An assessment of heterogeneity within the lithospheric mantle, Marie Byrd Land, West Antarctica

Author: Shaina Marie Cohen

Boston College Electronic Thesis or Dissertation, 2016

AN ASSESSMENT OF HETEROGENEITY WITHIN THE LITHOSPHERIC MANTLE, MARIE BYRD LAND, WEST ANTARCTICA

Shaina Marie Cohen

A thesis

submitted to the Faculty of

the Department of Earth and Environmental Sciences

in partial fulfillment

of the requirements for the degree of

Master of Science in Geology

Boston College

Morrissey College of Arts and Sciences

Graduate School

May 2016

AN ASSESSMENT OF HETEROGENEITY WITHIN THE LITHOSPHERIC MANTLE, MARIE BYRD LAND, WEST ANTARCTICA

Shaina M. Cohen

Advisor: Professor Seth Caley Kruckenberg, Ph.D.

The West Antarctic rift system is one of the most expansive regions of extended continental crust on Earth, but relatively little is known about the structure of the mantle lithosphere in this region. This research aims to examine a suite of ultramafic mantle xenoliths from several volcanic centers located throughout Marie Byrd Land, West Antarctica. Through the use of several complementary analytical methods, the deformational and compositional heterogeneity of the lithospheric mantle in this region is characterized.

The Marie Byrd Land xenoliths have equilibration temperatures between 779 and 1198°C, which is a range that corresponds to extraction depths between 39 and 72 km. These samples preserve significant mineralogical and microstructural heterogeneities that document both lateral and vertical heterogeneities within the Marie Byrd Land mantle lithosphere. The modal mineralogy of spinel peridotites varies between 40 – 99% olivine, 0 – 42% diopside, 0 – 45% enstatite and 0 – 5% chromite. Minimum olivine grain sizes range from 60 to 110 µm and maximum olivine grain sizes range from 2.5 to 10.0 mm. The geometric mean grain size of olivine in these samples ranges from 100 µm to 2 mm and has an average of 694 µm. The geometric mean grain size of diopside ranges from 90 to 865 µm and has an average of 325 µm, whereas that of enstatite ranges from 120 µm to 1.2 mm and has an average of 625 µm. Comparatively, the pyroxenites contain 0 – 29% olivine, 29 – 95% diopside, 1 – 36% enstatite and 1 – 11% chromite.

Deformation mechanism maps suggest that the olivine within the MBL peridotite xenoliths primarily accommodate strain through the operation of dislocation-accommodated grain-

boundary sliding at strain rates between 10^{-19}/s and 10^{-11}/s. This is consistent with microstructural observations of the suite made using optical microscopy (e.g., deformation bands and subgrains in olivine; aligned grain boundaries between contrasting phases). Application of the olivine grain size piezometer indicates that the suite preserves differential stresses ranging from 0.5 MPa to 50 MPa, with mean differential stresses ranging from 4 to 30 MPa. Values of mean differential stress only vary slightly throughout the field area, but generally decrease in magnitude towards the east with maximum values migrating upwards in the lithospheric mantle along this transect. The samples from some volcanic centers are highly homogenous with respect to their microstructural characteristics (e.g., Mount Avers – Bird Bluff), whereas others display heterogeneities on the sub-five-kilometer-scale (e.g., Demas Bluff). Comparatively, mineralogical heterogeneities are more consistent throughout the sample suite with variations generally being observed between the sub-five-kilometer-scale and the sub-ten-kilometer-scale.

Most samples within the MBL peridotite suite display axial-[010] or A-type olivine textures. Although less dominant, axial-[100], B-type and random olivine textures are also documented within the suite. Axial-[010] textures have J-indices and M-indices ranging from 1.7 – 4.1 and 0.08 – 0.21, respectively. The average value of the J-index for axial-[010] textures is 2.9, whereas the average M-index of these samples is equal to 0.15. Overall, A-type textures tend to be stronger with J- and M-indices ranging from 1.4 – 9.0 and 0.07 – 0.37, respectively. The olivine crystallographic textures of the MBL xenolith suite are heterogeneous on scales that are smaller than the highest resolution that is attainable using contemporary geophysical methods, which implies that patterns of mantle flow and deformation are far more complex than these studies suggest.

TABLE OF CONTENTS

LIST OF TABLES

LIST OF FIGURES

LIST OF APPENDICES

TABLE OF ABBREVIATIONS

Abbreviation	Meaning
1ppg	One-point-per grain
AD	Mount Aldaz, Usas Escarpment
AV	Mount Avers, Fosdick Mountains
AVBB	Mount Avers – Bird Bluff, Fosdick Mountains
BB	Bird Bluff, Fosdick Mountains
BC	Band contrast
BSE	Backscattered electron
ch	Chromite
CPO	Crystallographic preferred orientation
cpx	Clinopyroxene
DB	Demas Bluff, Fosdick Mountains
di	Diopside
disGBS	Dislocation-accommodated grain boundary sliding
DMM	Deformation mechanism map
EAC	East Antarctica craton
EBSD	Electron backscatter diffraction
en	Enstatite
EMPA	Electron microprobe analysis
FDM	Fosdick Mountains
fo	Forsterite
FTIR	Fourier transform infrared
KSP	Mount Cumming, Executive Committee Range
LAM	Large area map
Ma	Million years ago
MAD	Mean angular deviation
MBL	Marie Byrd Land
MJ	Marujupu Peak, Fosdick Mountains
ODF	Orientation distribution function
ol	Olivine
opx	Orthopyroxene
P	Pressure (kbar; MPa)
px	Pyroxene
RODF	Rotated orientation distribution function
RN	Recess Nunatak, Fosdick Mountains
SEM	Scanning electron microscope
SPO	Shape preferred orientation
T	Temperature (°C)
WARS	West Antarctic rift system
XRCT	X-ray computed tomography

ACKNOWLEDGMENTS

I would like to express my deepest gratitude to my advisor, Professor Seth C. Kruckenberg for the unwavering support, encouragement, and guidance he provided throughout my graduate studies. Early on, while working with Professor Kruckenberg, I was fortunate to attend a scanning electron microscope training course in Cranberry Township, PA offered by TESCAN – the company that manufactures the scanning electron microscope housed in Professor Kruckenberg's lab within the Department of Earth and Environmental Sciences at Boston College. As a result, I quickly gained expertise in the advanced operation of scanning electron microscopes, which ultimately expedited data collection for this research. Additionally, Professor Kruckenberg urged me to attend EBSD 2014 – a biannual electron backscatter diffraction (EBSD) conference in Pittsburgh, PA during June of 2014. Although I did not present my research at this conference, this was another incredibly valuable experience to attend a multitude of workshops and presentations that helped me understand the vast amount of meaningful information offered by electron backscatter diffraction analysis. During this time I was also fortunate enough to network with a number of reputable scientists within the EBSD community and discuss their research, which further broadened my understanding of the many applications of this powerful analytical method. Professor Kruckenberg has helped me grow immensely – as both a scientist and an individual – during the time I have spent as a part of the Department of Earth and Environmental Sciences at Boston College. In many ways, he has helped me to understand what I am capable of and fostered a deep sense of self-pride for all that I have accomplished. I am eternally grateful for the opportunity to work closely with someone who is both a remarkable researcher and a truly good-hearted person.

Secondly, I would like to extend thanks to Dr. Vasileios Chatzaras for his innumerable contributions to this thesis since I began working with Professor Kruckenberg. In addition to providing me with valuable data sets that were imperative to attaining my research goals (Sections 2.1 and 2.2), Dr. Chatzaras consistently provided insightful feedback on drafts of both my thesis proposal and my thesis in a timely manner. His input throughout this process has been indispensable because it has improved my understanding of the broader impacts associated with my research and allowed me to view this project from a different perspective. I am truly honored to be a contributing co-author on a manuscript recently submitted to the Journal of Geophysical Research (Appendix A). I look forward to collaborating with him again in the future when the content of this thesis becomes its own manuscript, which will also be submitted to an academic journal. At this point, it is also important for to acknowledge the immense contributions of the other co-authors listed on the manuscript submitted by Dr. Chatzaras: Professor L. Gordon Medaris Jr. (UW – Madison) for his vast knowledge of geothermobarometry, Professor Anthony C. Withers (University of Western Ontario) for the determination of volatile contents, and Dr. Brian Bagley (UMN – Twin Cities) for his assistance in using X-ray computed tomography to quantify the fabric ellipsoids preserved by the xenolith samples, which directly allowed for the production of thin sections that are successfully reoriented into their fabric frame of reference. The collective knowledge and expertise possessed by these gentlemen has been absolutely critical to understanding the conditions of the deformational environment(s) from which the Marie Byrd Land xenoliths were sourced.

I would also like to thank the other members of both my proposal committee and my thesis committee: Professor John Ebel, Professor J. Chris Hepburn, and Professor Ethan Baxter. As a seismologist, Professor Ebel provided critical insight from a geophysical perspective during my

oral examination. Due to the fact that his field of expertise is slightly outside of what I am most familiar with, many of the questions he asked during this time were incredibly thought-provoking and opened my eyes to how a geophysicist understands large-scale geodynamic processes for the first time, which was a rewarding experience that I look back upon fondly. Professor Hepburn is a metamorphic petrologist who was also an active member of my proposal committee. He met with me several times prior to my oral examination so we could have meaningful discussions regarding my research and how I could glean potential tectonic implications from my studies. In addition to this, Professor Hepburn helped me fulfill my duties as a teaching assistant for the undergraduate Petrology course at Boston College by helping me organize a field trip and offering to give a guest lecture to the class. Although these contributions are not directly related to my research, his generous acts were incredibly inspiring because they are something he did out of the kindness of his heart and his deeply-rooted passion for teaching geology. I will always remain thankful for all that he has done for the Department of Earth and Environmental Sciences. My first experience with Professor Baxter was as a student in his Isotope Geochemistry and Geochronology course that was offered at Boston University. At this time I didn't know that he would eventually become a member of my thesis committee, but I was immediately impressed by his teaching abilities and his enthusiasm for the course material. Although Professor Baxter is the most recent addition to my thesis committee, I am incredibly thankful that he has made time in his busy schedule to discuss my research and has provided me with insight that has helped clarify the final version of this thesis during the revision process. These professors have collectively helped me become a better analytical thinker and have shown me the immense power of truly loving what you do, which in turn has helped me stay focused on my long-term goal of obtaining a doctorate in geology and becoming a professor. For these reasons, I am eternally grateful for their contributions to this thesis and my academic career as a whole.

Special thanks are extended to: Brian Hess (UW – Madison) for his unrivaled expertise in preparing and polishing high-quality geological thin sections for EBSD analyses; Zach Michels (UW – Madison) for sharing his comprehensive knowledge of the MTEX textural analysis toolbox with me during one of his visits to Boston College; Dr. Lars Hansen (University of Oxford) for allowing me to use his MATLAB-based graphical user inference that is capable of quickly generating deformation mechanism maps based on the user-defined conditions of deformation and chosen flow law parameters; the U.S. Polar Rock Repository, Professor Kurt Panter (Bowling Green State University), and Professor Christine Siddoway (Colorado College) for providing the xenolith samples to Professor Kruckenberg for analysis; and all other members of the NSF-funded field expeditions to Marie Byrd Land for their contributions to sample acquisition.

In addition to all of the aforementioned individuals who have deeply impacted how my academic life has progressed, there are numerous people in my personal life that I must express immense gratitude towards because they have loved and supported me unconditionally while I have feverishly worked towards receiving my Master's degree in Geology. Admittedly, there have been numerous points along this journey that my academic priorities have taken precedence over my obligations to my family and close friends. Although I have become painfully aware of how this has negatively affected the people I love, I am truly blessed because they have never once turned their backs on me. In fact, they have done the exact opposite by encouraging me to persevere despite my struggles, reminding me of the immense internal strength I possess, and emphasizing that all of my hard work will eventually pay off. Although it is a small consolation for what these individuals have endured on my behalf, I would like to explicitly thank the following individuals: my mother, Linda Cohen, for always pushing me to be better than who I was yesterday; my father, Howard Cohen, for reminding me to take a deep breath when I am

overwhelmed and to take comfort in the many aspects of my life I have control over; my step-mother, Laurie Cohen, for her inspirational bravery and strength in the face of adversity as she goes through an aggressive treatment plan designed to battle a rare form of liver cancer; my boyfriend, Zachary Currier, for being able to see past the negative influences in my life and loving me for who I truly am despite them; my best friend, Michaela Zullo, for always understanding what I am going through, providing me with a judgment-free environment in which I am able to openly voice my opinions, and becoming the sister I never thought I would have; the other graduate students within my research group, Martha Parsons and Will Montz, for all of the ups and downs we have experienced by spending the past three years together; and all of the brilliant students that I have had the pleasure of interacting with as a teaching assistant for allowing me to learn so much about myself simply by sharing my passion for geology with your eager minds. I am eternally grateful for everything that you have done and I am incredibly proud of the person you have all collectively helped me become.

This research received funding from two primary sources: a National Science Foundation Antarctic Earth Sciences grant awarded to Professor Kruckenberg in January of 2013 (NSF-ANT 1246320), and a Graduate Student Research grant awarded to the author by the Geological Society of America in May of 2014. Two years of summer funding provided by the Department of Earth and Environmental Studies were also of paramount importance during my graduate studies; without these funds I would have had to obtain another job, which would have distracted me from my academic responsibilities and delayed the submission of this thesis.

PREFACE TO THE THESIS

The intent of this thesis is to assess the deformational and compositional heterogeneities preserved by a suite of young (ca. 1.4 Ma), chromite-bearing mantle xenoliths from Marie Byrd Land (MBL), West Antarctica. This is primarily accomplished through the acquisition and interpretation of electron-backscatter diffraction (EBSD) data, which allows for the crystallographic textures (i.e. crystallographic preferred orientations, CPOs) and mineralogical phases within the thin sections produced from the MBL xenoliths to be mapped and quantified (Section 2.4). Additional microstructural analyses are completed using optical and electron microscopy (Section 2.3). The research contained herein, which relies heavily on the EBSD data, has also been contributed to a co-authored manuscript submitted to the Journal of Geophysical Research (Chatzaras et al., in revision) and is therefore complementary. The entirety of the Chatzaras et al. (in revision) manuscript is Appendix A of this thesis.

Chatzaras et al. (in revision) evaluate the effects of finite strain and fabric ellipsoid geometries on the development of crystallographic texture, whereas this thesis assesses the extent to which the lithospheric mantle beneath MBL is a heterogeneous body. The former research applies both high-resolution X-ray computed tomography (XRCT) and well-established geothermometers in order to place the xenolith samples into their deformational frame of reference and to quantify their equilibration temperatures (Sections 2.1 and 2.2). Chatzaras et al. (in revision) also determine the extraction depths for the MBL xenolith suite by constructing a geotherm for the region at the time of eruption that accounts for the ubiquitous presence of spinel (Section 2.2).

This complementary manuscript is imperative for assessing the heterogeneity within the lithospheric mantle of MBL (i.e. the purpose of this thesis) for two reasons: 1) the assessment of the spinel shape-preferred orientation (SPO) using XRCT allows for the production of oriented thin sections oriented with respect to the strain induced fabric (i.e. parallel to lineation and perpendicular to foliation), which are subsequently evaluated using polarized light microscopy, electron microscopy and EBSD (Sections 2.3 and 2.4), and 2) the quantification of equilibration temperatures and extraction depths allows for a three-dimensional characterization of mantle properties based on the distribution of xenolith samples throughout MBL.

Likewise, the EBSD data collected as part of the research and described herein is imperative for characterizing the full range of CPOs preserved by the MBL xenolith suite (Section 2.4). These CPO data were critical to arriving at the conclusions presented in Chatzaras et al. (in revision). Furthermore, the results and conclusions surrounding the assessment of mantle heterogeneity beneath MBL are the subject of a co-authored manuscript that is currently in preparation.

1 INTRODUCTION TO THE THESIS

1.1 AIM OF THESIS

The purpose of this research is to investigate a diverse suite of recently exhumed (ca. 1.4 Ma) ultramafic xenoliths sourced from several volcanic centers throughout Marie Byrd Land (MBL), West Antarctica in order to characterize the deformational and compositional heterogeneity of the lithospheric mantle in an actively-deforming region that has a protracted tectonic history (e.g., Siddoway, 2008). In turn, this investigation will inform on the scales of anisotropic mantle textures observed in geophysical studies of MBL. Furthermore, all assessments of naturally deformed mantle xenoliths are of great importance because they allow for direct comparisons to be drawn between the true conditions of deformation that control the generation of microstructures in a natural setting and the results of experimental deformation studies that aim to quantify the deformational conditions (e.g., water fugacity) that are thought to be responsible for the existence of various known patterns of olivine crystallographic texture (e.g., Karato et al., 2008, and references contained therein). The research objectives are addressed using results obtained by a variety of complementary methods, including:

1. Optical microscopy is used to perform microstructural analyses of thin sections. Microstructural observations are used to infer the dominant deformation mechanism(s) operating within each xenolith sample based on the documented relationships that exist both between constituent mineral phases (i.e. forsterite, enstatite, diopside and chromite) and within individual mineral grains (e.g., the existence of dislocation walls). Microstructural analyses also allow for a

qualitative assessment of the structural and compositional heterogeneity that exists throughout the sample suite.

2. Electron backscatter diffraction (EBSD) is a scanning electron microscope (SEM) based method that is used to quantify the crystallographic orientation and phase identity of the mineral grains that constitute a sample. These data are subsequently used to identify the crystallographic texture (i.e. crystallographic preferred orientation, CPO), textural strength, grain size distribution and relative abundance of each phase present in a sample. It must be brought to the attention of the reader that there is an important distinction made between the terms texture and fabric as they are discussed within the confines of this thesis. Specifically, texture refers to the crystallographic orientation of constituent mineral grains, whereas fabric describes their shape preferred orientation (SPO).
3. Deformation mechanism maps (DMMs) are constructed and used in conjunction with the recrystallized olivine grain size piezometer (Karato et al., 1980; Van der Wal et al., 1993). The EBSD-determined grain sizes are subsequently used to infer the dominant deformation mechanisms that operated to accommodate strain in the sample, and to estimate the magnitude of differential stress it experienced prior to its entrainment and exhumation to Earth's surface.

1.2 Deformation in Earth's mantle

1.2.1 Characteristic properties of mantle lithologies

The lithospheric mantle is comprised of ultramafic tectonites (i.e. peridotites and pyroxenites) that accommodate strain through the operation of ductile deformation mechanisms (i.e. dislocation creep and/or diffusion creep ± grain-boundary sliding). Peridotite – the dominant lithology of the Earth's upper mantle above the transition zone (ca. 410 km; the depth at which olivine undergoes a phase transformation into wadsleyite) – is defined as a coarse-grained ultramafic rock containing at least 40% modal olivine commonly occurring with lesser amounts of clinopyroxene and/or orthopyroxene. Based on the relative proportions of these constituent minerals, peridotites are further classified as dunitic (>90% olivine), harzburgitic (<5% clinopyroxene), wehrlitic (<5% orthopyroxene), or lherzolitic (>5% both ortho- and clinopyroxene). Comparatively, pyroxenites contain less than 40% modal olivine by definition. These rocks are further classified as websterites, orthopyroxenites and clinopyroxenites (Le Maitre, 2002). The rocks of the upper mantle also contain a minor mineral phase (i.e. plagioclase feldspar, spinel or garnet), the presence of which is controlled by pressure-sensitive subsolidus metamorphic reactions (e.g., Winter, 2010).

1.2.2 Methods of assessing mantle rheology

As the most abundant and weakest mineral of the upper mantle, olivine exerts critical control over the rheology of the lithosphere (i.e. the quantitative response of such mantle rocks to the stress imposed by Earth's internal driving forces). Several complementary approaches are commonly used to assess mantle rheology, including geophysical methods, experimental studies of olivine aggregates and field studies of naturally deformed mantle materials (i.e. ophiolite belts, alpine peridotite massifs and mantle xenoliths). There are limitations inherent to each of these approaches for understanding mantle deformation that can only be overcome through the comparison and integration of their results.

The characteristic anisotropy that defines the upper mantle – macroscopically observable using contemporary geophysical methods (e.g., shear wave splitting) – is commonly interpreted to result from the generation of CPO in olivine, which is thought to develop as olivine aligns with the direction of viscoplastic mantle flow. Consequently, such reports of anisotropy are used to infer the kinematics of global mantle flow patterns and to elucidate information regarding active tectonic processes (e.g., Nicolas and Christensen, 1987; Mainprice, 2007; Bodmer et al., 2015). Despite the importance of such geophysically-derived information, these methods provide a low-resolution snapshot of mantle structure that cannot inform on the complexities of mantle flow at the scales of heterogeneity observed in exhumed mantle sections (e.g., Warren et al., 2008; Toy et al., 2010; Kruckenberg et al., 2013; Skemer et al., 2013).

Comparatively, experimental rock deformation studies constrain the rheology and microstructural (i.e. grain scale) response of the upper mantle by examining the patterns of olivine crystallographic texture that form in response to variations in important deformational parameters including, but not limited to: absolute temperature (T), confining pressure (P), differential stress (σ), strain rate ($\dot{\varepsilon}$), modal mineralogy, grain size (d), melt fraction (ϕ), and water fugacity (fH_2O). Based on the observed power law dependence of strain rate on differential stress, the rheology of olivine-rich lithologies is quantified (Brace and Kohlstedt, 1980; Kohlstedt et al., 1995; Hirth and Kohlstedt, 2003) using a flow law of the form:

$$\dot{\varepsilon} = A\sigma^n d^{-p} fH_2O^r \exp(\alpha\phi) \exp\left(-\frac{E^* + PV^*}{RT}\right) \qquad \text{(Equation 1)}$$

where A is a the material constant for olivine, n is the stress exponent, p is the grain size dependency exponent, r is the water fugacity exponent, α is the melt fraction constant, E* is the activation energy, V* is the activation volume, and R is the ideal gas constant. The values for A, n, p, r and α have mostly been empirically derived through experimental rock deformation studies and it has been determined that their magnitudes are dependent on the operative deformation mechanism(s) within a sample (e.g., Hirth, 2002; Hirth and Kohlstedt, 2003; Hansen et al., 2011). Although experimental studies are imperative for the parameterization of mantle rheology, there is a significant difference between the rates observed in natural and experimental systems, which requires the extrapolation of data. Furthermore, it should be recognized that natural rock samples are almost always multiphase systems that exhibit significant variations with respect to the distribution of the constituent phases and their relative grain sizes, which is a variable that has yet to be thoroughly explored through experimental studies.

The discrepancy between natural and experimental rates places heightened importance on the complementary information provided by field-based studies of exhumed mantle rocks. Although such samples are relatively rare, they provide invaluable information in the form of preserved microstructural features formed in a natural setting, which can be interpreted to understand the deformational processes behind their generation. Such field studies increasingly document that the lithospheric mantle is structurally and compositionally heterogeneous across a wide range of spatiotemporal scales (e.g., Warren et al., 2008; Skemer et al., 2010; Webber et al., 2010; Newman et al., 2011; Chatzaras et al., 2015). These studies also emphasize the role of heterogeneities on strain localization mechanisms in the upper mantle, which affect lithospheric strength and have implications for tectonic processes. Unlike ophiolites and alpine peridotites, which commonly experience tectonic overprinting during obduction or exhumation, mantle xenoliths in actively deforming regions preserve primary microstructures developed under deformation conditions characteristic of the lithospheric mantle. Their rapid ascent minimizes modification of crystallographic textures and/or mineral chemistries, thus preserving information about the mantle conditions from which they were extracted. This offers the unique opportunity to assess the deformation conditions within the upper mantle and the resultant crystallographic textures that form in response to changes in conditions or during strain localization. Xenolith samples are also advantageous in the sense that they inform on the spatial scales of mantle heterogeneity owing to the simple fact that they are derived from different depths and source regions. Together with insights gained from other methods, analyses of xenolith samples can be used to constrain variations in mantle rheology in tectonically active portions of the lithosphere (e.g., Behr and Hirth, 2014, Chatzaras et al., 2015), as is outlined in the subsequent methodology (Chapter 2).

1.2.3 Olivine deformation mechanisms and associated microstructures

During high-temperature ductile mantle flow, mineral grains change shape while maintaining cohesion at the grain scale. At the grain scale, intracrystalline deformation mechanisms accommodate strain by effectively altering the shape of mineral grains. Specifically, olivine-rich rocks in the mantle are known to deform by dislocation creep (i.e. the movement of linear defects in the lattice) or by grain boundary sliding (GBS), with the latter being accommodated either by diffusion (i.e. diffusion creep) or the movement of dislocations in adjacent grains, which is known as dislocation-accommodated grain boundary sliding (disGBS) (e.g., Hirth and Kohlstedt, 2003; Toy et al., 2010; Hansen et al., 2012). The activation of different deformation mechanisms is associated with the formation of distinct rock microstructures and crystallographic textures. These microstructures can be quantified using a combination of microstructural analysis and electron backscatter diffraction, which elucidates information concerning the mechanics of the deformational processes operating within the upper mantle, and therefore its rheology (e.g., Hirth, 2002; Hirth and Kohlstedt, 2003).

Dislocation creep – inferred to be the dominant deformation mechanism in the uppermost (ca. 250 km) of the mantle – results in a strong crystallographic texture as the axes of constituent mineral grains develop a non-random distribution, referred to as a crystallographic preferred orientation (CPO). During this process, dislocations within the crystal lattice migrate along slip systems that are defined by movement (i.e. slip) along a specific crystallographic plane and direction. The most energetically favorable (i.e. easiest) slip system dominates the CPO; activation of each slip system is highly dependent on the critical resolved shear stress experienced by the rock (Durham and Goetze, 1977; Bai et al., 1991; Passchier and Trouw, 2005; Karato et al., 2008).

The results of early deformation experiments on olivine-rich rocks conclude that the [100] axis is the easiest slip direction in olivine, but the preferred slip plane changes from being diffuse throughout the {0kl} family of planes to being concentrated along the (010) plane due to the effects of increasing temperature and decreasing strain rate (Carter and Avé Lallemant, 1970). Studies of olivine CPOs further document the presence of (010)[100] (i.e. A-type), axial-[100] (i.e. {0kl}[100] or D-type), and axial-[010] (i.e. {0kl}[010] or AG-type) olivine textures, and expect A-type textures to dominate the upper mantle (Ben Ismaïl and Mainprice, 1998).

Experimental deformation studies performed on olivine single crystals have identified the existence of additional olivine CPO textures that are dependent on variations in water content, pressure and stress (e.g., Jung and Karato, 2001; Couvy et al., 2004; Katayama et al., 2004; Jung et al., 2006; Mainprice, 2007; Ratteron et al., 2007; Karato et al., 2008, and references therein; Figure 1.1). Dominant slip in the [100] direction is also observed in E-type olivine CPO patterns, which are distinguished from A-type, axial-[100], and axial-[010] textures by slip on the (001) plane. At higher water contents, experimental results document the dominant slip changing from the [100] direction to the [001] direction. Such textures are either B- or C-type and are defined by slip occurring on the (010) and (100) planes, respectively. Field-studies of naturally deformed peridotites conclude that B-type olivine textures may form: 1) as a function of variations in water content (Mizukami et al., 2004), 2) due to the operation of disGBS (Précigout and Hirth, 2014), or 3) at elevated pressures (>3 GPa; Jung et al.,

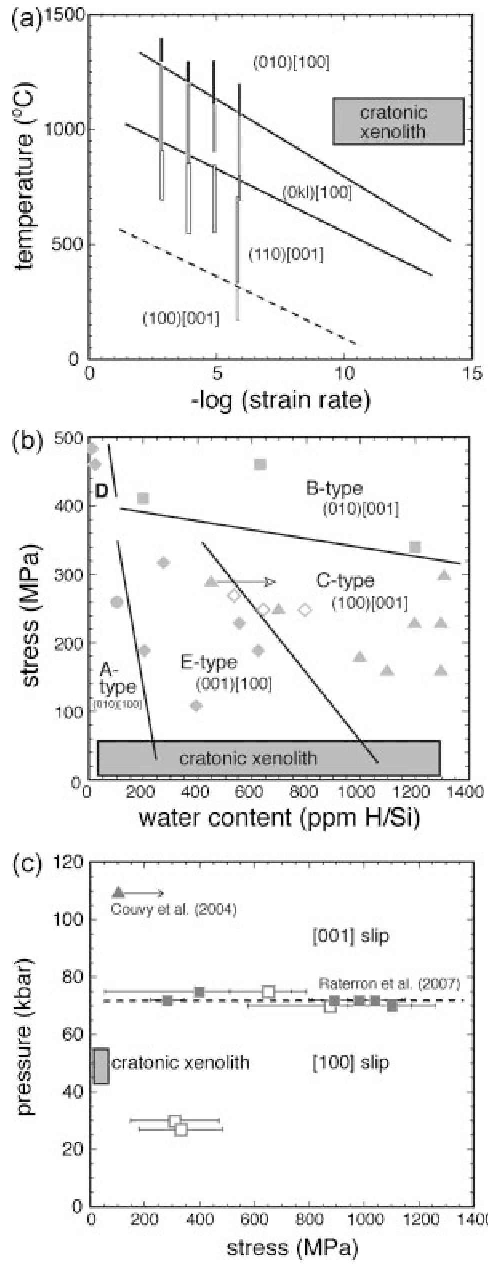

Figure 1.1. Results from experimental rock deformation studies show that there are three mechanisms capable of influencing the activity of various slip systems in olivine: (a) Temperature and strain rate (Carter and Avé Lallemant, 1970), (b) Water content (Jung and Karato, 2001), and (c) Pressure (Couvy et al., 2004; Ratteron et al., 2007). Image source: Katayama et al. (2011). Gray boxes are representative of the mantle xenoliths that formed the basis of their study.

2009; Couvy et al., 2009). Although generally thought to form exclusively in dry, high stress deformational environments, the development of axial-[100] textures has been documented in wet olivine (Demouchy et al., 2012) and related to the operation of disGBS (Warren et al., 2008). The axial-[010] pattern, which has been recognized in naturally deformed peridotites and numerical simulation studies, is characterized by sharp [100] and diffuse [001] girdles (Tommasi et al., 2000; Mainprice, 2007). This texture is thought to be transitional between A- and B-type textures and has been attributed to the flattening deformation in axial compression experiments (Avé Lallemant and Carter, 1970; Nicolas et al., 1973; Hansen et al., 2011). Furthermore, it has also been suggested that the existence of axial-[010] and B-type textures may be the direct result of deformation in the presence of melt (Holtzman et al., 2003).

The weakening of CPO in naturally deformed peridotites has been attributed to the process of grain-size sensitive diffusion creep (e.g., Hirth and Kohlstedt, 2003; Warren and Hirth, 2006; Falus et al., 2011; Précigout and Hirth, 2014), although experimental research shows this deformation mechanism is also capable of producing olivine CPO (Mainprice et al., 2005; Sundberg and Cooper, 2008; Miyazaki et al., 2013). The CPO texture of a rock undergoes complex transitions in response to variations in the conditions of deformation, and is therefore an important microstructural parameter for understanding the relationships between the kinematics of deformation, the observed patterns of anisotropy, and variations in intracrystalline deformation mechanisms within in the upper mantle (e.g., Nicolas and Christensen, 1987; Mainprice, 2007; Karato et al., 2008).

Despite the importance of relating olivine textures back to their deformation conditions, it is important to note that these relationships are not explicit. In addition to the examples provided above, there is a significant amount of literature that documents known olivine textures forming under deformation conditions that deviate from what is expected based on the results of the aforementioned studies (Karato et al., 2008, and references contained therein). Although a complete discussion of such variation is too extensive to cover within the confines of this thesis, the reader is encouraged to remember that the development of olivine texture is a poly-parametric issue. Thus, there is no clear-cut relationship that exists between any singular deformation condition and a specific olivine texture.

1.3 A brief geologic history of Marie Byrd Land, West Antarctica

1.3.1 An overview of present-day Antarctica

The Transantarctic Mountains extend across the continent of Antarctica and structurally separate its two distinct tectonic provinces: the East Antarctic craton (EAC) and the West Antarctic rift system (WARS), which is one of the most extensive regions of extended continental crust in the world (Figure 1.2). Despite the size of the WARS, the behavior of Antarctic lithosphere is poorly understood due to its extensive cover by ice sheets, which severely limits exposures of the crust. As a result, most of what is known about the rheology and structure of lithosphere in this area is quantified indirectly through geophysical methods (e.g., Behrendt et al., 1991, Ritzwoller et al., 2001).

Based on measurements of surface wave dispersion, Ritzwoller et al. (2001) present a model of the Antarctic lithosphere and estimate crustal thicknesses to be ca. 27 km in the thinned continental crust of the WARS and in excess of ca. 40 km in the stable EAC. Furthermore, the researchers determine that most of the WARS mantle is seismically slow, which is directly related to the presence of an asthenospheric anomaly at a depth of ca. 120

km. The thicker and rheologically stronger EAC is thought to have remained a cohesive crustal block since the fragmentation of Rodinia during the Neoproterozoic (Mukasa and Dalziel, 2000). The thin lithosphere comprising the WARS is significantly weaker and is structurally subdivided into five distinct microplates that have experienced multiple episodes of intracontinental deformation that are associated with dramatic WARS extension: the Antarctic Peninsula, Haag Nunataks, the Ellsworth-Whitmore Mountains, Thurston Island, and Marie Byrd Land (Siddoway, 2008; Harley et al., 2013). Of these crustal blocks, Marie Byrd Land (MBL) is the largest and is of great interest because it cradles portions of the West Antarctic Ice Sheet and because it is a tectonically active region that has been experiencing anomalous volcanism since ca. 30 Ma (Gaffney and Siddoway, 2007).

1.3.2 Tectonic overview

During Cambrian times, a subduction zone began to nucleate along the long-lived passive paleo-Pacific margin of Gondwana. This convergent boundary persisted until rifting began to fragment the supercontinent during the Jurassic. During this extended period of geologic time, the allochthonous tectonic blocks that comprise the present day WARS were sutured onto the Gondwanan margin along the evolving Transantarctic Mountains (Elliot, 2013). During the late Jurassic, East and West Gondwana began to break apart – an event that coincides with the initiation of WARS extension. The most rapid extension occurred during the Cretaceous (ca. 105-90 Ma), which dramatically thinned the West Antarctic crust as the Ross Sea opened away from the rheologically strong boundary of the EAC (e.g., LeMasurier, 2008). The final stage of rifting across Gondwana occurred when MBL was separated from the microcontinents of present-day New Zealand via sea-floor spreading at the newly formed Pacific-Antarctic ridge. This tectonic event is constrained by Chron 34 (84

Ma; Weaver et al., 1994) and is considered to be distinct from earlier stages of WARS extension because MBL and New Zealand rifted apart along high-angle faults, whereas all prior extension occurred orthogonal to the frontal scarp of the Transantarctic Mountains (Siddoway, 2008). The unexpected rift orientation and the rapid extension between MBL and its conjugate margin has been explained by both mantle plume activity (Weaver at al., 1994; Storey et al., 1999) and the subduction of the Phoenix-Pacific ridge (Mukasa and Dalziel, 2000; Finn, 2005).

Although minimal extension has occurred since the middle Cenozoic, increased regional heat flow is responsible for the anomalous volcanic activity that characterizes MBL (Lawver and Gahagan, 1994; Winberry and Anandakrishnan, 2004). The region of Cenozoic volcanism extends for ca. 1000 km through MBL and is defined by basaltic shield volcanoes and adjacent basanitic scoria cones (Gaffney and Siddoway, 2007). Some of the magmas produced at these volcanic centers have entrained and rapidly transported portions of the actively deforming lithospheric mantle beneath MBL to Earth's surface to be preserved as mantle xenoliths (Handler et al., 2003). These xenoliths, which are the basis of this research, represent access to naturally deformed peridotites that can be used to quantify the extent of heterogeneity within the lithospheric mantle of MBL and understand its rheology.

1.3.3 Marie Byrd Land xenoliths

The suite of ultramafic xenoliths that are the focus of this study are sourced from young Cenozoic volcanic flows (ca. 1.4 Ma) that are exposed within the Fosdick Mountains, the Usas Escarpment and the Executive Committee Range of MBL (Figure 1.2). Geochemical analyses of the alkaline basalts that host the ultramafic xenoliths show that the composition of the magma is heterogeneous between the volcanic centers, but remains relatively homogeneous within each individual volcanic center. This is interpreted to mean that distinct mantle sources are feeding the different volcanic centers found in MBL (Gaffney and Siddoway, 2007).

The xenolith samples comprising this suite have been previously characterized in a complementary study that uses electron microprobe analysis, high resolution X-ray computed tomography and electron backscatter diffraction to characterize the range of equilibration temperatures, fabric geometries and crystallographic textures displayed by the suite (Appendix A; Chatzaras et al., in revision). These xenoliths display substantial compositional and textural heterogeneities between and within individual volcanic centers. In combination with their vertical distribution, this makes them incredibly useful for performing a thorough assessment of heterogeneity and rheological structure of the lithospheric mantle beneath MBL.

1.3.3.1 Implications for ice sheet dynamics

The West Antarctic Ice Sheet is unique among the continental ice sheets of the world as it is the only marine-based continental ice sheet remaining. This simply means that the WAIS has a grounding line that is below sea level. It has long been hypothesized that marine-based ice sheets are inherently unstable and sensitive to anthropogenic climate warming (Mercer, 1978; Vaughn, 2008); ongoing subglacial volcanism associated with elevated heat flow poses a significant threat as it could potentially expedite deglaciation in West Antarctica via basal warming and associated feedbacks.

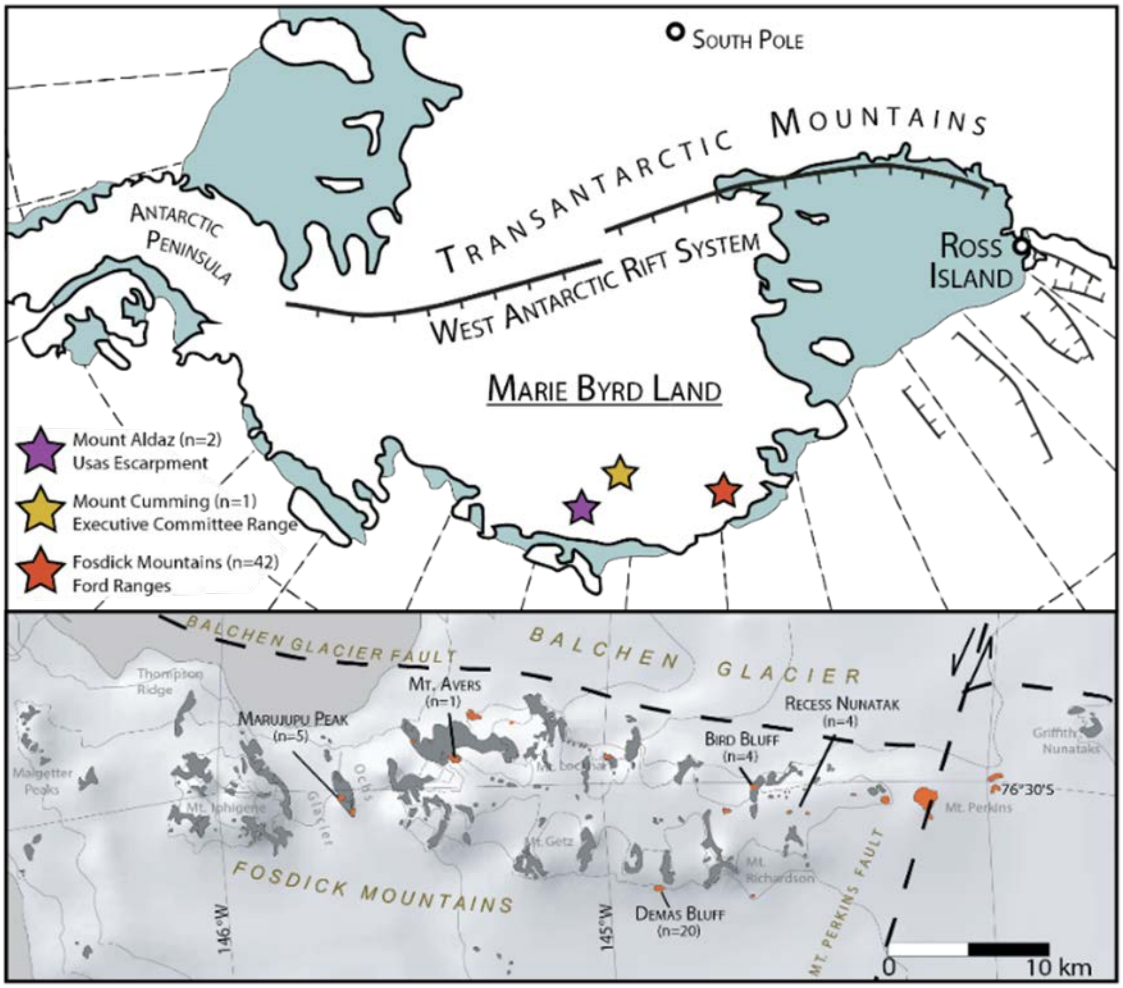

Figure 1.2. (Top) Map depicting the distribution and relative locations of the volcanic centers from which the ultramafic xenoliths are sourced. (Bottom) Enlarged view of the E-W trending Fosdick Mountains showing areas containing xenoliths in orange (modified from Gaffney and Siddoway, 2007). Not shown are eight samples that are sourced from volcanic centers between Mount Avers and Bird Bluff.

2 METHODOLOGY

2.1 SAMPLE ORIENTATION AND THIN SECTION PRODUCTION

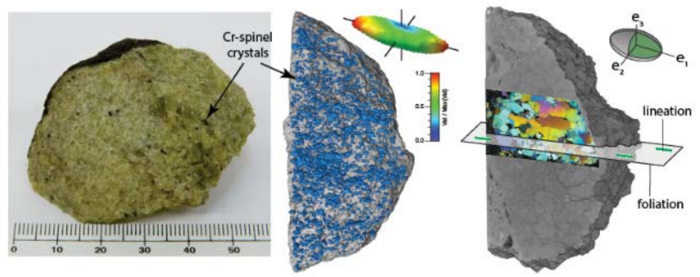

Figure 2.1. Spinel fabric (i.e. SPO) is quantified using XRCT and used to infer the orientation of the overall rock fabric (Image source: Chatzaras et al., in revision).

Studies of mantle xenoliths are complicated by the fact that samples are removed from their deformational frame of reference during their entrainment and rapid ascent to Earth's surface. This makes it nearly impossible to identify the lineation and/or foliation (i.e. the rock fabric) strictly from field-based observations, unless there is a deformed xenolith containing a visible fabric at the hand sample scale. In order to circumvent this problem, Chatzaras et al. (in revision; Appendix A) use high-resolution X-ray computed tomography to determine the three-dimensional fabric (i.e. shape preferred orientation, SPO) of constituent spinel grains. A fabric tensor is computed from the spinel SPO for each xenolith sample, which allows for the determination of the fabric geometry and degree of anisotropy (i.e. the fabric ellipsoid). Subsequently, rock billets are cut parallel to the XZ plane of the spinel SPO. This orientation is inferred to be representative of the overall rock fabric, which subsequently allows for the production of thin sections that have been reoriented into their fabric frame of reference (Figure 2.1). In turn, this allows for a meaningful interpretation of the crystallographic preferred orientation (CPO) of a sample with respect to its fabric geometry. It is important to note that Chatzaras et al. (in revision) use the crystallographic preferred orientation data from this study, which is acquired through the application of electron backscatter diffraction (EBSD) and subsequently processed using version 3.5 of the MTEX MATLAB toolbox (Bachmann et al., 2011; Appendix B).

2.2 ELECTRON MICROPROBE ANALYSES AND GEOTHERMOMETRY

Precise chemical compositions of mineral grains within the thin sections produced from each xenolith sample are determined by Chatzaras et al. (in revision) using the Cameca SX51 electron microprobe housed at the University of Wisconsin – Madison. The distribution of constituent elements between minerals is used to calculate the equilibration temperature using well-calibrated geothermometers (Figure 2.2). In almost all cases, an average of several two-pyroxene geothermometers are used to infer the equilibration temperature of the samples (i.e. Bertrand and Mercier, 1985; Brey and Kohler, 1990; Taylor, 1998). Due to the absence of pyroxene in the dunite from Mount Cumming (KSP89-181-X01), the olivine-spinel exchange geothermometers of O'Neill (1981) and Ballhaus et al. (1991) are applied. Based on the exclusive presence of spinel as the stable accessory phase, Chatzaras et al. (in revision) determine the depths from which the xenoliths are sourced by constructing a geotherm for the lithospheric mantle of Marie Byrd Land during the time period when mantle xenoliths were transported to the surface.

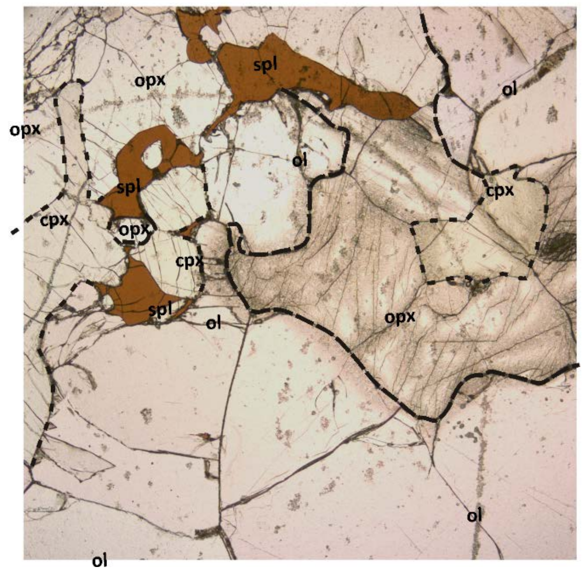

Figure 2.2. Photomicrograph showing the four constituent mineral phases analyzed for determination of the equilibration temperature. (Image source: Chatzaras et al., in revision).

2.3 OPTICAL AND ELECTRON MICROSCOPY

Although the vast majority of data is acquired through the application of electron backscatter diffraction (Section 2.4), the microstructures preserved by the MBL xenolith suite are also assessed through the application of less time-intensive methods (i.e. polarized light microscopy and backscattered electron imaging). Images of full thin sections are acquired using a Leica Z6 APO macroscope equipped with a SPOT Insight Firewire CCD camera, which allows for photomicrographs to be taken under both plane-polarized and cross-polarized light (Appendix C). Comparatively, all smaller-scale microstructures of interest (e.g., grain boundaries) are investigated and imaged using a Zeiss Axioskop 40 polarized light microscope, which is also fitted with a SPOT Insight Firewire CCD camera.

Backscattered electron (BSE) images of full thin sections are produced using the Tescan Vega 3 LMU scanning electron microscope that is housed within the Department of Earth and Environmental Sciences at Boston College. The Vega software is capable of stitching a multitude of BSE images into a panoramic view of an entire sample (Appendix C). It is important to note that all BSE images are grayscale because they effectively record the average atomic number (i.e. density) that the beam is being rastered across. As the electron beam strikes the polished sample surface, the electrons scatter elastically in response to the substrate they are coming into contact with. Atoms of heavier elements are larger and consequentially are more likely to produce elastic scattering of the beam. This allows a greater number of backscattered electrons to reach the detector, which in turn produces a bright region on the BSE map. Comparatively, regions containing lighter elements appear dark in BSE images. This is helpful because it allows for the user to quickly distinguish between the different constituent phases of a sample.

2.4 ELECTRON BACKSCATTER DIFFRACTION

Electron backscatter diffraction (EBSD) is a scanning electron microscope (SEM) based technique that is commonly used to quantify the crystallographic preferred orientation (CPO) of the mineral grains within a sample. The interaction of a stationary electron beam that is rastered across a tilted (70°) sample causes incident electrons to be inelastically scattered in all directions within the top few nanometers of a surface (i.e. the interaction volume). Backscattered electrons that satisfy the Bragg diffraction condition ($\sin\theta = n\lambda/2d$) diffract into a pair of cones around the respective diffracting crystallographic plane, which produces Kikuchi bands as they intersect an analytical detector phosphor screen. Collectively, the bands detected from all diffracting planes produce an electron backscatter diffraction pattern (EBSP). These EBSPs are then computationally solved for and indexed to known Miller indices as a function of the crystallographic lattice orientations of the mineral grain being analyzed (e.g., Prior et al., 1999; Maitland and Sitzman, 2007).

2.4.1 Data collection

The Department of Earth and Environmental Sciences at Boston College is equipped with a Tescan Vega 3 LMU scanning electron microscope with an Oxford Instruments NordlysMax2 EBSD detector capable of rapid determination of crystallographic textures and phase identification. In order to prevent electron charging during analysis, a thin (ca. 6 nm) carbon coat is applied to each sample using a Quorum/EMS 150TE high vacuum coating system prior to EBSD orientation and phase mapping. EBSD analyses are conducted under high vacuum conditions in the SEM, with 20-30 kV of accelerating voltage and beam current ranging between 20 and 40 nA. Electron backscatter patterns are indexed using 2x2 camera binning, a Hough resolution of 100 and a fixed step size of 7.5 µm. All four phases present within the suite (i.e. forsterite, enstatite, diopside, and chromite) are mapped.

Large area maps (LAMs) are constructed for each thin section. Each large area map contains approximately 1300-1500 smaller orientation maps (750µm × 750µm) that are montaged into a cohesive dataset using Oxford's AZtecHKL software (version 3.0 SP1). A 20% overlap is assigned between adjacent fields as this value optimizes the ability of Oxford's AZtecHKL software to auto-align adjacent fields during LAM construction. This software package allows crystallographic orientation and phase maps to be generated for entire thin sections, which offers a distinct advantage in the analysis of samples dominated by large grain sizes (i.e. peridotites) because a statistically significant amount of grains is required to confidently define the crystallographic texture of a sample.

2.4.2 Calculation of normalized phase abundances

The phase abundances tabulated by Oxford's AZtecHKL software during data acquisition allow for an assessment of the mineralogical heterogeneity within the xenolith suite. The abundance of the major constituent minerals (i.e. olivine, diopside, and enstatite) are normalized and plotted on the IUGS classification diagram for phaneritic ultramafic rocks (Figure 2.3). It is important to note that non-indexed portions of the sample are disregarded in these normalizations. Although LAMs are constructed for the pyroxenite samples, only peridotitic samples (n=41) are considered when performing textural analyses.

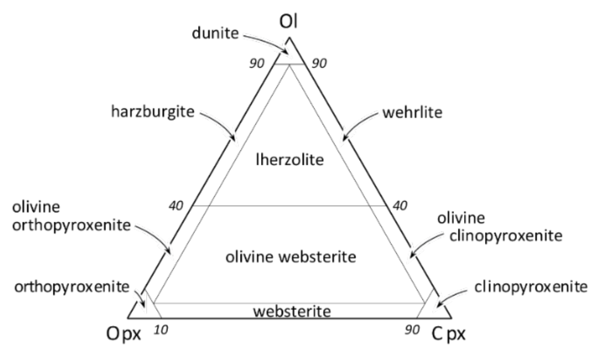

Figure 2.3. IUGS classification diagram for phaneritic ultramafic rocks containing orthopyroxene, clinopyroxene, and olivine as the major constituent minerals. (Image modified from: Le Maitre, 2002).

Table 2.1. Equilibration temperatures (Chatzaras et al., in revision) are shown alongside depth and pressure estimates, which are determined from the construction of a MBL geothermal gradient at the time of eruption. Black text is used for peridotitic xenolith samples that have been successfully reoriented into their fabric frame of reference, whereas samples that have not are shown in red (cf. Appendix A).

Volcanic Center	**Sample Name**	**T (± 25°C)**	**Depth (km)**	**Pressure (kbar)**
Mount Aldaz (AD)	AD6021-X01	1017	57	19
	AD6021-X02	1084	63	21
Mount Cumming (KSP)	KSP89-181-X01 (lo-Cr)	862	42	14
	KSP89-181-X01 (hi-Cr)	995	52	17
Mount Avers (AV)	FDM-AV01-X01	939	50	16
Mount Avers – Bird Bluff (AVBB)	FDM-AVBB01	937	50	16
	FDM-AVBB02	779	39	13
	FDM-AVBB03	949	51	17
	FDM-AVBB04	822	42	14
	FDM-AVBB05	814	42	14
	FDM-AVBB06	940	50	16
	FDM-AVBB07	805	41	13
	FDM-AVBB08	832	43	14
Bird Bluff (BB)	FDM-BB01-X01	945	51	17
	FDM-BB02-X01	1053	60	20
	FDM-BB03-X01	856	45	15
	FDM-BB04-X01	853	45	15
Demas Bluff (DB)	FDM-DB01-X01	1024	58	19
	FDM-DB02-X01	1183	71	23
	FDM-DB02-X02	978	54	18
	FDM-DB02-X03	999	55	18
	FDM-DB02-X04	933	50	16
	FDM-DB02-X05	958	51	17
	FDM-DB02-X06	1198	72	23
	FDM-DB02-X08	803	41	13
	FDM-DB02-X10	1020	57	19
	FDM-DB02-X11	1039	59	19
	FDM-DB02-X12	1036	59	19
	FDM-DB02-X13	911	49	16
	FDM-DB03-X01	856	44	14
	FDM-DB03-X02	861	44	14
	FDM-DB03-X03	982	54	18
	FDM-DB03-X04	1002	56	18
	FDM-DB04-X01	991	55	18
	FDM-DB04-X02	984	54	18
	FDM-DB04-X03	1165	69	23
	FDM-DB04-X04	968	53	17

Table 2.1. Continued.

Volcanic Center	Sample Name	T (± 25°C)	Depth (km)	Pressure (kbar)
Marujupu Peak (MJ)	FDM-MJ01-X01	898	48	16
	FDM-MJ01-X02	974	53	17
	FDM-MJ01-X03	929	50	16
	FDM-MJ01-X05	1014	57	19
	FDM-MJ01-X06	1070	61	20
Recess Nunatak (RN)	FDM-RN01-X01	961	52	17
	FDM-RN02-X01	828	42	14
	FDM-RN03-X01	943	51	17
	FDM-RN04-X01	812	42	14

2.4.3 Noise reduction and grain reconstruction

Noise reduction is completed using the HKL CHANNEL 5 software Tango (v. 5.12.56.0) in order to improve the quality of the EBSD dataset (Figure 2.4; Table 2.2). Isolated pixels that have been incorrectly indexed (i.e. wild spikes) are extrapolated first, followed by iterative extrapolation of non-indexed pixels (i.e. zero solutions) based on the 8, 7, and then 6 nearest neighbors of each pixel (Bestmann & Prior, 2003).

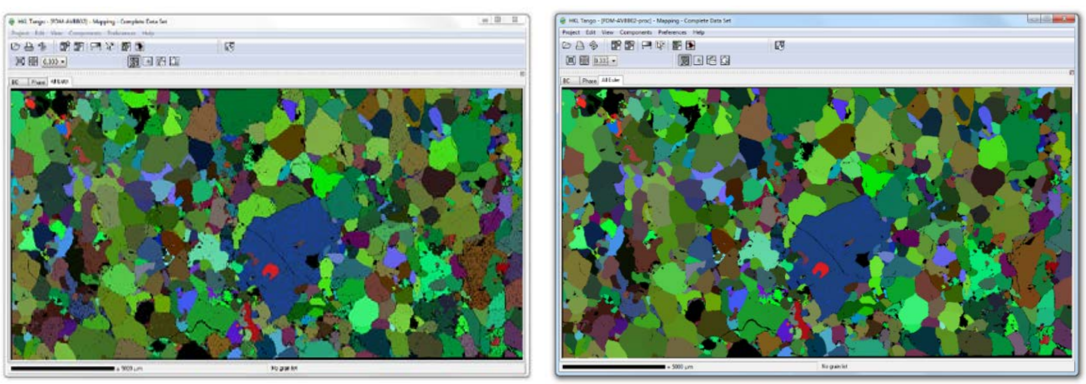

Figure 2.4. Sample FDM-AVBB02 is shown before and after noise reduction using Tango. (Left) The EBSD map prior to noise reduction in Tango. This map contains misindexed and non-indexed points, within the data set. (Right) An EBSD map after noise reduction is complete. A significant portion of wild spikes and zero solutions are removed. Notice that many of the anomalous black points visible in the upper image are no longer visible after noise reduction.

Table 2.2. Phase statistics for sample FDM-AVBB02 are shown before and after noise reduction is complete. This process reduces the abundance of zero solutions and corrects for any misindexed points, which improves the quality of the data set. BC = band contrast; MAD = mean angular deviation.

Phase	Raw Data			Processed Data		
	%	Mean BC	Mean MAD	%	Mean BC	Mean MAD
Zero solutions	6.99	39.59	n/a	4.98	34.25	n/a
Forsterite (Fo)	60.00	121.8	0.3386	60.83	120.6	0.3380
Enstatite (En)	17.42	82.56	0.4985	19.09	81.70	0.4941
Diopside (Di)	13.33	107.2	0.4484	12.80	107.7	0.4337
Chromite (Ch)	2.26	144.4	0.4547	2.30	144.0	0.4508

The post-processed EBSD dataset is subsequently imported into the MTEX MATLAB toolbox (version 3.5), which contains a number of powerful analytical algorithms for the reconstruction of grains and grain boundaries from the spatially indexed orientation measurements. In MTEX, the orientation measurements are further filtered and discarded if the mean angular deviation (MAD) of the indexed solution exceeds 1.0. The MAD is a numerical quantity that expresses how well the detected electron backscatter pattern matches the refined solution (i.e. quality of fit). Grain boundaries are then reconstructed using the MTEX algorithm, which operates under the assumption a grain boundary exists between two adjacent measurements if they are indexed as different phases or their relative misorientation angle exceeds a 10° threshold (Bachmann et al., 2011). Based on the large grain sizes observed in the samples, grains containing less than 50 pixels (i.e. grains that are smaller than ca. 2.8 mm^2) are removed from the grain set (Appendix B). This eliminates any influence of grain fragments on quantitative textural analyses of the observed mantle textures. The spatially indexed EBSD data contained within the resultant grain set contains all data used for subsequent textural analyses (Figure 2.5).

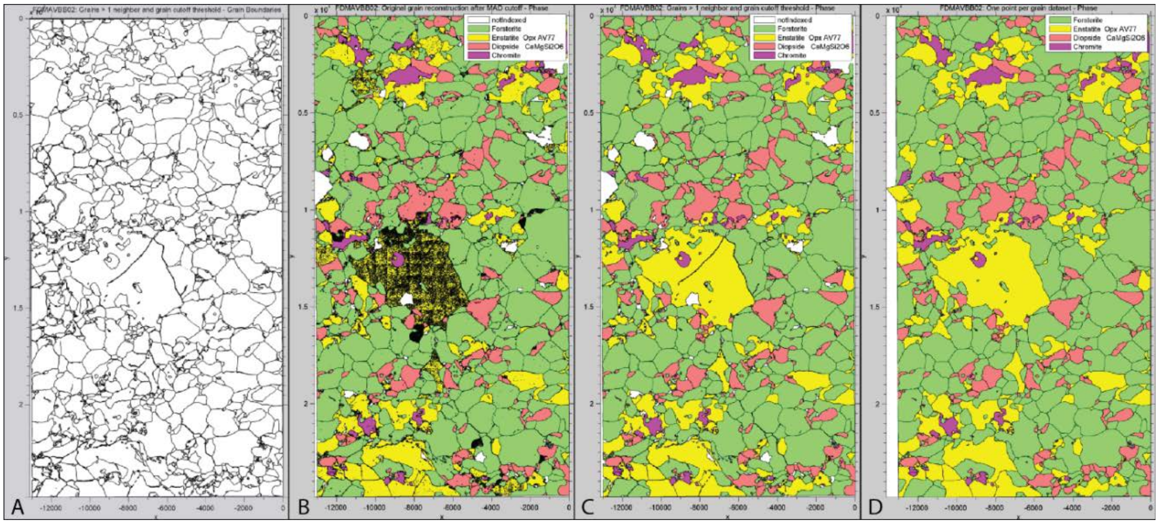

Figure 2.5. (A) Grain boundary reconstruction for sample FDM-AVBB02. The boundary map excludes solutions with a mean angular deviation (MAD) greater than 1 and grains containing less than 50 pixels. (B) Phase map of the EBSD data for sample FDM-AVBB02, which excludes solutions that have a MAD greater than 1. (C) Phase map of the EBSD data for sample FDM-AVBB02, which excludes solutions having a MAD greater than 1 and grains containing less than 50 pixels. (D) One point-per-grain phase map of sample FDM-AVBB02, which excludes solutions that have a MAD greater than 1 and grains containing less than 50 pixels. Additionally, this map reduces each constituent mineral grain to a single data point having a known phase and a single orientation, which is based on the average orientation of all indexed points within the confines of that mineral grain.

2.4.4 Textural analyses

2.4.4.1 Pole figures and orientation distribution functions (ODFs)

In order to visualize the crystallographic texture of a sample (i.e. its CPO) using MTEX, the reconstructed grain set is separated by phase. One point-per-grain (1ppg) data are used to plot pole figures and orientation distribution functions (ODFs) for the major phases present in each sample (i.e. forsterite, diopside and/or enstatite). Area-weighted data sets are useful for determining the bulk properties of a sample, whereas the one point-per-grain data sets are used to quantitatively measure the relative strength of the textures between xenolith samples (Appendix B). Plotting the crystallographic orientation of all phases allows for an evaluation of the relationships that exist between the textures of the constituent minerals.

Pole figures are a common approach to visualizing CPOs, but they are limited stereographic projections because they only describe the measured orientations in one crystallographic direction. Plotting an ODF is the preferred method because it provides a complete three-dimensional description of the crystallographic texture as a frequency distribution of the measured crystal orientations in Euler space (Wenk and Wilde, 1972; Ben Ismaïl and Mainprice, 1998). Using MTEX, pole figures and ODFs are generated for each major phase using both the area-weighted and the one point-per-grain data sets (Figure 2.6). The ODFs are then interpreted with respect to the patterns of CPO that have been extensively documented in studies of experimentally and naturally deformed mantle rocks (e.g., Karato et al., 2008).

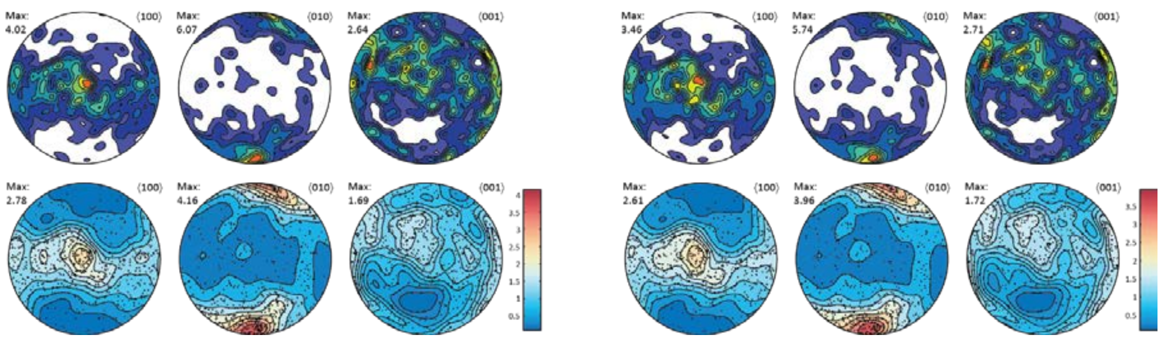

Figure 2.6. Examples of pole figures (top) and ODFs (bottom) created for the forsterite grains in sample FDM-AVBB02, which display an axial-[010] texture. (Left) Area-weighted data is plotted for 672 grains of olivine. (Right) One point-per-grain data is plotted for 630 grains of olivine.

2.4.4.2 Assessing the textural strength and symmetry of olivine texture

The intensity of olivine CPO for each sample is quantified by calculating the J-index (Bunge, 1982) and the misorientation index (i.e. M-index; Skemer et al., 2005) for both the one point-per-grain and area-weighted grain sets in MATLAB using the MTEX toolbox for quantitative textural analyses (Appendix B). Mathematically, the J-index is defined as the second moment of an ODF and its value ranges from zero (i.e. a random CPO) to infinity (i.e.

a single crystal CPO). Although the J-index is a commonly employed measure of texture intensity, it is sensitive to the number of grains measured and is thought to be difficult to interpret unambiguously (Skemer et al., 2005). Comparatively, the M-index is defined as the difference between some measured distribution of uncorrelated misorientation angles and the distribution expected for uncorrelated misorientation angles within a completely random texture. The M-index ranges from zero (i.e. a random CPO) to 1 (i.e. a single crystal CPO) and is thought to be a more reliable indicator of textural intensity (Skemer et al., 2005). The measured misorientation angles are exported as a number string into a text file that is subsequently imported into a MATLAB-based graphical user interface M-index calculator developed by Skemer (2008). The calculator generates a misorientation angle frequency histogram for each sample (Figure 2.7), which plots the measured misorientation distribution against a theoretical random distribution. In order to quantitatively assess the symmetry of the olivine textures preserved by the MBL peridotite samples, the BA-index is calculated (Mainprice et al., 2014). It is a quantitative method that is

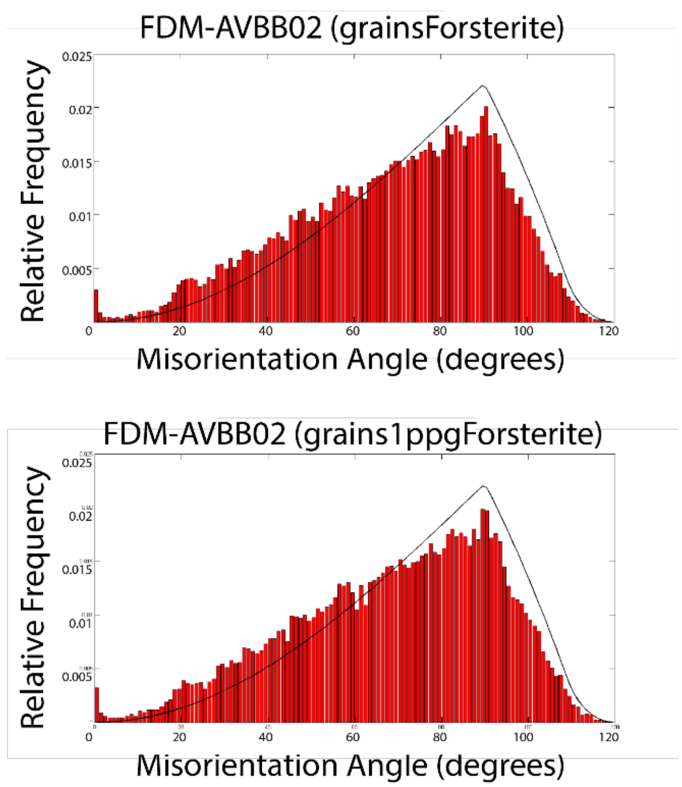

Figure 2.7. Examples of the histograms produced for sample FDM-AVBB02 using the M-index GUI developed by Skemer (2008). The M-index for the area-weighted grain set (top) is 0.105, whereas the M-index for the one point-per-grain data is 0.106.

used to determine if the olivine texture is axial-[010] ($0 \leq BA \leq 0.35$), orthorhombic ($0.35 \leq BA \leq 0.65$) or axial-[100] ($0.65 \leq BA \leq 1$). Mathematically, the BA-index is defined as:

$$BA = \frac{1}{2}\left(2 - \left(\frac{P_{010}}{G_{010}+P_{010}}\right) - \left(\frac{G_{100}}{G_{100}+P_{100}}\right)\right) \qquad \text{(Equation 2)}$$

Where P is equal to $\lambda_1 - \lambda_2$ and G equal to $2(\lambda_2 - \lambda_3)$, with $\lambda_1 \geq \lambda_2 \geq \lambda_3$ being the three eigenvalues determined from the orientation distribution function of each sample within the xenolith suite (Vollmer, 1990).

2.4.4.3 Grain size distributions

In order to quantify the grain size distribution of the constituent phases within each sample, the EBSD data is processed in the MTEX toolbox to calculate grain size statistics and plot grain size distribution histograms (Appendix B). The grain area is measured, from which the diameter of a circle with equivalent area to that of the measured grain is calculated. The geometric and arithmetic means are calculated for both the maximum diameter and equivalent diameter lengths observed in each sample. Grain size histograms are plotted from these data (Figure 2.8). Grain size distributions are then evaluated to determine the

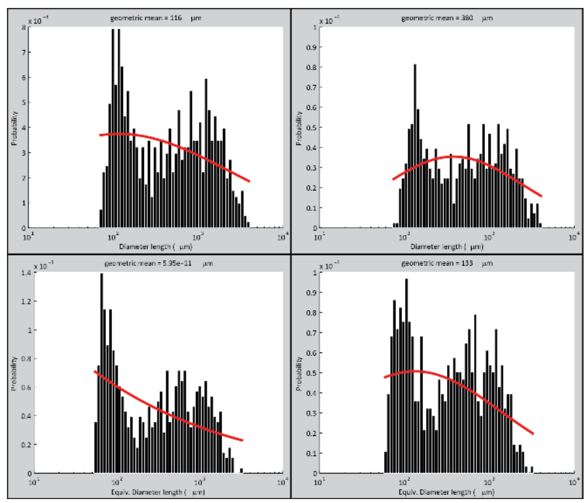

Figure 2.8. Example grain size histograms that show the grain size distribution of the olivine grains in sample FDM-AVBB02. (Left) The geometric mean of the area-weighted data is calculated for the maximum diameter and equivalent diameter lengths of olivine grains. (Right) The geometric mean of the one point-per-grain data is calculated for the maximum diameter and equivalent diameter lengths of olivine grains. Notice that in some cases (i.e. bottom left) the calculated geometric mean grain size is not properly calculated by the software. In such cases, the most dominant peak of the histogram is inferred to be equal to the geometric mean grain size.

minimum, maximum, and geometric mean grain sizes of the phases that constitute each peridotitic sample.

2.4.4.4 Deformation mechanism maps and piezometry

The conditions at which different deformation mechanisms are dominant may be evaluated using a deformation mechanism map (DMM). DMMs are plots of grain size (μs) against differential stress (MPa) that are contoured for strain rate (1/s) and constructed for specific pressure, temperature, and water content conditions (Figure 2.9). The DMM is split into different fields within which a specific deformation mechanism is interpreted to be the dominant means for accommodating strain based on the parameterization of the deformation conditions (Equation 1); it is important to remember that all deformation mechanisms are operating to some extent. These field boundaries are constructed using experimentally determined flow laws for dry olivine that have been calibrated for a wide range of deformation conditions (i.e. Evans and Goetze, 1979; Hirth and Kohlstedt, 2003). Due to uncertainties associated with the applied geothermometers, all samples are plotted on a series of DMMs that are constructed at a 100°C resolution between 800 and 1200°C. The recrystallized grain size piezometer of van der Wal et al. (1993) is overlain on each DMM

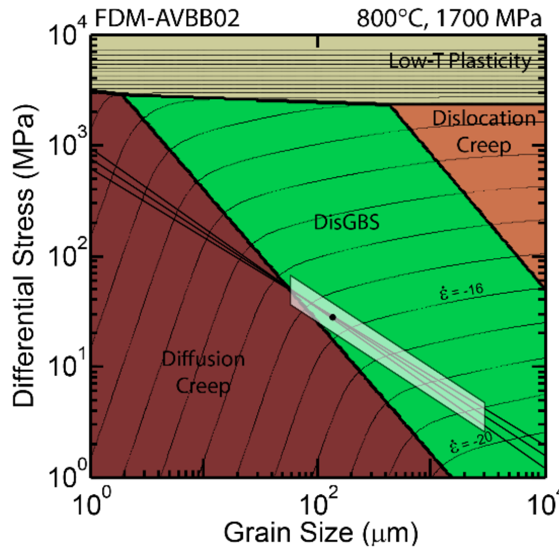

Figure 2.9. DMM for sample FDM-AVBB02, constructed for a temperature of 800°C and a pressure of 1700 MPa. Based on the observed grain size distribution (white box), estimates of differential stress range from 3 – 50 MPa. Comparatively, the geometric mean grain size for this sample (black circle; 133 μm) implies a mean differential stress of 30 MPa affected this rock prior to its exhumation. Strain rates for this sample range from approximately 10^{-15}/s – 10^{-19}/s with a geometric mean on the order of 10^{-16}/s.

in order to estimate the magnitude of mean differential stress experienced by each sample. The size of olivine grains within a sample is directly related to the paleostress state of that xenolith sample prior to entrainment by its host magma (Karato et al., 1980; Van der Wal et al., 1993). Although the sizes of recrystallized olivine grains are commonly used to estimate the maximum differential stress, in this study the mean grain size of olivine is used to estimate the mean differential stress for each sample due to the fact that most xenoliths are coarse-grained and typically lack significant recrystallization. Consequently, the estimates for the mean differential stresses are minima, given that grain size reduction due to recrystallization is associated with larger magnitudes of differential stress. Strain rates may also be approximated using a DMM, but proper parameterization of the variables in the olivine flow law (Equation 1) provides a more reliable estimate.

3 HETEROGENEITY OF THE LITHOSPHERIC MANTLE BENEATH MBL

3.1 ASSESSING HETEROGENEITY USING ELECTRON BACKSCATTER DIFFRACTION DATA

The amount and variety of data that electron backscatter diffraction (EBSD) is capable of generating may seem difficult to keep track of. At a result, it is important to reiterate the power of these datasets and remind the reader why they are imperative in assessing the heterogeneity of the lithospheric mantle beneath Marie Byrd Land. In the most direct sense, the EBSD data sets provide the relative abundances of the constituent mineral phases within each xenolith sample (Section 3.2) and allow for an assessment of their crystallographic preferred orientations (CPOs; Section 3.3). In turn, these data are used to confidently reconstruct a map of the grain boundaries and assess the grain size distribution of the constituent minerals within each sample (Section 3.2). The differential stress and strain rate that each sample records is then determined by placing the grain size statistics along the recrystallized olivine grain size piezometer, which itself is plotted on top of a deformation mechanism map (DMM; Section 3.4). In this way, the observed range in olivine grain sizes allows for an assessment of the dominant deformation mechanism that accommodates strain within each sample. This information is subsequently verified against observations made using optical microscopy (Section 3.2).

3.2 Mineralogical and Microstructural Characterization of the Xenolith Suite

The xenolith suite contains forty-one spinel-bearing peridotites and four spinel pyroxenites (Figure 3.1). Spinel is the stable metamorphic phase and its occurrence is documented in all samples (Table 3.1). The xenolith samples are more accurately classified as predominantly lherzolites (n=31) with lesser occurrences of harzburgite (n=4), wehrlite (n=3), dunite (n=3), olivine websterite (n=1), websterite (n=1) and clinopyroxenite (n=2) being documented. The MBL xenoliths are coarse-grained and typically display the characteristics of either a granular or a tabular microstructure, although it is important to note that there are also examples of porphyroclastic microstructures preserved within the suite.

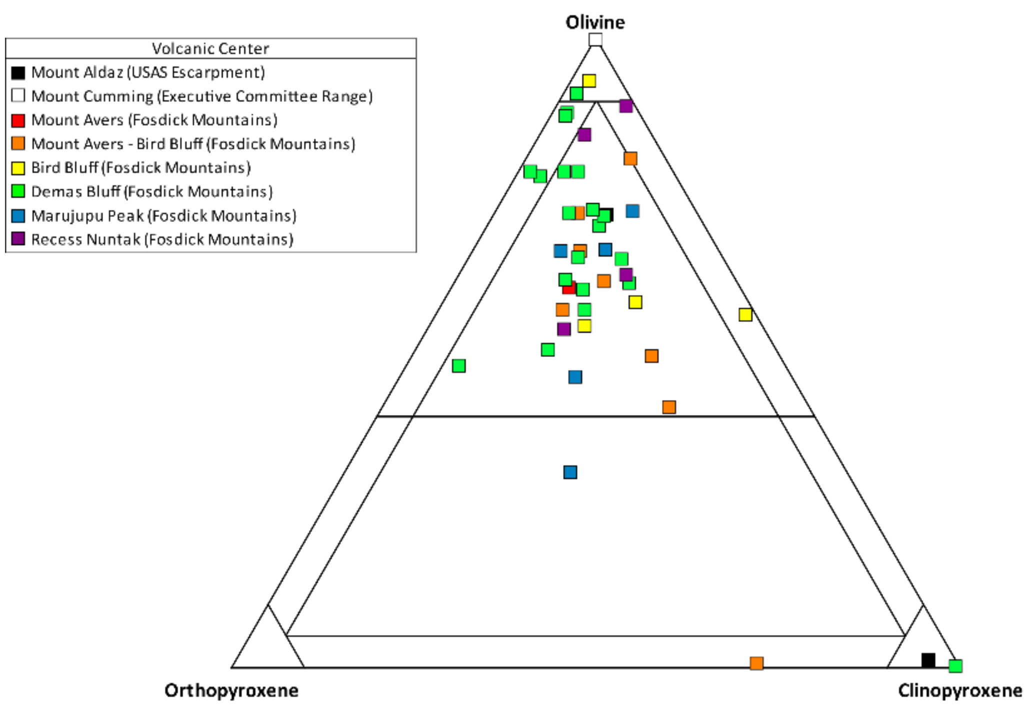

Figure 3.1. Ternary diagram showing the compositional variation observed within the suite of MBL xenoliths.

Table 3.1. Raw phase abundance data collected during EBSD acquisition and reported by Oxford's AZtec software. Non-indexed portions of the EBSD map (i.e. zero solutions) are included. Fo = forsterite, En = enstatite, Di = diopside and Ch = chromite.

Sample	Number of Fields	Phase Abundances (%)				
	(750 μm x 750 μm)	Fo	En	Di	Ch	Zero Solutions (Z.S.)
AD6021-X01	609	0.51	1.65	41.16	5.21	51.47
AD6021-X02	1536	65.11	11.41	14.05	0.61	8.81
KSP89-181-X01	957	91.54	0.01	0.15	0.53	7.76
FDM-AV01-X01	884	51.15	19.86	13.63	2.09	13.27
FDM-AVBB01	1479	48.35	14.39	16.12	2.06	19.08
FDM-AVBB02	902	60.00	17.34	13.37	2.30	6.99
FDM-AVBB03	1581	0.58	20.81	54.15	10.46	13.99
FDM-AVBB04	1349	27.64	9.86	18.38	1.54	42.59
FDM-AVBB05	1485	57.77	12.99	9.18	1.31	18.75
FDM-AVBB06	1469	48.88	22.47	14.65	1.16	12.83
FDM-AVBB07	1504	58.22	3.42	10.30	1.78	26.28
FDM-AVBB08	1180	24.25	11.31	23.14	1.83	39.46
FDM-BB01-X01	1581	41.94	0.99	31.77	0.81	24.50
FDM-BB02-X01	1386	47.68	21.44	18.75	1.76	10.37
FDM-BB03-X01	1333	63.31	2.93	1.65	0.26	31.85
FDM-BB04-X01	1048	43.47	11.58	19.70	0.85	24.40
FDM-DB01-X01	1458	44.45	10.77	17.47	2.35	24.96
FDM-DB02-X01	1145	56.64	11.70	12.32	0.72	18.63
FDM-DB02-X02	1535	71.78	8.02	1.58	0.37	18.25
FDM-DB02-X03	775	54.95	13.48	7.79	0.46	23.32
FDM-DB02-X04	1178	42.46	15.97	10.34	0.86	30.57
FDM-DB02-X05	1458	0.17	0.29	60.30	2.69	36.56
FDM-DB02-X06	1891	31.28	29.12	4.78	0.04	34.78
FDM-DB02-X08	1233	68.99	8.08	1.73	0.20	21.00
FDM-DB02-X10	1008	57.90	17.45	13.45	0.11	11.09
FDM-DB02-X11	1169	57.71	10.48	12.36	0.68	18.76
FDM-DB02-X12	865	48.76	10.65	15.82	2.09	22.69
FDM-DB02-X13	1215	53.59	10.34	9.69	1.86	24.52
FDM-DB03-X01	1581	66.79	5.15	1.41	1.06	25.58
FDM-DB03-X02	1334	41.69	17.01	14.69	3.49	23.12
FDM-DB03-X03	1530	49.97	18.11	15.01	2.07	14.84
FDM-DB03-X04	1271	54.83	8.95	5.69	1.93	28.59
FDM-DB04-X01	1298	59.02	11.24	4.58	0.13	25.03
FDM-DB04-X02	1380	43.33	26.73	15.63	2.52	11.80
FDM-DB04-X03	1377	66.28	15.85	2.73	0.87	14.26
FDM-MJ01-X01	1380	24.11	29.63	24.25	4.96	17.05
FDM-MJ01-X02	371	52.61	12.30	14.23	1.97	18.88
FDM-MJ01-X03	602	37.44	12.36	6.80	1.16	42.25
FDM-MJ01-X05	436	56.99	6.88	14.88	3.40	17.85
FDM-MJ01-X06	1258	35.71	22.95	18.66	0.80	21.89
FDM-RN01-X01	1500	53.92	0.74	5.88	0.85	38.62
FDM-RN02-X01	1298	54.59	12.81	19.97	1.76	10.87
FDM-RN03-X01	1914	62.01	6.86	4.54	0.34	26.25
FDM-RN04-X01	1350	45.25	23.03	15.66	1.19	14.86

The modal mineralogy of the spinel peridotites varies between 40.1 – 99.2% olivine, 0.2 – 42.1% diopside, 0 – 44.6% enstatite and 0.1 – 4.5% chromite (Table 3.2). The grain size distribution of the olivine in the peridotitic samples typically follows a log-normal distribution (Appendix D). Exceptions to this observation include the several samples that contain enough recrystallized olivine grains to generate a significant secondary peak in the grain size distribution histogram. Minimum olivine grain sizes range from 60 to 110 μm and maximum olivine grain sizes range from 2.5 to 10.0 mm. The geometric mean grain size of olivine in these samples ranges from 100 μm to 2 mm and has an average of 694 μm. The geometric mean grain size of diopside ranges from 90 to 865 μm and has an average of 325 μm, whereas that of enstatite ranges from 120 μm to 1.2 mm and has an average of 625 μm (Table 3.3). Comparatively, the pyroxenites contain 0.3 – 29.1% olivine, 29.2 – 95.0% diopside, 0.5 – 35.7% enstatite and 0.6 – 10.7% chromite. Grain-size statistics are not generated for the pyroxenites because these samples do not contain enough olivine to assess how the distribution, size and/or crystallographic texture of the pyroxene grains may influence the development of microstructures (e.g., CPO) in olivine.

3.2.1 Mount Aldaz, Usas Escarpment

The two spinel-bearing samples that are sourced from Mt. Aldaz contain 1.1 – 71.4% olivine, 15.4 – 84.8% diopside, 3.4 – 12.5% enstatite and 0.7 – 10.7% chromite. Sample AD6021-X01 is classified as a spinel clinopyroxenite, whereas sample AD6021-X02 is a spinel-bearing lherzolite. Equilibration temperatures for these samples are 1017 and 1084°C, respectively. These temperatures correspond to depths of 57 and 63 km.

Sample AD6021-X01 is a chromite-rich (10.7%) clinopyroxenite. Spinel grains are interstitial and occur as holly-leaf structures. Pyroxene grains are large with irregular to curvilinear boundaries that infrequently form 120° grain boundary junctions. Occurrences of undulose extinction and dislocation walls exist within the sample (Figure 3.2).

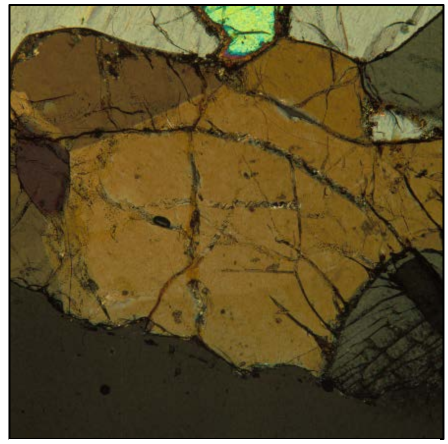

Figure 3.2. Photomicrograph (100X) of dislocation walls and curvilinear boundaries displayed by a grain of enstatite within sample AD6021-X01.

Comparatively, sample AD6021-X02 is a coarse-granular spinel-bearing lherzolite. Olivine grains range in size from 80 to 6000 μm with a geometric mean of 815 μm. The mean size of diopside grains is 376 μm and the range of grain sizes extends from 60 to 2500 μm. Enstatite grains range in size from 90 to 3000 μm and display a geometric mean of 746 μm. Grain bulging in this sample provides evidence for recrystallization via strain-induced grain boundary migration. Dislocation walls and subgrains are abundant in olivine with many grain boundaries forming 120° triple junctions (Figure 3.3). Pyroxenes are interstitial with curvilinear to polygonal grain boundaries. Infrequently, small grains of pyroxene occur within larger olivine grains. Chromite is rare (0.7%) and unevenly distributed throughout the sample as it is generally found in clusters that are interstitial to pyroxene grains.

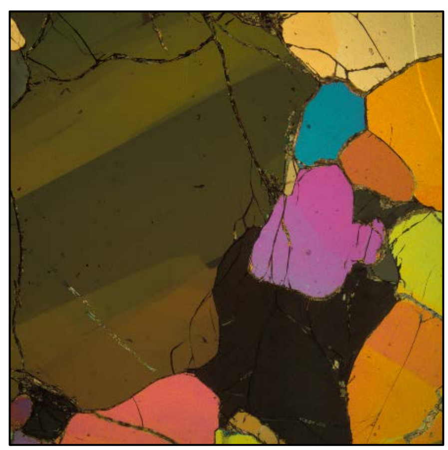

Figure 3.3. Photomicrograph (100X) of AD6021-X02 showing the presence of dislocation walls in olivine and the existence of 120° triple junctions along the boundaries of strain-free subgrains.

Table 3.2. Phase abundances are determined for forsterite (fo), enstatite (en), diopside (di) and chromite (ch) by removing zero solutions from the data set. Values are normalized to the primary mineralogy of the xenolith suite (i.e. fo, en and di) and plotted on the IUGS ternary diagram for phaneritic ultramafic rocks.

Sample	Phase Abundances (%)				Normalized Abundances (%)			Rock Name (IUGS)
	Fo	En	Di	Ch	Fo	En	Di	
AD6021-X01	1.1	3.4	84.8	10.7	1.2	3.8	95.0	Clinopyroxenite
AD6021-X02	71.4	12.5	15.4	0.7	71.9	12.6	15.5	Lherzolite
KSP89-181-X01	99.3	0.0	0.2	0.6	99.8	0.0	0.2	Dunite
FDM-AV01-X01	59.0	22.9	15.7	2.4	60.4	23.5	16.1	Lherzolite
FDM-AVBB01	59.8	17.8	19.9	2.5	61.3	18.2	20.4	Lherzolite
FDM-AVBB02	64.5	18.6	14.4	2.5	66.1	19.1	14.7	Lherzolite
FDM-AVBB03	0.7	24.2	62.9	12.2	0.8	27.6	71.6	Websterite
FDM-AVBB04	48.1	17.2	32.0	2.7	49.5	17.6	32.9	Lherzolite
FDM-AVBB05	71.1	16.0	11.3	1.6	72.3	16.2	11.5	Lherzolite
FDM-AVBB06	56.1	25.8	16.8	1.3	56.8	26.1	17.0	Lherzolite
FDM-AVBB07	79.0	4.6	14.0	2.4	80.9	4.8	14.3	Wehrlite
FDM-AVBB08	40.1	18.7	38.2	3.0	41.3	19.3	39.4	Lherzolite
FDM-BB01-X01	55.5	1.3	42.1	1.1	56.1	1.3	42.5	Wehrlite
FDM-BB02-X01	53.2	23.9	20.9	2.0	54.3	24.4	21.3	Lherzolite
FDM-BB03-X01	92.9	4.3	2.4	0.4	93.3	4.3	2.4	Dunite
FDM-BB04-X01	57.5	15.3	26.1	1.1	58.2	15.5	26.4	Lherzolite
FDM-DB01-X01	59.2	14.4	23.3	3.1	61.2	14.8	24.0	Lherzolite
FDM-DB02-X01	69.6	14.4	15.1	0.9	70.2	14.5	15.3	Lherzolite
FDM-DB02-X02	87.8	9.8	1.9	0.5	88.2	9.9	1.9	Harzburgite
FDM-DB02-X03	71.7	17.6	10.2	0.6	72.1	17.7	10.2	Lherzolite
FDM-DB02-X04	60.9	23.0	14.9	1.2	61.6	23.3	15.1	Lherzolite
FDM-DB02-X05	0.3	0.5	95.0	4.2	0.3	0.5	99.2	Clinopyroxenite
FDM-DB02-X06	48.0	44.6	7.3	0.1	48.0	44.7	7.3	Lherzolite
FDM-DB02-X08	87.3	10.2	2.2	0.3	87.6	10.3	2.2	Harzburgite
FDM-DB02-X10	65.1	19.6	15.1	0.1	65.2	19.7	15.1	Lherzolite
FDM-DB02-X11	71.0	12.9	15.2	0.8	71.6	13.0	15.3	Lherzolite
FDM-DB02-X12	63.1	13.8	20.5	2.7	64.8	14.2	21.0	Lherzolite
FDM-DB02-X13	71.0	13.7	12.8	2.5	72.8	14.0	13.2	Lherzolite
FDM-DB03-X01	89.8	6.9	1.9	1.4	91.1	7.0	1.9	Dunite
FDM-DB03-X02	54.2	22.1	19.1	4.5	56.8	23.3	20.0	Lherzolite
FDM-DB03-X03	58.7	21.3	17.6	2.4	60.1	21.8	18.1	Lherzolite
FDM-DB03-X04	76.8	12.5	8.0	2.7	78.9	12.9	8.2	Lherzolite
FDM-DB04-X01	78.7	15.0	6.1	0.2	78.9	15.0	6.1	Lherzolite
FDM-DB04-X02	49.1	30.3	17.7	2.9	50.6	31.2	18.2	Lherzolite
FDM-DB04-X03	77.3	18.5	3.2	1.0	78.1	18.7	3.2	Harzburgite
FDM-DB04-X04	78.7	19.5	1.6	0.2	78.9	19.5	1.6	Harzburgite
FDM-MJ01-X01	29.1	35.7	29.2	6.0	31.0	38.0	31.1	Olivine Websterite
FDM-MJ01-X02	64.9	15.2	17.5	2.4	66.5	15.5	18.0	Lherzolite
FDM-MJ01-X03	64.8	21.4	11.8	2.0	66.1	21.8	12.0	Lherzolite
FDM-MJ01-X05	69.4	8.4	18.1	4.1	72.4	8.7	18.9	Lherzolite
FDM-MJ01-X06	45.7	29.4	23.9	1.0	46.2	29.7	24.1	Lherzolite
FDM-RN01-X01	87.8	1.2	9.6	1.4	89.1	1.2	9.7	Wehrlite
FDM-RN02-X01	61.2	14.4	22.4	2.0	62.5	14.7	22.9	Lherzolite
FDM-RN03-X01	84.1	9.3	6.2	0.5	84.5	9.3	6.2	Lherzolite
FDM-RN04-X01	53.2	27.1	18.4	1.4	53.9	27.4	18.7	Lherzolite

Table 3.3. Minimum, maximum and geometric mean grain sizes are determined for olivine, diopside and enstatite. These values are reported alongside the number of grains (n) of each phase measured in the sample. Italicized values correspond to a mineral phase within a sample that has less than twenty grains. As a result, these values are not considered to be significant when reporting the grain-size ranges of that particular phase within the sample suite. Electron backscatter diffraction data is processed to determine grain sizes using the equivalent area method. Due to the limitations of using a two-dimensional section, a scaling factor of 1.2 is applied in order to approximate three-dimensional grain diameters (Van der Wal et al., 1993).

Sample	Olivine Grain Sizes (μm)				Diopside Grain Sizes (μm)				Enstatite Grain Sizes (μm)			
	n	Min.	Max.	Mean	n	Min.	Max.	Mean	n	Min.	Max.	Mean
AD6021-X02	312	80	6000	815	283	60	2500	376	132	90	3000	746
KSP89-181-X01	1354	55	3750	455	46	60	200	108	2	70	110	91
FDM-AV01-X01	412	60	4000	111	262	60	2000	200	122	80	4000	543
FDM-AVBB01	2681	60	2500	214	1466	60	2000	143	896	60	4000	166
FDM-AVBB02	630	60	3000	133	331	60	2000	192	195	60	5000	343
FDM-AVBB04	579	60	3000	587	425	60	3000	538	216	70	4500	563
FDM-AVBB05	743	60	5000	150	218	60	3000	369	188	70	5000	595
FDM-AVBB06	911	60	3750	192	475	50	2000	77	298	60	5000	474
FDM-AVBB07	677	70	4000	644	364	60	2000	414	165	100	2000	446
FDM-AVBB08	831	60	2750	285	559	60	4000	398	296	60	4000	421
FDM-BB01-X01	1698	60	3500	122	1215	60	4000	130	93	70	1500	120
FDM-BB02-X01	903	55	3000	322	712	60	2000	170	453	60	3000	393
FDM-BB03-X01	263	65	6000	1180	83	70	1500	383	129	90	3000	458
FDM-DB01-X01	274	80	6500	885	208	60	4000	451	144	100	4000	521
FDM-DB02-X01	620	60	4250	494	357	60	1500	373	308	60	2000	484
FDM-DB02-X02	111	70	9000	2000	60	70	1000	113	53	150	5000	594
FDM-DB02-X03	91	70	9000	210	63	60	2000	500	26	100	8000	960
FDM-DB02-X04	103	70	6000	1230	88	100	2000	865	39	200	7000	902

Table 3.3. Continued.

Sample	Olivine Grain Sizes (μm)				Diopside Grain Sizes (μm)				Enstatite Grain Sizes (μm)			
	n	Min.	Max.	Mean	n	Min.	Max.	Mean	n	Min.	Max.	Mean
FDM-DB02-X06	117	60	1000	356	629	50	3000	102	127	70	8000	1160
FDM-DB02-X08	107	90	8000	1310	9	100	2000	600	48	200	4000	1200
FDM-DB02-X10	145	70	7000	736	123	60	3000	236	37	70	7000	1000
FDM-DB02-X11	224	70	4000	1610	206	60	2000	302	89	80	3000	795
FDM-DB02-X12	135	70	6000	599	87	70	4000	377	52	70	7000	444
FDM-DB02-X13	273	80	4500	933	168	80	2500	480	131	100	5000	471
FDM-DB03-X01	133	110	10000	1460	39	80	1500	411	47	100	4000	1150
FDM-DB03-X02	343	70	5500	545	202	60	2000	470	155	100	4000	601
FDM-DB03-X03	274	70	5000	898	236	60	2500	405	142	60	6000	553
FDM-DB03-X04	149	60	7000	100	29	80	5000	297	59	80	9000	524
FDM-DB04-X01	117	80	9000	1450	68	60	2000	491	58	100	5000	1100
FDM-DB04-X02	208	60	4500	647	168	60	3000	150	106	60	5000	1040
FDM-DB04-X03	150	70	7000	1360	41	70	2000	100	73	90	6000	1010
FDM-DB04-X04	114	60	8500	1310	78	60	1500	124	49	90	7000	1000
FDM-MJ01-X02	244	65	3000	513	161	60	1250	315	90	80	2000	356
FDM-MJ01-X03	220	60	4000	600	85	70	2000	377	86	80	5000	480
FDM-MJ01-X05	163	60	5000	350	164	60	2000	186	75	60	2000	467
FDM-MJ01-X06	1110	60	2750	122	718	60	2000	127	216	60	7000	530
FDM-RN01-X01	292	70	4000	1290	155	70	2000	580	35	100	1500	357
FDM-RN02-X01	383	70	4000	604	406	60	3000	317	154	60	4000	297
FDM-RN03-X01	445	70	6000	406	906	60	3000	115	236	60	5000	291
FDM-RN04-X01	377	60	4250	528	306	60	2000	432	219	80	6000	497

3.2.2 Mount Cumming, Executive Committee Range

The only sample sourced from Mount Cumming (KSP89-181-X01) is a porphyroclastic spinel dunite containing 99.2% olivine, 0.2% diopside and 0.6% chromite. This sample contains low-Cr and high-Cr chromite grains from which two equilibration temperatures are determined: 850°C (low) and 990°C (high). This corresponds to extraction depths of 42 and 52 km, respectively. Olivine grains range in size from 55 to 3750 μm and have a geometric mean grain size of 455 μm. There are relatively few diopside grains in this sample (n=46). Diopside displays a narrow range of grain sizes from 60 to 200 μm, and has a geometric mean grain size of 108 μm. Only two small (ca. 70 and 110 μm) grains of enstatite are indexed in this sample.

Olivine porphyroclasts in this sample are defined by their larger size, an abundance of dislocation walls and the serrated to irregular shape of their boundaries. Comparatively, the recrystallized grains that are spalled off from the porphyroclast during subgrain rotation recrystallization are unstrained, smaller, and display polygonal to curvilinear boundaries that commonly meet to form 120° triple junctions (Figure 3.4).

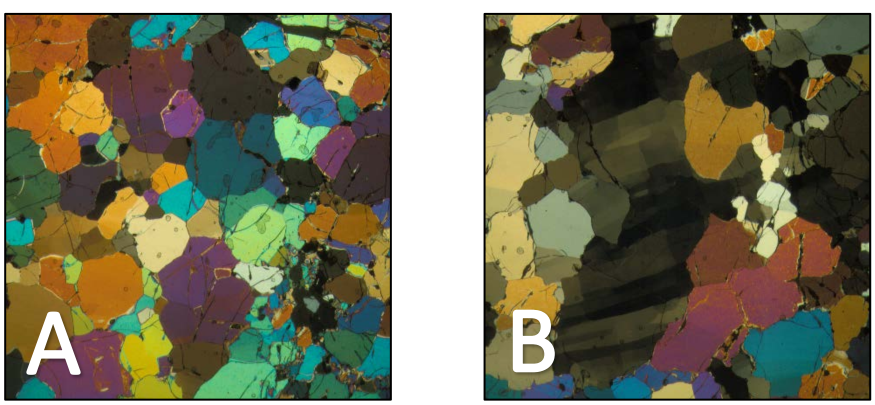

Figure 3.4. Photomicrographs (25X) of the Mount Cumming dunite (KSP89-181-X01). (A) Recrystallized grains are dislocation-free and commonly approach 120° triple junctions. (B) Large porphyroclast containing dislocation walls, a serrated grain boundary and is surrounded by smaller, strain-free subgrains.

3.2.3 Mount Avers, Fosdick Mountains

Sample FDM-AV01-X01 is a coarse-granular spinel-bearing lherzolite with 59.0% olivine, 15.7% diopside, 22.9% enstatite and 2.4% chromite. The sample equilibrated at 939°C, which corresponds to a depth of 50 km. Olivine grains range in size between 60 and 4000 μm with a geometric mean grain size of 111 μm. Diopside grains range in size between 60 and 2000 μm with a geometric mean grain size of 200 μm. Enstatite grains display a range of 80 to 4000 μm with a geometric mean grain size of 543 μm.

The olivine grains are relatively small and characterized by curvilinear to irregular boundaries that sometimes meet to form 120° triple junctions (Figure 3.5A). Most olivine only has a small amount of internal strain, but there are examples of dislocation walls and subgrains developing in some grains (Figure 3.5B). Diopside occurs primarily as small, irregularly shaped grains that are interstitial to other phase. In this sample, enstatite is quite large compared to the other phases. These grains have irregularly-shaped boundaries and contain deformation twins (Figure 3.5C).

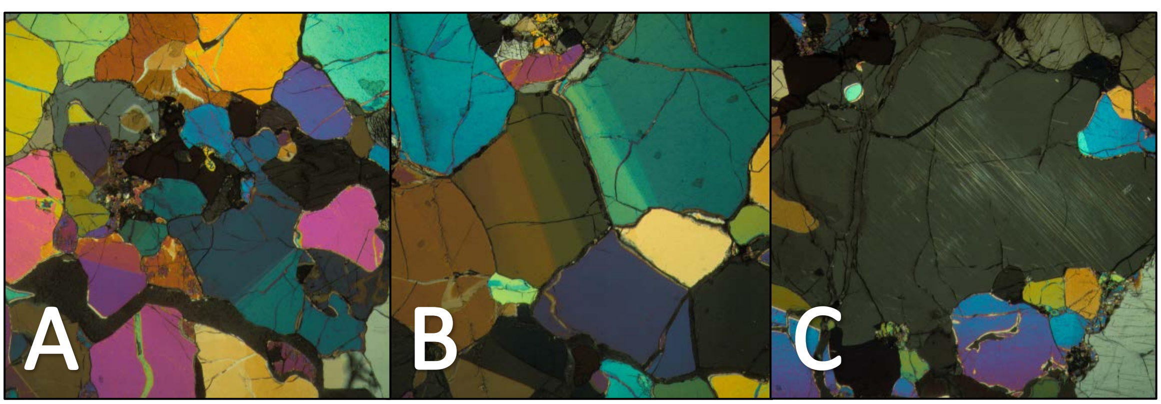

Figure 3.5. Photomicrographs (25X) of sample FDM-AV01-X01. (A) Grain boundaries are curvilinear and/or irregular, although 120° triple junctions do occur. (B) Dislocation walls and subgrain development is documented in olivine grains. (C) Enstatite grains are irregularly shaped and contain deformation twins. These grains are quite large compared to the other phases in this sample.

3.2.4 Mount Avers – Bird Bluff, Fosdick Mountains

Of the eight samples sourced from volcanic centers located between Mount Avers and Bird Bluff, six are lherzolites, one is a wehrlite (FDM-AVBB07) and one is a websterite (FDM-AVBB03). The spinel-bearing peridotites contain 40.1 – 79.0% olivine, 4.6 – 25.8% enstatite, 11.3 – 38.2% diopside and 1.3 – 3.0% spinel. These samples equilibrated at temperatures between 779 and 940°C, which corresponds to extraction depths between 39 and 50 km. The spinel websterite contains 0.7% olivine, 24.2% enstatite, 62.9% diopside and 12.2% spinel. This sample has an equilibration temperature of 949°C, which corresponds to a depth of 51 km.

Grain size distributions are compiled and evaluated for the constituent silicate phases of the seven peridotitic samples. Minimum and maximum olivine grain sizes range from 60 to 70 μm and 2500 to 5000 μm, respectively. The geometric mean grain size of olivine ranges from 133 to 644 μm with an average of 315 μm. Minimum and maximum diopside grain sizes range from 50 to 60 μm and 2000 to 4000 μm, respectively. Diopside grains constitute the smallest grains contained within the samples sourced from Mount Avers – Bird Bluff. Other phases in these xenoliths have minimum grain size ranges that are greater than that displayed by diopside. The geometric mean grain size of diopside ranges from 77 to 538 μm with an average of 304 μm. Minimum and maximum enstatite grain sizes show the largest range of values, which range from 60 to 100 μm and 2000 to 5000 μm, respectively. Enstatite generally constitutes the largest grains within these samples with a geometric mean grain size ranging from 166 to 595 μm and an average geometric mean grain size of 430 μm.

Sample FDM-AVBB01 is a spinel-bearing porphyroclastic lherzolite. Olivine porphyroclasts are defined by their larger size, an abundance of dislocation walls and the serrated to irregular shape of their boundaries (Figure 3.6A). Comparatively, the recrystallized olivine grains are unstrained, smaller, and display polygonal to curvilinear boundaries that commonly meet to form 120° triple junctions (Figure 3.6B). Diopside grains are small, interstitial to other phases and well-dispersed throughout the sample. These grains display highly irregular to curvilinear boundaries that commonly bulge into other constituent grains. Enstatite grains may be small, but there are several large grains that occur in clusters throughout the sample. These grains have lobate – cuspate boundaries and are mostly strain-free, although faint deformation twins are observed in a few grains. Bulging relationships in this sample are complex with each phase seeming to indiscriminately bulge into other phases (Figure 3.6C). Spinel grains are interstitial and spatially associated with pyroxene grains.

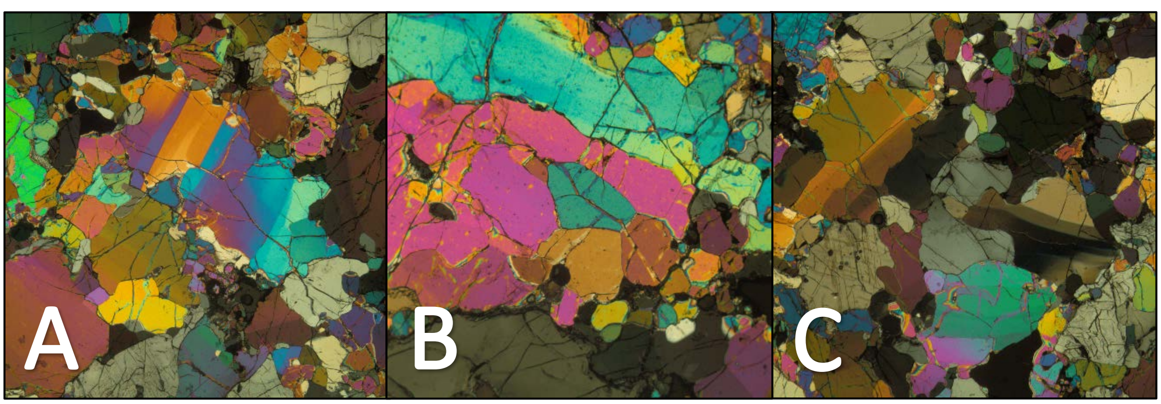

Figure 3.6. Photomicrographs of FDM-AVBB01. (A, 25X) Highly-strained olivine porphyroclast with abundant dislocation walls and a serrated boundary. Grain bulging and subgrain development are also evident. (B, 50X) Smaller olivine grains are free of internal strain and commonly approach 120° triple junctions. (C, 25X) Grain bulging is evident between all constituent phases.

Samples FDM-AVBB02, FDM-AVBB04, FDM-AVBB06, FDM-AVBB07 and FDM-AVBB08 are coarse-granular peridotites with similar microstructures (Figure 3.7). Olivine microstructures include: undulose extinction (Figure 3.7A), well-developed triple junctions in strain-free grains (Figure 3.7B), curvilinear to irregular grain boundaries in strained grains (Figures 3.7A, C, E, F, G, and I), dislocation walls (Figures 3.7C, E, F, G and I), and triple junctions approaching 120° intersections (Figure 3.7E). Large enstatite grains have irregular boundaries and deformation twins (Figures 3.7D and E). Rare subgrain development is noted in enstatite grains (Figure 3.7E). Diopside generally occurs interstitially, but some large grains have exsolution lamellae and irregular boundaries that bulge into adjacent grains (Figure 3.7H). Spinel grains are interstitial and spatially associated with pyroxenes.

Sample FDM-AVBB05 is a coarse-tabular lherzolite with aligned spinel trails and a weak olivine fabric (Figure 3.8). Olivine microstructures include dislocation walls and linear to curvilinear boundaries that often join to form 120° triple junctions. Boundaries between adjacent olivine grains are linear, whereas boundaries between olivine and pyroxene are curvilinear to irregular. Neither pyroxene shows any deformational microstructures except for grain bulging. Both pyroxene phases occur as relatively large grains throughout the sample, but the boundaries of large enstatite grains are irregular to serrated, whereas the grain boundaries of diopside and smaller enstatite grains are curvilinear.

Sample FDM-AVBB03 is a spinel websterite and is the only pyroxenite from Mount Avers – Bird Bluff (Figure 3.9). This sample has the greatest equilibration temperature, and is thus interpreted to have been extracted from the greatest depth (i.e. 66 km) of the xenoliths from this volcanic center. Although grain size distributions are not constructed for this

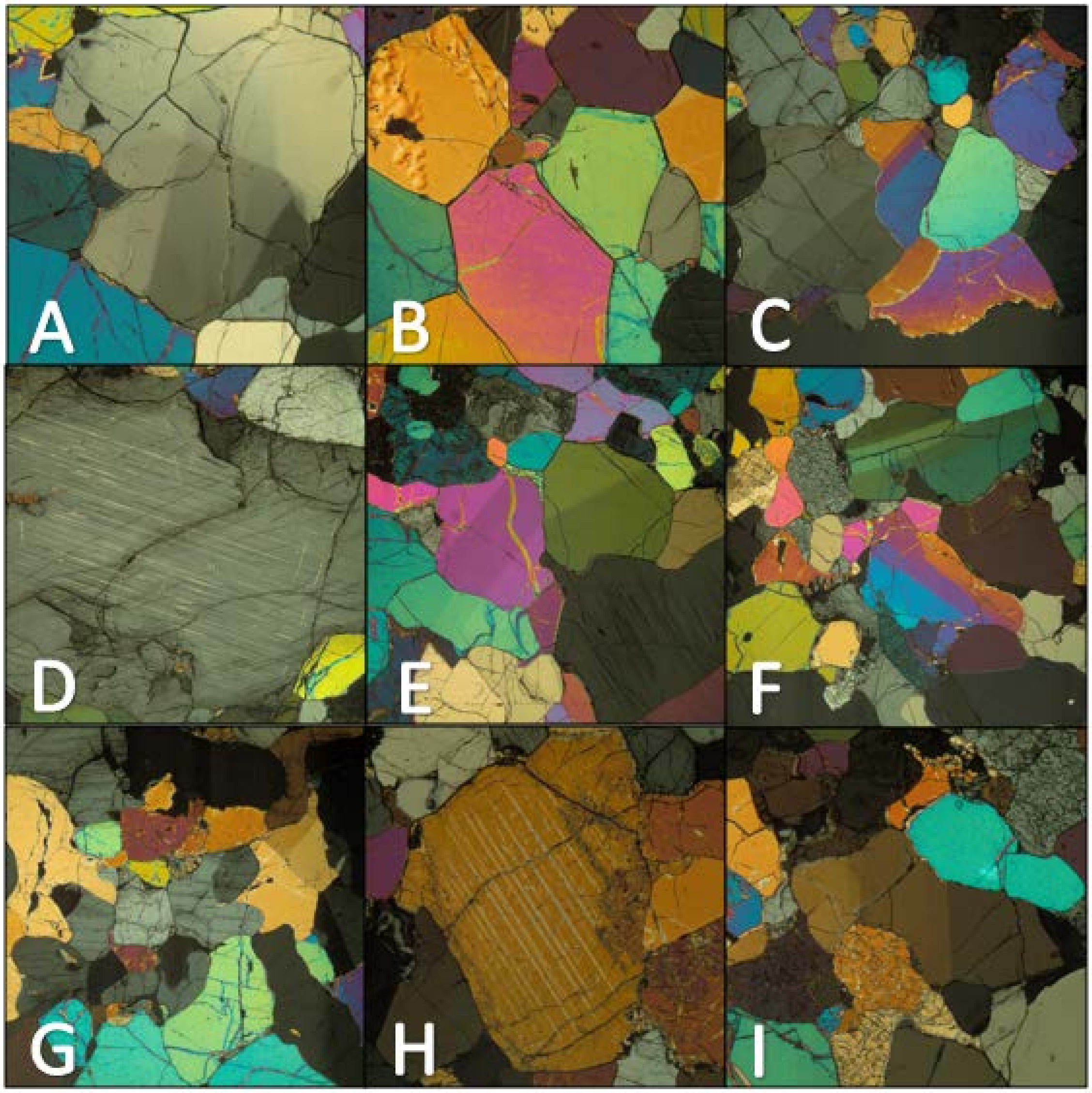

Figure 3.7. Photomicrographs of microstructures displayed by the coarse-granular peridotites sourced from Mount Avers – Bird Bluff. (A, 50X) Olivine grain in sample FDM-AVBB02, which displays undulose extinction and irregular to curvilinear boundaries. (B, 50X) Well-developed 120° triple junctions in olivine grains from sample FDM-AVBB02. (C, 25X) Olivine grains from sample FDM-AVBB04 contain abundant dislocation walls, have irregular boundaries and show evidence for subgrain development. (D, 25X) Deformation twins form in an irregularly shaped enstatite grain from sample FDM-AVBB04. (E, 25X) A combination of curvilinear and irregular grain boundaries are displayed by sample FDM-AVBB06. Some olivine grains contain dislocation walls and are forming triple junctions that approach a 120° intersection. Enstatite displays deformation twins. (F, 25X) Highly strained olivine grains in sample FDM-AVBB07 have strongly oriented dislocation walls, irregular boundaries and show evidence for subgrain development. (G, 25X) Enstatite forms subgrains in sample FDM-AVBB07. (H, 50X) Large grains of diopside in sample FDM-AVBB08 contain deformation twins. (I, 50X) Olivine grains in sample FDM-AVBB08 have well-developed dislocation walls and irregular boundaries.

sample and a large range of grain sizes is observed for both pyroxenes, the grain size trends observed in the rest of the Mount Avers – Bird Bluff suite hold true. Enstatite constitutes the largest grain size fraction of this sample and diopside constitutes the smallest grain size fraction. Exsolution lamellae are abundant in both diopside and enstatite grains. Grain boundaries are spatially variable throughout the thin section with cuspate – lobate, linear to curvilinear and irregular boundaries observed. The predominance of equilibrium textures also varies spatially in thin section - some portions display one- and two-pyroxene 120° triple junctions, whereas others are dominated by irregular to serrated boundaries.

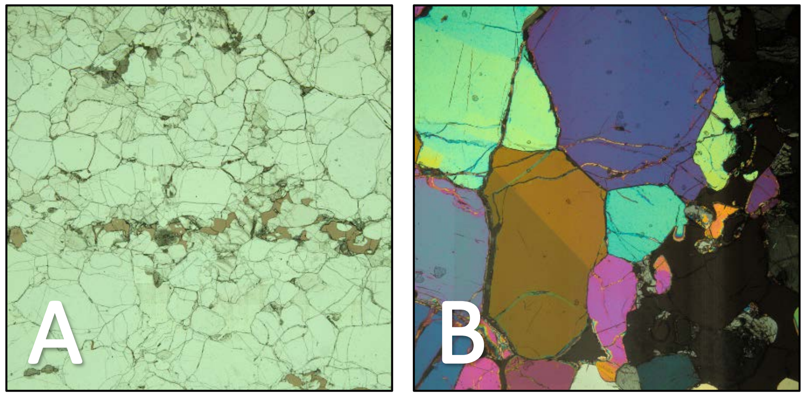

Figure 3.8. Photomicrographs of sample FDM-AVBB05. (A, 12.5X) Photomicrograph showing the presence of spinel trains. (B, 25X) Photomicrograph showing olivine grains that have widely spaced dislocation walls and form 120° triple junctions.

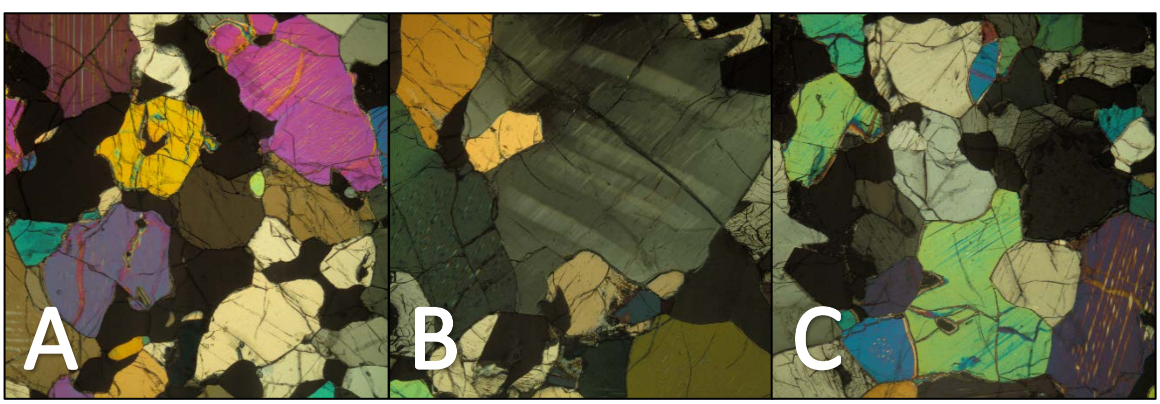

Figure 3.9. Photomicrographs (25X) of sample FDM-AVBB03. (A) Exsolution lamellae in diopside grains that display cuspate – lobate and linear to curvilinear boundaries. There are also isolated examples of 120° triple junctions in this portion of the thin section. (B) Exsolution lamellae in a large enstatite grain, which displays an irregular grain boundary. (C) Pyroxenes in this portion of the thin section dominantly display linear to curvilinear boundaries, which frequently form 120° triple junctions.

3.2.5 Bird Bluff, Fosdick Mountains

The four samples from Bird Bluff are spinel-bearing peridotites ranging in composition from lherzolitic to dunitic, with one sample of intermediate composition being wehrlitic. These samples contain 53.2 – 92.9% olivine, 1.3 – 23.9% enstatite, 2.4 – 42.1% diopside and 0.4 – 2.0% spinel and have equilibration temperatures between 853 and 1053°C, which corresponds to a depth range extending from 45 to 60 km.

Grain size distributions are only generated for the samples from this volcanic center that are successfully reoriented into their kinematic frame of reference using XRCT. One lherzolitic sample (i.e. FDM-BB04-X01) does not meet this requirement. Minimum and maximum olivine grain sizes range from 55 to 65 μm and 3000 to 6000 μm, respectively. The geometric mean grain size of olivine ranges between 122 and 1180 μm with an average of 541 μm. Minimum and maximum diopside grain sizes range from 60 to 70 and 1500 to 4000, respectively. The mean grain size of diopside in the Bird Bluff xenoliths ranges from 130 to 383 μm with an average of 228 μm. Enstatite grains in these samples display minimum and maximum grain sizes ranging from 60 to 90 μm and 1500 to 3000 μm, respectively. Mean enstatite grain sizes range from 120 to 458 μm with an average of 324 μm. All three silicate phases in the wehrlitic sample from Bird Bluff (FDM-BB01-X01) display similar mean grain sizes, with diopside and olivine grains displaying the largest maximum grain size values. Comparatively, olivine grain sizes are more than 60% larger than the pyroxenes in the dunitic sample (FDM-BB03-X01), whereas the enstatite grains are largest within the successfully oriented lherzolite (FDM-BB02-X01) and their mean grain size exceeds that of olivine by about 20%.

The dunite (FDM-BB03-X01) and the unsuccessfully reoriented lherzolite (FDM-BB04-X01) from Bird Bluff are both sourced from a depth of 45 km within the lithospheric mantle. Despite this similarity, these samples are compositionally heterogeneous and preserve different microstructures that are evident in thin section. In terms of its microstructures, sample FDM-BB03-X01 is a coarse-granular dunite that is characterized by large olivine grains with infrequent dislocation walls and sparse evidence for grain bulging (Figure 3.10A). Olivine grains typically display linear to curvilinear boundaries that approach 120° triple junctions when it is the only phase along the interface (Figure 3.10B), whereas the pyroxenes display more irregular grain boundaries (Figure 3.10C).

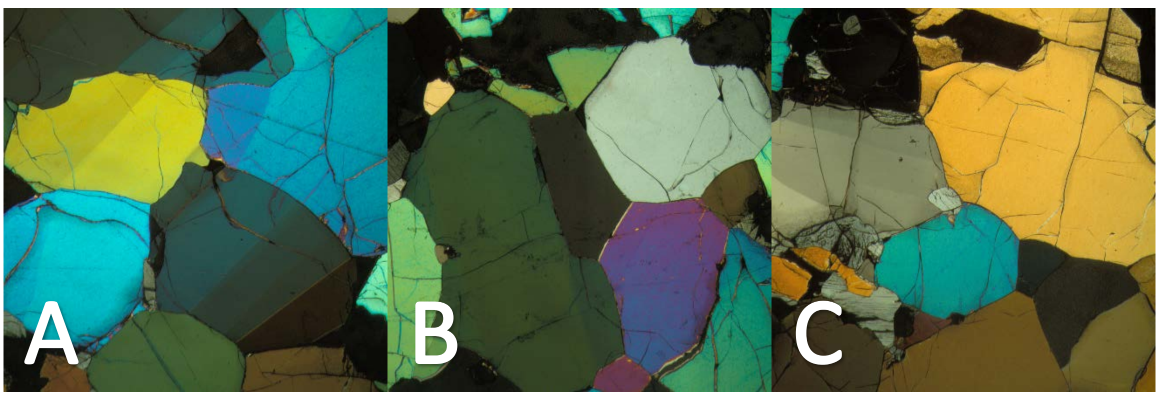

Figure 3.10. Photomicrographs of FDM-BB03-X01. (A, 25X) Dislocation walls and olivine are rarely present in olivine. (B, 25X) Olivine grain boundaries are linear to curvilinear and commonly approach 120° triple junctions when in exclusive contact with other olivine grains. (C, 25X) Grain boundaries are more irregular along pyroxene interfaces.

Compared to the dunite, the lherzolite from the same depth (FDM-BB04-X01) contains smaller grains that preserve microstructural evidence that implies strain is more unevenly distributed within this sample. Unlike the dunite, deformation twins are preserved in both pyroxenes (Figure 3.11A), which is likely a function of their abundance in a fertile lherzolite. Both grain bulging and dislocation walls are more commonly documented in this sample and have led to the formation of subgrains (Figure 3.11B). Grain boundaries within this sample are mostly irregular, but it is important to note that when three olivine grains meet at a triple junction they sometimes approach 120° intersections (Figure 3.11C), which is similar to what is documented for sample FDM-BB03-X01.

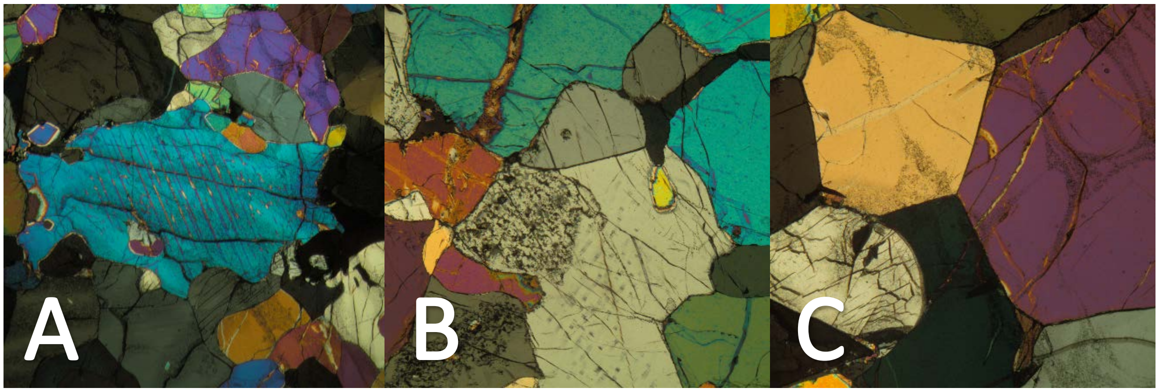

Figure 3.11. Photomicrographs of sample FDM-BB04-X01. (A, 25X) Deformation twins in a diopside grain that is characterized by highly irregular boundaries. (B, 50X) Grain bulging is common and leads to the formation of subgrains. (C, 50X) Triple junctions infrequently meet to for 120° angles when three olivine grains come into contact with one another.

Sample FDM-BB01-X01 is a coarse-grained wehrlite sourced from a depth of 51 km that is characterized by the abundant presence of dislocation walls in olivine and irregular grain boundaries that commonly bulge into adjacent grains (Figure 3.12A). These microstructures are remarkably similar to those observed in sample FDM-BB02-X01 – a coarse-grained lherzolite sourced from a depth of 60 km – but grain boundaries tend to be more curvilinear rather than irregular (Figure 3.12B). Furthermore, some of the larger enstatite grains within this sample display undulose extinction, which indicates that the crystal lattice is accommodating some of the imposed strain via the movement of dislocations. It is also important to note that this lherzolitic sample preserves larger grains with wider ranges of grain sizes and contains enstatite that displays undulose extinction (Figure 3.12C).

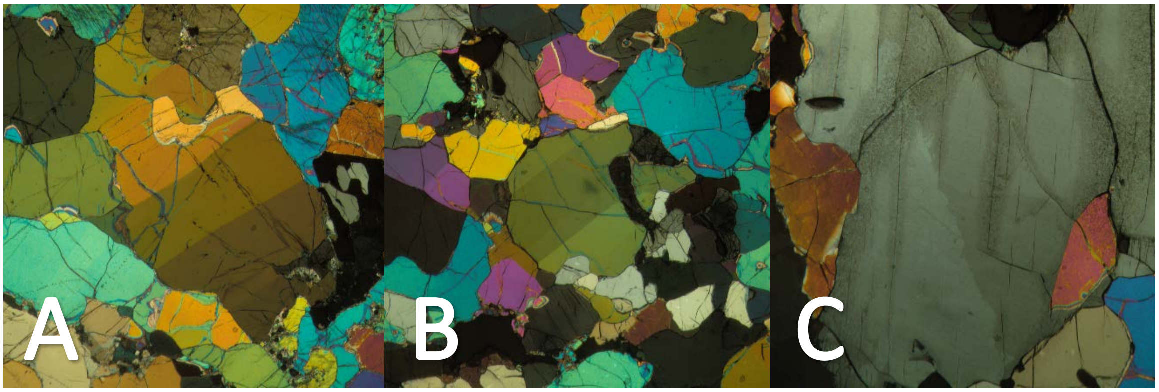

Figure 3.12. Photomicrographs of FDM-BB01-X01 and FDM-BB02-X01. (A, 25X) Sample FDM-BB01-X01 contains abundant dislocation walls and irregular grain boundaries that commonly bulge. (B, 25X) Sample FDM-BB02-X01 preserves similar microstructures, but contains grain boundaries that tend toward curvilinear. (C, 50X) Sample FDM-BB02-X01 contains enstatite grains that display undulose extinction.

3.2.6 Demas Bluff, Fosdick Mountains

A significant proportion of the samples within the MBL xenolith suite are sourced from Demas Bluff (n=20), which necessitates discussing their mineralogical and microstructural characteristics by grouping the samples based on their lithology (e.g., lherzolite). The Demas Bluff spinel-bearing ultramafic xenoliths are comprised of: fourteen lherzolites, four harzburgites, one dunite and one clinopyroxenite. It is important to note that Demas Bluff is unique as it is the only volcanic center from which harzburgites are sourced. The samples from this location have equilibration temperatures ranging from 803 to 1198°C, which correspond to extraction depths between 41 and 72 km.

3.2.6.1 Lherzolites

The mineralogy of the spinel-bearing lherzolites from Demas Bluff varies between 48.0 – 78.7% olivine, 12.5 – 30.3% enstatite, 6.1 – 23.3% diopside and 0.2 – 4.5% chromite. Equilibration temperatures for these samples range from 861 – 1198°C, which corresponds to extraction depths between 57 and 98 km. Olivine grains display minimum and maximum grain sizes ranging from 60 to 80 μm and 1000 to 9000 μm, respectively. The geometric mean grain size of the olivine within these rocks ranges from 100 to 1610 μm and has an average of 764 μm. Enstatite grains have minimum and maximum grain sizes ranging from 60 to 200 μm and 2000 to 9000 μm, respectively. The geometric mean grain size of enstatite ranges from 444 to 1160 μm and has an average value of 754 μm, which is almost the same as the average geometric mean grain size determined for the olivine grains in the lherzolites. Comparatively, diopside is a smaller phase and displays minimum and maximum grain sizes that range from 60 to 100 μm and 1500 to 5000 μm, respectively. The geometric mean grain size of diopside ranges from 150 to 865 μm and has an average of 393 μm, which is approximately half the grain size of the other constituent mineral phases.

Due to the large number of lherzolites sourced from Demas Bluff (n=14), their variations with respect to mineralogy and preserved microstructures are discussed in order of increasing extraction depth (Table 3.4). Although there are microstructural variations that exist between individual xenolith samples, the Demas Bluff lherzolites can be generally classified as having coarse-granular and tabular microstructures that are interpreted to have formed in response to changes in the conditions of deformation with depth. Pyroxenes commonly contain deformation twins and grains of chromite within these samples tend to be interstitial and randomly distributed. Exceptions to these observations are discussed on a case-by-case basis. Furthermore, it is important to note that the error associated with the geothermometry is not currently being considered during this assessment. Thus, it must be remembered that samples having

Table 3.4. The microstructures preserved by the Demas Bluff lherzolites (n=14) are discussed in order of increasing extraction depth.

Sample	Extraction Depth (km)
FDM-DB03-X02	44
FDM-DB02-X13	49
FDM-DB02-X04	50
FDM-DB03-X03	54
FDM-DB04-X02	54
FDM-DB02-X03	55
FDM-DB04-X01	55
FDM-DB03-X04	56
FDM-DB02-X10	57
FDM-DB01-X01	58
FDM-DB02-X11	59
FDM-DB02-X12	59
FDM-DB02-X01	71
FDM-DB02-X06	72

similar extraction depths may have actually been extracted from the same depth within the lithospheric mantle of MBL.

Sample FDM-DB03-X02 is a coarse-granular lherzolite containing 54.2% olivine, 41.2% pyroxene (22.1% enstatite and 19.1%) diopside and 4.5% chromite. Olivine grains in this sample are dominated by linear to curvilinear boundaries and often contain dislocation walls. Comparatively, diopside and enstatite grains are characterized as having irregular grain boundaries (Figure 3.13). Although examples do exist, grains of different phases infrequently meet to form 120° triple junctions. It is more common to observe this microstructure forming between three adjacent grains of olivine. The major mineral phases in this sample are similarly sized with the geometric mean grain sizes of olivine, diopside and enstatite grains being equal to 545 μm, 470 μm and 601 μm, respectively.

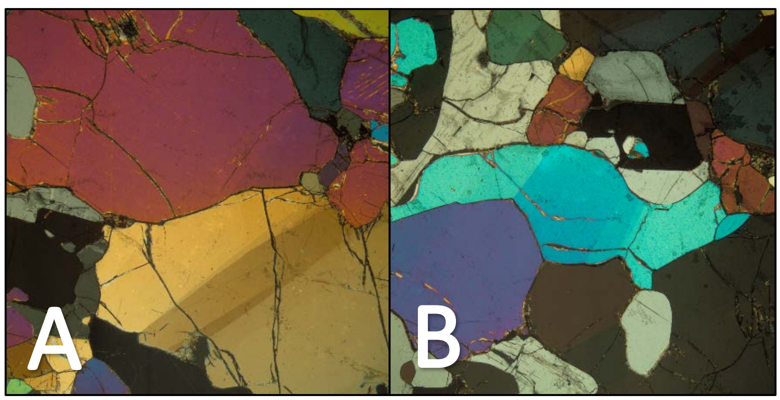

Figure 3.13. Photomicrographs (25X) of sample FDM-DB03-X02. (A) Dislocation walls in olivine. (B) Grain boundaries rarely form 120° triple junction, but some examples are observed. Pyroxenes are generally characterized by irregular grain boundaries.

Sample FDM-DB02-X13 is a coarse-granular lherzolite containing 71.0% olivine, 26.5% pyroxene (13.7% enstatite and 12.8% diopside) and 2.5% chromite. This xenolith was extracted from a similar depth as sample FDM-DB02-X04, which is also a coarse-granular lherzolite. Despite this, sample FDM-DB02-X04 differs from FDM-DB02-X13 in terms of both its mineralogy (i.e. 60.9% olivine, 23.0% enstatite, 14.9% diopside and 1.2% chromite) and its preserved microstructures. Olivine grains in FDM-DB02-X13 tend to have linear grain boundaries and commonly meet to form 120° triple junctions (Figure 3.14A), whereas olivine grains in FDM-DB02-X04 are characterized by irregular boundaries (Figure 3.14B). Both samples are characterized by irregularly-shaped pyroxenes that bulge into adjacent grains and the presence of dislocation walls in olivine, although only sample FDM-DB02-X04 contains evidence for well-developed olivine subgrains (Figure 3.14C). The olivine grains in sample FDM-DB02-X13 have a geometric mean grain size of 933 μm, which is approximately twice that of either diopside (480 μm) or enstatite (471 μm).The grains in FDM-DB02-X04 are generally larger, but olivine displays the largest geometric mean grain size (1230 μm). Despite this, the geometric mean grain sizes of both diopside (865 μm) and enstatite (902 μm) are larger relative to the geometric mean grain size of olivine in this sample.

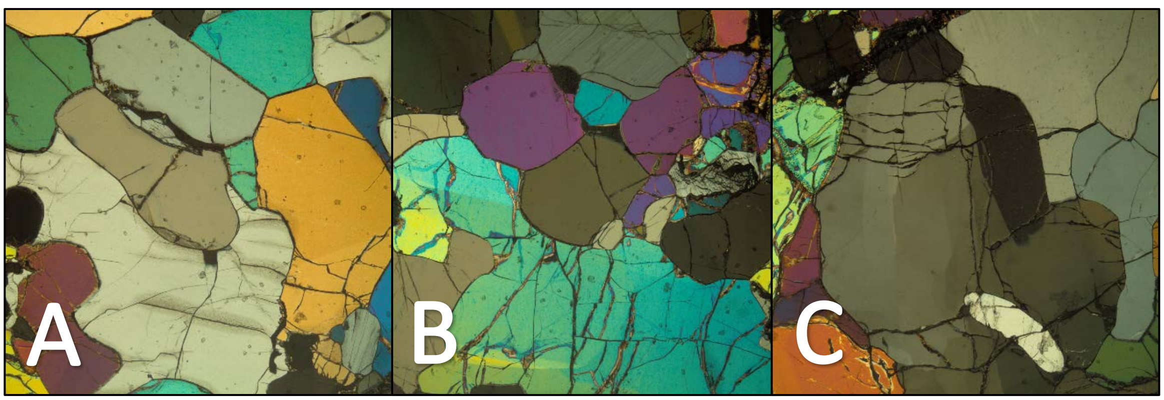

Figure 3.14. Photomicrographs (25X) of samples FDM-DB02-X13 and FDM-DB02-X04. (A) Well-developed 120° triple junctions and linear boundaries are observed in the olivine grains of FDM-DB02-X13, whereas pyroxene grains are defined by having highly irregular boundaries that commonly bulge into adjacent grains. (B) Some olivine grains within sample FDM-DB02-X13 contain a significant amount of internal strain, which is clearly shown by the yellow and blue deformation bands. (C) Well-developed olivine subgrains.

Samples FDM-DB03-X03 and FDM-DB04-X02 are coarse-granular lherzolites that are both inferred to have been extracted from a depth of 54 km. Although these samples vary slightly with respect to their mineralogies (i.e. FDM-DB03-X03 is ca. 9% more olivine rich, whereas FDM-DB04-X02 is ca. 9% more enstatite rich), both are classified as having a coarse-granular microstructure. Olivine grains display grain boundaries that vary between linear, curvilinear and/or lobate-cuspate (Figure 3.15). Linear boundaries are generally associated with strain-free grains and meet to form 120° triple junctions, whereas curvilinear and lobate-cuspate boundaries are generally associated with highly-strained grains that bulge into adjacent grains. These samples also contain evidence for the development of dislocation walls and subgrains in olivine grains. Comparatively, grains of pyroxene display irregularly-shaped grain boundaries and contain characteristic deformation twins. Olivine grains are the largest in sample FDM-DB03-X03 and display a geometric mean grain size of 898 μm, which is nearly twice the geometric mean grain size of both diopside (405 μm) and enstatite (553 μm). Comparatively, sample FDM-DB04-X02 is characterized by having large grains of enstatite (1040 μm), with smaller grains of olivine (647 μm) and even smaller grains of diopside (150 μm).

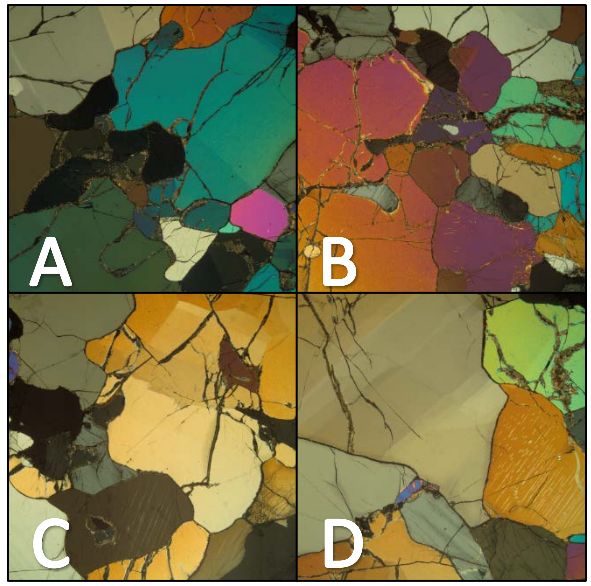

Figure 3.15. Photomicrographs (25X) of samples FDM-DB03-X03 (A and B) and FDM-DB04-X02 (C and D). (A) Olivine grains contain dislocation walls and display a wide range of boundary relationships between adjacent grains. (B) Linear grain boundaries are commonly associated with strain-free grains and form 120° triple junctions.

Samples FDM-DB02-X03 and FDM-DB04-X01 are also coarse-granular lherzolites that are interpreted to be extracted from the same depth within the MBL lithosphere (i.e. 55 km). In terms of their mineralogies, these samples are similar with the primary exception being that

FDM-DB02-X03 is negligibly more diopside rich (ca. 4%), whereas FDM-DB04-X01 contains slightly more (ca. 6%) olivine. Microstructurally, both samples are characterized by abundant 120° triple junctions, linear to curvilinear boundaries and the occasional presence of widely-spaced dislocation bands in olivine (Figure 3.16).

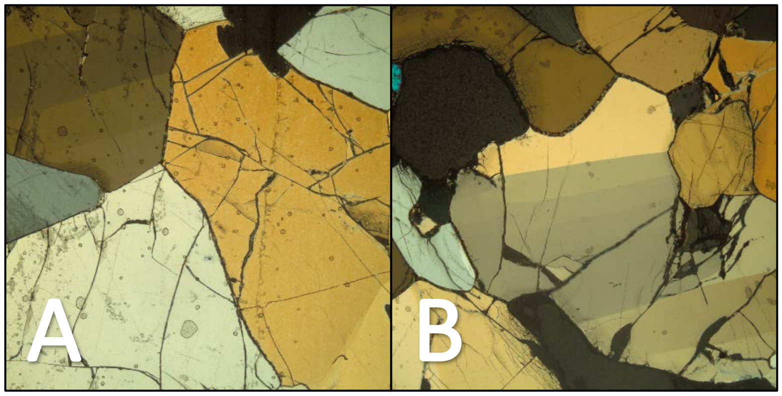

Figure 3.16. Photomicrographs (25X) of samples (A) FDM-DB02-X03 and (B) FDM-DB04-X01, which show dislocation bands in olivine and the prevalence of 120° triple junctions.

Sample FDM-DB03-X04 is interpreted to be sourced from a similar depth as these xenoliths. In terms of its mineralogy, this sample is nearly identical to FDM-DB04-X01. Microstructurally, this sample contains the same features described above, but is classified as having a tabular microstructure due to the presence of spinel trains (Figure 3.17). Based on the geometric mean grain sizes calculated for these samples, there is considerable variation with respect to the sizes of their constituent mineral grains. Sample FDM-DB02-X03 contains small grains of olivine (210 μm), with larger grains of diopside (500 μm) and even larger grains of enstatite (960 μm). Although the observed grain sizes are smaller for sample FDM-DB03-X04, the same relative size difference between olivine and the pyroxenes is observed. In the case of this sample, the geometric mean grain sizes of olivine, diopside and enstatite are 100 μm, 297 μm and 524 μm, respectively. Unlike the other two

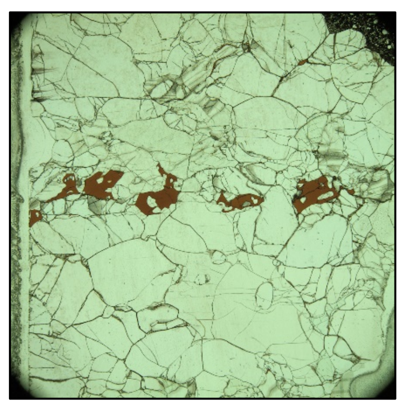

Figure 3.17. Photomicrograph (12.5X) of sample FDM-DB03-X04 showing the spinel trails observed in thin section.

samples extracted from this approximate depth, olivine grains are largest in sample FDM-DB04-X01 and have a geometric mean grain size of 1450 μm. The geometric mean grain size of enstatite is slightly smaller (1100 μm) and that of diopside is significantly smaller (491 μm). In all three cases, the calculated geometric mean grain size of diopside is approximately half that of enstatite.

Samples FDM-DB02-X10, FDM-DB01-X01, FDM-DB02-X11 and FDM-DB02-X12 are all coarse-granular lherzolites that are interpreted to have been extracted from slightly greater depths of the MBL lithosphere (i.e. 57 – 59 km). In terms of their respective mineralogies, these samples are quite diverse. Sample FDM-DB01-X01 is relatively olivine-poor (59.2%) and contains the most pyroxene (34.3%) and chromite (3.1%), whereas sample FDM-DB02-X11 is more olivine-rich (71.0%) and contains the least pyroxene (28.1%). Comparatively, samples FDM-DB02-X10 and FDM-DB02-X12 have compositions that fall between the two endmember cases, with the only difference between them being that FDM-DB02-X10 is significantly more depleted with respect to chromite (0.1%) than FDM-DB02-X12 (2.7%). Microstructurally, sample FDM-DB02-X10 contains olivine grains that display dislocation walls and the development of subgrains. Most grain boundaries are lobate – cuspate, although some are linear to curvilinear in nature and rarely meet to form 120° junctions (Figure 3.18A). In addition to the aforementioned microstructures, sample FDM-DB01-X01 contains enstatite grains with deformation twins and infrequently displays examples of 120° triple junctions (Figure 3.18B). Comparatively, samples FDM-DB02-X11 and FDM-DB02-X12 are characterized by the presence of dislocation walls in olivine, the predominance of linear to curvilinear boundaries and grains that commonly meet to form 120° triple junctions (Figure 3.18C). The geometric mean grain sizes of olivine, diopside and enstatite in sample

FDM-DB02-X10 are equal to 736 μm, 236 μm and 1000 μm, respectively. The largest grains contained within this sample are made of enstatite, whereas the largest constituent grains of the other three samples are made of olivine. The geometric mean grain sizes of olivine in samples FDM-DB01-X01 and FDM-DB02-X12 are equal to 885 μm and 599 μm, respectively. Furthermore, the diopside in these two samples have geometric mean grain sizes that are only slightly smaller (ca. 70 μm) than those of enstatite. Comparatively, sample FDM-DB02-X11 has a geometric mean olivine grain size of 1610 μm and a geometric mean diopside grain size (302 μm) that is approximately 40% that of enstatite (795 μm).

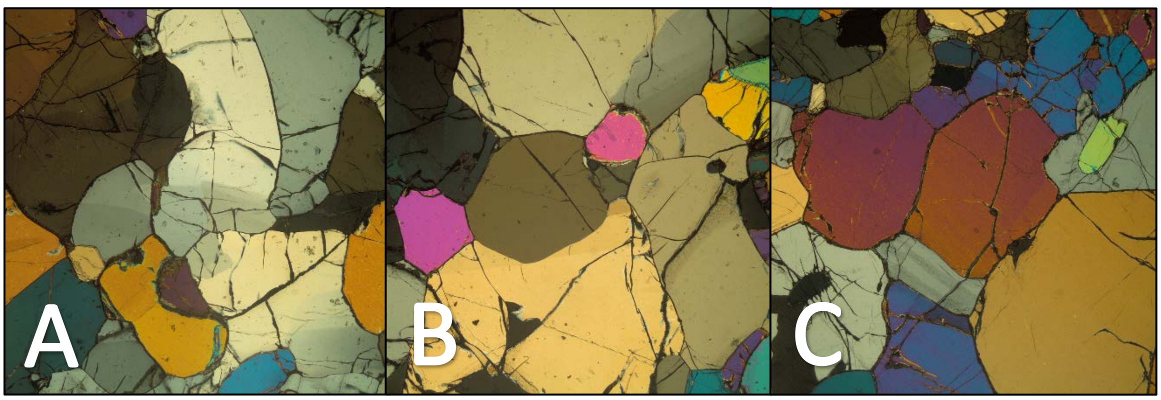

Figure 3.18. Photomicrographs (25X) of (A) FDM-DB02-X10 showing the development of dislocation walls and subgrains in olivine with rare examples of 120° triple junctions, (B) FDM-DB01-X01 showing the presence of dislocation walls and more abundant examples of 120° triple junctions, and (C) FDM-DB02-X11 showing the characteristic microstructures of this sample and FDM-DB02-X12, which both contain linear to curvilinear boundaries are more abundant 120° triple junctions.

Samples FDM-DB02-X01 and FDM-DB02-X06 are the most deeply-sourced xenolith samples from MBL and are interpreted to be extracted from depths of 71 and 72 km, respectively. These xenoliths vary considerable in their mineralogies; FDM-DB02-X01 contains 69.6% olivine, 29.5% pyroxene (14.4% enstatite and 15.1% diopside; approximately equal amounts) and 0.9% chromite, whereas FDM-DB02-X06 contains 48.0% olivine, 51.9% pyroxene (44.6% enstatite and 7.3% diopside; significantly depleted with respect to diopside) and 0.1% chromite. Microstructurally, sample FDM-DB02-X01 is a coarse-granular lherzolite that displays linear to curvilinear and lobate – cuspate boundaries, dislocation walls in olivine, and undulose extinction in enstatite. Although some exceptions exist, most grains in this sample do not meet to form 120° triple junctions (Figure 3.19). Sample FDM-DB02-X06 is also a coarse-granular lherzolite, but it preserves different microstructures. Specifically, this sample is dominated by lobate – cuspate grain boundaries, which form as highly-strained grains bulge into adjacent grains that have less stored strain in their crystal lattice. Olivine grains in this sample display dislocation walls and develop subgrains, especially when the adjacent grains are pyroxenes (Figure 3.20). Furthermore, the geometric mean grain sizes observed in these two samples are quite different. Sample FDM-DB02-X01 displays a geometric mean olivine grain size of 494 μm, which is quite similar to that of enstatite (484 μm), whereas diopside grains are smaller (ca. 100 μm). Comparatively, the largest grains in sample FDM-DB02-X06 are enstatite, which display a geometric mean grain size of 1160 μm. Olivine is significantly smaller and displays a geometric mean grain size of 356 μm, whereas diopside is again the smallest phase with a geometric mean grain size of 102 μm.

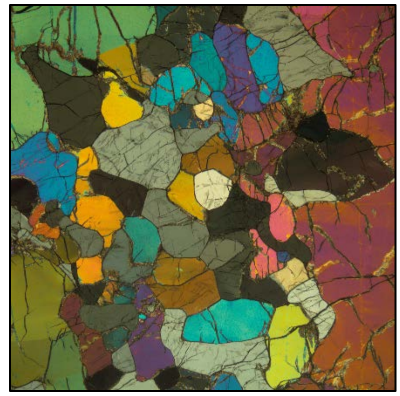

Figure 3.19. Photomicrograph (25X) of FDM-DB02-X01 showing the character of its grain boundaries and the rare occurrence of 120° triple junctions.

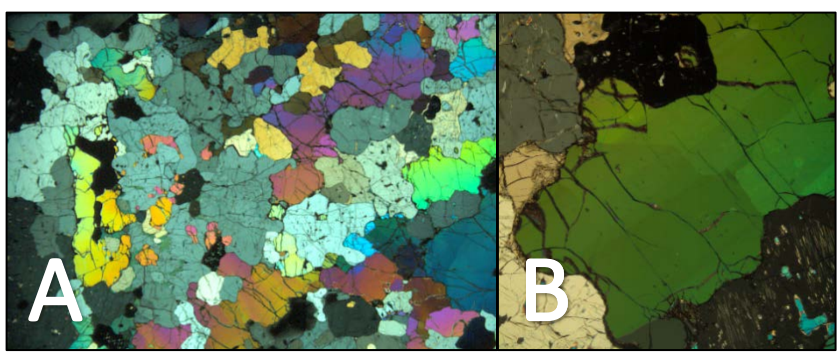

Figure 3.20. Photomicrographs of sample FDM-DB02-X06. (A, 12.5X) Grain boundaries that are typical of this sample. (B, 25X) Subgrains in an olivine grain that is adjacent to grains of pyroxene.

3.2.6.2 Harzburgites

The mineralogical composition of the four spinel-bearing harzburgites from Demas Bluff ranges from 77.3 – 87.8% olivine, 9.8 – 19.5% enstatite, 1.6 – 3.2 diopside and 0.2 – 1.0% chromite. These samples are the only samples within the MBL xenolith suite that are classified as harzburgites and their equilibration temperatures range from 803 - 1102°C, which corresponds to extraction depths between 41 and 69 km. Olivine grains display minimum and maximum size ranges of 60 to 90 μm and 7000 to 9000 μm, respectively. The geometric mean grain size of olivine ranges from 1310 to 2000 μm and has an average value of 1495 μm. In addition to being the most abundant mineral, olivine is also the phase that displays the largest grain sizes. Enstatite is far less abundant than olivine, but displays minimum and maximum grain size ranges of 90 to 200 μm and 4000 to 7000 μm, respectively. The geometric mean grain size of enstatite ranged from 594 to 1200 μm and has an average value of 1239 μm, which is only marginally smaller than the average geometric mean grain size of olivine. Although harzburgites are clinopyroxene-poor peridotites, the grain size distribution of diopside is evaluated for these samples. The minimum and maximum size of diopside grains range from 60 – 100 μm and 1000 – 2000 μm, respectively. The geometric mean grain size of diopside ranges from 100 to 600 μm and has an average of 234 μm, which is significantly smaller than the sizes obtained by the phases that have not been depleted from the rock (i.e. olivine and enstatite).

All of the harzburgites have tabular microstructures, which is based on the alignment of elongated olivine grains in thin section (Figure 3.21). Sample FDM-DB02-X02 is dominated by lobate – cuspate grain boundaries, but linear boundaries separate some aligned grains of olivine. Olivine generally displays dislocation walls, although some display undulatory extinction (Figure 3.22A). Samples FDM-DB02-X08 and FDM-DB04-X04 contain similar microstructures to FDM-DB02-X02, but they contain a moderate amount of 120° triple junctions and display linear grain between aligned olivine grains. Unlike the other harzburgites, sample FDM-DB04-X03 preserves aligned grains of both olivine, enstatite and diopside (Figure 3.22B). Otherwise, it is microstructurally similar to samples FDM-DB02-X08 and FDM-DB04-X04. Three of the harzburgites have large geometric mean olivine grain sizes with marginally smaller geometric mean enstatite grain sizes, and small (ca. 100 μm) geometric mean diopside grain sizes. Comparatively, sample FDM-DB02-X02 contains the largest geometric mean olivine grain size of the MBL xenolith suite (2000 μm), but displays a geometric mean enstatite grain size (594 μm) that is approximately 70% smaller than that of olivine.

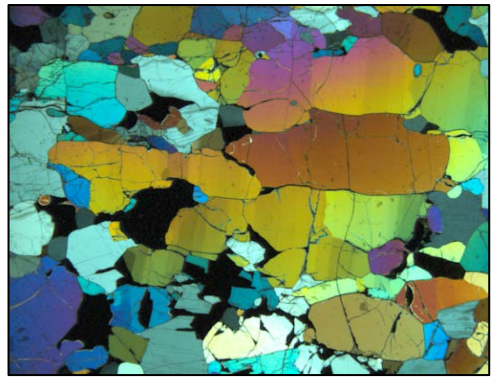

Figure 3.21. Photomicrograph (12.5X) showing the alignment of elongated olivine grains in sample FDM-DB02-X08.

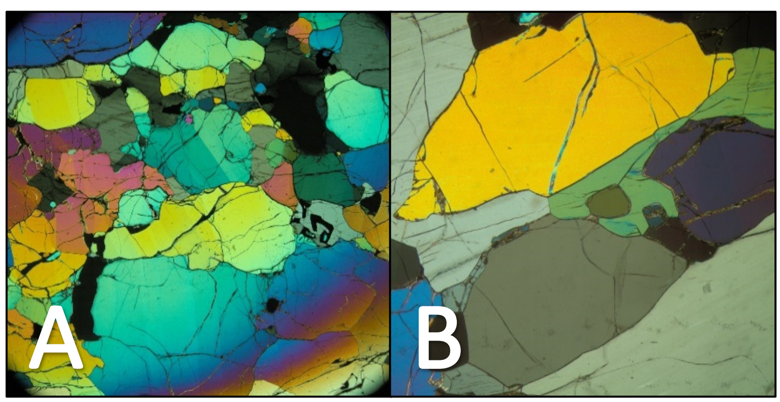

Figure 3.22. (A, 12.5X) Photomicrograph of sample FDM-DB02-X02 showing dislocation walls and undulatory extinction in olivine. (C, 25X) Photomicrograph of FDM-DB04-X03 showing aligned grain boundaries between olivine, enstatite and diopside.

3.2.6.3 Dunite

The spinel-bearing dunite from Demas Bluff (FDM-DB03-X01) contains 89.8% olivine, 6.9% enstatite, 1.9% diopside and 1.4% chromite. When these values are normalized for plotting on an IUGS ternary diagram, they become 91.1% olivine, 7.0% enstatite and 1.9% diopside. This sample straddles the mineralogical threshold between being a dunite and a harzburgite, and is in fact quite similar in composition to the most depleted harzburgite of the MBL xenolith suite (FDM-DB02-X02). Based on the application of the olivine – spinel geothermometer, this dunite either equilibrated at 862°C (42 km) or 995°C (52 km). This discrepancy is the direct result of this sample containing to spinel grains that contain different concentrations of chromium. Olivine grain sizes in this sample range from 110 to 10000 μm and display a geometric mean grain size of 1460 μm. These are the largest values determined for both the minimum and maximum olivine grain size out of the entire suite of MBL peridotites. Although much less abundant than olivine, enstatite grains are also quite large with sizes ranging from 100 to 4000 μm and a geometric mean of 1150 μm. Diopside grains range in size from 80 to 1500 μm and have a geometric mean of 411 μm, which is significantly smaller than the grain sizes of the other silicate phases.

This tabular xenolith is unique in terms of its preserved microstructures because it contains a quadruple-junction boundary between grains of olivine and enstatite (Figure 3.23A), which is a disequilibrium microstructure that is generally accepted as evidence for the operation of grain-boundary sliding (Ashby and Verrall, 1973). Comparatively, 120° triple junctions are observed between adjacent grains of olivine, which are also characterized by the presence of dislocation walls, evidence for subgrain formation, and curvilinear to linear grain boundaries (Figure 3.23B). Grains of enstatite generally display lobate – cuspate grain boundaries (Figure 3.23C).

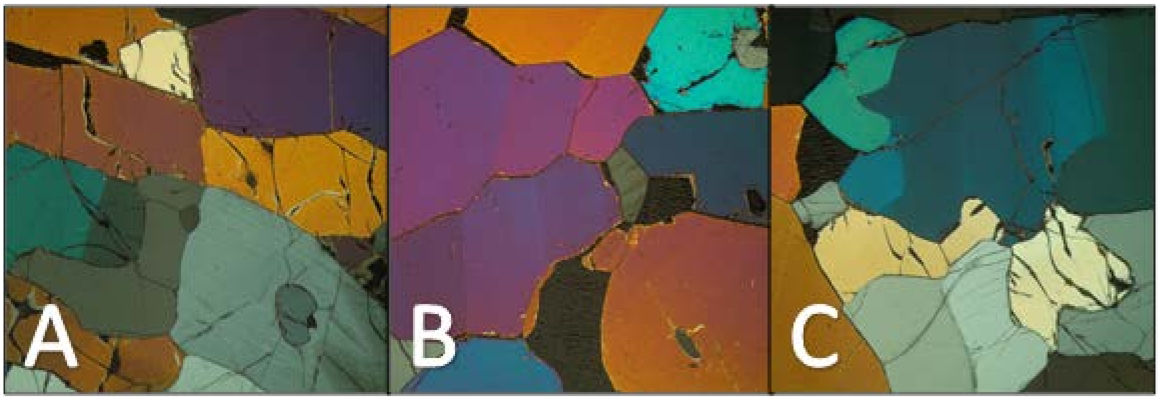

Figure 3.23. Photomicrographs (25X) of the tabular dunite sourced from Demas Bluff (FDM-DB03-X01). (A) Quadruple-junction grain boundary between grains of olivine and enstatite is preserved. (B) Olivine grains that are in contact with other grains of olivine are generally characterized by having dislocation walls, showing evidence for subgrain formation and meeting to form 120° triple junctions. (C) Grains of enstatite have lobate – cuspate grain boundaries.

3.2.6.4 Clinopyroxenite

The spinel-bearing clinopyroxenite from Demas Bluff (FDM-DB02-X05) contains 0.3% olivine, 0.5% enstatite, 95.0% diopside and 4.2% chromite. This sample has an equilibration temperature of 958°C, which corresponds to an extraction depth of 51 km. This sample contains abundant interstitial glass that presumably formed as melt during exhumation and rapidly cooled once at the surface (Figure 3.24A and B). Although infrequent, some diopside grains display minor undulose extinction (Figure 3.24C).

3.2.7 Marujupu Peak, Fosdick Mountains

Four of the five xenoliths sourced from Marujupu Peak are lherzolites and the remaining sample is an olivine websterite. The equilibration temperatures for the lherzolites range from 929 to 1070°C (50 – 61 km), whereas the olivine websterite has an equilibration temperature of 898°C (48 km). In terms of their mineralogies, the lherzolites contain 45.7 –

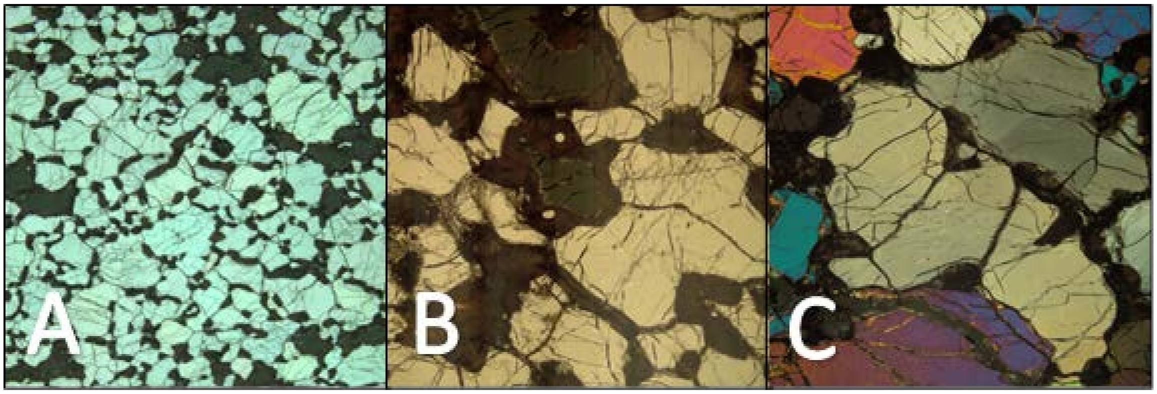

Figure 3.24. Photomicrographs of FDM-DB02-X05. (A, 12.5X) Photomicrograph of the thin section as viewed through plane-polarized light. There is an abundant amount of interstitial glass along grain boundaries. (B, 25X) Photomicrograph viewed through plane-polarized light focusing on chromite grains surrounded by glass. (C, 25X) Photomicrograph viewed through cross-polarized light that shows an example of weak undulose extinction that has developed in diopside.

69.4% olivine, 26.5 – 53.3% pyroxene (8.4 – 29.4% enstatite and 11.8 – 23.9% diopside) and 1.0 – 4.1% chromite. Interestingly, samples FDM-MJ01-X02 and FDM-MJ01-X03 are almost identical in terms of their mineralogies (i.e. 64.8 – 64.9% olivine, 32.7 – 33.2% pyroxene and 2.0 – 2.4% chromite) and have similar equilibration temperatures of 974°C and 929°C, respectively. Comparatively, the olivine websterite contains 29.1% olivine, 64.9% pyroxene (35.7% enstatite and 29.2% diopside) and 6.0% chromite.

The minimum and maximum sizes of olivine grains in the lherzolites range from 60 – 65 μm and 2750 – 5000 μm, respectively. The geometric mean grain size of olivine size ranges from 122 – 600 μm. Diopside grains are generally smaller with minimum, maximum and geometric mean grain sizes ranging from 60 – 70 μm, 1250 – 2000 μm and 127 – 377 μm. Similar to olivine, the grains of enstatite are also relatively large in these samples and display minimum, maximum and geometric mean grain sizes ranging from 60 – 80 μm, 2000 – 7000 μm and 356 – 530 μm, respectively. The geometric mean grain size of the olivine grains in samples FDM-MJ01-X02 (513 μm) and FDM-MJ01-X03 (600 μm) indicates that the olivine grains are the largest in this sample, whereas both enstatite and diopside have smaller geometric mean grain sizes (356 – 480 μm and 315 – 377 μm, respectively). Comparatively, the largest geometric mean grain sizes contained within samples FDM-MJ01-X05 (467 μm) and FDM-MJ01-X06 (530 μm) are displayed by enstatite. The olivine in sample FDM-MJ01-X05 displays a slightly smaller geometric mean grain size (350 μm) than enstatite, which is also larger than that of diopside (186 μm), whereas the olivine in sample FDM-MJ01-X06 is significantly smaller than enstatite (122 μm) and is similar in size to diopside (127 μm).

All of the xenolith samples from Marujupu Peak have coarse-granular microstructures that are characterized by olivine grains containing dislocation walls (Figure 3.22). The grain boundaries preserved in the olivine websterite (FDM-MJ01-X01) generally have a lobate – cuspate appearance, although there are examples of linear boundaries between olivine and enstatite that approach 120° triple junctions (Figure 3.25A). The grain boundaries preserved within the Marujupu Peak lherzolites generally have a more linear geometry. There are also lobate – cuspate boundaries preserved by these xenolith samples, which tend to be more common when adjacent grains are not of the same phase (Figure 3.25B).

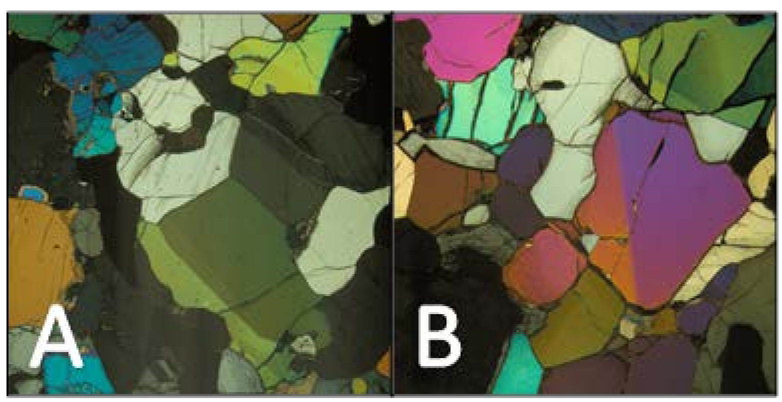

Figure 3.25. Photomicrographs (25X) of xenolith samples sourced from Marujupu Peak, which both show the existence of dislocation walls in olivine. (A) Olivine websterite (FDM-MJ01-X01) dominated by lobate – cuspate grain boundaries with linear boundaries between grains of contrasting phase. (B) Lherzolites are dominated by linear boundaries, but there are examples of lobate – cuspate boundaries, which are favored between grains of contrasting phase.

3.2.8 Recess Nunatak, Fosdick Mountains

Three of the four peridotite samples from Recess Nunatak are lherzolites and the final sample (FDM-RN01-X01) is a wehrlite. The equilibration temperatures for these samples ranges from 812 to 961°C (42 – 52 km), but it should be noted that there is a bimodal distribution of the samples between the extremes of this temperature range. Samples FDM-RN02-X01 and FDM-RN04-X01 equilibrated at the low end (828°C and 812°C, respectively), whereas samples FDM-RN01-X02 and FDM-RN03-X01 equilibrated at the high end (961°C and 943°C, respectively). Due to this observation, these samples are discussed in the aforementioned pairs.

In terms of their mineralogies observed within these xenoliths, FDM-RN02-X01 and FDM-RN04-X01 contain 53.2 – 61.2% olivine, 36.8 – 45.5% pyroxene (14.4 – 27.1% enstatite and 18.4 – 22.4% diopside) and 1.4 – 2.0% chromite. Olivine constitutes the largest grains within these samples with minimum, maximum and geometric mean grain sizes ranging from 60 – 70 μm, 4000 – 4250 μm and 528 – 604 μm, respectively. The diopside grains in sample FDM-RN02-X01 range in size from 60 – 3000 μm and have a geometric mean of 317 μm. Although diopside has a smaller range of grain sizes than that displayed by enstatite (60 – 4000 μm), the geometric mean grain size of enstatite is marginally smaller (297 μm). Comparatively, the enstatite grains in sample FDM-RN04-X01 range in size from 80 – 6000 μm and have a geometric mean grain size of 497 μm. In this case, the diopside grains display a smaller range of grain sizes (60 – 2000 μm) and have a marginally smaller geometric mean grain size (432 μm) compared to enstatite. Both samples FDM-RN02-X01 and FDM-RN04-X01 have a coarse-granular microstructure, which is characterized by the presence of dislocation walls and subgrains in olivine, deformation twins in diopside, and grain boundaries that are variable between curvilinear and lobate – cuspate (Figure 3.26)

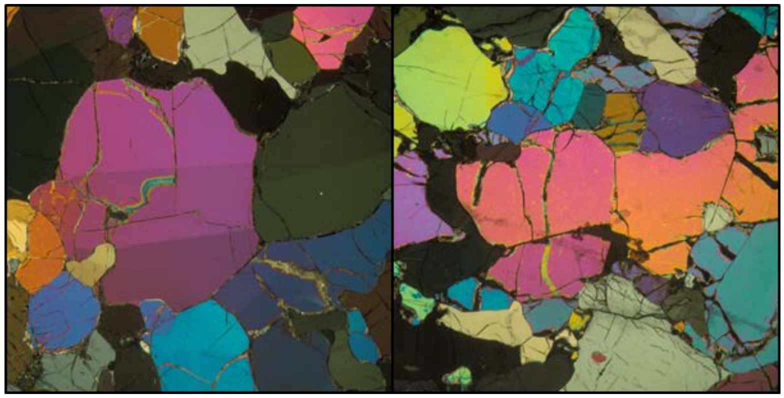

Figure 3.26. Photomicrographs (25X) of the coarse-granular lherzolite samples from Recess Nunatak. (A) FDM-RN02-X01 is a coarse-granular lherzolite that contains olivine with dislocation walls and has grain boundaries that vary from curvilinear to lobate – cuspate. (B) In addition to what is observed in FDM-RN02-X01, sample FDM-RN04-X01 also preserves evidence for the development of olivine subgrains.

Samples FDM-RN01-X01 and FDM-RN03-X01 contain 84.1 – 87.8% olivine, 10.8 – 15.5% pyroxene (1.2 – 9.3% enstatite and 6.2 – 9.6% diopside) and 0.5 – 1.4 chromite. Despite the fact FDM-RN01-X01 is a wehrlite and FDM-RN03-X01 is a lherzolite, both samples are depleted with respect to pyroxene relative to the samples sourced from a shallower depth beneath this volcanic center (i.e. approaching a dunitic composition). The grain sizes observed in the wehrlite are large compared to those in the lherzolite. Olivine grain sizes for sample FDM-RN01-X01 range in size from 70 – 4000 μm and have a geometric mean grain size of 1290 μm. Diopside grains in this sample are significantly smaller as they range in size from 70 – 2000 μm and have a geometric mean grain size of 580 μm. As is expected of the most depleted phase within a sample, the enstatite grains within this sample are the smallest and range in size from 100 – 1500 μm with a geometric mean grain size of 357 μm. Comparatively, the olivine grains in FDM-RN03-X01 are smaller than those observed in the wehrlite and range in size from 70 – 6000 μm with a geometric mean grain size of 406 μm. The enstatite grains within this sample are smaller and range in size from 60 – 5000 μm with a geometric mean grain size of 291 μm. The smallest grains within this sample are diopside, which displays grain sizes ranging from 60 – 3000 μm and has a geometric mean grain size of 115 μm. Sample FDM-RN01-X01 is a porphyroclastic wehrlite (Figure 3.27A). In the sample, the larger grains of olivine contain store more strain energy on their crystal lattice than the smaller subgrains, which is evidenced by the presence of dislocation walls in olivine porphyroclasts and their absence in subgrains. The strained grains preserved within this sample are also generally characterized as having lobate – cuspate grain boundaries (Figure 3.27A), whereas the grain boundaries of unstrained grains are linear to curvilinear and commonly approach or attain 120° intersections at their triple junctions (Figure 3.27B). Comparatively, sample FDM-RN03-X01 is a coarse-granular lherzolite that is microstructurally similar to samples FDM-RN02-X01 and FDM-RN04-X01.

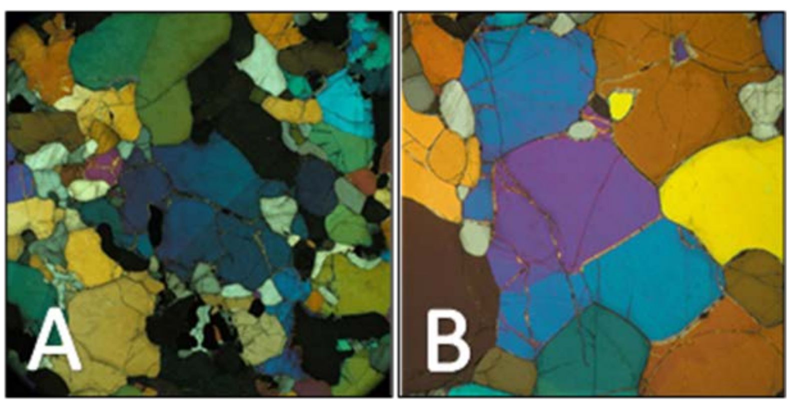

Figure 3.27. Photomicrographs of sample FDM-RN01-X01. (A, 25X) Photomicrograph showing the porphyroclastic texture of this sample, the presence of dislocation walls in olivine and the lobate – cuspate grain boundaries associated with strained grains. (B, 25X) Photomicrograph showing the linear to curvilinear appearance of grain boundaries surrounding unstrained grains.

3.3 OLIVINE CRYSTALLOGRAPHIC PREFERRED ORIENTATION AND TEXTURAL STRENGTH

The crystallographic preferred orientation (CPO) of the constituent silicate phases is quantified for all peridotite samples that meet two important criteria (n=38): (1) the sample must be reoriented into its fabric frame of reference successfully and (2) it must contain a sufficient amount of grains of each phase to quantitatively assess its textural strength (i.e. J- and M-indices) and the symmetry of its crystallographic axes (i.e. the BA-index; Figure 3.28). Two lherzolite samples sourced from Demas Bluff (FDM-DB02-X06 and FDM-DB03-X04) do not fit this criteria because they contain an insufficient number of olivine grains, and there is one lherzolite from Bird Bluff (FDM-BB04-X01) that is not considered for textural analyses because it was not successfully reoriented using high-resolution XRCT.

The sections that follow summarize the results of EBSD analyses in order to thoroughly assess the extent to which the lithospheric mantle beneath Marie Byrd Land is texturally heterogeneous. These results also constitute a critical dataset for the manuscript by Chatzaras et al. (in revision; Appendix A) that complements the interpretations that are further described within this thesis. The work of Chatzaras et al. (in revision) relies on the EBSD data obtained as part of this thesis to examine the relationship between fabric geometry (i.e. SPO) and the development of multiple known olivine textures (i.e. CPOs). Based on the results of experimental studies, variations in olivine texture are generally attributed to the activation of different slip systems in response to variations in the parameters of deformation (e.g., temperature, water content) rather than the geometry of deformation. The conclusions drawn from the manuscript of Chatzaras et al. (in revision) vary dramatically from what is expected based solely on the results of experimental work, and in turn have the potential to change the long-standing paradigm surrounding what variables ultimately control the development of various olivine textures. In order to investigate the complete findings discussed within the confines of the Chatzaras et al. (in revision) manuscript, the reader is directed to Appendix A, which contains the full journal article that is currently awaiting publication.

The majority of samples within the MBL peridotite suite display axial-[010] (n=15) or A-type (n=15) olivine textures (Appendix E). Despite this predominance, axial-[100] (n=6), B-type (n=1) and random (n=1) textures are also documented within the suite (Figure 3.29). The axial-[010] textures have J-indices and M-indices ranging from 1.7 – 4.1 and 0.08 – 0.21, respectively. The average value of the J-index for axial-[010] textures is 2.9, whereas the average M-index of these samples is equal to 0.15. Overall, A-type textures tend to be stronger with J- and M-indices ranging from 1.4 – 9.0 and 0.07 – 0.37, respectively (Table 3.5).

3.3.1 Mount Aldaz, Usas Escarpment

Sample AD6021-X02 is a lherzolite that displays an axial-[010] olivine texture with a J-index of 3.5 and an M-index of 0.19, which means that the olivine grains in this sample are texturally stronger than the average observed in samples having the same texture. The grains of enstatite and diopside in this sample both display stronger crystallographic textures than olivine. Enstatite has J- and M-indices equal to 6.0 and 0.20, respectively, whereas diopside has J- and M-indices equal to 3.6 and 0.44, respectively.

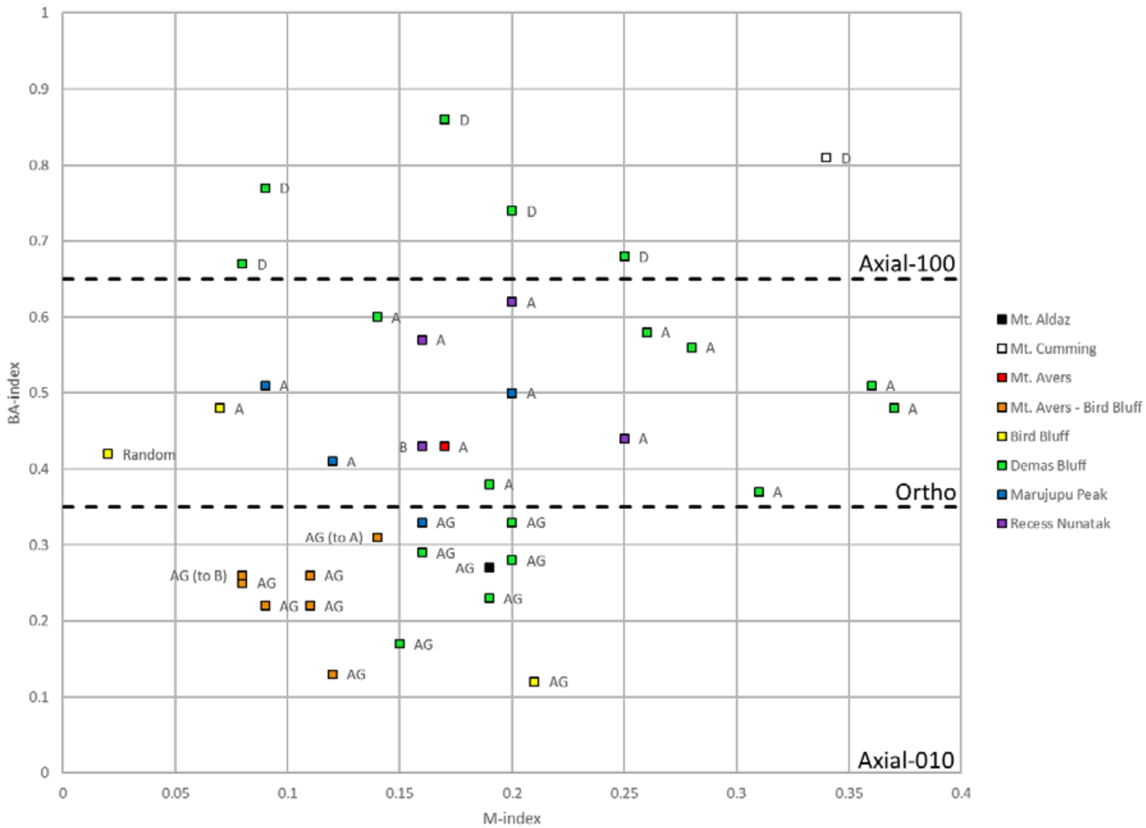

Figure 3.28. Plot of the M-index of olivine versus the BA-index of olivine, which is used to quantitatively discriminate between different olivine textures. If the BA-index is less than 0.35 the olivine has an axial-[010] texture (i.e. AG-type), whereas a BA-index greater than 0.65 is indicative of an axial-[100] texture (i.e. D-type) in olivine. Samples with a BA-index between 0.35 and 0.65 have an orthorhombic olivine texture (i.e. A or B-type textures).

Table 3.5. The peridotite samples sourced from MBL are listed alongside their lithology and the olivine textures they preserve. Textural strength indices (M and J) are provided for all three silicate phases provided there are a sufficient number of grains to characterize the sample, whereas the BA-index is only provided for olivine because it is a diagnostic tool that is used to quantitatively determine the olivine texture when ODFs are ambiguous. Ol = olivine, en = enstatite and di = diopside. Axial-[010] and axial-[100] textures are listed as AG and D-type olivine textures, respectively.

Sample	Lithology	Olivine				Enstatite		Diopside	
		Olivine Texture	J	M	BA	J	M	J	M
AD6021-X02	Lherzolite	AG	3.5	0.19	0.27	6.0	0.20	3.6	0.44
KSP89-181-X01	Dunite	D	4.3	0.34	0.81	-	-	-	-
FDM-AV01-X01	Lherzolite	A	2.9	0.17	0.43	4.7	0.21	3.6	0.43
FDM-AVBB01	Lherzolite	AG	2.2	0.12	0.13	1.7	0.06	1.6	0.44
FDM-AVBB02	Lherzolite	AG	2.0	0.11	0.22	3.6	0.16	2.7	0.42
FDM-AVBB04	Lherzolite	AG	1.9	0.09	0.22	7.4	0.15	5.3	0.44
FDM-AVBB05	Lherzolite	AG	1.7	0.14	0.31	4.7	0.20	3.7	0.43
FDM-AVBB06	Lherzolite	AG	1.9	0.08	0.25	2.7	0.10	2.5	0.42
FDM-AVBB07	Wehrlite	AG	1.9	0.08	0.26	7.6	0.13	2.6	0.42
FDM-AVBB08	Lherzolite	AG	3.3	0.11	0.26	3.1	0.16	5.3	0.39
FDM-BB01-X01	Wehrlite	A	1.4	0.07	0.48	-	-	3.0	0.42
FDM-BB02-X01	Lherzolite	Random	1.4	0.02	0.42	2.0	0.05	2.5	0.43
FDM-BB03-X01	Dunite	AG	4.1	0.21	0.12	3.4	0.24	-	-
FDM-DB01-X01	Lherzolite	A	2.8	0.14	0.60	4.8	0.22	4.2	0.45
FDM-DB02-X01	Lherzolite	D	3.0	0.20	0.74	2.0	0.05	4.0	0.43
FDM-DB02-X02	Harzburgite	A	9.0	0.36	0.51	-	-	-	-
FDM-DB02-X03	Lherzolite	A	4.5	0.31	0.37	-	-	-	-
FDM-DB02-X04	Lherzolite	AG	3.9	0.20	0.33	-	-	-	-
FDM-DB02-X08	Harzburgite	A	7.1	0.37	0.48	-	-	-	-
FDM-DB02-X10	Lherzolite	A	4.3	0.26	0.58	-	-	10.0	0.46
FDM-DB02-X11	Lherzolite	A	3.5	0.19	0.38	-	-	5.4	0.48
FDM-DB02-X12	Lherzolite	AG	3.3	0.15	0.17	-	-	-	-
FDM-DB02-X13	Lherzolite	D	2.3	0.08	0.67	5.6	0.26	4.0	0.45
FDM-DB03-X01	Dunite	D	5.5	0.25	0.68	-	-	-	-
FDM-DB03-X02	Lherzolite	AG	2.8	0.20	0.28	4.4	0.15	5.4	0.45
FDM-DB03-X03	Lherzolite	D	2.7	0.09	0.77	3.7	0.33	5.0	0.43
FDM-DB04-X01	Lherzolite	AG	4.0	0.19	0.23	-	-	-	-
FDM-DB04-X02	Lherzolite	AG	3.4	0.16	0.29	5.2	0.18	4.2	0.45
FDM-DB04-X03	Harzburgite	D	4.9	0.17	0.86	-	-	-	-
FDM-DB04-X04	Harzburgite	A	4.4	0.28	0.56	-	-	-	-
FDM-MJ01-X02	Lherzolite	A	4.0	0.20	0.50	-	-	4.0	0.44
FDM-MJ01-X03	Lherzolite	A	2.7	0.09	0.51	-	-	-	-
FDM-MJ01-X05	Lherzolite	AG	3.8	0.16	0.33	-	-	6.7	0.48
FDM-MJ01-X06	Lherzolite	A	1.5	0.12	0.41	2.6	0.22	2.8	0.42
FDM-RN01-X01	Wehrlite	A	4.3	0.25	0.44	-	-	4.6	0.46
FDM-RN02-X01	Lherzolite	A	2.7	0.16	0.57	4.9	0.28	3.7	0.43
FDM-RN03-X01	Lherzolite	B	2.8	0.16	0.43	1.5	0.33	9.8	0.47
FDM-RN04-X01	Lherzolite	A	2.7	0.20	0.62	3.2	0.20	3.5	0.46

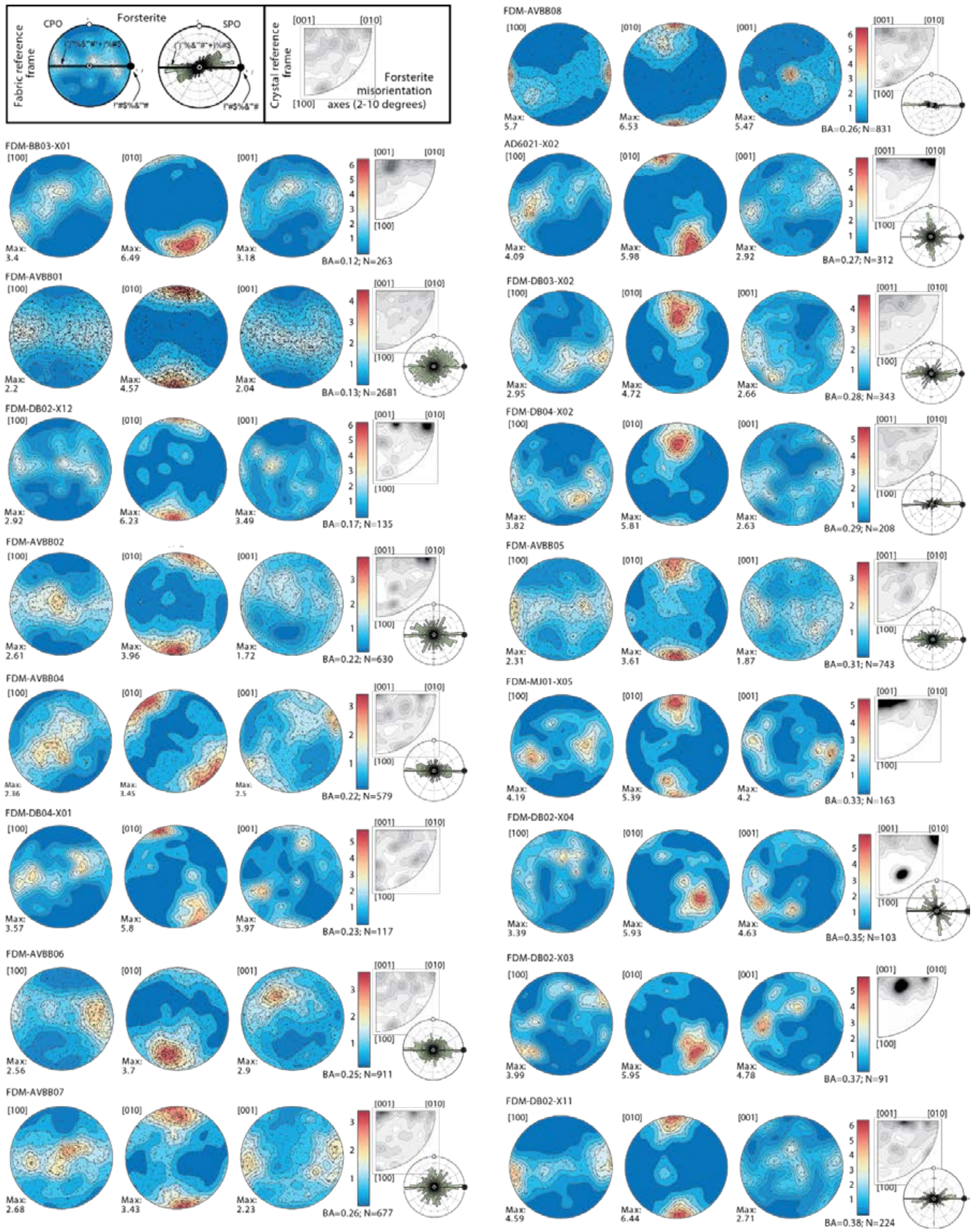

Figure 3.29. (1 of 3). Crystallographic preferred orientation (CPO), low-angle misorientation and shape preferred orientation (SPO) of olivine grains are shown for the MBL xenolith suite. Samples are arranged in order of increasing BA-index. Image source: Chatzaras et al. (in revision).

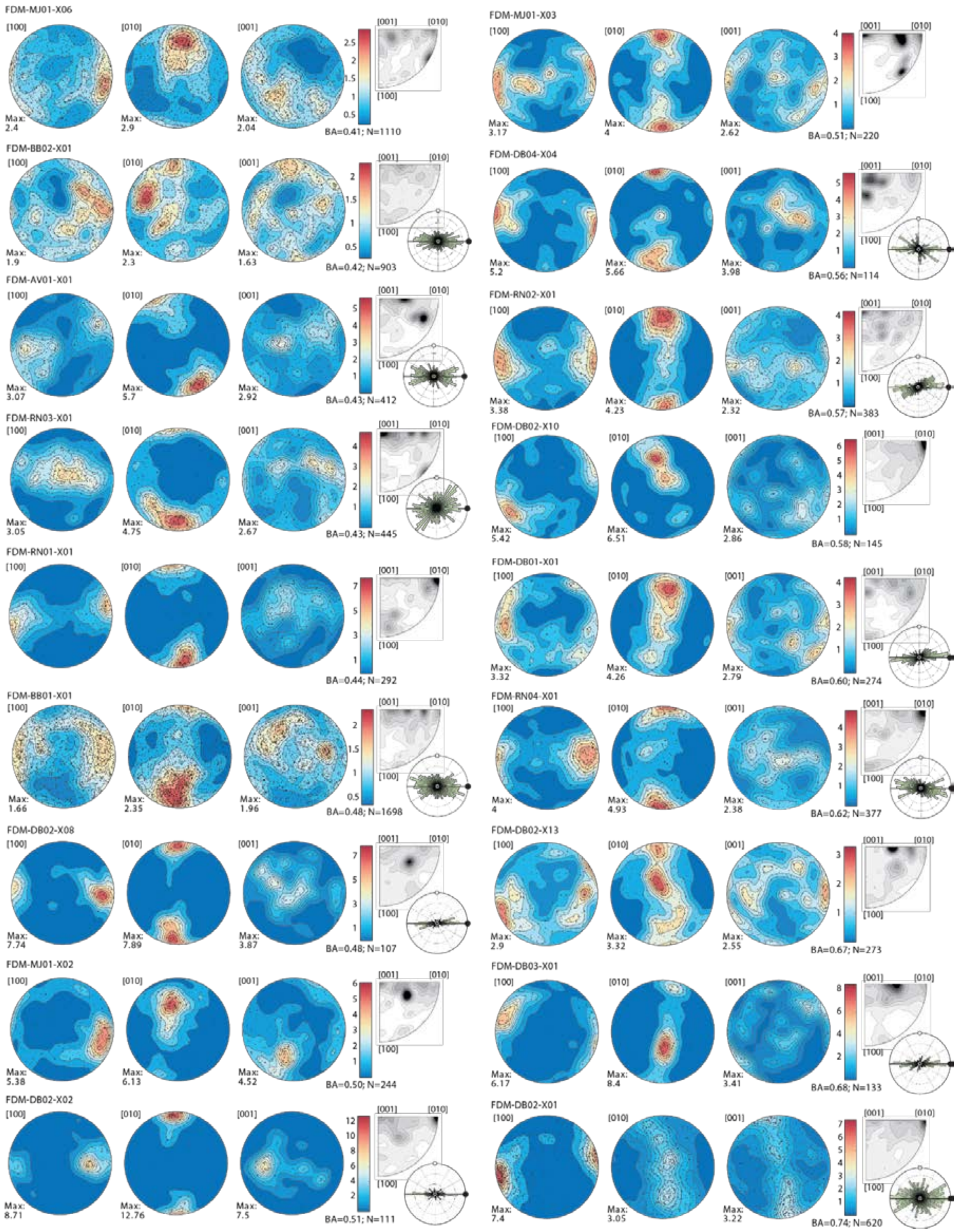

Figure 3.29. (2 of 3).

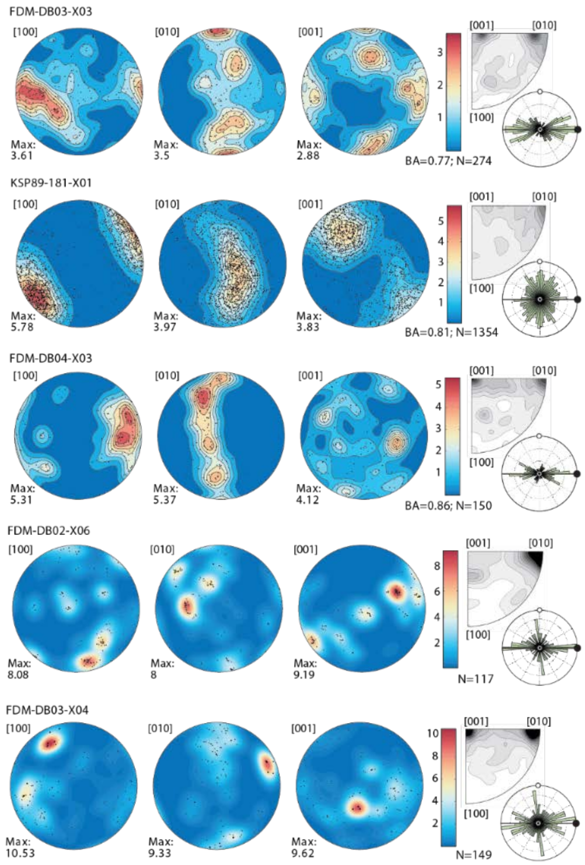

Figure 3.29. (3 of 3).

3.3.2 Mount Cumming, Executive Committee Range

Sample KSP89-181-X01 is a dunite that displays an axial-[100] olivine texture with the J- and M-indices of olivine equal to 4.3 and 0.34, respectively. As these values are greater than the average values calculated for the samples with axial-[100] textures, this sample is texturally stronger. Textural strength is not evaluated for the pyroxenes in this sample because there are too few grains to be statistically significant.

3.3.3 Mount Avers, Fosdick Mountains

Sample FDM-AV01-X01 is a lherzolite that displays an A-type olivine texture with J- and M-indices equal to 2.9 and 0.17, respectively, which indicates that this sample is texturally weak compared to other peridotites characterized by the same texture. The textural indices for both enstatite and diopside are greater than those calculated for olivine, with J-indices equal to 4.7 and 3.6, respectively, and M-indices equal to 0.21 and 0.43, respectively.

3.3.4 Mount Avers – Bird Bluff, Fosdick Mountains

The seven peridotites sourced from Mount Avers – Bird Bluff all display axial-[010] olivine textures. The J-indices for these samples range from 1.7 – 3.3, whereas the M-indices range from 0.08 to 0.14. Interestingly, the sample having the largest M-index value also has the smallest value of the J-index. Based solely on the values calculated for the J-index, it seems that these samples are both texturally stronger and weaker than other samples having an axial-[010] texture. Despite this observation, it is important to note that all of the M-index values calculated for these samples are less than the average M-index value calculated for all samples with an axial-[010] texture, which implies they are all texturally weak compared to the other samples.

Although there are exceptions to this observation, the textural indices calculated for enstatite are generally greater than those calculated for diopside, which are in turn usually greater than those calculated for olivine. Specifically, the J- and M-indices of enstatite range from 1.7 – 7.6 and 0.06 – 0.20, respectively, whereas the J- and M-indices of diopside range from 1.6 – 5.3 and 0.39 – 0.44, respectively. Sample FDM-AVBB01 is unique because the values calculated for the J-indices of enstatite (1.7) and diopside (1.6) are both less than the value determined for the olivine grains (2.2). Comparatively, the M-index of enstatite (0.06) is also less than that of olivine for this sample, whereas the M-index of diopside (0.44) is significantly higher than the other values calculated for this sample. Additionally, sample FDM-AVBB08 is of interest because it contains enstatite grains with a J-index of 3.1 (i.e. less than that of olivine) and an M-index of 0.16 (i.e. greater than that of olivine), whereas the textural intensity of the diopside in this sample is greater than that of the other two silicate phases. All the peridotites from this volcanic center are lherzolites except for FDM-AVBB07, which is a wehrlite. Although this does not seem to impact the textural strength of olivine or diopside, it should be noted that the enstatite grains within this sample seem to have a strong texture based on their J-index value of 7.6. Despite this observation, the M-index of enstatite in this sample is equal to 0.13, which implies a somewhat weaker crystallographic texture developed in enstatite.

3.3.5 Bird Bluff, Fosdick Mountains

Each of the three samples sourced from Bird Bluff displays a different olivine texture. Sample FDM-BB01-X01 is a wehrlite with an A-type texture. The J- and M-indices for olivine in this sample are quite weak and are equal to 1.4 and 0.07, respectively, whereas the diopside grains display stronger textures with J- and M-indices equal to 3.0 and 0.42, respectively. This sample does not contain a statistically significant number of enstatite grains. Comparatively, sample FDM-BB02-X01 is a lherzolite with a random (i.e. annealed) olivine texture. The J- and M-indices for olivine are 1.4 and 0.02, respectively, which are comparable to the values determined for FDM-BB01-X01. Both the enstatite and the diopside within this sample preserve stronger textures than olivine. The J- and M-indices of enstatite are equal to 2.0 and 0.05, respectively, whereas diopside is texturally strongest with J- and M-indices of 2.5 and 0.43, respectively. Sample FDM-BB03-X01 is a dunite that preserves an axial-[010] olivine texture with J- and M-indices equal to 4.1 and 0.21, respectively, which means this sample is texturally strong compared to the other samples that display an axial-[010] olivine texture. The enstatite grains within this sample have a J-index that is less than that of olivine (3.4) and an M-index that is greater than that of olivine (0.24), whereas there are too few diopside grains to adequately assess their crystallographic texture in this sample.

3.3.6 Demas Bluff, Fosdick Mountains

Considering ca. 45% of the MBL peridotite xenoliths that meet the criteria for textural analyses are sourced from Demas Bluff (n=17), these samples are grouped and discussed based on the olivine CPO that they preserve. Five lherzolitic samples from Demas Bluff display axial-[010] olivine textures, which have average J-, M-, and BA-indices equal to 3.5, 0.18 and 0.25, respectively. Of these samples, only two have a sufficient number of enstatite and diopside grains to quantify the textural indices of these phases. The average J- and M-indices for enstatite are 4.8 and 0.17, respectively, whereas those for diopside are equal to 4.8 and 0.45, respectively. Seven peridotites (i.e. lherzolites and harzburgites) have A-type olivine textures. The average J-, M- and BA-indices for olivine are 5.1, 0.27 and 0.50, respectively. Sample FDM-DB01-X01 is the only Demas Bluff sample with an A-type olivine texture that also has enough enstatite grains to determine its textural strength. The enstatite within this sample has J- and M-indices of 4.8 and 0.22, respectively. This sample and two other A-type lherzolites from Demas Bluff contain enough grains of diopside to determine average J- and M-index values of 6.5 and 0.46, respectively. The five remaining samples are peridotites (i.e. lherzolites, a harzburgite and a dunite) that preserve axial-[100] olivine textures, and have average J-, M- and BA-index values of 3.7, 0.16 and 0.74, respectively. The three axial-[100] lherzolites from Demas Bluff also contain a sufficient number of enstatite and diopside grains to assess their textural strength. The average J- and M-indices of enstatite are equal to 3.8 and 0.21, respectively, whereas those of diopside are equal to 4.3 and 0.44, respectively.

3.3.6.1 Xenoliths that display axial-[010] olivine textures

The five peridotite samples from Demas Bluff with an axial-[010] olivine texture are classified as lherzolites. The J- and M-indices for the olivine within these samples range from 2.8 – 4.0 and 0.15 – 0.20, respectively. The textural strength of pyroxene is evaluated in samples FDM-DB03-X02 and FDM-DB04-X02. Although the values for the J-index of enstatite are higher than those of olivine (4.4 – 5.2), the M-indices of enstatite (0.15 – 0.18) fall within the range of those displayed by olivine. Comparatively, the J-index of diopside ranges from 4.2 – 4.5 and the M-index for both samples is equal to 0.45, which imply it is the phase that displays the strongest texture in these two samples.

3.3.6.2 Xenoliths that display A-type olivine textures

Four of the seven peridotite samples from Demas Bluff that preserve an A-type olivine texture are lherzolites, whereas the other three are classified as harzburgites. The J- and M--indices of olivine in the lherzolites range from 2.8 – 5.1 and 0.14 – 0.31, respectively, whereas those calculated for the harzburgites range from 4.4 – 9.0 and 0.28 – 0.37, respectively. Although there is some overlap between the calculated ranges, olivine generally develops a stronger texture in harzburgites than in lherzolites sourced from Demas Bluff. No harzburgites contain a sufficient amount of enstatite or diopside grains to quantify their textural strength or their crystallographic symmetry. In fact, there is only one A-type lherzolite from Demas Bluff (FDM-DB01-X01) that contains enough grains of both enstatite and diopside to assess their textures. Both the J- and M-indices for enstatite in this sample (i.e. 4.8 and 0.22, respectively) are greater than those of olivine (i.e. 2.8 and 0.14, respectively). Two additional lherzolites (FDM-DB02-X10 and FDM-DB02-X11) contain enough diopside grains to evaluate its textural strength. The J- and M-indices for diopside in these two samples ranges from 5.4 – 10.0 and 0.46 – 0.48, respectively. These values are larger than any other textural index calculated for all of the Demas Bluff peridotites.

3.3.6.3 Xenoliths that display axial-[100] olivine textures

Three of the five peridotite samples sourced from Demas Bluff that preserve an axial-[100] olivine texture are lherzolites, whereas one is classified a harzburgite (FDM-DB04-X03) and the final sample from this volcanic center is classified as a dunite (FDM-DB03-X01). The J- and M-indices of olivine in the lherzolites range from 2.3 – 3.0 and 0.08 – 0.20, respectively. The olivine textures preserved in the depleted samples are stronger with J- and M-indices ranging from 4.9 – 5.5 and 0.17 – 0.25, respectively. Only the lherzolites contain a sufficient number of enstatite and diopside grains to quantify the textural strength of these phases. The J- and M-indices for enstatite range from 2.0 – 3.7 and 0.05 – 0.33, respectively, whereas those calculated for diopside are the largest with values ranging from 4.0 – 5.0 and 0.43 – 0.45, respectively. The textural strength of the pyroxenes is greater than that of olivine in samples FDM-DB02-X13 and FDM-DB03-X03, but the enstatite contained within sample FDM-DB02-X01 displays the weakest texture within this sample.

3.3.7 Marujupu Peak, Fosdick Mountains

Three of the four lherzolites sourced from Marujupu Peak preserve A-type olivine textures, whereas the remaining lherzolite displays an axial-[010] olivine texture. The J- and M-indices for these samples range from 2.7 – 4.3 and 0.16 – 0.25, respectively. The A-type olivine texture preserved in sample FDM-MJ01-X02 is the strongest quantified for the samples from this volcanic center. Interestingly, the strength of the two other A-type olivine textures is similar to that of the sample with an axial-[010] olivine texture (FDM-MJ01-X05). Although samples FDM-MJ01-X02 and FDM-MJ01-X05 do not have enough enstatite grains to assess their textural strength, they do contain a sufficient number of diopside grains. In sample FDM-MJ01-X01 the J-index of diopside is equal to 4.0 (i.e. less than that calculated for olivine), whereas the M-index of diopside is equal to 0.44 (i.e. greater than that calculated for olivine). Comparatively, the J- and M-indices of diopside in this sample are equal to 6.7 and 0.48, respectively, both of which are greater than the values calculated for olivine. The J- and M-indices can be calculated for both the enstatite and the diopside in sample FDM-MJ01-X06. Enstatite grains display J- and M-indices equal to 2.6 and 0.22, respectively. The diopside grains in this sample display the largest values for J- and M-indices, which equal 2.8 and 0.42, respectively. Sample FDM-MJ01-X01 is the only sample from this volcanic center that does not contain enough enstatite or diopside grains to draw any conclusions about the textural strength of these phases.

3.3.8 Recess Nunatak, Fosdick Mountains

Three of the four peridotite samples sourced from Recess Nunatak are lherzolites, whereas the remaining sample (FDM-RN01-X01) is classified as a wehrlite. The wehrlitic sample displays an A-type olivine texture that is the strongest of all the Recess Nunatak xenoliths and has J- and M-indices that are equal to 4.3 and 0.25, respectively. Although this sample does not contain enough grains of enstatite to quantify its texture, the grains of diopside within FDM-RN01-X01 display a J-index of 4.6 and an M-index of 0.46, which implies their crystallographic texture is stronger than the texture developed in olivine grains.

Two of the lherzolitic samples (FDM-RN02-X01 and FDM-RN04-X01) display weaker A-type olivine textures, which both have a J-index equal to 2.7 and M-indices equal to 0.16 and 0.20, respectively. The third lherzolite from Recess Nunatak (FDM-RN03-X01) is the only sample that displays a B-type olivine texture within the MBL xenolith suite. This texture is quantified as having a J-index of 2.8 and an M-index of 0.16, which is quite similar to the textural indices that are quantified for the other lherzolites from this volcanic center. The results of experimental studies imply a significant amount of water (>200 ppm H/Si) is required to activate the slip systems that are thought to be responsible for the development of a B-type olivine CPO (e.g., Jung and Karato, 2001).

The grains of pyroxene that occur in the lherzolitic samples with A-type olivine textures (i.e. FDM-RN02-X01 and FDM-RN04-X01) display stronger crystallographic textures than the olivine grains in these samples. In sample FDM-RN02-X01 the J- and M- indices for enstatite are 4.9 and 0.28, respectively, whereas the J- and M-indices for enstatite in sample FDM-RN04-X01 are equal to 3.2 and 0.20, respectively. The J- and M-indices for the diopside in sample FDM-RN02-X01 are equal to 3.7 and 0.43, respectively, which are greater than the values calculated for olivine and less than those determined for the grains of enstatite within this sample. The diopside in sample FDM-RN04-X01 has J- and M-indices that are equal to 3.5 and 0.46, respectively, which are greater than the values determined for both the olivine and the enstatite in this sample. The lherzolitic sample with a B-type olivine texture contains enstatite grains that display a J-index of 1.5, which is less than the value of the J-index for olivine in this sample. Despite this, the M-index for enstatite in this sample is equal to 0.33, which is greater than that of the olivine within this sample. Comparatively, both the J- and M-indices calculated for the grains of diopside in this sample are equal to 9.8

and 0.47, respectively, which implies that these grains preserve a significantly stronger crystallographic texture either olivine or enstatite.

3.3.9 Phase abundance and textural strength

A significant amount of research has been focused on understanding the rheological behavior of Earth's lithospheric mantle through the application of laboratory-derived flow laws that are only applicable to olivine (Equation 1), which comprises most (ca. 60-65%) of the upper mantle. As a result, there is uncertainty surrounding how secondary phases (i.e. pyroxenes) influence olivine deformation processes in naturally deformed peridotites (Hansen and Warren, 2015). This uncertainty is exacerbated by the fact that some researchers have suggested that pyroxenes in mantle rocks inhibit the growth of olivine grains, which in turn promotes the operation of grain-size sensitive deformation mechanisms (i.e. diffusion creep; e.g., Warren and Hirth, 2006; Toy et al., 2010). Alternatively, conclusions drawn from field-based observations imply pyroxene is stronger than olivine in a natural setting, which would counteract the effect of inhibited grain growth in olivine (e.g., Tikoff et al., 2010). Furthermore, there is an increasing body of research being conducted on polyphase aggregates that implies both phase morphology and phase arrangement can significantly impact how a rock accommodates strain at the microstructural level, which directly influences its bulk strength (e.g., Tullis et al., 1991).

Due to the potential influence of pyroxene abundance, morphology, and/or distribution on olivine deformation, it is important to discuss how the presence of these secondary phases (i.e. enstatite and diopside) may have influenced the type and intensity of the olivine CPO textures preserved within the MBL peridotite suite. The discussion that follows focuses on how olivine textures and grain sizes vary with respect to the abundance of secondary phases (i.e. lithology). Prior to examining these interphase relationships, it is helpful to develop an understanding of how the textural strength indices calculated for all silicate phases vary throughout the sample suite (Table 3.6). Although values are given for the J-index, the reader is reminded that this value is highly sensitive to the number of grains measured and is difficult to interpret (Skemer et al., 2005).

Overall, diopside CPO textures display the highest values of both the M- and J-index; values range from 0.39 – 0.48 and 1.6 – 10.0, respectively. The values for the M-index of diopside are significantly higher than those calculated for the other phases, whereas the range of values for the J-index of diopside is only slightly greater than what is observed in either olivine or enstatite. Despite this, recent research concludes that olivine deformation is not sensitive to the morphology of clinopyroxene (Gerbi et al., 2015). Although the two orthorhombic silicate minerals (i.e. olivine and enstatite) have textures that are comparable in strength, olivine textures are marginally stronger. Values for the M- and J-indices of enstatite range from 0.05 – 0.33 and 1.5 – 7.6, respectively. Comparatively, the M- and J-indices of olivine range from 0.02 – 0.37 and 1.4 – 9.0, respectively.

Table 3.6. Ranges of values for the textural indices are calculated for the three silicate phases within the MBL xenolith suite and subdivided according to sample lithology. Ranges for the entire suite are also given.

M-index	Olivine		Enstatite		Diopside	
	Minimum	Maximum	Minimum	Maximum	Minimum	Maximum
Dunites	0.21	0.34	0.24	0.24	-	-
Harzburgites	0.17	0.37	-	-	-	-
Lherzolites	0.02	0.31	0.05	0.33	0.39	0.48
Wehrlites	0.07	0.25	0.13	0.13	0.42	0.46
Overall	*0.02*	*0.37*	*0.05*	*0.33*	*0.39*	*0.48*
J-index	Olivine		Enstatite		Diopside	
	Minimum	Maximum	Minimum	Maximum	Minimum	Maximum
Dunites	4.1	5.5	3.4	3.4	-	-
Harzburgites	4.4	9.0	-	-	-	-
Lherzolites	1.4	4.5	1.5	7.4	1.6	10
Wehrlites	1.4	4.3	7.6	7.6	2.6	4.6
Overall	*1.4*	*9.0*	*1.5*	*7.6*	*1.6*	*10*

In order to discuss how olivine deforms in response to variations in the abundance of secondary phases for each sample within the MBL xenolith suite, the total pyroxene content is plotted against values calculated for: the geometric mean grain size of olivine, the mean differential stress determined from the olivine grain size piezometer, the M-index of olivine, and the J-index of olivine (Figure 3.30). The geometric mean grain size of olivine displays an inverse relationship with respect to pyroxene content, whereas values of mean differential stress increase with pyroxene content. This follows logic based on the application of the olivine grain size piezometer – smaller grains are inherently associated with larger values of differential stress. Comparatively, the geometric mean grain sizes calculated for both diopside and enstatite display no correlation with pyroxene content (Figure 3.31).

Plotting the values of the M- and J-indices against total pyroxene content shows that textural strength decreases with increasing pyroxene content (Figure 3.32). This observation follows logic – when a higher percentage of secondary phases exist, these phases will also be responsible for accommodating strain within a body of rock. It must also be considered that higher percentages of pyroxene content are associated with smaller olivine grains that are more likely to deform by diffusion creep, which is a deformation mechanism that is thought to weaken crystallographic textures in naturally deformed peridotites (e.g., Hirth and Kohlstedt, 2003; Warren and Hirth, 2006; Falus et al., 2011; Précigout and Hirth, 2014).

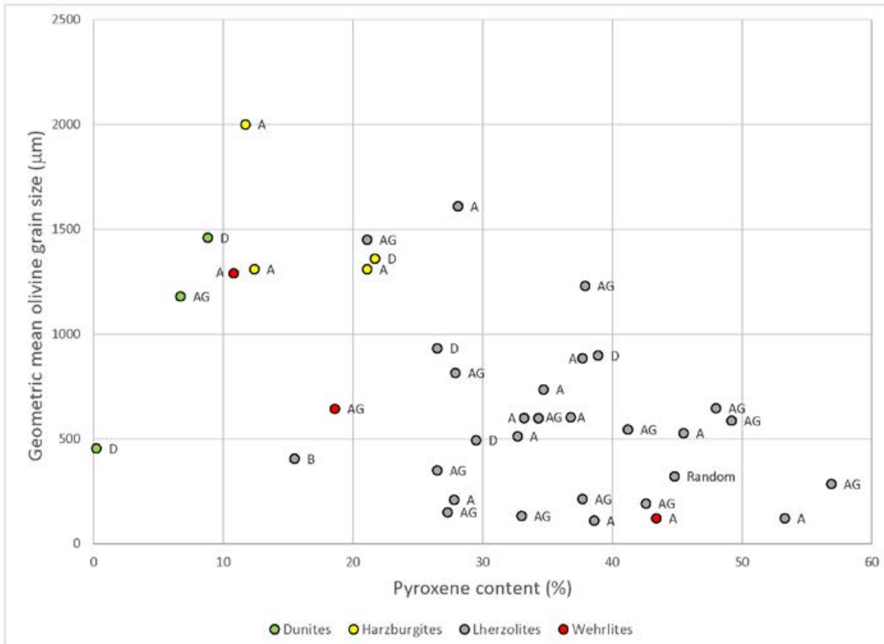

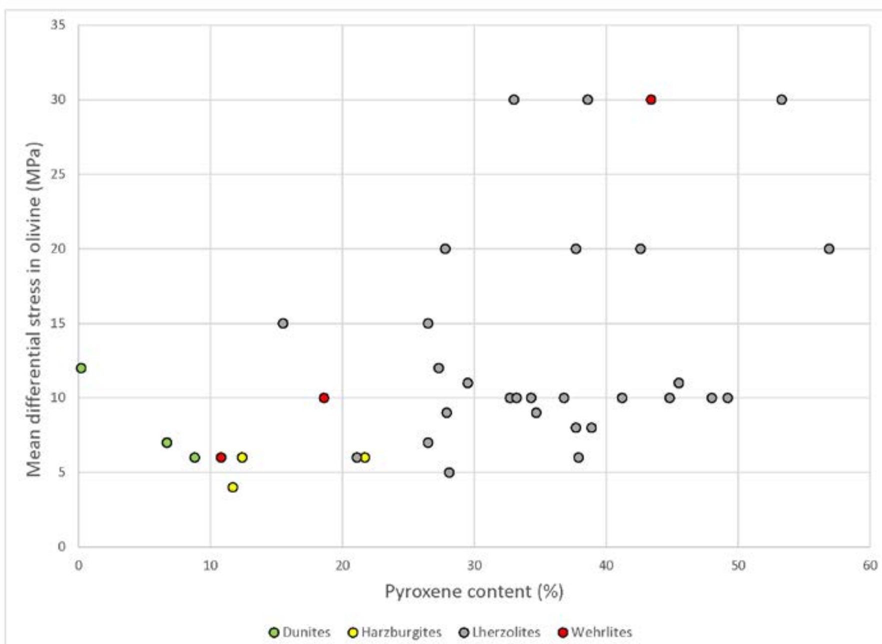

Figure 3.30. (Top) Plot showing an inverse relationship exists between pyroxene abundance and the geometric mean grain size of olivine. Olivine textures are labelled with axial-[010] and axial-[100] textures referred to as "AG" and "D," respectively. Notice that there is no correlation between grain size, texture, and/or pyroxene content. (Bottom) Plot showing the direct relationship between pyroxene abundance and the mean differential stress values determined using the olivine grain size piezometer.

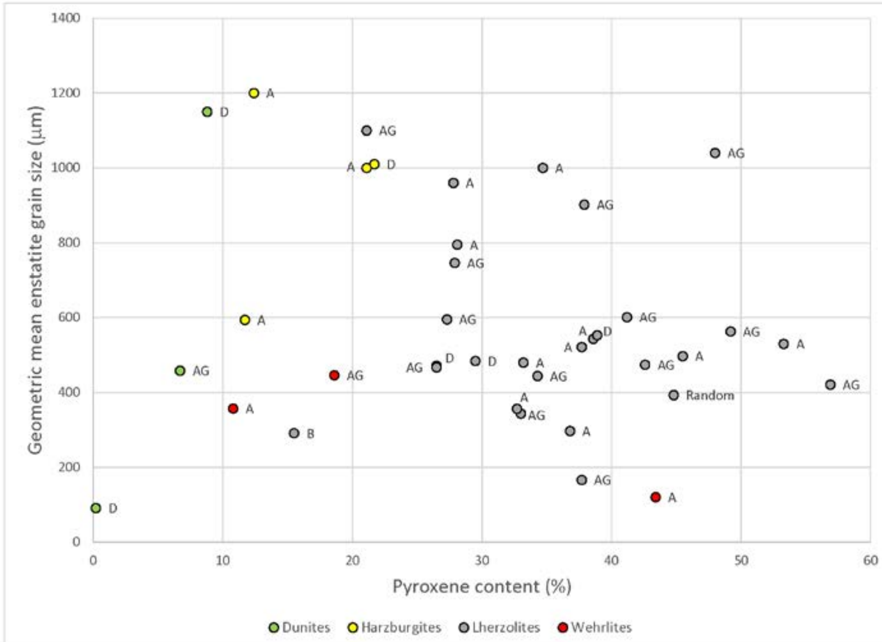

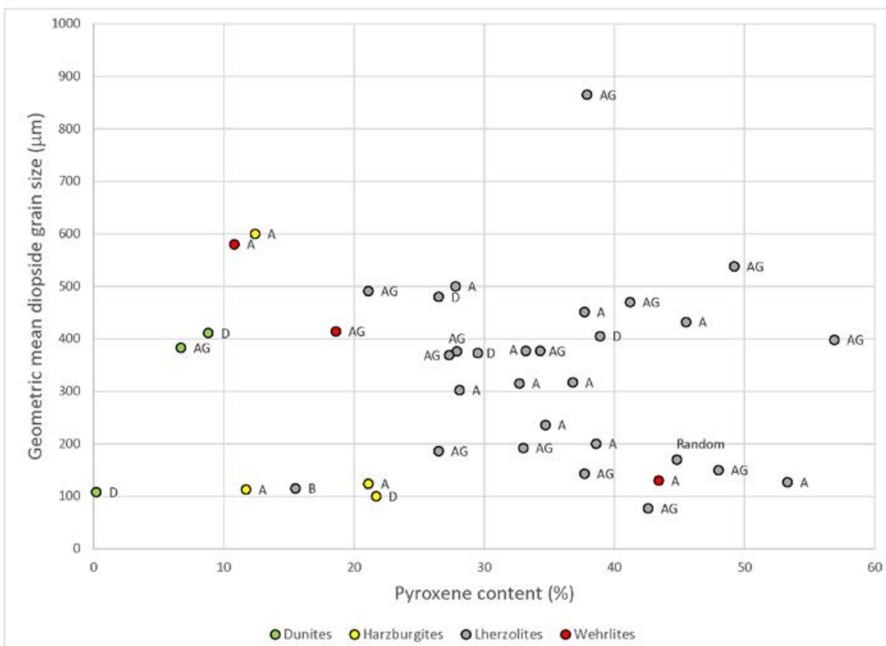

Figure 3.31. Plots showing the lack of correlation between the grain sizes for either of the pyroxenes and total pyroxene content. Olivine textures are labelled with axial-[010] and axial-[100] textures referred to as "AG" and "D," respectively. Notice that there is no correlation between grain size, olivine texture, and/or pyroxene content. (Top) Enstatite. (Bottom) Diopside.

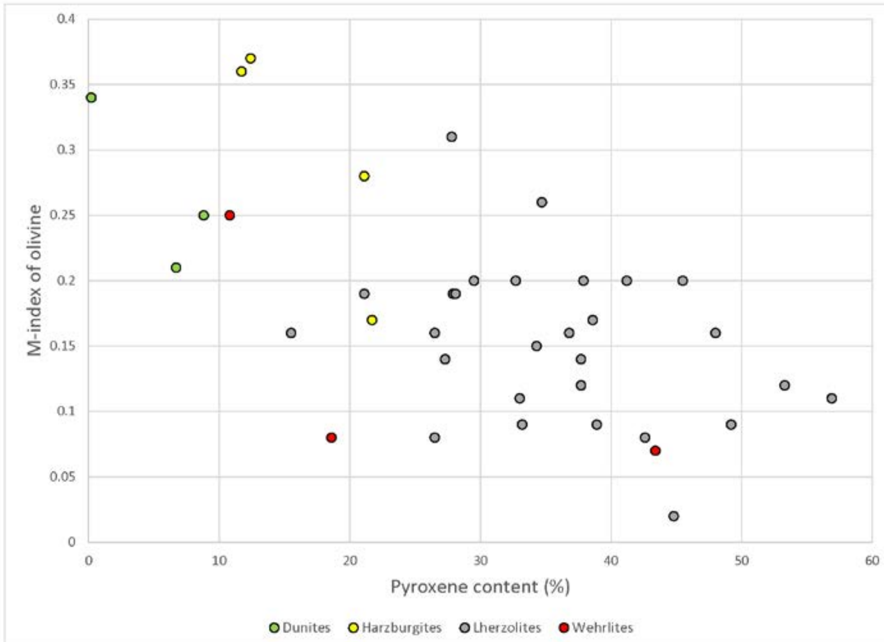

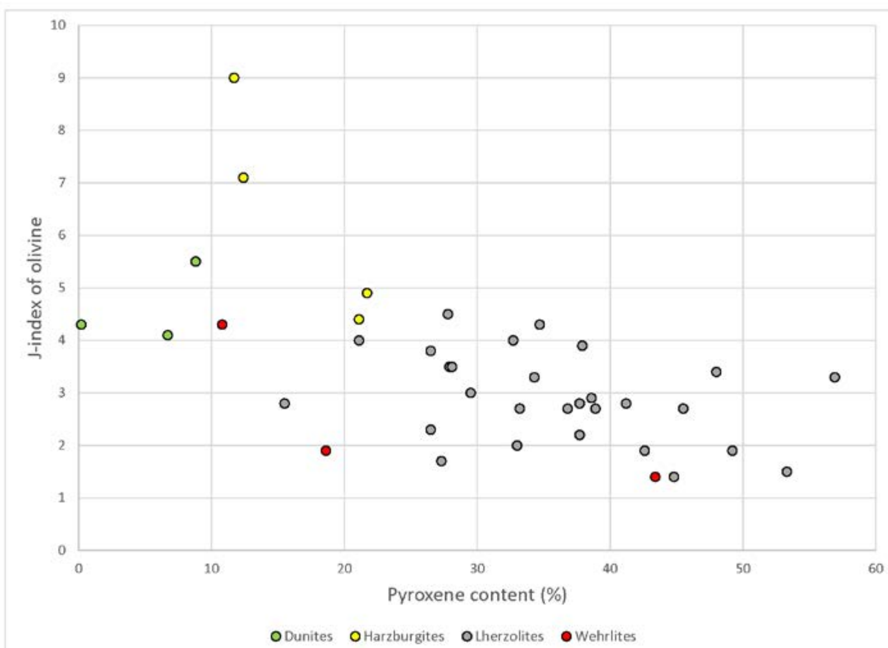

Figure 3.32 Plots showing the inverse relationship that exists between pyroxene content and both of the textural strength indices. (Top) M-index. (Bottom) J-index.

3.4 DEFORMATION MECHANISMS AND ESTIMATIONS OF PALEOSTRESS MAGNITUDE

Deformation mechanism maps (DMMs) imply that the olivine grains within the MBL peridotite xenoliths store strain on their crystal lattices primarily through the operation of dislocation-accommodated grain-boundary sliding (Figure 3.33; Appendix F), which is consistent with microstructural observations of the suite (e.g., the existence of quadruple junctions between grains of contrasting phase; Section 3.1). Application of the olivine grain size piezometer indicates that the suite experienced differential stresses ranging from 0.5 MPa to 50 MPa with mean differential stresses ranging from 4 to 30 MPa and an average mean differential stress of 15 MPa (Table 3.7).

It is important to note that some of the estimates of differential stress provided herein differ from those presented by Chatzaras et al. (in revision; cf. Appendix A). The complementary manuscript aims to quantify the values of maximum differential stress recorded by the MBL xenolith suite, which requires the mean grain size of recrystallized grains to be used for piezometry. By doing this, Chatzaras et al. (in revision) are able to examine how olivine textures change as a function of maximum stress, which is not a goal of this thesis. Comparatively, this study aims to quantify values of mean differential stress, which consider the entire grain size distribution (i.e. recrystallized grain populations are ignored).

Twenty-two of the thirty-eight xenoliths (ca. 58%) that constitute the peridotitic samples sourced from MBL preserve a mean differential stress that is between 6 and 10 MPa. Only two samples, both of which are sourced from Demas Bluff, display values of mean differential stress that are less than or equal to 5 MPa. An additional six samples preserve mean differential stresses between 11 and 15 MPa, whereas the remaining eight samples preserve mean differential stresses that are greater than 15 MPa. The four samples displaying the highest value of mean differential stress within the MBL suite (i.e. 30 MPa) are sourced from Marujupu Peak, Mount Avers, Bird Bluff and a volcanic center located between the latter two volcanic centers (AVBB). Furthermore, it is important to note that the range of mean differential stresses estimated for each volcanic center generally tend to increase towards the western-most longitudes of the study area (Table 3.8). Demas Bluff – the southernmost volcanic center within the Fosdick Mountains – deviates from this trend. Despite this, one of the samples sourced from this location preserves a mean differential stress of 20 MPa, which is greater than the average of the mean differential stresses preserved by the entire MBL peridotite xenolith suite. The strain rates associated with the deformation of the MBL xenolith suite range from 10^{-17}/s to 10^{-11}/s.

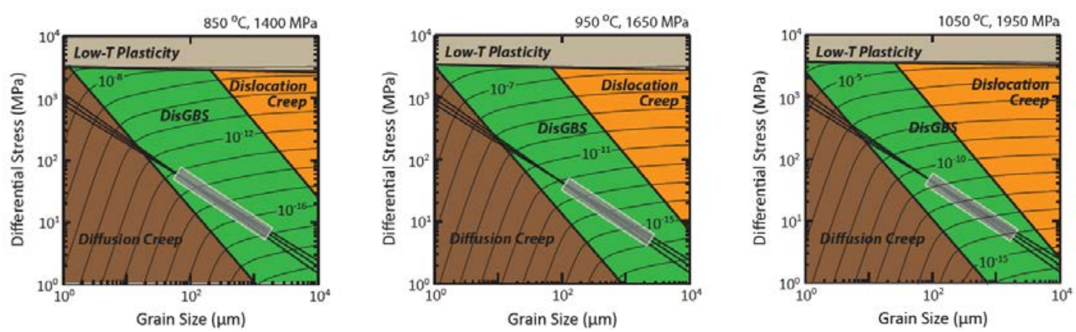

Figure 3.33. Deformation mechanism maps are constructed for olivine based on the operation of four deformation mechanisms (i.e. low-temperature plasticity, dislocation creep, dislocation-accommodated grain boundary sliding (disGBS) and diffusion creep. The piezometer corresponds to that described by Warren and Hirth (2006) and is based on the data of Karato et al. (1980) and Van der Wal et al. (1993). Gray boxes correspond to the range of mean grain sizes within the xenoliths that deformed at the set of pressure and temperature conditions. Based on the distribution of grain sizes, the extrapolation of the disGBS flow law of Hansen et al. (2011) implies the dominant deformation mechanism operating within the MBL xenoliths is disGBS. Image source: Chatzaras et al. (in revision).

Table 3.7. The minimum, maximum and geometric mean grain sizes for olivine are given for all peridotitic samples from MBL. The minimum differential stress corresponds with the maximum grain size, whereas the maximum differential stress corresponds with the minimum grain size. The geometric mean grain size calculated for each sample is used to estimate the mean differential stress experienced by each sample. These values differ from those presented in Chatzaras et al. (in revision; cf. Appendix A) because subpopulations of recrystallized grains are disregarded within the confines of this study. Values for mean differential stress that vary significantly (i.e. >10 MPa) are denoted with an asterisk.

Sample	Min. Grain Size (μm)	Max. Grain Size (μm)	Geo. Mean Grain Size (μm)	Min. Δσ (MPa)	Max. Δσ (MPa)	Geo. Mean Δσ (MPa)
AD6021-X02	80	6000	815	2	40	9
KSP89-181-X01	55	3750	455	3	50	12
FDM-AV01-X01	60	4000	111	3	50	30
FDM-AVBB01	60	2500	214	4	50	20
FDM-AVBB02	60	3000	133	3	50	30
FDM-AVBB04	60	3000	587	3	50	10
*FDM-AVBB05	60	5000	150	2	50	12
FDM-AVBB06	60	3750	192	3	50	20
FDM-AVBB07	70	4000	644	3	45	10
FDM-AVBB08	60	2750	285	3	50	20
FDM-BB01-X01	60	3500	122	3	50	30
FDM-BB02-X01	55	3000	322	3	50	10
FDM-BB03-X01	65	6000	1180	2	45	7
FDM-DB01-X01	80	6500	885	2	40	8
FDM-DB02-X01	60	4250	494	2	50	11
FDM-DB02-X02	70	9000	2000	0.5	45	4
FDM-DB02-X03	70	9000	210	0.5	45	20
FDM-DB02-X04	70	6000	1230	2	45	6
FDM-DB02-X08	60	1000	356	1	40	6
FDM-DB02-X10	90	8000	1310	1	45	9
FDM-DB02-X11	70	7000	736	3	45	5
FDM-DB02-X12	70	4000	1610	2	45	10
FDM-DB02-X13	70	6000	599	2	40	7
FDM-DB03-X01	80	4500	933	0.5	30	6
FDM-DB03-X02	110	10000	1460	2	45	10
FDM-DB03-X03	70	5500	545	2	45	8
FDM-DB04-X01	70	5000	898	0.5	40	6
FDM-DB04-X02	60	7000	100	2	50	10
FDM-DB04-X03	80	9000	1450	1	45	6
FDM-DB04-X04	60	4500	647	0.5	50	6
FDM-MJ01-X02	70	7000	1360	3	45	10
*FDM-MJ01-X03	60	8500	1310	3	50	10
*FDM-MJ01-X05	65	3000	513	2	50	15
FDM-MJ01-X06	60	4000	600	3	50	30
FDM-RN01-X01	60	5000	350	3	45	6
FDM-RN02-X01	60	2750	122	3	45	10
FDM-RN03-X01	70	4000	1290	2	45	15
FDM-RN04-X01	70	4000	604	2	50	11

Table 3.8. Xenolith-bearing volcanic centers of MBL listed in order of increasing westward longitude (modified from Chatzaras et al., in revision).

Volcanic Center	Latitude (°S)	Longitude (°W)	Range of Mean $\Delta\sigma$ Values (MPa)	Average of Mean $\Delta\sigma$ Values (MPa)
USAS Escarpment				
Mount Aldaz	76.051	124.417	9	9
Executive Committee Range				
Mount Cumming	76.667	125.820	12	12
Fosdick Mountains				
Recess Nunatak	76.519	144.507	6 – 15	11
Bird Bluff	76.504	144.598	7 – 30	16
Demas Bluff	76.568	144.853	4 – 20	8
Mount Avers	76.481	145.396	30	30
Marujupu Peak	76.508	145.670	10 – 30	16

4 CONCLUSIONS AND SYNOPSIS

In order to describe the heterogeneity of the lithospheric mantle of MBL, it is imperative to consider the microstructural variations occurring both within and between the individual volcanic centers. Studying variations that occur with depth at an individual volcanic center allows for the development of a more detailed view of the vertical structure of the lithospheric mantle at that point. Subsequent assessments focusing on how vertical heterogeneities differ between each of the volcanic centers provide the means to understand lateral variations. Collectively, these assessments help improve our three-dimensional understanding of how deformation is being accommodated within the lithospheric mantle of MBL today. In turn, this may directly inform on the behavior of the West Antarctic Rift System and the extent to which active rifting may be continuing to drive subaerial and subglacial volcanism in West Antarctica.

4.1 VERTICAL HETEROGENEITIES WITHIN INDIVIDUAL VOLCANIC CENTERS OF MBL

The volcanic centers from which more than one peridotitic xenolith sample is sourced are ideal for assessing the vertical structure of the lithospheric mantle beneath MBL. There are three volcanic centers (i.e. Mount Aldaz, Mount Cumming and Mount Avers) from which only one peridotite xenolith is sourced. Although there is a significant amount of information recorded within these samples, there is no way to assess the vertical heterogeneities that are documented in the mantle by the rocks from these locations.

4.1.1 Mount Aldaz, Usas Escarpment

The samples from Mount Aldaz preserve equilibration temperatures ranging from 1017 to 1084°C, which is a range that corresponds to depths between 57 and 63 kilometers. Due to the fact there is only one peridotite sourced from this volcanic center, the microstructural heterogeneity occurring with depth cannot be assessed at this location. Despite this, it is apparent that the samples display mineralogical heterogeneities on the sub-ten-kilometer-scale because both a clinopyroxenite and a lherzolite occur over a narrow six kilometer depth interval (Table 4.1; Figure 4.1).

Table 4.1. Xenoliths from Mount Aldaz are arranged in order of increasing equilibration temperature alongside a summary of their microstructural and mineralogical properties. Note that sample AD6021-X01 is a clinopyroxenite (< 40% olivine), which means that it does not contain enough grains of olivine to either quantify the CPO or apply the recrystallized grain size piezometer.

Sample	T (°C)	h (km)	Rock Name	CPO (ol)	J (ol)	M (ol)	Abundance (%) and Mean G.S. (μm)				Mean Δσ (MPa)
							ol	di	en	% px	
AD6021-X01	1017	57	Clinopyroxenite	-	-	-	1.2 -	95.0 -	3.8 -	98.8	-
AD6021-X02	1084	63	Lherzolite	AG	3.5	0.19	71.9 815	15.5 376	12.6 746	28.1	9

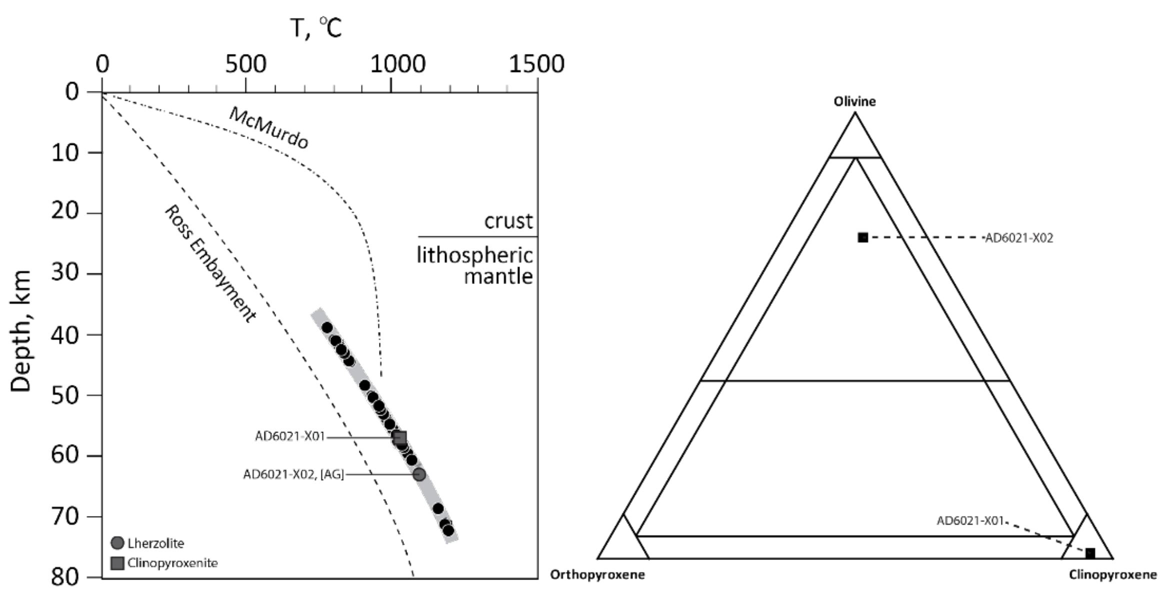

Figure 4.1. (Left) Relative extraction depths for the Mount Aldaz xenoliths are plotted on the geothermal gradient calculated by Chatzaras et al. (in revision). (Right) Ternary diagram showing the mineralogical variations of the Mount Aldaz xenoliths.

4.1.2 Mount Cumming, Executive Committee Range

Neither the microstructural nor the mineralogical heterogeneity of the lithospheric mantle can be assessed at Mount Cumming because there is only one sample sourced from this volcanic center (Table 4.2; Figure 4.2). This sample is an axial-[100] dunite that equilibrated between 862 and 995°C.

Table 4.2. Microstructural and mineralogical properties of the xenolith from Mount Cumming. There are two equilibration temperatures because spinel grains show compositional heterogeneity in terms of Cr-content on the thin section scale.

Sample	**T (°C)**	**h (km)**	**Rock Name**	**CPO (ol)**	**J (ol)**	**M (ol)**	**Abundance (%) and Mean G.S. (μm)**				**Mean Δσ (MPa)**
							ol	**di**	**en**	**% px**	
KSP89-181-X01 (lo-Cr)	862	42	Dunite	D	4.3	0.34	99.8 455	0.2 108	0.0 91	0.2	12
KSP89-181-X01 (hi-Cr)	995	52									

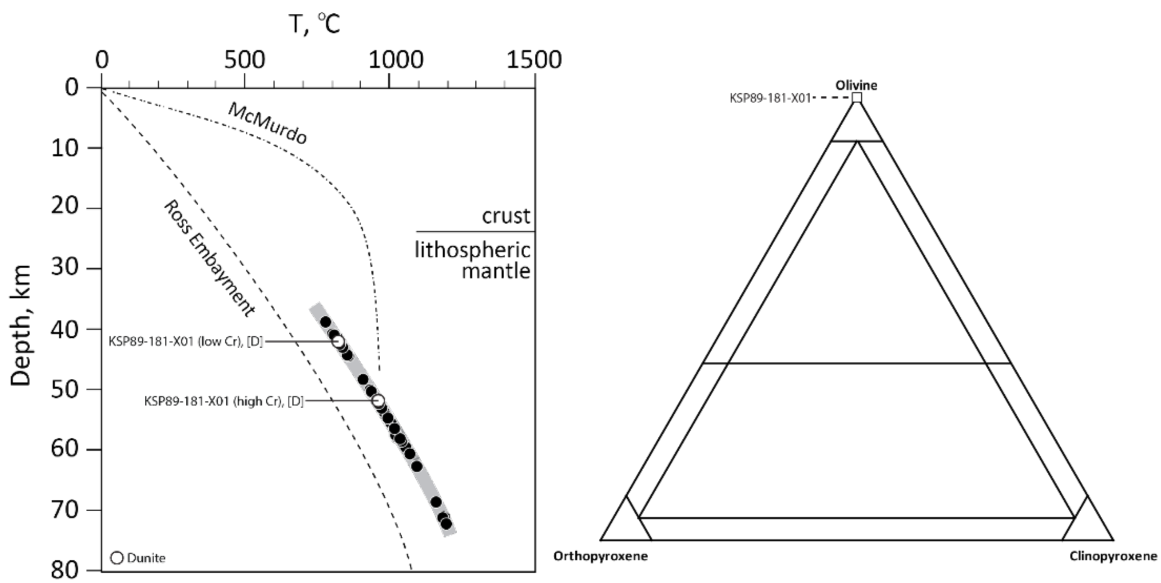

Figure 4.2. (Left) Two extraction depths for the Mount Cumming xenolith are plotted on the geothermal gradient. Due to the absence of pyroxene, the olivine-spinel exchange thermometer is applied, which leads to the calculation of two extraction depths based on variations in chromium (Cr) content. (Right) Ternary diagram that shows the mineralogical composition of the Mount Cumming dunite.

4.1.3 Mount Avers, Fosdick Mountains

Similar to Mount Cumming, there is only one sample sourced from Mount Avers, which prevents heterogeneity from being evaluated at this volcanic center (Table 4.3; Figure 4.3). This sample displays an A-type olivine fabric and equilibrated at a depth of 50 km.

Table 4.3. Microstructural and mineralogical properties of the xenolith from Mount Avers.

Sample	T (°C)	h (km)	Rock Name	CPO (ol)	J (ol)	M (ol)	Abundance (%) and Mean G.S. (μm)				Mean Δσ (MPa)
							ol	di	en	% px	
FDM-AV01-X01	939	50	Lherzolite	A	2.9	0.17	60.4 111	16.1 200	23.5 543	39.6	30

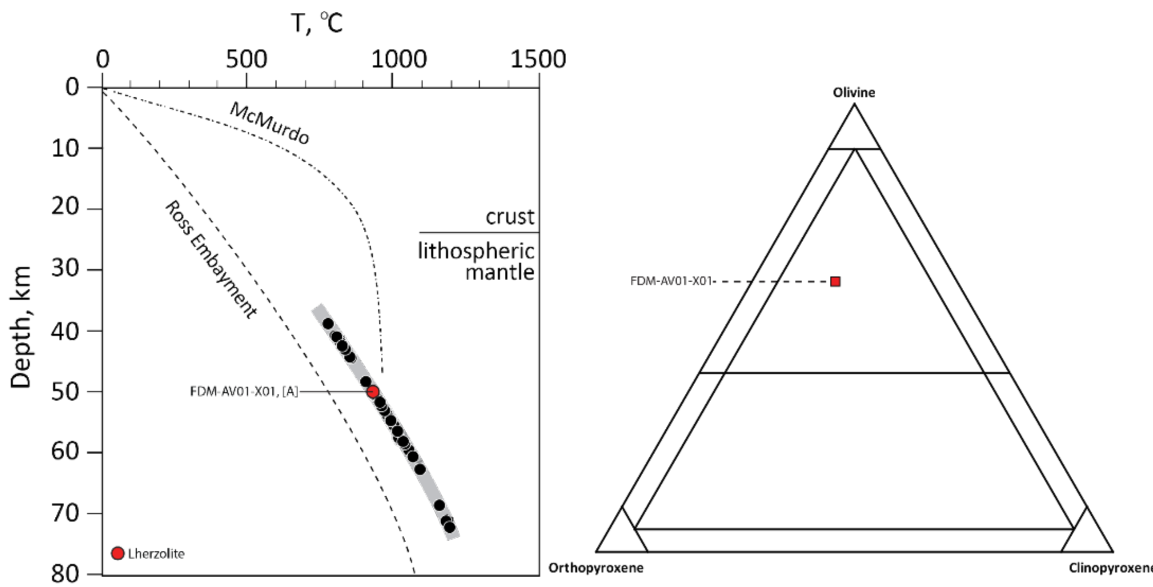

Figure 4.3. (Left) Extraction depth for the Mount Avers lherzolite is plotted on the geothermal gradient calculated. (Right) Ternary diagram showing the mineralogical composition of the Mount Avers lherzolite.

4.1.4 Mount Avers – Bird Bluff, Fosdick Mountains

The seven peridotitic xenoliths sourced from Mount Avers – Bird Bluff display extraction depths ranging from 39 – 51 km and remain microstructurally homogeneous over this 12 km interval (Table 4.4; Figure 4.4). All samples preserve axial-[010] textures that display average J- and M-indices of 2.1 and 0.10, respectively. Furthermore, the xenoliths record a narrow range of mean differential stresses (10 – 30 MPa) with an average of 17 MPa. There is no apparent correlation between the magnitude of the textural strength indices and temperature, phase abundance, mean grain size or mean differential stress.

Despite their similarities, the peridotitic samples are slightly heterogeneous with respect to their compositions as they range from slightly peridotitic (i.e. 41.3% olivine) to borderline wehrlitic (i.e. 4.8% enstatite). This variation does not coincide with variations in temperature. The mineralogical heterogeneity within this subset of the MBL xenolith suite is further exacerbated by the existence of a websterite containing almost no olivine (0.8%). This sample is interpreted to have been sourced from a depth of 51 km, which is a depth at with lherzolites are also documented. Thus, mineralogical heterogeneity is inferred to vary on the sub-kilometer-scale within this portion of the lithospheric mantle of MBL.

Table 4.4. Xenoliths from Mount Avers – Bird Bluff are arranged in order of increasing equilibration temperature alongside a summary of their microstructural and mineralogical properties. Note that sample FDM-AVBB03 is a pyroxenite (< 40% olivine), which means that it does not contain enough grains of olivine to either quantify the CPO or apply the recrystallized grain size piezometer.

Sample	T (°C)	h (km)	Rock Name	CPO (ol)	J (ol)	M (ol)	Abundance (%) and Mean G.S. (μm)				Mean Δσ (MPa)
							ol	di	en	% px	
FDM-AVBB02	779	39	Lherzolite	AG	2.0	0.11	66.1% 214	14.7% 192	19.1% 343	33.8	30
FDM-AVBB07	805	41	Wehrlite	AG	1.9	0.08	80.9% 644	14.3% 414	4.8% 446	19.1	10
FDM-AVBB05	814	42	Lherzolite	AG	1.7	0.14	72.3% 150	11.5% 369	16.2% 595	27.7	12
FDM-AVBB04	822	42	Lherzolite	AG	1.9	0.09	49.5% 587	32.9% 538	17.6% 563	50.5	10
FDM-AVBB08	832	43	Lherzolite	AG	3.3	0.11	41.3% 285	39.4% 398	19.3% 421	58.7	20
FDM-AVBB01	937	50	Lherzolite	AG	2.2	0.12	61.3% 214	20.4% 143	18.2% 166	38.6	20
FDM-AVBB06	940	50	Lherzolite	AG	1.9	0.08	56.8% 192	17.0% 77	26.1% 474	43.1	20
FDM-AVBB03	949	51	Websterite	-	-	-	0.8% -	71.6% -	27.6% -	99.2	-

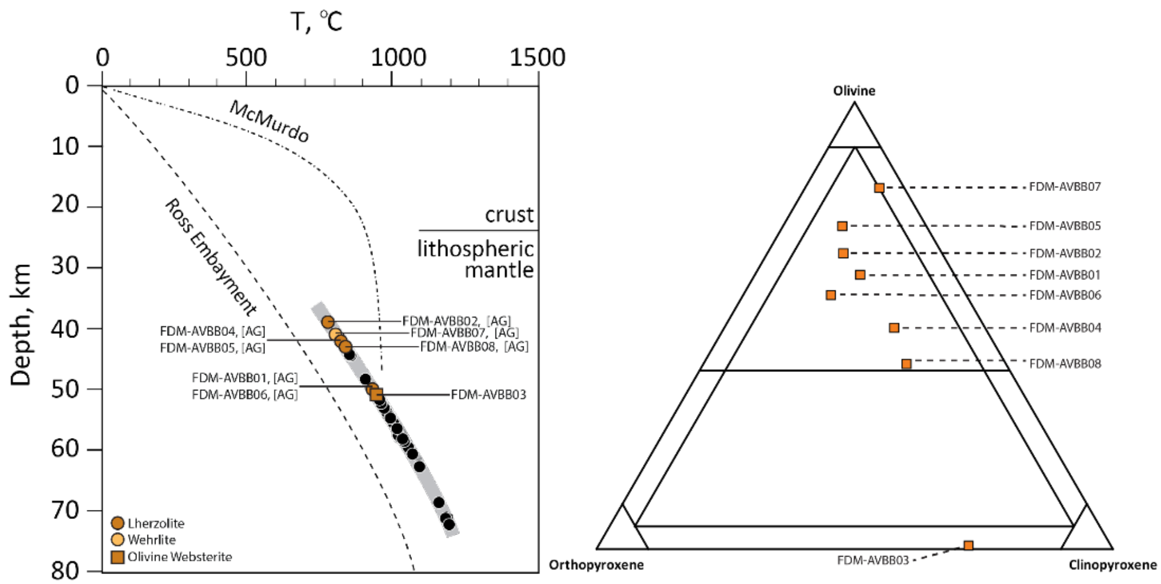

Figure 4.4. (Left) Extraction depths for the Mount Avers – Bird Bluff xenoliths are plotted on the geothermal gradient. (Right) Ternary diagram showing the mineralogical variation between the Mount Avers – Bird Bluff samples.

4.1.5 Bird Bluff, Fosdick Mountains

The peridotite xenoliths sourced from Bird Bluff equilibrated at temperatures between 853 and 1053°C, which corresponds to extraction depths spanning from 45 to 60 km. There are significant variations with respect to the microstructural and mineralogical properties of these rocks that occur over this 15 km depth range (Table 4.5; Figure 4.5). Crystallographic textures are heterogeneous on the sub-ten- kilometer-scale with samples preserving axial-[010], A-type and random olivine CPOs. The axial-[010] texture preserved in the dunite is stronger than either the A-type or the random texture, with the latter two displaying approximately the same values for both the J- and M-indices. Furthermore, this sample preserves the highest percentage (93.3%) and largest diameter (1180 μm) of olivine grains at this volcanic center, but is also inferred to be the weakest with a low mean differential stress value of 7 MPa. Comparatively, the strongest xenolith from this volcanic center is a wehrlite that preserves a mean differential stress of 30 MPa. Although this is a minor variation, these samples are sourced from similar depths (i.e. 45 and 51 km), which further supports the conclusion that this portion of the lithospheric mantle is structurally heterogeneous on the sub-ten-kilometer-scale.

Table 4.5. Xenoliths from Bird Bluff are arranged in order of increasing equilibration temperature alongside a summary of their microstructural and mineralogical properties. Note that XRCT analyses for sample FDM-BB04-X01 did not successfully reorient the samples into its kinematic frame of reference.

Sample	T (°C)	h (km)	Rock Name	CPO (ol)	J (ol)	M (ol)	Abundance (%) and Mean G.S. (μm)				Mean Δσ (MPa)
							ol	di	en	% px	
FDM-BB04-X01	853	45	Lherzolite	-	-	-	58.2% -	26.4% -	15.5% -	41.9	-
FDM-BB03-X01	856	45	Dunite	AG	4.1	0.21	93.3% 1180	2.4% 383	4.3% 458	6.7	7
FDM-BB01-X01	945	51	Wehrlite	A	1.4	0.07	56.1% 122	42.5% 130	1.3% 120	43.8	30
FDM-BB02-X01	1053	60	Lherzolite	Rand.	1.4	0.02	54.3% 322	21.3% 170	24.4% 393	45.7	10

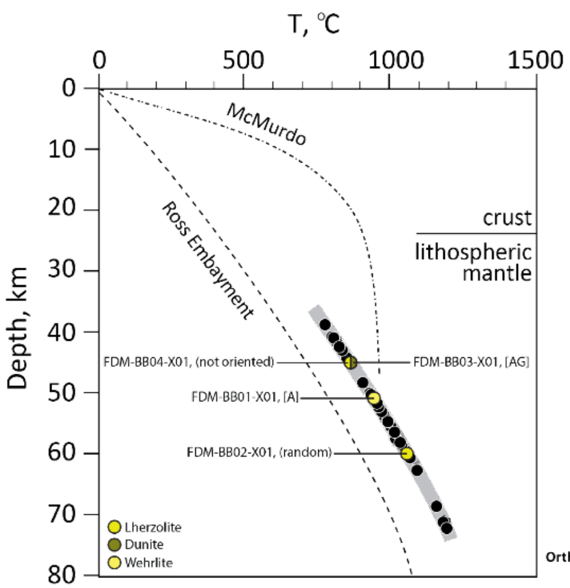

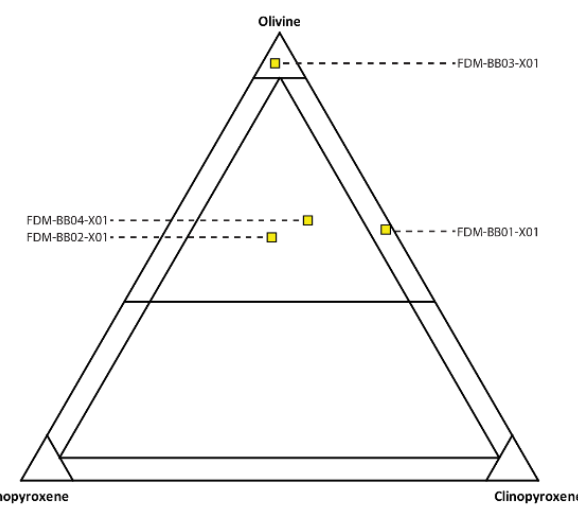

Figure 4.5. (Left) Extraction depths for the Bird Bluff xenoliths are plotted on the geothermal gradient. (Right) Ternary diagram showing the mineralogical variation between the Mount Avers – Bird Bluff samples.

Both a fertile mantle lherzolite and the pyroxene-depleted dunite are inferred to have been extracted from the same depth beneath this volcanic center (i.e. 45 km). As temperature increases, the samples from this volcanic center quickly transition from lherzolitic to dunitic and subsequently evolve towards lithologies with increasingly higher pyroxene contents. These observations lead to the conclusion that the lithospheric mantle beneath Bird Bluff displays mineralogical heterogeneities on the sub-ten-kilometer-scale. Although the wehrlite is depleted with respect to enstatite, the total amount of pyroxene in this sample (43.8%) is consistent with the total amount of pyroxene documented in the lherzolites from this volcanic center, which implies the operation of some geological process that allows for diopside enrichment (e.g., melt migration).

4.1.6 Demas Bluff, Fosdick Mountains

The Demas Bluff xenoliths sample the lithospheric mantle of MBL between depths of 41 and 72 km. These samples are microstructurally heterogeneous on the sub-five-kilometer scale and mineralogically heterogeneous on the sub-ten-kilometer scale (Table 4.6; Figure 4.6). Olivine textures alternate between axial-[010], A- and axial-[100] independent of variations in either grain size or temperature. Interestingly, only the lherzolites display all three textures documented at this volcanic center and they are also the only samples that record axial-[010] textures. The textural strength indices calculated for these axial-[010] CPOs is relatively consistent with J- and M- indices ranging from 2.8 to 4.0 and 0.15 to 0.20, respectively. Comparatively, the xenoliths that are depleted with respect to pyroxene display either A-type or axial-[100] textures. Axial-[100] textures (i.e. D-type) are marginally stronger and more variable than the axial-[010] textures, whereas A-type (i.e. orthogonal) textures are the strongest and span a larger range of values than either other CPO (i.e. 2.8 $\leq$

$J \leq 9.0$ and $0.14 \leq M \leq 0.37$). The strongest textures within the Demas Bluff xenoliths belong to two of the harzburgitic samples with A-type olivine CPOs that occur at different depths within the MBL mantle (i.e. 41 and 54 km), which further emphasizes the extent to which heterogeneity is observed at this volcanic center.

In terms of mineralogy, the Demas Bluff xenolith suite is predominantly comprised of lherzolites with other lithologies occurring over several narrow depth intervals (i.e. 41 – 44 km, 54 – 59 km and 71 – 72 km). Harzburgitic and dunitic samples occur at the shallowest depths (i.e. 41 – 44 km) and samples quickly transition to lherzolites between depths of 44 and 50 km. These samples are separated from another sequence of lherzolites (54 – 59 km) by the Demas Bluff clinopyroxenite and two harzburgites. Mineralogical heterogeneity cannot be assessed between 60 and 68 km because no samples are sourced from these depths. Importantly, the most deeply-sourced harzburgite occurs at a depth of 69 km, which is used to infer the existence of mineralogical heterogeneities between the lherzolites at 59 and 71 km.

When focusing on the mineralogy of the four harzburgites from this volcanic center, it is important to mention that they fall into two groups. Samples FDM-DB02-X08 and FDM-DB02-X02 are remarkably similar in terms of their mineralogies even though they are separated by a distance of approximately 13 km. Comparatively, sample FDM-DB04-X04 is sourced from approximately the same depth as FDM-DB02-X02, but its mineralogy parallels that of FDM-DB04-X02, which is from 16 km deeper within the lithospheric mantle of MBL. There is also vertical variation with respect to the modal mineralogy of the Demas Bluff lherzolites. Although most contain more than 60% olivine, three samples contain between 48.0 and 56.8% olivine. These xenoliths are sourced from dramatically different depths within the lithospheric mantle (i.e. 44, 54 and 72 km). Thus, is it concluded that there is no apparent correlation between phase abundance and equilibration temperature.

Table 4.6. The twenty xenoliths from Demas Bluff are arranged in order of increasing equilibration temperature alongside a summary of their microstructural and mineralogical properties. Note that samples FDM-DB02-X06 and FDM-DB03-X04 did not contain enough olivine grains to confidently assess the preserved textures or apply the piezometer.

Sample	T (°C)	h (km)	Rock Name	CPO (ol)	J (ol)	M (ol)	Abundance (%) and Mean G.S. (μm)				Mean Δσ (MPa)
							ol	di	en	% px	
FDM-DB02-X08	803	41	Harzburgite	A	7.1	0.37	87.6 1310	2.2 600	10.3 1200	12.5	6
FDM-DB03-X01	856	44	Dunite	D	5.5	0.25	91.1 1460	1.9 411	7.0 1150	8.9	6
FDM-DB03-X02	861	44	Lherzolite	AG	2.8	0.20	56.8 545	20.0 470	23.3 601	43.3	10
FDM-DB02-X13	911	49	Lherzolite	D	2.3	0.08	72.8 933	13.2 480	14.0 471	27.2	7
FDM-DB02-X04	933	50	Lherzolite	AG	3.9	0.20	61.6 1230	15.1 865	23.3 902	38.4	6
FDM-DB02-X05	958	52	Clinopyroxenite	-	-	-	0.3 -	99.2-	0.5 -	99.7	-
FDM-DB04-X04	968	53	Harzburgite	A	4.4	0.28	78.9 1310	1.6 124	19.5 1000	21.1	6
FDM-DB02-X02	978	54	Harzburgite	A	9.0	0.36	88.2 2000	1.9 113	9.9 594	11.8	4
FDM-DB03-X03	982	54	Lherzolite	D	2.7	0.09	60.1 898	18.1 405	21.8 553	39.9	8
FDM-DB04-X02	984	54	Lherzolite	AG	3.4	0.16	50.6 647	18.2 150	31.2 1040	49.4	10
FDM-DB04-X01	991	55	Lherzolite	AG	4.0	0.19	78.9 1450	6.1 491	15.0 1100	21.1	6
FDM-DB02-X03	999	55	Lherzolite	A	4.5	0.31	72.1 210	10.2 500	17.7 960	27.9	20

Table 4.6. Continued.

Sample	T (°C)	h (km)	Rock Name	CPO (ol)	J (ol)	M (ol)	Abundance (%) and Mean G.S. (μm) ol	di	en	% px	Mean Δσ (MPa)
FDM-DB03-X04	1002	56	Lherzolite	-	-	-	78.9 100	8.2 297	12.9 524	21.1	-
FDM-DB02-X10	1020	57	Lherzolite	A	4.3	0.26	65.2 736	15.1 236	19.7 1000	34.8	9
FDM-DB01-X01	1024	58	Lherzolite	A	2.8	0.14	61.2 885	24.0 451	14.8 521	38.8	8
FDM-DB02-X12	1036	59	Lherzolite	AG	3.3	0.15	64.8 599	21.0 377	14.2 444	35.2	10
FDM-DB02-X11	1039	59	Lherzolite	A	3.5	0.19	71.6 1610	15.3 302	13.0 795	28.3	5
FDM-DB04-X03	1165	69	Harzburgite	D	4.9	0.17	78.1 1360	3.2 100	18.7 1010	21.9	6
FDM-DB02-X01	1183	71	Lherzolite	D	3.0	0.20	70.2 494	15.3 373	14.5 484	29.8	11
FDM-DB02-X06	1198	72	Lherzolite	-	-	-	48.0 356	7.3 102	44.7 1160	52.0	-

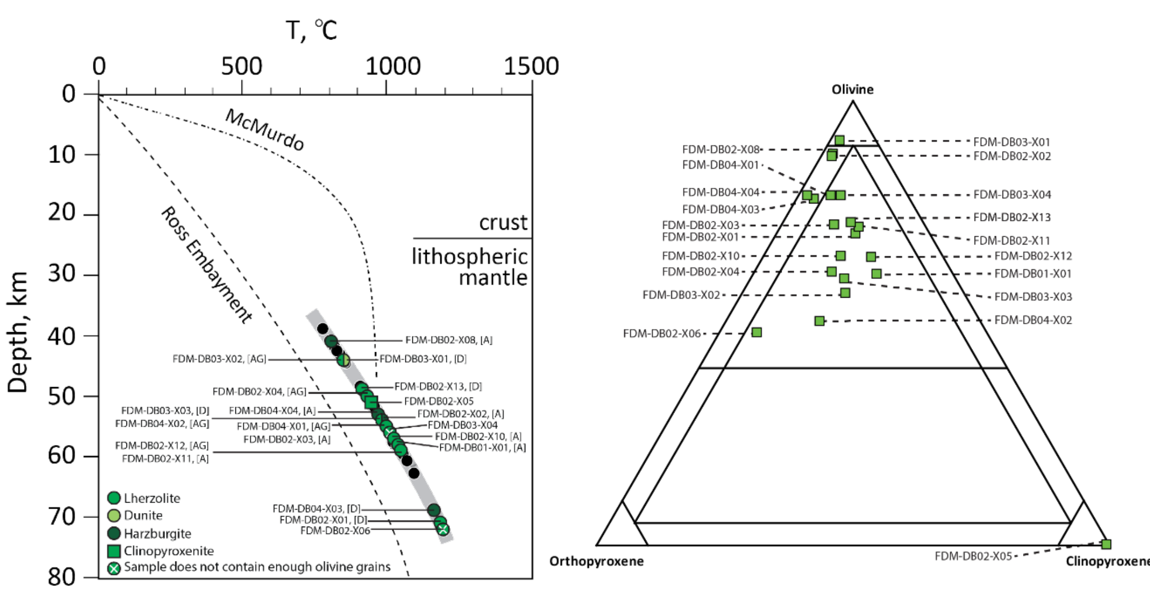

Figure 4.6. (Left) Extraction depths for the Demas Bluff xenoliths are plotted on the geothermal gradient. (Right) Ternary diagram showing the mineralogical variation between the Demas Bluff samples.

4.1.7 Marujupu Peak, Fosdick Mountains

The xenoliths from Marujupu Peak originated at depths between 48 and 61 km. The values for mean differential stress range from 10 to 30 MPa and seem to increase with temperature. Over this depth range, microstructural heterogeneities exist on the sub-five-kilometer scale. This conclusion is based on the observation of axial-[010] and A-type textures and the variations in the textural strength indices calculated for A-type textures (Table 4.7; Figure 4.7).

Comparatively, the mineralogy of the xenoliths sourced from this volcanic center is slightly more consistent. An olivine websterite is documented at the shallowest depth, but at deeper levels all remaining samples from Marujupu Peak are classified as lherzolites. The A-type lherzolites occurring at 50 and 53 km differ in regards to the strength of their olivine textures, but they display nearly identical phase abundances and preserve the same value for mean differential stress. Despite this, there is some variation with respect to the abundances of the constituent mineral phases deeper within the lithospheric mantle of MBL. Specifically, the most deeply-sourced sample – FDM-MJ01-X06 – preserves phase abundances that approach the composition one would expect to be contained within a pyroxenite. As a result, it is inferred that this portion of the lithospheric mantle displays minor mineralogical heterogeneities on the sub-ten-kilometer scale. These variations are classified as minor because they are noticeable, but do not cause variations in the lithology of the peridotites encountered at these depths.

Table 4.7. Five xenoliths from Marujupu Peak are arranged in order of increasing equilibration temperature alongside a summary of their microstructural and mineralogical properties. Note that sample FDM-MJ01-X01 is a pyroxenite (< 40% olivine), which means that it does not contain enough grains of olivine to either quantify the CPO or apply the recrystallized grain size piezometer.

Sample	T (°C)	h (km)	Rock Name	CPO (ol)	J (ol)	M (ol)	Abundance (%) and Mean G.S. (μm)				Mean Δσ (MPa)
							ol	di	en	% px	
FDM-MJ01-X01	898	48	Olivine Websterite	-	-	-	31.0% -	31.1% -	38.0% -	69.1	-
FDM-MJ01-X03	929	50	Lherzolite	A	2.7	0.09	66.1% 600	12.0% 377	21.8% 480	33.8	10
FDM-MJ01-X02	974	53	Lherzolite	A	4.0	0.20	66.5% 513	18.0% 315	15.5% 356	33.5	10
FDM-MJ01-X05	1014	57	Lherzolite	AG	3.8	0.16	72.4% 350	18.9% 186	8.7% 467	27.6	15
FDM-MJ01-X06	1070	61	Lherzolite	A	1.5	0.12	46.2% 122	24.1% 127	29.7% 530	53.8	30

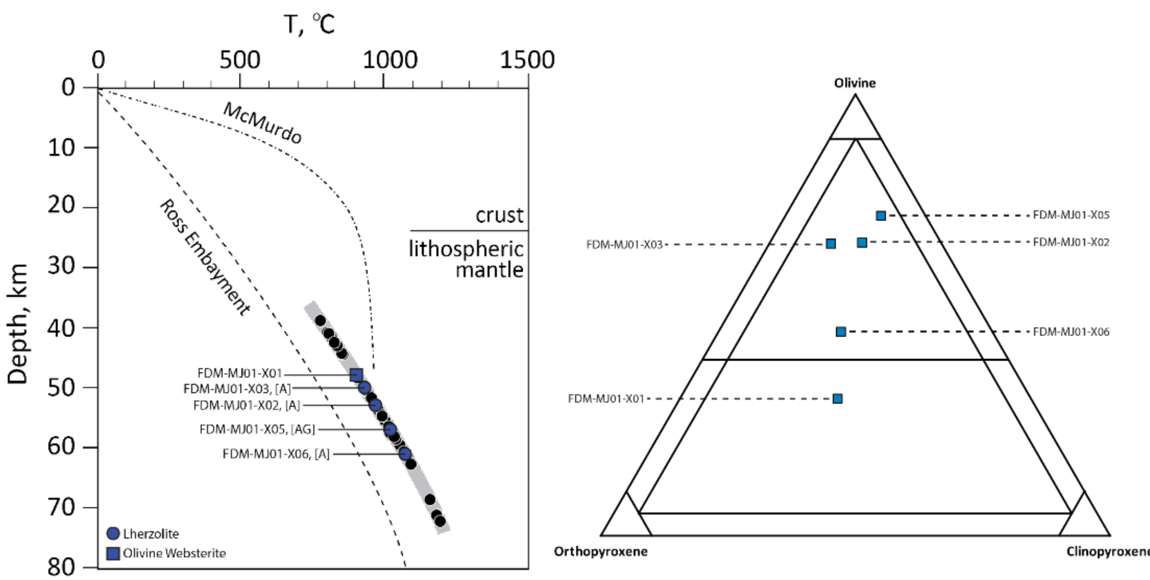

Figure 4.7. (Left) Extraction depths for the Marujupu Peak xenoliths are plotted on the geothermal gradient. (Right) Ternary diagram showing the mineralogical variation between the Marujupu Peak samples.

4.1.8 Recess Nunatak, Fosdick Mountains

The samples from Recess Nunatak are all peridotites that equilibrated at temperatures between 812 and 961°C, which correspond to depths ranging from 42 to 52 kilometers. These xenoliths display microstructural and mineralogical heterogeneities on the sub-ten-kilometer-scale (Table 4.8; Figure 4.8). Over a span of 10 kilometers, both A- and B-type olivine CPOs are documented in lherzolites and a wehrlite. Although the two most shallowly-sourced samples with A-type textures are homogeneous with respect to the values of textural indices, there is an abrupt switch from B-type to A-type occurring approximately between 51 and 52 kilometers. Furthermore, the A-type texture of the wehrlitic sample (FDM-RN01-X01) is the strongest of all textures documented at this volcanic center. Comparatively, the B-type texture is similar in strength to the A-type textures that occur above it. The values for mean differential stress are low, vary over a narrow range between 6 and 15 MPa and do not correlate with changes in temperature.

Two lherzolites interpreted to be extracted from a depth of 42 kilometers only display minor mineralogical variations between each other. The more deeply-sourced B-type lherzolite contains a higher percentage of olivine even though it occurs only nine kilometers deeper than the other two, which makes this sample more mineralogically similar to the wehrlite that is sourced from approximately the same depth. Despite their mineralogical similarities, it is important to reiterate that these two samples do not preserve the similar microstructures. The grain sizes preserved by the Recess Nunatak peridotites do not show any correlation with changes in depth, but it is interesting to note that there is an apparent increase in the abundance of olivine with increases in temperature at this volcanic center.

Table 4.8. Four xenoliths from Recess Nunatak are arranged in order of increasing equilibration temperature alongside a summary of their microstructural and mineralogical properties.

Sample	T (°C)	h (km)	Rock Name	CPO (ol)	J (ol)	M (ol)	Abundance (%) and Mean G.S. (μm)				Mean Δσ (MPa)
							ol	di	en	% px	
FDM-RN04-X01	812	42	Lherzolite	A	2.7	0.20	53.9% 528	18.7% 432	27.4% 497	46.1	11
FDM-RN02-X01	828	42	Lherzolite	A	2.7	0.16	62.5% 604	22.9% 317	14.7% 297	37.6	10
FDM-RN03-X01	943	51	Lherzolite	B	2.8	0.16	84.5% 406	6.2% 115	9.3% 291	15.5	15
FDM-RN01-X01	961	52	Wehrlite	A	4.3	0.25	89.1% 1290	9.7% 580	1.2% 357	10.9	6

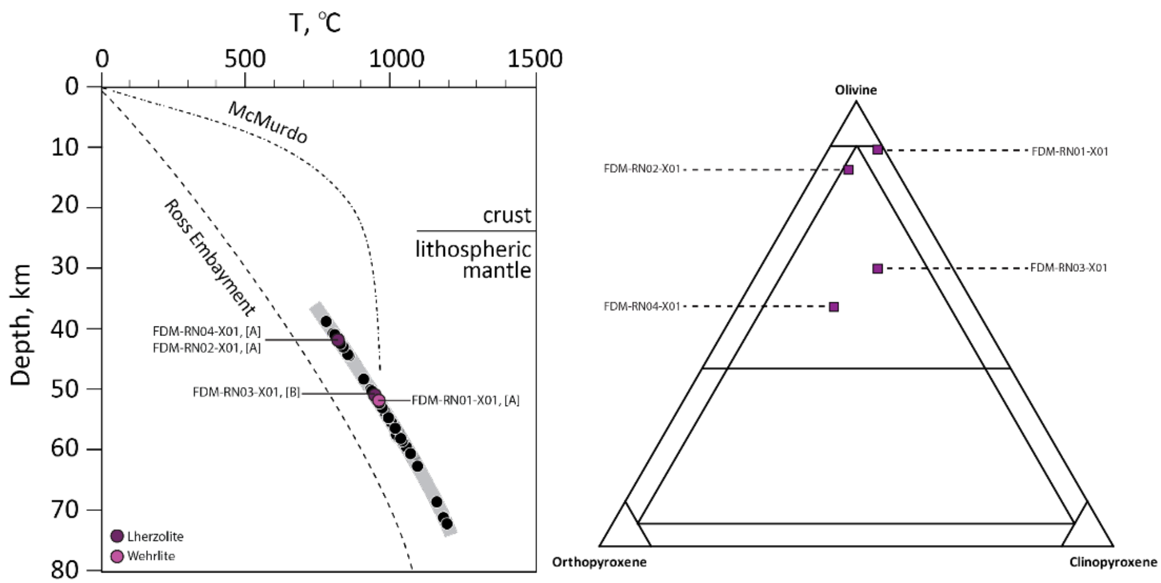

Figure 4.8. (Left) The extraction depths for the Recess Nunatak xenoliths are plotted on the geothermal gradient. (Right) Ternary diagram showing the mineralogical variation between the Recess Nunatak samples.

4.2 AN OVERVIEW OF VERTICAL HETEROGENEITIES IN MARIE BYRD LAND

The lithospheric mantle beneath MBL is deforming heterogeneously, which is supported by the observed variations in the microstructural and mineralogical properties of the xenolith samples sourced from individual volcanic centers. Some locations are highly homogenous with respect to their microstructural characteristics (e.g., Mount Avers – Bird Bluff), whereas others display heterogeneities on the sub-five-kilometer-scale (e.g., Demas Bluff). Comparatively, mineralogical heterogeneities are more consistent throughout the sample suite with variations generally being observed between the sub-five-kilometer-scale and the sub-ten-kilometer-scale. Furthermore, it is important to note that some volcanic centers that display unique properties (e.g., Demas Bluff is the only location at which harzburgites are documented; Recess Nunatak is the only volcanic center with a sample that preserves a B-type olivine CPO), which further reinforces the interpretation that this portion of Earth's mantle is deforming in a highly heterogeneous manner. Within the MBL xenoliths, dislocation-accommodated grain-boundary sliding is the dominant deformation mechanism and it operates at strain rates between 10^{-19}/s and 10^{-11}/s (Figure 4.9).

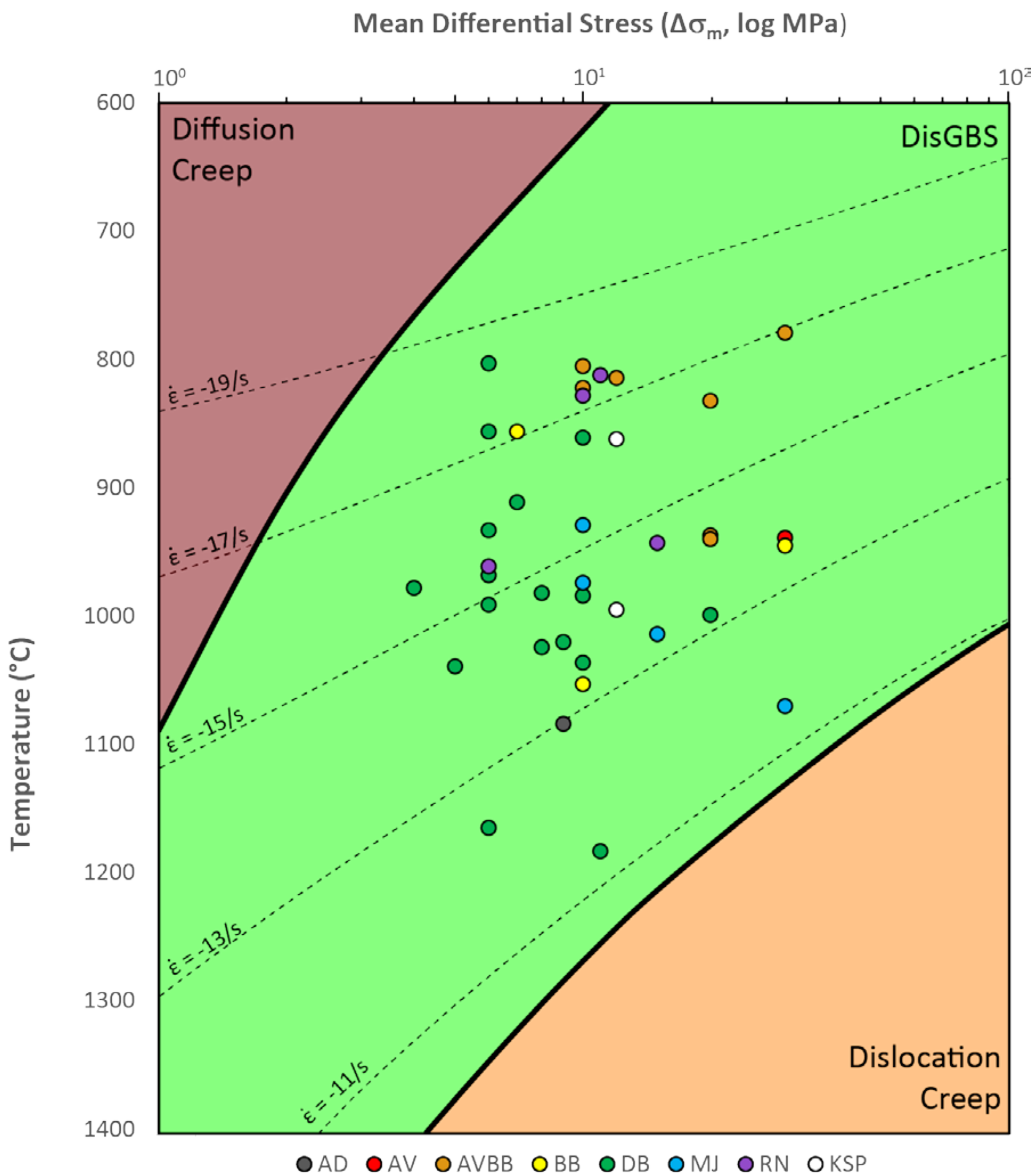

Figure 4.9. Deformation mechanism map showing that dislocation-accommodated grain-boundary sliding (disGBS) is the dominant method through which the MBL xenoliths store internal strain. Samples plot between strain rates of 10^{-19} and 10^{-11}/s.

4.3 LATERAL VARIATIONS ACROSS MARIE BYRD LAND

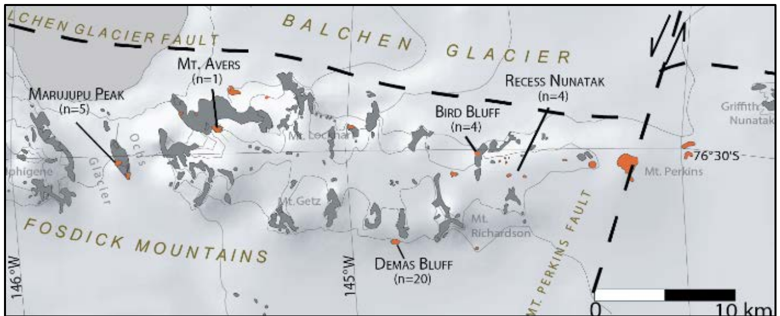

Volcanic Center	Latitude (°S)	Longitude (°W)
Recess Nunatak	76.519	144.507
Bird Bluff	76.504	144.598
Demas Bluff	76.568	144.853
Mount Avers	76.481	145.396
Marujupu Peak	76.508	145.670

Figure 4.10. Map of the Fosdick Mountains showing associated xenolith localities (modified from Gaffney and Siddoway, 2007). Not shown are the eight samples sourced from volcanic centers located between Mount Avers and Bird Bluff.

In addition to evaluating the heterogeneities documented at individual volcanic centers, understanding how mantle deformation varies laterally throughout MBL is imperative to assessing the extent and intensity of ongoing tectonic processes that are continuously influencing landscape evolution beneath the West Antarctic ice sheet (e.g., volcanism). This is accomplished by evaluating variations in heterogeneity as they change from west to east throughout the study area. The reason for choosing this transect is two-fold. Firstly, the majority of samples comprising the xenolith suite represent the Fosdick Mountains (n=42; Figure 4.10) in western MBL, whereas a total of three xenolith samples are from eastern MBL (i.e. Usas Escarpment and Executive Committee Range). Secondly, variations in the tectonic histories of western and eastern MBL imply they behaved as two distinct geographical provinces (i.e. the Ross and Amundsen Provinces, respectively) until mid-Cretaceous times (Pankhurst et al., 1998). As a result, it is logical to expect any important microstructural and/or mineralogical trends to appear along an east to west transect of MBL.

4.3.1 Western Marie Byrd Land

The xenoliths from volcanic centers within the Fosdick Mountains continuously sample a 33 kilometer thick portion of the actively deforming lithospheric mantle that underlies the West Antarctic Rift system. Taken as a whole, these xenoliths imply microstructural and mineralogical heterogeneities exist beneath the Fosdick Mountains between the sub-kilometer-scale and the sub-ten-kilometer scale with fewer lithological variations occurring with depth. Despite the abundant heterogeneities throughout the region, the majority of samples are lherzolites that preserve axial-[010] textures and record a narrow range of mean differential stresses that does not exceed 30 MPa (Figure 4.11). Deformation mechanism maps imply that all samples accommodate strain by the dominant operation of dislocation-accommodated grain-boundary sliding (disGBS) with strain rates ranging from 10^{-17} to 10^{-11}/s.

The westernmost volcanic center within the Fosdick Mountains is Marujupu Peak (Figure 4.12A). The five xenoliths from this location sample the lithospheric mantle over a 13 kilometer depth range. The mean differential stresses of these samples increase with temperature. A maximum of 30 MPa is recorded by an A-type lherzolite that was extracted from a depth of 61 kilometers. The most shallowly-sourced sample from this volcanic center is an olivine websterite. This sample is also the most shallowly-sourced and olivine-rich pyroxenite sample of the MBL suite. Other samples from Marujupu Peak are lherzolites that preserve an axial-[010] and three A-type textures, all of which are heterogeneous with respect to their relative strengths and vary on a sub-five-kilometer-scale. Compared to the average of all axial-[010] lherzolites, the axial-[010] sample from Marujupu Peak is finer-grained, enriched with respect to olivine and depleted with respect to enstatite. Two of the

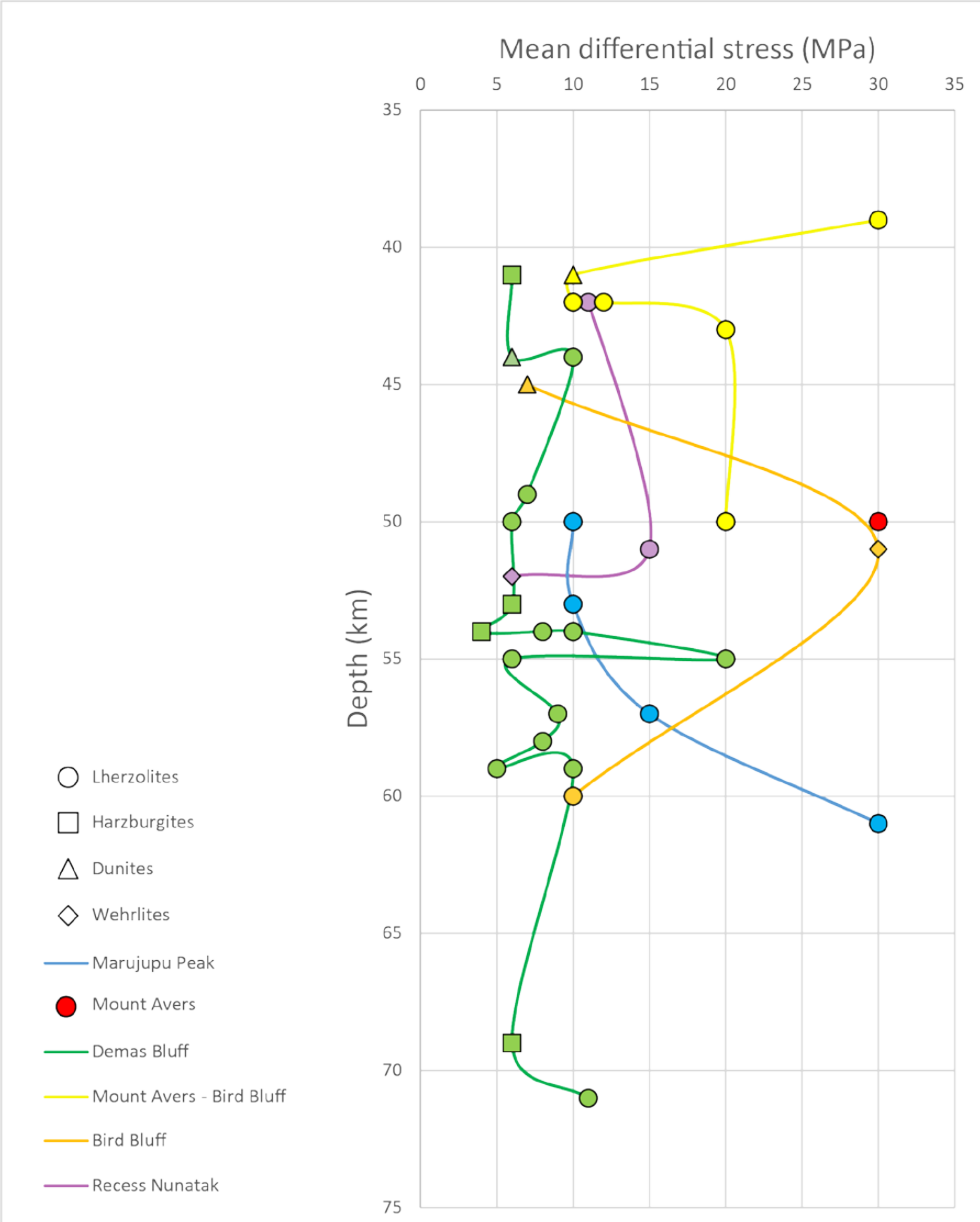

Figure 4.11. Lithospheric strength profiles for all xenoliths sourced from western MBL. The Cenozoic volcanic centers of the Fosdick Mountains in order from west to east are: Marujupu Peak, Mount Avers, Demas Bluff, Mount Avers – Bird Bluff, Bird Bluff, and Recess Nunatak. Only one sample is sourced from Mount Avers, which prevents any interpretation of how bulk rock strength changes with depth at this location.

A-type samples (i.e. FDM-MJ01-X02 and FDM-MJ01-X03) are representative of the average A-type lherzolite from MBL in terms of phase abundances, grain sizes and values of mean differential stress. Comparatively, sample FDM-MJ01-X06 is the most deeply-sourced A-type sample contained within the xenolith suite. It is more fine-grained and olivine-poor than any other A-type lherzolite and it is the sample that records the maximum differential stress at this volcanic center.

Moving eastward, the next volcanic center is Mount Avers (Figure 4.12B). The sole xenolith from this location is an A-type lherzolite that originated at a depth of 50 kilometers. Although there is only one Mount Avers sample, it preserves a mean differential stress of 30 MPa, which is the maximum mean differential stress recorded by the MBL suite. This sample is representative of the average A-type lherzolite from MBL in terms of the observed phase abundances and enstatite grain sizes, but contains smaller grains of both olivine and diopside (Table 4.11). There is an A-type lherzolite from Marujupu Peak that also preserves a mean differential stress of 30 MPa, but it occurs deeper within the lithospheric mantle (i.e. 61 km). This variation may imply that the strongest point within the lithospheric mantle migrates to shallower structural levels towards the eastern portion of the study area.

Demas Bluff is the volcanic center to the southeast of Mount Avers (Figure 4.13A). The twenty xenoliths from this location sample depths within the lithospheric mantle between 41 and 72 kilometers. Unlike the samples from Marujupu Peak, mean stresses do not increase with temperature and a maximum differential stress of 20 MPa is recorded by an A-type lherzolite that originated at a depth of 55 kilometers below this volcanic center. Although the difference is negligible, this value is 10 MPa less than the maximum value

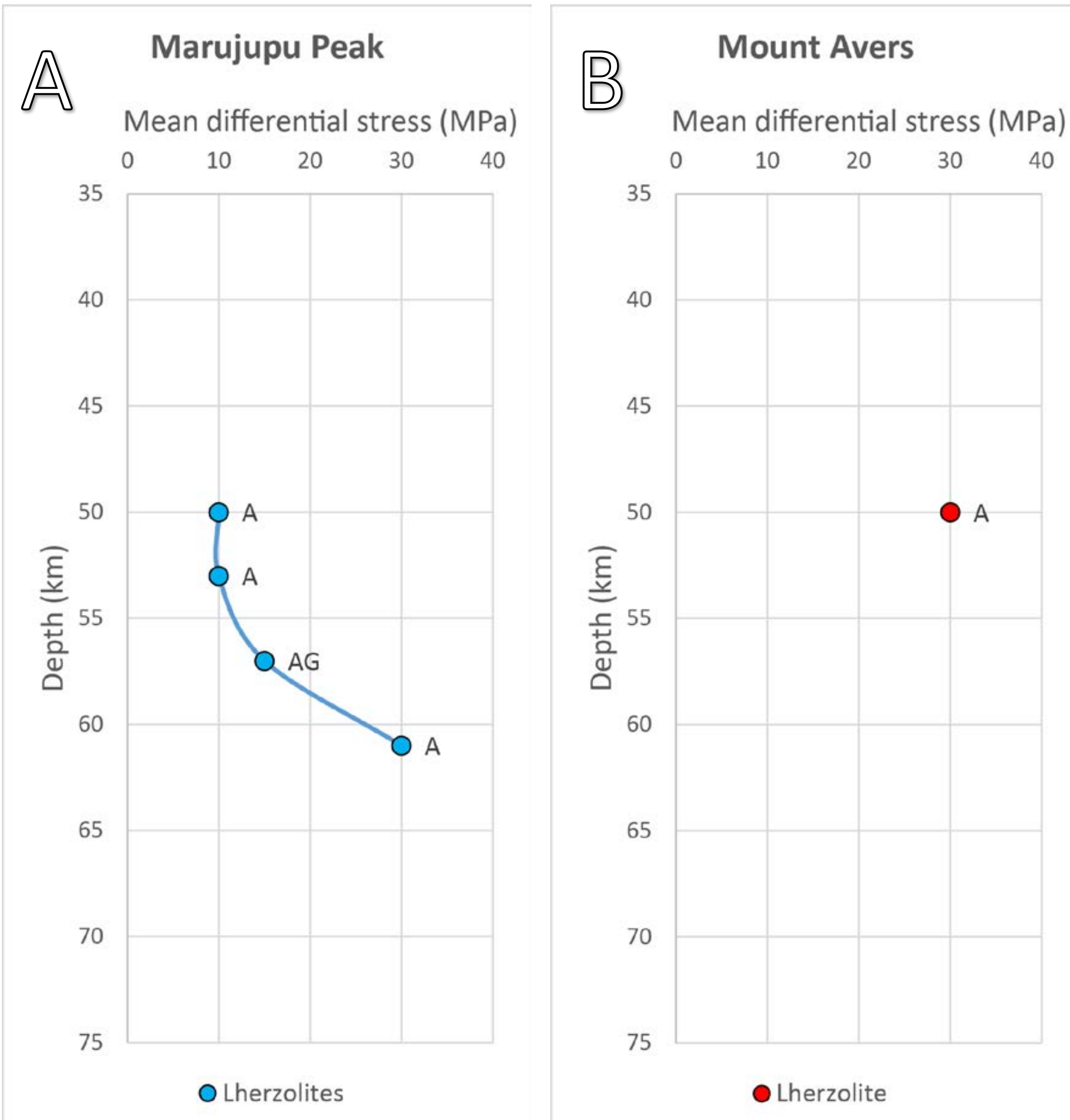

Figure 4.12. Lithospheric strength profiles for xenolith samples sourced from (A) Marujupu Peak, and (B) Mount Avers. Axial-[010] olivine textures are termed AG.

determined for the MBL xenolith suite and may imply the lithospheric mantle is slightly weaker in this region. Compared to Marujupu Peak, this region is also more mineralogically heterogeneous as fourteen lherzolites, four harzburgites, a dunite and a clinopyroxenite are all sourced from this location. The Demas Bluff clinopyroxenite is almost entirely diopside and contains some interstitial glass, which implies there is a significant amount of melt migrating through the lithospheric mantle beneath this volcanic center. This conclusion is also supported by the significant mineralogical heterogeneities that occur with depth beneath this volcanic center. There are five axial-[010], three axial-[100] and four A-type lherzolites from Demas Bluff.

The axial-[010] xenoliths sample depths between 44 and 50 kilometers. These samples are texturally strong and preserve low mean differential stresses when compared to other xenoliths that preserve this olivine texture. The A-type lherzolites from this volcanic center are mineralogically homogeneous and show olivine grain sizes increasing with depth, which does not agree with the overall trend observed throughout the MBL suite. Except for sample FDM-DB01-X01, these xenoliths display stronger than average values for both the J- and M-index. All axial-[100] lherzolites are from Demas Bluff and are relatively homogeneous. The most deeply-sourced sample (i.e. FDM-DB02-X01) only varies slightly in regards to its smaller olivine grain sizes. The dunite from this volcanic center also preserves an axial-[100] texture. Interestingly, these four samples are the only axial-[100] textures of the western Marie Byrd Land xenolith suite. Furthermore, the four harzburgites from Demas Bluff are the only harzburgitic samples identified within the entire MBL suite. These xenoliths are mineralogically homogeneous and quite weak as they preserve mean differential stresses between 4 and 6 MPa. The three harzburgites that preserve A-type olivine CPOs are texturally strong relative to those developed in other lithologies. Comparatively, the most deeply-sourced harzburgite preserves an axial-[100] texture that is slightly stronger than those preserved in axial-[100] lherzolites and slightly weaker than that preserved in the axial-[100] dunite.

The eight xenoliths sourced from volcanic centers located between Mount Avers and Bird Bluff sample the lithospheric mantle between depths of 39 and 51 kilometers and preserve mean differential stresses between 10 and 30 MPa (Figure 4.13B). At the shallowest structural levels sampled, lherzolites and wehrlites coexist and quickly transition to being exclusively lherzolitic between depths of 42 and 50 kilometers. This region is subsequently underlain by websterites, although the extent of this potential pyroxenite lens cannot be determined. Compared to samples from other volcanic centers, the Mount Avers – Bird Bluff peridotites are remarkably homogenous with respect to their microstructures as they all preserve axial-[010] textures of the same approximate intensity. The values of mean differential stress for these samples is consistently greater than those determined for any other axial-[010] peridotites. Specifically, sample FDM-AVBB02 records the largest value for mean differential stress and is sourced from a depth of 39 kilometers. Interestingly, this xenolith is the only axial-[010] lherzolite to record a mean value of 30 MPa and it is also more-shallowly sourced than the other MBL xenoliths that preserve a mean differential stress of equal magnitude. Compared to the entire suite, these samples are relatively strong overall with several peridotites recording mean differential stresses of 20 MPa between depths of 43 and 50 kilometers. The maximum value of mean differential stress at Marujupu Peak (i.e. 20 MPa) is recorded at a greater depth of 55 kilometers. Thus, the strength of the lithospheric mantle resides closer towards the base of the crust relative to other volcanic

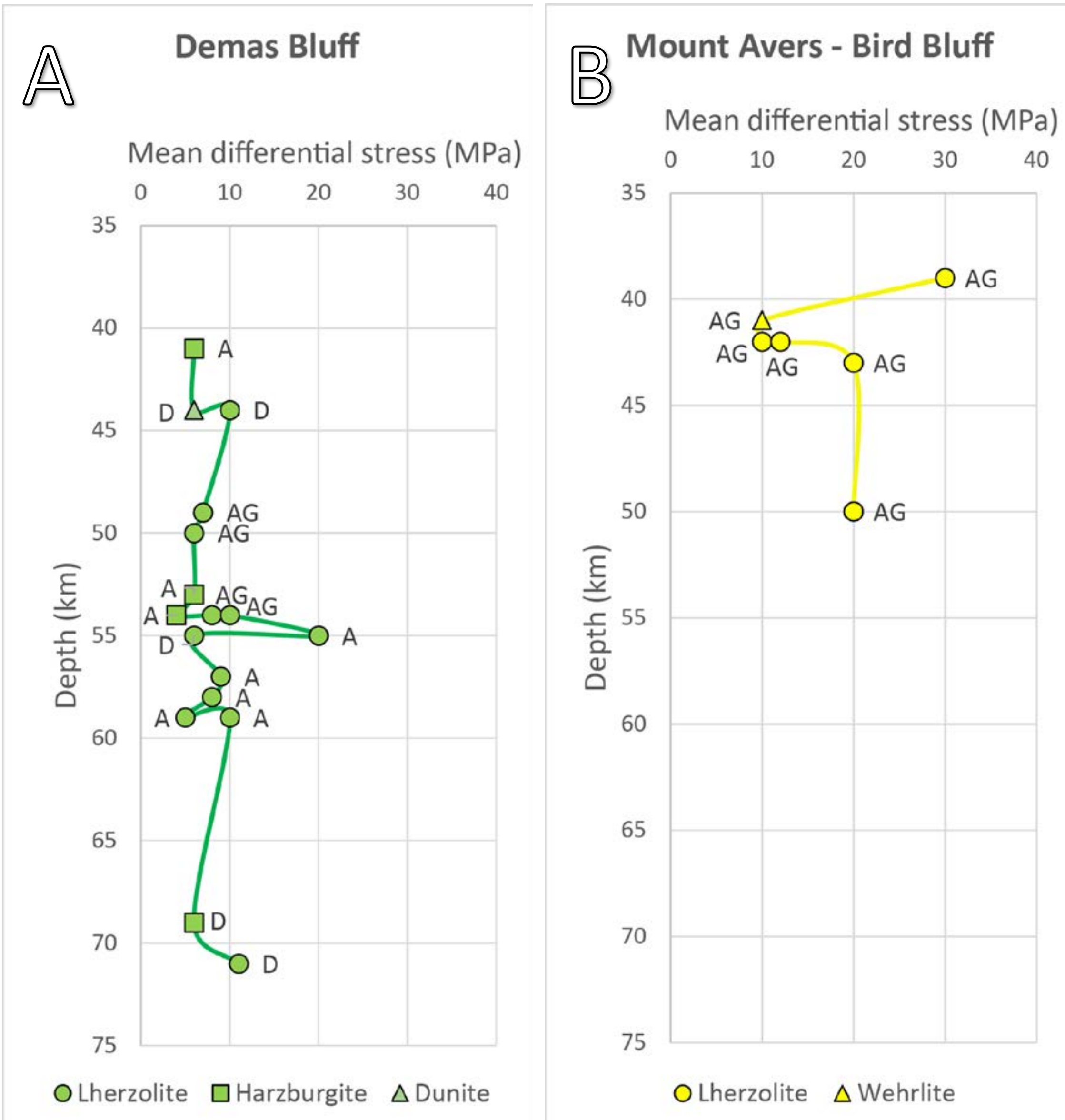

Figure 4.13. Lithospheric strength profiles for xenolith samples sourced from (A) Demas Bluff, and (B) volcanic centers located between Mount Avers and Bird Bluff. Axial-[010] and axial-[100] olivine textures are termed AG and D, respectively.

centers, which supports the observation that the strongest point within the lithospheric mantle migrates to shallower structural levels towards the eastern portion of the study area.

Bird Bluff is located to the north east of Demas Bluff (Figure 4.14A). The four xenoliths sourced from this volcanic center sample depths between 45 and 60 kilometers within the lithospheric mantle and record mean differential stresses ranging from 7 to 30 MPa. These samples display mineralogical and microstructural heterogeneities on the sub-five kilometer scale that do not correlate with changes in temperature. At the shallowest depths samples, lherzolite and dunite are inferred to coexist. Unfortunately, this lherzolitic sample (i.e. FDM-BB04-X01) is not reoriented into its kinematic frame of reference and its texture cannot be evaluated as a result. The dunite preserves the strongest axial-[010] texture recorded within the MBL xenolith suite. At a slightly greater depth of 51 kilometers, an A-type is documented. This sample is the most fine-grained and olivine-poor wehrlite of the suite and it preserves the maximum mean differential stress (i.e. 30 MPa) within this volcanic center, which implies the strongest portion of the lithospheric mantle beneath Bird Bluff is at approximately the same depth as that of Mount Avers. This is not in line with previous observations that suggest the strength of the lithospheric mantle migrates to higher structural levels towards the eastern portion of the study area. The final xenolith from this location is an olivine-poor lherzolite that preserves a random olivine CPO. Despite this, the textural indices calculated for this sample are similar to those calculated for the wehrlite that occurs above it. This is the only random CPO documented within the xenolith suite, but it is only the fourth most deeply-sourced sample. Thus, it can be inferred that recovery processes are dominant of intracrystalline deformation mechanisms in some parts of the lithospheric mantle beneath MBL. Comparatively, samples from Marujupu Peak and Demas Bluff record olivine textures up to depths of 61 and 71 kilometers, respectively.

The easternmost volcanic center of interest within the Fosdick Mountains is Recess Nunatak (Figure 4.14B). Three lherzolites and one wehrlite are sourced from this volcanic center. They collectively sample depths between 42 and 52 kilometers and record mean differential stresses between 6 and 15 MPa. The two most shallowly-sourced samples are A-type lherzolites that are microstructurally and mineralogically homogenous. Although the third lherzolite displays similar values for its textural indices, it is more olivine-rich than the others and it preserves the only B-type olivine texture of all samples contained within the MBL xenolith suite. This sample also preserves the greatest value of mean differential stress at this volcanic center (i.e. 15 MPa). Although this value is less than what is observed at other volcanic centers, it implies that the strongest portion of the mantle is at a depth of approximately 51 kilometers, which is also the conclusion made for Mount Avers and Bird Bluff. Importantly, analyses to determine the water content of olivine within this B-type sample show that it is dry (Chatzaras et al., in revision). This is in direct opposition to the findings of many experimental studies (e.g., Jung and Karato, 2001). The most deeply-sourced sample from Recess Nunatak is an A-type wehrlite that has higher J- and M-index values than any other xenolith from this location.

4.3.2 Eastern Marie Byrd Land

There are three samples sourced from eastern MBL, of which only two are peridotites that directly inform on microstructural variations that develop in response to the conditions of deformation. The third is a clinopyroxenite from Mount Aldaz that is sourced from depths greater than any pyroxenite in western MBL. Similarly, the axial-[010] lherzolite from Mount

Aldaz is more deeply-sourced than any axial-[010] peridotite from western MBL (Figure 3.15A). Furthermore, this xenolith preserves a mean differential stress of 9 MPa, which is relatively low compared to the values displayed by other samples having axial-[010] textures. The unique sample from Mount Cumming is a dunite with an axial-[100] olivine CPO. This is the only xenolith that does not contain enough pyroxene to apply geothermometers associated with the chemistry of diopside and enstatite. Application of the olivine-spinel exchange geothermometer shows an extraction depth between 42 and 52 kilometers (Figure 4.15B). These samples imply that western MBL is likely mineralogically heterogeneous at the sub-ten-kilometers scale, whereas scales of microstructural heterogeneity are more difficult to assess. Despite this, mineralogical variations are intimately related to microstructural variations, so it is reasonable to assume this region of MBL is also microstructurally heterogeneous at the sub-ten-kilometer-scale.

4.4 SUMMARY OF LATERAL HETEROGENEITY

Collectively, the MBL xenoliths continuously sample a 33 kilometer thick portion of the actively deforming lithospheric mantle that underlies portions of the slowly-expanding West Antarctic Rift system. These samples preserve significant mineralogical and microstructural heterogeneities that are documented laterally and vertically throughout the study area, which imply mantle deformation varies complexly at the sub-kilometer to sub-ten-kilometer scale. Values of mean differential stress only vary slightly throughout the field area, but generally seem to decrease in magnitude towards the east with maximum values migrating upwards in the lithospheric mantle along this transect. Although there is a strong sample bias towards Demas Bluff, the amount of mineralogical heterogeneity seems to decrease

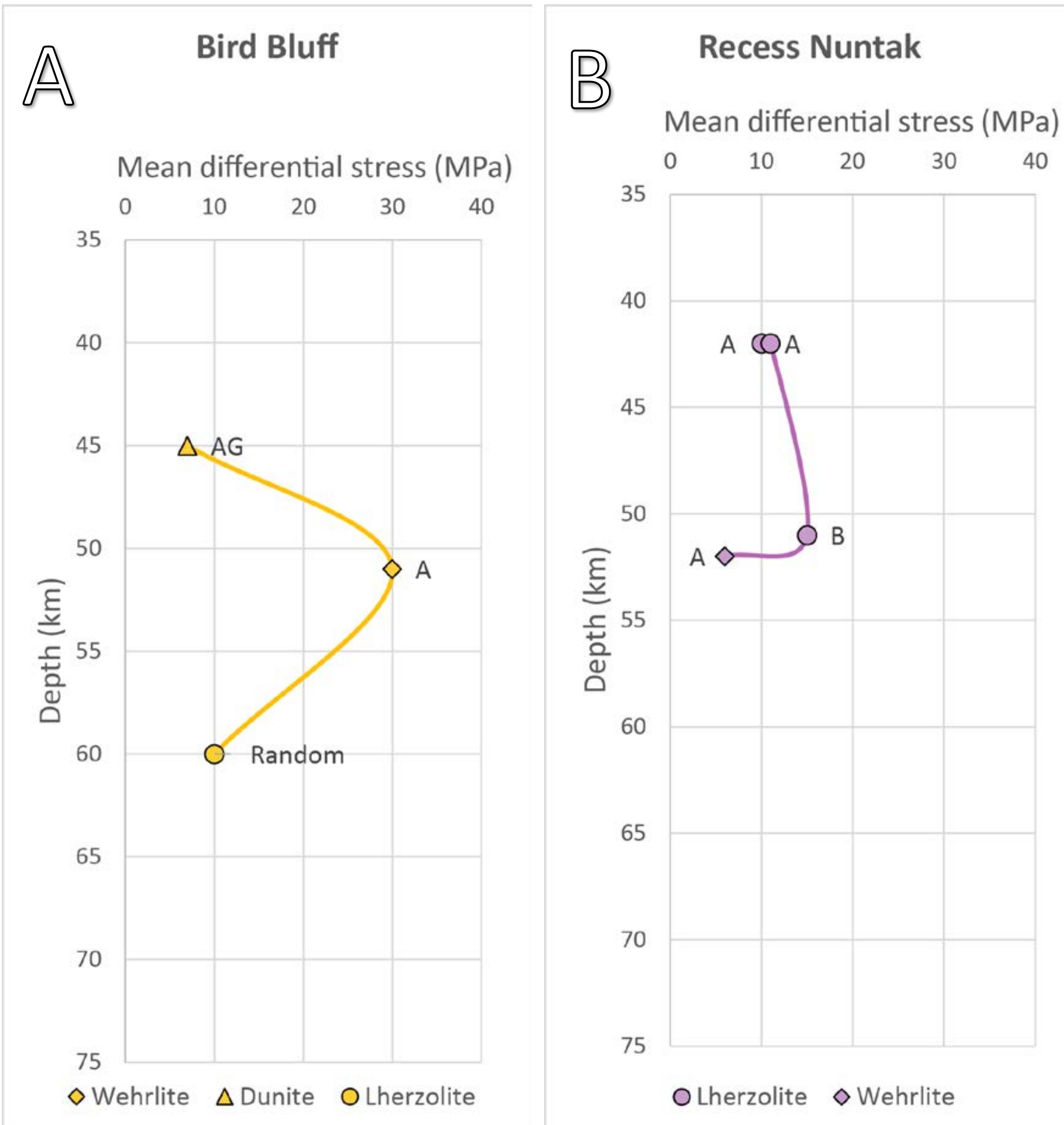

Figure 4.14. Lithospheric strength profiles for xenolith samples sourced from (A) Bird Bluff, and (B) Recess Nunatak. Axial-[010] olivine textures are termed AG.

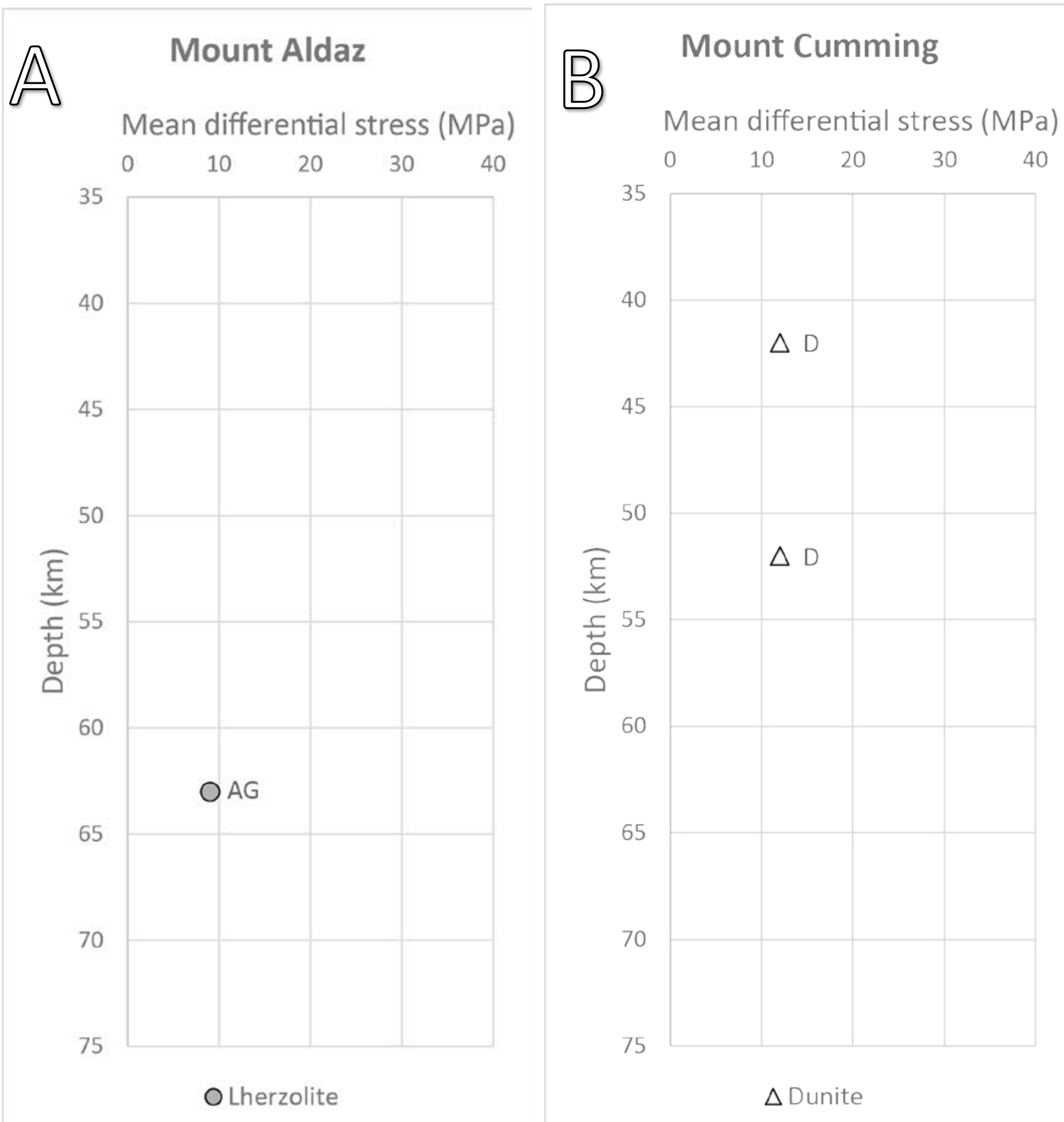

Figure 4.15. Lithospheric strength profiles for the xenolith samples from eastern Marie Byrd Land. (A) Mount Aldaz, Usas Escarpment, and (B) Mount Cumming, Executive Committee Range. Note that the dunite from Mount Cumming has two equilibration temperatures because spinel grains show compositional heterogeneity in terms of Cr-content on the thin section scale. Axial-[010] and axial-[100] olivine textures are termed AG and D, respectively.

with increasing depth, whereas microstructural heterogeneities exist at all depths. Despite these heterogeneities, most samples can be accurately described as lherzolites having either AG- or A-type olivine CPOs. Furthermore, the entirety of the MBL xenolith suite is inferred to deform primarily by the operation of disGBS at strain rates between 10^{-17} and 10^{-11}/s.

4.5 Broader Impacts

Although the West Antarctic rift system is one of the most expansive regions of extended continental crust on Earth, relatively little is known about the structure and heterogeneity of the mantle lithosphere in this region. This deficiency is attributable to the harsh Antarctic climate, the extensive cover of outcrop by the West Antarctic ice sheet, and the fact that seismic stations have only become commonplace across the continent within the last decade. Prior to the establishment of the GPS and seismic instrumentation network by POLENET/ANET in International Polar Year 2007-08, most data that aimed to inform on the lithospheric structure of Antarctica was derived from aeromagnetic surveys (e.g., Behrendt et al., 1996), surface wave dispersion measurements (e.g., Ritzwoller et al., 2001), shipboard geophysical studies (e.g., Luyendyk et al., 2001), determinations of seismic anisotropy using shear wave splitting (e.g., Müller, 2001), surface wave tomography (e.g., Sieminski et al., 2003), and teleseismic broad-band events (e.g., Winberry and Anandakrishnan, 2004). Although these studies were imperative for improving our understanding of the Antarctic lithosphere, their results are generally low-resolution and do not directly inform on the complexities of lithospheric structure that are observed at the outcrop scale (e.g., Kruckenberg et al., 2013).

Since the installation of the POLENET/ANET array across West Antarctica and the Transantarctic Mountains, geophysical researchers have used the resultant seismic data to place better constraints on the patterns of mantle seismic anisotropy within this largely enigmatic continental rift system. The characteristic seismic anisotropy that defines Earth's upper mantle is commonly interpreted to result from the generation of CPO in olivine, which in turn is thought to develop as olivine aligns with the direction of viscoplastic mantle flow. Consequently, such reports of anisotropy are used to infer the kinematics of global mantle flow patterns and to elucidate information regarding active tectonic processes (e.g., Nicolas and Christensen, 1987; Mainprice, 2007; Bodmer et al., 2015). Furthermore, the known olivine textures are thought to transmit seismic waves differently. For example, the fast axis of olivine having an A-type texture is thought to align with the extension and/or flow direction, whereas the fast axis aligns itself normal to the direction of maximum shear in B-type olivine textures (Zhang and Karato, 1995; Jung and Karato, 2001).

Due to the relationship that exists between olivine texture (i.e. CPO) and seismic anisotropy, the results of this study provide constraints for interpreting the results of shear wave splitting studies conducted in West Antarctica (e.g., Accardo et al., 2014). This is of great importance because the olivine crystallographic textures documented within the MBL xenolith suite are heterogeneous on scales that are smaller than the highest resolution attainable using contemporary geophysical methods. In turn, this implies that patterns of mantle flow and deformation are far more complex than these indirect studies suggest. Thus, the results of experimental, geophysical, and field studies must be considered collectively in order to develop a reliable model that describes the structure of West Antarctic lithosphere. Continued efforts towards developing this model will allow researchers to better understand how continental rifting is being accommodated within the Antarctic lithosphere with possible implications for the stability of the West Antarctic ice sheet (Shapiro and Ritzwoller, 2004).

REFERENCES CITED

Accardo, N.J., Wiens, D.A., Hernandez, S., Aster, R.C., Nyblade, A., Huerta, A., Anandakrishnan, S., Wilson, T., Heeszel, D.S., and Dalziel, I.W.D. (2014), Upper mantle seismic anisotropy beneath the West Antarctic Rift System and surrounding region from shear wave analysis. *Geophysics Journal International*, v. 198, pp. 414-429.

Ashby, M.F. and Verrall, R.A. (1973), Diffusion accommodated flow and superplasticity. *Acta Metallurgica*, v. 36, pp. 469-491.

Avé Lallemant, H.G. and Carter, N.L. (1970), Syntectonic recrystallization of olivine and modes of flow in the upper mantle. *Geological Society of America Bulletin*, v. 81, pp. 2203-2220.

Bai, Q., Mackwell, S.J., and Kohlstedt, D.L. (1991), High temperature creep of olivine single crystals 1. Mechanical results for buffered samples. *Journal of Geophysical Research*, v. 96, pp. 2441-2463.

Bachmann, F., Hielscher, R., and Schaeben, H. (2011), Grain detection from 2d and 3d EBSD data – Specification of the MTEX algorithm. *Ultramicroscopy*, v. 111, pp. 1720-1733.

Ballhaus, F., Berry, R.F., and Green, D.H. (1991), High pressure experimental calibration of olivine-orthopyroxene-spinel oxygen geobarometer: implications for the oxidations state of the upper mantle. *Contributions to Mineralogy and Petrology*, v. 107, pp. 27-40.

Behr, W.M., and Hirth, G. (2014), Rheological properties of the mantle lid beneath the Mojave region in southern California. *Earth and Planetary Science Letters*, v. 393, pp. 60-72.

Behrendt, J.C., LeMasurier, W.E., Cooper, A.K., Tessensohn, F., Trehu, A., and Damaske, D. (1991), Geophysical studies of the West Antarctic Rift System. *Tectonics*, v. 10, pp. 1257-1273.

Behrendt, J.C., Saltus, R., Damaske, D., McCafferty, A., Finn, C.A., Blankenship, D., and Bell, R.E. (1996), Patterns of late Cenozoic volcanic and tectonic activity in the West Antarctic rift system revealed by aeromagnetic surveys. *Tectonics*, v. 15, pp. 660-676.

Ben Ismaïl, W., and Mainprice, D. (1998), An olivine fabric database: an overview of upper mantle fabrics and seismic anisotropy. *Tectonophysics*, v. 296, pp. 145-157.

Bertrand, P., and Mercier, J.C.C. (1985), The mutual solubility of coexisting ortho- and clinopyroxene: toward an absolute geothermometer for the natural system? *Earth and Planetary Science Letters*, v. 76, pp. 109-122.

Bestmann, M., and Prior, D.J. (2003), Intragranular dynamic recrystallization in naturally deformed calcite marble: diffusion accommodated grain boundary sliding as a result of subgrain rotation recrystallization. *Journal of Structural Geology*, v. 25(10), pp. 1597-1613.

Bodmer, M., Toomey, D.R., Hooft, E.E., Nábělek, J., and Braunmiller, J. (2015), Seismic anisotropy beneath the Juan de Fuca plate system: Evidence for heterogeneous mantle flow. *Geology*, v. 43(12), pp. 1095-1098.

Brace, W.F., and Kohlstedt, D.L. (1980), Limits of lithospheric stress imposed by laboratory experiments. *Journal of Geophysical Research*, v. 85, pp. 6248-6252.

Brey, G.P., and Köhler (1990), Geothermobarometry in four-phase lherzolites: II. New Thermobarometers and practical assessment of existing thermobarometry. *Journal of Petrology*, v. 31, pp. 1352-1378.

Bunge, H. (1982), Texture Analysis in Materials Science: Mathematical Models. Butterworths, London. 593 pp.

Carter, N.L., and Avé Lallemant, H.G. (1970), High temperature deformation of dunite and peridotite. *Geological Society of America Bulletin*, v. 81, pp. 2181-2202.

Chatzaras, V., Tikoff, B., Newman, J., Withers, A.C., and Drury, M.R. (2015), Mantle strength of the San Andreas fault system and the role of mantle-crust feedbacks. *Geology*, v. 43(10), pp. 891-894.

Chatzaras, V., Kruckenberg, S.C., Cohen, S.M., Medaris Jr., L.G., Withers, A.C., and Bagley, B. (in revision), Axial-type olivine crystallographic preferred orientations: the effect of strain geometry on mantle texture. *Journal of Geophysical Research*.

Couvy, H., Frost, D.J., Heidelbach, F., Nyils, K., Ungar, T., Mackwell, S.J., and Cordier, P. (2004), Shear deformation experiments of forsterite at 11 GPa - 1400°C in the multianvil apparatus. *European Journal of Mineralogy*, v. 16, pp. 877-889.

Demouchy, S., Tommasi, A., Barou, F., Mainprice, D., and Cordier, P. (2012), Deformation of olivine in torsion under hydrous conditions. *Physics of the Earth and Planetary Interiors*, v. 202-203, pp. 85-99.

Durham, W.B. and Goetze, C. (1977), Plastic flow of oriented single crystals of olivine: 1. Mechanical data. *Journal of Geophysical Research*, v. 82, pp. 5737-5753.

Elliot, D.H. (2013), The geological and tectonic evolution of the Transarctic Mountains: a review, in *Antarctic Palaeoenvironments and Earth-Surface Processes*, eds. M.J. Hambrey, P.F. Barker, P.J. Barrett, V. Bowman, B. Davies, J.L. Smellie, and M. Tranter, Geological Society, London, Special Publications, v. 381, pp. 7-35.

Evans, B. and Goetze, C. (1979), The temperature variation of hardness of olivine and its implication for polycrystalline yield stress. *Journal of Geophysical Research*, v. 84, doi: 10.1029/JB080i010p05505.

Falus, G., Tommasi, A., and Soustelle, V. (2011), The effect of dynamic recrystallization on olivine crystal preferred orientations in mantle xenoliths deformed under varied stress conditions. *Journal of Structural Geology*, v. 33, pp. 1528-1540.

Finn, C.A., Muller, R.D., and Panter, K.S. (2005), A Cenozoic diffuse alkaline magmatic province (DAMP) in the southwest Pacific without rift or plume origin. *Geochemistry Geophysics Geosystems*, v. 6(1), Q02005, doi:10.1029/2004GC000723.

Gaffney, A.M., and Siddoway, C.S. (2007), Heterogeneous sources for Pleistocene laves of Marie Byrd Land, Antarctica: new data from the SW Pacific diffuse alkaline magmatic province. *U.S. Geological Survey Open-File Report 07-1047*, Extended Abstract 063.

Gerbi, C., Johnson, S.E., Cook, A., and Vel, S.S. (2015), Effect of phase morphology on bulk strength for power-law materials. *Geophysical Journal International*, v. 200, pp. 374-389, doi:10.1093/gji/ggu388.

Handler, M.R., Wysoczanski, R.J., and Gamble, J.A. (2003), Proterozoic lithosphere in Marie Byrd Land, West Antarctica: Re-Os systematics of spinel peridotite xenoliths. *Chemical Geology*, v. 196 (1-4), p. 131-145.

Hansen, L.N. and Warren, J.M. (2015), Quantifying the effect of pyroxene on deformation of peridotite in a natural shear zone. *Journal of Geophysical Research*, v. 120, pp. 2717-2738, doi:10.1002/2014JB011584.

Hansen, L.N., Zimmerman, M.E., and Kohlstedt D.L. (2011), Grain boundary sliding in San Carlos olivine: Flow law parameters and crystallographic preferred orientation. *Journal of Geophysical Research*, v. 116, B08201, doi:10.1029/2011JB008220.

Hansen, L.N., Zimmerman, M.E., and Kohlstedt, D.L. (2012), The influence of microstructure on deformation of olivine in the grain-boundary sliding regime. *Journal of Geophysical Research*, v. 117, B09201.

Harley, S.L., Fitzsimmons, I.C.W., and Zhao, Y. (2013), Antarctica and supercontinent evolution: historical perspectives, recent advances and unresolved issues. *Geological Society of London, Special Publications*, v. 383, p. 1-34.

Hirth, G. (2002), Laboratory constraints on the rheology of the upper mantle, in *Plastic Deformation of Minerals and Rocks, Reviews in Mineralogy and Geochemistry*, eds. S. Karato and H. Wenk, v. 51, pp. 97-120.

Hirth, G. and Kohlstedt, D.L. (2003), Rheology of the upper mantle and the mantle wedge: A view from the experimentalists, in *Inside the Subduction Factory*, ed. J. Eiler, Geophysical Monograph American Geophysical Union, Washington, D.C., v. 138, pp. 83-105.

Holtzman, B.K., Kohlstedt, D.L., Zimmerman, M.E., Heidelback, F., Hiraga, T., and Hustoft, J. (2003), Melt Segregation and Strain Partitioning: Implications for Seismic Anisotropy and Mantle Flow. *Science*, v. 301 (5637), pp. 1227-1230.

Jung, H., and Karato, S. (2001), Water-Induced Fabric Transitions in Olivine. *Science*, v. 293, pp. 1460-1463.

Jung, H., Katayama, I., Jiang, Z., Hiraga, T., and Karato, S. (2006), Effect of water and stress on the lattice-preferred orientation of olivine. *Tectonophysics*, v. 421, pp. 1-22.

Jung, H., Mo, W., and Green, H.W. (2009), Upper mantle seismic anisotropy resulting from pressure-induced slip transition in olivine. *Nature Geoscience*, v. 2, pp. 73-77.

Karato, S.I., Toriumi, M., and Fuji, T. (1980), Dynamic recrystallization of olivine single crystals during high-temperature creep. *Geophysical Research Letters*, v. 7, pp. 649-652.

Karato, S., Jung, H., Katayama, I., and Skemer, P. (2008), Geodynamic significance of Seismic Anisotropy of the Upper Mantle: New Insights from Laboratory Studies. *Annual Review of Earth and Planetary Sciences*, v. 36, pp. 59-95.

Katayama, I., Jung, H., and Karato, S. (2004), New type of olivine fabric from deformation experiments at modest water content and low stress. *Geology*, v. 32(12), pp. 1045-1048.

Katayama, I., Michibayashi, K., Terao, R., Ando, J.I., and Komiya, T. (2011), Water content of the mantle xenoliths from Kimberley and implications for explaining textural variations in cratonic roots. *Geological Journal*, v. 46, pp. 173-182.

Kohlstedt, D.L., Evans, B., and Mackwell, S.J. (1995), Strength of the lithosphere: constraints imposed by laboratory experiments. *Journal of Geophysical Research*, v. 100, pp. 17587-17602.

Kruckenberg, S.C., Tikoff, B., Toy, V.G., Newman, J., and Young, L.I. (2013), Strain localization associated with channelized melt migration in upper mantle lithosphere: insights from the Twin Sisters ultramafic complex, Washington, USA. *Journal of Structural Geology*, v. 50, pp. 133-147.

Lawver, R.L., and Gahagan, L.M. (1994), Constraints on timings of extension of the Ross Sea region. *Terra Antarctica*, v. 1, p. 545-552.

Le Maitre, R. W. (2002), Igneous Rocks: a Classification and Glossary of Terms: Recommendations of the International Union of Geological Sciences Subcommission on the Systematics of Igneous Rocks, Cambridge: Cambridge University Press, 236 pp.

LeMasurier, W.E. (2008), Neogene extension and basin deepening in the West Antarctic rift inferred from comparisons with the East African rift and other analogs. *Geology*, v. 36, pp. 247-250.

Luyendyk, B.P., Sorlien, C.C., Wilson, D.S., Bartek, L.R., and Siddoway, C.S. (2001), Structural and tectonic evolution of the Ross Sea Rift in the Cape Colbeck region, Easteron Ross Sea, Antarctica. *Tectonics*, v. 20, pp. 933-958.

Mainprice, D. (2007), Seismic anisotropy of the deep Earth from a mineral and rock physics perspective, ed. G Schubert. *Treatise on Geophysics*, v. 2, pp. 437-492.

Mainprice, D., Bachmann, F., Hielscher, R., and Schaeben, H. (2014), Descriptive tools for the analysis of texture projects with large datasets using MTEX – strength, symmetry and components. *Geological Society of London Special Publication*, Field Experiment and Theory: In Honour of Ernest Rutter.

Mainprice, D., Tommasi, A., Couvy, H., Cordier, P, and Frost, D.J. (2005), Pressure sensitivity of olivine slip systems and seismic anisotropy of Earth's upper mantle. *Nature*, v. 433, pp. 731-733.

Maitland, T., and Sitzman, S. (2007), Electron Backscatter Diffraction (EBSD) Technique and Materials Characterization Examples, in *Scanning Microscopy for Nanotechnology Techniques and Applications*, eds. W. Zhou and Z.L. Wang, 522 pp.

Mercer, J.H. (1978), West Antarctica ice sheet and CO_2 greenhouse effect: a threat of disaster. *Nature*, v. 271, pp. 321-325.

Miyazaki, T., Sueyoshi, K., and Hiraga, T. (2013), Olivine crystals align during diffusion creep of Earth's upper mantle. *Nature*, v. 502, pp. 321-326.

Mizukami, T., Wallis, S.R., and Yamamoto, J. (2004), Natural examples of olivine lattice preferred orientation patterns with a flow-normal a-axis maximum. *Nature*, v. 427, pp. 432-436.

Mukasa, S.B., and Dalziel, I.W.D. (2000), Marie Byrd Land, West Antarctica: Evolution of Gondwana's Pacific margin constrained by zircon U-Pb geochronology and feldspar common-Pb isotopic compositions. *Geological Society of America Bulletin*, v. 112(4), pp. 611-627.

Müller, C. (2001), Upper mantle seismic anisotropy beneath Antarctica and the Scotia Sea region. *Geophysical Journal International*, v. 147, pp. 105-122.

Newman, J., Stewart, E.D., Toy, V.G., Kruckenberg, S.C., and Tikoff, B. (2011), Heterogeneous mantle fabrics in the Red Hills ultramafic massif, South Island, New Zealand. *AGU Fall Meeting Abstracts*, Abstract T12C-2396.

Nicolas, A., Boudier, F., and Boullier, A.M. (1973), Mechanisms of flow in naturally and experimentally deformed peridotites. *American Journal of Science*, v. 273, pp. 853-876.

Nicolas, A., and Christensen, N. (1987), Formation of anisotropy in upper mantle peridotites – a review. Composition, Structure and Dynamics of the Lithosphere – Asthenosphere System. *American Geophysical Union – Geodynamic Series*, v. 16, pp. 111-123.

O'Neill, H.S.T.C. (1981), The transition between spinel lherzolite and garnet lherzolite, and its use as a geobarometer. *Contributions to Mineralogy and Petrology*, v. 77, pp. 185-194.

Pankhurst, R.J., Weaver, S.D., Bradshaw, J.D., Storey, B.C., and Ireland, T.R. (1998), Geochronology and geochemistry of pre-Jurassic superterranes in Marie Byrd Land, Antarctica. *Journal of Geophysical Research*, v. 103, pp. 2529-2547.

Passchier, C.W., and Trouw, R.A.J. (2005), Microtectonics, 2nd ed. Springer, 364 pp.

Précigout, J., and Hirth, G. (2014), B-type olivine fabric induced by grain boundary sliding. *Earth and Planetary Science Letters*, v. 395, pp. 231-240.

Prior, D.J., Boyle, A.P., Brenker, F., Cheadle, M.C., Day, A., Lopez, G., Peruzzo, L., Potts, G.J., Reddy, S., Spiess, R., Timms, N.E., Trimby, P., Wheeler, J., and Zetterström, L. (1999), The application of electron backscatter diffraction and orientation contrast imaging in the SEM to textural problems in rocks. *American Mineralogist*, v. 84, pp. 1741-1759.

Ratteron, P., Chen, J., Li, L., Weidner, D., and Cordier, P. (2007), Pressure-induced slip0system transition in forsterite: single-crystal rheological properties at mantle temperature and pressure. *American Mineralogist*, v. 92, pp. 1436-1445.

Ritzwoller, M.H., Shapiro, N.M., Levshin, A.L., and Leahy, G.M. (2001), Crustal and upper mantle structure beneath Antarctica and surrounding oceans. *Journal of Geophysical Research*, v. 106, p. 1-26.

Siddoway, C.S. (2008), Tectonics of the West Antarctica Rift System: New light on the history and dynamics of distributed intracontinental extension, in *Antarctica: A Keystone in a Changing World* – Online proceedings of the 10th ISAES, eds. A.K. Cooper and C.R. Raymond et al., USGS Open-File Report 2007, pp. 91-114.

Sieminski, A., Debayle, E., and Lévêque, J-J. (2003), Seismic evidence for deep low-velocity anomalies in the transition zone beneath West Antarctica. *Earth and Planetary Science Letters*, v. 216, pp. 645-661.

Skemer, P., Katayama, I., Jiang, Z., and Karato, S. (2005), The misorientation index: Development of a new method for calculating the strength of lattice-preferred orientation. *Tectonophysics*, v. 411, pp. 157-167.

Skemer, P., Warren, J.M., Kelemen, P.B., and Hirth, G. (2010), Microstructural and rheological evolution of a mantle shear zone. *Journal of Petrology*, v. 51(1-2), pp. 43-53.

Skemer, P., Warren, J.M., Hansen, L.N., Hirth, G., and Kelemen, P.B. (2013), The influence of water and LPO on the initiation and evolution of mantle shear zones. *Earth and Planetary Science Letters*, v. 375, pp. 222-233.

Storey, B.C., Leat, P.T., Weaver, S.D, Pankhurst, J.D., and Kelley, S. (1999), Mantle plumes and Antarctica-New Zealand rifting: Evidence from mid-Cretaceous mafic dykes. *Journal of the Geological Society*, v. 156, p. 659-671.

Sundberg, M. and Cooper, R.F. (2008), Crystallographic preferred orientation produced by diffusional creep of harzburgite: Effects of chemical interactions among phases during plastic flow. *Journal of Geophysical Research*, v. 113, B12208, doi:10.1039/2008JB005618.

Taylor, W.R. (1998), An experimental test of some geothermometry and geobarometer formulations for upper mantle peridotites with application to the thermobarometry of fertile lherzolite and garnet websterite. *Neues Jahrbuch für Geologie und Paläontologie Abhandlungen*, v. 172, pp. 381-408.

Tikoff, B., Larson, C.E., Newman, J., and Little, T. (2010), Field-based constraints on finite strain and rheology of the lithospheric mantle, Twin Sisters, Washington. *Lithosphere*, v. 2(6), 418, doi:10.1130/L97.1.

Tommasi, A., Mainprice, D., Canova, G., and Chastel Y. (2000), Viscoplastic self-consistent and equilibrium-based modeling of olivine lattice preferred orientations: Implications for the upper mantle seismic anisotropy. *Journal of Geophysical Research*, v. 105 (B4), pp. 7893-7908.

Toy, V.G., Newman, J., Lamb, W., and Tikoff, B. (2010), The Role of Pyroxenites in Formation of Shear Instabilities in the Mantle: Evidence from an Ultramafic Ultramylonite, Twin Sisters Massif, Washington. *Journal of Petrology*, v. 51(1-2), pp. 55-80.

Tullis, T.E., Horowitz, F.G., and Tullis, J. (1991), Flow laws of polyphase aggregates from end-members flow laws. *Journal of Geophysical Research*, v. 96, pp. 8081-8096.

Van der Wal, D., Chopra, P., Drury, M., and FitzGerald, J. (1993), Relationships between dynamically recrystallized grains size and deformation conditions in experimentally deformed olivine rocks. *Geophysical Research Letters*, v. 20, pp. 1479-1482.

Vaughan, D.G. (2008), West Antarctic Ice Sheet collapse – the fall and rise of a paradigm. *Climate Change*, v. 91, pp. 65-79.

Vollmer, F.W. (1990), An application of eigenvalue methods to structural domain analysis. *Geological Society of America Bulletin*, v. 102, pp. 786-791.

Warren, J.M., Hirth, G., and Kelemen, P.B. (2008), Evolution of olivine lattice preferred orientation during simple shear in the mantle. *Earth and Planetary Science Letters*, v. 272, pp. 501-512.

Warren, J.M., and Hirth, G. (2006), Grain size sensitive deformation mechanisms in naturally deformed peridotites. *Earth and Planetary Science Letters*, v. 248, pp. 438-450.

Weaver, S.D., Storey, B.C., Pankhurst, R.J., Mukasa, S.B., DiVenere, V., and Bradshaw, J.D. (1994), Antarctic-New Zealand rifting and Marie Byrd Land lithospheric magmatism linked to ridge subduction and mantle plume activity. *Geology*, v. 22, p. 811-814.

Webber, C., Newman, J., Holyoke, C., Little, T., and Tikoff, B. (2010), Fabric development in cm-scale shear zones in ultramafic rocks, Red Hills, New Zealand. *Tectonophysics*, v. 489, pp. 55-75

Wenk, H.R., and Wilde, W.R. (1972), Orientation Distribution Diagrams for Three Yule Marble Fabrics, in *Flow and Fracture of Rocks*, eds. H.C. Heard, I.Y. Borg, N.L. Carter, and C.B. Raleigh, American Geophysical Union, Washington, D.C. doi: 10.1029/GM016p0083.

Winberry, J.P. and Anandakrishnan, S. (2004), Crustal structure of the West Antarctic rift system and Marie Byrd Land hotspot. *Geology*, v. 32, p. 977-980.

Winter, J.D. (2010), Principles of Igneous and Metamorphic Petrology, 2nd ed. Pearson Prentice Hall, 702 pp.

Zhang, S., and Karato, S. (1995), Lattice preferred orientation of olivine aggregates deformed in simple shear. *Nature*, v. 375, pp. 774-777.

APPENDIX A

Axial-type olivine crystallographic preferred orientations: the effect of strain geometry on mantle texture

Vasileios Chatzaras[1,*], Seth C. Kruckenberg[1], Shaina M. Cohen[1], L. Gordon Medaris Jr.[2], Anthony C. Withers[3], Brian Bagley[4]

[1]*Department of Earth and Environmental Sciences, Boston College, Chestnut Hill, MA 02467, USA*
[2]*Department of Geoscience, University of Wisconsin-Madison, Madison, WI 53706, USA*
[3]*Department of Earth Sciences and the Centre for Planetary Science and Exploration, University of Western Ontario, 1151 Richmond Street, London, Ontario N6A 5B7, Canada*
[4]*Department of Earth Sciences, University of Minnesota - Twin Cities, 310 Pillsbury Dr. SE, Minneapolis, MN 55455, USA*

[*]*Present address: Department of Geoscience, University of Wisconsin-Madison, Madison, WI 53706, USA; Department of Earth Sciences, Utrecht University, PO Box 80.021, 3508 TA Utrecht, The Netherlands*

Key points:

- X-ray computed tomography was used to quantitatively describe 3D spinel shape fabric
- Relationship between finite strain geometry and olivine texture is established for the first time in naturally deformed mantle rocks
- Axial-[010] and axial-[100] olivine crystallographic preferred orientations form by flattening and constrictional strain, respectively

Abstract

The effect of finite strain geometry on crystallographic preferred orientation (CPO), which is well known for the crust, is poorly constrained in the upper mantle. Significantly, the relationship between mineral shape preferred orientation (SPO) and CPO in the upper mantle remains unclear. We analyzed a suite of 40 spinel peridotite xenoliths from Marie Byrd Land, west Antarctica. X-ray computed tomography allows for quantification of spinel SPO, which ranges from prolate to oblate fabric geometries. Electron backscatter diffraction analysis reveals a range of olivine CPO patterns, including the A-type, axial-[010], axial-[100], and B-type patterns. Until now, these CPO types were associated with different deformation conditions, deformation mechanisms, or strain magnitudes. Microstructures and deformation mechanism maps suggest that deformation in all studied xenoliths is dominated by dislocation-accommodated grain boundary sliding. For the range of temperatures (779–1198 ^{o}C), extraction depths (39–72 km), differential stresses (2–60 MPa), and water content (up to 500 H/10^6Si) of the xenolith suite, variations in olivine CPO symmetry do not correlate with changes in deformation conditions. Here we establish for the first time in naturally deformed mantle rocks that finite strain geometry controls the development of axial-type olivine CPOs; axial-[010] and axial-[100] CPOs form in relation to oblate and prolate fabric ellipsoids, respectively. Associated girdling of olivine crystal axes is the combined result of intracrystalline slip with activation of multiple slip systems, and grain boundary sliding. Our results highlight that mantle deformation may deviate from simple shear. Olivine texture in field studies and seismic anisotropy in geophysical investigations can provide critical constraints for the 3D strain in the upper mantle.

1. Introduction

Mantle flow produces olivine crystallographic preferred orientation (CPO), which is the dominant cause of mechanical and seismic anisotropy [*Christensen*, 1984; *Tommasi et al.*, 1999; *Karato et al.*, 2008]. Deformation experiments have established that olivine CPO pattern depends on the degree of activation of different olivine slip systems [*Durham and Goetze*, 1977; *Bai et al.*, 1991], which in turn depends on temperature, pressure, differential stress, and water content (Figure 1a) [*Carter and Avé Lallemant*, 1970; *Jung and Karato*, 2001; *Couvy et al.*, 2004; *Katayama et al.*, 2004; *Karato et al.*, 2008; *Demouchy et al.*, 2012; *Raterron et al.*, 2012]. Studies of naturally deformed rocks support the results of deformation experiments [*Vauchez et al.*, 2005; *Mizukami et al.*, 2004; *Lee and Jung*, 2014], and in many cases extrapolate experimental results to nature using olivine CPO to infer deformation conditions [e.g., *Saruwatari et al.*, 2001; *Katayama and Korenaga*, 2011].

To add complexity, presence of melt, deformation history (e.g., existence of inherited CPO, strain partitioning), type of deformation (e.g., pure shear, simple shear, transpression, and transtension), and strain magnitude also affect olivine CPO development and evolution [*Avé Lallemant and Carter*, 1970; *Nicolas et al.*, 1973; *McKenzie*, 1979; *Ribe and Yu*, 1991; *Wenk et al.*, 1991; *Tommasi et al.*, 1999; *Holtzman et al.*, 2003; *Webber et al.*, 2010; *Boneh and Skemer*, 2014; *Hansen et al.*, 2014]. The role of strain on olivine CPO evolution is less well understood compared to the effects of melt or changing deformation conditions.

For crustal minerals (e.g., quartz, calcite, mica, and amphibole), it is well established that the shape of the finite strain ellipsoid (i.e., prolate, oblate, plane strain) affects CPO [e.g., *Lister and Hobbs*, 1980; *Law et al.*, 1984; *Scmid and Casey*, 1986; *Kruckenberg et al.*, 2010; *Lloyd et al.*, 2011; *Xypolias et al.*, 2013; *Llana-Funez and Rutter*, 2014]. In these minerals, flattening strain produces girdles parallel to the foliation, constriction is associated with girdles at high angle to the lineation, and plane strain produces clustered distributions of crystallographic axes (Figure 1b); an exception is the girdled quartz c-axis pattern formed in plane strain at low temperature conditions. A relationship between finite strain geometry and CPO symmetry has also been observed in experimental and numerical simulation studies of olivine deformation [*Avé Lallemant and Carter*, 1970; *Nicolas et al.*, 1973; *Wenk et al.*, 1991; *Tommasi et al.*, 1999]. Yet, to the best of our knowledge, such a relationship has not been described for naturally deformed mantle rocks.

Mantle xenoliths transported to the surface by erupted lavas are ideal materials for exploring the relationship between shape preferred orientation (SPO) and CPO under natural deformation conditions. Mantle xenoliths are commonly unaffected by exhumation-related processes (e.g., low-temperature recrystallization and CPO overprinting) that may affect peridotites in exhumed ultramafic massifs. One limitation inherent to xenolith studies is that samples are detached from their original deformation context. When combined with small sample sizes, the identification of mineral SPO (foliation and lineation) is often difficult. The lack of a SPO reference framework in xenolith studies further hampers distinction between olivine CPO patterns that share similar crystal axis symmetry, but of variable orientation relative to the orientation of foliation and lineation (e.g., orthorhombic A-, B-, C-, and E-type olivine CPO patterns) (Figure 1a). Therefore, our understanding of upper mantle deformation and seismic anisotropy - particularly below continents where exhumed xenoliths are the only source of direct information - is hindered without a methodology that incorporates a quantitative 3D characterization of SPO, which in turn allows for an unbiased characterization and interpretation of CPO.

In this study, we develop a new workflow that allows for evaluation of the relationship between spinel SPO and olivine CPO in mantle materials. Using a combination of X-ray computed tomography and electron backscatter diffraction analysis we show how limitations inherent to the study of 3D shape fabric in mantle materials can be overcome to gain new insights into mantle deformation processes and the development of axial-type CPOs in olivine.

2. Geological setting

The samples analyzed in this study were collected from the Marie Byrd Land volcanic province in west Antarctica (Figure 2a). Marie Byrd Land has experienced a complex deformation history that includes Cretaceous transcurrent to oblique extensional deformation [*Siddoway et al.*, 2005; *McFadden et al.*, 2010] followed by mid-Cenozoic to present extension and widespread basaltic volcanism [e.g., *Finn et al.*, 2005]. West Antarctica is also characterized by slow mantle seismic velocities [e.g., *Sieminski et al.*, 2003], strong and consistent seismic anisotropy [*Accardo et al.*, 2014], and thinned continental crust [*Winberry and Anandakrishnan*, 2004]; crustal thickness in Marie Byrd Land is approximately 23 km [*Ferraccioli et al.*, 2002].

The mantle xenoliths analyzed have been sampled from six volcanic centers; five centers are located in the Fosdick Mountains (Marujupu Peak, Mt. Avers, Demas Bluff, Bird Bluff and Recess Nunatak), one in the Usas Escarpment (Mt. Aldaz) and one in the Executive Committee Range (Mt. Cumming) (Figure 2a; Table 1 in supporting information). In the Fosdick Mountains, mantle xenoliths were entrained in ca. 1.4 Ma basaltic to basanitic cinder cones and flows [*Gaffney and Siddoway*, 2007] (Figure 2b and c). Geochemical analyses show that the xenolith-bearing lavas are compositionally homogeneous within each volcanic center, but heterogeneous among the centers [*Gaffney and Siddoway*, 2007]. We studied 40 spinel-bearing mantle xenoliths of variable composition, including 30 lherzolites, 6 harzburgites, 3 werhlites, and 1 dunite. Xenoliths range between 3 and 15 cm in diameter, are extremely fresh (i.e. lack of significant alteration), and have sharp contacts with the enclosing basalts (Figures 2d and 3a).

3. Methods

To understand what controls the development of olivine CPO in the Marie Byrd Land xenoliths, we compare how changes in deformation conditions and SPO relate to olivine CPO variations. We use X-ray computed tomography to quantitatively describe spinel SPO in terms of orientation (in the hand specimen reference framework), shape, and anisotropy. Electron backscatter diffraction is used to determine patterns of olivine CPO, misorientation axis distributions, olivine SPO, and grain size. Olivine CPO data are plotted relative to the spinel SPO reference framework (i.e. foliation and lineation), which allows for robust and unbiased identification of CPO symmetry and type. We determine mineral compositions and equilibration temperatures by means of electron probe microanalysis. Water content in olivine and orthopyroxene is estimated with Fourier Transform Infrared Spectroscopy. Details for each of the applied methods are provided below.

3.1. X-ray computed tomography

We used high-resolution X-ray computed tomography (XRCT) to visualize and quantify the mineral shape fabric defined by the three-dimensional SPO of spinel grains (Figure 3a and b; and Supplementary Movie S1). XRCT was carried out at the University of Minnesota-Twin Cities, which houses a X5000 high-resolution microCT system with a twin head 225 kV cone-beam X-ray source and a Dexela area detector (3073 x 3889 pixels). Because the analyzed xenoliths cover a wide range of sizes, different scan parameters were tested and applied (Table S2) to maximize resolution and contrast. Samples were placed on a rotary stage, and 1080 radiographs were collected through 360° of rotation. To reduce noise 3-4 radiographs were collected at each angle and averaged (frame averaging), resulting in scan times of 45 min to 2 h and voxel sizes of 10–50 μm. The individual radiographs were then reconstructed into a 3D volume using the commercial software efX-CT. During the reconstruction a correction was applied to reduce the effects of beam hardening.

Voxels corresponding to spinel were segmented from the voxels corresponding to the remaining constituent phases (olivine, orthopyroxene, and clinopyroxene) following the procedure described in *Ketcham* [2005a]. In case of spinel aggregates, we separated spinel grains manually following an object-based analysis, implemented by the BLOB3D software [*Ketcham,* 2005b]. Spinel grain separation was shape- rather than CPO-based. Where spinel grain separation was not possible, the shape of spinel aggregates was analyzed. We used the 3D shapes and orientations of the spinel grains and aggregates to determine rock fabric. The SPO of spinel grains was analyzed with QUANT3D software [*Ketcham and Ryan*, 2004]. To calculate the fabric tensor we used the star length distribution method [*Odgaard et al.*, 1997]. To obtain the fabric tensor, the method uses a moment of inertia calculation to define an orientation matrix [*Launeau and Robin*, 1996] from which a fabric tensor is derived by normalizing the eigenvalues to sum to 1. The fabric tensor eigenvectors and eigenvalues define orthogonal principal axes, with the maximum and minimum eigenvector corresponding to the axes along which the moment of inertia is minimized and maximized, respectively. The eigenvalues are related to the moment of inertia about each axis. Thus, the fabric tensor takes into account both spinel grain shapes and orientations. We used the corrected degree of anisotropy (*P'*) and the shape factor (*T*) to quantify the anisotropy and shape of fabric ellipsoid [*Jelínek*, 1981]. *P'* is given by:

$$P' = \exp\sqrt{2\left[(f_1 - f)^2 + (f_2 - f)^2 + (f_3 - f)^2\right]} \qquad (1)$$

where f_1, f_2, and f_3 are the natural logs of the normalized magnitudes of the maximum (Φ_1), intermediate (Φ_2), and minimum (Φ_3) axes of the fabric ellipsoid and $f = (f_1 + f_2 + f_3)/3$ [*Jelínek*, 1981]. *P′* varies from one (sphere – no anisotropy) to infinity (with increasing ellipticity toward a material line or material plane). *P′* is similar in mathematical formulation to the better-known octahedral shear strain [*Nadai*, 1963] used in Hsu plots [*Hossack*, 1968], but P′ magnitude does not necessarily coincide with the strain magnitude.

The shape factor (*T*) is mathematically similar to Lode's parameter [*Hossack*, 1968] used in Hsu plots, and is defined as:

$$T = \frac{2f_2 - f_1 - f_3}{f_1 - f_3} \qquad (2)$$

The values of the shape parameter have the range $-1 < T < 1$, where $T < 0$ corresponds to prolate, $T = 0$ to neutral (plane strain), and $T > 0$ to oblate ellipsoids.

From the fabric tensor we determined the orientations of the three principal fabric ellipsoid axes, which define the foliation plane (contains Φ_1 and Φ_2 axes) and the lineation (parallel to Φ_1) of each xenolith (Figure 3b and c). The commercial software Avizo®Fire was used to project the fabric ellipsoid axes on the reconstructed rock volume, and subsequently on the rock sample. In 29 samples, thin sections were produced parallel to the $\Phi_1\Phi_3$ plane of the fabric ellipsoid with the long axis of each thin section parallel to Φ_1 (Figure 3c). Thin sections from 11 samples had to be produced at random orientations relative to the spinel fabric due to restrictions imposed by small xenolith size. In these samples, the spinel SPO was determined by means of XRCT analysis of the randomly oriented rock billets.

3.2. Electron backscatter diffraction

Crystallographic preferred orientations for all constituent mineral phases in the Marie Byrd Land xenoliths were collected by means of electron backscatter diffraction (EBSD) on polished thin sections. EBSD data were acquired on a Tescan Vega 3 LMU scanning electron microscope (SEM) equipped with a LaB6 source and an Oxford Instruments Nordyls Max2 EBSD detector housed within the Department of Earth and Environmental Sciences at Boston College. Typical operating conditions for analyses were 20-100 nA for beam currents and an accelerating voltage of 30 kV. Crystallographic texture maps of full thin sections (26x46 mm) were acquired and indexed using the Oxford Instruments AZtecHKL acquisition and analysis software (version 2.3). The analytical method is described in detail by *Prior et al.* [1999].

To ensure a high density of crystallographic orientation data and multiple solutions within individual grains, a step size of 7.5 μm was used throughout map regions; EBSD datasets correspondingly comprise approximately 10 million individual solutions with indexing rates typically >90%. Microstructural maps were constructed from the unprocessed EBSD datasets using version 3.5 of the MTEX Matlab toolbox for textural analysis (http://mtex-toolbox.github.io), from which one point per grain data (i.e. mean crystallographic orientation of each grain) were calculated for grains separated by misorientation boundaries of ≥10º [*Bachmann et al.*, 2011] (Figure 4a–d). Pole figures were produced from the one point per grain datasets for comparison of olivine CPO patterns (Figure 4e). In all samples, the olivine CPO data are plotted in the 3D spinel SPO reference frame (i.e. relative to the spinel-defined foliation and lineation). Misorientation axes were calculated for correlated misorientation angles between 2° and 10° and their distributions are plotted relative to the olivine crystal reference framework.

To quantify the strength of olivine CPO, we use the J-index [*Bunge*, 1982] and M-index [*Skemer et al.*, 2005]. The J-index is calculated from the orientation distribution functions using MTEX [*Bachmann et al.*, 2010] and has a value of 1 (random) to infinity (single crystal). The M-index is calculated from the distribution of uncorrelated misorientation axes and has a value of 0 (random) to 1 (single crystal). We use the BA-index [*Mainprice et al.*, 2014] to quantify the tendency of the olivine CPO toward end-member axial-[010] (BA = 0) or axial-[100] (BA = 1) symmetries. The BA-index is defined as:

$$BA\,index = \frac{1}{2}\left(2 - \left(\frac{P_{010}}{G_{010} + P_{010}}\right) - \left(\frac{G_{100}}{G_{100} + P_{100}}\right)\right) \qquad (3)$$

where P and G are the Point and Girdle pattern symmetry characteristics of *Vollmer* [1990] for olivine [100] and [010]. The P and G indices were calculated from the eigenvalues of the normalized orientation matrix using the MTEX [*Mainprice et al.*, 2011].

Two-dimensional olivine SPO (Figure 4d inset) was determined from grain-set properties of the EBSD maps analyzed in MTEX. No olivine SPO data were acquired from thin sections produced at random orientation relative to the spinel fabric. The olivine grain size was determined with the equivalent area diameter method on grains defined by a grain boundary misorientation angle of 10°, constructed from the EBSD data in MTEX. To convert between the mean equivalent area diameter on a two-dimensional section and the mean grain diameter in three dimensions, a scaling factor of 1.2 was used [*Underwood, 1970; Van der Wal et al.*, 1993].

3.3. Electron probe microanalysis

The major and minor element compositions of olivine, spinel, orthopyroxene, and clinopyroxene were analyzed by wavelength-dispersion spectrometry (WDS) with a Cameca SX50 instrument at the Department of Geoscience, University of Wisconsin-Madison. Operating conditions were: 15 kV accelerating voltage, 20 nA beam current (Faraday cup), and beam diameter of 1 µm. Combinations of natural minerals and synthetic materials were used as standards for each mineral species, and data reduction was performed by Probe for Windows software, utilizing the $\phi(\rho z)$ matrix correction of *Armstrong* [1988].

Mineral compositions were analyzed in each sample in several domains, situated at different structural positions relative to the determined foliation. Constituent phases of interest were analyzed in each domain and compositions were determined for cores and rims in each phase. Where possible, adjacent grains of olivine, spinel, orthopyroxene and clinopyroxene were analyzed. No significant compositional differences were found on the inter- or intragranular scales. However, enstatite and Cr-diopside grains in a few samples contain exsolution lamellae of the complementary pyroxene and spinel, although such lamellae were too thin to allow for accurate analyses. Consequently, the host compositions of coexisting orthopyroxene and clinopyroxene were used to calculate temperature. Representative analyses of constituent minerals are summarized in Table S3.

Equilibration temperatures for the Marie Byrd Land xenoliths were determined by application of three different calibrations of the two-pyroxene geothermometer (Table S4), namely those by *Bertrand and Mercier* [1985] (BM85), *Brey and Köhler* [1990] (BK90), and *Taylor* [1998] (T98). For the dunite sample we used the olivine-spinel Fe-Mg exchange geothermometer of *Ballhaus et al.* [1991] (BBG91). Temperatures were calculated at an assumed pressure of 15 kbar, because of the uncertainty in estimating pressures for spinel peridotites (see section 4.3). The effect of pressure on calculated two-pyroxene temperatures is 2 °C/kbar.

3.4. Fourier transform infrared spectroscopy

Fourier transform infrared (FTIR) spectroscopic measurements were made to determine the H content of olivine and orthopyroxene from seven peridotite xenoliths (FDM-AV01-X01, FDM-BB01-X01, FDM-DB03-X01, FDM-RN03-X01, FDM-RN04-X01, FDM-AVBB02, and AD6021-X02) and olivine from a dunite xenolith (KSP89-181-X01). Polarized spectra were collected in transmission mode using a Bruker Tensor 37 FTIR spectrometer and Hyperion 2000 microscope with 15×

objective and condenser. An infrared globar source and MCT detector were used and 128 scans were taken over spectral range of 1000-5000 cm^{-1} with a sampling interval of 1 cm^{-1}. The aperture was adjusted so that the analyzed area formed a square with edge length between 50 and 100 μm. After they had been disaggregated from the xenoliths, orthopyroxene and olivine grains that appeared to have the best-developed faces were selected for FTIR analysis. We prepared polished sections perpendicular to the **α** axes of the infrared indicatrices by polishing parallel to the (100) faces of orthopyroxene and (010) faces of olivine. Sample orientation was confirmed, and **β** and **γ** directions were identified, by comparing spectra in the region from 1400 to 2300 cm^{-1}, where diagnostic Si-O overtone bands occur, with reference spectra for olivine from *Asimow et al.* [2006] and for orthopyroxene from *Mosenfelder and Rossman* [2013]. Well-oriented samples were selected and repolished to prepare sections orthogonal to those containing the **β** and **γ** directions, so that principal spectra with the electric vector of the infrared light polarized parallel to the **α** axis of the infrared indicatrix (the "**α**-spectra") could be measured. The spectra for orthopyroxene are a close match to the respective principal polarized spectra for sample KBH-1 of *Bell et al.* [1995; Figure S1], so we calculated H_2O concentration for the orthopyroxene using the molar absorption coefficient of *Bell et al.* [1995], while for olivine we used the molar absorption coefficient of *Withers et al.* [2012].

4. Results

4.1. Microstructures

Microstructures in the Marie Byrd Land xenoliths were studied by combined optical (Figure 5) and electron microscopy (e.g., EBSD maps; Figure 4) techniques. The xenoliths are coarse-grained and have a granular or tabular microstructure (Figures 4b and c; 5a and b). Spinel occurs as discrete, euhedral to subhedral grains, and commonly forms characteristic spinel trails (Figure 5c). Interstitial, symplectic or complexly shaped irregular intergrowths of spinel with pyroxene are also present but less common. Olivine grains show undulose extinction (Figure 5d) and well-developed subgrain boundaries (Figures 4a; 5a, b, e, f, h, i). The subgrain boundaries are usually oriented perpendicular or oblique (at high angle) to the foliation (Figures 4a; 5a, e, f); however, subgrain boundaries subparallel or at low angle to the foliation are also present (Figure 5b, e, i). Gently curved to straight olivine-olivine grain boundaries, which lead to polygonal crystal shapes with 120° triple junctions, are indicative of an equilibrium microstructure (Figure 5g). Recrystallization, accommodated by grain boundary migration, is inferred from interpenetrating olivine grain boundaries [*Drury and Urai*, 1990].

Several microstructures identified in the xenoliths are indicative of grain boundary sliding: 1) Olivine tabular grains with straight grain boundaries oriented subparallel to the foliation (Figure 5a); 2) Presence of diamond-shaped grains with grain boundaries forming conjugate sets trending at 20–50^{o} to the foliation (Figure 5e, f); 3) Along strike continuity between subgrain and grain boundaries, the subgrain boundaries forming in zones of sliding accommodation-strain at triple points (Figure 5i); 4) Presence of four-grain junctions (Figure 5j) [*Ashby and Verall*, 1973; *Drury and Humphries*, 1988; *Ree*, 1994; *Newman et al.*, 1999; *Sundberg and Cooper*, 2008]

4.2. Mineral compositions

Minerals in the Marie Byrd Land mantle xenoliths are highly magnesian, and have compositional characteristics typical for those in subcontinental peridotite xenoliths [e.g., *Arai*, 1994]. Spinel shows significant variation in both Mg# (100×[Mg/(Mg+Fe)]) and Cr# (100×[Cr/(Cr+Al)]), which range from 56.7 to 84.6 and 1.3 to 63.1, respectively (Figure 6a). The majority of the xenoliths (77%) contain spinel with Mg-rich and Cr-poor (Cr#<20) compositions, which are typical for relatively undepleted mantle peridotites. Olivine is Mg-rich, with Mg# values ranging between 88.2 and 92.1, and the Mg# in olivine tends to increase with an increase in Cr# in coexisting spinel (Figure 6b). With the exception of the dunite sample (KSP89-181-X01), all xenoliths plot within or at the border of the olivine-spinel mantle array (OSMA), as established by *Arai* [1994] (Figure 6b).

Orthopyroxene and clinopyroxene are Mg-rich, with Mg# ranging between 83.7–92.5 and 82.4–94.8, respectively. Pyroxenes show large sample-to-sample variation in Al_2O_3 and Cr_2O_3 contents, where the range in Al_2O_3 for orthopyroxene is 1.86–6.14 wt%, and for clinopyroxene is 1.82–8.61 wt%, as illustrated for coexisting pyroxenes in Figure 6c. The positions of the data points reflect equilibration temperatures (higher Al_2O_3 generally representing higher temperatures) and whole-rock Cr_2O_3/Al_2O_3 ratios. Tie-lines are sub-parallel for most xenoliths, which implies chemical equilibrium for Al_2O_3 and Cr_2O_3 in the coexisting pyroxenes. Two samples (FDM-DB02-X02, and FDM-DB04-X03) display discordant tie-lines relative to the other samples, reflecting disequilibrium with respect to Al_2O_3 and Cr_2O_3. Pyroxenes in sample FDM-DB02-X08 contain relatively small amounts of Al_2O_3 and Cr_2O_3 and equilibrated at a lower temperature than did other xenoliths from the same volcanic center.

4.3. Equilibration temperatures and extraction depths

Temperatures from the three two-pyroxene geothermometers are in very good agreement (Figure 7a), and the average temperature estimates range from 780 to 1200 ^{o}C, calculated at a pressure of 15 kbar (Table 1). These temperatures are thought to represent the xenolith temperatures at the time of extraction from the mantle, but note that samples that contain pyroxene exsolution lamellae must have cooled from some unknown higher temperature prior to extraction.

The average of the three two-pyroxene geothermometers is used to estimate temperatures for the Marie Byrd Land xenoliths at the time of extraction. The regular distribution of sub-parallel Al_2O_3 and Cr_2O_3 tie lines in pyroxenes (Figure 6c) and the excellent agreement between the results of the three two-pyroxene geothermometers (Figure 7a), together indicate the attainment and preservation of equilibrium in pyroxenes with respect to Ca, Mg, Fe, Al, and Cr.

Currently, there is no reliable geobarometer for direct calculation of pressure, and therefore depth, for spinel peridotites. However, we can predict the maximum extraction depth for each xenolith by calculating the maximum pressure at which spinel, rather than garnet, would be stable in each peridotite xenolith [*O' Neill*, 1981]. This approach is valid for the Marie Byrd Land xenoliths, which are devoid of garnet. The compositionally-controlled stability limit for spinel ranges from 49 to 105 km, and corresponds to the predicted maximum possible extraction depth of the studied peridotite xenoliths (Figure 7b; Table S4). The wide range in the predicted maximum depths is due to the large variation in Cr# of spinel in the xenolith suite, i.e., higher Cr contents stabilize spinel to higher pressures.

Further constraints on the depths of xenolith extraction can be placed by combining the results of geothermometry with a geotherm at the time of eruption [e.g., *Medaris et al.*, 2015]. Such an approach can be applied to the Marie Byrd Land spinel peridotite xenoliths by combining the average results of the two-pyroxene geothermometers with an appropriate geotherm. Two geotherms have been established in the region: the McMurdo petrologic geotherm [*Berg et al.*, 1989] and the present-day Ross Embayment geotherm [*ten Brink et al.*, 1997] (Figure 7b). However, neither geotherm is appropriate for the Marie Byrd Land xenolith suite, because use of the McMurdo geotherm would place 50% of the xenoliths above the Moho, and application of the Ross Embayment geotherm would require that 73% of the samples contain garnet, rather than spinel (Figure 7b). Alternatively, a geotherm shown by the thick gray line in Figure 7b, has been constructed that is consistent with the stability of spinel in all xenoliths (the thick gray line in Figure 7b, whose width corresponds to the ±25 °C precision of the two-pyroxene geothermometers). Depths for the Marie Byrd Land xenoliths are then estimated by intersecting their pressure-dependent two-pyroxene temperatures with the hypothetical geotherm (Figure 7b and Table S4). The range of xenolith temperatures represents depths between 39 and 72 km, indicating that the Marie Byrd Land xenoliths have been extracted from moderate to relatively deep levels of the lithospheric mantle.

4.4. Three-dimensional spinel shape preferred orientation

The Marie Byrd Land xenoliths are characterized by low values of the degree of anisotropy (P') of the spinel fabric ellipsoid, which range from 1.09 to 1.61 (Figure 8 and Table 1). Low anisotropy suggests small deviation of the shape of the mean spinel fabric ellipsoid from a sphere. Nonetheless, the low P' values are comparable to the orthopyroxene fabric ellipsoid anisotropy (P' = 1.08–1.15) reported from spinel peridotites from the Bogota Peninsula shear zone in New Caledonia [*Titus et al.*, 2011]. The shape parameter (T) ranges from -0.94 to 0.84, showing large variation in the geometry of the spinel fabric ellipsoid (Table 1; Figure 8). The Marie Byrd Land xenoliths are mainly characterized by either oblate or prolate fabric ellipsoids, and only eight samples have neutral ellipsoid shapes (T close to 0). Our data show no obvious correlation between the degree of anisotropy and the geometry of the spinel fabric ellipsoid (Figure 8).

Visual comparison of the orientation of the XRCT-derived 3D spinel shape fabric and the microstructures observed in the xenoliths, suggests correlation between the two. The determined $\Phi_1\Phi_2$ plane (foliation) of the fabric ellipsoid is oriented parallel to the 3D spatial distribution of spinel grains in layers. Further, the Φ_1 axis (lineation) of the fabric ellipsoid, which corresponds to the trend of spinel grains' long axis alignment (Figure 3b and c), coincides with the trend of observed spinel trails (Figure 5c).

To explore the relationship between the spinel and olivine shape fabric, we analyze the 2D olivine SPO in thin sections cut parallel to the $\Phi_1\Phi_3$ plane of the spinel fabric ellipsoid. In 80% of the xenoliths for which olivine SPO was determined, olivine grains show a clear tendency to align with their long axes parallel or at a small angle (<10°) to the spinel lineation (Figure 9). The long axes of olivine grains are oriented at intermediate or high angle to the spinel lineation in six samples (AD6021-X02, FDM-AV01-X01, FDM-RN03-X01, FDM-BB01-X01, FDM-DB02-X01, KSP89-181-X01). Our data indicate that the 2D olivine SPO is consistent with the orientation of the spinel fabric ellipsoid. However, the 2D treatment of the olivine SPO imposes restrictions on further exploring the relationship between the spinel and olivine fabric ellipsoids in 3D.

4.5. Crystallographic preferred orientations

Olivine CPOs from the analyzed xenoliths are presented in Figure 9; samples are organized based on their BA-index value. Olivine CPOs are plotted with respect to the spinel foliation and lineation as determined with XRCT for all samples, which allows for the accurate identification of the CPO symmetry and type. The Marie Byrd Land xenoliths exhibit a variety of olivine CPO types; four out of six CPO types observed in nature and reproduced by deformation experiments (Figure 1a) are recognized. The observed CPO types include the A- and B-type with orthorhombic symmetry, as well as the axial-[010] and axial-[100] symmetries (Figure 9; Table 1). The variation in olivine CPO is also expressed by the BA index, which ranges from 0.12 to 0.86 (Figure 9; Table 1).

Olivine A-type CPO with orthorhombic symmetry is recognized in 12 xenoliths (Figure 9; Table 1). The A-type is characterized by point concentrations of the three olivine crystal axes, with the [100] axes aligned parallel or at small angle to the spinel lineation (Φ_1), the [010] axes parallel or at small angle to the pole to the foliation (Φ_3), and the [001] axes oriented normal to the lineation within the foliation plane (parallel to Φ_2) (Figure 9). The agreement in the orientation of the olivine crystal axes and the spinel fabric ellipsoid axes observed for the A-type pattern provides further evidence for the robustness of the determined spinel fabric ellipsoid, used to plot and interpret the olivine CPO data.

Olivine axial-[010] symmetry is recognized in 15 xenoliths (Figure 9; Table 1). The CPOs are characterized by [010] point concentrations normal or at high angle to the foliation plane, while [100] and [001] axes form girdles within, or close to the foliation plane. Within the [100] and [001] girdles, the maxima of the crystal axis distributions trend either parallel or oblique to Φ_1 and Φ_2 fabric ellipsoid axes.

Olivine CPO in eight samples is characterized by point concentrations of [100] near Φ_1 axis, while [010] are typically distributed along girdles at high angle to the lineation (Figure 9). Within the [010] girdles, the maximum concentration of axes is near either Φ_2 or Φ_3. In sample FDM-DB02-X01, the [001] axes show girdle distribution normal to the spinel lineation. However, in the rest of the xenoliths, the orientation of [001] axes is commonly dispersed leading to more complex or random distributions, which can be a common characteristic of deformed, polyphase rocks [*Ben Ismail and Mainprice*, 1998; *Bystricky et al.*, 2006]. The olivine CPO in these eight xenoliths may therefore be classified as having an axial-[100] symmetry (Figure 9; Table 1). Such classification is also supported by the high BA-index values (typically >0.6) in these samples.

The B-type olivine CPO pattern is recognized in sample FDM-RN03-X01 (Figure 9). The CPO is characterized by Φ_2-parallel [100] axes that lie within the foliation plane, [010] axes normal to the foliation (parallel to Φ_3), and [001] axes oblique to Φ_1.

One xenolith (FDM-BB02-X01), with equigranular microstructure and abundant 120^o triple junctions of olivine grains, has a random texture (Figure 9). Insufficient number of analyzed olivine grains in two xenoliths (FDM-DB02-X04 and FDM-DB03-X04), prevents us from ascribing the poorly developed crystallographic texture to a specific CPO symmetry (Figure 9).

Most xenoliths have moderate to low olivine CPO strength. The J-index varies from 1.39 to 14.34 with an arithmetic mean of 3.67 (Figure 9; Table 1). This mean J-index value is smaller than the value of 8–10 characterizing most natural peridotites [*Ben Ismail and Mainprice*, 1998; *Tommasi et al.*, 2000]. In agreement with J-index, the calculated M-index is moderate to low, ranging between 0.07 and 0.37 (arithmetic mean of 0.18).

4.6. Crystallographic misorientations and active slip systems

Low-angle (2–10^{o}) boundaries in deformed grains develop as a result of dislocation creep and organization of dislocations into planes of lower energy due to recovery. Organization of edge dislocations produces tilt boundaries, while organization of screw dislocations forms twist boundaries (Figure 10b). The combined analysis of CPO and low-angle misorientation axes allows the determination of the slip systems that must be active for the formation of the low-angle boundaries [*Lloyd et al.*, 1997]. Using EBSD mapping, we analyzed low-angle (2–10^{o}) misorientation axes to investigate: 1) the olivine slip systems that produce the subgrain boundaries for the different CPO types; and 2) intracrystalline deformation of spinel grains.

4.6.1. Olivine

The majority of the xenoliths with A-type pattern are characterized by low-angle misorientation axes distributed along girdles between [001] and [010] (Figure 9; FDM-DB02-X11, FDM-BB02-X01, FDM-AV01-X01, FDM-BB01-X01, FDM-DB02-X08, FDM-MJ01-X02, and FDM-MJ01-X03). Such distribution of misorientation axes is characteristic of {0kl}[100] slip system (Figure 10a). In the remaining xenoliths with A-type CPO pattern, the misorientation axes are clustered near either [001] (FDM-DB04-X04, and FDM-RN02-X01), or [010] (FDM-RN01-X01, and FDM-DB02-X10), or both (FDM-MJ01-X06, and FDM-DB02-X02). Concentration of misorientation axes near [001] is indicative of the presence of tilt boundaries in (100), and therefore for the activity of (010)[100] slip system (Figure 10a). Clustering of misorientation axes near [010] is possibly related to the existence of twist boundaries in (010) (Figure 10a). Formation of either tilt boundaries in (001) associated with (100)[001] slip, or tilt boundaries in (100) associated with (001)[100] slip is a less plausible explanation because in A-type, olivine [010] axes cluster normal to the foliation (Figure 9) implying that (010) is the dominant slip plane.

The xenoliths with olivine CPO of axial-[010] symmetry are predominantly characterized by low-angle misorientation axes that show girdle distributions between [001] and [010] (Figure 9). Within the girdles, the misorientation axis distributions exhibit maxima oblique to both [001] and [010] (FDM-BB03-X01, FDM-DB04-X02, FDM-AVBB05, and FDM-DB02-X03), which suggests activity of the {0kl}[100] slip system (Figure 10a). Maxima of the misorientation axis distributions near [001] in four xenoliths (FDM-AVBB07, FDM-AVBB08, FDM-DB03-X02, FDM-MJ01-X05) indicate arrangement of dislocations along [100] tilt boundaries via (010)[100] slip. Clustering of misorientation axes near [010] (FDM-DB02-X12, FDM-AVBB02, and AD6021-X02) can be the result of: 1) tilt boundaries in (001) built of (100)[001] dislocations; 2) tilt boundaries in (100) associated with (001)[100] dislocations; or 3) twist boundaries in (010) (Figure 10a). Concentration of olivine [010] axes at high angle to the foliation (Figure 9) suggests that (010) is the primary dislocation slip plane and therefore (100)[001] and (001)[100] slip seems less favorable for the formation of the subgrain boundaries. Thus, we attribute the clustering of misorientation axes near [010] to the existence of twist boundaries in (010). In support to the existence of twist boundaries is the presence of subgrain boundaries subparallel to the foliation plane, and therefore, to (010) planes (Figure 5b). Furthermore, coexistence of misorientation axes near [001] and [100] (FDM-AVBB01, FDM-AVBB06, FDM-AVBB07, and FDM-AVBB08) implies activity of both (010)[100] and (010)[001] slip systems.

Olivine low-angle misorientation axis distributions in the xenoliths with CPO of axial-[100] symmetry are characterized by maxima either oblique (FDM-DB01-X01, FDM-DB02-X13, and FDM-DB03-X01) or parallel (FDM-RN04-X01, FDM-DB02-X01, FDM-DB03-X03, KSP89-181-X01, and FDM-DB04-X03) to [001] and [010] (Figure 9). These misorientation axis distributions suggest operation of a variety of dislocations in the {0kl}[100] family of slip systems. The existence of [001] misorientations fits with subgrains characterized by tilt boundaries built of (010)[100] dislocations, while [010] misorientations most easily fit with tilt boundaries built of (001)[100] dislocations (Figure 10a). The xenoliths with [010] misorientations are characterized by lack of olivine [100] crystal axes trending parallel to Φ_3, which would indicate (100)[001] slip, as well as lack of [100] crystal axes parallel to Φ_2 that could suggest occurrence of (010) twist boundaries built from (010)[100] and (010)[001] dislocations.

The xenolith with the B-type CPO pattern contains misorientation axes that are distributed along a girdle between [001] and [010], with the maximum concentration of axes being parallel to [001]. This distribution of misorientations suggests that subgrain boundaries are built of {0kl}[100] dislocations, with predominant occurrence of tilt boundaries in (100) associated with (010)[100] dislocations.

4.6.2. Spinel

Spinel is characterized by random distribution of crystallographic axes orientations irrespective of fabric anisotropy and geometry. Misorientation analysis of spinel reveals that only few grains have internal misorientation of maximum 6°, which indicates limited intragrain deformation (Figure S2).

4.7. Grain size and differential stress

For viscously deforming rocks, the piezometric relationship that relates the recrystallized grain size to the differential stress follows a power law:

$$D_g = A\sigma^{-n} \qquad (4)$$

where D_g is the recrystallized grain size, σ is the differential stress, and A and n are empirically derived constants. We use the calibrations of *Karato et al.* [1980] and *Van der Wal et al.* [1993] to estimate differential stress. Olivine grain sizes generally show continuous, log-normal distributions (Figure 4f). In coarse-grained peridotites with continuous grain size distributions, such as those in the Marie Byrd Land xenoliths, it is difficult to discriminate between recrystallized and relict grains. We use the geometric mean of the grain size distribution in a sample to describe the recrystallized grain size. The use of mean grain size may lead to overestimation of the recrystallized grain size and, therefore, underestimation of differential stress. On the other hand, presence of pyroxene in the xenoliths may have caused pinning of olivine grain boundaries during growth, reducing olivine grain size. Thus, we believe that the use of mean grain size can be justified for the Marie Byrd Land xenoliths. The geometric means of the grain size distributions range from 61 to 2000 μm (Table 1); the average of the geometric means for the whole xenolith suite is 665 μm. The estimated grain sizes correspond to differential stresses of 2–60 MPa (Table 1; Figure 11).

4.8. Water content

Xenoliths chosen for FTIR measurement included examples with each of the four different olivine CPO types (Table 2). Olivine H contents vary from below the detection limit (sub-ppm) to 5 ppm H_2O, and coexisting orthopyroxenes have from 34 to 153 ppm H_2O. Olivine in mantle xenoliths is susceptible to diffusive loss of H during emplacement [e.g., *Demouchy et al.*, 2006; *Warren and Hauri*, 2014]. Orthopyroxene, on the other hand, has been shown to preserve its pre-emplacement H content with greater fidelity [*Warren and Hauri*, 2014]. We therefore use the equilibrium partition coefficient for H between orthopyroxene and olivine, $D^{opx/ol}$, to determine the pre-emplacement H content of olivine. Experiments show that $D^{opx/ol}$ is strongly dependent upon the Al_2O_3 content of the orthopyroxene [*Hirschmann et al.*, 2009]. The analyzed orthopyroxenes have between 3.1 and 4.8 wt.% Al_2O_3, from which we estimate that $D^{opx/ol}$ is between 5 and 15 [e.g., *Ardia et al.*, 2012], which suggests equilibrium H concentration in olivine of up to 31 ppm H_2O (500 $H/10^6$ Si) (Table 2).

4.9. Deformation mechanisms

To assess the dominant deformation mechanism(s) in the Marie Byrd Land xenoliths, we constructed deformation mechanism maps using experimentally derived olivine flow laws. For each xenolith, we constructed the deformation mechanism map based on the estimated deformation conditions (temperature, pressure, and differential stress), assuming a dry lithospheric mantle. In Figure 11, we present deformation mechanism maps constructed for temperature intervals (and corresponding pressures) of 850, 950, and 1050 °C. Data from individual samples are plotted on the deformation mechanism map that most closely matches calculated equilibration temperatures. Extrapolation of laboratory flow laws from *Hansen et al.* [2011] to the deformation conditions estimated for the Marie Byrd Land xenoliths indicates that deformation was primarily achieved by dislocation-accommodated grain boundary sliding (Figure 11). Deformation by dislocation-accommodated grain boundary sliding is also consistent with the observed microstructures in the xenolith suite, which are indicative of intragrain deformation and grain boundary sliding (see section 4.1).

5. Discussion

5.1. Significance of spinel shape fabric

The lack of spinel CPO and the limited presence of low-angle misorientations in the spinel grains suggest limited intracrystalline deformation of spinel. This observation is in agreement with deformation experiments on spinel-olivine aggregates showing that, at high temperature and confining pressure conditions, spinel is stronger than olivine and behaves as a rigid phase [*Mecklenburgh et al.*, 2006]. We can therefore infer that spinel must have undergone rigid rotation, relative to adjacent olivine and pyroxene grains, via grain boundary sliding.

In each xenolith, the spinel shape fabric ellipsoid describes the distribution of orientations of spinel grains rather than the mean 3D shape of individual grains. We emphasize that the estimated degree of anisotropy of the spinel shape fabric does not represent the finite strain magnitude quantitatively [*Giorgis and Tikoff*, 2004; *Arbaret et al.*, 2007]. In several xenoliths we observe subparallelism of: 1) the Φ_1 axis of the spinel fabric ellipsoid; 2) the long axes of olivine grains measured on the $\Phi_1\Phi_3$ plane of the fabric ellipsoid; and 3) the maxima of [100] or [001] olivine crystal axis distributions (Figure 9; e.g., FDM-AVBB06, FDM-AVBB07, FDM-AVBB08, FDM-DB03-X02, FDM-AVBB05, FDM-DB02-X11, FDM-DB02-X08 FDM-RN02-X01, FDM-DB01-X01, FDM-DB03-X03, and FDM-DB04-X03). We interpret the alignment between these three deformation features as an indication that the 3D spinel shape fabric may have reached a steady state orientation. The parallelism between 3D spinel SPO, 2D olivine SPO, and olivine CPO, does not depend on the deformation mechanism; spinel SPO formed by rotation of rigid grains, while olivine SPO and CPO formed by dislocation-accommodated grain boundary sliding.

At high strain, dynamic recrystallization may affect SPO; the long axes of the recrystallized grains acquire a steady state orientation at high angle (40–70°) to the shear plane [e.g., *Herwegh and Handy*, 1998; *Tasaka et al.*, 2016]. Due to limited modification of spinel grain shape by dynamic recrystallization, we can rule out this hypothesis. Experimental and numerical studies demonstrate that in simple shear, a viscous material containing a population of rigid particles (e.g., non-recrystallized porphyroclasts) develops a steady shape fabric at large strains [*Ildefonse et al.*, 1997]. This shape fabric can be subparallel to the shear plane and shear direction [*Mancktelow et al.*, 2002; *Arbaret et al.*, 2007], as well as to the finite strain ellipsoid [*Bhattacharyya and Hudleston*, 2001; *Bystricky et al.*, 2006]. We can therefore assume that the XRCT-derived spinel SPO can provide a robust reference framework relative to which we can plot and interpret the olivine CPO data.

The geometries of the fabric ellipsoid and finite strain ellipsoid are likely to be similar. In places where finite strain can be studied in detail, it typically conforms well to shape fabric [e.g., *Cloos*, 1947; *Bhattacharyya and Hudleston*, 2001]. Consequently, while the magnitudes of the axes may vary, the overall shape of the fabric ellipsoid should parallel the finite strain ellipsoid. Deviations from this pattern are expected only in the cases of highly planar markers, highly linear markers, or deformations with large vorticity components [*Giorgis and Tikoff*, 2004]. In the following discussion we assume that spinel fabric geometry adequately describes the finite strain geometry.

5.2. Effect of deformation conditions

The Marie Byrd Land xenoliths have equilibrated at temperatures ranging from 780 to 1200 °C, and assuming a geotherm which satisfies the stability of spinel in all the xenoliths, the corresponding ranges in pressures and depths are 13–23 kbar and 39–72 km, respectively (Figure 6c). The estimated deformation conditions suggest a lithospheric rather than asthenospheric origin for all the xenoliths; the asthenospheric mantle beneath Marie Byrd Land is marked by a seismic low velocity zone imaged below 80 km depth [*Ritzwoller et al.*, 2001]. Water content and paleopiezometry analysis suggest that the Marie Byrd Land lithospheric mantle is variably hydrated (with olivine H content of up to 500 $H/10^6Si$) and has been deformed under low flow stress (2–60 MPa).

Combining the estimated deformation conditions with the observed olivine CPOs in the Marie Byrd Land xenoliths, we can explore how variations in temperature, pressure, differential stress, and water content are associated with the type of olivine CPO. Plotting our data in differential stress versus temperature/pressure space, we do not observe systematic variation in CPO type relative to temperature and pressure (Figure 12a). There is, however, a tendency of axial-[100] patterns to develop at lower flow stress. To further provide an unbiased discriminator of the relationship between deformation conditions and olivine CPO, we use the BA-index. The BA-index shows no correlation with equilibration temperature and pressure (Figure 12b). Higher BA-index values (> 0.5), though, are associated with low differential stress (Figure 12c).

We observe a correlation between the BA-index and the estimated pre-emplacement OH concentration in olivine; water content increases with the BA-index (Figure 12d; Table 2). Olivine in xenoliths with the axial-[010] symmetry is only slightly hydrated (<150 $H/10^6Si$), and it becomes moderately hydrated (100–500 $H/10^6Si$) toward the axial-[100] symmetry. In the orthorhombic symmetry, the xenolith with the B-type CPO is characterized by minor water content (73–219 $H/10^6Si$), while the two xenoliths with A-type CPO have minor to modest water content (40–288 $H/10^6Si$).

The development of the A-type olivine CPO in the range of deformation conditions estimated for the Marie Byrd Land xenoliths is in agreement with the results of experimental studies, which show that the A-type CPO typically forms at low stress, and low water content [*Carter and Avé Lallemant*, 1970; *Jung and Karato*, 2001; *Katayama et al.*, 2004; *Karato et al.*, 2008]. Particularly, in the low stress levels estimated for the studied xenoliths, the range of water content at which the formation of the A-type is observed can increase up to 300 $H/10^6Si$ (Figure 1a) [*Katayama et al.*, 2004], which is in agreement with our observations.

The transition from A-type to axial-[100] type pattern is predominantly considered to be stress-controlled, and the axial-[100] CPO is typically related to high stress and dry conditions (Figure 1a) [*Carter and Avé Lallemant, 1970*; *Katayama et al.*, 2004]. However, decrease of temperature decreases the stress threshold above which the axial-[100] type forms. Xenoliths with the axial-[100] CPO are characterized by low stresses (<20 MPa), but span the whole range of the estimated deformation conditions (Figure 12a–c). This implies that the formation of the axial-[100] CPO at low flow stress is not the result of decreasing deformation temperature. High-temperature experiments show development of the axial-[100] type at relatively low stresses and under hydrous [*Demouchy et al.*, 2012] or dry [*Bystricky et al.*, 2000; *Hansen et al.*, 2014] conditions. Our results provide further support for the development of the axial-[100] CPO in low flow stress and moderate water content. Combining the experimental results with observations from naturally deformed rocks [e.g., *Saruwatari et al.*, 2001; *Warren et al.*, 2008; *Webber et al.*, 2010; this study], it becomes evident that the axial-[100] CPO can form in a wide range of deformation conditions, which makes it difficult to assign this CPO type to a specific set of conditions.

Increased activity of the (010)[001] slip system with increased pressure (>30 kbar) [*Couvy et al.*, 2004; *Raterron et al.*, 2012; *Jung et al.*, 2009; *Lee and Jung*, 2015] or water content (>200 $H/10^6Si$) [*Jung and Karato*, 2001; *Mizukami et al.*, 2004; *Karato et al.*, 2008] may lead to the development of the B-type and the axial-[010] CPOs. Despite the uncertainty included in the determination of the geotherm for the Marie Byrd Land lithospheric mantle, the xenoliths with axial-[010] and B-type CPOs are characterized by equilibration pressures of less than 21 kbar and contain relatively dry olivine. Development of the axial-[010] and B-type patterns at pressures lower than 30 kbar and/or dry conditions has been described both in nature [*Newman et al.*, 1999; *Dijkstra et al.*, 2002; *Hidas et al.*, 2007; *Drury et al.*, 2011; *Precigout and Hirth*, 2014] and experiments [*Avé Lallemant and Carter,* 1970; *Nicolas et al.*, 1973].

Experimental, theoretical, and natural studies have substantiated that changes in deformation conditions induce variations in olivine CPO [e.g., *Carter and Avé Lallemant*, 1970; *Tommasi et al.*, 2000; *Karato et al.*, 2008]. Our dataset confirms the development of the A-type under low flow stress, low to moderate water content, and intermediate pressure. However, our results emphasize that the development of the axial-type and B-type CPOs in the Marie Byrd Land xenoliths cannot be solely explained on the basis of variations in deformation conditions.

5.3. Effect of finite strain

5.3.1. Strain magnitude

Strain markers are rare in the mantle, and as a result, the relationship between strain magnitude and olivine CPO is difficult to evaluate in naturally deformed mantle rocks. Strain can affect the CPO asymmetry [*Zhang and Karato*, 2000; *Kaminski and Ribe*, 2002; *Warren et al.*, 2008; *Webber et al.*, 2010], the CPO type [*Boneh and Skemer*, 2014; *Hansen et al.*, 2014], as well as the CPO strength [*Tommasi et al.*, 2000; *Kaminski and Ribe*, 2001; *Hansen et al.*, 2014]. Experimental and numerical simulation studies suggest that CPO strength may increase as a function of shear strain [*Bystricky et al.*, 2000; *Kaminski and Ribe*, 2001; *Hansen et al.*, 2014], in which case it is possible to use olivine CPO strength to qualitatively describe strain magnitude.

An increase in strain may cause transient development of the axial-[100] type in olivine during CPO evolution from random to A-type [*Hansen et al.*, 2014]. To explore potential effect of strain magnitude on olivine CPO development for the Marie Byrd Land xenoliths, we plot the BA-index against the J- and M-indices. Unlike experimental observations, our data show no correlation between CPO symmetry and strength (Figure 13a and b). Furthermore, the mean J- and M-index values for the A-type (J=3.49, M=0.15) and axial-[100] (J=3.48, M=0.18) CPOs are similar. These observations suggest that either there is no correlation between strain magnitude and CPO strength, or that the CPO type does not depend on strain magnitude. Lack of J- and M-indices increase with increasing shear strain has also been reported along a strain gradient in naturally deformed peridotites [*Warren et al.*, 2008].

To further explore the relationship between strain magnitude and CPO type, we use the spinel shape fabric. The degree of spinel fabric anisotropy does not describe strain magnitude in a quantitative way, but can provide qualitative constraints [*Giorgis and Tikoff*, 2004]. We observe no correlation between the BA-index and the fabric anisotropy (Figure 13c). Thus, our data provide indirect evidence that the variation in olivine CPO symmetry observed in the Marie Byrd Land xenoliths may not be the result of strain magnitude changes.

5.3.2. Strain geometry

In addition to fabric anisotropy, we explore the relationship between fabric geometry and CPO symmetry (Figure 14a). The xenoliths with A-type CPO spread over the whole range of fabric ellipsoid geometries; five xenoliths plot in the prolate field, four in the oblate field, and three plot near the neutral ellipsoid shape line. The majority (10 out of 15) of the xenoliths with an axial-[010] symmetry are characterized by fabric ellipsoids with neutral shape to oblate geometries. On the other hand, the majority (6 out of 8) of the xenoliths with axial-[100] CPO are associated with prolate spinel fabric ellipsoid geometries. The sample with the B-type pattern has a highly oblate fabric (*T*=0.68) (Figure 14a). To explore the relationship between fabric geometry and olivine CPO further, we compare the BA-index with the shape parameter of the spinel fabric (Figure 14b). The BA-index increases with decreasing *T*, which suggests a transition from axial-[010], to orthorhombic symmetry, and finally to axial-[100] CPO, with an associated change from oblate to prolate fabric geometry (Figure 14b). Assuming correlation between the shape of the fabric and finite strain ellipsoid, our data provide evidence that olivine CPO type depends on finite strain geometry.

In support of this result, laboratory-based studies and numerical simulations demonstrate that different deformation boundary conditions will produce different olivine CPOs. The axial-[010] CPO has largely been produced in axial compression experiments [*Avé Lallemant and Carter*, 1970; *Nicolas et al.*, 1973; *Hansen et al.*, 2011; *Miyazaki et al.*, 2013], which involve flattening strain [*Avé Lallemant and Carter*, 1970; *Nicolas et al.*, 1973; *Llana-Funez and Rutter*, 2014]. Axial compression of olivine aggregates results in clusters of [010] axes and girdles of [100] axes; girdling of [100] axes comprises the primary distinction between the axial-[010] and A-type CPOs. Olivine CPOs with [100] girdles have also been produced in direct shear experiments [*Zhang et al.*, 2000; *Holtzman et al.*, 2003; *Hansen et al.*, 2014]. Deformation in direct shear experiments is simple shear-dominated but it also includes a component of compression, with the overall deformation being transpressional [*Zhang et al.*, 2000; *Holtzman et al.*, 2003; *Karato et al.*, 2008; *Hansen et al.*, 2014]. Transpression generally produces oblate ellipsoids due to flattening strain [e.g., *Fossen and Tikoff*, 1998]. Numerical simulations suggest that axial shortening and transpression result in axial-[010] CPOs, similar to those observed in the Marie Byrd Land xenoliths with oblate fabric geometries [*Wenk et al.*, 1991; *Tommasi et al.*, 1999].

Numerical simulations also suggest that transtension (constrictional strain) will produce axial-[100] CPOs, similar to those identified in the xenoliths with prolate fabric geometries

[*Tommasi et al.*, 1999]. Girdling versus clustering of [010] axes comprises the primary distinction between the axial-[100] and A-type CPOs, respectively. In laboratory-based studies, the axial-[100] CPO is primarily produced in torsion experiments [*Bystricky et al.*, 2000, 2006; *Demouchy et al.*, 2012; *Hansen et al.*, 2014]. Deformation in torsion is considered to approach simple shear, and therefore plane strain. This questions the universality of the correlation between axial-[100] and prolate strain observed in both the numerical models and our xenoliths. An explanation in line with our results could be that the geometry of the strain ellipsoid in torsion experiments conducted at moderate shear strain, where the axial-[100] CPO forms [*Hansen et al.*, 2014], may deviate from plane strain. Because the evolution of strain geometry in these torsion experiments has not been reported, we cannot currently test this hypothesis.

The A-type has been produced in direct shear and high shear strain torsion experiments under dominant simple shear deformation [*Zhang et al.*, 2000; *Hansen et al.*, 2014]. Development of the A-type in simple shear is also supported by olivine CPO simulation studies [*Wenk et al.*, 1991; *Tommasi et al.*, 1999; *Kaminski and Ribe*, 2001]. Our results do not show any correlation of A-type with fabric geometry, which may imply that the role of deformation conditions may dominate in the development of this CPO in the studied xenoliths.

The presence of only one sample with B-type olivine CPO pattern in the analyzed suite of xenoliths, does not allow for definitive predictions concerning the relationship between this CPO and strain geometry. We note, however, that our observations are in agreement with the results of *Lee and Jung* [2015], which also show correlation between the olivine B-type and flattening strain. Furthermore, the B-type is predominantly formed in direct shear experiments [*Jung and Karato*, 2001; *Holtzman et al.*, 2003]; samples are subjected to transpressional deformation, which may produce oblate strain ellipsoids.

To summarize, our results emphasize that in the Marie Byrd Land xenoliths, strain geometry controls the development of axial-type olivine CPO patterns (Figure 15). The axial-[010] CPO forms in flattening strain and the axial-[100] CPO in constriction. This relationship is also supported by deformation experiments and numerical simulation studies of CPO evolution.

5.4. Mechanism of olivine axial-type CPO development

We propose that development of olivine axial-type CPOs in the Marie Byrd Land xenoliths results from the combination of: 1) 3D strain; 2) deformation by dislocation-accommodated grain boundary sliding; and 3) activation of multiple slip systems. The kinematic boundary conditions of deformation control the orientation and shape of the finite strain ellipsoid [*Fossen and Tikoff*, 1998]. The 3D strain induces changes in the shape of grains. Movement of dislocations along slip planes and sliding along grain boundaries, induce shape changes at the grain scale. Concurrent slip along multiple glide planes allows for accommodation of more complex types of non-coaxial deformation [*Tommasi et al.*, 1999], while grain boundary sliding relaxes strain compatibility constraints, and may facilitate grain rotations [*Tommasi et al.*, 2000; *Warren et al.*, 2008; *Drury et al.*, 2011; *Hansen et al.*, 2014; *Précigout and Hirth*, 2014].

Correlation of [100], [001], and [010] olivine crystallographic axes with ε_1, ε_2, and ε_3 strain ellipsoid axes, respectively, has been proposed [*Avé Lallemant and Carter*, 1970; *Nicolas et al.*, 1973; *McKenzie*, 1979; *Ribe and Yu*, 1991; *Miyazaki et al.*, 2013]. In addition, a fundamental relationship exists between the distributions of the orientations of olivine crystallographic axes in axial-type CPOs and the orientations of axes in the corresponding fabric ellipsoids, i.e., between crystal lattice and grain shape. The [100], [001], and [010] axes show similar distributions in their orientations with Φ_1, Φ_2, and Φ_3 fabric ellipsoid axes, respectively (Figure 15). In flattening strain, the Φ_1 and Φ_2 axes of grains have similar magnitudes and tend to disperse along the foliation plane due to multi-directional stretching occurring on that plane. Similarly, the [100] and [001] olivine crystallographic axes of the axial-[010] CPO, which forms with oblate strain geometries, tend to make girdles along the foliation (Figure 15). Both Φ_3 and [010] cluster parallel to the shortening orientation. In constrictional strain, the Φ_2 and Φ_3 axes of grains have similar magnitudes and tend to disperse on a plane normal to the lineation (Figure 15). Both Φ_1 and [100] cluster parallel to the stretching orientation. The described relationship between the crystallographic and grain shape axes implies that their orientation is controlled by the strain geometry, and therefore, by the kinematic boundary conditions imposed by the deformation.

The grain-scale processes that produce the girdled patterns in axial-type CPOs in the Marie Byrd Land xenoliths are as follows. Flattening strain involves multi-directional stretching along the foliation plane. This stretching can be accommodated by dislocation glide toward a range of directions within the foliation plane [*Tommasi et al.*, 1999]. In the xenoliths with axial-[010] CPO, intracrystalline deformation exhibited by subgrain boundary formation is accommodated by {0kl}[100] and (010)[001] slip. Numerical simulations of *Tommasi et al.* [2000] show that, in axial shortening, relaxation of strain compatibility constraints (e.g., due to grain boundary sliding) may increase the activity of the otherwise "hard" (010)[001] slip system. The combination of microstructures, misorientation axes analysis, and CPO data suggests the existence of twist boundaries in (010), which involve rotation along (010) planes (Figure 10b) [*Lloyd et al.*, 1997]. Such rotation may induce spreading of [100] and [001] axes within the foliation plane and produce more girdled patterns. Development of the axial-[010] CPO in dislocation-accommodated grain boundary sliding with dominant activity of (010)[100] is also reported by *Précigout and Hirth* [2014]; the axial-[010] CPO is considered transitional between the A- and B-type CPOs, with the alignment of [001] axes parallel to Φ_1 being the result of rigid grain rotations guided by the olivine crystal habit.

In the xenoliths with axial-[100] CPO, olivine grains contain subgrain boundaries comprised of dislocations in the {0kl}[100] family of slip systems and (001)[100] dislocations. In agreement with the results of previous studies, development of [010] and [001] girdles in the Marie Byrd Land xenoliths seem to result from the activation of multiple glide systems [*Tommasi et al.*, 1999, 2000; *Warren et al.*, 2008; *Demouchy et al.*, 2012]. Multislip on {0kl}[100] systems and/or combined operation of (010)[100] and (001)[100] slip systems, which is favored by grain boundary sliding, both may lead to the formation of [010] and [001] girdles at high angle to the lineation.

5.5. Implications for the interpretation of olivine CPO

Several experimental and numerical simulation studies have substantiated the role of deformation conditions, melt, and strain magnitude on the development and evolution of olivine CPO [*Avé Lallemant and Carter*, 1970; *Carter and Avé Lallemant*, 1970; *Wenk et al.*, 1991; *Tommasi et al.*, 1999, 2000; *Jung and Karato*, 2001; *Holtzman et al.*, 2003; *Couvy et al.*, 2004; *Katayama et al.*, 2004; *Karato et al.*, 2008; *Demouchy et al.*, 2012; *Raterron et al.*, 2012; *Hansen et al.*, 2014]. In the present study, we highlight the role of finite strain geometry as fundamental parameter affecting olivine CPO, and particularly controlling the development of the axial-type CPOs. We should note that the relationship between strain geometry and olivine CPO was initially described in early compression experiments [*Avé Lallemant and Carter*, 1970; *Nicolas et al.*, 1973] and later numerical studies [*McKenzie*, 1979; *Ribe and Yu*, 1991; *Wenk et al.*, 1991; *Tommasi et al.*, 1999, 2000], however, little attention has been given to this relationship since then. Additionally, correlation between finite strain geometry and clinopyroxene CPO has been described in mantle xenolith studies [*Helmstaedt et al.*, 1972; *Ulrich and Mainprice*, 2005]. Thus, our results emphasize that both deformation conditions and finite strain geometry may affect mantle texture, which makes it difficult to deduce the effect of each parameter separately.

Despite the complexities inherent in the interpretation of CPO patterns, particularly in naturally deformed rocks that may have followed complex deformation histories, three lines of evidence suggest that our results form the Marie Byrd Land xenoliths can be of broad significance for upper mantle studies. First, the importance of dislocation-accommodated grain boundary sliding, which contributes to the development of the axial-type CPOs [*Tommasi et al.*, 2000; *Warren et al.*, 2008; *Hansen et al.*, 2014; *Précigout and Hirth*, 2014], is increasingly recognized. Extrapolation of experimental flow laws shows that dislocation-accommodated grain boundary sliding may contribute to the deformation over a wide range of conditions in a dry upper mantle [*Hansen et al.*, 2011]. Second, polyphase materials such as the Marie Byrd Land xenoliths (predominantly lherzolites and harzburgites) are the norm rather than the exception in nature. Grain and phase boundary sliding is facilitated by the coexistence of olivine and pyroxene [*Sundberg and Cooper*, 2008; *Newman et al.*, 1999]. Third, there are a large number of studies reporting axial-type CPOs in naturally deformed rocks from a range of tectonic settings [e.g., *Saruwatari et al.,* 2001; *Dijkstra et al.*, 2002; *Vauchez et al.*, 2005; *Hidas et al.*, 2007; *Warren et al.,* 2008; *Webber et al.*, 2010; *Précigout and Hirth*, 2014]. Assuming that olivine CPO contains information about strain geometry, the occurrence of axial-type patterns implies that deviation of upper mantle deformation from simple shear may not be an uncommon phenomenon. Furthermore, since olivine CPO is the major contributor to lithospheric seismic anisotropy [*Christensen*, 1984; *Ben Ismail and Mainprice*, 1998; *Tommasi et al.*, 1999; *Karato et al.*, 2008; *Précigout and Almqvist*, 2014], there is great potential for using seismic anisotropy to map finite strain variations in the lithosphere, and to interrogate new geodynamic interpretations with a revised view of the development of olivine CPO.

6. Conclusions

Using X-ray computed tomography we determine the spinel fabric ellipsoid in a suite of spinel peridotite xenoliths from Marie Byrd Land, west Antarctica. The xenoliths show a range of fabric ellipsoid geometries (oblate, neutral shape, and prolate) and are characterized by a variety of olivine CPO types (A-type, axial-[010], axial-[100], and B-type). For the range of temperature, pressure, differential stress, and water content conditions estimated in the xenoliths, the development of girdled olivine CPO patterns is predominantly controlled by the geometry of the finite strain ellipsoid rather than the deformation conditions. We therefore establish for the first time in naturally deformed peridotites a relationship between finite strain geometry and olivine CPO symmetry. The axial-[010] and axial-[100] patterns form by flattening and constrictional strain, respectively. Importantly, our observations suggest that mantle deformation may deviate from simple shear. Our results emphasize that future studies of laboratory and naturally deformed rocks should incorporate the role of finite strain geometry as a possible cause of textural transitions in the mantle. Olivine texture and seismic anisotropy could potentially be used to map 3D strain variations in the upper mantle.

Acknowledgements

We thank the United States Polar Rock Repository, Christine Siddoway and Kurt Panter for providing us with xenolith samples. We thank John Fournelle (UW-Madison) for his advice and assistance with the microprobe analyses. Brian Hess (UW-Madison) is thanked for the production of high quality thin sections used in EBSD analysis, and Zach Michels is also thanked for assistance with MTEX. Marc Hirschmann and Jed Mosenfelder (U. Minnesota) kindly provided access to FTIR facilities. The quality of this work was benefited greatly from constructive comments from reviewers Lars Hansen and Jacques Précigout, as well as the comments of the editors Michael

Walter and Stephen Parman. Finally, we thank Basil Tikoff, Julie Newman, Martyn Drury, and members of the structure and tectonics groups at Boston College and UW-Madison for insightful discussions. The EPMA data used are listed in Table S3. Requests for XRCT and EBSD data sets can be made by contacting the corresponding author. This research was supported by NSF-ANT 1246320 grant to S.C. Kruckenberg and NSERC discovery grant to A.C. Withers.

References

Accardo, N. J., D. A. Wiens, S. Hernandez, R. C. Aster, A. Nyblade, et al. (2014), Upper mantle seismic anisotropy beneath the West Antarctic Rift System and surrounding region from shear wave splitting analysis, *Geophys. J. Int., 198*, 414–429, doi:10.1093/gji/ggu117.

Arai, S. (1994), Characterization of spinel peridotites by olivine-spinel compositional relationships: review and interpretation, *Chem. Geol., 113*, 191–204, doi:10.1016/0009-2541(94)90066-3.

Arbaret, L., M. Bystricky, and R. Champallier (2007), Microstructures and rheology of hydrous synthetic magmatic suspensions deformed in torsion at high pressure, *J. Geophys. Res., 112*, B10208, doi:10.1029/2006JB004856.

Ardia, P., M. M. Hirschmann, A. C. Withers, and T. J. Tenner (2012), H_2O storage capacity of olivine at 5–8 GPa and consequences for dehydration partial melting of the upper mantle, *Earth Planet. Sci. Lett., 345– 348*, 104–116, doi:10.1016/j.epsl.2012.05.038.

Armstrong, J. T. (1988), Quantitative analysis of silicate and oxide materials: comparison of Monte Carlo, ZaF, an ϕ(pz) procedures, in *Proceedings of the 23rd annual conference of the Microbeam analysis Society*, edited by D. E. Newbury, pp 239–246, *San Francisco Press, San Francisco.*

Ashby, M. F., Verrall, R. A., 1973, Diffusion accommodated flow and superplasticity, *Acta Metall.*, *21*, 149–163, doi:10.1016/0001-6160(73) 90057-6.

Asimow, P. D., L. C. Stein, J. L. Mosenfelder, and G. R. Rossman (2006), Quantitative polarized FTIR analysis of trace OH in populations of randomly oriented mineral grains, *Am. Mineral.*, *91*, 278–284 doi:10.2138/am.2006.1937.

Avé Lallemant, H. G., and N. L. Carter (1970), Syntectonic recrystallization of olivine and modes of flow in the upper mantle, *Geol. Soc. Am. Bullet.*, *81*, 2203–2020, doi:10.1130/0016-7606(1970)81[2203:SROOAM]2.0.CO;2.

Bachmann, F., R. Hielscher, and H. Schaeben (2010), Texture analysis with MTEX-Free and Open Source Software Toolbox, *Diffus. Defect Data Solid State Data Part B Solid State Phenom.*, 160, 63–68.

Bachmann, F., R. Hielscher, and H. Schaeben (2011), Grain detection from 2d and 3d EBSD data – Specification of the MTEX algorithm, *Ultramicroscopy*, *111*, 1720–1733.

Bai, Q., S. J. Mackwell, and D. L. Kohlstedt (1991), High-temperature creep of olivine single crystals, 1, Mechanical results for buffered samples, *J. Geophys. Res.*, 96, 2441–2463, doi: 10.1029/90JB01723.

Ballhaus C., R. F. Berry, and D. H. Green (1991) High pressure experimental calibration of olivine-orthopyroxene-spinel oxygen geobarometer: implications for the oxidation state of the upper mantle, *Contrib. Mineral. Petrol.*, *107*, 27–40, doi:10.1007/BF00311183.

Ben Ismail, W., and D. Mainprice (1998), An olivine fabric database: an overview of upper mantle fabrics and seismic anisotropy, *Tectonophysics*, *296*, 145–158, doi:10.1016/S0040-1951(98)00141-3.

Bell, D.R., P. D. Ihinger, and G. R. Rossman (1995), Quantitative analysis of trace OH in garnet and pyroxenes, *Am. Mineral.*, *80*, 465–474.

Berg, J. H., R. J. Moscati, and D. L. Herz (1989), A petrologic geotherm from a continental rift in Antarctica, *Earth Planet. Sci. Lett.*, *93*, 98–108, doi:10.1016/0012-821X(89)90187-8.

Bertrand P, and J-C. C. Mercier (1985), The mutual solubility of coexisting ortho- and clinopyroxene: toward an absolute geothermometer for the natural system? *Earth Planet. Sci. Lett.*, *76*, 109–122, doi:10.1016/0012-821X(85)90152-9.

Bhattacharyya, P. and P. J. Hudleston (2001), Strain in ductile shear zones in the Caledonides of northern Sweden: a three-dimensional puzzle, *J. Struct. Geol.*, *23*, 1549–1565, doi:10.1016/S0191-8141(01)00020-7.

Boneh, Y., and P. Skemer (2014), The effect of deformation history on the evolution of olivine CPO, *Earth Planet. Sci. Lett.*, *406*, 213–222, doi:10.1016/j.epsl.2014.09.018.

Brey, G. P., and T. Köhler (1990), Geothermobarometry in four-phase lherzolites: II. new thermobarometers and practical assessment of existing thermobarometry, *J. Petrol.*, *31*, 1352–1378, doi:10.1093/petrology/31.6.1353.

Bunge, H. J. (1982), *Texture Analysis in Materials Science*, Butterworths, Boston, Mass.

Bystricky, M., K. Kunze, L. Burlini, and J. –P. Burg (2000), High shear strain of olivine aggregates: rheological and seismic consequences, *Science*, *290*, 1564–1567, doi: 10.1126/science.290.5496.1564.

Bystricky, M., F. Heidelbach, and S. Mackwell (2006), Large-strain deformation and strain partitioning in polyphase rocks: Dislocation creep of olivine-magnesiowüstite aggregates, *Tectonophysics*, *427*, 115–132, doi: 10.1016/j.tecto.2006.05.025.

Carter, N. L., and H. G. Avé Lallemant (1970), High temperature deformation of dunite and peridotite, *Geol. Soc. Am. Bull.*, *81*, 2181–202, doi:10.1130/0016-7606(1970)81[2181:HTFODA]2.0.CO;2.

Christensen, N. I. (1984), The magnitude, symmetry and origin of upper mantle anisotropy based on fabric analyses of ultramafic tectonites, *Geophys. J. R. Astron. Soc.*, *76*, 89–111, doi:10.1111/j.1365-246X.1984.tb05025.x.

Cloos, E. (1947), Oolite deformation in the South Mountain fold, Marybank, Geol. Soc. Bull., 58, 843–918.

Couvy, H., D. J. Frost, F. Heidelbach , K. Nyilas, T. Ungar, et al. (2004), Shear deformation experiments of forsterite at 11 GPa-1400°C in the multianvil apparatus. *Eur. J. Mineral., 16*, 877–89, doi:10.1127/0935-1221/2004/0016-0877.

De Kloe, R. (2001), Deformation mechanisms and melt nano-structures in Experimentally deformed olivine–orthopyroxene rocks with low melt fractions. An electron microscopy study. Ph.D. Thesis. Utrecht University, 173 pp.

Demouchy, S., S. D. Jacobsen, F. Gaillard, and C. R. Stern (2006), Rapid magma ascent recorded by water diffusion profiles in mantle olivine, *Geology, 34*, 429–432, doi:10.1130/G22386.1.

Demouchy, S., A. Tommasi, F. Barou, D. Mainprice, and P. Cordier (2012), Deformation of olivine in torsion under hydrous conditions, *Phys. Earth Planet. Inter.*, *202–203*, 57–70, doi: 10.1016/j.pepi.2012.05.001.

Dijkstra, A. H., M. R. Drury, and R. M. Frijhoff (2002), Microstructures and lattice fabrics in the Hilti mantle section (Oman Ophiolite): evidence for shear localiza- tion and melt weakening in the crust- mantle transition zone? *J. Geophys. Res., 107*, ETG 2-1, doi: 10.1029/2001JB000458.

Drury, M. R., and F. J. Humphreys (1988), Microstructural shear criteria associated with grain boundary sliding during ductile deformation, *J. Struct. Geol., 10*, 83–89, doi:10.1016/0191-8141(88)90130-7.

Drury, M.R., and J. L. Urai (1990), Deformation-related recrystallisation processes, *Tectonophysics, 172*, 235–253, doi: 10.1016/0040-1951(90)90033-5.

Drury, M. R., H. G. Avé Lallemant, G. M. Pennock, and L. N. Palasse (2011), Crystal preferred orientation in peridotite ultramylonites deformed by grain size sensitive creep, Étang de Lers, Pyrenees, France, *J. Struct, Geol., 33*, 1776–1789, doi: 10.1016/j.jsg.2011.10.002.

Durham, W. B., and G. Goetze (1977), Plastic flow of oriented single crystals of olivine, 1, Mechanical data, J. Geophys. Res., *82*, 5737–5753, doi: 10.1029/JB082i036p05737.

Evans, B., and C. Goetze (1979), The temperature variation of hardness of olivine and its implication for polycrystalline yield stress, *J. Geophys. Res. 84*, 5505–5524, .doi: 10.1029/JB084iB10p05505

Ferraccioli, F., E. Bozzo, and D. Damaske (2002), Aeromagnetic signatures over western Marie Byrd Land provide insight into magmatic arc basement, mafic magmatism and structure of the eastern Ross Sea rift flank, *Tectonophysics, 347*,139–165, doi:10.1029/2001GL014138.

Finn, C. A., R. D. Müller, and K. S. Panter (2005), A Cenozoic diffuse alkaline magmatic province (DAMP) in the southwest Pacific without rift or plume origin, *Geochem. Geophys. Geosyst., 6*, doi:10.1029/2004GC000723.

Fossen, H., and B. Tikoff (1998), Extended models of transpression and transtension, and application to tectonic settings, in *Continental Traspressional and Transtensional Tectonics*, Geol. Soc. Lond. Spec. Publ., vol. 135, pp. 15–33, doi: 10.1144/GSL.SP.1998.135.01.02.

Gaffney, A. M., and C. S. Siddoway (2007), Heterogeneous sources for Pleistocene lavas of Marie Byrd Land, Antarctica: new data from the SW Pacific diffuse alkaline magmatic province: U.S. Geological Survey Open-File Report 07-1047, Extended Abstract 063.

Giorgis, S., and B. Tikoff (2004), Constraints on kinematics and strain from feldspar porphyroclast populations, in Flow Processes in Faults and Shear Zones edited by G. I. Alsop et al., pp. 265–285, Geol. Soc. Lon Sp. Publ., doi:10.1144/GSL.SP.2004.224.01.17.

Goetze, C. (1978), The mechanisms of creep in olivine, *Philos. Trans. R. Soc. Lond., A 288*, 99–119.

Hansen, L. N., M. E. Zimmerman, and D. L. Kohlstedt (2011), Grain boundary sliding in San Carlos olivine: Flow law parameters and crystallographic-preferred orientation, *J. Geophys. Res., 116*, B08201, doi:10.1029/2011JB008220.

Hansen, L. N., M. E. Zimmerman, and D. L. Kohlstedt (2014), Protracted fabric evolution in olivine: Implications for the relationship among strain, crystallographic fabric, and seismic anisotropy, *Earth Planet. Sci. Lett., 387*, 157–168, doi:10.1016/j.epsl.2013.11.009.

Helmstaedt, H., O. L. Anderson, and A. T. Gavasci (1972), Petrofabric studies of eclogite, spinel–websterite, and spinel–lherzolite xenoliths from kimberlite-bearing breccia pipes in southeastern Utah and northeastern Arizona, *J. Geophys. Res., 77*, 4350–4365, doi:10.1029/JB077i023p04350.

Herwegh, M., and M. Handy (1998), The origin of shape preferred orientation in mylonite: Inferences from in-situ experiments on poly-crystalline norcamphor, *J. Struct. Geol., 20*, 681–694, doi: 10.1016/S0191-8141(98)00011-X.

Hidas, K., G. Falusa, C. Szabó, P. J. Szabó, I. Kovács, and T. Földes (2007), Geodynamic implications of flattened tabular equigranular textured peridotites from the Bakony-Balaton Highland Volcanic Field (Western Hungary), *J. Geodyn., 43*, 484–503, doi:10.1016/j.jog.2006.10.007.

Hirth, G., and D. Kohlstedt (2003), Rheology of the upper mantle and the mantle wedge: a view from the experimentalists, in The Subduction Factory, Geophysical Monograph, vol. 138, edited by J. Eiler , Am. Geophys. Union, pp. 83–105.

Holtzman, B. K., D. L. Kohlstedt, M. E. Zimmerman, F. Heidelbach, T. Hiraga, and J. Hustoft (2003), Melt segregation and strain partitioning: implications for seismic anisotropy and mantle flow, *Science 301*, 1227–1230, doi:10.1126/science.1087132.

Hossack, J. (1968), Pebble deformation and thrusting in the Bygdin Area (Norway), *Tectonophysics, 5*, 315-339, doi: 10.1016/0040-1951(68)90035-8.

Ildefonse, B., L. Arbaret, and H. Diot (1997), Rigid particles in simple shear flow: Is their preferred orientation periodic or steady state? in *Granites: From Segregation of Melt to Emplacement Fabrics*, edited by J. L. Bouchez, D. H. W. Hutton, and W. E. Stephens, pp. 177–185, Kluwer Acad., Dordrecht, Netherlands.

Jelínek, V. 1981. Characterization of the magnetic fabrics of rocks, *Tectonophysics*, *79*, T63-T67, doi: 10.1016/0040-1951(81)90110-4.

Jung, H., and S. Karato (2001), Water-induced fabric transitions in olivine, *Science, 293*, 1460–1463, doi:10.1126/science.1062235.

Jung, H., W. Mo, and H. W. Green (2009), Upper mantle seismic anisotropy resulting from pressure-induced slip transition in olivine. *Nat. Geosci. 2*, 73–77, doi: 10.1038/NGEO389.

Kaminski, E., and N. M. Ribe (2001), A kinematic model for recrys- tallization and texture development in olivine polycrystals, *Earth Planet. Sci. Lett., 189*, 253–267, doi: 10.1016/S0012-821X(01)00356-9.

Karato, S.-I., M. Toriumi, and T. Fuji, (1980), Dynamic recrystallization of olivine single crystals during high-temperature creep, *Geoph. Res. Lett., 7*, 649–652, doi:10.1029/GL007i009p00649.

Karato, S., H. Jung, I. Katayama, and P. A. Skemer (2008), Geodynamic significance of seismic anisotropy of the upper mantle: new insights from laboratory studies, *Annu. Rev. Earth Planet. Sci., 36*, 59–95, doi:10.1146/annurev.earth.36.031207.124120.

Katayama, I., H. Jung, and S. I. Karato (2004), New type of olivine fabric from deformation experiments at modest water content and low stress, *Geology, 32*, 1045–1048, doi:10.1130/G20805.1.

Katayama, I., and J. Korenaga (2011), Is the African cratonic lithosphere wet or dry?, in *Volcanism and Evolution of the African Lithosphere*, Geol. Soc. Am. Sp. Paper, vol. 478, edited by Beccaluva, L., G. Bianchini, and M. Wilson, pp. 249–256, doi:10.1130/2011.2478(13).

Ketcham, R. A. (2005a), Computational methods for quantitative analysis of three-dimensional features in geological specimens, *Geosphere, 1*, 32–41, doi:10.1130/GES00001.1.

Ketcham, R. A. (2005b), Three-dimensional grain fabric measurements using high-resolution X-ray computed tomography, *J. Struct. Geol., 27*, 1217–1228, doi: 10.1016/j.jsg.2005.02.006.

Ketcham, R. A., and T. Ryan (2004), Quantification and visualization of anisotropy in trabecular bone, J. Microsc., 213, 158–171, doi: 10.1111/j.1365-2818.2004.01277.x.

Kruckenberg, S. C., E. C. Ferré, C. Teyssier, O. Vanderhaeghe, D. L. Whitney, N. C. A. Seaton, and J. A. Skord (2010), Viscoplastic flow in migmatites deduced from fabric anisotropy: An example from the Naxos dome, Greece, *J. Geophys. Res.*, 115, B09401, doi:10.1029/2009JB007012.

Launeau, P., and P. -Y. F. Robin (1996), Fabric analysis using the intercept method, *Tectonophysics, 267*, 91–119, doi: 10.1016/S0040-1951(96)00091-1.

Law, R. D., R. J. Knipe, and H. Dayan (1984), Strain path partitioning within thrust sheets: microstructural and petrofabric evidence from the Moine thrust zone at Loch Eriboll, NW Scotland, *J. Struct. Geol.*, *6*, 477–497, doi: 10.1016/0191-8141(84)90060-9.

Lee, J., and H. Jung (2015), Lattice-preferred orientation of olivine found in diamond-bearing garnet peridotites in Finsch, South Africa and implications for seismic anisotropy, *J. Struct. Geol.*, *70*, 12–22, doi:10.1016/j.jsg.2014.10.015.

Lister G.S., and B. E. Hobbs (1980) The simulation of fabric development during plastic deformation and its application to quartzite: the influence of deformation history. *J. Struct. Geol.*, *2*, 355–371, doi:10.1016/0191-8141(80)90023-1.

Llana-Fúnez, S., and E. H. Rutter (2014), Effect of strain geometry on the petrophysical properties of plastically deformed aggregates: experiments on Solnhofen limestone, in *Deformation Structures and Processes within the Continental Crust*, edited by S. Llana-Fúnez, A. Marcos, and F. Bastida, Geol. Soc. Spec. Publ. London, p.p. 167–187, doi:10.1144/SP394.12.

Lloyd, G. E., A. B. Farmer, and D. Mainprice (1997), Misorientation analysis and the formation and orientation of subgrain and grain boundaries, *Tectonophysics*, *279*, 55–78, doi: 10.1016/S0040-1951(97)00115-7.

Lloyd, G. E, R. H. W. Butler, M. Casey, D. J. Tatham, and D. Mainprice (2011), Constraints on the seismic properties of the middle and lower continental crust, in *Deformation Mechanisms, Rheology and Tectonics: Microstructures, Mechanics and Anisotropy*, edited by D. J. Prior, E. H. Rutter, and D. J. Tatham, Geol. Soc. Spec. Publ. London, p.p. 7–32, doi:10.1144/SP360.2.

Mainprice, D., R. Hielscher, and H. Schaeben (2011), Calculating anisotropic physical properties from texture data using the MTEX open-source package. In *Deformation Mechanisms, Rheology and Tectonics: Micro- structures, Mechanics and Anisotropy*, Geol. Soc. Sp. Publ.

London, vol. 360, edited by Prior, D. J., E. H. Rutter, and D. J. Tatham, pp. 175–192, doi: 10.1144/SP360.10.

Mainprice, D., F. Bachmann, R. Hielscher, and H. Schaeben (2014), Descriptive tools for the analysis of texture projects with large datasets using MTEX — strength, symmetry and components, In *Rock Deformation from Field, Experiments and Theory: A Volume in Honour of Ernie Rutter*, Geol. Soc. Sp. Publ. London, vol. 409, edited by Faulkner, D. R., E. Mariani, and J. Mecklenburgh, doi: 10.1144/SP409.8.

Mancktelow, N. S., L. Arbaret, and G. Pennacchioni (2002), Experimental observations on the effect of interface slip on rotation and stabilisation of rigid particles in simple shear and a comparison with natural mylonites, *J. Struct. Geol., 24*, 567–585, doi:10.1016/S0191-8141(01)00084-0.

McFadden, R. R., C. S. Siddoway, C. Teyssier, and C. M. Fanning (2010a), Cretaceous oblique extensional deformation and magma accumulation in the Fosdick Mountains migmatite-cored gneiss dome, West Antarctica, *Tectonics, 29*, TC4022, doi:10.1029/2009TC002492.

McKenzie, D. P. (1979), Finite deformation during fluid flow, *Geophys. J. R. Astron. Soc., 58*, 689–715, doi:10.1111/j.1365-246X.1979.tb04803.x.

Medaris Jr, L. G., L. Ackerman, E. Jelínek, and T. Magna (2015), Depletion, cryptic metasomatism, and modal metasomatism of central European lithospheric mantle: evidence from elemental and Li isotope compositions of spinel peridotite xenoliths, Kozákov volcano, Czech Republic, *Int. J. Earth Sci.*, *104*, 1925–1956, doi:10.1007/s00531-014-1065-y.

Mecklenburgh, J., Y-H. Zhao, F. Heidelbach,and S. Mackwell (2006), Deformation of olivine-spinel aggregates in the system $(Mg,Ni)_2GeO_4$ deformed to high strain in torsion: Implications for upper mantle anisotropy, *J. Geophys. Res., 111*, B11209, doi:10.1029/2006JB004285.

Miyazaki, T., K. Sueyoshi, and T. Hiraga (2013), Olivine crystals align during diffusion creep of Earth's upper mantle, *Nature, 502*, 321–326, doi:10.1038/nature12570.

Mizukami, T., S. R. Wallis, and J. Yamamoto (2004), Natural examples of olivine lattice preferred orientation patterns with a flow-normal a-axis maximum, *Nature, 427*, 432–436, doi:10.1038/nature02179.

Mosenfelder, J.D., and G. R. Rossman (2013), Analysis of hydrogen and fluorine in pyroxenes by SIMS and FTIR. Part 1. Orthopyroxene, *Am. Mineral., 98*, 1026–1041, doi:10.2138/am.2013.4413.

Nadai, A. (1963), Theory of flow and fracture of solids, New York, McGraw-Hill, p. 705.

Newman, J., W. M. Lamb, M. R. Drury, and R. L M. Vissers (1999) Deformation processes in a peridotite shear zone: reaction-softening by an H2O-deficient, continuous net transfer reaction. *Tectonophysics, 303*, 193–222, doi:10.1016/S0040-1951(98)00259-5.

Nicolas, A., F. Boudier, and A. M. Boullier (1973), Mechanisms of flow in naturally and experimentally deformed peridotites, *Am. J. Sci., 273*, 853–876, doi:10.2475/ajs.273.10.853.

Odgaard, A., J. Kabel, B. van Rietbergen, M. Dalstra, and R. Huiskes (1997), Fabric and elastic principle directions of cancellous bone are closely related, J. Biomech., 30, 487–495, doi:10.1016/S0021-9290(96)00177-7.

O'Neill H. S. T. C. (1981), The transition between spinel lherzolite and garnet lherzolite, and its use as a geobarometer, *Contrib. Mineral. Petrol., 77*, 185–194, doi:10.1007/BF00636522.

Précigout, J., and G. Hirth (2014), B-type olivine fabric induced by grain boundary sliding, *Earth Planet. Sci. Lett., 395*, 231–240, doi:10.1016/j.epsl.2014.03.052.

Précigout, J., and B. S. G. Almqvist (2014), The Ronda peridotite (Spain): A natural template for seismic anisotropy in subduction wedges, *Geophys. Res. Lett., 41*, 8752–8758, doi: 10.1002/2014GL062547.

Prior, D. J., A. P. Boyle, F. Brenker, M. C. Cheadle, A. Day, et al. (1999), The application of electron backscatter diffraction and orientation contrast imaging in the SEM to textural problems in rocks, *Am. Mineral.*, *84*, 1741–1759.

Raterron, P., J. Girard, and J. Chen (2012), Activities of olivine slip systems in the upper mantle, *Phys. Earth Planet. Inter.*, *200*, 105–112, doi:10.1016/j.pepi.2012.04.006.

Ree, J. H. (1994), Grain boundary sliding and development of grain boundary openings in experimentally deformed octachloropropane, *J. Struct. Geol.*, *16*, 403–418, doi: 10.1016/0191-8141(94)90044-2.

Ribe, N. M., and Y. Yu (1991), A theory for plastic deformation and textural evolution of olivine polycrystals, *J. Geophys. Res.*, *96*, 8325–8335, doi:10.1029/90JB02721.

Ritzwoller, M. H., N. M. Shapiro, A. L. Levshin, and G. M. Leahy (2001), Crustal and upper mantle structure beneath Antarctica and surrounding oceans, *J. Geophys. Res.*, *106*, 1–26, doi:10.1029/2001JB000179.

Saruwatari, K., S. Ji, C. Long, and M. H. Salisbury, (2001), Seismic anisotropy of mantle xenoliths and constraints on upper mantle structure beneath the southern Canadian Cordillera, *Tectonophysics*, *339*, 403–426, doi: 10.1016/S0040-1951(01)00136-6.

Schmid, S. M., and M. Casey (1986), Complete fabric analysis of some commonly observed quartz [c]-axis patterns, in *Mineral and Rock Deformation: Laboratory Studies* Geoph. Monogr, vol. 36, edited by Hobbs, B. E., and H. C. Heard, Am. Geoph. Un, Washington, DC, pp. 263–286.

Siddoway, C. S., L. C. Sass III, and R. Esser (2005), Kinematic history of Marie Byrd Land terrane, West Antarctica: Direct evidence from Cretaceous mafic dykes, in *Terrane Processes at the Margin of Gondwana*, edited by A. Vaughan et al., Geol. Soc. Spec. Publ., 246, 417–438, doi:10.1144/GSL.SP.2005.246.01.17

Sieminski, A., E. Debayle, and J. J. Leveque (2003), Seismic evidence for deep low-velocity anomalies in the transition zone beneath West Antarctica, *Earth Planet. Sci. Lett., 216*, 645–661, doi:10.1016/S0012-821X(03)00518-1.

Skemer, P., I. Katayama, Z. Jiang, and S. Karato (2005), The misorientation index: Development of a new method for calculating the strength of lattice-preferred orientation, *Tectonophysics, 411(1–4)*, 157–167, doi:10.1016/j.tecto.2005.08.023.

Sundberg, M., and R. F. Cooper (2008) Crystallographic preferred orientation produced by diffusional creep of harzburgite: effects of chemical interactions among phases during plastic flow, *J. Geoph. Res., 113*, B12208, doi:10.1029/2008JB005618.

Tasaka, M., M. E. Zimmerman, and D. L. Kohlstedt (2016), Evolution of the rheological and microstructural properties of olivine aggregates during dislocation creep under hydrous conditions, *J. Geophys. Res. Solid Earth, 121*, doi:10.1002/2015JB012134.

Taylor, W. R. (1998), An experimental test of some geothermometer and geobarometer formulations for upper mantle peridotites with application to the thermobarometry of fertile lherzolite and garnet websterite, *Neues Jahrb. Geol. Palaontol. Abh., 172*, 381–408, doi:10.1127/njma/172/1998/381.

ten Brink, U. T., R. I. Hackney, S. Bannister, T. A. Stern, and Y. Makovsky (1997), Uplift of the Transantarctic Mountains and the bedrock beneath the East Antarctic ice sheet, *J. Geophys. Res., 102*, 27,603–27,621, doi:10.1029/97JB02483.

Titus, S. J., S. M. Maes, B. Benford, E. C. Ferré, and B. Tikoff, (2011) Fabric development in the mantle section of a paleotransform fault and its effect on ophiolite obduction, New Caledonia, *Lithosphere, 3*, 221–244, doi: 10.1130/L122.1.

Tommasi, A., B. Tikoff, and A. Vauchez (1999), Upper mantle tectonics: Three-dimensional deformation, olivine crystallographic fabrics and seismic properties, *Earth Planet. Sci. Lett., 168*, 173–186, doi:10.1016/S0012-821X(99)00046-1.

Tommasi, A., D. Mainprice, G. Canova, and Y. Chastel (2000), Viscoplastic self-consistent and equilibrium-based modeling of olivine lattice preferred orientations: Implications for the upper mantle seismic anisotropy, *J. Geophys. Res., 105*, 7893–7908, doi: 10.1029/1999JB900411.

Ulrich, S., and D. Mainprice (2005), Does cation ordering in omphacite influence development of lattice-preferred orientation? *J. Struct. Geol., 27*, 419–431, doi:10.1016/j.jsg.2004.11.003.

Underwood, E., 1970. Quantitative Stereology. Addison-Wesley, Reading, MA.

Van der Wal, D., P. Chopra, M. Drury, and J. FitzGerald (1993), Relationships between dynamically recrystallized grain size and deformation conditions in experimentally deformed olivine rocks, *Geoph. Res. Lett., 20*, 1479–1482, doi:10.1029/93GL01382.

Vauchez, A., F. Dineur, and R. Rudnick (2005), Microstructure, texture and seismic anisotropy of the lithospheric mantle above a mantle plume: insights from the Labait volcano xenoliths (Tanzania), *Earth Planet. Sci. Lett., 232*, 295–314, doi:10.1016/j.epsl.2005.01.024.

Vollmer, F. W. (1990) An application of eigenvalue methods to structural domain analysis, *Geol. Soc. Am. Bull., 102*, 786–791, doi:10.1130/0016-7606.

Warren, J., and G. Hirth (2006), Grain size sensitive deformation mechanisms in naturally deformed peridotites, *Earth Planet. Sci. Lett., 248*, 438–450, doi:10.1016/j.epsl.2006.06.006.

Warren, J. M., G. Hirth, and P. B. Kelemen (2008), Evolution of olivine lattice preferred orientation during simple shear in the mantle, *Earth Planet. Sci. Lett., 272(3–4)*, 501–512, doi:10.1016/j.epsl.2008.03.063.

Warren, J. M., and E. H. Hauri (2014), Pyroxenes as tracers of mantle water variations, *J. Geoph. Res., 119*, 1851–1881, doi:10.1002 /2013JB010328.

Webber, C., J. Newman, C. W. Holyoke III, T. Little, B. Tikoff (2010), Fabric devel- opment in cm-scale shear zones in ultramafic rocks, Red Hills, New Zealand, *Tectonophysics*, *489*, 55–75. http://dx.doi.org/10.1016/j.tecto.2010.04.001.

Wenk, H. R., K. Bennett, G. R. Canova, and A. Molinari (1991), Modeling plastic-deformation of peridotite with the self-consistent theory, *J. Geoph. Res., 96(B5)*, 8337–8349, doi:10.1029/91JB00117.

Winberry, J. P., and S. Anandakrishnan (2004), Crustal structure of the West Antarctic rift system and Marie Byrd Land hotspot, *Geology, 32*, 977–980, doi:10.1130/G20768.1.

Withers, A. C., H. Bureau, C. Raepsaet, and M. M. Hirschmann (2012), Calibration of infrared spectroscopy by elastic recoil detection analysis of H in synthetic olivine, *Chemical Geology, 334*, 92–98, doi: 10.1016/j.chemgeo.2012.10.002.

Xypolias, P., V. Chatzaras, R. Beane, and S. Papadopoulou (2013), Heterogeneous constrictional deformation in a ductile shear zone resulting from the transposition of a lineation-parallel fold, *J. Struct. Geol., 52*, 44–59, doi:10.1016/j.jsg.2013.05.0 01.

Zhang, S., S. -I. Karato, J. Fitz Gerald, U. H. Faul, and Y. Zhou (2000), Simple shear deformation of olivine aggregates, *Tectonophysics, 316*, 133–152, doi: 10.1016/S0040-1951(99)00229-2.

Figure Captions

Figure 1. Common interpretation of CPO types in mantle and crust. (a) *Left*: Schematic depiction of the typical olivine CPO types. Equal area, lower hemisphere projections are shown for each of the principal olivine crystallographic axes. Shaded regions denote the dominant crystal axis orientations for each textural type. *Right*: Olivine CPO type as a function of stress and water content at high temperatures (1200–1300 ^{o}C). Modified after *Katayama et al.* [2004]. (b) Relationship between finite strain geometry and CPO symmetry for calcite, quartz, biotite, and hornblende. We note that CPO changes as a function of deformation conditions has also been described for crustal minerals (e.g., quartz CPO transitions with temperature). Crystallographic texture data based on: calcite, *Llana-Funez and Rutter* [2014]; quartz, *Scmid and Casey* [1986]; biotite and hornblende, *Lloyd et al.* [2011]. Data are shown on Flinn plots.

Figure 2. (a) Map of west Antarctica showing the location of the Fosdick Mountains and Executive Committee Range in Marie Byrd Land. (b and c) Field photos of volcanic centers from which the studied mantle xenoliths were sampled. Demas Bluff basalt flow (b) and Marujupu diatreme (c); note two people in red parkas for scale in (c). (d) Example of mantle xenoliths from Demas Bluff basalt flow.

Figure 3. Determination of the spinel shape fabric using X-ray computed tomography. (a) Dunite from Mt. Cumming. Black grains are spinel. (b) Reconstructed volume of the scanned xenolith in (a). Blue objects correspond to spinel grains that have been separated from the olivine mass (grey) on the basis of their density contrast. 3D rose diagram produced with QUANT3D software describes the fabric ellipsoid calculated from the SPO of the spinel grains. (c) Reconstructed volume of a

spinel harzburgite from Demas Bluff. The slice through the volume is parallel to the $\Phi_1\Phi_3$ plane of the spinel fabric ellipsoid. The thin section that was produced from the specific slice of the xenolith is shown as an overlay. The thin section is normal to the foliation plane (contains Φ_1 and Φ_2) and parallel to the lineation (Φ_1).

Figure 4. Examples of EBSD maps and representative CPO, SPO, and grain size data. (a) EBSD inverse pole figure map of olivine crystallographic axis orientations in the dunite KSP89-181-X01. Olivine crystal axes orientations are colored relative to Φ_1 axis of the spinel fabric ellipsoid (IPF-X coloring). All maps have upper edge parallel to the XRCT-determined Φ_1 spinel ellipsoid axis (lineation) with the foliation normal to the map. White arrows highlight subgrain boundaries in olivine grains. (b) Combined EBSD phase map and inverse pole figure map of olivine crystallographic axis orientations for the spinel lherzolite FDM-AV01-X01. Grains are: white, spinel; light grey, clinopyroxene; and dark grey, orthopyroxene. Olivine grains are shown with IPF-X coloring. (c) Combined EBSD phase map and olivine IPF-X map for the spinel lherzolite FDM-RN02-X01. Map coloring as in (b). (d) EBSD phase map of (c). The inset rose diagram describes the orientation of the long axis of olivine grains plotted relative to the spinel fabric ellipsoid axes. Note strong alignment of olivine long axes subparallel to long Φ_1 axis of the spinel fabric ellipsoid. (e) Lower-hemisphere equal area projections of olivine crystallographic axis orientations. Data from the EBSD map in (c), plotted as one point per grain. Pole figures are plotted in the reference frame of the spinel fabric ellipsoid as determined by XRCT. Note strong concentration of [100] axes near Φ_1, which agrees with the IPF-X map in (c). (f) Frequency distribution of olivine grain size calculated as equivalent area diameter. The histogram has a logarithmic scale. The red curve represents the lognormal distribution fit to the measured distribution. Olivine grain size data are from the map in (c), calculated as one point per grain.

Figure 5. Typical microstructures in the Marie Byrd Land spinel peridotite xenoliths. In all photomicrographs lineation is parallel to the top edge and foliation is normal to the photomicrograph. (a) Coarse-grained harzburgite characterized by alignment of tabular olivine crystals with straight grain boundaries parallel to the foliation; widely spaced subgrain boundaries (white arrows) are oriented perpendicular to the foliation (FDM-DB02-X08). (b) Coarse-grained lherzolite with granular microstructure. Olivine subgrain boundaries are predominantly oriented at low angle to the foliation but subgrain boundaries oblique to the foliation are also present (AD6021-X02). (c) Lherzolite with spinel trail formed by discrete, subhedral spinel grains (FDM-DB03-X04). (d) Olivine crystal with undulose extinction in a coarse-grained granular harzburgite (FDM-DB02-X02). (e) Aligned olivine-orthopyroxene grain boundaries in a spinel harzburgite. Arrow points to one of the aligned boundaries. Olivine subgrain boundaries are oriented both perpendicular and at low angle to the foliation. In the latter case, the subgrain boundaries are parallel to the olivine-orthopyroxene grain boundaries. Note the diamond grain structure of the orthopyroxene grain in the center, which is indicative of grain boundary sliding (FDM-DB04-X03). (f) Granular lherzolite with alignment of olivine grain boundaries oblique (lower left to upper right) to the spinel foliation (FDM-AV01-X01). (g) Granular lherzolite with 120° triple junctions (white arrows) between olivine grains (FDM-AVBB02). (h) Olivine grain with two sets of subgrain boundaries, at high angle to each other. Both subgrain boundary sets are oriented oblique to the foliation (FDM-DB02-X10). (i) Detail of the aligned olivine-orthopyroxene grain boundaries shown in (e). Olivine subgrain boundary aligned to the olivine-orthopyroxene grain boundary. This microstructure may suggest phase boundary sliding (FDM-DB04-X03). (f) Olivine and orthopyroxene grains forming a four-grain junction, characteristic of grain boundary sliding (FDM-DB03-X01). All photomicrographs are under crossed-polarized light, except (c), which is taken in plane-polarized light.

Figure 6. Graphical representation of geochemical data. (a) Variation in spinel composition in terms of Cr# and Mg#. (b) Correlation of Cr# in spinel with Mg# in olivine in the Marie Byrd Land peridotite xenoliths. The field for subcontinental spinel xenoliths is shown for comparison [*Arai*, 1994]. OSMA: olivine-spinel mantle array. (c) Contents of Cr_2O_3 and Al_2O_3 in coexisting orthopyroxene and clinopyroxene in the studied peridotite xenoliths. The subparallel tie lines between orthopyroxene and clinopyroxene indicate chemical equilibration among the pairs of pyroxenes. Three samples with discordant tie lines are identified by their names.

Figure 7. Equilibration temperatures and extraction depths estimated for the Marie Byrd Land xenoliths. (a) Comparison of temperature estimates (calculated at 15 kbar) from the three two-pyroxene geothermometers (BM85 - *Bernard and Mercier* [1985], BK90 – *Brey and Köhler* [1990], and T98 – *Taylor* [1998]) with their average. (b) Estimated equilibration temperatures and extraction depths for the spinel peridotite xenoliths. Black symbols indicate temperature-depth values obtained by combining the averages of the three, two-pyroxene geothermometers with a hypothetical geotherm at 1.5 Ma. Grey symbols represent the maximum depths for spinel stability in each sample, and the thick grey line indicates an inferred geotherm at 1.5 Ma that is consistent with the stability of spinel in all samples of the xenolith suite. The McMurdo petrologic geotherm [*Berg et al.*, 1989], and the present-day Ross Embayment geotherm [*ten Brink et al.*, 1997] are shown for comparison.

Figure 8. Hsu plot showing the relationship between the degree of anisotropy (*P'*, radial component) and the shape factor (*T*, tangential component) as determined by means of XRCT for the Marie Byrd Land xenoliths.

Figure 9. Crystallographic orientations, low-angle misorientations and shape preferred orientations of olivine grains. Samples are organized with increasing BA-index value. Crystallographic orientations are plotted as one point per grain datasets in lower-hemisphere equal area projections, relative to the spinel fabric ellipsoid axes. Color scales are for multiples of uniform distribution. For each sample, the BA-, J-, and M-indices, as well as the number of grains analyzed are given. Misorientation axes are from correlated misorientation angles between 2° and 10°. Inverse pole figures are in the crystallographic reference frame. Orientations of the long axes of olivine grains relative to the spinel fabric ellipsoid axes are shown in rose diagrams.

Figure 10. (a) Inverse pole figure showing the misorientation axis distributions expected for different slip systems in olivine. Modified after *De Kloe* [2001]. (b) Schematic diagram showing lattice rotations across subgrain tilt and twist boundaries. Modified after *Lloyd et al.* [1997].

Figure 11. Olivine deformation mechanism maps calculated using four deformation mechanisms, as described in *Warren and Hirth* [2006]: dislocation creep; dislocation-accommodated grain boundary sliding (DisGBS); diffusion creep; and low-temperature plasticity. The deformation mechanism maps have been constructed using the flow laws of *Goetze* [1978], *Evans and Goetze* [1979], *Hirth and Kohlstedt* [2003], and *Hansen et al.* [2011]. The temperature and pressure are chosen based on the estimated deformation conditions in the Marie Byrd Land xenoliths (this study). The maps are constructed at 850, 950 and 1050^{0}C, and data are plotted on the map that most closely matches the calculated equilibration temperature. We use a piezometric line that corresponds to the linear least squares fit to data of *Karato et al.* [1980] and *Van der Wal et al.* [1993], based on *Warren and Hirth* [2006]. Extrapolations of the Hansen et al. flow law predict deformation by dominantly

dislocation-accommodated grain boundary sliding. The grey boxes in the maps correspond to the range of mean grain sizes in the xenoliths for the deformation conditions for which each map has been constructed.

Figure 12. Relationship between deformation conditions and olivine CPO type. (a) Olivine CPO type as a function of differential stress, temperature, and pressure. (b) Olivine CPO type expressed by the BA-index, as a function of temperature and pressure. (c) BA-index as a function of differential stress. (d) Relationship between BA-index and water content. Water content is the estimated range of pre-emplacement OH concentrations in olivine.

Figure 13. (a-b) Relationship between olivine CPO symmetry (BA-index) and strength described by the M-index (a) and J-index (b). (c) Degree of spinel fabric anisotropy versus olivine CPO symmetry.

Figure 14. Relationship between fabric geometry and CPO symmetry. (a) Spinel fabric anisotropy versus geometry. Data are coded based on their olivine CPO type. (b) Spinel fabric geometry versus olivine CPO symmetry, expressed by the BA-index. Red lines describe the existing trend between fabric geometry and BA-index data; the value of the BA-index increases with transition from oblate to prolate fabric geometries.

Figure 15. Relationship between finite strain geometry and olivine CPO symmetry.

Table 1. Equilibration temperature, grain size, differential stress, olivine CPO type, CPO strength, and spinel fabric

Volcanic center	Xenolith	Temp (°C)	*D* (μm)	*σ* (MPa)	Olivine CPO type	J	M	BA	*P′*	*T*
Bird Bluff	FDM-BB03-X01	856	1180	06	Axial-[010]	4.07	0.21	0.12	1.16	-0.19
Mt. Avers – Bird Bluff	FDM-AVBB01	937	214	25	Axial-[010]	2.19	0.12	0.13	1.11	0.01
Demas Bluff	FDM-DB02-X12	1036	599	10	Axial-[010]	3.32	0.16	0.17	1.22	0.67
Mt. Avers – Bird Bluff	FDM-AVBB02	779	133	35	Axial-[010]	1.97	0.11	0.22	1.29	0.65
Mt. Avers – Bird Bluff	FDM-AVBB04	822	587	10	Axial-[010]	1.88	0.09	0.22	1.10	0.02
Demas Bluff	FDM-DB04-X01	991	1450	06	Axial-[010]	4.03	0.20	0.23	1.09	0.15
Mt. Avers – Bird Bluff	FDM-AVBB06	940	192	25	Axial-[010]	1.90	0.08	0.25	1.14	0.13
Mt. Avers – Bird Bluff	FDM-AVBB07	805	644	10	Axial-[010]	1.87	0.08	0.26	1.28	0.35
Mt. Avers – Bird Bluff	FDM-AVBB08	832	285	19	Axial-[010]	3.27	0.12	0.26	1.12	0.84
Mt. Aldaz	AD6021-X02	1084	815	09	Axial-[010]	3.54	0.20	0.27	1.14	-0.06
Demas Bluff	FDM-DB03-X02	861	545	10	Axial-[010]	2.77	0.20	0.28	1.24	-0.11
Demas Bluff	FDM-DB04-X02	984	647	10	Axial-[010]	3.37	0.16	0.29	1.25	-0.23
Mt. Avers – Bird Bluff	FDM-AVBB05	814	61	60	Axial-[010]	1.73	0.14	0.31	1.23	-0.08
Marujupu	FDM-MJ01-X05	1014	90	46	Axial-[010]	3.80	0.16	0.33	1.24	0.25
Demas Bluff	FDM-DB02-X04	933	1230	07	n/a	–	–	0.35	1.32	0.53
Demas Bluff	FDM-DB02-X03	999	210	25	Axial-[010]	4.50	0.31	0.37	1.15	0.36
Demas Bluff	FDM-DB02-X11	1039	1610	06	A	3.54	0.20	0.38	1.25	-0.22
Marujupu	FDM-MJ01-X06	1070	133	35	A	1.46	0.13	0.41	1.23	0.60
Bird Bluff	FDM-BB02-X01	1053	322	20	Random	1.40	0.02	0.42	1.23	-0.34
Mt. Avers	FDM-AV01-X01	939	111	40	A	2.92	0.18	0.43	1.15	0.02
Recess Nunatak	FDM-RN03-X01	943	346	15	B	3.30	0.15	0.43	1.13	0.68
Recess Nunatak	FDM-RN01-X01	961	1290	07	A	14.34	0.24	0.44	1.30	-0.32
Bird Bluff	FDM-BB01-X01	945	122	35	A	1.39	0.07	0.48	1.15	0.22
Demas Bluff	FDM-DB02-X08	803	1310	05	A	7.07	0.37	0.48	1.18	-0.56
Marujupu	FDM-MJ01-X02	974	513	10	A	4.00	0.20	0.50	1.40	-0.08
Demas Bluff	FDM-DB02-X02	978	2000	05	A	8.95	0.36	0.51	1.34	0.11
Marujupu	FDM-MJ01-X03	929	100	42	A	2.70	0.09	0.51	1.32	0.16
Demas Bluff	FDM-DB04-X04	968	1310	06	A	4.40	0.28	0.56	1.21	-0.43
Recess Nunatak	FDM-RN02-X01	828	604	10	A	2.75	0.16	0.57	1.32	0.20
Demas Bluff	FDM-DB02-X10	1020	736	10	A	4.30	0.26	0.58	1.15	-0.94
Demas Bluff	FDM-DB01-X01	1024	885	08	Axial-[100]	2.82	0.14	0.60	1.29	0.28
Recess Nunatak	FDM-RN04-X01	812	528	10	Axial-[100]	2.71	0.20	0.62	1.27	-0.24
Demas Bluff	FDM-DB02-X13	911	933	08	Axial-[100]	2.33	0.08	0.67	1.23	-0.09
Demas Bluff	FDM-DB03-X01	856	1460	06	Axial-[100]	5.55	0.25	0.68	1.29	-0.85
Demas Bluff	FDM-DB02-X01	1183	494	13	Axial-[100]	3.05	0.20	0.74	1.27	-0.35
Demas Bluff	FDM-DB03-X03	982	898	08	Axial-[100]	2.72	0.09	0.77	1.19	-0.08
Mt. Cumming	KSP89-181-X01	862/955	455	15	Axial-[100]	4.34	0.34	0.81	1.61	0.44
Demas Bluff	FDM-DB04-X03	1165	1360	06	Axial-[100]	4.88	0.17	0.86	1.23	-0.67
Demas Bluff	FDM-DB02-X06	1198	314	20	n/a	–	–	0.45	1.13	-0.36
Demas Bluff	FDM-DB03-X04	1002	900	08	n/a	–	–	0.38	1.15	-0.66

Temp, 2-Px average equilibration temperature; D, equivalent area diameter grain size; σ, differential stress; *P′*, fabric anisotrpy; *T*, shape parameter.

Table 2. OH concentrations in olivine and orthopyroxene

Xenolith	Olivine CPO type	Olivine[a] OH concentrations (wt. ppm H_2O)	Orthopyroxene[b] OH concentrations (wt. ppm H_2O)	Pre-emplacement olivine OH concentrations (ppm wt. H_2O)	Pre-emplacement olivine OH concentrations (wt. H/10^6 Si)
FDM-AV01-X01	A	1.31	88	06–18	96–288
FDM-BB01-X01	A	0.00	37	02–07	40–120
FDM-DB03-X01	Axial-[100]	0.29	111	07–22	120–360
FDM-RN03-X01	B	3.27	68	05–14	73–219
FDM-RN04-X01	Axial-[100]	3.40	153	10–31	167–501
FDM-AVBB02	Axial-[010]	2.95	38	03–08	42–125
AD6021-X02	Axial-[010]	0.18	34	02–07	37–111
KSP89-181-X01	Axial-[100]	4.86	–	–	–

[a] Olivine OH concentrations from this study calculated using the calibration of *Withers et al.* [2012]

[b] Orthopyroxene OH concentrations from this study calculated using the calibration of *Bell et al.* [1995]

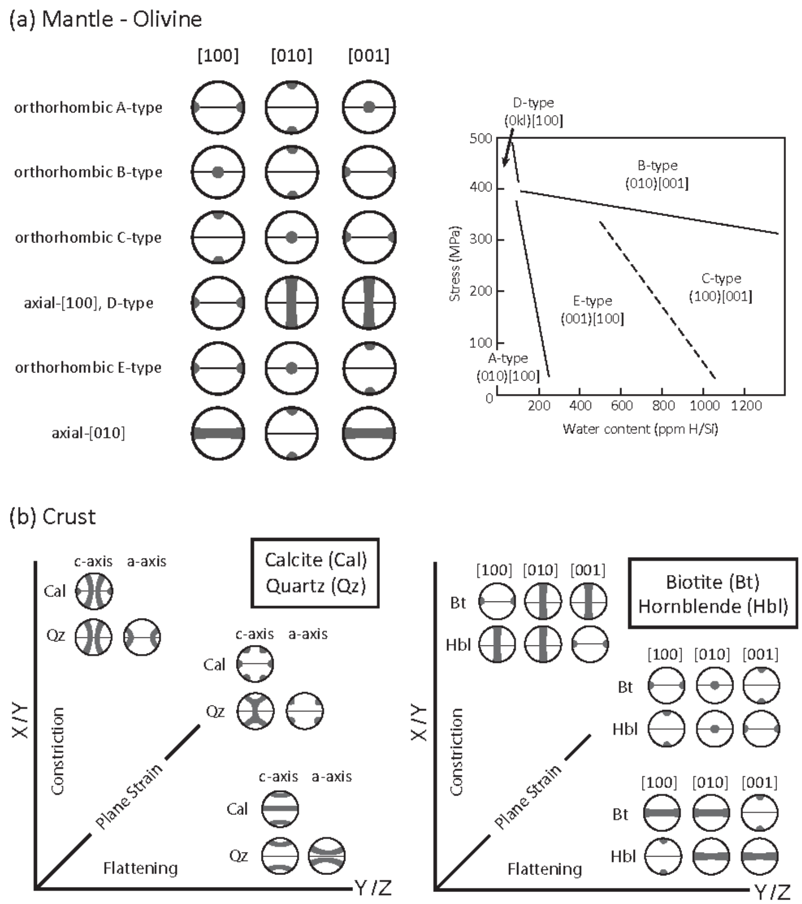

(a) Mantle - Olivine
[100]
[010]
[001]
orthorhombic A-type
orthorhombic B-type
orthorhombic C-type
axial-[100], D-type
orthorhombic E-type
axial-[010]
D-type
{0kl}[100]
B-type
{010}[001]
C-type
{100}[001]
E-type
{001}[100]
A-type
{010}[100]
Stress (MPa)
Water content (ppm H/Si)
(b) Crust
Calcite (Cal)
Quartz (Qz)
c-axis
a-axis
Cal
Qz
X/Y
Constriction
Plane Strain
Flattening
Y/Z
Biotite (Bt)
Hornblende (Hbl)
Bt
Hbl

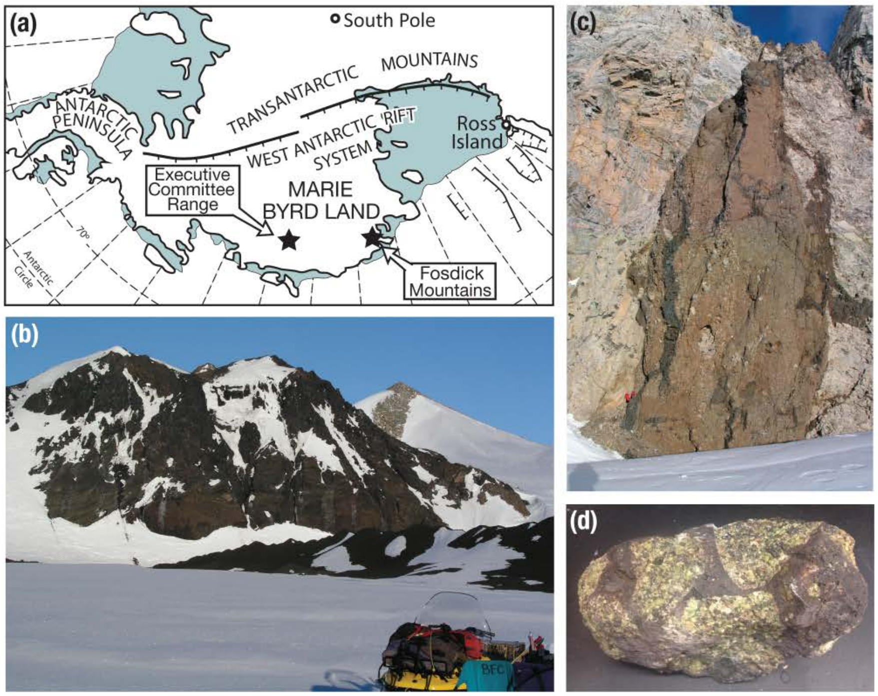
(a)
South Pole
ANTARCTIC PENINSULA
TRANSANTARCTIC
MOUNTAINS
WEST ANTARCTIC RIFT SYSTEM
Ross Island
Executive Committee Range
MARIE BYRD LAND
Fosdick Mountains
70°
Antarctic Circle
(b)
(c)
(d)

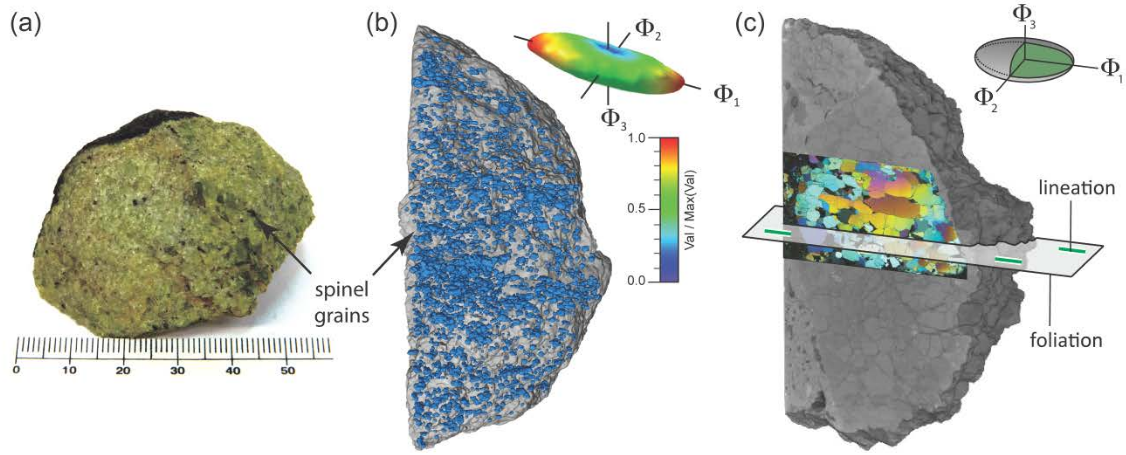

(a)
spinel
grains
0
10
20
30
40
50
(b)
Φ_2
Φ_1
Φ_3
1.0
0.5
0.0
Val / Max(Val)
(c)
Φ_3
Φ_1
Φ_2
lineation
foliation

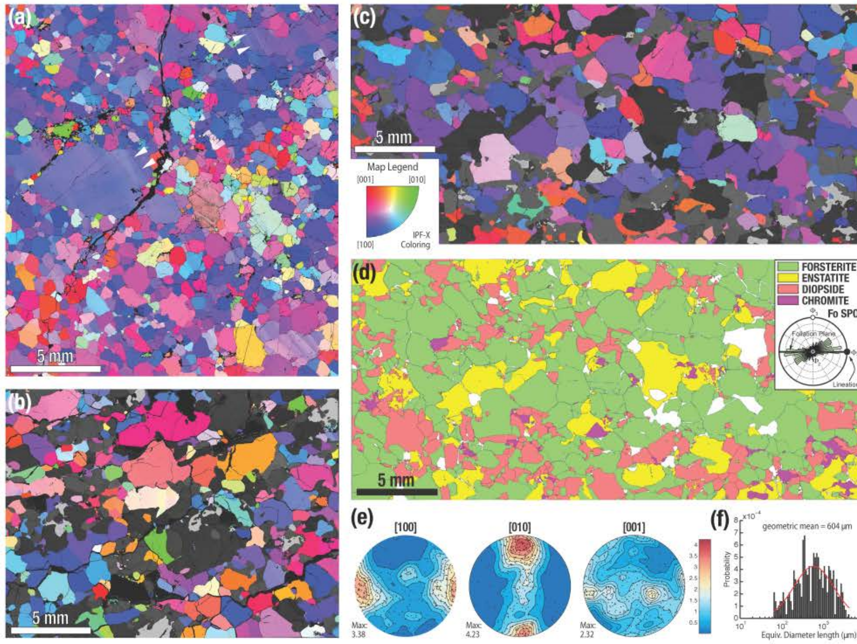

(a)
5 mm
(b)
5 mm
(c)
5 mm
Map Legend
[001]
[010]
[100]
IPF-X Coloring
(d)
FORSTERITE
ENSTATITE
DIOPSIDE
CHROMITE
Fo SPO
Foliation Plane
Lineation
5 mm
(e)
[100]
[010]
[001]
Max: 3.38
Max: 4.23
Max: 2.32
(f)
geometric mean = 604 µm
Probability
Equiv. Diameter length (µm)

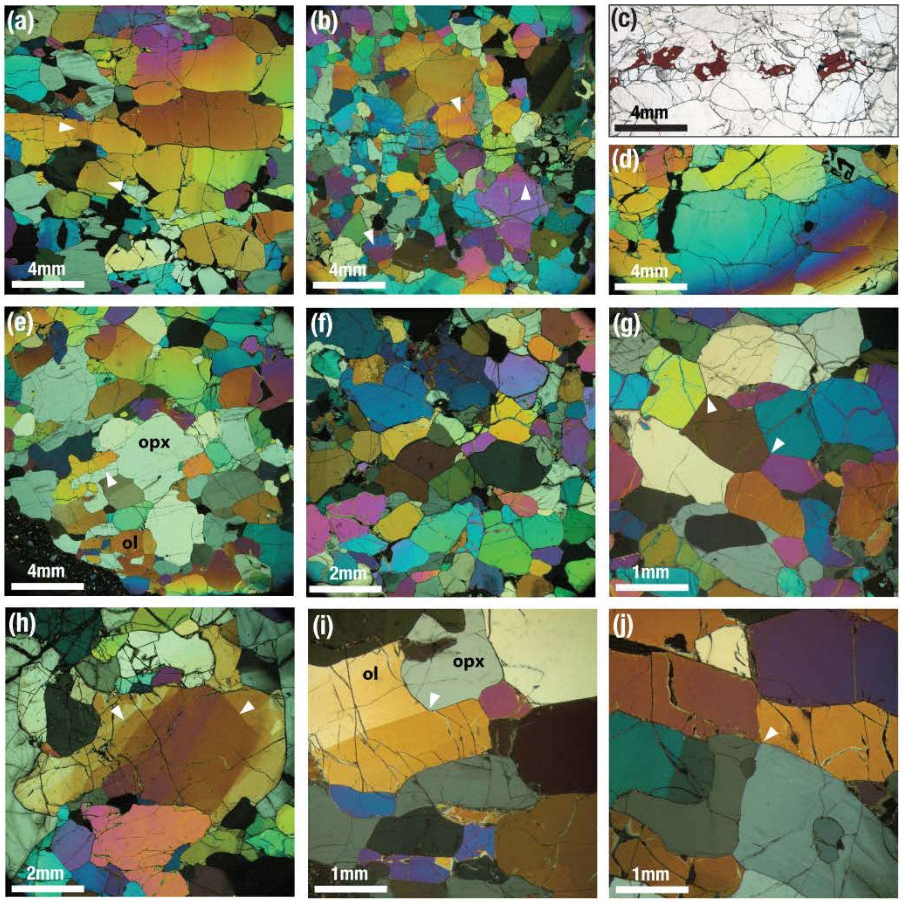
(a)
4mm
(b)
4mm
(c)
4mm
(d)
4mm
(e)
opx
ol
4mm
(f)
2mm
(g)
1mm
(h)
2mm
(i)
ol
opx
1mm
(j)
1mm

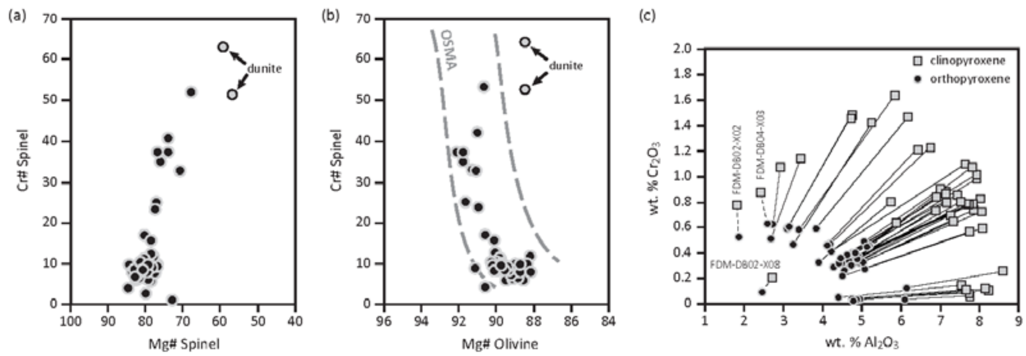

(a)
Cr# Spinel
Mg# Spinel
dunite
(b)
Cr# Spinel
Mg# Olivine
OSMA
dunite
(c)
wt. % Cr_2O_3
wt. % Al_2O_3
clinopyroxene
orthopyroxene
FDM-DB02-X02
FDM-DB04-X03
FDM-DB02-X08

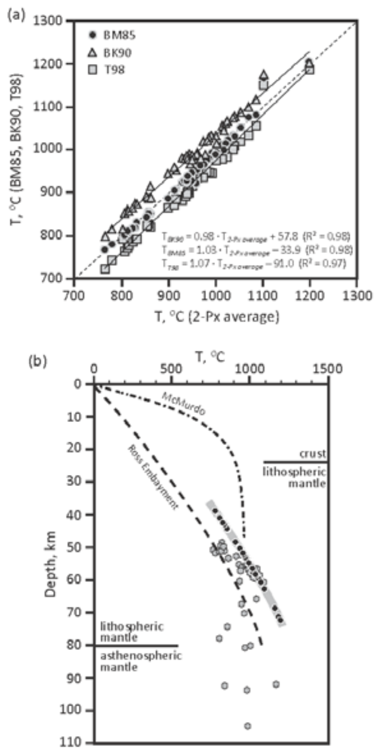
(a)
BM85
BK90
T98
T, °C (BM85, BK90, T98)
T, °C (2-Px average)
$T_{BK90} = 0.98 \cdot T_{2\text{-}Px\ average} + 57.8$ ($R^2 = 0.98$)
$T_{BM85} = 1.03 \cdot T_{2\text{-}Px\ average} - 33.9$ ($R^2 = 0.98$)
$T_{T98} = 1.07 \cdot T_{2\text{-}Px\ average} - 91.0$ ($R^2 = 0.97$)
(b)
T, °C
Depth, km
McMurdo
Ross Embayment
crust
lithospheric mantle
lithospheric mantle
asthenospheric mantle

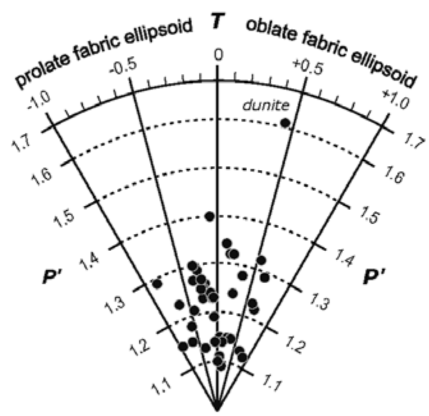
T
prolate fabric ellipsoid
oblate fabric ellipsoid
-1.0
-0.5
0
+0.5
+1.0
dunite
1.7
1.6
1.5
1.4
1.3
1.2
1.1
P'
P'

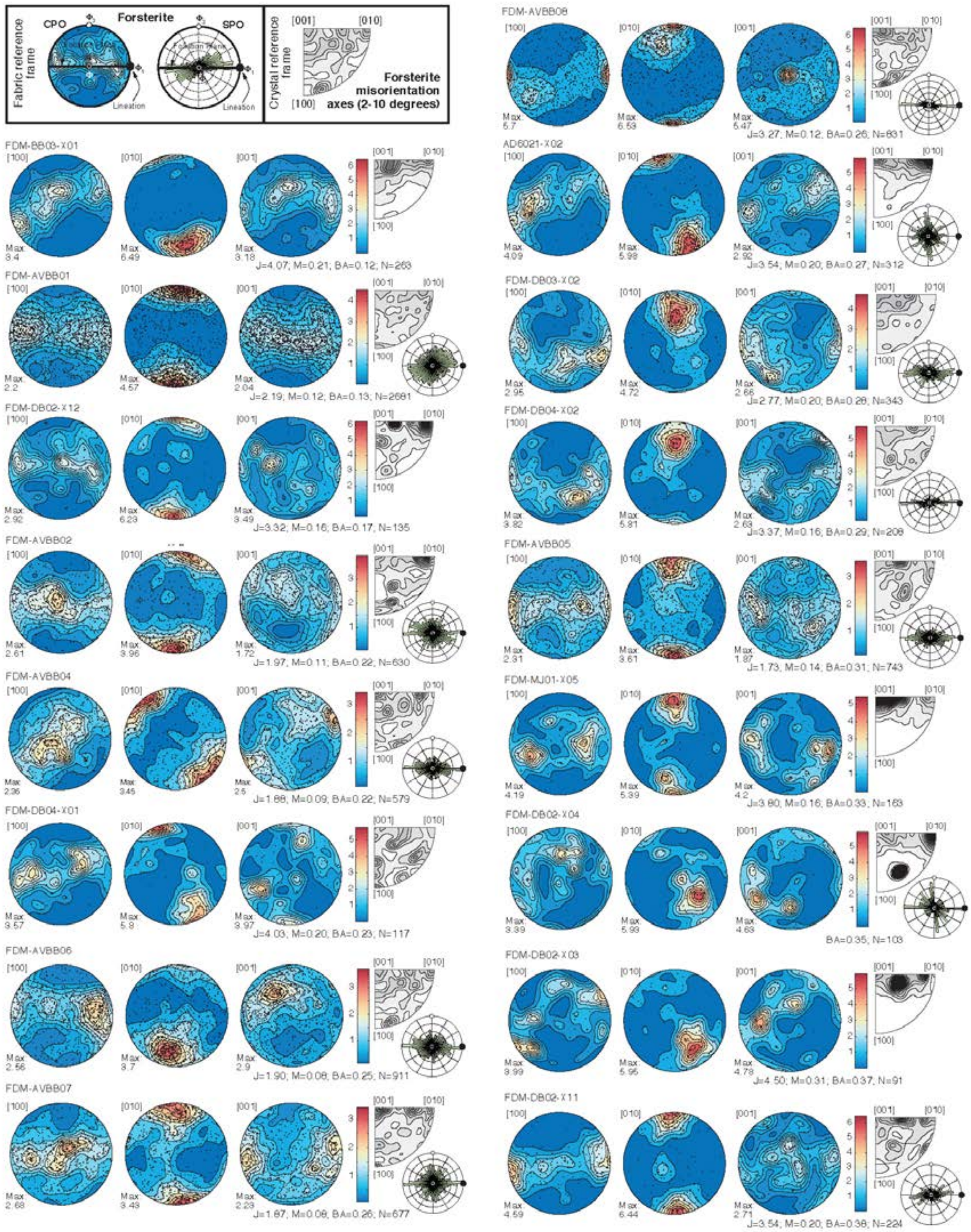
Forsterite
CPO
SPO
Fabric reference frame
Lineation
Crystal reference frame
Forsterite misorientation axes (2-10 degrees)
FDM-BB03-X01
J=4.07; M=0.21; BA=0.12; N=263
FDM-AVBB01
J=2.19; M=0.12; BA=0.13; N=2681
FDM-DB02-X12
J=3.32; M=0.16; BA=0.17; N=135
FDM-AVBB02
J=1.97; M=0.11; BA=0.22; N=630
FDM-AVBB04
J=1.88; M=0.09; BA=0.22; N=579
FDM-DB04-X01
J=4.03; M=0.20; BA=0.23; N=117
FDM-AVBB06
J=1.90; M=0.08; BA=0.25; N=911
FDM-AVBB07
J=1.87; M=0.08; BA=0.26; N=677
FDM-AVBB08
J=3.27; M=0.12; BA=0.26; N=631
AD6021-X02
J=3.54; M=0.20; BA=0.27; N=312
FDM-DB03-X02
J=2.77; M=0.20; BA=0.28; N=343
FDM-DB04-X02
J=3.37; M=0.16; BA=0.29; N=208
FDM-AVBB05
J=1.73; M=0.14; BA=0.31; N=743
FDM-MJ01-X05
J=3.80; M=0.16; BA=0.33; N=163
FDM-DB02-X04
BA=0.35; N=103
FDM-DB02-X03
J=4.50; M=0.31; BA=0.37; N=91
FDM-DB02-X11
J=3.54; M=0.20; BA=0.38; N=224

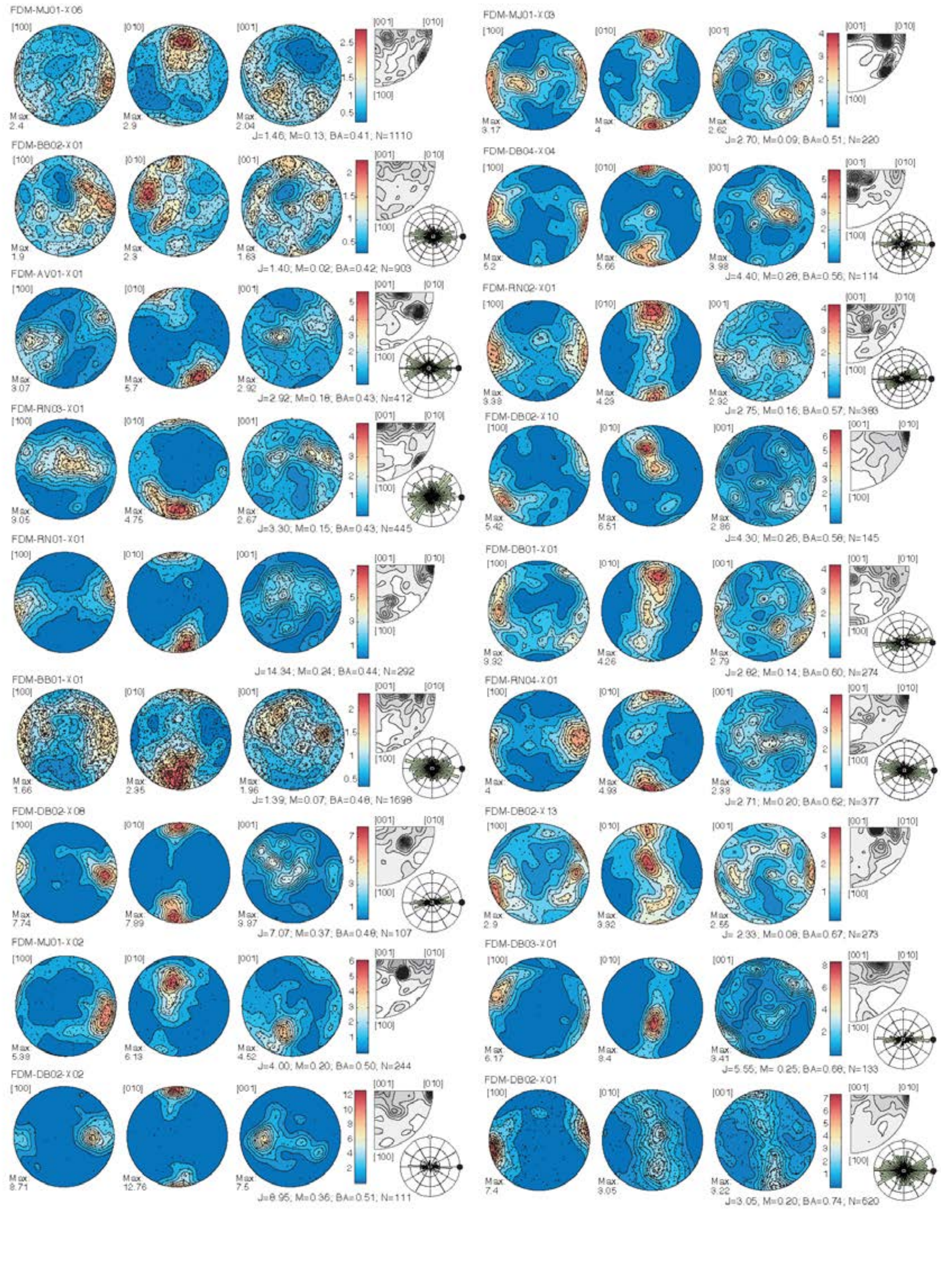
FDM-MJ01-X06
J=1.46; M=0.13; BA=0.41; N=1110
FDM-MJ01-X03
J=2.70; M=0.09; BA=0.51; N=220
FDM-BB02-X01
J=1.40; M=0.02; BA=0.42; N=903
FDM-DB04-X04
J=4.40; M=0.28; BA=0.56; N=114
FDM-AV01-X01
J=2.92; M=0.18; BA=0.43; N=412
FDM-RN02-X01
J=2.75; M=0.16; BA=0.57; N=383
FDM-RN03-X01
J=3.30; M=0.15; BA=0.43; N=445
FDM-DB02-X10
J=4.30; M=0.26; BA=0.58; N=145
FDM-RN01-X01
J=14.34; M=0.24; BA=0.44; N=292
FDM-DB01-X01
J=2.62; M=0.14; BA=0.60; N=274
FDM-BB01-X01
J=1.39; M=0.07; BA=0.48; N=1698
FDM-RN04-X01
J=2.71; M=0.20; BA=0.62; N=377
FDM-DB02-X08
J=7.07; M=0.37; BA=0.48; N=107
FDM-DB02-X13
J= 2.33; M=0.08; BA=0.67; N=273
FDM-MJ01-X02
J=4.00; M=0.20; BA=0.50; N=244
FDM-DB03-X01
J=5.55; M= 0.25; BA=0.68; N=133
FDM-DB02-X02
J=8.95; M=0.36; BA=0.51; N=111
FDM-DB02-X01
J=3.05; M=0.20; BA=0.74; N=520

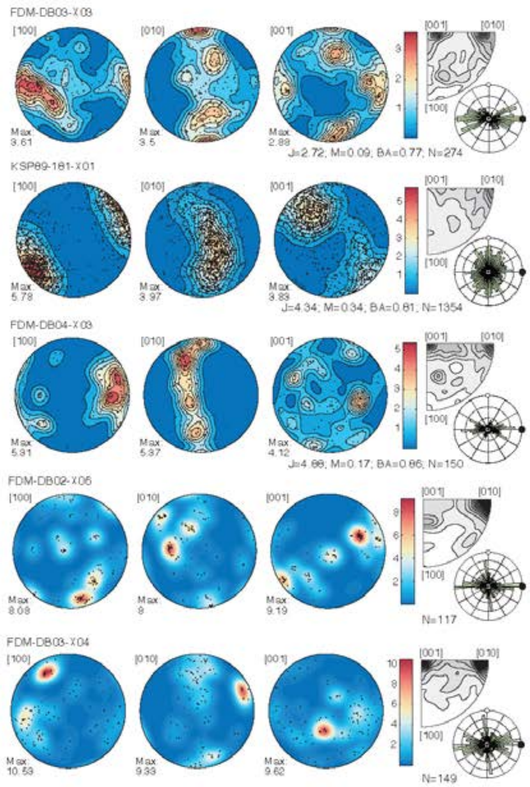
FDM-DB03-X03
[100]
[010]
[001]
Max
3.61
Max
3.5
Max
2.88
J=2.72; M=0.09; BA=0.77; N=274
KSP89-181-X01
[100]
[010]
[001]
Max
5.78
Max
3.97
Max
3.83
J=4.34; M=0.34; BA=0.81; N=1354
FDM-DB04-X03
[100]
[010]
[001]
Max
5.31
Max
5.37
Max
4.12
J=4.66; M=0.17; BA=0.86; N=150
FDM-DB02-X06
[100]
[010]
[001]
Max
8.08
Max
9
Max
9.19
N=117
FDM-DB03-X04
[100]
[010]
[001]
Max
10.53
Max
9.33
Max
9.62
N=149

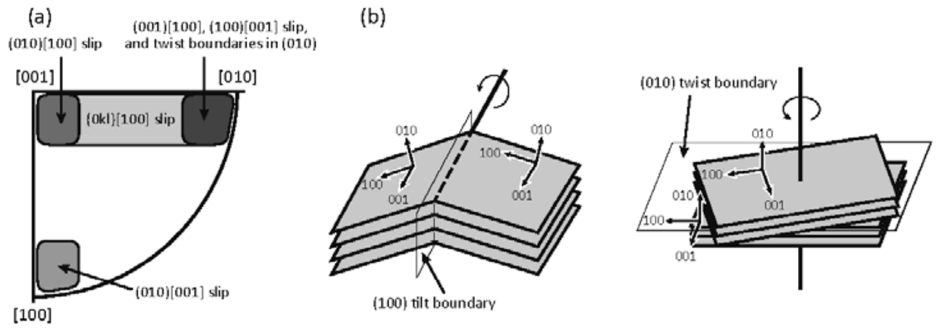
(a)
(010)[100] slip
(001)[100], (100)[001] slip,
and twist boundaries in (010)
[001]
[010]
{0kl}[100] slip
(010)[001] slip
[100]
(b)
010
100
001
(100) tilt boundary
(010) twist boundary

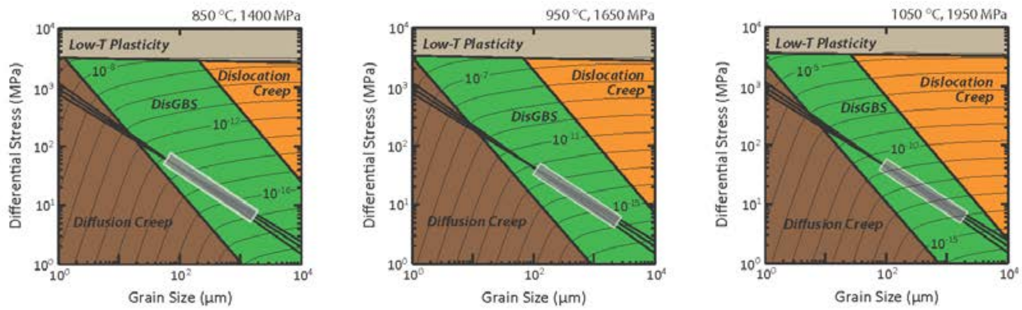
850 °C, 1400 MPa
Low-T Plasticity
Dislocation Creep
DisGBS
Diffusion Creep
10^{-8}
10^{-12}
10^{-16}
950 °C, 1650 MPa
Low-T Plasticity
Dislocation Creep
DisGBS
Diffusion Creep
10^{-7}
10^{-11}
10^{-15}
1050 °C, 1950 MPa
Low-T Plasticity
Dislocation Creep
DisGBS
Diffusion Creep
10^{-5}
10^{-10}
10^{-15}
Differential Stress (MPa)
Grain Size (µm)

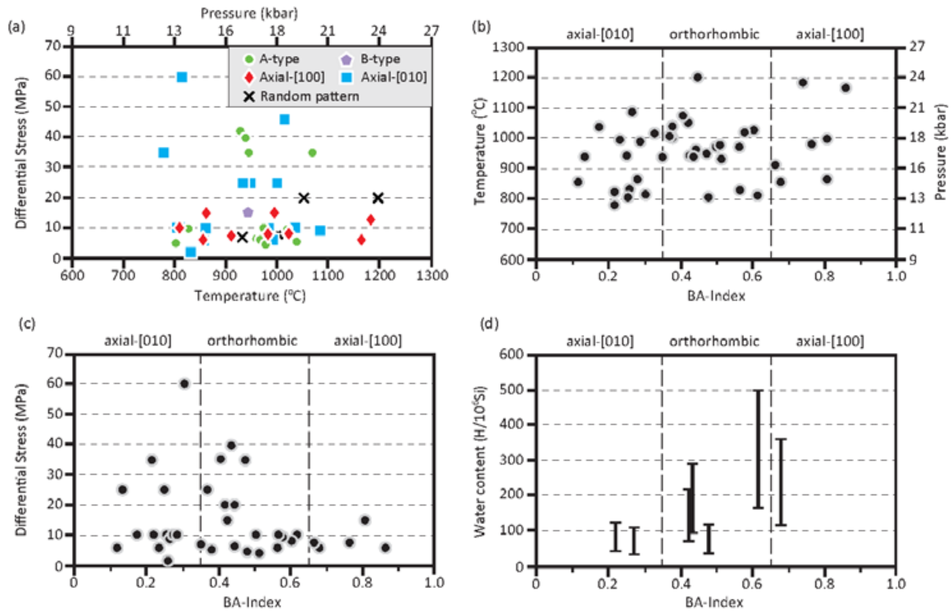

(a)
Pressure (kbar)
Differential Stress (MPa)
Temperature (°C)
A-type
B-type
Axial-[100]
Axial-[010]
Random pattern
(b)
axial-[010]
orthorhombic
axial-[100]
Temperature (°C)
Pressure (kbar)
BA-Index
(c)
axial-[010]
orthorhombic
axial-[100]
Differential Stress (MPa)
BA-Index
(d)
axial-[010]
orthorhombic
axial-[100]
Water content (H/10⁶Si)
BA-Index

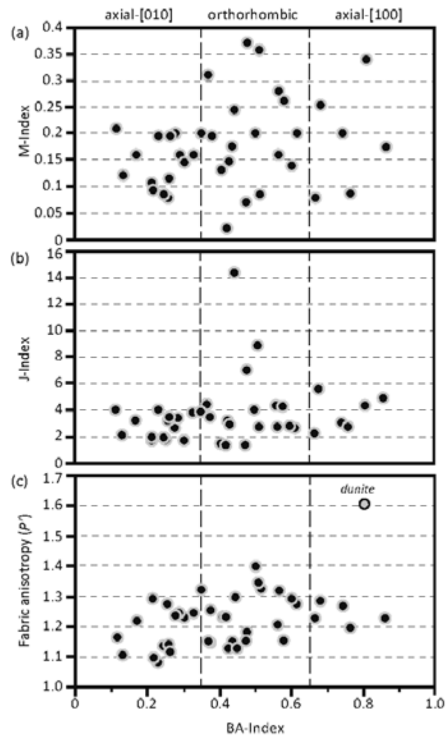

axial-[010]
orthorhombic
axial-[100]
(a)
M-Index
(b)
J-Index
(c)
Fabric anisotropy (P')
dunite
BA-Index

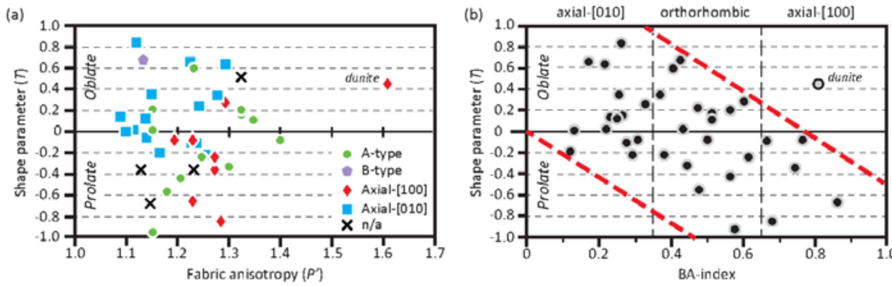
(a)
Shape parameter (T)
Oblate
Prolate
dunite
A-type
B-type
Axial-[100]
Axial-[010]
n/a
Fabric anisotropy (P')
(b)
axial-[010]
orthorhombic
axial-[100]
BA-index

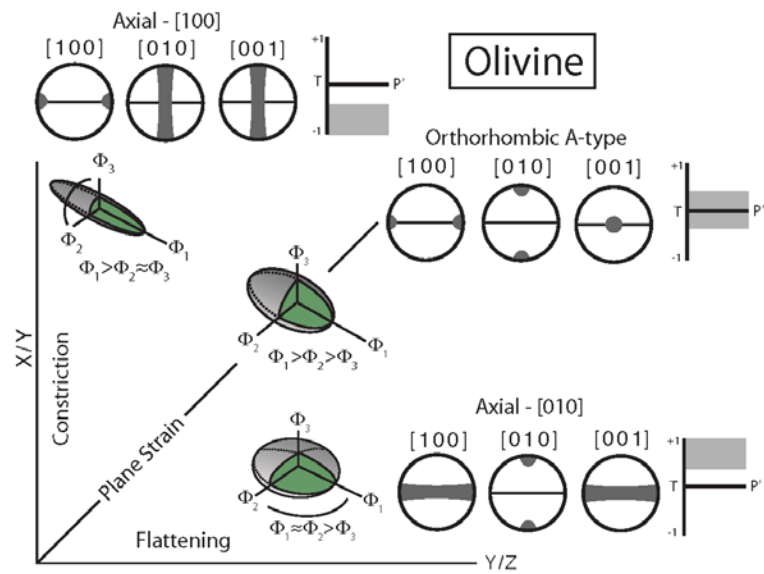
Axial - [100]
[100]
[010]
[001]
+1
T
P'
-1
Olivine
Orthorhombic A-type
[100]
[010]
[001]
Φ_3
Φ_2
Φ_1
$\Phi_1 > \Phi_2 \approx \Phi_3$
$\Phi_1 > \Phi_2 > \Phi_3$
X/Y
Constriction
Plane Strain
Axial - [010]
$\Phi_1 \approx \Phi_2 > \Phi_3$
Flattening
Y/Z

AGU PUBLICATIONS

Journal of Geophysical Research: Solid Earth

Supporting Information for

Effect of strain-induced fabric geometry on olivine crystallographic texture evolution

Vasileios Chatzaras[1], Seth C. Kruckenberg[1], Shaina M. Cohen[1], L. Gordon Medaris Jr.[2], Anthony C. Withers[3], Brian Bagley[4]

[1]Department of Earth and Environmental Sciences, Boston College, Chestnut Hill, MA 02467, USA
[2]Department of Geoscience, University of Wisconsin-Madison, Madison, WI 53706, USA
[3]Department of Earth Sciences and the Centre for Planetary Science and Exploration, University of Western Ontario, 1151 Richmond Street, London, Ontario N6A 5B7, Canada
[4]Department of Earth Sciences, University of Minnesota - Twin Cities, 310 Pillsbury Dr. SE, Minneapolis, MN 55455, USA

Contents of this file

Additional Supporting Information (Files uploaded separately)

Introduction

This supporting document contains a detailed record of data produced in the course of this work, and adds to the data presented in the manuscript. The supporting information provide the opportunity to the reader to explore the depth of the analysis performed on the FTIR, XRCT, and EPMA data, presented in the manuscript.

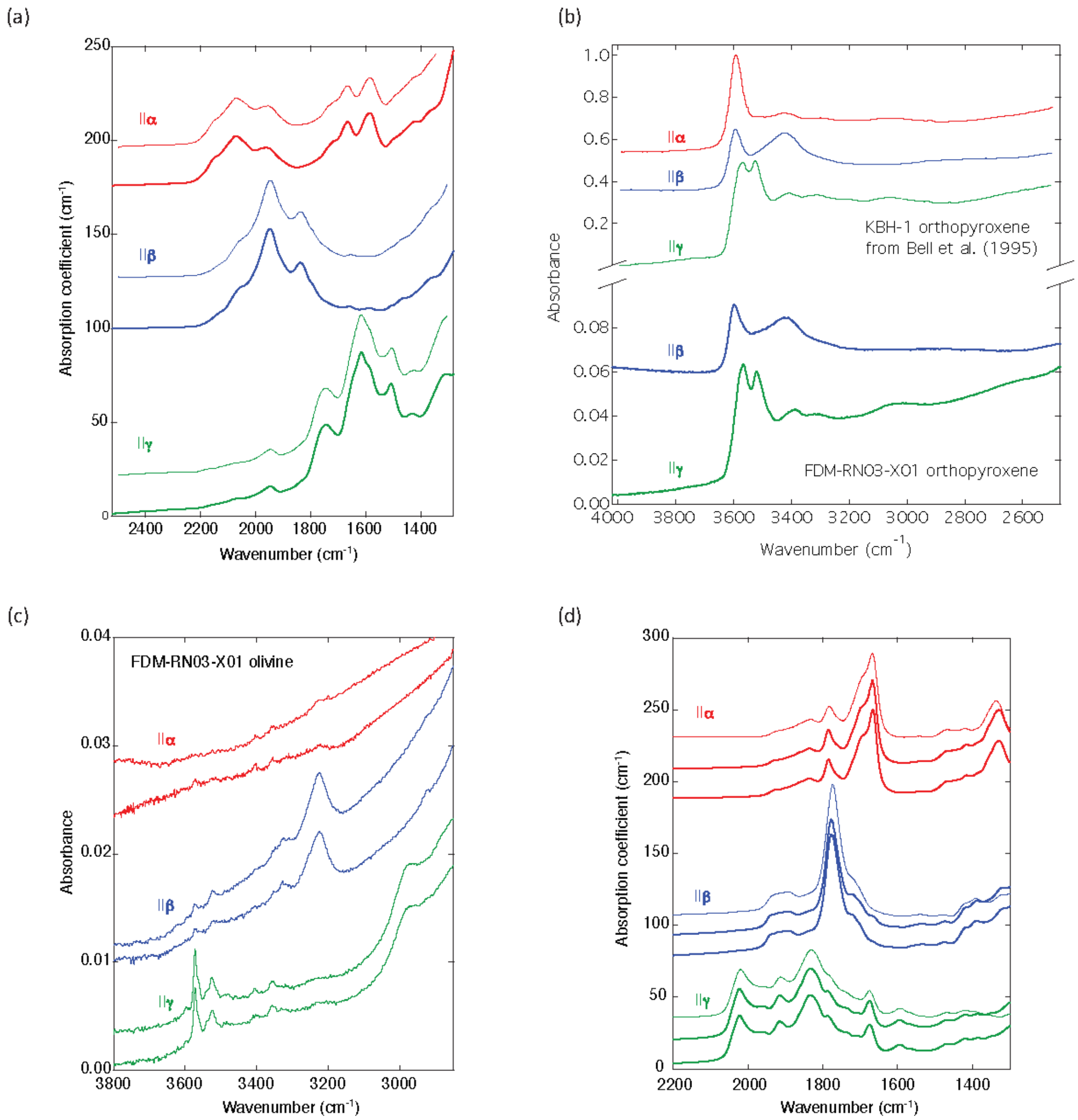

Figure S1. (a) Comparison of the Si-O overtone bands used to orient FDM-RN03-X01 orthopyroxene (solid curves) and the equivalent polarized principal spectra for KBH-1 from *Mosenfelder and Rossman* [2013; dotted curves]. (b) Polarized principal spectra from FDM-RN03-X01 orthopyroxene (lower panel). Sample thickness is 0.185mm (||β and ||γ) and 0.240mm (||α) . Polarized spectra in the upper panel are from sample KBH-1 of *Bell et al.* [1995], from which the molar absorption coefficient was derived. Spectra have been offset for clarity. (c) Representative polarized principal spectra from FDM-RN03-X01 olivine. Sample thickness is 0.305 mm (upper ||β and ||γ), 0.285 mm (lower ||β and ||γ), 0.350 mm (upper ||α) and 0.478 (lower ||α). Spectra have been offset for clarity. (d) Principal polarized spectra used to orient the olivine samples in Figure S1c (solid curves), compared with the principal polarized spectra for sample GRR997 of *Asimow et al.* [2006; dotted curves]. Spectra are normalized to 1 cm thickness. Spectra collected in this study are shown without baseline subtraction, and are offset for clarity.

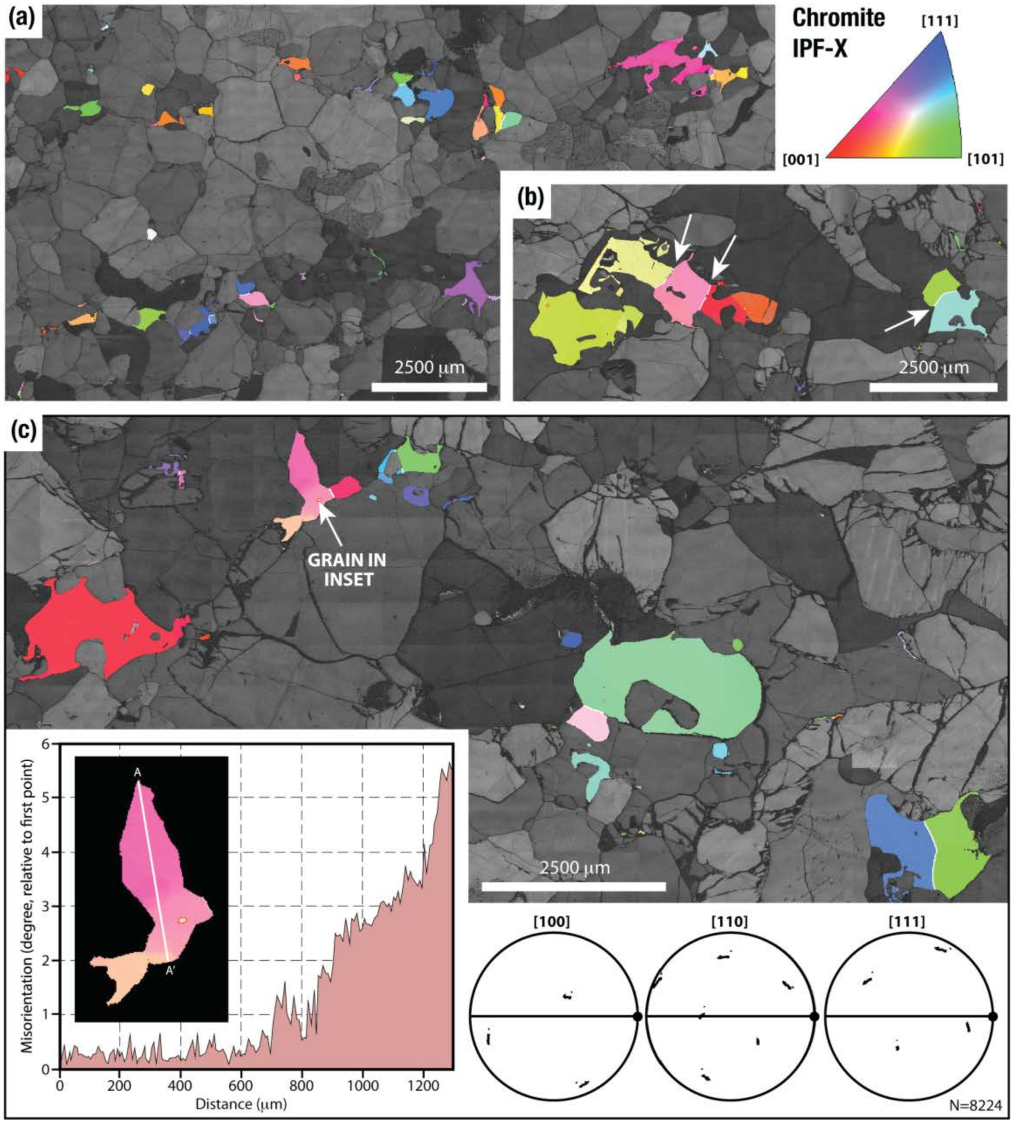

Figure S2. Representative EBSD maps of crystallographic preferred orientations in spinel (chromite). The orientations of spinel crystal axes are colored relative to Φ_1 axis of the spinel fabric ellipsoid (IPF-X coloring); all other phases are shown in gray (based on EBSD band contrast) for clarity. (a) Sample FDM-AVBB07 showing spinel grains with random distribution of crystallographic axes orientations. Spinel grains have minimal internal deformation, as indicated by homogeneous internal microstructure, characteristic of spinel crystallographic patterns in the xenolith suite analyzed. (b) FDM-DB03-X02: White arrows highlight examples of adjacent spinel grains, calculated with 10° misorientation boundaries (white lines), which otherwise lack evidence of significant internal deformation or recrystallization. (c) Spinel grains within sample FDM-DB01-X01 predominately show homogeneous intragrain and random intergrain crystallographic orientations. Limited intracrystalline deformation is observed in some spinel grains, as denoted by misorientations less than 10° (see inset) and minimal dispersion of crystallographic axes orientations in corresponding pole figures (lower-hemisphere, equal area projection).

References

Asimow, P. D., L. C. Stein, J. L. Mosenfelder, and G. R. Rossman (2006), Quantitative polarized FTIR analysis of trace OH in populations of randomly oriented mineral grains, *Am. Mineral., 91,* 278–284, doi: 10.2138/am.2006.1937.

Bell, D.R., P. D. Ihinger, and G. R. Rossman (1995), Quantitative analysis of trace OH in garnet and pyroxenes, *Am. Mineral*, 80, 465–474.

Mosenfelder, J.D., and G. R. Rossman (2013) Analysis of hydrogen and fluorine in pyroxenes by SIMS and FTIR. Part 1. Orthopyroxene, *Am. Mineral.,98,*1026–1041, doi: 10.2138/am.2013.4413.

Volcanic center	Latitude (S)	Longitude (W)
Fosdick Mountains		
Mt. Avers	76.481°	145.396°
Bird Bluff	76.504°	144.598°
Demas Bluff	76.568°	144.853°
Marujupu	76.508°	145.670°
Recess Nunatak	76.519°	144.507°
Usas Escarpment		
Mt. Aldaz	76.051°	124.417°
Executive Committee Range		
Mt. Cumming	76.667°	125.820°

Table S1. Geographic coordinates of the volcanic centers from which xenoliths were sampled.

Voltage	150-200 kV
Current	150-700 µA
Frame rate	1.3-9.2 fps
Source to detector distance	794-997 mm
Source to sample distance	126-643 mm
Number of projections	1080
Frame averaging	3-4
Voxel size (isotropic)	9.74-48.4 µm

Table S2. Parameters of X-ray computed tomography scans.

Table S3. Mineral compositions for the Marie Byrd Land spinel peridotite xenoliths

Sample	T (°C) calculated at an assumed pressure of 15 kbar					Ol-Spl	P (kbar)	$Depth_{max}$ (km)	H (km)
	2-Px BM[a]	2-Px BK[b]	2-Px T[c]	2-Px Avg	1 std dev	BBG[d]		O[e]	
Fosdick Mountains									
FDM-AV01-X01	937	978	902	939	38	---	16	57	50
FDM-BB01-X01	931	968	937	945	20	---	17	56	51
FDM-BB02-X01	1052	1088	1019	1053	34	---	20	56	60
FDM-BB03-X01	855	886	826	856	30	---	15	74	45
FDM-DB01-X01	1023	1065	983	1024	41	---	19	57	58
FDM-DB02-X01	1178	1200	1169	1183	16	---	23	71	71
FDM-DB02-X02	970	985	978	978	7	---	18	94	54
FDM-DB02-X03	987	1034	976	999	31	---	18	58	55
FDM-DB02-X04	927	980	892	933	44	---	16	60	50
FDM-DB02-X06	1205	1203	1186	1198	11	---	23	---	72
FDM-DB02-X08	801	814	792	803	11	---	13	78	41
FDM-DB02-X10	1014	1060	987	1020	37	---	19	59	57
FDM-DB02-X11	1032	1076	1009	1039	34	---	19	66	59
FDM-DB02-X12	1033	1074	1001	1036	37	---	19	59	59
FDM-DB02-X13	906	957	870	911	44	---	16	53	49
FDM-DB03-X01	855	886	826	856	30	---	14	74	44
FDM-DB03-X02	851	913	820	861	47	---	14	53	44
FDM-DB03-X03	975	1022	948	982	37	---	18	55	54
FDM-DB03-X04	995	1015	995	1002	11	---	18	80	56
FDM-DB04-X01	993	1033	945	991	44	---	18	57	55
FDM-DB04-X02	980	1026	947	984	40	---	18	56	54
FDM-DB04-X03	1171	1174	1152	1165	12	---	23	92	69
FDM-DB04-X04	963	980	962	968	10	---	17	81	53
FDM-MJ01-X02	966	1019	937	974	41	---	17	55	53
FDM-MJ01-X03	924	979	882	929	49	---	16	55	50
FDM-MJ01-X05	1010	1054	976	1014	39	---	19	58	57
FDM-MJ01-X06	1076	1099	1033	1070	34	---	20	58	61
FDM-RN01-X01	953	995	934	961	31	---	17	70	52
FDM-RN02-X01	818	875	791	828	43	---	14	50	42
FDM-RN03-X01	941	989	899	943	45	---	17	68	51
FDM-RN04-X01	806	860	771	812	45	---	14	49	42
FDM-AVBB01	930	984	898	937	44	---	16	51	50
FDM-AVBB02	781	814	743	779	36	---	13	52	39
FDM-AVBB04	817	861	788	822	37	---	14	49	42
FDM-AVBB05	810	855	777	814	39	---	14	51	42
FDM-AVBB06	930	980	910	940	36	---	16	52	50
FDM-AVBB07	801	850	764	805	43	---	13	51	41
FDM-AVBB08	831	873	791	832	41	---	14	51	43
USAS Escarpment									
AD6021-X02	1081	1116	1056	1084	30	---	21	61	63
Executive Committee Range									
KSP89-181-X01	---	---	---	---	---	862	14	93	42
KSP89-181-X01	---	---	---	---	---	995	17	105	52

[a]*Bertrand and Mercier* [1985]; [b]*Brey and Köhler* [1990]; [c]*Taylor* [1998]; [d]*Ballhaus et al.* [1991], T from Fe-Mg exchange in Ol-Spl; [e]*O'Neil* [1981]; H, estimated extraction depth

Table S4. Temperature, pressure, and extraction depth estimates for the Marie Byrd Land spinel peridotite xenoliths

Movie S1. Tomographic visualization of the three-dimensional shape preferred orientation of the spinel grains in the xenolith shown in Figure 3a and 3b of the manuscript. Red objects represent the spinel grains.

VOLCANIC CENTER	*Mt. Avers*	*Bird Bluff*	*Bird Bluff*	*Bird Bluff*	*Demas Bluff*	*Demas Bluff*	*Demas Bluff*	*Demas Bluff*	*Demas Bluff*	*Demas Bluff*
SAMPLE	**FDM-AV01-X01**	**FDM-BB01-X01**	**FDM-BB02-X01**	**FDM-BB03-X01**	**FDM-DB01-X01**	**FDM-DB02-X01**	**FDM-DB02-X02**	**FDM-DB02-X03**	**FDM-DB02-X04**	**FDM-DB02-X06**
T°C @ 15 kbar	*939*	*945*	*1053*	*856*	*1024*	*1183*	*978*	*999*	*933*	*1198*
OLIVINE										
wt. %										
SiO2	40.79	40.51	40.25	41.08	40.62	40.75	41.11	40.79	40.81	39.41
FeO	9.65	11.34	11.36	8.59	10.26	9.19	8.26	9.47	9.60	15.64
MnO	0.13	0.08	0.07	0.12	0.07	0.12	0.11	0.15	0.14	0.18
MgO	49.08	47.51	47.41	49.82	48.32	49.20	50.08	49.01	48.94	43.99
NiO	0.35	0.38	0.39	0.36	0.36	0.38	0.36	0.36	0.37	0.24
CaO	0.04	0.03	0.05	0.001	0.02	0.09	0.04	0.04	0.06	0.04
Sum	100.04	99.84	99.53	99.97	99.66	99.74	99.95	99.82	99.90	99.49
Si	1.000	1.002	1.000	1.002	1.002	1.000	1.002	1.001	1.001	0.999
Fe	0.198	0.235	0.236	0.175	0.212	0.189	0.168	0.194	0.197	0.331
Mn	0.003	0.002	0.001	0.002	0.001	0.002	0.002	0.003	0.003	0.004
Mg	1.793	1.752	1.755	1.812	1.776	1.801	1.819	1.793	1.790	1.662
Ni	0.007	0.008	0.008	0.007	0.007	0.008	0.007	0.007	0.007	0.005
Ca	0.001	0.001	0.001	0.000	0.001	0.002	0.001	0.001	0.001	0.001
Sum	3.001	2.999	3.002	2.998	2.999	3.002	2.999	3.000	3.000	3.002
Mg#	90.1	88.2	88.2	91.2	89.4	90.5	91.5	90.2	90.1	83.4
ORTHOPYROXENE										
wt. %										
SiO2	54.49	54.69	54.34	55.12	54.39	53.49	56.18	54.10	54.27	52.43
TiO2	0.10	0.10	0.13	0.02	0.14	0.12	0.02	0.12	0.11	0.31
Al2O3	4.22	3.91	4.57	3.10	4.70	5.84	1.86	5.18	4.19	6.10
Cr2O3	0.41	0.32	0.26	0.59	0.33	0.63	0.52	0.46	0.47	0.04
FeO	6.62	7.39	6.90	5.63	6.49	5.80	5.24	6.25	6.26	9.82
MnO	0.16	0.16	0.16	0.13	0.14	0.12	0.14	0.13	0.14	0.17
MgO	33.05	32.89	32.60	34.43	32.94	32.29	35.12	33.17	33.35	29.05
CaO	0.44	0.41	0.58	0.40	0.54	1.37	0.45	0.50	0.51	1.63
Na2O	0.03	0.02	0.11	0.03	0.09	0.14	0.02	0.08	0.09	0.19
Sum	99.50	99.89	99.74	99.43	99.77	99.78	99.55	99.99	99.38	99.74
Si	1.895	1.901	1.889	1.911	1.886	1.856	1.941	1.871	1.889	1.853
Ti	0.003	0.002	0.003	0.000	0.004	0.003	0.001	0.003	0.003	0.008
Al	0.173	0.160	0.187	0.127	0.192	0.239	0.076	0.211	0.172	0.254
Cr	0.011	0.009	0.007	0.016	0.009	0.017	0.014	0.013	0.013	0.001
Fe	0.192	0.215	0.203	0.163	0.188	0.168	0.151	0.181	0.182	0.290
Mn	0.005	0.005	0.005	0.004	0.004	0.004	0.004	0.004	0.004	0.005
Mg	1.714	1.704	1.690	1.780	1.703	1.670	1.809	1.710	1.731	1.531
Ca	0.016	0.015	0.022	0.015	0.020	0.051	0.017	0.019	0.019	0.062
Na	0.002	0.001	0.007	0.002	0.006	0.009	0.001	0.005	0.006	0.013
Sum	4.011	4.013	4.014	4.018	4.012	4.017	4.014	4.017	4.019	4.017
Ca	0.8	0.8	1.1	0.8	1.0	2.7	0.8	1.0	1.0	3.3
Mg	89.1	88.1	88.3	90.9	89.1	88.4	91.5	89.6	89.6	81.3
Fe	10.0	11.1	10.6	8.3	9.8	8.9	7.7	9.5	9.4	15.4
Mg #	89.9	88.8	89.3	91.6	90.1	90.8	92.3	90.4	90.5	84.1
CLINOPYROXENE										
wt. %										
SiO2	51.71	52.46	52.17	53.70	52.22	51.22	54.18	52.43	51.85	50.66
TiO2	0.62	0.47	0.64	0.13	0.65	0.27	0.03	0.52	0.57	0.78
Al2O3	7.64	5.76	7.33	4.74	7.71	6.90	1.82	6.91	6.75	7.76
Cr2O3	1.10	0.80	0.65	1.48	0.78	1.05	0.78	0.84	1.23	0.06
FeO	2.32	2.58	2.90	1.96	2.66	3.32	1.76	2.66	2.59	6.34
MnO	0.08	0.10	0.12	0.08	0.07	0.10	0.05	0.10	0.08	0.15
MgO	14.19	15.20	15.03	15.39	14.71	17.20	18.09	15.17	14.79	16.63
CaO	19.71	20.74	18.66	20.88	18.76	18.25	22.44	19.74	19.70	16.41
Na2O	1.96	1.30	1.89	1.82	2.12	1.17	0.30	1.77	2.04	1.30
Sum	99.33	99.41	99.39	100.20	99.60	99.40	99.47	100.14	99.60	100.09
Si	1.876	1.906	1.888	1.935	1.883	1.857	1.966	1.888	1.882	1.84
Ti	0.017	0.013	0.017	0.004	0.018	0.007	0.001	0.014	0.016	0.02
Al	0.327	0.247	0.313	0.201	0.328	0.295	0.078	0.293	0.289	0.33
Cr	0.032	0.023	0.019	0.042	0.022	0.030	0.022	0.024	0.035	0.00
Fe	0.071	0.078	0.088	0.059	0.080	0.101	0.053	0.080	0.079	0.19
Mn	0.002	0.003	0.004	0.002	0.002	0.003	0.002	0.003	0.002	0.00
Mg	0.768	0.823	0.811	0.827	0.791	0.930	0.978	0.814	0.800	0.90
Ca	0.766	0.807	0.724	0.806	0.725	0.709	0.872	0.761	0.766	0.64
Na	0.138	0.092	0.133	0.127	0.148	0.082	0.021	0.123	0.144	0.09
Sum	3.996	3.992	3.995	4.004	3.998	4.014	3.994	4.001	4.012	4.019
Ca	47.8	47.2	44.6	47.6	45.4	40.8	45.8	46.0	46.6	36.9
Mg	47.8	48.2	50.0	48.9	49.6	53.4	51.4	49.2	48.6	52.0
Fe	4.4	4.6	5.4	3.5	5.0	5.8	2.8	4.8	4.8	11.1
Mg #	91.6	91.3	90.2	93.3	90.8	90.2	94.8	91.0	91.0	82.4
SPINEL										
wt. %										
TiO2	0.07	0.04	0.11	0.02	0.11	0.17	0.04	0.11	0.15	---
Al2O3	56.06	55.71	59.42	39.21	59.58	52.47	26.49	57.58	52.68	---
Cr2O3	11.99	11.24	7.57	28.64	7.94	14.59	42.97	9.76	14.88	---
V2O3	0.05	0.07	0.05	0.09	0.04	0.04	0.19	0.04	0.06	---
FeO	10.73	12.06	10.57	13.46	9.87	10.32	14.05	10.52	11.31	---
MnO	0.10	0.06	0.04	0.14	0.04	0.09	0.19	0.08	0.12	---
MgO	19.87	19.67	21.34	16.44	21.85	20.83	15.02	20.95	19.66	---
CaO	0.00	0.00	0.00	0.00	0.00	0.00	0.00	0.00	0.00	---
ZnO	0.15	0.16	0.12	0.25	0.08	0.07	0.12	0.08	0.13	---
NiO	0.34	0.35	0.41	0.18	0.38	0.34	0.11	0.35	0.34	---
Sum	99.35	99.34	99.65	98.43	99.88	98.91	99.17	99.45	99.32	---
Ti	0.001	0.001	0.002	0.000	0.002	0.003	0.001	0.002	0.003	---
Al	1.733	1.730	1.803	1.324	1.798	1.644	0.942	1.762	1.652	---
Cr	0.249	0.234	0.154	0.649	0.161	0.307	1.025	0.200	0.313	---
V	0.001	0.001	0.001	0.002	0.001	0.001	0.005	0.001	0.001	---
Fe	0.235	0.266	0.228	0.322	0.212	0.229	0.354	0.228	0.252	---
Mn	0.002	0.001	0.001	0.003	0.001	0.002	0.005	0.002	0.003	---
Mg	0.777	0.773	0.819	0.702	0.834	0.826	0.676	0.811	0.780	---
Ca	0.000	0.000	0.000	0.000	0.000	0.000	0.000	0.000	0.000	---
Zn	0.003	0.003	0.002	0.005	0.002	0.001	0.003	0.002	0.003	---
Ni	0.007	0.007	0.008	0.004	0.008	0.007	0.003	0.007	0.007	---
Sum	3.008	3.016	3.019	3.012	3.018	3.021	3.013	3.016	3.014	---
Fe2+	0.215	0.222	0.178	0.290	0.163	0.174	0.320	0.186	0.215	---
Fe3+	0.020	0.044	0.050	0.033	0.048	0.055	0.035	0.043	0.037	---
XMg	0.783	0.777	0.822	0.708	0.836	0.826	0.679	0.814	0.784	---
XCr	0.125	0.119	0.079	0.329	0.082	0.157	0.521	0.102	0.159	---
YCr	0.124	0.117	0.077	0.324	0.080	0.153	0.512	0.100	0.156	---
YAl	0.866	0.862	0.898	0.660	0.896	0.820	0.471	0.879	0.825	---
YFe3+	0.010	0.022	0.025	0.016	0.024	0.028	0.017	0.021	0.018	---
Spl	0.685	0.684	0.757	0.475	0.768	0.696	0.325	0.731	0.659	---
Hc	0.190	0.197	0.164	0.196	0.150	0.147	0.154	0.167	0.182	---
MgChr	0.098	0.093	0.065	0.233	0.069	0.130	0.354	0.083	0.125	---
Chr	0.027	0.027	0.014	0.096	0.013	0.027	0.167	0.019	0.034	---
Sum	1.000	1.000	1.000	1.000	1.000	1.000	1.000	1.000	1.000	---
ρ	3.84	3.84	3.77	4.07	3.76	3.83	4.25	3.79	3.87	---

Demas Bluff	Demas Bluff	Demas Bluff	Demas Bluff	Demas Bluff	Demas Bluff	Demas Bluff	Demas Bluff	Demas Bluff	Demas Bluff	Demas Bluff
FDM-DB02-X08	**FDM-DB02-X10**	**FDM-DB02-X11**	**FDM-DB02-X12**	**FDM-DB02-X13**	**FDM-DB03-X01**	**FDM-DB03-X02**	**FDM-DB03-X03**	**FDM-DB03-X04**	**FDM-DB04-X01**	**FDM-DB04-X02**
803	*1020*	*1039*	*1036*	*911*	*856*	*861*	*982*	*1002*	*991*	*984*
41.11	40.72	41.01	40.82	40.59	41.08	40.63	40.93	40.54	40.71	40.46
8.04	9.82	9.16	9.67	10.18	8.59	10.17	10.02	8.03	8.63	9.89
0.11	0.13	0.14	0.14	0.12	0.12	0.14	0.15	0.13	0.14	0.14
50.49	48.67	49.46	48.80	48.13	49.82	48.47	48.77	50.31	49.75	48.87
0.39	0.37	0.40	0.36	0.36	0.36	0.37	0.37	0.40	0.40	0.40
0.04	0.03	0.07	0.03	0.00	0.00	0.04	0.05	0.035	0.03	0.035
100.19	99.73	100.23	99.82	99.39	99.97	99.82	100.28	99.44	99.66	99.79
0.999	1.002	1.001	1.00	1.003	1.002	1.001	1.002	0.993	0.998	0.996
0.163	0.202	0.187	0.20	0.210	0.175	0.209	0.205	0.165	0.177	0.204
0.002	0.003	0.003	0.00	0.003	0.002	0.003	0.003	0.003	0.003	0.003
1.829	1.785	1.800	1.79	1.773	1.812	1.779	1.780	1.838	1.817	1.793
0.008	0.007	0.008	0.01	0.007	0.007	0.007	0.007	0.008	0.008	0.008
0.001	0.001	0.0019	0.00	0.000	0.000	0.001	0.001	0.001	0.001	0.001
3.002	2.999	3.001	2.998	2.997	2.998	3.001	2.999	3.008	3.003	3.005
91.8	89.8	90.6	90.0	89.4	91.2	89.5	89.7	91.8	91.1	89.8
56.27	53.66	54.79	54.43	54.37	55.12	54.37	54.28	55.80	54.99	54.17
0.01	0.15	0.08	0.13	0.16	0.02	0.14	0.14	0.02	0.12	0.11
2.45	5.08	4.10	4.83	4.48	3.10	4.42	4.90	2.69	3.41	4.74
0.09	0.49	0.46	0.40	0.31	0.59	0.05	0.35	0.51	0.58	0.31
5.20	6.44	5.84	6.32	6.58	5.63	6.58	6.56	5.14	5.66	6.37
0.13	0.14	0.12	0.14	0.16	0.13	0.15	0.14	0.11	0.13	0.16
35.08	32.74	33.90	33.17	33.09	34.43	33.11	33.49	34.86	33.92	32.98
0.53	0.52	0.59	0.54	0.43	0.40	0.53	0.46	0.45	0.46	0.55
0.02	0.07	0.10	0.09	0.05	0.03	0.08	0.07	0.03	0.08	0.09
99.79	99.30	99.98	100.05	99.64	99.43	99.43	100.37	99.61	99.35	99.45
1.936	1.871	1.892	1.881	1.888	1.911	1.892	1.872	1.926	1.909	1.884
0.000	0.004	0.002	0.003	0.004	0.000	0.004	0.004	0.001	0.003	0.003
0.099	0.209	0.167	0.197	0.183	0.127	0.181	0.199	0.109	0.139	0.194
0.003	0.013	0.012	0.011	0.009	0.016	0.001	0.009	0.014	0.016	0.008
0.150	0.188	0.169	0.183	0.191	0.163	0.191	0.189	0.148	0.164	0.185
0.004	0.004	0.004	0.004	0.005	0.004	0.004	0.004	0.003	0.004	0.005
1.800	1.702	1.745	1.709	1.713	1.780	1.717	1.723	1.793	1.755	1.710
0.019	0.019	0.022	0.020	0.016	0.015	0.020	0.017	0.017	0.017	0.020
0.001	0.005	0.007	0.006	0.003	0.002	0.006	0.004	0.002	0.005	0.006
4.013	4.016	4.020	4.014	4.013	4.018	4.016	4.022	4.013	4.013	4.015
1.0	1.0	1.1	1.0	0.8	0.8	1.0	0.9	0.9	0.9	1.1
91.4	89.1	90.2	89.4	89.2	90.9	89.0	89.3	91.6	90.6	89.3
7.6	9.8	8.7	9.6	10.0	8.3	9.9	9.8	7.6	8.5	9.7
92.3	90.1	91.2	90.3	90.0	91.6	90.0	90.1	92.4	91.4	90.2
53.99	51.79	52.37	52.51	51.63	53.70	51.69	52.15	53.85	52.78	52.10
0.04	0.60	0.34	0.55	0.79	0.13	0.66	0.63	0.05	0.50	0.62
2.72	7.00	6.41	7.15	7.84	4.74	7.54	7.52	3.45	5.84	7.64
0.20	0.90	1.21	0.88	0.79	1.48	0.14	0.80	1.14	1.64	0.79
1.79	2.83	2.63	2.71	2.53	1.96	2.81	2.60	1.79	2.27	2.54
0.06	0.09	0.08	0.08	0.08	0.08	0.09	0.10	0.07	0.08	0.07
17.37	15.09	15.56	15.23	14.22	15.39	14.51	14.66	17.07	15.08	14.44
23.28	18.91	19.41	18.96	19.89	20.88	20.25	19.46	21.54	19.21	19.16
0.65	1.98	1.65	1.98	2.04	1.82	2.05	1.97	0.73	2.04	2.10
100.11	99.20	99.67	100.06	99.82	100.20	99.75	99.89	99.70	99.44	99.46
1.950	1.883	1.894	1.889	1.867	1.935	1.873	1.881	1.946	1.912	1.885
0.001	0.016	0.009	0.015	0.022	0.004	0.018	0.017	0.001	0.014	0.017
0.116	0.300	0.273	0.303	0.334	0.201	0.322	0.320	0.147	0.249	0.326
0.006	0.026	0.035	0.025	0.022	0.042	0.004	0.023	0.033	0.047	0.023
0.054	0.086	0.080	0.082	0.076	0.059	0.085	0.079	0.054	0.069	0.077
0.002	0.003	0.002	0.002	0.003	0.002	0.003	0.003	0.002	0.002	0.002
0.935	0.818	0.839	0.816	0.767	0.827	0.783	0.788	0.920	0.815	0.779
0.901	0.737	0.752	0.731	0.770	0.806	0.786	0.752	0.834	0.746	0.743
0.046	0.140	0.116	0.138	0.143	0.127	0.144	0.138	0.051	0.144	0.147
4.011	4.008	4.001	4.002	4.005	4.004	4.018	4.000	3.988	3.998	3.998
47.7	44.9	45.0	44.9	47.7	47.6	47.5	46.5	46.1	45.8	46.5
49.5	49.9	50.2	50.1	47.5	48.9	47.3	48.7	50.9	50.0	48.7
2.9	5.2	4.8	5.0	4.7	3.5	5.2	4.9	3.0	4.2	4.8
94.5	90.5	91.3	90.9	90.9	93.3	90.2	90.9	94.4	92.2	91.0
0.05	0.12	0.12	0.11	0.07	0.02	0.12	0.08	0.04	0.10	0.10
36.78	56.97	51.49	57.47	58.34	39.21	58.26	59.09	38.59	59.31	59.31
32.43	10.75	15.71	10.25	8.48	28.64	8.45	8.67	30.91	8.43	8.43
0.07	0.08	0.06	0.06	0.05	0.09	0.05	0.05	0.09	0.05	0.05
11.82	10.66	11.24	10.54	10.19	13.46	10.89	10.43	11.75	10.76	10.76
0.15	0.09	0.12	0.09	0.06	0.14	0.10	0.10	0.15	0.08	0.08
18.04	20.71	20.04	20.91	20.23	16.44	21.51	20.78	17.98	20.92	20.92
0.00	0.00	0.00	0.00	0.00	0.00	0.00	0.00	0.00	0.00	0.00
0.11	0.07	0.10	0.10	0.12	0.25	0.13	0.14	0.14	0.13	0.13
0.17	0.39	0.36	0.37	0.38	0.18	0.38	0.41	0.20	0.42	0.42
99.61	99.81	99.24	99.88	97.92	98.43	99.89	99.75	99.84	100.18	100.18
0.001	0.002	0.002	0.002	0.001	0.0005	0.002	0.001	0.001	0.002	0.002
1.232	1.745	1.622	1.755	1.804	1.3238	1.773	1.796	1.281	1.795	1.795
0.729	0.221	0.332	0.210	0.176	0.6488	0.172	0.177	0.688	0.171	0.171
0.002	0.002	0.001	0.001	0.001	0.0020	0.001	0.001	0.002	0.001	0.001
0.281	0.232	0.251	0.228	0.223	0.3224	0.235	0.225	0.277	0.231	0.231
0.003	0.002	0.003	0.002	0.001	0.0033	0.002	0.002	0.004	0.002	0.002
0.764	0.802	0.799	0.808	0.791	0.7019	0.828	0.799	0.755	0.801	0.801
0.000	0.000	0.000	0.000	0.000	0.0000	0.000	0.000	0.000	0.000	0.000
0.002	0.001	0.002	0.002	0.002	0.0053	0.003	0.003	0.003	0.002	0.002
0.004	0.008	0.008	0.008	0.008	0.0042	0.008	0.008	0.005	0.009	0.009
3.018	3.014	3.020	3.015	3.008	3.012	3.024	3.012	3.014	3.014	3.014
0.233	0.194	0.198	0.188	0.201	0.290	0.170	0.193	0.240	0.193	0.193
0.048	0.038	0.053	0.040	0.022	0.033	0.065	0.032	0.037	0.038	0.038
0.766	0.805	0.801	0.811	0.797	0.708	0.830	0.805	0.759	0.806	0.806
0.372	0.112	0.170	0.107	0.089	0.329	0.089	0.090	0.350	0.087	0.087
0.363	0.110	0.165	0.105	0.088	0.324	0.086	0.088	0.343	0.085	0.085
0.613	0.871	0.808	0.875	0.901	0.660	0.882	0.896	0.638	0.896	0.896
0.024	0.019	0.026	0.020	0.011	0.016	0.032	0.016	0.018	0.019	0.019
0.481	0.715	0.665	0.724	0.726	0.475	0.756	0.733	0.494	0.736	0.736
0.147	0.173	0.165	0.169	0.185	0.196	0.155	0.177	0.157	0.177	0.177
0.285	0.090	0.136	0.087	0.071	0.233	0.074	0.072	0.265	0.070	0.070
0.087	0.022	0.034	0.020	0.018	0.096	0.015	0.017	0.084	0.017	0.017
1.000	1.000	1.000	1.000	1.000	1.000	1.000	1.000	1.000	1.000	1.000
4.06	3.81	3.86	3.80	3.80	4.07	3.77	3.79	4.05	3.79	3.79

Demas Bluff	*Demas Bluff*	*Marujupu*	*Marujupu*	*Marujupu*	*Marujupu*	*Recess Nunatak*	*Recess Nunatak*	*Recess Nunatak*	*Recess Nunatak*	*Mt. Avers – Bird Bluff*
FDM-DB04-X03	**FDM-DB04-X04**	**FDM-MJ01-X02**	**FDM-MJ01-X03**	**FDM-MJ01-X05**	**FDM-MJ01-X06**	**FDM-RN01-X01**	**FDM-RN02-X01**	**FDM-RN03-X01**	**FDM-RN04-X01**	**FDM-AVBB01**
1165	*960*	*974*	*929*	*1014*	*1070*	*961*	*820*	*943*	*812*	*763*
40.87	41.12	40.55	40.63	40.75	40.55	41.04	40.47	40.95	40.54	40.61
7.90	7.74	10.61	9.91	9.90	11.20	8.16	10.78	8.77	10.54	10.09
0.11	0.11	0.15	0.13	0.15	0.16	0.15	0.13	0.13	0.13	0.14
50.39	50.44	48.06	48.67	48.77	47.72	50.13	48.03	49.50	48.43	48.62
0.41	0.38	0.36	0.36	0.35	0.38	0.37	0.38	0.34	0.39	0.37
0.035	0.03	0.03	0.03	0.03	0.04	0.06	0.04	0.076	0.03	0.06
99.71	99.82	99.76	99.71	99.95	100.03	99.89	99.84	99.77	100.08	99.89
0.998	1.001	1.001	1.000	1.001	1.001	1.001	0.999	1.002	0.998	0.999
0.161	0.157	0.219	0.204	0.203	0.231	0.166	0.223	0.180	0.217	0.208
0.002	0.002	0.003	0.003	0.003	0.003	0.003	0.003	0.003	0.003	0.003
1.834	1.831	1.769	1.786	1.785	1.756	1.822	1.768	1.806	1.777	1.784
0.008	0.007	0.007	0.007	0.007	0.007	0.007	0.008	0.007	0.008	0.007
0.001	0.001	0.001	0.001	0.001	0.001	0.002	0.001	0.002	0.001	0.001
3.003	3.000	3.000	3.001	3.000	3.000	3.001	3.002	3.000	3.003	3.002
91.9	92.1	89.0	89.8	89.8	88.4	91.6	88.8	91.0	89.1	89.6
55.97	55.70	53.81	54.04	54.27	53.59	55.33	54.33	54.83	54.15	54.26
0.01	0.02	0.09	0.11	0.13	0.10	0.06	0.12	0.13	0.12	0.11
2.59	2.75	4.42	4.63	4.44	5.12	3.25	4.70	3.83	4.86	4.50
0.63	0.63	0.32	0.39	0.36	0.45	0.47	0.03	0.60	0.03	0.28
5.14	5.07	6.78	6.61	6.34	7.33	5.44	7.14	5.72	6.93	6.48
0.14	0.14	0.15	0.16	0.17	0.17	0.14	0.16	0.12	0.15	0.14
34.80	34.85	33.05	33.14	33.24	32.55	34.24	32.90	33.44	32.98	32.92
0.46	0.40	0.38	0.43	0.43	0.32	0.48	0.49	0.67	0.40	0.62
0.02	0.01	0.03	0.06	0.10	0.06	0.02	0.04	0.15	0.05	0.20
99.75	99.65	99.03	99.54	99.40	99.66	99.43	99.99	99.40	99.60	99.59
1.929	1.924	1.883	1.880	1.887	1.868	1.916	1.884	1.902	1.882	1.886
0.000	0.001	0.002	0.003	0.003	0.002	0.002	0.003	0.003	0.003	0.003
0.105	0.112	0.182	0.190	0.182	0.210	0.133	0.195	0.157	0.199	0.188
0.017	0.017	0.009	0.011	0.010	0.012	0.013	0.001	0.016	0.001	0.008
0.148	0.146	0.198	0.192	0.184	0.214	0.158	0.207	0.166	0.201	0.188
0.004	0.004	0.004	0.005	0.005	0.005	0.004	0.005	0.004	0.004	0.004
1.788	1.792	1.724	1.719	1.723	1.692	1.767	1.701	1.730	1.708	1.706
0.017	0.015	0.014	0.016	0.016	0.012	0.018	0.018	0.025	0.015	0.023
0.001	0.001	0.002	0.004	0.007	0.004	0.001	0.002	0.010	0.003	0.014
4.010	4.011	4.020	4.019	4.017	4.020	4.011	4.016	4.013	4.017	4.020
0.9	0.8	0.7	0.8	0.8	0.6	0.9	0.9	1.3	0.8	1.2
91.5	91.7	89.0	89.2	89.6	88.2	91.0	88.3	90.1	88.8	89.0
7.6	7.5	10.2	10.0	9.6	11.1	8.1	10.8	8.6	10.5	9.8
92.3	92.5	89.7	89.9	90.3	88.8	91.8	89.1	91.2	89.5	90.1
54.38	53.78	51.61	51.56	52.13	50.81	52.66	51.90	52.34	51.69	51.97
0.01	0.08	0.61	0.68	0.55	0.83	0.24	0.65	0.48	0.64	0.58
2.42	2.93	7.91	7.94	7.14	7.81	5.24	8.14	6.18	8.23	7.25
0.88	1.07	0.90	1.02	0.87	1.07	1.43	0.12	1.47	0.11	0.69
2.09	1.68	2.71	2.59	2.63	2.82	2.19	2.74	2.38	2.67	2.77
0.08	0.08	0.08	0.09	0.09	0.07	0.10	0.10	0.07	0.09	0.08
19.57	17.22	13.99	13.83	14.88	15.24	15.40	14.02	15.05	14.06	15.06
19.93	21.79	19.11	19.06	18.99	18.45	20.31	20.44	19.62	20.49	19.83
0.44	0.74	2.06	2.35	1.99	1.78	1.52	2.12	2.10	2.14	2.08
99.79	99.37	99.05	99.13	99.28	98.88	99.10	100.24	99.70	100.13	100.31
1.956	1.952	1.877	1.875	1.890	1.852	1.918	1.870	1.896	1.865	1.872
0.000	0.002	0.017	0.019	0.015	0.023	0.007	0.018	0.013	0.017	0.016
0.103	0.125	0.339	0.340	0.305	0.335	0.225	0.346	0.264	0.350	0.308
0.025	0.031	0.026	0.029	0.025	0.031	0.041	0.003	0.042	0.003	0.020
0.063	0.051	0.083	0.079	0.080	0.086	0.067	0.083	0.072	0.081	0.084
0.002	0.002	0.002	0.003	0.003	0.002	0.003	0.003	0.002	0.003	0.003
1.049	0.932	0.759	0.750	0.804	0.828	0.836	0.753	0.813	0.756	0.809
0.768	0.847	0.745	0.743	0.738	0.721	0.793	0.789	0.761	0.792	0.766
0.030	0.052	0.145	0.166	0.140	0.126	0.107	0.148	0.148	0.150	0.144
3.996	3.994	3.995	4.004	4.000	4.005	3.996	4.012	4.012	4.016	4.020
40.8	46.3	47.0	47.3	45.5	44.1	46.8	48.6	46.2	48.6	46.2
55.8	50.9	47.8	47.7	49.6	50.6	49.3	46.4	49.4	46.4	48.8
3.3	2.8	5.2	5.0	4.9	5.3	3.9	5.1	4.4	5.0	5.0
94.3	94.8	90.2	90.5	91.0	90.6	92.6	90.1	91.9	90.4	90.6
0.02	0.06	0.05	0.05	0.07	0.03	0.09	0.04	0.02	0.04	0.08
34.34	36.60	58.31	57.93	57.30	57.92	45.39	60.98	47.00	61.40	59.11
35.17	32.41	9.56	9.67	10.58	9.37	22.80	6.43	21.64	6.09	8.26
0.11	0.09	0.05	0.05	0.05	0.04	0.09	0.04	0.09	0.05	0.05
12.40	11.83	10.96	11.42	10.61	12.17	11.55	10.78	10.95	10.47	10.49
0.15	0.17	0.08	0.12	0.09	0.10	0.13	0.08	0.12	0.09	0.09
17.14	17.13	20.12	20.41	20.72	19.57	18.74	21.38	18.87	21.62	20.81
0.00	0.00	0.00	0.00	0.00	0.00	0.00	0.00	0.00	0.00	0.00
0.11	0.11	0.20	0.17	0.08	0.21	0.14	0.13	0.13	0.13	0.15
0.17	0.18	0.38	0.33	0.34	0.38	0.25	0.41	0.27	0.39	0.41
99.59	98.58	99.71	100.13	99.82	99.77	99.16	100.27	99.10	100.27	99.45
0.000	0.001	0.001	0.001	0.001	0.001	0.002	0.001	0.000	0.001	0.002
1.166	1.240	1.782	1.768	1.752	1.779	1.471	1.832	1.511	1.839	1.800
0.801	0.737	0.196	0.198	0.217	0.193	0.495	0.130	0.467	0.122	0.169
0.002	0.002	0.001	0.001	0.001	0.001	0.002	0.001	0.002	0.001	0.001
0.299	0.284	0.238	0.247	0.230	0.265	0.265	0.230	0.250	0.223	0.227
0.004	0.004	0.002	0.003	0.002	0.002	0.003	0.002	0.003	0.002	0.002
0.736	0.734	0.778	0.788	0.801	0.760	0.768	0.812	0.767	0.819	0.802
0.000	0.000	0.000	0.000	0.000	0.000	0.000	0.000	0.000	0.000	0.000
0.002	0.002	0.004	0.003	0.001	0.004	0.003	0.002	0.003	0.002	0.003
0.004	0.004	0.008	0.007	0.007	0.008	0.006	0.008	0.006	0.008	0.008
3.015	3.009	3.009	3.016	3.013	3.013	3.014	3.018	3.009	3.018	3.013
0.259	0.260	0.213	0.206	0.194	0.231	0.227	0.182	0.225	0.175	0.191
0.040	0.025	0.025	0.042	0.036	0.035	0.038	0.048	0.025	0.047	0.036
0.740	0.739	0.785	0.793	0.805	0.767	0.771	0.817	0.773	0.824	0.808
0.407	0.373	0.099	0.101	0.110	0.098	0.252	0.066	0.238	0.062	0.086
0.399	0.368	0.098	0.099	0.108	0.096	0.247	0.065	0.233	0.061	0.084
0.581	0.620	0.890	0.881	0.874	0.887	0.734	0.912	0.755	0.915	0.898
0.020	0.012	0.012	0.021	0.018	0.017	0.019	0.024	0.012	0.024	0.018
0.438	0.463	0.707	0.713	0.716	0.692	0.577	0.763	0.591	0.772	0.738
0.154	0.164	0.193	0.186	0.174	0.210	0.171	0.171	0.173	0.165	0.176
0.301	0.275	0.078	0.080	0.089	0.075	0.194	0.054	0.182	0.051	0.069
0.106	0.097	0.021	0.021	0.021	0.023	0.058	0.012	0.053	0.011	0.016
1.000	1.000	1.000	1.000	1.000	1.000	1.000	1.000	1.000	1.000	1.000
4.11	4.08	3.82	3.81	3.81	3.83	3.96	3.76	3.94	3.75	3.79

Mt. Avers - Bird Bluff	Mt. Avers - Bird Bluff	Mt. Avers - Bird Bluff	Mt. Avers - Bird Bluff	Mt. Avers - Bird Bluff	Mt. Avers - Bird Bluff	Mt. Aldaz	Mt. Cumming	Mt. Cumming
FDM-AVBB02	**FDM-AVBB04**	**FDM-AVBB05**	**FDM-AVBB06**	**FDM-AVBB07**	**FDM-AVBB08**	**AD6021-X02**	**KSP89-181-X01**	**KSP89-181-X01**
							low-Cr Spl	hghi-Cr Spl
779	*822*	*814*	*940*	*805*	*832*	*1084*	*838*	*984*
40.42	40.16	40.29	40.45	40.37	40.78	40.45	40.70	40.70
9.54	10.21	9.59	10.84	10.24	9.71	9.92	10.24	10.24
0.14	0.14	0.13	0.15	0.13	0.13	0.05	0.16	0.16
49.28	48.58	49.08	47.84	48.51	48.79	48.66	48.40	48.40
0.42	0.43	0.40	0.39	0.40	0.41	0.37	0.29	0.29
0.07	0.072	0.072	0.053	0.075	0.054	0.04	0.05	0.05
99.88	99.60	99.56	99.72	99.73	99.87	99.49	99.84	99.84
0.993	0.993	0.994	1.000	0.997	1.002	0.998	1.002	1.002
0.20	0.211	0.198	0.224	0.211	0.199	0.205	0.211	0.211
0.00	0.003	0.003	0.003	0.003	0.003	0.001	0.003	0.003
1.81	1.791	1.804	1.764	1.785	1.787	1.790	1.776	1.776
0.01	0.008	0.008	0.008	0.008	0.008	0.007	0.006	0.006
0.002	0.002	0.002	0.001	0.002	0.001	0.001	0.001	0.001
3.008	3.009	3.008	3.001	3.005	3.000	3.003	2.999	2.999
90.2	89.4	90.1	88.7	89.4	90.0	89.7	89.4	89.4
54.34	53.77	53.98	53.45	54.33	54.15	54.41	---	---
0.10	0.11	0.12	0.11	0.09	0.12	0.12	---	---
4.75	5.09	4.95	5.04	4.28	4.88	4.78	---	---
0.40	0.27	0.32	0.33	0.29	0.38	0.35	---	---
6.43	6.84	6.43	7.23	6.91	6.46	6.12	---	---
0.14	0.16	0.15	0.17	0.15	0.13	0.13	---	---
33.25	32.72	32.96	32.37	32.98	33.14	32.96	---	---
0.53	0.50	0.48	0.57	0.45	0.45	0.74	---	---
0.05	0.03	0.04	0.05	0.03	0.03	0.10	---	---
100.00	99.48	99.44	99.31	99.53	99.73	99.71	---	---
1.880	1.873	1.878	1.870	1.892	1.878	1.886	---	---
0.003	0.003	0.003	0.003	0.002	0.003	0.003	---	---
0.194	0.209	0.203	0.208	0.176	0.200	0.195	---	---
0.011	0.008	0.009	0.009	0.008	0.010	0.010	---	---
0.186	0.199	0.187	0.212	0.201	0.187	0.177	---	---
0.004	0.005	0.005	0.005	0.004	0.004	0.004	---	---
1.715	1.699	1.709	1.689	1.712	1.713	1.703	---	---
0.020	0.018	0.018	0.021	0.017	0.017	0.027	---	---
0.004	0.002	0.003	0.003	0.002	0.002	0.007	---	---
4.017	4.017	4.014	4.020	4.015	4.015	4.012	---	---
1.0	1.0	0.9	1.1	0.9	0.9	1.4	---	---
89.3	88.6	89.3	87.9	88.7	89.4	89.3	---	---
9.7	10.4	9.8	11.0	10.4	9.8	9.3	---	---
90.2	89.5	90.1	88.9	89.5	90.1	90.6	---	---
52.02	51.77	51.42	51.82	51.74	51.69	52.44	---	---
0.56	0.52	0.63	0.55	0.58	0.56	0.51	---	---
7.42	8.08	8.07	7.84	7.72	8.03	6.89	---	---
0.86	0.60	0.72	0.74	0.78	0.82	0.73	---	---
2.21	2.44	2.36	2.79	2.58	2.31	2.81	---	---
0.08	0.09	0.07	0.08	0.08	0.09	0.08	---	---
14.51	14.25	14.20	14.42	14.16	14.42	15.78	---	---
21.37	20.84	20.91	19.70	20.75	20.79	18.92	---	---
1.86	1.98	1.92	2.04	2.03	2.00	1.64	---	---
100.87	100.56	100.30	99.98	100.43	100.71	99.81	---	---
1.866	1.861	1.854	1.871	1.865	1.856	1.890	---	---
0.015	0.014	0.017	0.015	0.016	0.015	0.014	---	---
0.314	0.342	0.343	0.334	0.328	0.340	0.293	---	---
0.024	0.017	0.021	0.021	0.022	0.023	0.021	---	---
0.066	0.073	0.071	0.084	0.078	0.069	0.085	---	---
0.002	0.003	0.002	0.002	0.003	0.003	0.003	---	---
0.776	0.764	0.763	0.776	0.761	0.772	0.847	---	---
0.821	0.803	0.808	0.762	0.801	0.800	0.731	---	---
0.129	0.138	0.134	0.143	0.142	0.139	0.114	---	---
4.014	4.014	4.014	4.008	4.015	4.017	3.997	---	---
49.4	49.0	49.2	47.0	48.9	48.7	43.9	---	---
46.6	46.6	46.5	47.8	46.4	47.0	51.0	---	---
4.0	4.5	4.3	5.2	4.7	4.2	5.1	---	---
92.1	91.2	91.5	90.2	90.7	91.8	90.9	---	---
0.03	0.03	0.03	0.04	0.05	0.03	0.13	0.4	0.44
58.37	61.38	59.35	59.76	58.13	59.43	57.92	23	16.87
9.25	6.03	8.17	7.68	8.90	8.08	9.26	36.17	42.92
0.04	0.04	0.07	0.05	0.05	0.04	0.05	0.21	0.22
10.53	10.51	10.43	11.53	11.21	10.40	9.87	25.74	24.22
0.10	0.09	0.10	0.11	0.11	0.10	0.03	0.24	0.28
20.15	20.50	20.36	19.82	19.87	20.34	21.87	12.12	12.32
0.00	0.00	0.00	0.00	0.00	0.00	0.00	0.00	0.00
0.18	0.14	0.18	0.16	0.14	0.16	0.09	0.22	0.06
0.41	0.48	0.37	0.38	0.39	0.43	0.39	0.18	0.14
99.04	99.20	99.06	99.54	98.86	99.01	99.61	98.28	97.47
0.001	0.001	0.001	0.001	0.001	0.001	0.002	0.010	0.011
1.791	1.859	1.813	1.822	1.791	1.816	1.763	0.871	0.659
0.190	0.122	0.167	0.157	0.184	0.166	0.189	0.919	1.125
0.001	0.001	0.001	0.001	0.001	0.001	0.001	0.005	0.006
0.229	0.226	0.226	0.250	0.245	0.225	0.213	0.692	0.671
0.002	0.002	0.002	0.002	0.002	0.002	0.001	0.007	0.008
0.782	0.785	0.787	0.765	0.775	0.786	0.842	0.580	0.609
0.000	0.000	0.000	0.000	0.000	0.000	0.000	0.000	0.000
0.003	0.003	0.003	0.003	0.003	0.003	0.002	0.005	0.001
0.009	0.010	0.008	0.008	0.008	0.009	0.008	0.005	0.004
3.008	3.008	3.008	3.009	3.011	3.008	3.021	3.093	3.094
0.207	0.204	0.203	0.226	0.217	0.203	0.157	0.444	0.420
0.022	0.022	0.023	0.024	0.029	0.022	0.056	0.248	0.251
0.791	0.794	0.795	0.772	0.781	0.795	0.843	0.567	0.592
0.096	0.062	0.085	0.079	0.093	0.084	0.097	0.513	0.631
0.095	0.061	0.084	0.078	0.092	0.083	0.094	0.451	0.553
0.894	0.928	0.905	0.910	0.894	0.906	0.878	0.427	0.324
0.011	0.011	0.011	0.012	0.014	0.011	0.028	0.122	0.123
0.715	0.745	0.727	0.711	0.709	0.728	0.761	0.276	0.219
0.189	0.193	0.188	0.210	0.198	0.188	0.142	0.211	0.151
0.076	0.049	0.067	0.061	0.073	0.066	0.082	0.291	0.373
0.020	0.013	0.017	0.018	0.020	0.017	0.015	0.222	0.258
1.000	1.000	1.000	1.000	1.000	1.000	1.000	1.000	1.000
3.81	3.78	3.80	3.81	3.81	3.79	3.77	4.33	4.40

APPENDIX B

The following code is an .m file that is intended for use with version 3.5 of the MTEX MATLAB toolbox (Bachmann et al., 2011). The purpose of this script is to import and process noise-reduced EBSD datasets. This is accomplished through the creation of grain sets, which reconstruct grain boundaries between adjacent data points that are either indexed as different mineral phases or have a relative misorientation angle equal to or greater than 10°. Once a grain set exists, the data are further reduced by calculating an average crystallographic orientation for every crystal defined within the grain set (i.e. a one-point-per-grain data set) and visually representing this data set as an orientation distribution function (ODF). Using a one-point-per-grain (1ppg) data set allows for the quantitative measurement of the relative strength of the textures developed throughout the xenolith suite (i.e. J- and M-indices). This script also calculates grain size statistics and generates grain size distribution histograms.

```
-----------------------------------------------------------------
%% Begin MTEX script

clear all;
close all;


%% Get MATLAB files for processing
[filename, pathname] = uigetfile('*.m','Pick your Matlab(*.m)
file(s)','MultiSelect', 'on');
filename=cellstr(filename);


%% Begin the sample processing scripts
for i=1:numel(filename)

s=char(filename{i}); % Get sample name without .m extension
l=length(s)-2;
samplename=[];
for k=1:l
    samplename=[samplename,s(k)];
end

run(filename{i});


% Calculate grains and generate maps
[grains, grains1ppg] = ebsd2grains(pathname, samplename,
ebsd,1,10,25);


% Get num grains of interest and export
n_Fo = numel(grains('Forsterite'));
n_Fo_1ppg = numel(grains1ppg('Forsterite'));
```

```
mkdir([pathname samplename '_Exports']);
epath = ([pathname samplename '_Exports']);
dlmwrite([epath '/N_Fo_Grains.txt'], 'Your number of Forsterite
 grains and 1ppg grains, respectively are =','');
dlmwrite([epath '/N_Fo_Grains.txt'], n_Fo,'-append');
dlmwrite([epath '/N_Fo_Grains.txt'], n_Fo_1ppg,'-append');

n_En = numel(grains('Enstatite  Opx AV77'));
n_En_1ppg = numel(grains1ppg('Enstatite  Opx AV77'));

mkdir([pathname samplename '_Exports']);
epath = ([pathname samplename '_Exports']);
dlmwrite([epath '/N_En_Grains.txt'], 'Your number of Enstatite
 grains and 1ppg grains, respectively are =','');
dlmwrite([epath '/N_En_Grains.txt'], n_En,'-append');
dlmwrite([epath '/N_En_Grains.txt'], n_En_1ppg,'-append');

n_Di = numel(grains('Diopside   CaMgSi2O6'));
n_Di_1ppg = numel(grains1ppg('Diopside   CaMgSi2O6'));

mkdir([pathname samplename '_Exports']);
epath = ([pathname samplename '_Exports']);
dlmwrite([epath '/N_Di_Grains.txt'], 'Your number of Diopside
 grains and 1ppg grains, respectively are =','');
dlmwrite([epath '/N_Di_Grains.txt'], n_Di,'-append');
dlmwrite([epath '/N_Di_Grains.txt'], n_Di_1ppg,'-append');


%% SPO Forsterite
% For the 'grains' dataset...
SPO_MP(grains('Forsterite'));

mkdir([pathname samplename '_Exports'])
epath = ([pathname samplename '_Exports']);
export_fig([epath '/grainsForsterite_SPO.pdf'])
close;

% For the 'grains1ppg' datzaset...
SPO_MP(grains1ppg('Forsterite'));

mkdir([pathname samplename '_Exports'])
epath = ([pathname samplename '_Exports']);
export_fig([epath '/grains1ppgForsterite_SPO.pdf'])
close;


%% Grain size plots
grainSizePlots( pathname, samplename, 'grainsForsterite',
 grains('Forsterite'), 50, 2 );
```

```
grainSizePlots( pathname, samplename, 'grains1ppgForsterite',
 grains1ppg('Forsterite'), 50, 2 );

grainSizePlots( pathname, samplename, 'grainsEnstatite',
 grains('Enstatite  Opx AV77'), 50, 2 );
grainSizePlots( pathname, samplename, 'grains1ppgEnstatite',
 grains1ppg('Enstatite  Opx AV77'), 50, 2 );

grainSizePlots( pathname, samplename, 'grainsDiopside',
 grains('Diopside   CaMgSi2O6'), 50, 2 );
grainSizePlots( pathname, samplename, 'grains1ppgDiopside',
 grains1ppg('Diopside   CaMgSi2O6'), 50, 2 );

%% Define coordinate system, plot pole figures and calculate ODF
h=[Miller(1,0,0,'direction'),Miller(0,1,0,'direction'),Miller(0,0
 ,1,'direction')];

[ol_odf,ol_mo]=plotPoleFigures(pathname, samplename, grains,
 'Forsterite', h, 'grains');

[maxMUD] = maxODF(ol_odf,h);
if maxMUD > maxMUDgrainsALL
   maxMUDgrainsALL = maxMUD;
end

[ol_odf_1ppg,ol_mo_1ppg]=plotPoleFigures(pathname, samplename,
 grains1ppg, 'Forsterite', h, 'grains1ppg');

[maxMUD] = maxODF(ol_odf_1ppg,h);
if maxMUD > maxMUDgrains1ppgALL
   maxMUDgrains1ppgALL = maxMUD;
end

[en_odf,en_mo]=plotPoleFigures(pathname, samplename, grains,
 'Enstatite  Opx AV77', h, 'grains');
[en_odf_1ppg,en_mo_1ppg]=plotPoleFigures(pathname, samplename,
 grains1ppg, 'Enstatite  Opx AV77', h, 'grains1ppg');

[di_odf,di_mo]=plotPoleFigures(pathname, samplename, grains,
 'Diopside   CaMgSi2O6', h, 'grains');
[di_odf_1ppg,di_mo_1ppg]=plotPoleFigures(pathname, samplename,
 grains1ppg, 'Diopside   CaMgSi2O6', h, 'grains1ppg');


%% PGR Olivine
calcPGR( pathname, samplename, ol_odf, 'Forsterite', 'grains' );
calcPGR( pathname, samplename, ol_odf_1ppg, 'Forsterite',
'grains1ppg' );
```

```
%% BAindex Olivine
calcBALSindex( pathname, samplename, ol_odf, 'Forsterite',
'grains' );
calcBALSindex( pathname, samplename, ol_odf_1ppg, 'Forsterite',
 'grains1ppg' );

%% Rotate ODF?
if exist('E')
    % For the 'grains' dataset...
    % Rotate the olivine ODF based upon the correct X-Ray CT
      Eigenvectors and Eigenvalues and plot

[ol_rodf]=eigen_rot_ANT(ol_odf,E(1),E(2),E(3),E(4),E(5),E(6));
    [ol_rmo]=eigen_rot_ANT(ol_mo,E(1),E(2),E(3),E(4),E(5),E(6));

[en_rodf]=eigen_rot_ANT(en_odf,E(1),E(2),E(3),E(4),E(5),E(6));
    [en_rmo]=eigen_rot_ANT(en_mo,E(1),E(2),E(3),E(4),E(5),E(6));

[di_rodf]=eigen_rot_ANT(di_odf,E(1),E(2),E(3),E(4),E(5),E(6));
    [di_rmo]=eigen_rot_ANT(di_mo,E(1),E(2),E(3),E(4),E(5),E(6));

    plotRotatedPoleFigures(pathname, samplename, ol_rodf, ol_rmo,
      'Forsterite', h, 'grains');
    plotRotatedPoleFigures(pathname, samplename, en_rodf, en_rmo,
      'Enstatite  Opx AV77', h, 'grains');
    plotRotatedPoleFigures(pathname, samplename, di_rodf, di_rmo,
      'Diopside   CaMgSi2O6', h, 'grains');

    % Set colormap
    map = flipud(lbmap(64,'RedBlue'));

    % Plot Rotated Olivine ODF
    figure('position',[0, 0, 1024, 1024]);
    plotpdf(ol_rodf, h, 'lower','contourf');
    title(['Contoured Rotated ODF ' samplename ': Forsterite']);
    colorbar;
    colormap(map)
    mkdir([pathname samplename '_Exports']);
    epath = ([pathname samplename '_Exports']);
    export_fig([epath '/PF-grainsForsterite-
      RODF_contoured_color.pdf']);
    close;

    figure('position',[0, 0, 1024, 1024]);
    plotpdf(ol_rodf, h, 'lower', 'contourf');
    title(['Rotated Contoured ODF ' samplename ': Forsterite']);
    colorbar;
    mtexColorMap white2black
    mkdir([pathname samplename '_Exports']);
    epath = ([pathname samplename '_Exports']);
```

```
export_fig([epath '/PF-grainsForsterite-
 RODF_contoured_BW.pdf']);
close;

% Plot Rotated Enstatite ODF
figure('position',[0, 0, 1024, 1024]);
plotpdf(en_rodf, h, 'lower','contourf');
title(['Contoured Rotated ODF ' samplename ': Enstatite']);
colorbar;
colormap(map)
mkdir([pathname samplename '_Exports']);
epath = ([pathname samplename '_Exports']);
export_fig([epath '/PF-grainsEnstatite-
 RODF_contoured_color.pdf']);
close;


figure('position',[0, 0, 1024, 1024]);
plotpdf(en_rodf, h, 'lower', 'contourf');
title(['Rotated Contoured ODF ' samplename ': Enstatite']);
colorbar;
mtexColorMap white2black
mkdir([pathname samplename '_Exports']);
epath = ([pathname samplename '_Exports']);
export_fig([epath '/PF-grainsEnstatite-
 RODF_contoured_BW.pdf']);
close;

% Plot Rotated Diopside ODF
figure('position',[0, 0, 1024, 1024]);
plotpdf(di_rodf, h, 'lower','contourf');
title(['Contoured Rotated ODF ' samplename ': Diopside']);
colorbar;
colormap(map)
mkdir([pathname samplename '_Exports']);
epath = ([pathname samplename '_Exports']);
export_fig([epath '/PF-grainsDiopside-
 RODF_contoured_color.pdf']);
close;

figure('position',[0, 0, 1024, 1024]);
plotpdf(di_rodf, h, 'lower', 'contourf');
title(['Rotated Contoured ODF ' samplename ': Diopside']);
colorbar;
mtexColorMap white2black
mkdir([pathname samplename '_Exports']);
epath = ([pathname samplename '_Exports']);
export_fig([epath '/PF-grainsDiopside-
 RODF_contoured_BW.pdf']);
close;
```

```
    % For the 'grains1ppg' dataset...
    % Rotate the olivine ODF based upon the correct X-Ray CT
     Eigenvectors and
     Eigenvalues and plot

[ol_rodf_1ppg]=eigen_rot_ANT(ol_odf_1ppg,E(1),E(2),E(3),E(4),E(5)
,E(6));

[ol_rmo_1ppg]=eigen_rot_ANT(ol_mo_1ppg,E(1),E(2),E(3),E(4),E(5),E
(6));

[en_rodf_1ppg]=eigen_rot_ANT(en_odf_1ppg,E(1),E(2),E(3),E(4),E(5)
,E(6));

[en_rmo_1ppg]=eigen_rot_ANT(en_mo_1ppg,E(1),E(2),E(3),E(4),E(5),E
(6));

[di_rodf_1ppg]=eigen_rot_ANT(di_odf_1ppg,E(1),E(2),E(3),E(4),E(5)
,E(6));

[di_rmo_1ppg]=eigen_rot_ANT(di_mo_1ppg,E(1),E(2),E(3),E(4),E(5),E
(6));

    plotRotatedPoleFigures(pathname, samplename, ol_rodf_1ppg,
     ol_rmo_1ppg, 'Forsterite', h, 'grains1ppg');
    plotRotatedPoleFigures(pathname, samplename, en_rodf_1ppg,
     en_rmo_1ppg, 'Enstatite  Opx AV77', h, 'grains1ppg');
    plotRotatedPoleFigures(pathname, samplename, di_rodf_1ppg,
     di_rmo_1ppg, 'Diopside   CaMgSi2O6', h, 'grains1ppg');

    % Set colormap
    map = flipud(lbmap(64,'RedBlue'));

    % Plot Rotated Olivine ODF
    figure('position',[0, 0, 1024, 1024]);
    plotpdf(ol_rodf_1ppg, h, 'lower','contourf');
    title(['Contoured Rotated ODF 1ppg ' samplename ':
     Forsterite']);
    colorbar;
    colormap(map)
    mkdir([pathname samplename '_Exports']);
    epath = ([pathname samplename '_Exports']);
    export_fig([epath '/PF-grainsForsterite1ppg-
     RODF_contoured_color.pdf']);
    close;


    figure('position',[0, 0, 1024, 1024]);
    plotpdf(ol_rodf_1ppg, h, 'lower', 'contourf');
    title(['Rotated Contoured ODF 1ppg ' samplename ':
     Forsterite']);
```

```
colorbar;
mtexColorMap white2black
mkdir([pathname samplename '_Exports']);
epath = ([pathname samplename '_Exports']);
export_fig([epath '/PF-grainsForsterite1ppg-
 RODF_contoured_BW.pdf']);
close;

% Plot Rotated Enstatite ODF
figure('position',[0, 0, 1024, 1024]);
plotpdf(en_rodf_1ppg, h, 'lower','contourf');
title(['Contoured Rotated ODF 1ppg ' samplename ':
 Enstatite']);
colorbar;
colormap(map)
mkdir([pathname samplename '_Exports']);
epath = ([pathname samplename '_Exports']);
export_fig([epath '/PF-grainsEnstatite1ppg-
 RODF_contoured_color.pdf']);
close;

figure('position',[0, 0, 1024, 1024]);
plotpdf(en_rodf_1ppg, h, 'lower', 'contourf');
title(['Rotated Contoured ODF 1ppg' samplename ':
 Enstatite']);
colorbar;
mtexColorMap white2black
mkdir([pathname samplename '_Exports']);
epath = ([pathname samplename '_Exports']);
export_fig([epath '/PF-grainsEnstatite1ppg-
 RODF_contoured_BW.pdf']);
close;

% Plot Rotated Diopside ODF
figure('position',[0, 0, 1024, 1024]);
plotpdf(di_rodf_1ppg, h, 'lower','contourf');
title(['Contoured Rotated ODF 1ppg ' samplename ':
 Diopside']);
colorbar;
colormap(map)
mkdir([pathname samplename '_Exports']);
epath = ([pathname samplename '_Exports']);
export_fig([epath '/PF-grainsDiopside1ppg-
 RODF_contoured_color.pdf']);
close;

figure('position',[0, 0, 1024, 1024]);
plotpdf(di_rodf_1ppg, h, 'lower', 'contourf');
title(['Rotated Contoured ODF 1ppg ' samplename ':
 Diopside']);
colorbar;
```

```
    mtexColorMap white2black
    mkdir([pathname samplename '_Exports']);
    epath = ([pathname samplename '_Exports']);
    export_fig([epath '/PF-grainsDiopside1ppg-
      RODF_contoured_BW.pdf']);
    close;
    end

    %% Clear some variables
    clear samplename; clear s; clear l; clear E;
    end


%% Export misorientations to a .txt file, which will be used to
produce M-index histogram using a MATLAB GUI written by Skemer
(2007).

    uncorr_ol=angle(calcMisorientation(grains('Forsterite'),'unco
    rrelated'))
      /degree;
    dlmwrite(sprintf('%s Olivine M-index.txt', crcname),
    uncorr_ol,' ');

    uncorr_di=angle(calcMisorientation(grains('Diopside'),'uncorr
    elated'))
      /degree;
    dlmwrite(sprintf('%s Diopside M-index.txt', crcname),
    uncorr_di,' ');

    uncorr_en=angle(calcMisorientation(grains('Enstatite'),'uncor
    related'))
      /degree;
    dlmwrite(sprintf('%s Enstatite M-index.txt', crcname),
    uncorr_en,' ');

%% Calculate the J-index (Bunge, 1982) for olivine

    J_ol=textureindex(ol_odf);
    J_di=textureindex(di_odf);
    J_en=textureindex(en_odf);


%% End MTEX script
-----------------------------------------------------------------
```

Appendix C

<u>Volcanic Center</u>: Mount Aldaz, Usas Escarpment
<u>Xenolith ID</u>: AD6021-X01

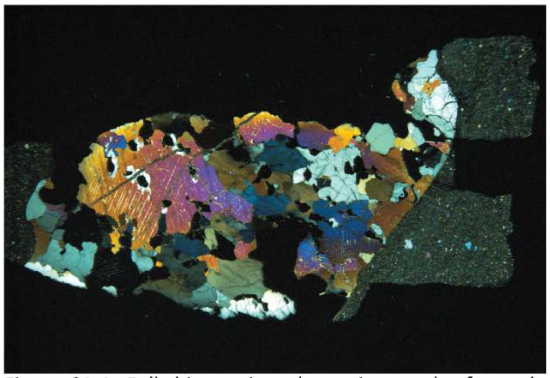

Figure C1-A. Full thin section photomicrograph of sample AD6021-X01 viewed through cross-polarized light (XPL).

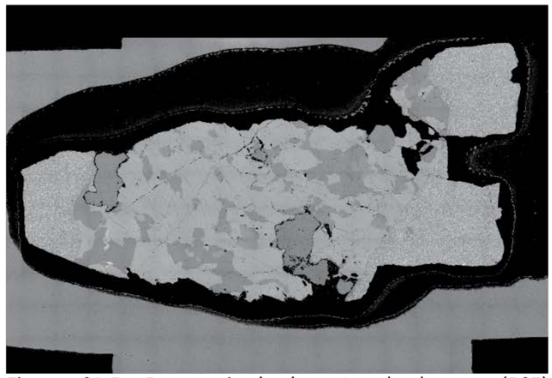

Figure C1-B. Panoramic back-scattered electron (BSE) image of sample AD6021-X01.

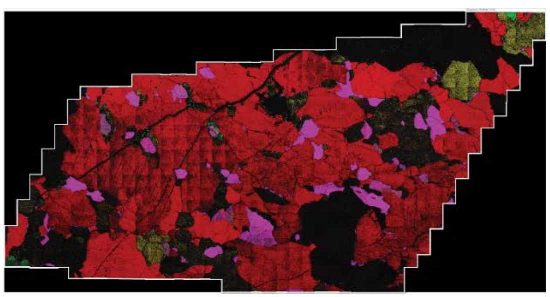

Figure C1-C. Phase map of sample AD6021-X01, generated by the AZtec software based on the EBSD dataset. Each mineralogical phase is represented by a different color: green is olivine, yellow is enstatite, red is diopside, and magenta is chromite. Black pixels are non-indexed portions of the map.

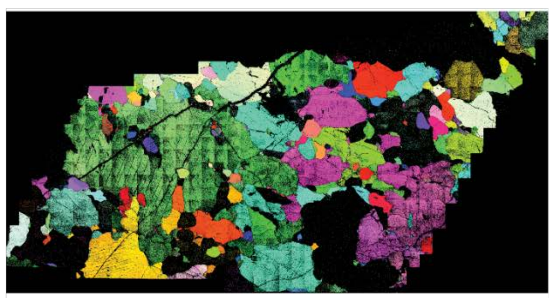

Figure C1-D. Inverse pole figure map of sample AD6021-X01, generated by the AZtec analysis software (v. 3.0 SP1). Coloring of crystallographic orientations are shown with respect to the x-direction. The olivine texture of this sample is not assessed because it is a pyroxenite.

<u>Volcanic Center</u>: Mount Aldaz, Usas Escarpment
<u>Xenolith ID</u>: AD6021-X02

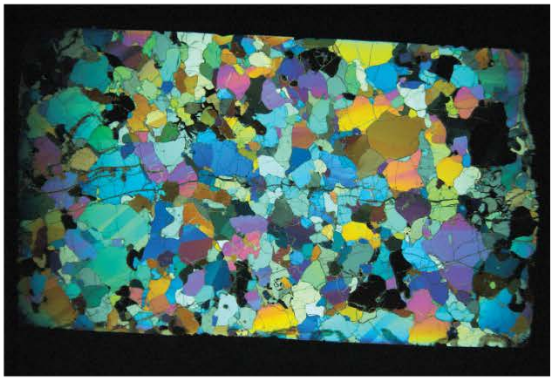

Figure C2-A. Full thin section photomicrograph of sample AD6021-X02 viewed through cross-polarized light (XPL).

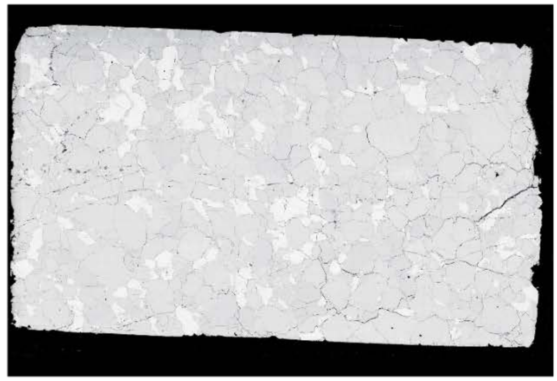

Figure C2-B. Panoramic back-scattered electron (BSE) image of sample AD6021-X02.

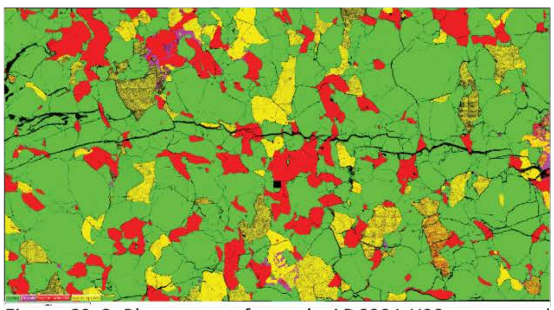

Figure C2-C. Phase map of sample AD6021-X02, generated by the AZtec software based on the EBSD dataset. Each mineralogical phase is represented by a different color: green is olivine, yellow is enstatite, red is diopside, and magenta is chromite. Black pixels are non-indexed portions of the map.

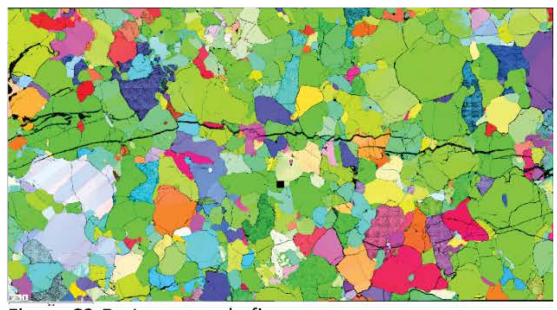

Figure C2-D. Inverse pole figure map of sample AD6021-X02, generated by the AZtec analysis software (v. 3.0 SP1). Coloring of crystallographic orientations are shown with respect to the x-direction (e.g., inverse pole figure of olivine, right).

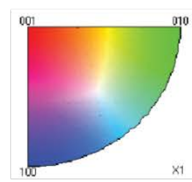

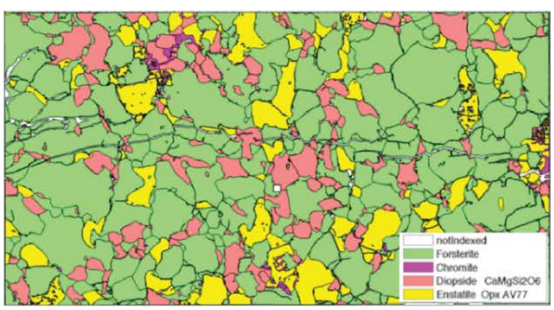

Figure C2-E. Phase map of sample AD6021-X02, generated using the MTEX toolbox (v. 3.5.0), shows the reconstructed grain set comprising the noise-reduced EBSD dataset. Non-indexed regions are not removed from the dataset during the production of this map.

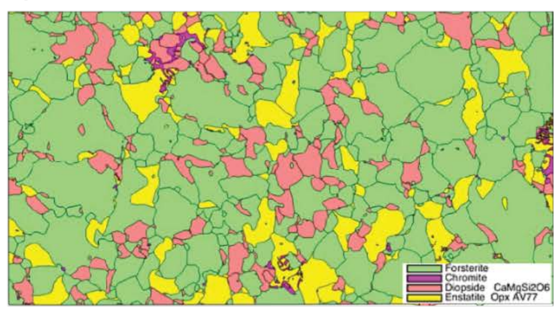

Figure C2-F. Phase map of sample AD6021-X02, generated using the MTEX toolbox (v. 3.5.0), shows the reconstructed grain set comprising the one-point-per-grain (1ppg) dataset. Non-indexed regions are removed from the dataset during the production of this map.

VOLCANIC CENTER: MOUNT CUMMING, EXECUTIVE COMMITTEE RANGE
XENOLITH ID: KSP89-181-X01

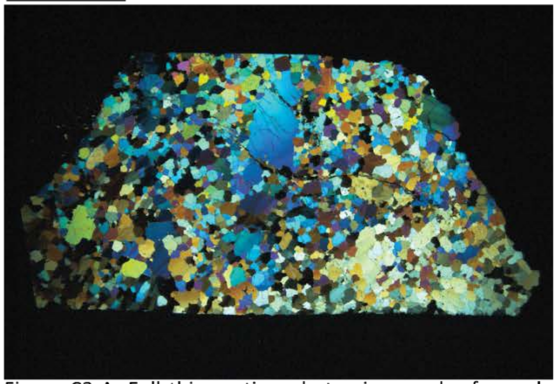

Figure C3-A. Full thin section photomicrograph of sample KSP89-181-X01 viewed through cross-polarized light (XPL).

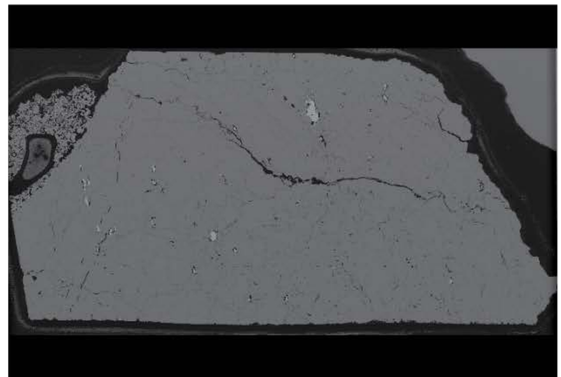

Figure C3-B. Panoramic back-scattered electron (BSE) image of sample KSP89-181-X01.

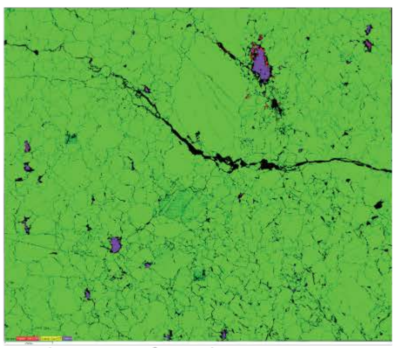

Figure C3-C. Phase map of sample KSP89-181-X01, generated by the AZtec software based on the EBSD dataset. Each mineralogical phase is represented by a different color: green is olivine, yellow is enstatite, red is diopside, and magenta is chromite. Black pixels are non-indexed portions of the map.

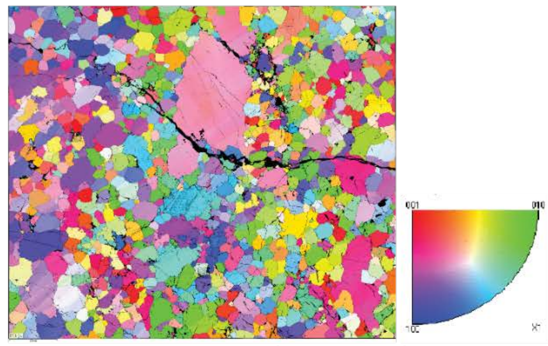

Figure C3-D. Inverse pole figure map of sample KSP89-181-X01, generated by the AZtec analysis software (v. 3.0 SP1). Coloring of crystallographic orientations are shown with respect to the x-direction (e.g., inverse pole figure of olivine, right).

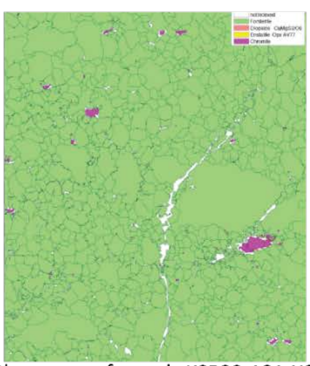

Figure C3-E. Phase map of sample KSP89-181-X01, generated using the MTEX toolbox (v. 3.5.0), shows the reconstructed grain set comprising the noise-reduced EBSD dataset. Non-indexed regions are not removed from the dataset during the production of this map.

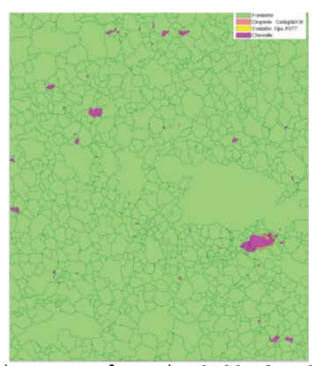

Figure C3-F. Phase map of sample KSP89-181-X01, generated using the MTEX toolbox (v. 3.5.0), shows the reconstructed grain set comprising the one-point-per-grain (1ppg) dataset. Non-indexed regions are removed from the dataset during the production of this map.

<u>Volcanic Center</u>: Mount Avers, Fosdick Mountains
<u>Xenolith ID</u>: FDM-AV01-X01

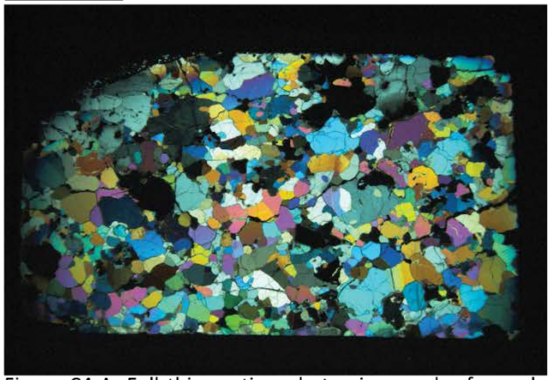

<u>Figure C4-A</u>. Full thin section photomicrograph of sample FDM-AV01-X01 viewed through cross-polarized light (XPL).

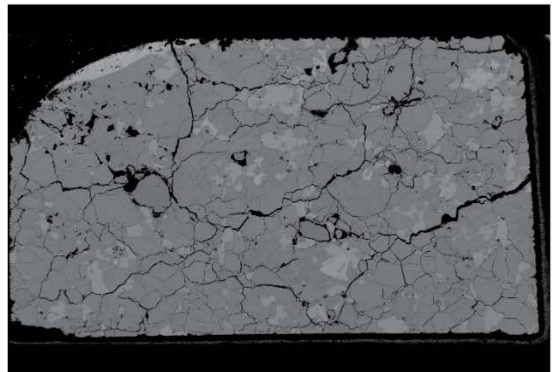

<u>Figure C4-B</u>. Panoramic back-scattered electron (BSE) image of sample FDM-AV01-X01.

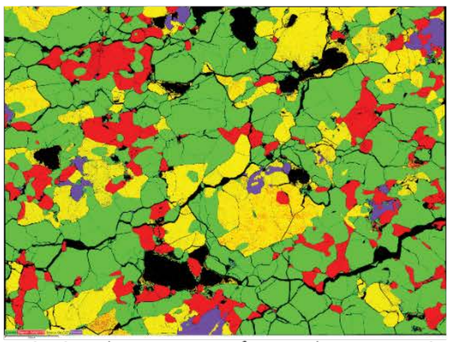

<u>Figure C4-C</u>. Phase map of sample FDM-AV01-X01, generated by the AZtec software based on the EBSD dataset. Each mineralogical phase is represented by a different color: green is olivine, yellow is enstatite, red is diopside, and magenta is chromite. Black pixels are non-indexed portions of the map.

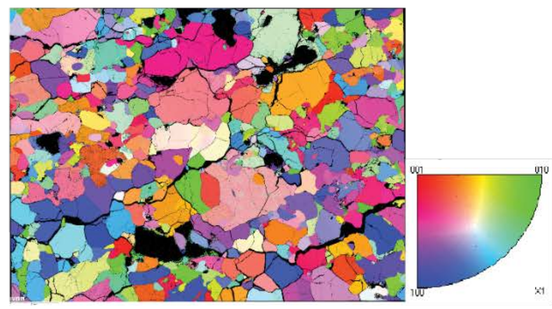

<u>Figure C4-D</u>. Inverse pole figure map of sample FDM-AV01-X01, generated by the AZtec analysis software (v. 3.0 SP1). Coloring of crystallographic orientations are shown with respect to the x-direction (e.g., inverse pole figure of olivine, right).

<u>Figure C4-E</u>. Phase map of sample FDM-AV01-X01, generated using the MTEX toolbox (v. 3.5.0), shows the reconstructed grain set comprising the noise-reduced EBSD dataset. Non-indexed regions are not removed from the dataset during the production of this map.

<u>Figure C4-F</u>. Phase map of sample FDM-AV01-X01, generated using the MTEX toolbox (v. 3.5.0), shows the reconstructed grain set comprising the one-point-per-grain (1ppg) dataset. Non-indexed regions are removed from the dataset during the production of this map.

Volcanic Center: Mount Avers - Bird Bluff, Fosdick Mountains
Xenolith ID: FDM-AVBB01

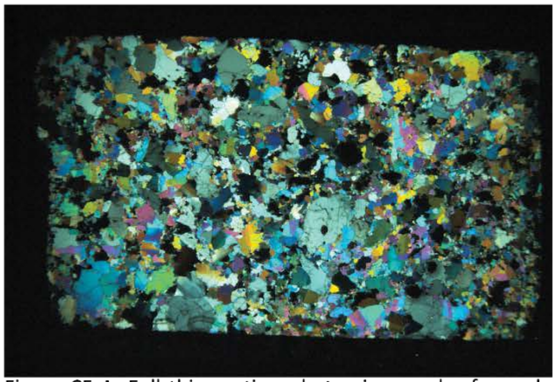

Figure C5-A. Full thin section photomicrograph of sample FDM-AVBB01 viewed through cross-polarized light (XPL).

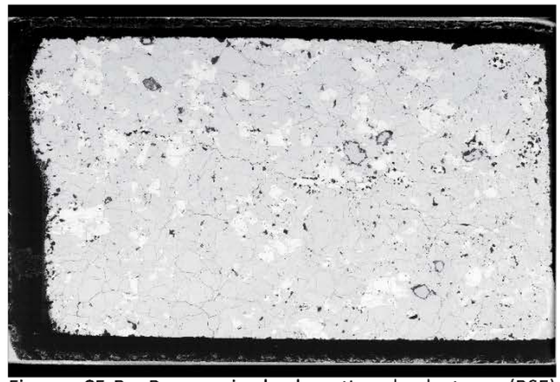

Figure C5-B. Panoramic back-scattered electron (BSE) image of sample FDM-AVBB01.

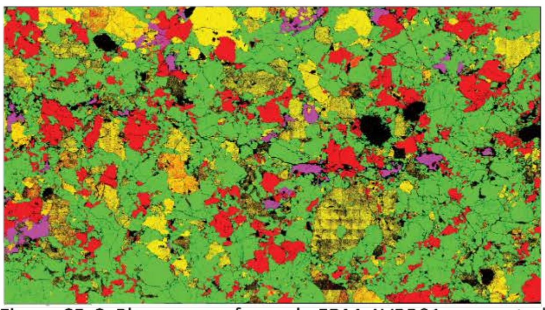

Figure C5-C. Phase map of sample FDM-AVBB01, generated by the AZtec software based on the EBSD dataset. Each mineralogical phase is represented by a different color: green is olivine, yellow is enstatite, red is diopside, and magenta is chromite. Black pixels are non-indexed portions of the map.

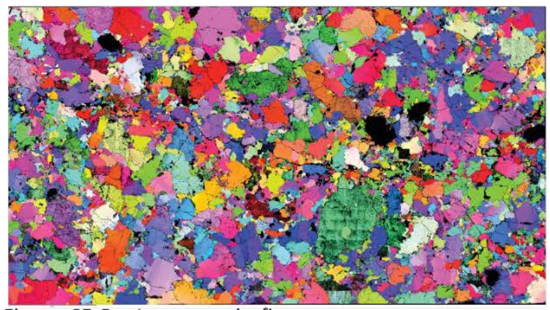

Figure C5-D. Inverse pole figure map of sample FDM-AVBB01, generated by the AZtec analysis software (v. 3.0 SP1). Coloring of crystallographic orientations are shown with respect to the x-direction (e.g., inverse pole figure of olivine, right).

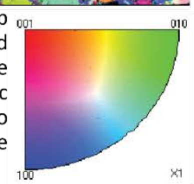

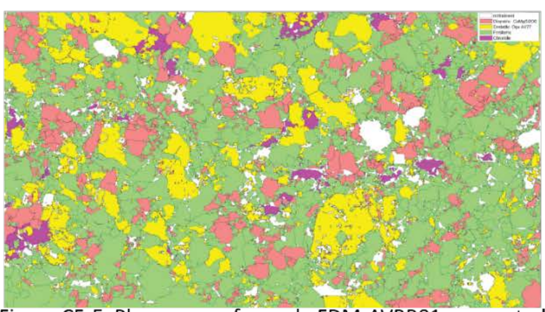

Figure C5-E. Phase map of sample FDM-AVBB01, generated using the MTEX toolbox (v. 3.5.0), shows the reconstructed grain set comprising the noise-reduced EBSD dataset. Non-indexed regions are not removed from the dataset during the production of this map.

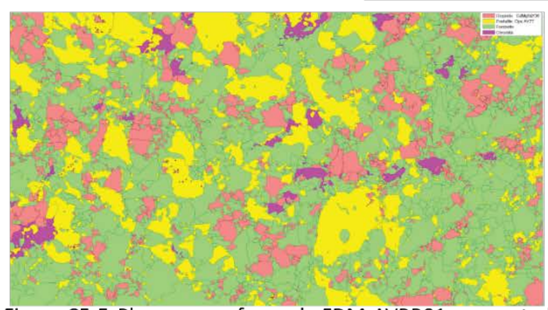

Figure C5-F. Phase map of sample FDM-AVBB01, generated using the MTEX toolbox (v. 3.5.0), shows the reconstructed grain set comprising the one-point-per-grain (1ppg) dataset. Non-indexed regions are removed from the dataset during the production of this map.

<u>VOLCANIC CENTER</u>: MOUNT AVERS - BIRD BLUFF, FOSDICK MOUNTAINS
<u>XENOLITH ID</u>: FDM-AVBB02

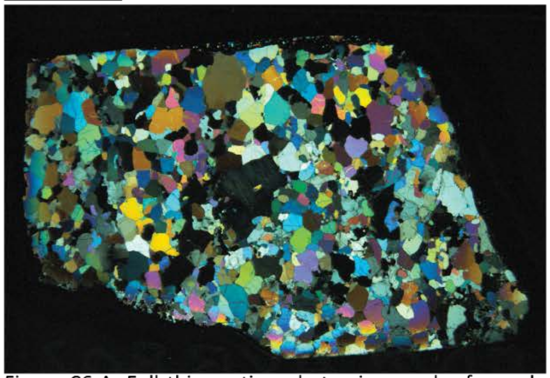

<u>Figure C6-A</u>. Full thin section photomicrograph of sample FDM-AVBB02 viewed through cross-polarized light (XPL).

<u>Figure C6-B</u>. Panoramic back-scattered electron (BSE) image of sample FDM-AVBB02.

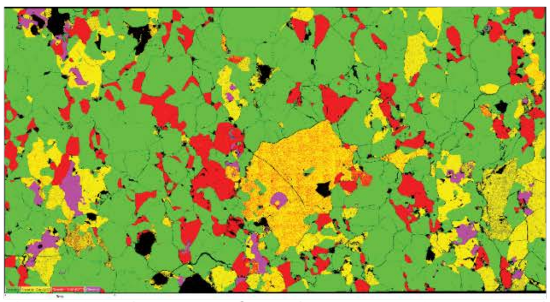

<u>Figure C6-C</u>. Phase map of sample FDM-AVBB02, generated by the AZtec software based on the EBSD dataset. Each mineralogical phase is represented by a different color: green is olivine, yellow is enstatite, red is diopside, and magenta is chromite. Black pixels are non-indexed portions of the map.

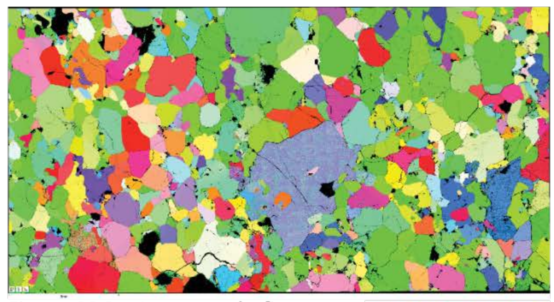

<u>Figure C6-D</u>. Inverse pole figure map of sample FDM-AVBB02, generated by the AZtec analysis software (v. 3.0 SP1). Coloring of crystallographic orientations are shown with respect to the x-direction (e.g., inverse pole figure of olivine, right).

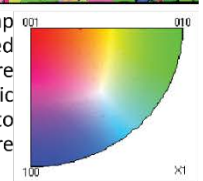

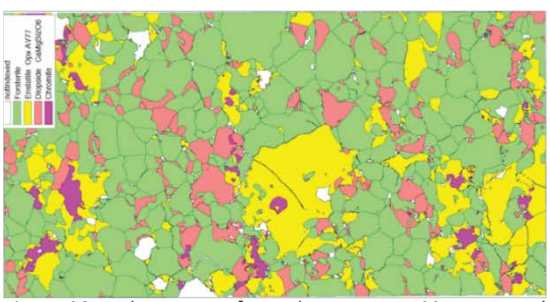

<u>Figure C6-E</u>. Phase map of sample FDM-AVBB02, generated using the MTEX toolbox (v. 3.5.0), shows the reconstructed grain set comprising the noise-reduced EBSD dataset. Non-indexed regions are not removed from the dataset during the production of this map.

<u>Figure C6-F</u>. Phase map of sample FDM-AVBB02, generated using the MTEX toolbox (v. 3.5.0), shows the reconstructed grain set comprising the one-point-per-grain (1ppg) dataset. Non-indexed regions are removed from the dataset during the production of this map.

Volcanic Center: Mount Avers - Bird Bluff, Fosdick Mountains

Xenolith ID: FDM-AVBB03

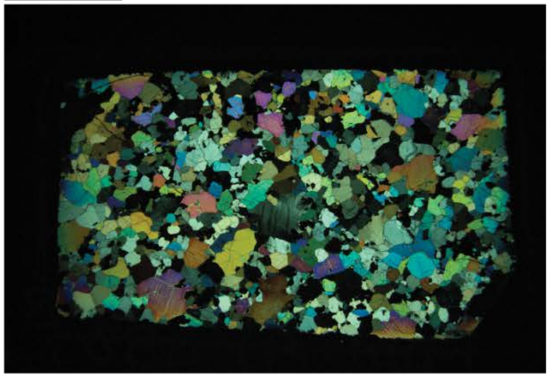

Figure C7-A. Full thin section photomicrograph of sample FDM-AVBB03 viewed through cross-polarized light (XPL).

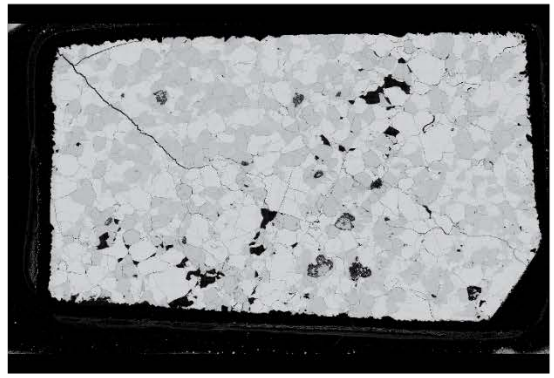

Figure C7-B. Panoramic back-scattered electron (BSE) image of sample FDM-AVBB03.

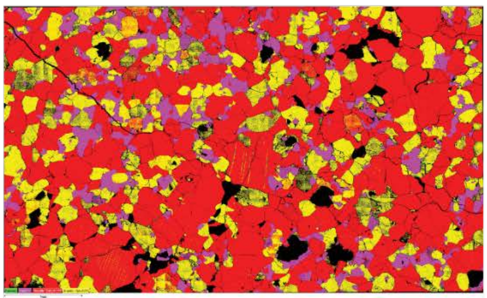

Figure C7-C. Phase map of sample FDM-AVBB03, generated by the AZtec software based on the EBSD dataset. Each mineralogical phase is represented by a different color: green is olivine, yellow is enstatite, red is diopside, and magenta is chromite. Black pixels are non-indexed portions of the map.

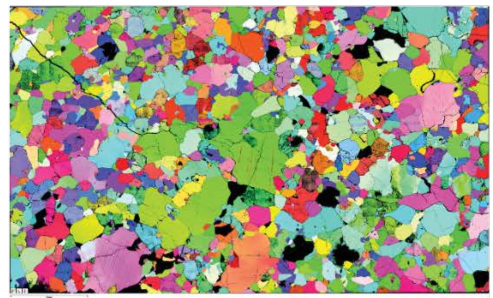

Figure C7-D. Inverse pole figure map of sample FDM-AVBB03, generated by the AZtec analysis software (v. 3.0 SP1). Coloring of crystallographic orientations are shown with respect to the x-direction. The olivine texture of this sample is not assessed because it is a pyroxenite.

Volcanic Center: Mount Avers - Bird Bluff, Fosdick Mountains

Xenolith ID: FDM-AVBB04

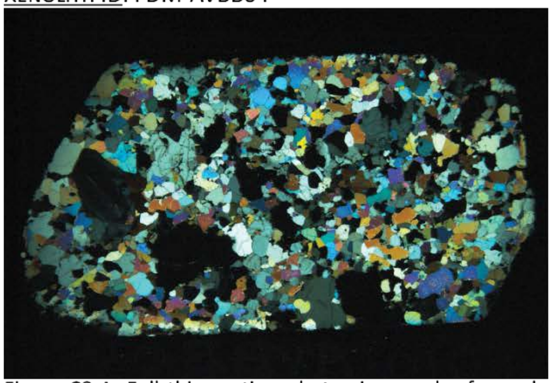

Figure C8-A. Full thin section photomicrograph of sample FDM-AVBB04 viewed through cross-polarized light (XPL).

Figure C8-B. Panoramic back-scattered electron (BSE) image of sample FDM-AVBB04.

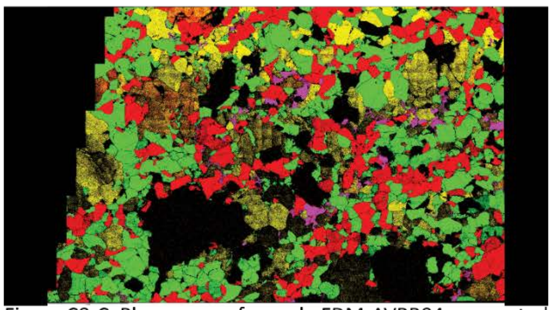

Figure C8-C. Phase map of sample FDM-AVBB04, generated by the AZtec software based on the EBSD dataset. Each mineralogical phase is represented by a different color: green is olivine, yellow is enstatite, red is diopside, and magenta is chromite. Black pixels are non-indexed portions of the map.

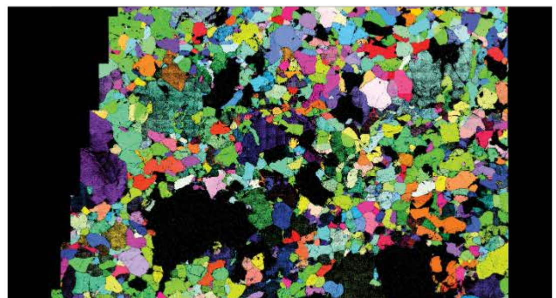

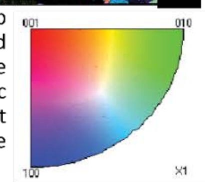

Figure C8-D. Inverse pole figure map of sample FDM-AVBB04, generated by the AZtec analysis software (v. 3.0 SP1). Coloring of crystallographic orientations are shown with respect to the x-direction (e.g., inverse pole figure of olivine, right).

Figure C8-E. Phase map of sample FDM-AVBB04, generated using the MTEX toolbox (v. 3.5.0), shows the reconstructed grain set comprising the noise-reduced EBSD dataset. Non-indexed regions are not removed from the dataset during the production of this map.

Figure C8-F. Phase map of sample FDM-AVBB04, generated using the MTEX toolbox (v. 3.5.0), shows the reconstructed grain set comprising the one-point-per-grain (1ppg) dataset. Non-indexed regions are removed from the dataset during the production of this map.

VOLCANIC CENTER: MOUNT AVERS - BIRD BLUFF, FOSDICK MOUNTAINS

XENOLITH ID: FDM-AVBB05

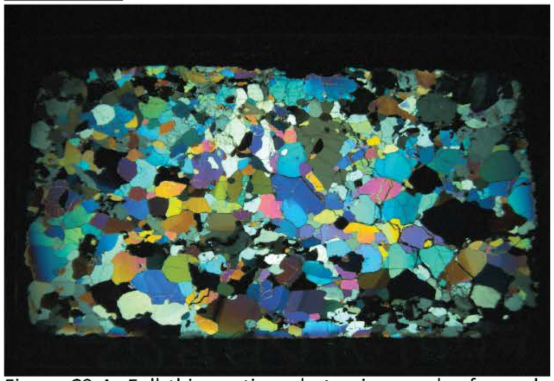

Figure C9-A. Full thin section photomicrograph of sample FDM-AVBB05 viewed through cross-polarized light (XPL).

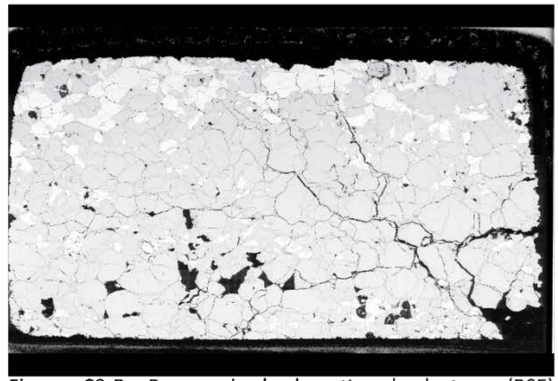

Figure C9-B. Panoramic back-scattered electron (BSE) image of sample FDM-AVBB05.

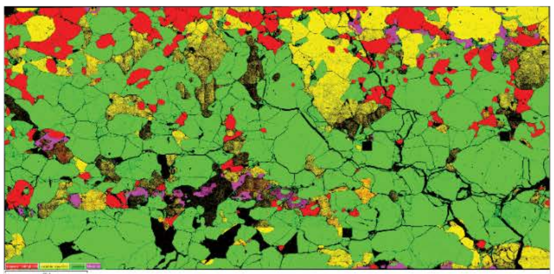

Figure C9-C. Phase map of sample FDM-AVBB05, generated by the AZtec software based on the EBSD dataset. Each mineralogical phase is represented by a different color: green is olivine, yellow is enstatite, red is diopside, and magenta is chromite. Black pixels are non-indexed portions of the map.

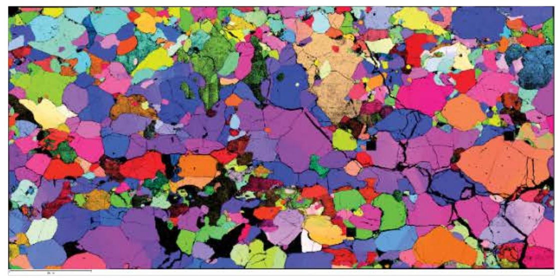

Figure C9-D. Inverse pole figure map of sample FDM-AVBB05, generated by the AZtec analysis software (v. 3.0 SP1). Coloring of crystallographic orientations are shown with respect to the x-direction (e.g., inverse pole figure of olivine, right).

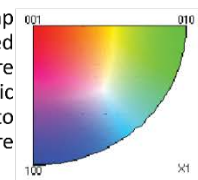

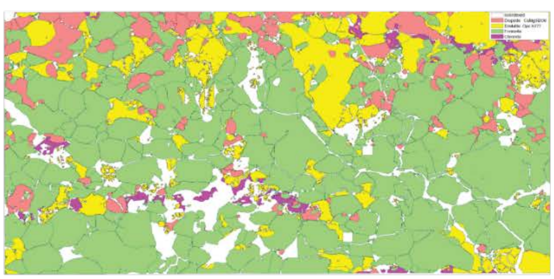

Figure C9-E. Phase map of sample FDM-AVBB05, generated using the MTEX toolbox (v. 3.5.0), shows the reconstructed grain set comprising the noise-reduced EBSD dataset. Non-indexed regions are not removed from the dataset during the production of this map.

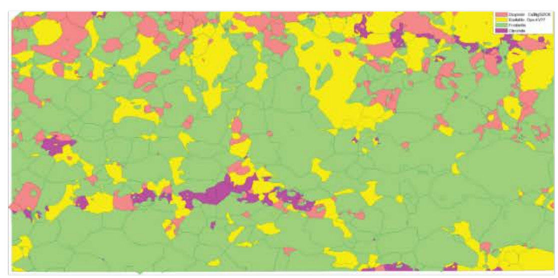

Figure C9-F. Phase map of sample FDM-AVBB05, generated using the MTEX toolbox (v. 3.5.0), shows the reconstructed grain set comprising the one-point-per-grain (1ppg) dataset. Non-indexed regions are removed from the dataset during the production of this map.

Volcanic Center: Mount Avers - Bird Bluff, Fosdick Mountains

Xenolith ID: FDM-AVBB06

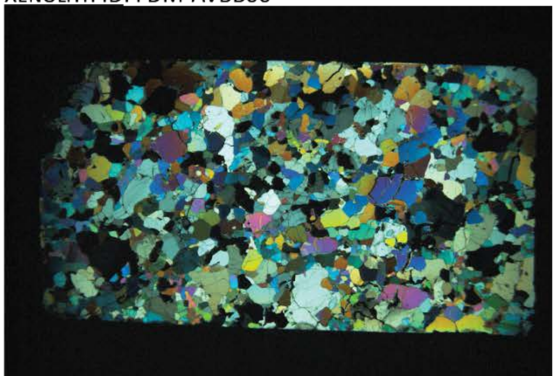

Figure C10-A. Full thin section photomicrograph of sample FDM-AVBB06 viewed through cross-polarized light (XPL).

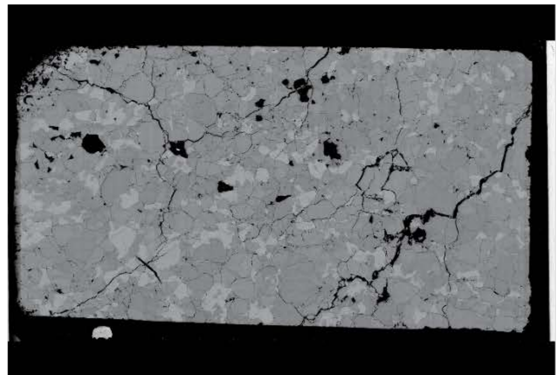

Figure C10-B. Panoramic back-scattered electron (BSE) image of sample FDM-AVBB06.

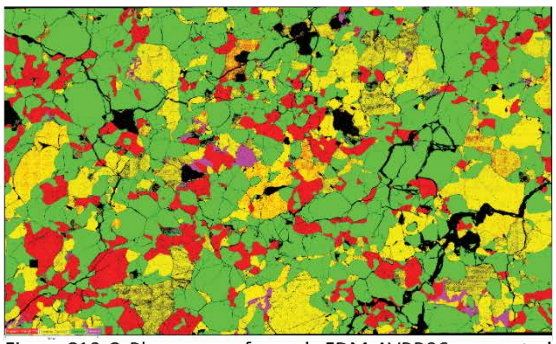

Figure C10-C. Phase map of sample FDM-AVBB06, generated by the AZtec software based on the EBSD dataset. Each mineralogical phase is represented by a different color: green is olivine, yellow is enstatite, red is diopside, and magenta is chromite. Black pixels are non-indexed portions of the map.

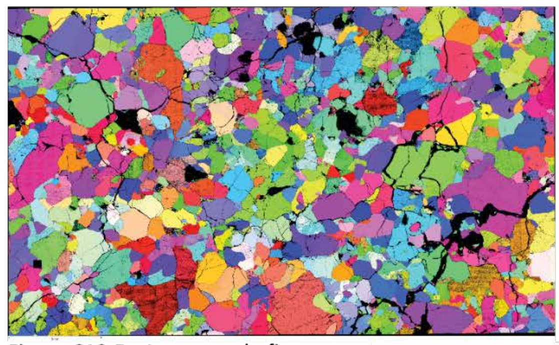

Figure C10-D. Inverse pole figure map of sample FDM-AVBB06, generated by the AZtec analysis software (v. 3.0 SP1). Coloring of crystallographic orientations are shown with respect to the x-direction (e.g., inverse pole figure of olivine, right).

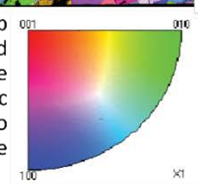

Figure C10-E. Phase map of sample FDM-AVBB06, generated using the MTEX toolbox (v. 3.5.0), shows the reconstructed grain set comprising the noise-reduced EBSD dataset. Non-indexed regions are not removed from the dataset during the production of this map.

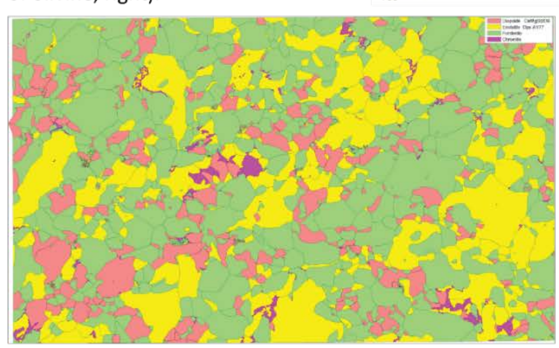

Figure C10-F. Phase map of sample FDM-AVBB06, generated using the MTEX toolbox (v. 3.5.0), shows the reconstructed grain set comprising the one-point-per-grain (1ppg) dataset. Non-indexed regions are removed from the dataset during the production of this map.

VOLCANIC CENTER: MOUNT AVERS - BIRD BLUFF, FOSDICK MOUNTAINS
XENOLITH ID: FDM-AVBB07

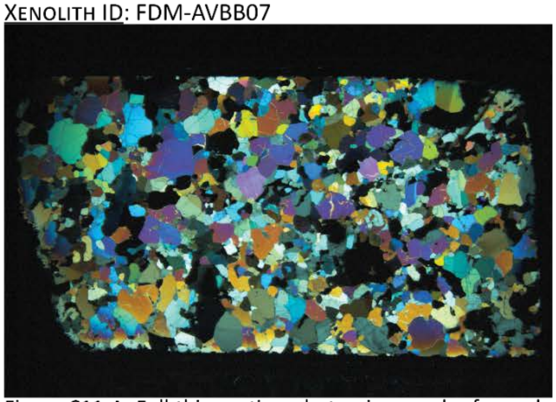

Figure C11-A. Full thin section photomicrograph of sample FDM-AVBB07 viewed through cross-polarized light (XPL).

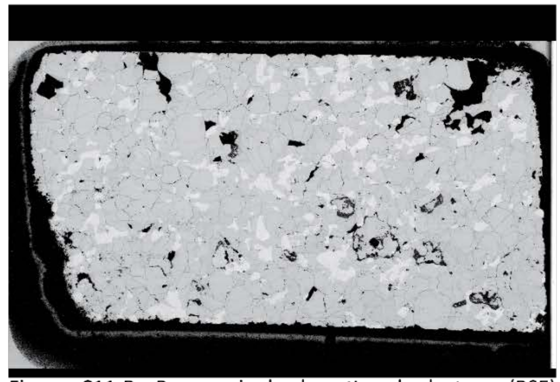

Figure C11-B. Panoramic back-scattered electron (BSE) image of sample FDM-AVBB07.

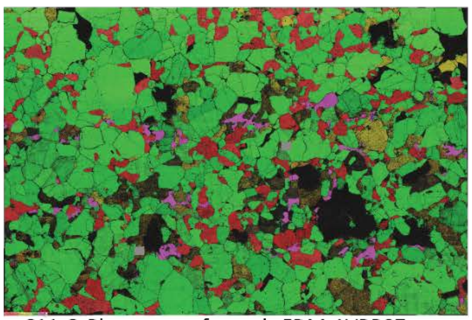

Figure C11-C. Phase map of sample FDM-AVBB07, generated by the AZtec software based on the EBSD dataset. Each mineralogical phase is represented by a different color: green is olivine, yellow is enstatite, red is diopside, and magenta is chromite. Black pixels are non-indexed portions of the map.

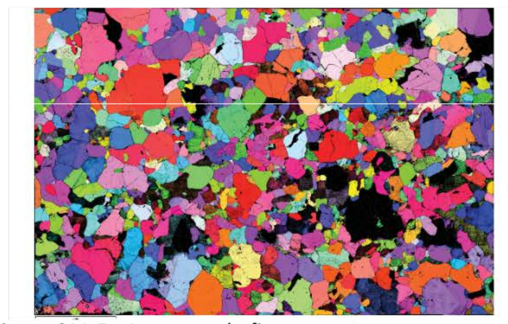

Figure C11-D. Inverse pole figure map of sample FDM-AVBB07, generated by the AZtec analysis software (v. 3.0 SP1). Coloring of crystallographic orientations are shown with respect to the x-direction (e.g., inverse pole figure of olivine, right).

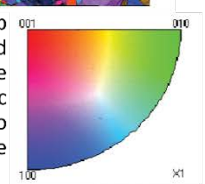

Figure C11-E. Phase map of sample FDM-AVBB07, generated using the MTEX toolbox (v. 3.5.0), shows the reconstructed grain set comprising the noise-reduced EBSD dataset. Non-indexed regions are not removed from the dataset during the production of this map.

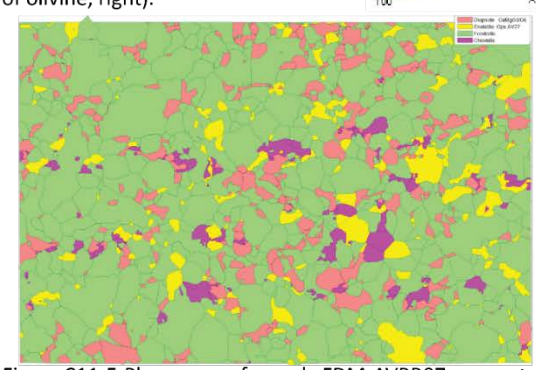

Figure C11-F. Phase map of sample FDM-AVBB07, generated using the MTEX toolbox (v. 3.5.0), shows the reconstructed grain set comprising the one-point-per-grain (1ppg) dataset. Non-indexed regions are removed from the dataset during the production of this map.

Volcanic Center: Mount Avers - Bird Bluff, Fosdick Mountains

Xenolith ID: FDM-AVBB08

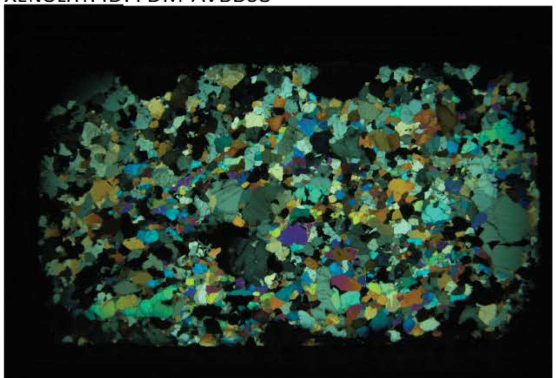

Figure C12-A. Full thin section photomicrograph of sample FDM-AVBB08 viewed through cross-polarized light (XPL).

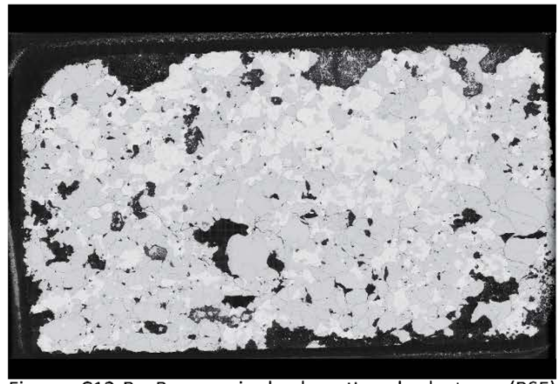

Figure C12-B. Panoramic back-scattered electron (BSE) image of sample FDM-AVBB08.

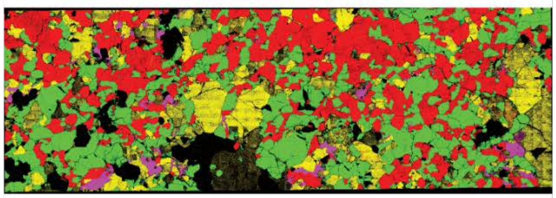

Figure C12-C. Phase map of sample FDM-AVBB08, generated by the AZtec software based on the EBSD dataset. Each mineralogical phase is represented by a different color: green is olivine, yellow is enstatite, red is diopside, and magenta is chromite. Black pixels are non-indexed portions of the map.

Figure C12-D. Inverse pole figure map of sample FDM-AVBB08, generated by the AZtec analysis software (v. 3.0 SP1). Coloring of crystallographic orientations are shown with respect to the x-direction (e.g., inverse pole figure of olivine, right).

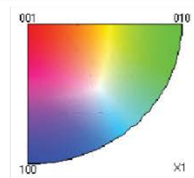

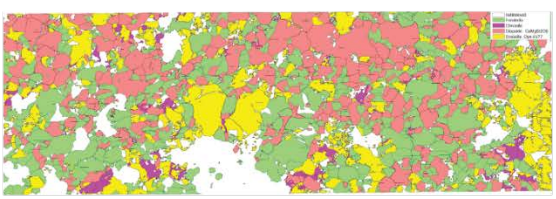

Figure C12-E. Phase map of sample FDM-AVBB08, generated using the MTEX toolbox (v. 3.5.0), shows the reconstructed grain set comprising the noise-reduced EBSD dataset. Non-indexed regions are not removed from the dataset during the production of this map.

Figure C12-F. Phase map of sample FDM-AVBB08, generated using the MTEX toolbox (v. 3.5.0), shows the reconstructed grain set comprising the one-point-per-grain (1ppg) dataset. Non-indexed regions are removed from the dataset during the production of this map.

VOLCANIC CENTER: BIRD BLUFF, FOSDICK MOUNTAINS
XENOLITH ID: FDM-BB01-X01

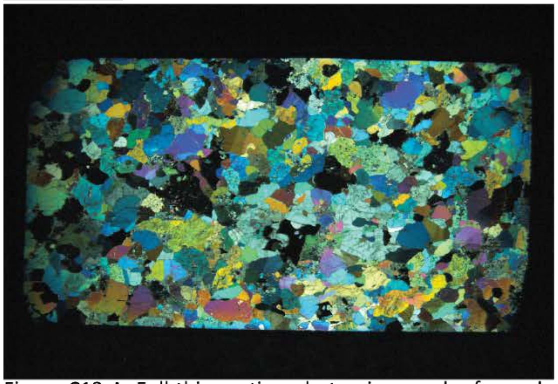

Figure C13-A. Full thin section photomicrograph of sample FDM-BB01-X01 viewed through cross-polarized light (XPL).

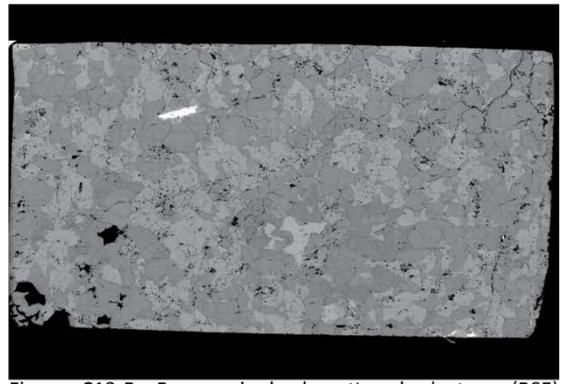

Figure C13-B. Panoramic back-scattered electron (BSE) image of sample FDM-BB01-X01.

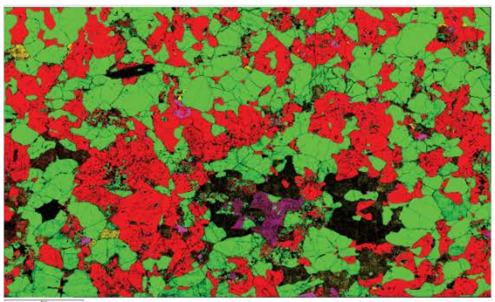

Figure C13-C. Phase map of sample FDM-BB01-X01, generated by the AZtec software based on the EBSD dataset. Each mineralogical phase is represented by a different color: green is olivine, yellow is enstatite, red is diopside, and magenta is chromite. Black pixels are non-indexed portions of the map.

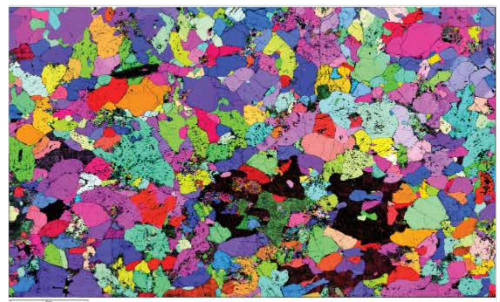

Figure C13-D. Inverse pole figure map of sample FDM-BB01-X01, generated by the AZtec analysis software (v. 3.0 SP1). Coloring of crystallographic orientations are shown with respect to the x-direction (e.g., inverse pole figure of olivine, right).

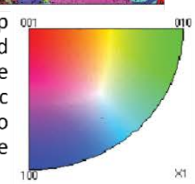

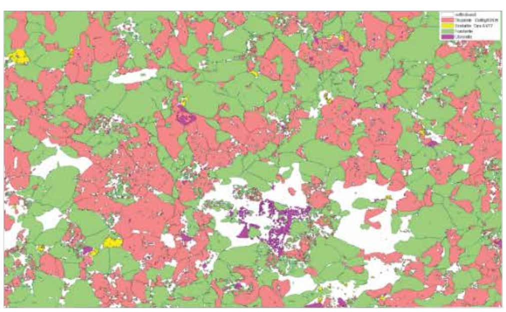

Figure C13-E. Phase map of sample FDM-BB01-X01, generated using the MTEX toolbox (v. 3.5.0), shows the reconstructed grain set comprising the noise-reduced EBSD dataset. Non-indexed regions are not removed from the dataset during the production of this map.

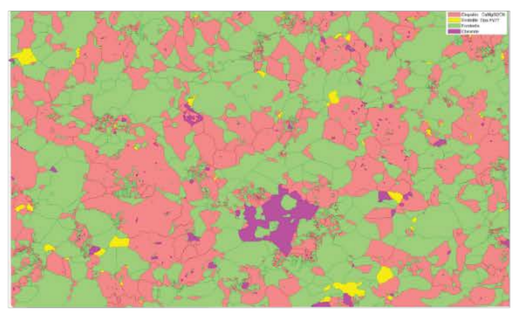

Figure C13-F. Phase map of sample FDM-BB01-X01, generated using the MTEX toolbox (v. 3.5.0), shows the reconstructed grain set comprising the one-point-per-grain (1ppg) dataset. Non-indexed regions are removed from the dataset during the production of this map.

VOLCANIC CENTER: BIRD BLUFF, FOSDICK MOUNTAINS
XENOLITH ID: FDM-BB02-X01

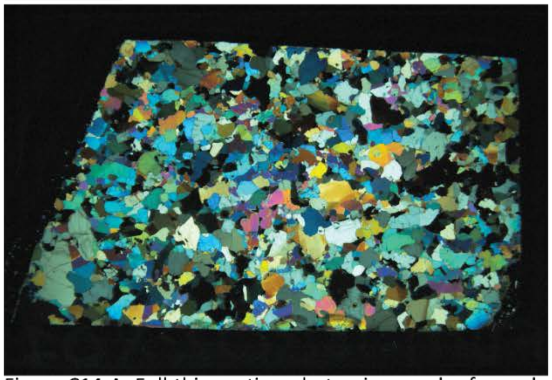

Figure C14-A. Full thin section photomicrograph of sample FDM-BB02-X01 viewed through cross-polarized light (XPL).

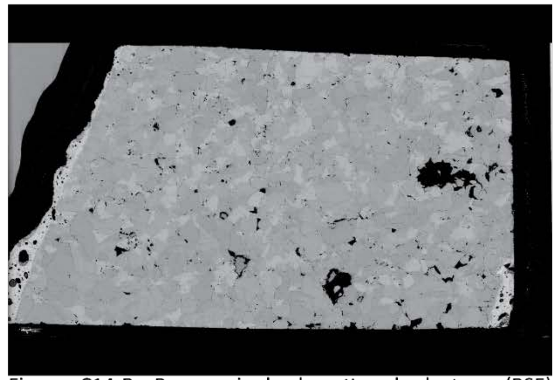

Figure C14-B. Panoramic back-scattered electron (BSE) image of sample FDM-BB02-X01.

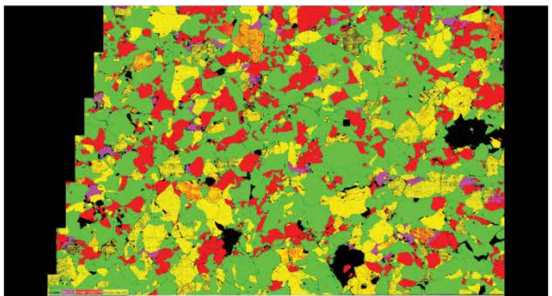

Figure C14-C. Phase map of sample FDM-BB02-X01, generated by the AZtec software based on the EBSD dataset. Each mineralogical phase is represented by a different color: green is olivine, yellow is enstatite, red is diopside, and magenta is chromite. Black pixels are non-indexed portions of the map.

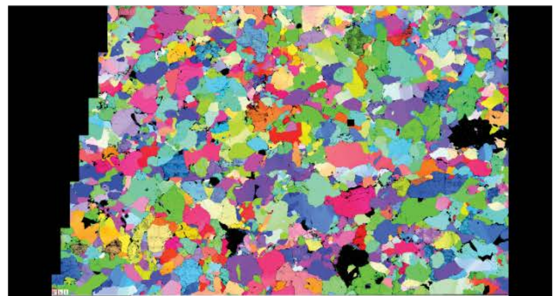

Figure C14-D. Inverse pole figure map of sample FDM-BB02-X01, generated by the AZtec analysis software (v. 3.0 SP1). Coloring of crystallographic orientations are shown with respect to the x-direction (e.g., inverse pole figure of olivine, right).

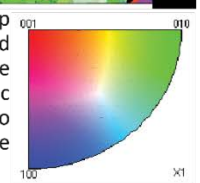

Figure C14-E. Phase map of sample FDM-BB02-X01, generated using the MTEX toolbox (v. 3.5.0), shows the reconstructed grain set comprising the noise-reduced EBSD dataset. Non-indexed regions are not removed from the dataset during the production of this map.

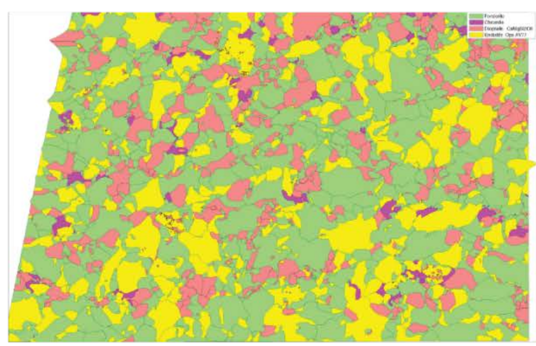

Figure C14-F. Phase map of sample FDM-BB02-X01, generated using the MTEX toolbox (v. 3.5.0), shows the reconstructed grain set comprising the one-point-per-grain (1ppg) dataset. Non-indexed regions are removed from the dataset during the production of this map.

VOLCANIC CENTER: BIRD BLUFF, FOSDICK MOUNTAINS
XENOLITH ID: FDM-BB03-X01

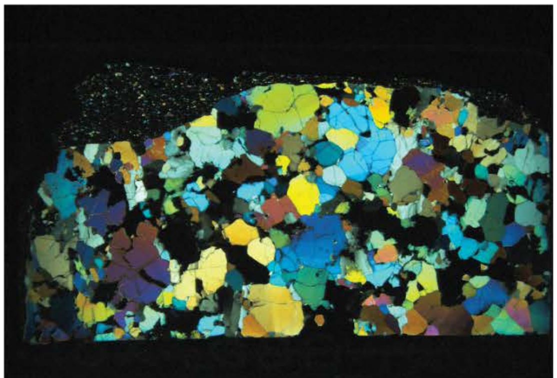

Figure C15-A. Full thin section photomicrograph of sample FDM-BB03-X01 viewed through cross-polarized light (XPL).

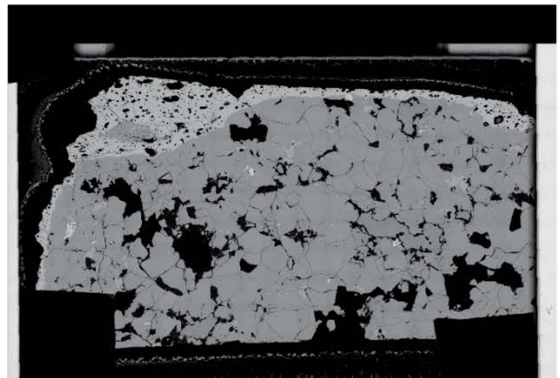

Figure C15-B. Panoramic back-scattered electron (BSE) image of sample FDM-BB03-X01.

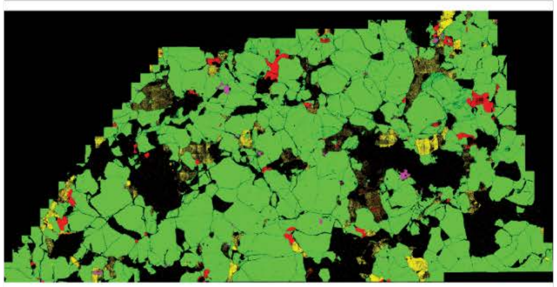

Figure C15-C. Phase map of sample FDM-BB03-X01, generated by the AZtec software based on the EBSD dataset. Each mineralogical phase is represented by a different color: green is olivine, yellow is enstatite, red is diopside, and magenta is chromite. Black pixels are non-indexed portions of the map.

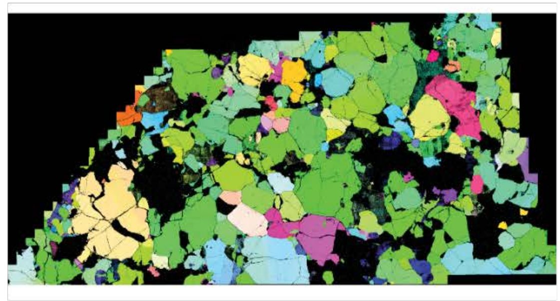

Figure C15-D. Inverse pole figure map of sample FDM-BB03-X01, generated by the AZtec analysis software (v. 3.0 SP1). Coloring of crystallographic orientations are shown with respect to the x-direction (e.g., inverse pole figure of olivine, right).

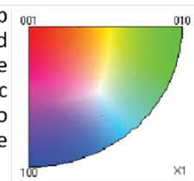

Figure C15-E. Phase map of sample FDM-BB03-X01, generated using the MTEX toolbox (v. 3.5.0), shows the reconstructed grain set comprising the noise-reduced EBSD dataset. Non-indexed regions are not removed from the dataset during the production of this map.

Figure C15-F. Phase map of sample FDM-BB03-X01, generated using the MTEX toolbox (v. 3.5.0), shows the reconstructed grain set comprising the one-point-per-grain (1ppg) dataset. Non-indexed regions are removed from the dataset during the production of this map.

<u>Volcanic Center</u>: Bird Bluff, Fosdick Mountains
<u>Xenolith ID</u>: FDM-BB04-X01

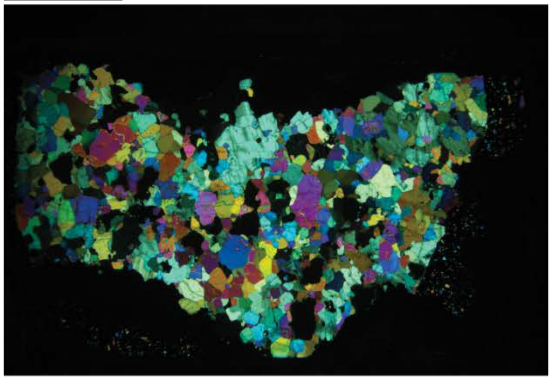

<u>Figure C16-A</u>. Full thin section photomicrograph of sample FDM-BB04-X01 viewed through cross-polarized light (XPL).

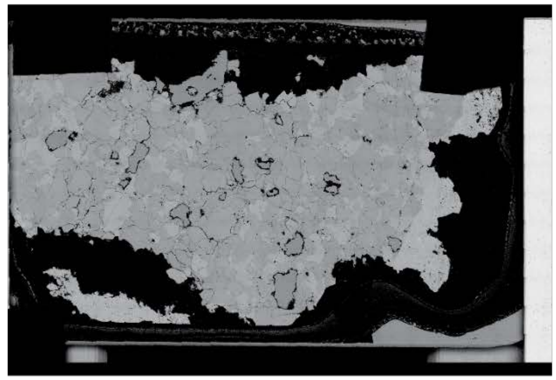

<u>Figure C16-B</u>. Panoramic back-scattered electron (BSE) image of sample FDM-BB04-X01.

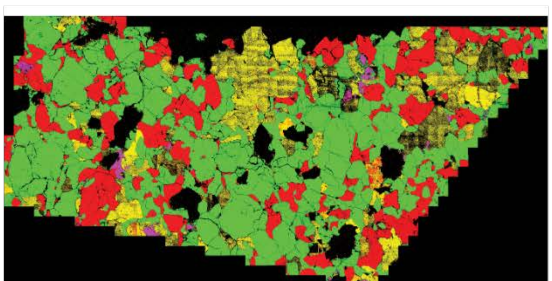

<u>Figure C16-C</u>. Phase map of sample FDM-BB04-X01, generated by the AZtec software based on the EBSD dataset. Each mineralogical phase is represented by a different color: green is olivine, yellow is enstatite, red is diopside, and magenta is chromite. Black pixels are non-indexed portions of the map.

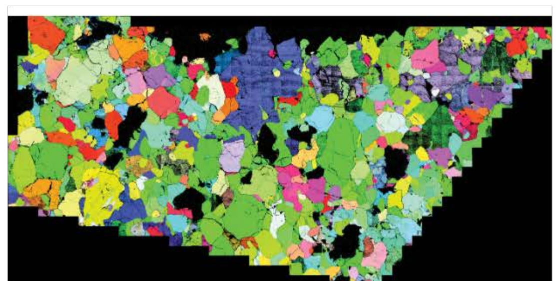

<u>Figure C16-D</u>. Inverse pole figure map of sample FDM-BB04-X01, generated by the AZtec analysis software (v. 3.0 SP1). Coloring of crystallographic orientations are shown with respect to the x-direction (e.g., inverse pole figure of olivine, right).

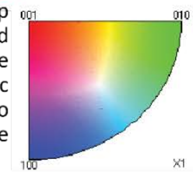

<u>Volcanic Center</u>: Demas Bluff, Fosdick Mountains
<u>Xenolith ID</u>: FDM-DB01-X01

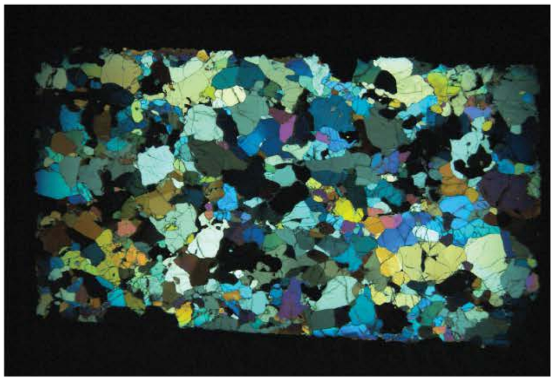

<u>Figure C17-A</u>. Full thin section photomicrograph of sample FDM-DB01-X01 viewed through cross-polarized light (XPL).

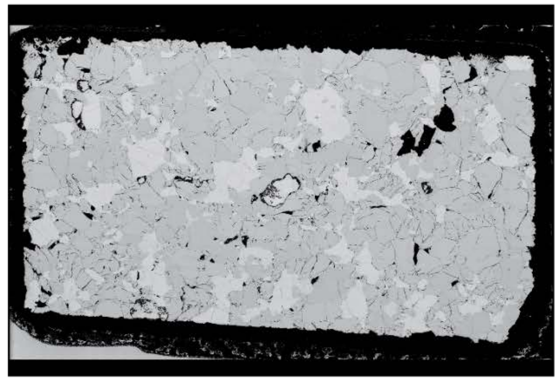

<u>Figure C17-B</u>. Panoramic back-scattered electron (BSE) image of sample FDM-DB01-X01.

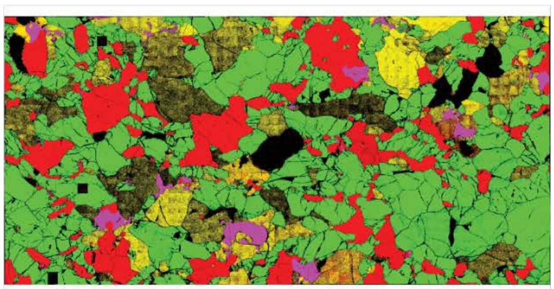

<u>Figure C17-C</u>. Phase map of sample FDM-DB01-X01, generated by the AZtec software based on the EBSD dataset. Each mineralogical phase is represented by a different color: green is olivine, yellow is enstatite, red is diopside, and magenta is chromite. Black pixels are non-indexed portions of the map.

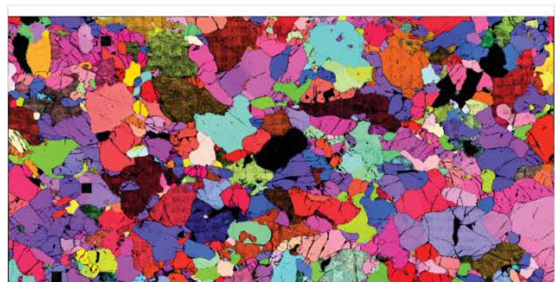

<u>Figure C17-D</u>. Inverse pole figure map of sample FDM-DB01-X01, generated by the AZtec analysis software (v. 3.0 SP1). Coloring of crystallographic orientations are shown with respect to the x-direction (e.g., inverse pole figure of olivine,

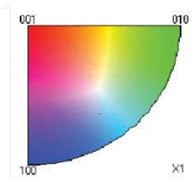

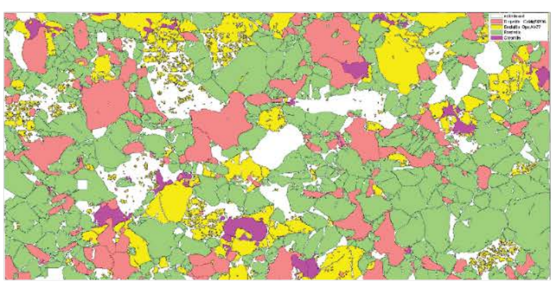

<u>Figure C17-E</u>. Phase map of sample FDM-DB01-X01, generated using the MTEX toolbox (v. 3.5.0), shows the reconstructed grain set comprising the noise-reduced EBSD dataset. Non-indexed regions are not removed from the dataset during the production of this map.

<u>Figure C17-F</u>. Phase map of sample FDM-DB01-X01, generated using the MTEX toolbox (v. 3.5.0), shows the reconstructed grain set comprising the one-point-per-grain (1ppg) dataset. Non-indexed regions are removed from the dataset during the production of this map.

Volcanic Center: Demas Bluff, Fosdick Mountains
Xenolith ID: FDM-DB02-X01

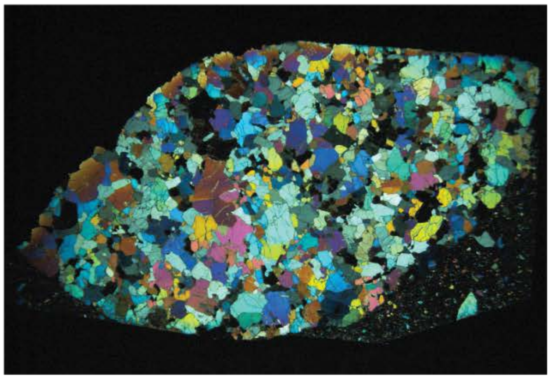

Figure C18-A. Full thin section photomicrograph of sample FDM-DB02-X01 viewed through cross-polarized light (XPL).

Figure C18-B. Panoramic back-scattered electron (BSE) image of sample FDM-DB02-X01.

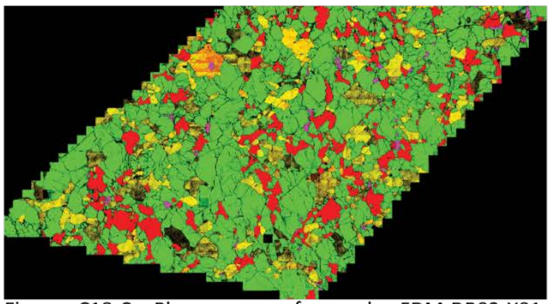

Figure C18-C. Phase map of sample FDM-DB02-X01, generated by the AZtec software based on the EBSD dataset. Each mineralogical phase is represented by a different color: green is olivine, yellow is enstatite, red is diopside, and magenta is chromite. Black pixels are non-indexed portions of the map.

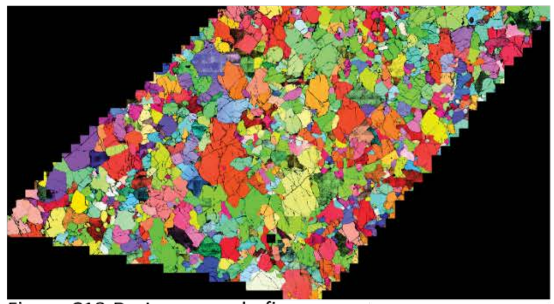

Figure C18-D. Inverse pole figure map of sample FDM-DB02-X01, generated by the AZtec analysis software (v. 3.0 SP1). Coloring of crystallographic orientations are shown with respect to the x-direction (e.g., inverse pole figure of olivine, right).

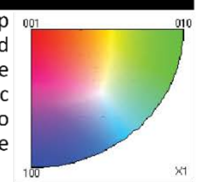

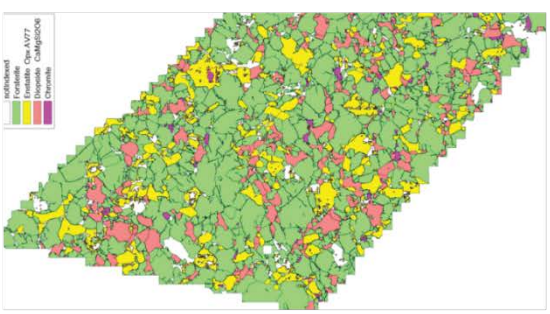

Figure C18-E. Phase map of sample FDM-DB02-X01, generated using the MTEX toolbox (v. 3.5.0), shows the reconstructed grain set comprising the noise-reduced EBSD dataset. Non-indexed regions are not removed from the dataset during the production of this map.

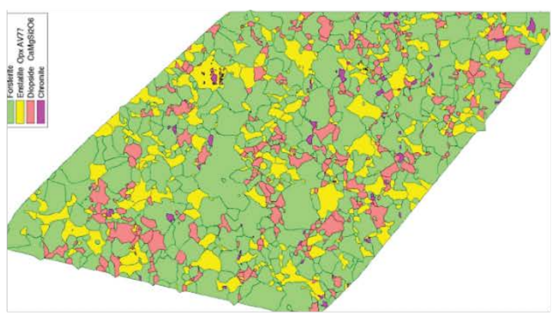

Figure C18-F. Phase map of sample FDM-DB02-X01, generated using the MTEX toolbox (v. 3.5.0), shows the reconstructed grain set comprising the one-point-per-grain (1ppg) dataset. Non-indexed regions are removed from the dataset during the production of this map.

Volcanic Center: Demas Bluff, Fosdick Mountains
Xenolith ID: FDM-DB02-X02

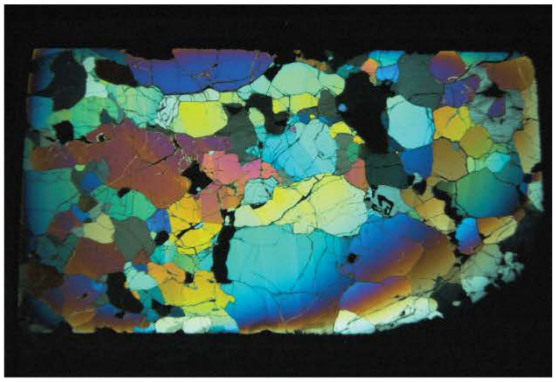

Figure C19-A. Full thin section photomicrograph of sample FDM-DB02-X02 viewed through cross-polarized light (XPL).

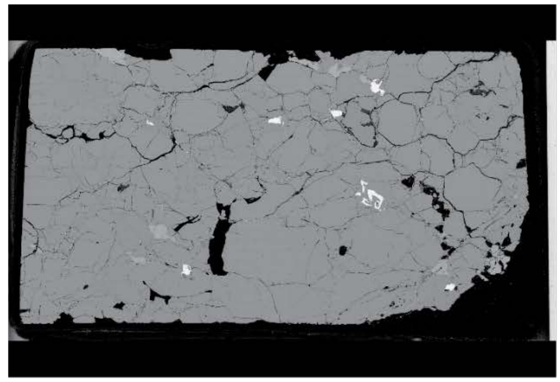

Figure C19-B. Panoramic back-scattered electron (BSE) image of sample FDM-DB02-X02.

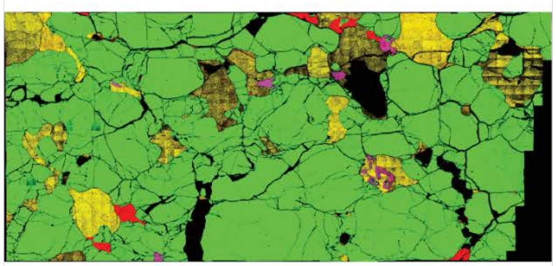

Figure C19-C. Phase map of sample FDM-DB02-X02, generated by the AZtec software based on the EBSD dataset. Each mineralogical phase is represented by a different color: green is olivine, yellow is enstatite, red is diopside, and magenta is chromite. Black pixels are non-indexed portions of the map.

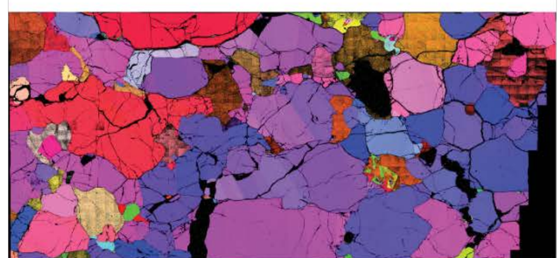

Figure C19-D. Inverse pole figure map of sample FDM-DB02-X02, generated by the AZtec analysis software (v. 3.0 SP1). Coloring of crystallographic orientations are shown with respect to the x-direction (e.g., inverse pole figure of olivine, right).

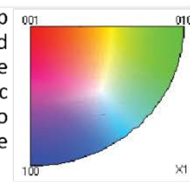

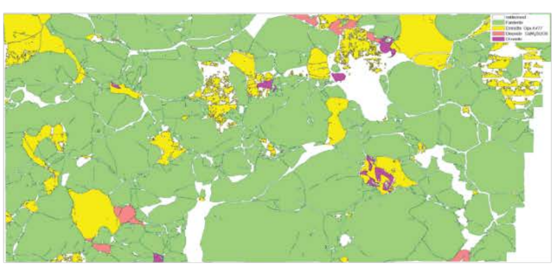

Figure C19-E. Phase map of sample FDM-DB02-X02, generated using the MTEX toolbox (v. 3.5.0), shows the reconstructed grain set comprising the noise-reduced EBSD dataset. Non-indexed regions are not removed from the dataset during the production of this map.

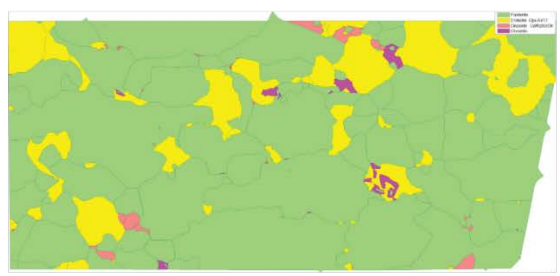

Figure C19-F. Phase map of sample FDM-DB02-X02, generated using the MTEX toolbox (v. 3.5.0), shows the reconstructed grain set comprising the one-point-per-grain (1ppg) dataset. Non-indexed regions are removed from the dataset during the production of this map.

Volcanic Center: Demas Bluff, Fosdick Mountains
Xenolith ID: FDM-DB02-X03

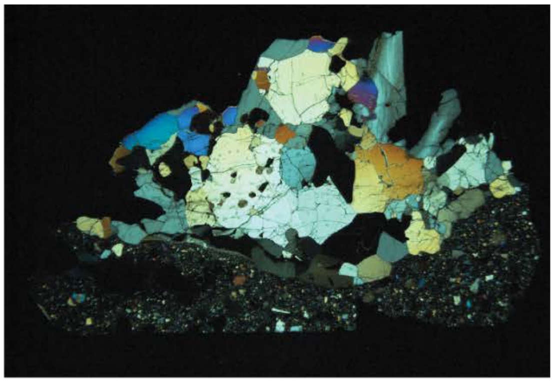

Figure C20-A. Full thin section photomicrograph of sample FDM-DB02-X03 viewed through cross-polarized light (XPL).

Figure C20-B. Panoramic back-scattered electron (BSE) image of sample FDM-DB02-X03.

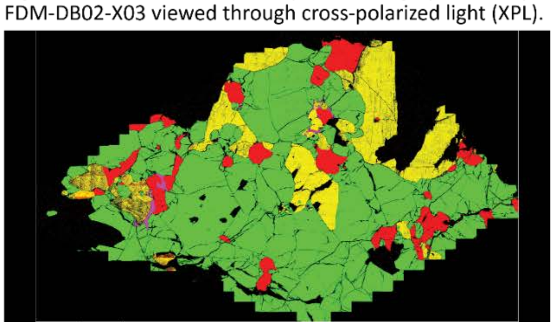

Figure C20-C. Phase map of sample FDM-DB02-X03, generated by the AZtec software based on the EBSD dataset. Each mineralogical phase is represented by a different color: green is olivine, yellow is enstatite, red is diopside, and magenta is chromite. Black pixels are non-indexed portions of the map.

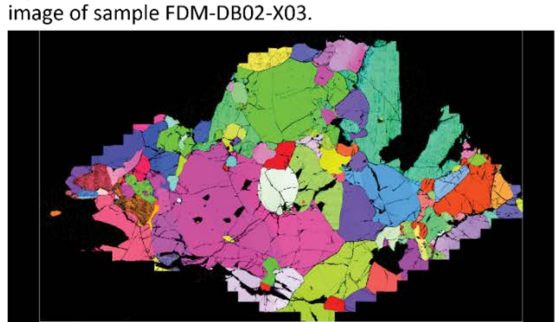

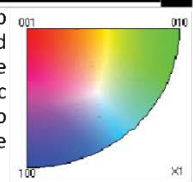

Figure C20-D. Inverse pole figure map of sample FDM-DB02-X03, generated by the AZtec analysis software (v. 3.0 SP1). Coloring of crystallographic orientations are shown with respect to the x-direction (e.g., inverse pole figure of olivine, right).

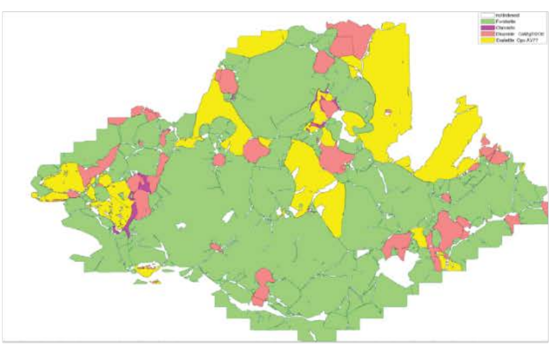

Figure C20-E. Phase map of sample FDM-DB02-X03, generated using the MTEX toolbox (v. 3.5.0), shows the reconstructed grain set comprising the noise-reduced EBSD dataset. Non-indexed regions are not removed from the dataset during the production of this map.

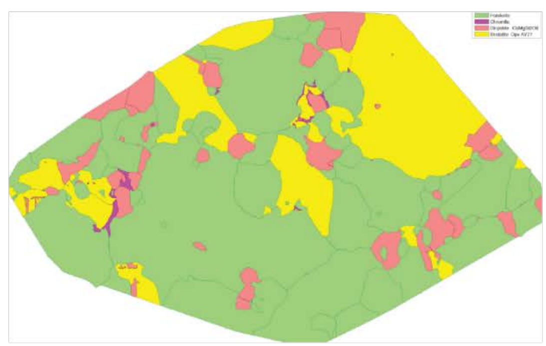

Figure C20-F. Phase map of sample FDM-DB02-X03, generated using the MTEX toolbox (v. 3.5.0), shows the reconstructed grain set comprising the one-point-per-grain (1ppg) dataset. Non-indexed regions are removed from the dataset during the production of this map.

VOLCANIC CENTER: DEMAS BLUFF, FOSDICK MOUNTAINS
XENOLITH ID: FDM-DB02-X04

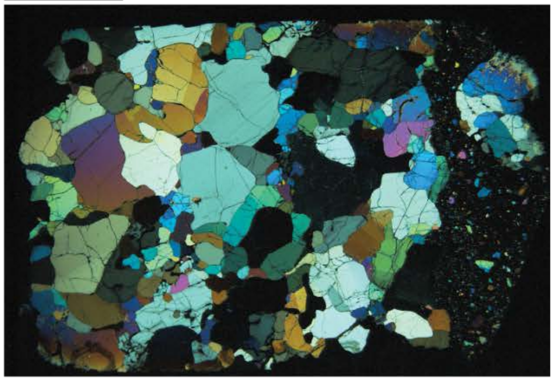

Figure C21-A. Full thin section photomicrograph of sample FDM-DB02-X04 viewed through cross-polarized light (XPL).

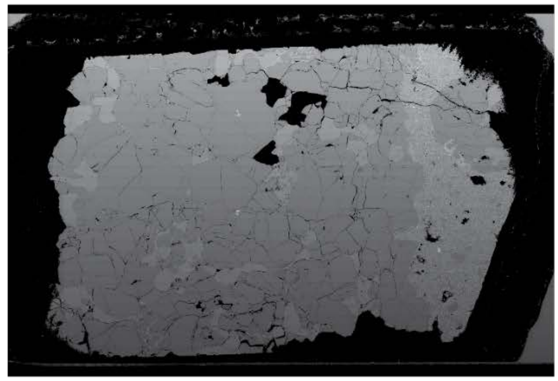

Figure C21-B. Panoramic back-scattered electron (BSE) image of sample FDM-DB02-X04.

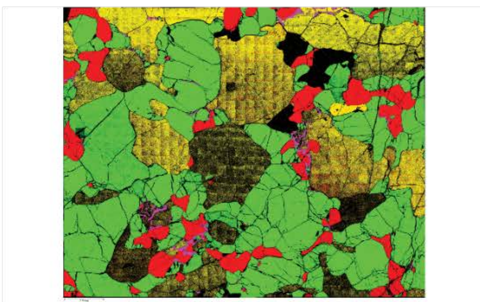

Figure C21-C. Phase map of sample FDM-DB02-X04, generated by the AZtec software based on the EBSD dataset. Each mineralogical phase is represented by a different color: green is olivine, yellow is enstatite, red is diopside, and magenta is chromite. Black pixels are non-indexed portions of the map.

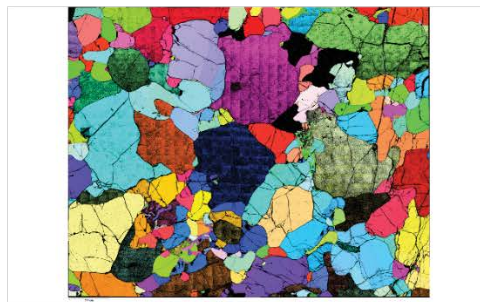

Figure C21-D. Inverse pole figure map of sample FDM-DB02-X04, generated by the AZtec analysis software (v. 3.0 SP1). Coloring of crystallographic orientations are shown with respect to the x-direction (e.g., inverse pole figure of olivine, right).

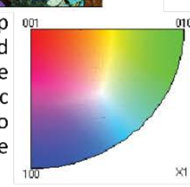

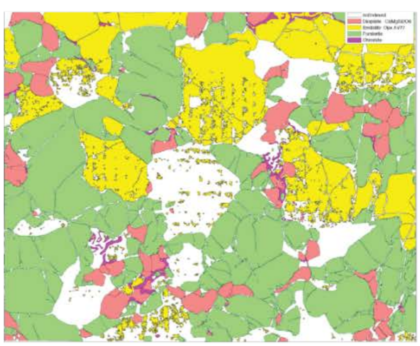

Figure C21-E. Phase map of sample FDM-DB02-X04, generated using the MTEX toolbox (v. 3.5.0), shows the reconstructed grain set comprising the noise-reduced EBSD dataset. Non-indexed regions are not removed from the dataset during the production of this map.

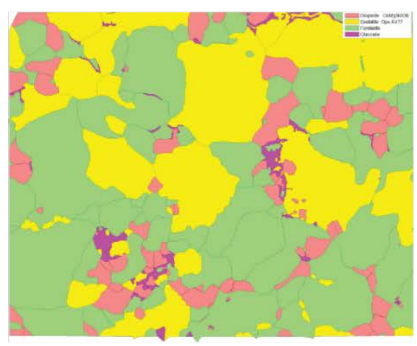

Figure C21-F. Phase map of sample FDM-DB02-X04, generated using the MTEX toolbox (v. 3.5.0), shows the reconstructed grain set comprising the one-point-per-grain (1ppg) dataset. Non-indexed regions are removed from the dataset during the production of this map.

Volcanic Center: Demas Bluff, Fosdick Mountains
Xenolith ID: FDM-DB02-X05

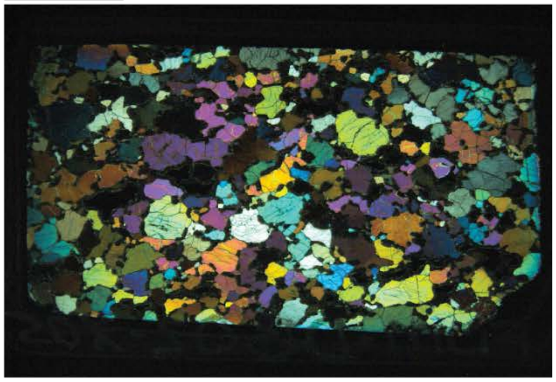

Figure C22-A. Full thin section photomicrograph of sample FDM-DB02-X05 viewed through cross-polarized light (XPL).

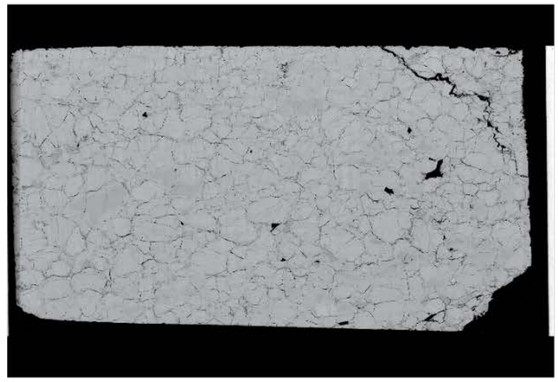

Figure C22-B. Panoramic back-scattered electron (BSE) image of sample FDM-DB02-X05.

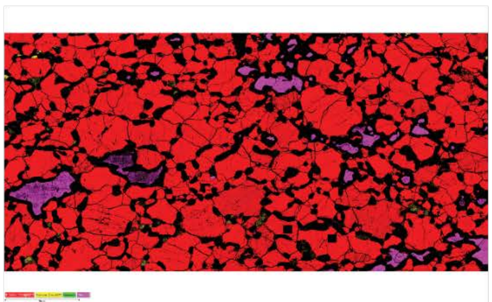

Figure C22-C. Phase map of sample FDM-DB02-X05, generated by the AZtec software based on the EBSD dataset. Each mineralogical phase is represented by a different color: green is olivine, yellow is enstatite, red is diopside, and magenta is chromite. Black pixels are non-indexed portions of the map.

Figure C22-D. Inverse pole figure map of sample FDM-DB02-X05, generated by the AZtec analysis software (v. 3.0 SP1). Coloring of crystallographic orientations are shown with respect to the x-direction. The olivine texture of this sample is not assessed because it is a pyroxenite.

VOLCANIC CENTER: DEMAS BLUFF, FOSDICK MOUNTAINS
XENOLITH ID: FDM-DB02-X06

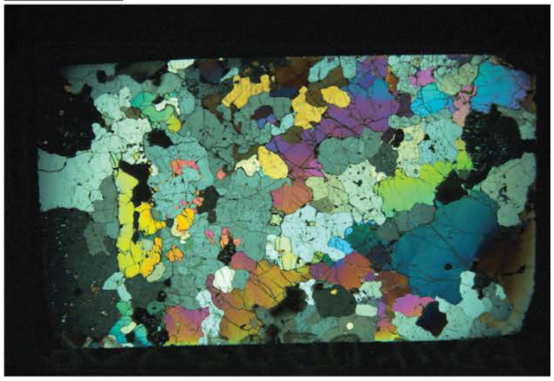

Figure C23-A. Full thin section photomicrograph of sample FDM-DB02-X06 viewed through cross-polarized light (XPL).

Figure C23-B. Panoramic back-scattered electron (BSE) image of sample FDM-DB02-X06.

Figure C23-C. Phase map of sample FDM-DB02-X06, generated by the AZtec software based on the EBSD dataset. Each mineralogical phase is represented by a different color: green is olivine, yellow is enstatite, red is diopside, and magenta is chromite. Black pixels are non-indexed portions of the map.

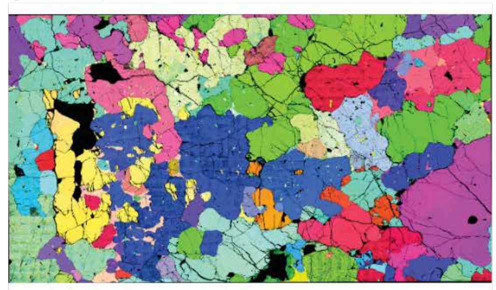

Figure C23-D. Inverse pole figure map of sample FDM-DB02-X06, generated by the AZtec analysis software (v. 3.0 SP1). Coloring of crystallographic orientations are shown with respect to the x-direction (e.g., inverse pole figure of olivine, right).

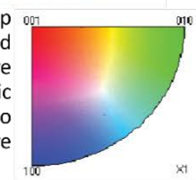

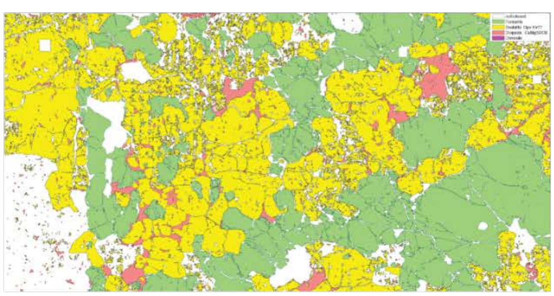

Figure C23-E. Phase map of sample FDM-DB02-X06, generated using the MTEX toolbox (v. 3.5.0), shows the reconstructed grain set comprising the noise-reduced EBSD dataset. Non-indexed regions are not removed from the dataset during the production of this map.

Figure C23-F. Phase map of sample FDM-DB02-X06, generated using the MTEX toolbox (v. 3.5.0), shows the reconstructed grain set comprising the one-point-per-grain (1ppg) dataset. Non-indexed regions are removed from the dataset during the production of this map.

VOLCANIC CENTER: DEMAS BLUFF, FOSDICK MOUNTAINS
XENOLITH ID: FDM-DB02-X08

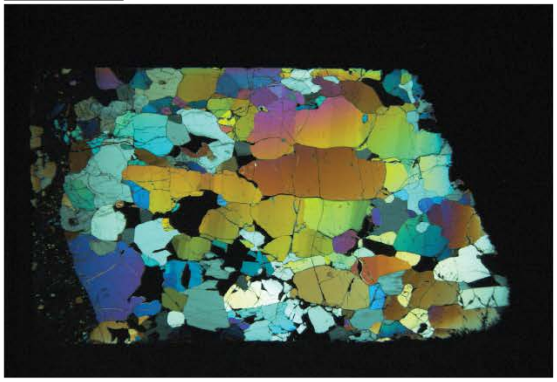

Figure C24-A. Full thin section photomicrograph of sample FDM-DB02-X08 viewed through cross-polarized light (XPL).

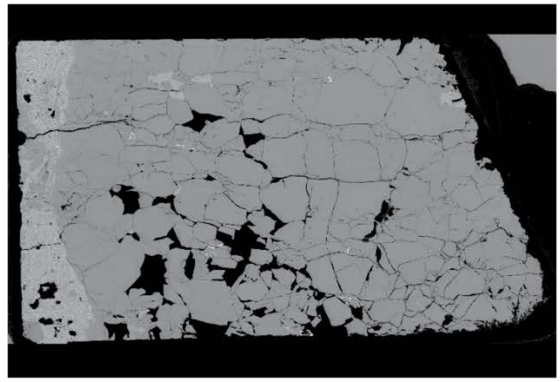

Figure C24-B. Panoramic back-scattered electron (BSE) image of sample FDM-DB02-X08.

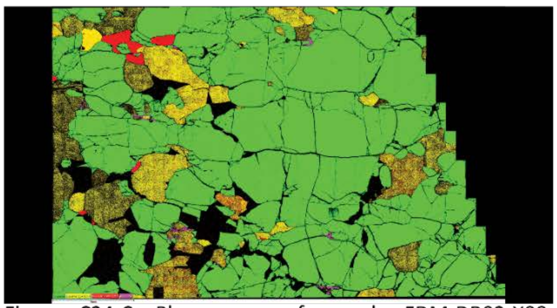

Figure C24-C. Phase map of sample FDM-DB02-X08, generated by the AZtec software based on the EBSD dataset. Each mineralogical phase is represented by a different color: green is olivine, yellow is enstatite, red is diopside, and magenta is chromite. Black pixels are non-indexed portions of the map.

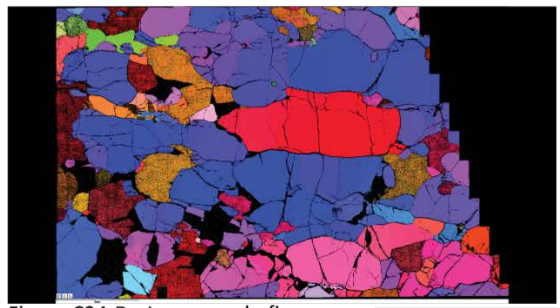

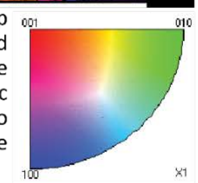

Figure C24-D. Inverse pole figure map of sample FDM-DB02-X08, generated by the AZtec analysis software (v. 3.0 SP1). Coloring of crystallographic orientations are shown with respect to the x-direction (e.g., inverse pole figure of olivine, right).

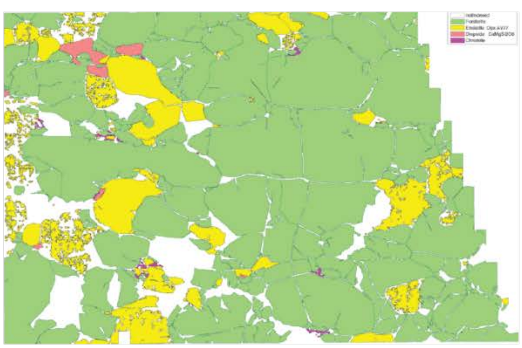

Figure C24-E. Phase map of sample FDM-DB02-X08, generated using the MTEX toolbox (v. 3.5.0), shows the reconstructed grain set comprising the noise-reduced EBSD dataset. Non-indexed regions are not removed from the dataset during the production of this map.

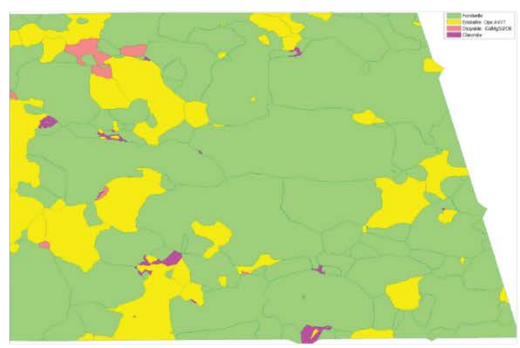

Figure C24-F. Phase map of sample FDM-DB02-X08, generated using the MTEX toolbox (v. 3.5.0), shows the reconstructed grain set comprising the one-point-per-grain (1ppg) dataset. Non-indexed regions are removed from the dataset during the production of this map.

<u>Volcanic Center</u>: Demas Bluff, Fosdick Mountains
<u>Xenolith ID</u>: FDM-DB02-X10

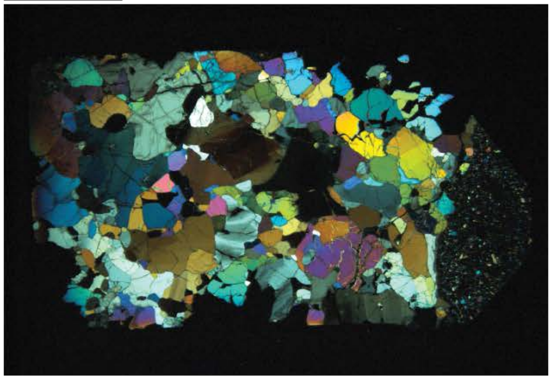

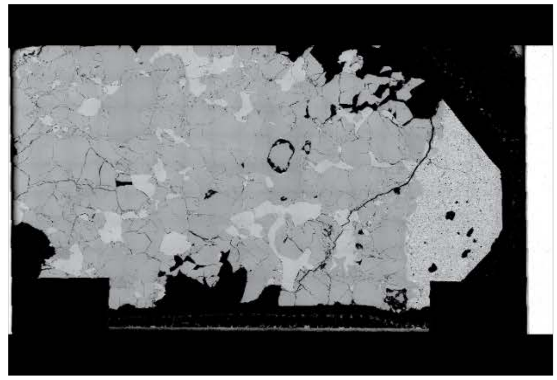

<u>Figure C25-A</u>. Full thin section photomicrograph of sample FDM-DB02-X10 viewed through cross-polarized light (XPL).

<u>Figure C25-B</u>. Panoramic back-scattered electron (BSE) image of sample FDM-DB02-X10.

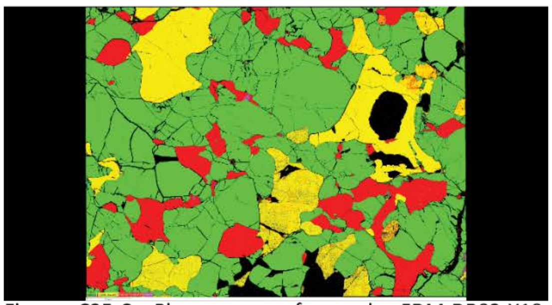

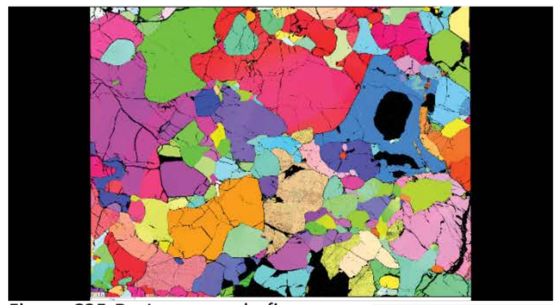

<u>Figure C25-C</u>. Phase map of sample FDM-DB02-X10, generated by the AZtec software based on the EBSD dataset. Each mineralogical phase is represented by a different color: green is olivine, yellow is enstatite, red is diopside, and magenta is chromite. Black pixels are non-indexed portions of the map.

<u>Figure C25-D</u>. Inverse pole figure map of sample FDM-DB02-X10, generated by the AZtec analysis software (v. 3.0 SP1). Coloring of crystallographic orientations are shown with respect to the x-direction (e.g., inverse pole figure of olivine, right).

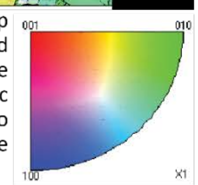

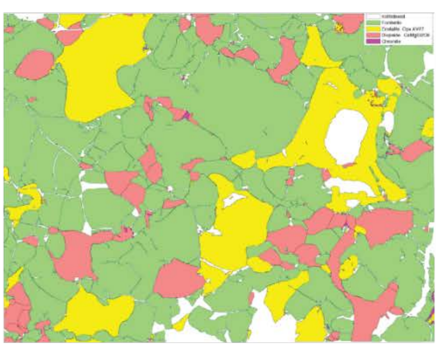

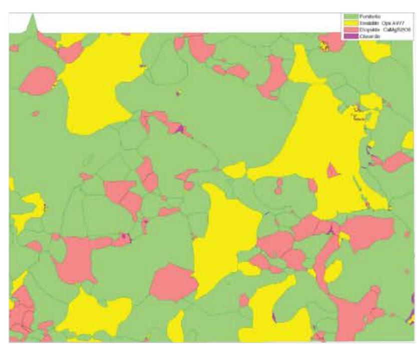

<u>Figure C25-E</u>. Phase map of sample FDM-DB02-X10, generated using the MTEX toolbox (v. 3.5.0), shows the reconstructed grain set comprising the noise-reduced EBSD dataset. Non-indexed regions are not removed from the dataset during the production of this map.

<u>Figure C25-F</u>. Phase map of sample FDM-DB02-X10, generated using the MTEX toolbox (v. 3.5.0), shows the reconstructed grain set comprising the one-point-per-grain (1ppg) dataset. Non-indexed regions are removed from the dataset during the production of this map.

Volcanic Center: Demas Bluff, Fosdick Mountains
Xenolith ID: FDM-DB02-X11

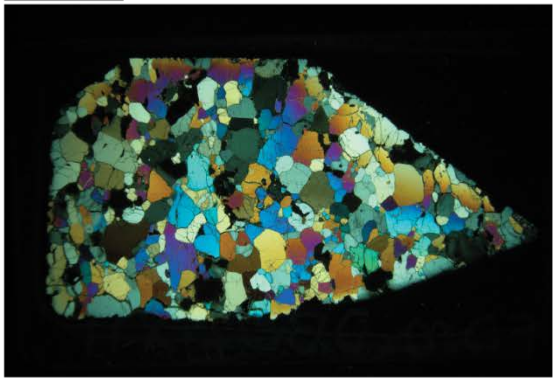

Figure C26-A. Full thin section photomicrograph of sample FDM-DB02-X11 viewed through cross-polarized light (XPL).

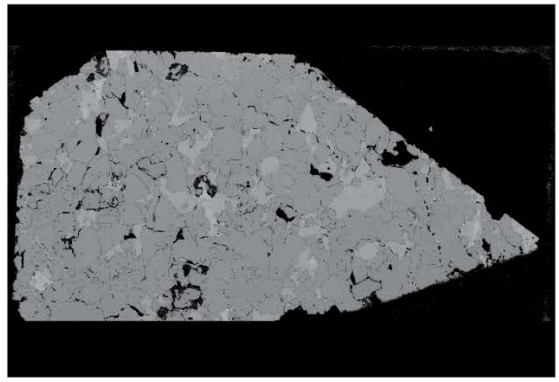

Figure C26-B. Panoramic back-scattered electron (BSE) image of sample FDM-DB02-X11.

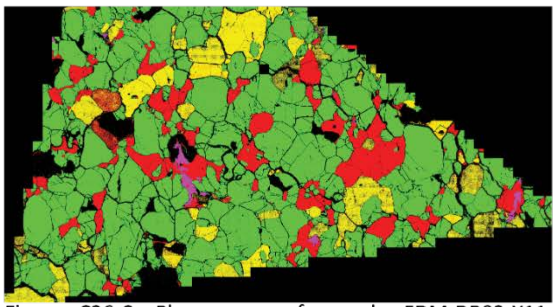

Figure C26-C. Phase map of sample FDM-DB02-X11, generated by the AZtec software based on the EBSD dataset. Each mineralogical phase is represented by a different color: green is olivine, yellow is enstatite, red is diopside, and magenta is chromite. Black pixels are non-indexed portions of the map.

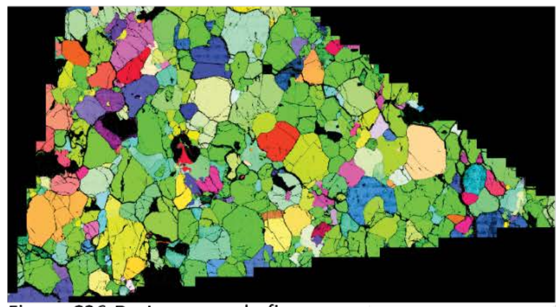

Figure C26-D. Inverse pole figure map of sample FDM-DB02-X11, generated by the AZtec analysis software (v. 3.0 SP1). Coloring of crystallographic orientations are shown with respect to the x-direction (e.g., inverse pole figure of olivine, right).

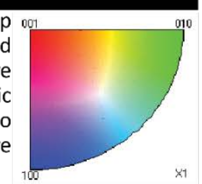

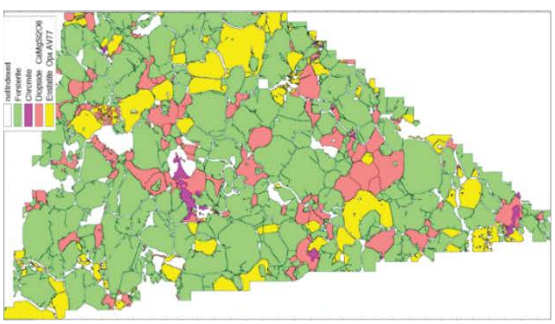

Figure C26-E. Phase map of sample FDM-DB02-X11, generated using the MTEX toolbox (v. 3.5.0), shows the reconstructed grain set comprising the noise-reduced EBSD dataset. Non-indexed regions are not removed from the dataset during the production of this map.

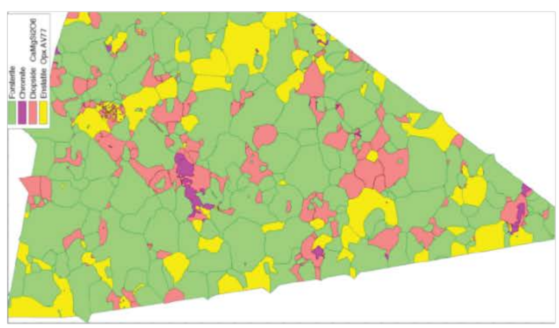

Figure C26-F. Phase map of sample FDM-DB02-X11, generated using the MTEX toolbox (v. 3.5.0), shows the reconstructed grain set comprising the one-point-per-grain (1ppg) dataset. Non-indexed regions are removed from the dataset during the production of this map.

<u>Volcanic Center</u>: Demas Bluff, Fosdick Mountains
<u>Xenolith ID</u>: FDM-DB02-X12

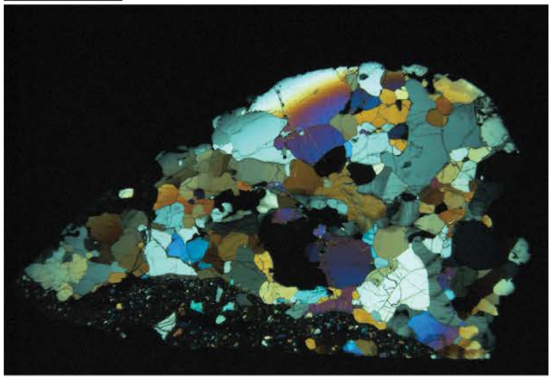

<u>Figure C27-A</u>. Full thin section photomicrograph of sample FDM-DB02-X12 viewed through cross-polarized light (XPL).

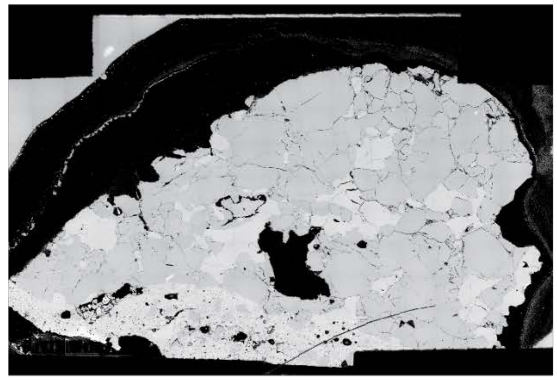

<u>Figure C27-B</u>. Panoramic back-scattered electron (BSE) image of sample FDM-DB02-X12.

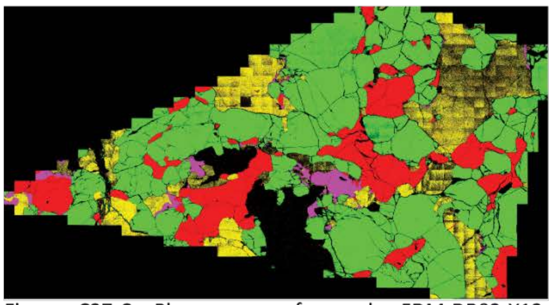

<u>Figure C27-C</u>. Phase map of sample FDM-DB02-X12, generated by the AZtec software based on the EBSD dataset. Each mineralogical phase is represented by a different color: green is olivine, yellow is enstatite, red is diopside, and magenta is chromite. Black pixels are non-indexed portions of the map.

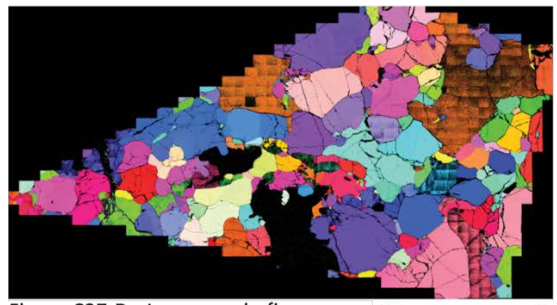

<u>Figure C27-D</u>. Inverse pole figure map of sample FDM-DB02-X12, generated by the AZtec analysis software (v. 3.0 SP1). Coloring of crystallographic orientations are shown with respect to the x-direction (e.g., inverse pole figure of olivine, right).

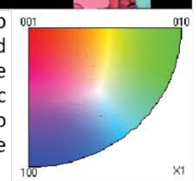

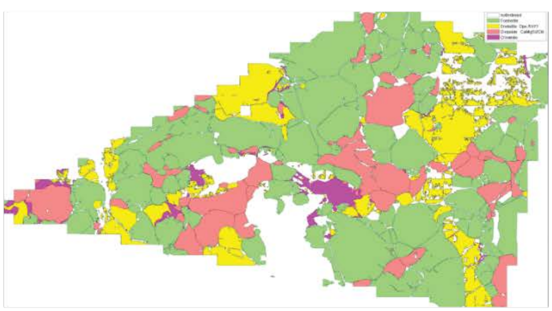

<u>Figure C27-E</u>. Phase map of sample FDM-DB02-X12, generated using the MTEX toolbox (v. 3.5.0), shows the reconstructed grain set comprising the noise-reduced EBSD dataset. Non-indexed regions are not removed from the dataset during the production of this map.

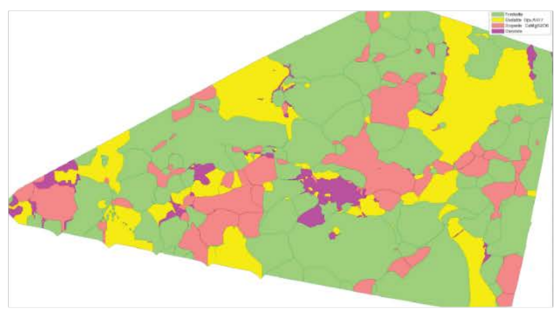

<u>Figure C27-F</u>. Phase map of sample FDM-DB02-X12, generated using the MTEX toolbox (v. 3.5.0), shows the reconstructed grain set comprising the one-point-per-grain (1ppg) dataset. Non-indexed regions are removed from the dataset during the production of this map.

Volcanic Center: Demas Bluff, Fosdick Mountains
Xenolith ID: FDM-DB02-X13

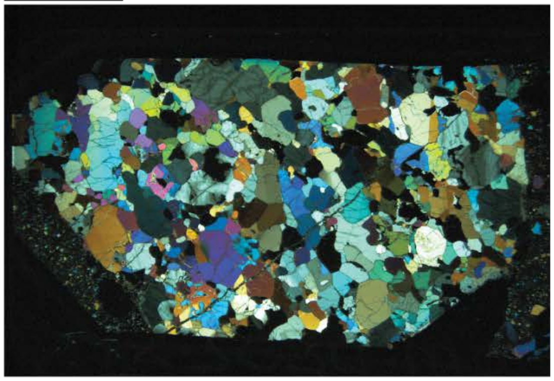

Figure C28-A. Full thin section photomicrograph of sample FDM-DB02-X13 viewed through cross-polarized light (XPL).

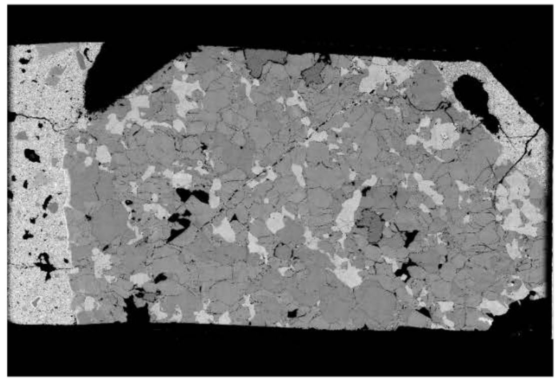

Figure C28-B. Panoramic back-scattered electron (BSE) image of sample FDM-DB02-X13.

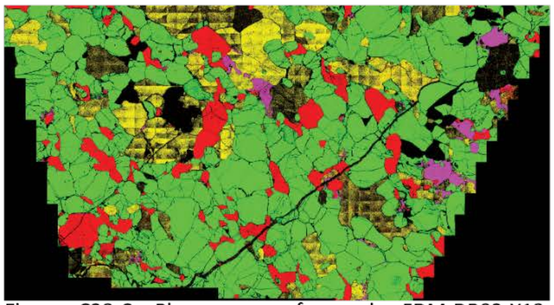

Figure C28-C. Phase map of sample FDM-DB02-X13, generated by the AZtec software based on the EBSD dataset. Each mineralogical phase is represented by a different color: green is olivine, yellow is enstatite, red is diopside, and magenta is chromite. Black pixels are non-indexed portions of the map.

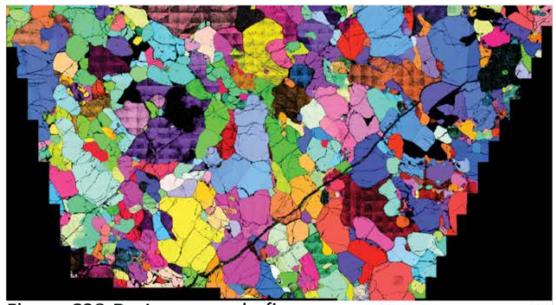

Figure C28-D. Inverse pole figure map of sample FDM-DB02-X13, generated by the AZtec analysis software (v. 3.0 SP1). Coloring of crystallographic orientations are shown with respect to the x-direction (e.g., inverse pole figure of olivine, right).

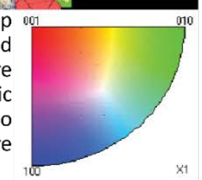

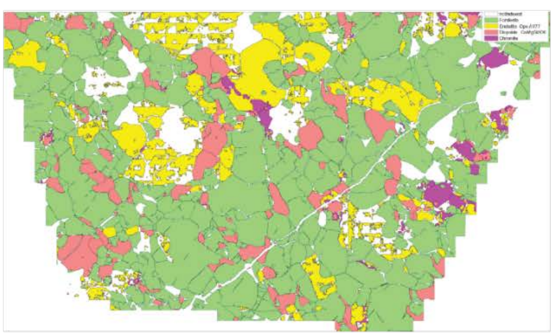

Figure C28-E. Phase map of sample FDM-DB02-X13, generated using the MTEX toolbox (v. 3.5.0), shows the reconstructed grain set comprising the noise-reduced EBSD dataset. Non-indexed regions are not removed from the dataset during the production of this map.

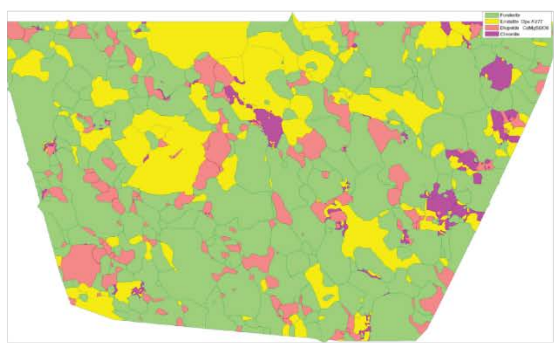

Figure C28-F. Phase map of sample FDM-DB02-X13, generated using the MTEX toolbox (v. 3.5.0), shows the reconstructed grain set comprising the one-point-per-grain (1ppg) dataset. Non-indexed regions are removed from the dataset during the production of this map.

Volcanic Center: Demas Bluff, Fosdick Mountains

Xenolith ID: FDM-DB03-X01

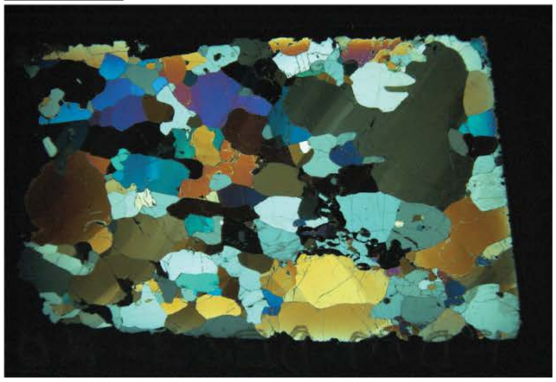

Figure C29-A. Full thin section photomicrograph of sample FDM-DB03-X01 viewed through cross-polarized light (XPL).

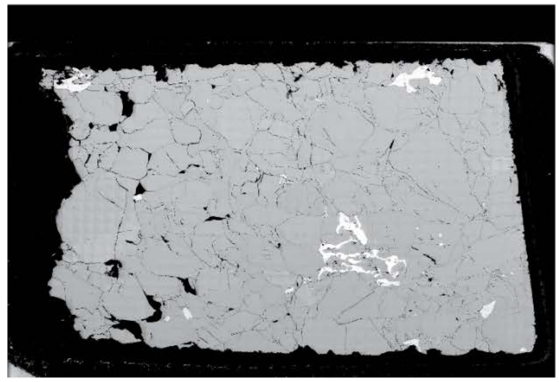

Figure C29-B. Panoramic back-scattered electron (BSE) image of sample FDM-DB03-X01.

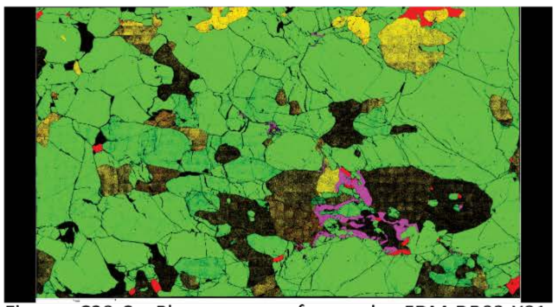

Figure C29-C. Phase map of sample FDM-DB03-X01, generated by the AZtec software based on the EBSD dataset. Each mineralogical phase is represented by a different color: green is olivine, yellow is enstatite, red is diopside, and magenta is chromite. Black pixels are non-indexed portions of the map.

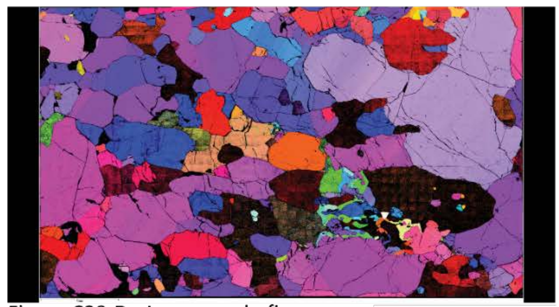

Figure C29-D. Inverse pole figure map of sample FDM-DB03-X01, generated by the AZtec analysis software (v. 3.0 SP1). Coloring of crystallographic orientations are shown with respect to the x-direction (e.g., inverse pole figure of olivine, right).

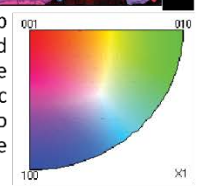

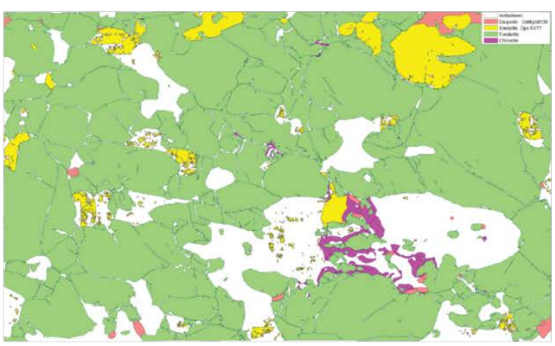

Figure C29-E. Phase map of sample FDM-DB03-X01, generated using the MTEX toolbox (v. 3.5.0), shows the reconstructed grain set comprising the noise-reduced EBSD dataset. Non-indexed regions are not removed from the dataset during the production of this map.

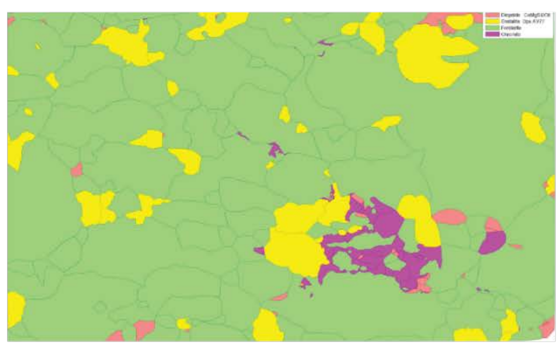

Figure C29-F. Phase map of sample FDM-DB03-X01, generated using the MTEX toolbox (v. 3.5.0), shows the reconstructed grain set comprising the one-point-per-grain (1ppg) dataset. Non-indexed regions are removed from the dataset during the production of this map.

Volcanic Center: Demas Bluff, Fosdick Mountains
Xenolith ID: FDM-DB03-X02

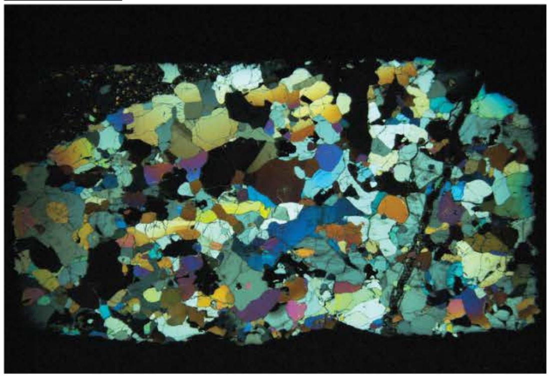

Figure C30-A. Full thin section photomicrograph of sample FDM-DB03-X02 viewed through cross-polarized light (XPL).

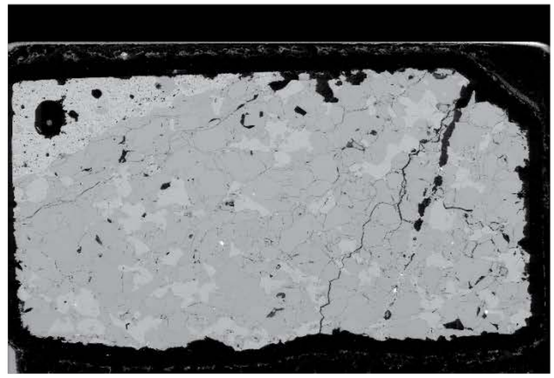

Figure C30-B. Panoramic back-scattered electron (BSE) image of sample FDM-DB03-X02.

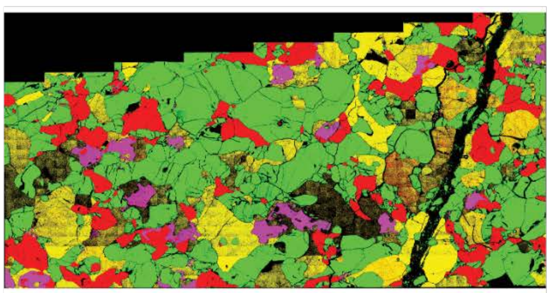

Figure C30-C. Phase map of sample FDM-DB03-X02, generated by the AZtec software based on the EBSD dataset. Each mineralogical phase is represented by a different color: green is olivine, yellow is enstatite, red is diopside, and magenta is chromite. Black pixels are non-indexed portions of the map.

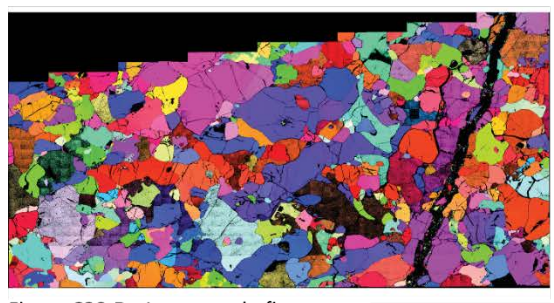

Figure C30-D. Inverse pole figure map of sample FDM-DB03-X02, generated by the AZtec analysis software (v. 3.0 SP1). Coloring of crystallographic orientations are shown with respect to the x-direction (e.g., inverse pole figure of olivine, right).

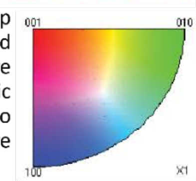

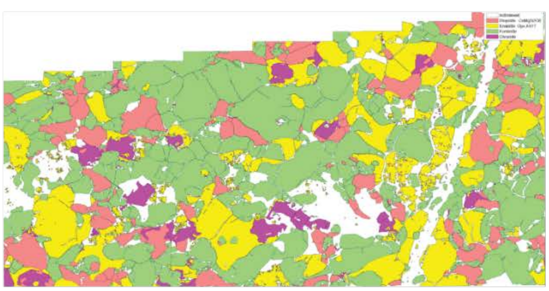

Figure C30-E. Phase map of sample FDM-DB03-X02, generated using the MTEX toolbox (v. 3.5.0), shows the reconstructed grain set comprising the noise-reduced EBSD dataset. Non-indexed regions are not removed from the dataset during the production of this map.

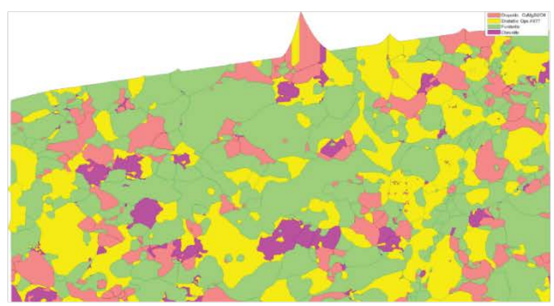

Figure C30-F. Phase map of sample FDM-DB03-X02, generated using the MTEX toolbox (v. 3.5.0), shows the reconstructed grain set comprising the one-point-per-grain (1ppg) dataset. Non-indexed regions are removed from the dataset during the production of this map.

VOLCANIC CENTER: DEMAS BLUFF, FOSDICK MOUNTAINS
XENOLITH ID: FDM-DB03-X03

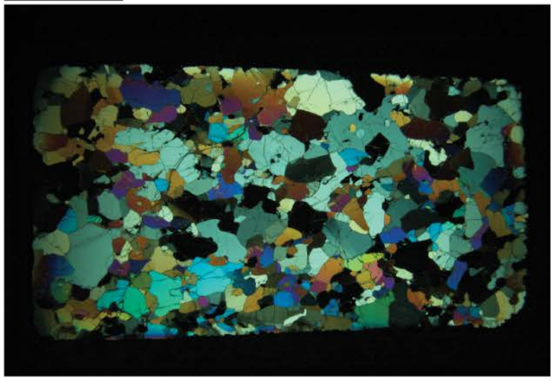

Figure C31-A. Full thin section photomicrograph of sample FDM-DB03-X03 viewed through cross-polarized light (XPL).

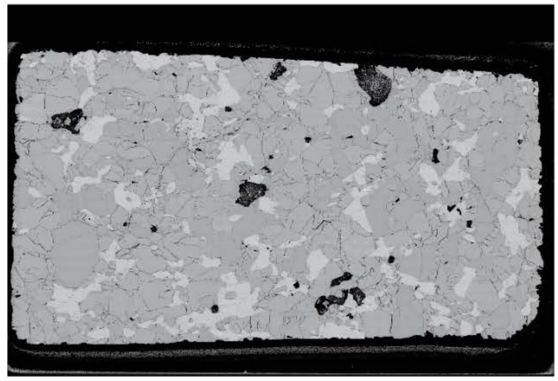

Figure C31-B. Panoramic back-scattered electron (BSE) image of sample FDM-DB03-X03.

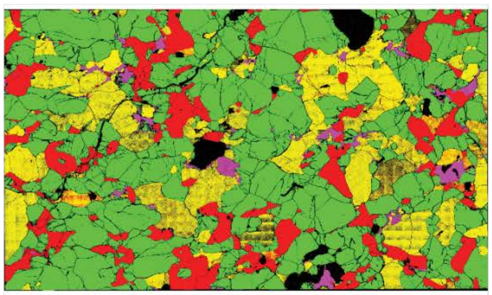

Figure C31-C. Phase map of sample FDM-DB03-X03, generated by the AZtec software based on the EBSD dataset. Each mineralogical phase is represented by a different color: green is olivine, yellow is enstatite, red is diopside, and magenta is chromite. Black pixels are non-indexed portions of the map.

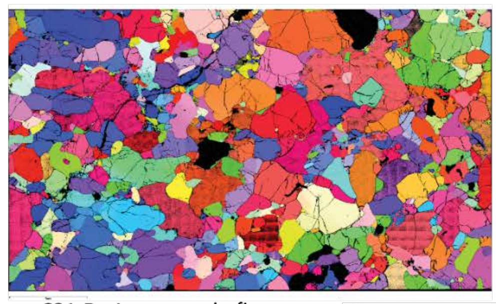

Figure C31-D. Inverse pole figure map of sample FDM-DB03-X03, generated by the AZtec analysis software (v. 3.0 SP1). Coloring of crystallographic orientations are shown with respect to the x-direction (e.g., inverse pole figure of olivine, right).

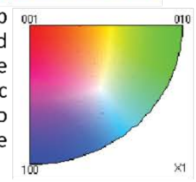

Figure C31-E. Phase map of sample FDM-DB03-X03, generated using the MTEX toolbox (v. 3.5.0), shows the reconstructed grain set comprising the noise-reduced EBSD dataset. Non-indexed regions are not removed from the dataset during the production of this map.

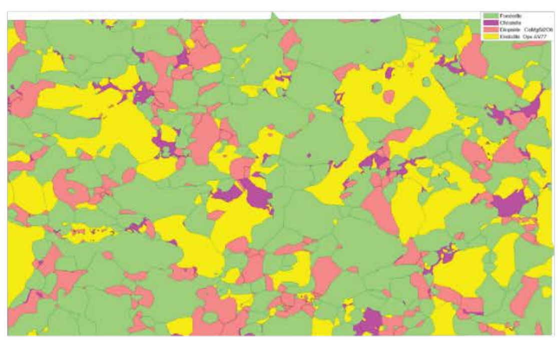

Figure C31-F. Phase map of sample FDM-DB03-X03, generated using the MTEX toolbox (v. 3.5.0), shows the reconstructed grain set comprising the one-point-per-grain (1ppg) dataset. Non-indexed regions are removed from the dataset during the production of this map.

Volcanic Center: Demas Bluff, Fosdick Mountains
Xenolith ID: FDM-DB03-X04

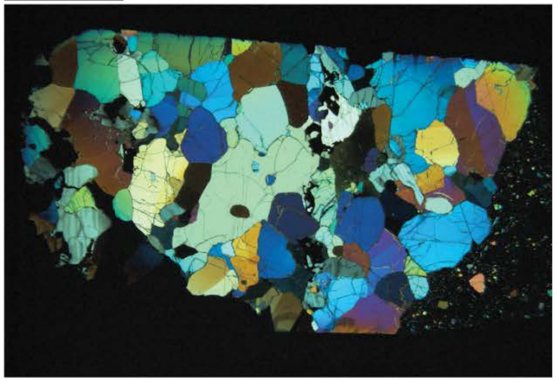

Figure C32-A. Full thin section photomicrograph of sample FDM-DB03-X04 viewed through cross-polarized light (XPL).

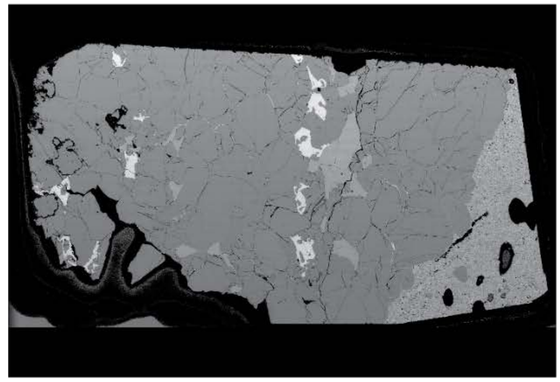

Figure C32-B. Panoramic back-scattered electron (BSE) image of sample FDM-DB03-X04.

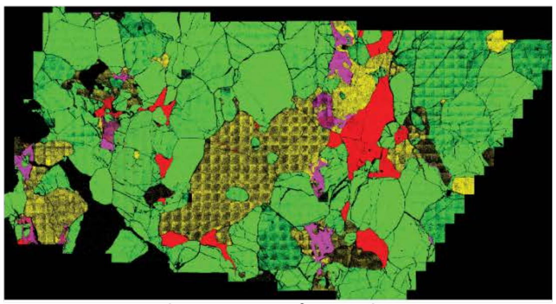

Figure C32-C. Phase map of sample FDM-DB03-X04, generated by the AZtec software based on the EBSD dataset. Each mineralogical phase is represented by a different color: green is olivine, yellow is enstatite, red is diopside, and magenta is chromite. Black pixels are non-indexed portions of the map.

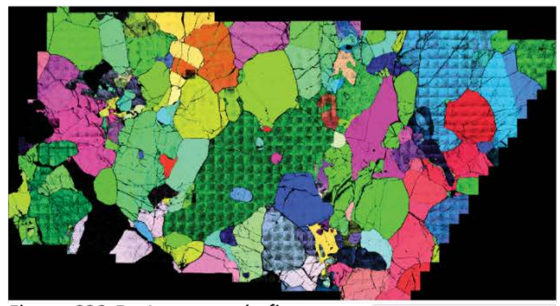

Figure C32-D. Inverse pole figure map of sample FDM-DB03-X04, generated by the AZtec analysis software (v. 3.0 SP1). Coloring of crystallographic orientations are shown with respect to the x-direction (e.g., inverse pole figure of olivine, right).

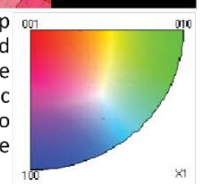

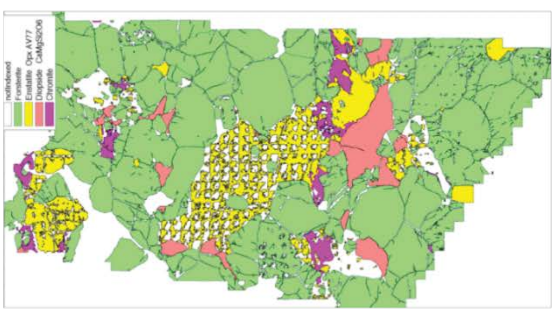

Figure C32-E. Phase map of sample FDM-DB03-X04, generated using the MTEX toolbox (v. 3.5.0), shows the reconstructed grain set comprising the noise-reduced EBSD dataset. Non-indexed regions are not removed from the dataset during the production of this map.

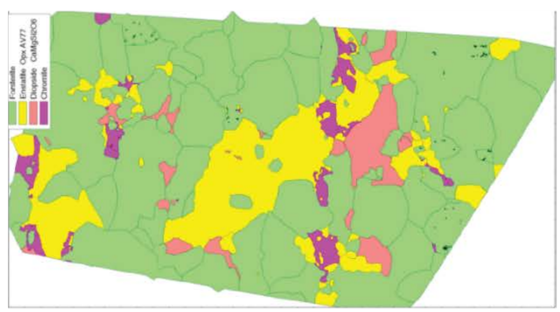

Figure C32-F. Phase map of sample FDM-DB03-X04, generated using the MTEX toolbox (v. 3.5.0), shows the reconstructed grain set comprising the one-point-per-grain (1ppg) dataset. Non-indexed regions are removed from the dataset during the production of this map.

Volcanic Center: Demas Bluff, Fosdick Mountains
Xenolith ID: FDM-DB04-X01

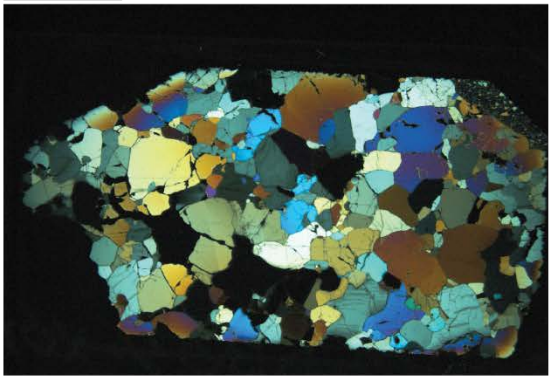

Figure C33-A. Full thin section photomicrograph of sample FDM-DB04-X01 viewed through cross-polarized light (XPL).

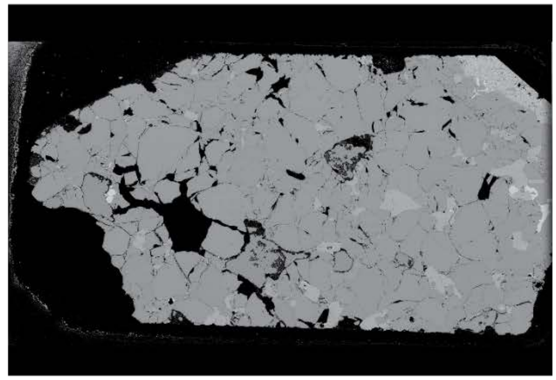

Figure C33-B. Panoramic back-scattered electron (BSE) image of sample FDM-DB04-X01.

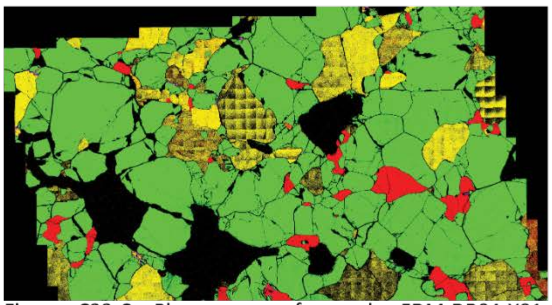

Figure C33-C. Phase map of sample FDM-DB04-X01, generated by the AZtec software based on the EBSD dataset. Each mineralogical phase is represented by a different color: green is olivine, yellow is enstatite, red is diopside, and magenta is chromite. Black pixels are non-indexed portions of the map.

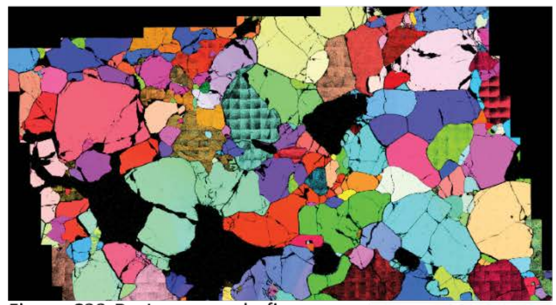

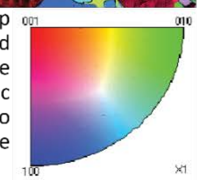

Figure C33-D. Inverse pole figure map of sample FDM-DB04-X01, generated by the AZtec analysis software (v. 3.0 SP1). Coloring of crystallographic orientations are shown with respect to the x-direction (e.g., inverse pole figure of olivine, right).

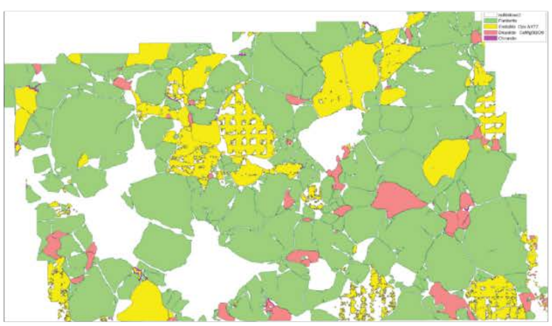

Figure C33-E. Phase map of sample FDM-DB04-X01, generated using the MTEX toolbox (v. 3.5.0), shows the reconstructed grain set comprising the noise-reduced EBSD dataset. Non-indexed regions are not removed from the dataset during the production of this map.

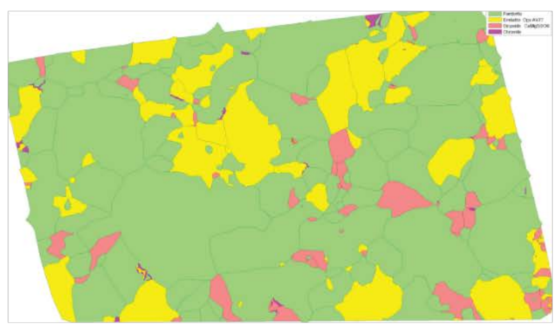

Figure C33-F. Phase map of sample FDM-DB04-X01, generated using the MTEX toolbox (v. 3.5.0), shows the reconstructed grain set comprising the one-point-per-grain (1ppg) dataset. Non-indexed regions are removed from the dataset during the production of this map.

Volcanic Center: Demas Bluff, Fosdick Mountains
Xenolith ID: FDM-DB04-X02

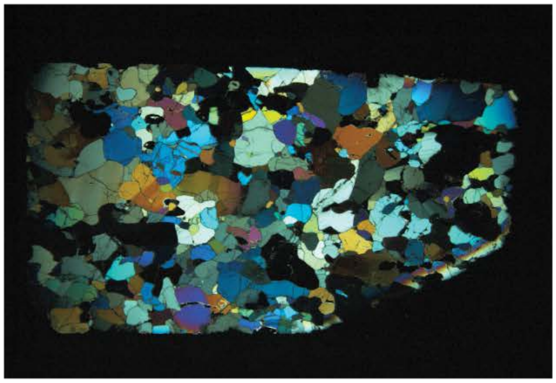

Figure C34-A. Full thin section photomicrograph of sample FDM-DB04-X02 viewed through cross-polarized light (XPL).

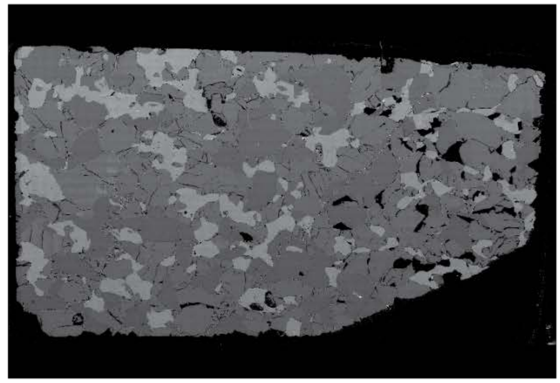

Figure C34-B. Panoramic back-scattered electron (BSE) image of sample FDM-DB04-X02.

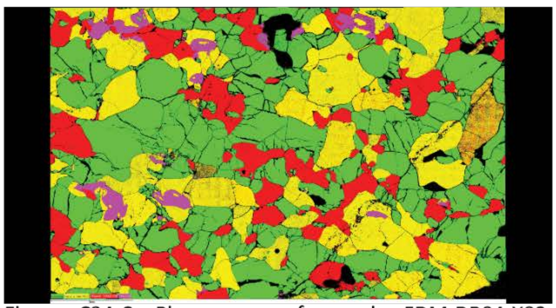

Figure C34-C. Phase map of sample FDM-DB04-X02, generated by the AZtec software based on the EBSD dataset. Each mineralogical phase is represented by a different color: green is olivine, yellow is enstatite, red is diopside, and magenta is chromite. Black pixels are non-indexed portions of the map.

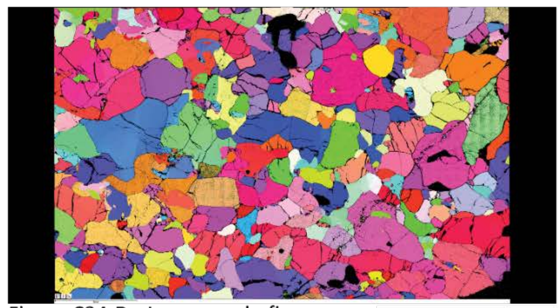

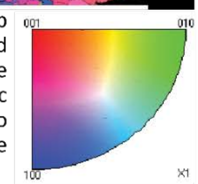

Figure C34-D. Inverse pole figure map of sample FDM-DB04-X02, generated by the AZtec analysis software (v. 3.0 SP1). Coloring of crystallographic orientations are shown with respect to the x-direction (e.g., inverse pole figure of olivine, right).

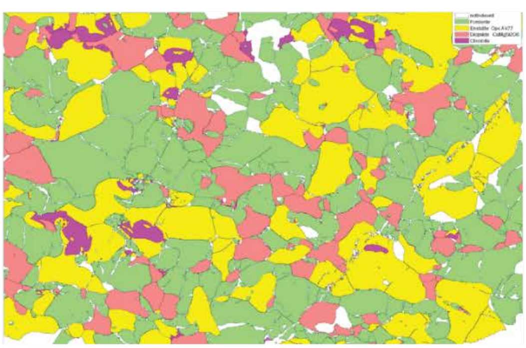

Figure C34-E. Phase map of sample FDM-DB04-X02, generated using the MTEX toolbox (v. 3.5.0), shows the reconstructed grain set comprising the noise-reduced EBSD dataset. Non-indexed regions are not removed from the dataset during the production of this map.

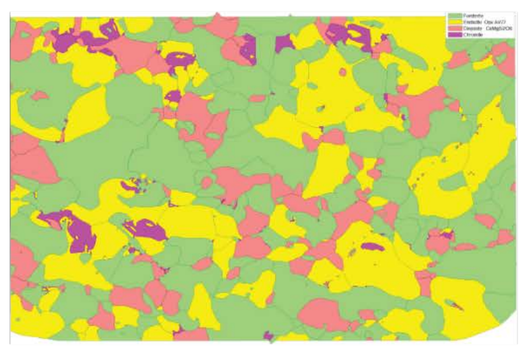

Figure C34-F. Phase map of sample FDM-DB04-X02, generated using the MTEX toolbox (v. 3.5.0), shows the reconstructed grain set comprising the one-point-per-grain (1ppg) dataset. Non-indexed regions are removed from the dataset during the production of this map.

<u>Volcanic Center</u>: Demas Bluff, Fosdick Mountains
<u>Xenolith ID</u>: FDM-DB04-X03

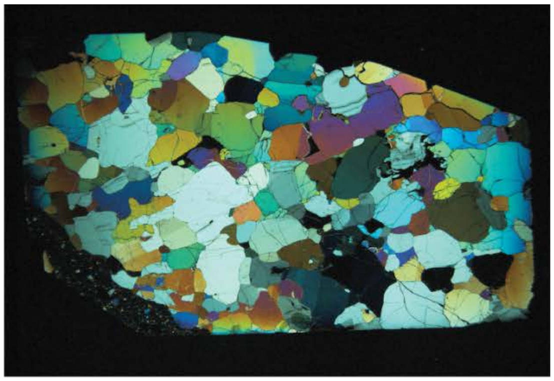

Figure C35-A. Full thin section photomicrograph of sample FDM-DB04-X03 viewed through cross-polarized light (XPL).

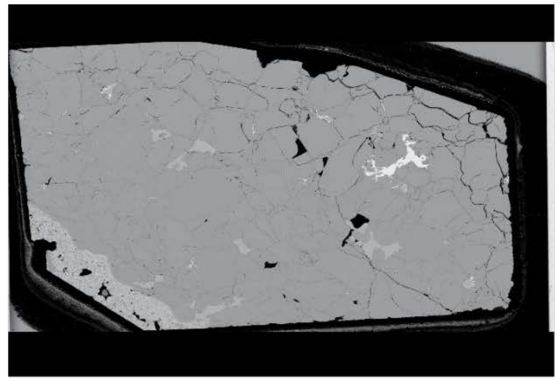

Figure C35-B. Panoramic back-scattered electron (BSE) image of sample FDM-DB04-X03.

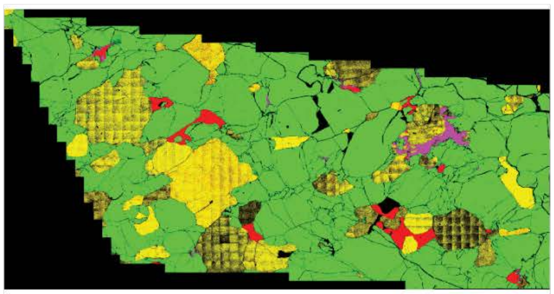

Figure C35-C. Phase map of sample FDM-DB04-X03, generated by the AZtec software based on the EBSD dataset. Each mineralogical phase is represented by a different color: green is olivine, yellow is enstatite, red is diopside, and magenta is chromite. Black pixels are non-indexed portions of the map.

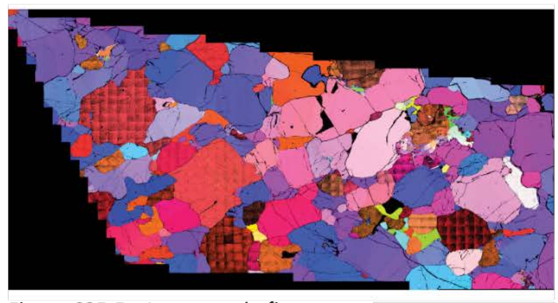

Figure C35-D. Inverse pole figure map of sample FDM-DB04-X03, generated by the AZtec analysis software (v. 3.0 SP1). Coloring of crystallographic orientations are shown with respect to the x-direction (e.g., inverse pole figure of olivine, right).

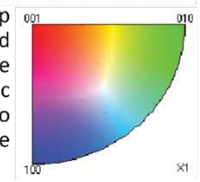

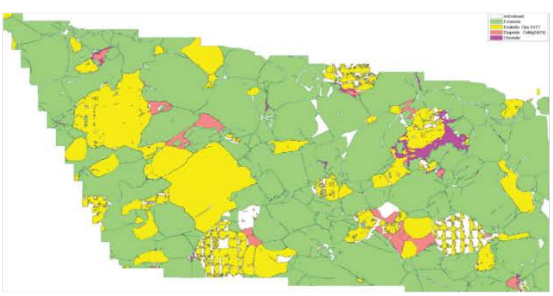

Figure C35-E. Phase map of sample FDM-DB04-X03, generated using the MTEX toolbox (v. 3.5.0), shows the reconstructed grain set comprising the noise-reduced EBSD dataset. Non-indexed regions are not removed from the dataset during the production of this map.

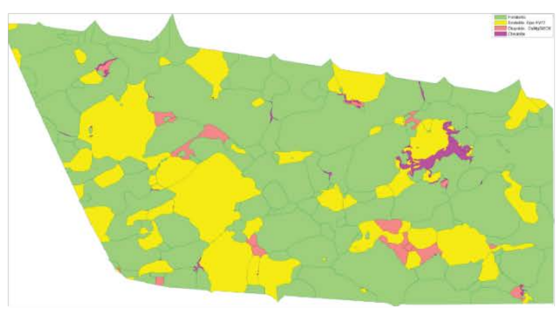

Figure C35-F. Phase map of sample FDM-DB04-X03, generated using the MTEX toolbox (v. 3.5.0), shows the reconstructed grain set comprising the one-point-per-grain (1ppg) dataset. Non-indexed regions are removed from the dataset during the production of this map.

Volcanic Center: Demas Bluff, Fosdick Mountains
Xenolith ID: FDM-DB04-X04

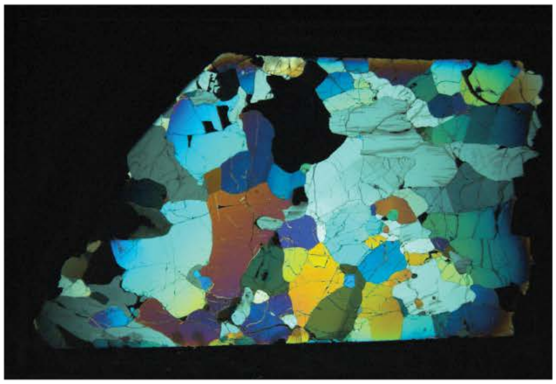

Figure C36-A. Full thin section photomicrograph of sample FDM-DB04-X04 viewed through cross-polarized light (XPL).

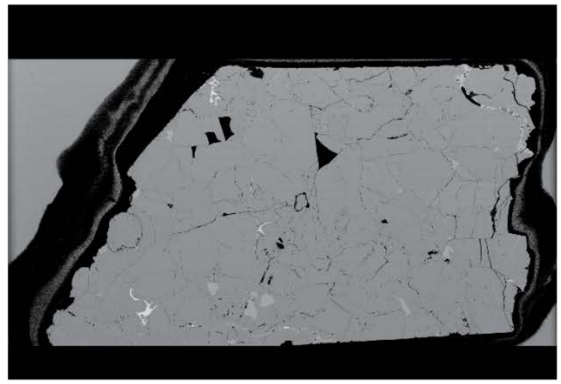

Figure C36-B. Panoramic back-scattered electron (BSE) image of sample FDM-DB04-X04.

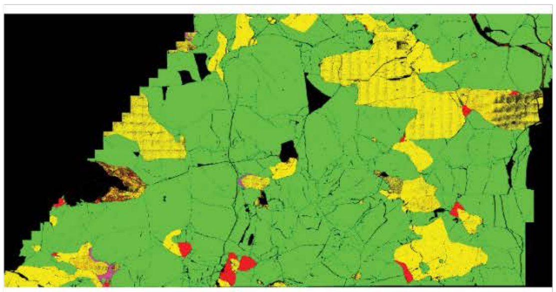

Figure C36-C. Phase map of sample FDM-DB04-X04, generated by the AZtec software based on the EBSD dataset. Each mineralogical phase is represented by a different color: green is olivine, yellow is enstatite, red is diopside, and magenta is chromite. Black pixels are non-indexed portions of the map.

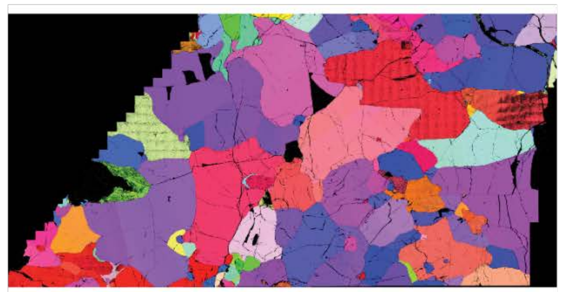

Figure C36-D. Inverse pole figure map of sample FDM-DB04-X04, generated by the AZtec analysis software (v. 3.0 SP1). Coloring of crystallographic orientations are shown with respect to the x-direction (e.g., inverse pole figure of olivine, right).

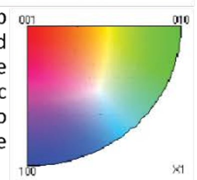

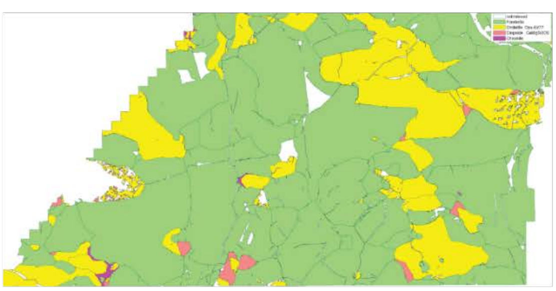

Figure C36-E. Phase map of sample FDM-DB04-X04, generated using the MTEX toolbox (v. 3.5.0), shows the reconstructed grain set comprising the noise-reduced EBSD dataset. Non-indexed regions are not removed from the dataset during the production of this map.

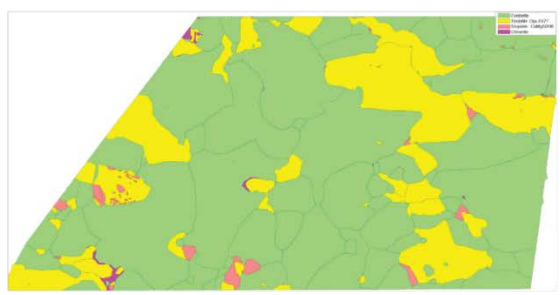

Figure C36-F. Phase map of sample FDM-DB04-X04, generated using the MTEX toolbox (v. 3.5.0), shows the reconstructed grain set comprising the one-point-per-grain (1ppg) dataset. Non-indexed regions are removed from the dataset during the production of this map.

VOLCANIC CENTER: MARUJUPU PEAK, FOSDICK MOUNTAINS
XENOLITH ID: FDM-MJ01-X01

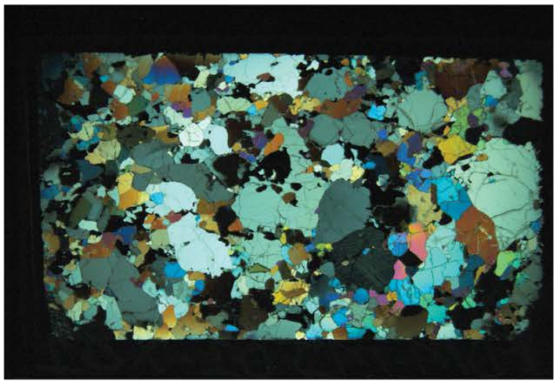

Figure C37-A. Full thin section photomicrograph of sample FDM-MJ01-X01 viewed through cross-polarized light (XPL).

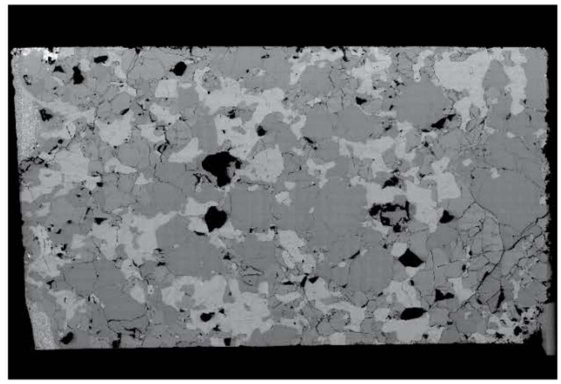

Figure C37-B. Panoramic back-scattered electron (BSE) image of sample FDM-MJ01-X01.

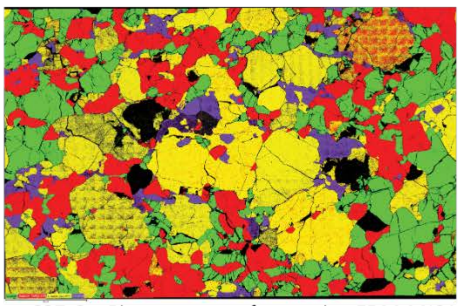

Figure C37-C. Phase map of sample FDM-MJ01-X01, generated by the AZtec software based on the EBSD dataset. Each mineralogical phase is represented by a different color: green is olivine, yellow is enstatite, red is diopside, and magenta is chromite. Black pixels are non-indexed portions of the map.

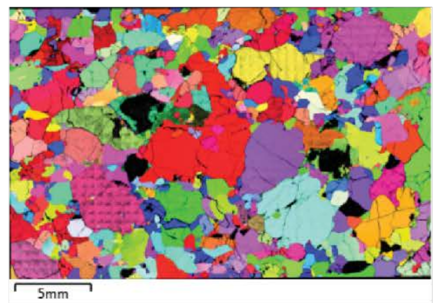

Figure C37-D. Inverse pole figure map of sample FDM-MJ01-X01, generated by the AZtec analysis software (v. 3.0 SP1). Coloring of crystallographic orientations are shown with respect to the x-direction. The olivine texture of this sample is not assessed because it is a pyroxenite.

Volcanic Center: Marujupu Peak, Fosdick Mountains
Xenolith ID: FDM-MJ01-X02

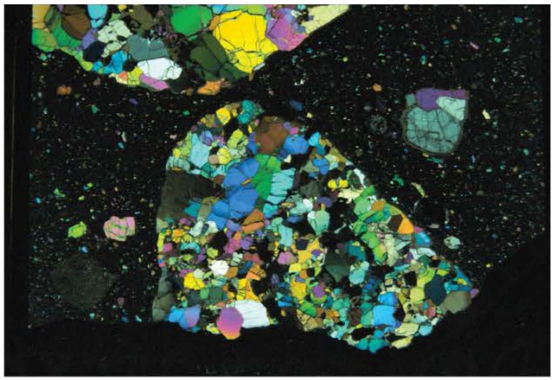

Figure C38-A. Full thin section photomicrograph of sample FDM-MJ01-X02 viewed through cross-polarized light (XPL).

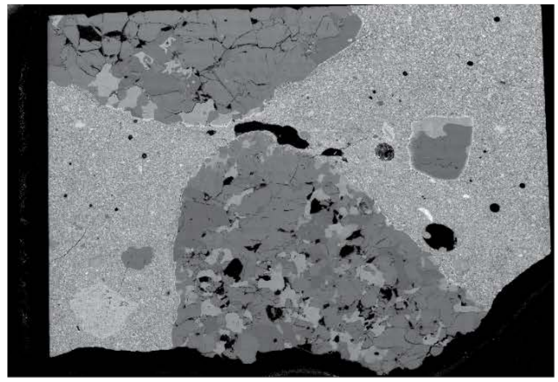

Figure C38-B. Panoramic back-scattered electron (BSE) image of sample FDM-MJ01-X02.

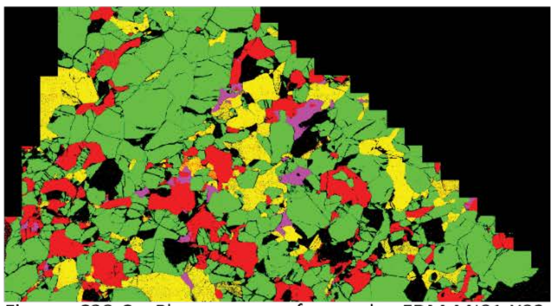

Figure C38-C. Phase map of sample FDM-MJ01-X02, generated by the AZtec software based on the EBSD dataset. Each mineralogical phase is represented by a different color: green is olivine, yellow is enstatite, red is diopside, and magenta is chromite. Black pixels are non-indexed portions of the map.

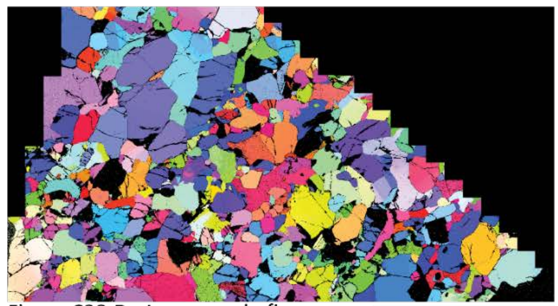

Figure C38-D. Inverse pole figure map of sample FDM-MJ01-X02, generated by the AZtec analysis software (v. 3.0 SP1). Coloring of crystallographic orientations are shown with respect to the x-direction (e.g., inverse pole figure of olivine, right).

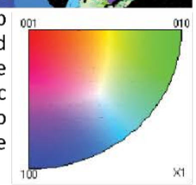

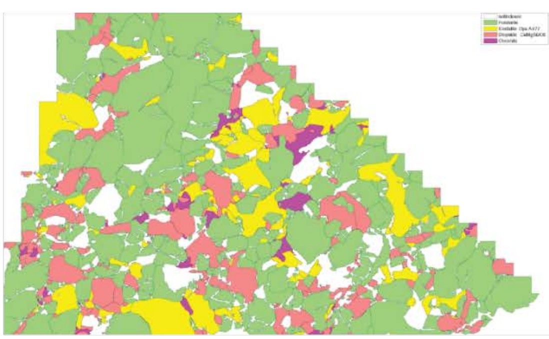

Figure C38-E. Phase map of sample FDM-MJ01-X02, generated using the MTEX toolbox (v. 3.5.0), shows the reconstructed grain set comprising the noise-reduced EBSD dataset. Non-indexed regions are not removed from the dataset during the production of this map.

Figure C38-F. Phase map of sample FDM-MJ01-X02, generated using the MTEX toolbox (v. 3.5.0), shows the reconstructed grain set comprising the one-point-per-grain (1ppg) dataset. Non-indexed regions are removed from the dataset during the production of this map.

Volcanic Center: Marujupu Peak, Fosdick Mountains
Xenolith ID: FDM-MJ01-X03

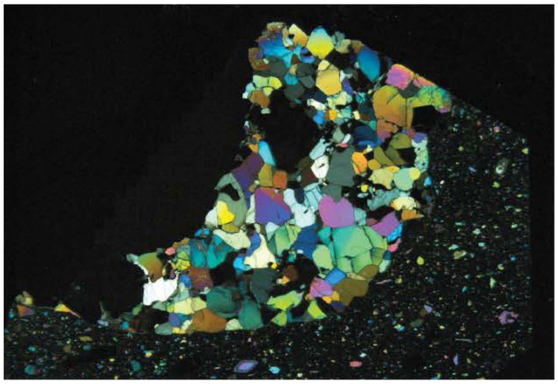

Figure C39-A. Full thin section photomicrograph of sample FDM-MJ01-X03 viewed through cross-polarized light (XPL).

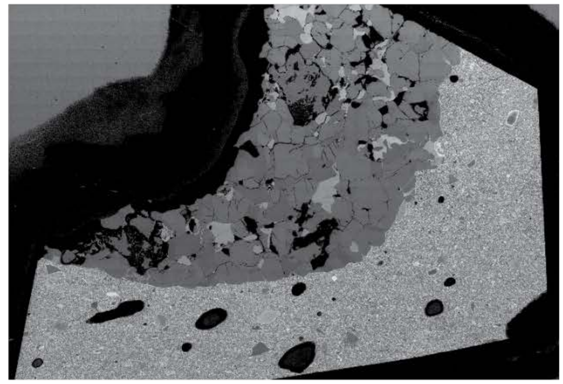

Figure C39-B. Panoramic back-scattered electron (BSE) image of sample FDM-MJ01-X03.

Figure C39-C. Phase map of sample FDM-MJ01-X03, generated by the AZtec software based on the EBSD dataset. Each mineralogical phase is represented by a different color: green is olivine, yellow is enstatite, red is diopside, and magenta is chromite. Black pixels are non-indexed portions of the map.

Figure C39-D. Inverse pole figure map of sample FDM-MJ01-X03, generated by the AZtec analysis software (v. 3.0 SP1). Coloring of crystallographic orientations are shown with respect to the x-direction (e.g., inverse pole figure of olivine, right).

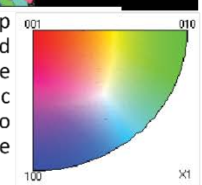

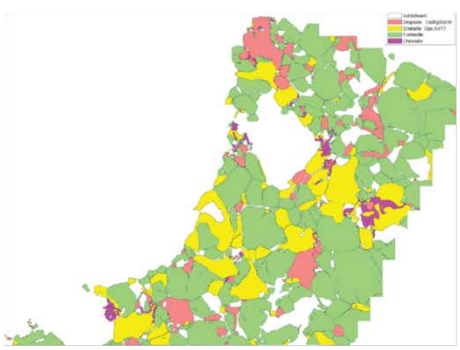

Figure C39-E. Phase map of sample FDM-MJ01-X03, generated using the MTEX toolbox (v. 3.5.0), shows the reconstructed grain set comprising the noise-reduced EBSD dataset. Non-indexed regions are not removed from the dataset during the production of this map.

Figure C39-F. Phase map of sample FDM-MJ01-X03, generated using the MTEX toolbox (v. 3.5.0), shows the reconstructed grain set comprising the one-point-per-grain (1ppg) dataset. Non-indexed regions are removed from the dataset during the production of this map.

Volcanic Center: Marujupu Peak, Fosdick Mountains
Xenolith ID: FDM-MJ01-X05

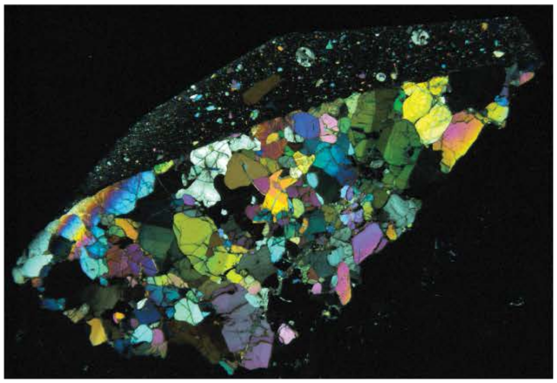

Figure C40-A. Full thin section photomicrograph of sample FDM-MJ01-X05 viewed through cross-polarized light (XPL).

Figure C40-B. Panoramic back-scattered electron (BSE) image of sample FDM-MJ01-X05.

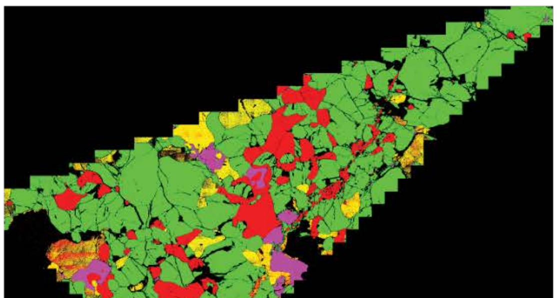

Figure C40-C. Phase map of sample FDM-MJ01-X05, generated by the AZtec software based on the EBSD dataset. Each mineralogical phase is represented by a different color: green is olivine, yellow is enstatite, red is diopside, and magenta is chromite. Black pixels are non-indexed portions of the map.

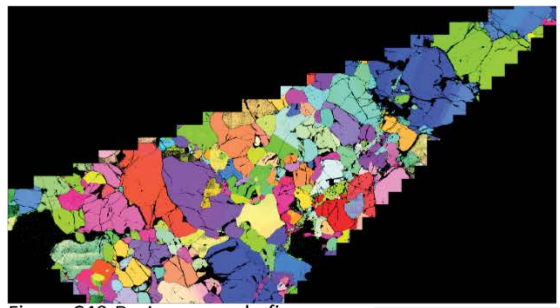

Figure C40-D. Inverse pole figure map of sample FDM-MJ01-X05, generated by the AZtec analysis software (v. 3.0 SP1). Coloring of crystallographic orientations are shown with respect to the x-direction (e.g., inverse pole figure of olivine, right).

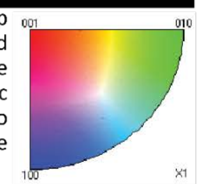

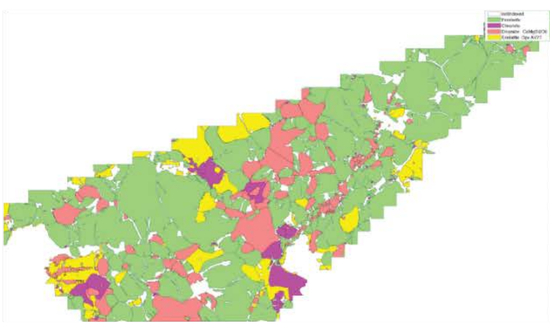

Figure C40-E. Phase map of sample FDM-MJ01-X05, generated using the MTEX toolbox (v. 3.5.0), shows the reconstructed grain set comprising the noise-reduced EBSD dataset. Non-indexed regions are not removed from the dataset during the production of this map.

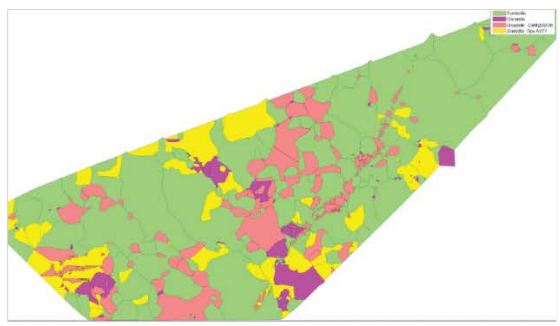

Figure C40-F. Phase map of sample FDM-MJ01-X05, generated using the MTEX toolbox (v. 3.5.0), shows the reconstructed grain set comprising the one-point-per-grain (1ppg) dataset. Non-indexed regions are removed from the dataset during the production of this map.

VOLCANIC CENTER: MARUJUPU PEAK, FOSDICK MOUNTAINS
XENOLITH ID: FDM-MJ01-X06

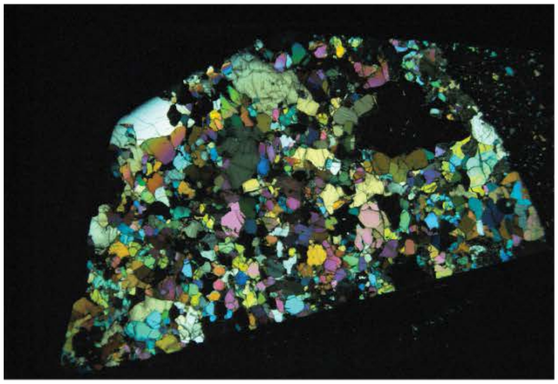

Figure C41-A. Full thin section photomicrograph of sample FDM-MJ01-X06 viewed through cross-polarized light (XPL).

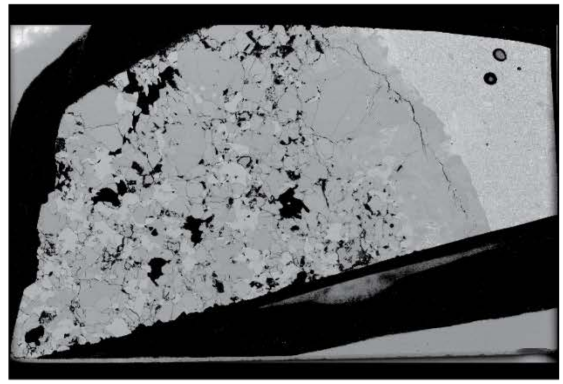

Figure C41-B. Panoramic back-scattered electron (BSE) image of sample FDM-MJ01-X06.

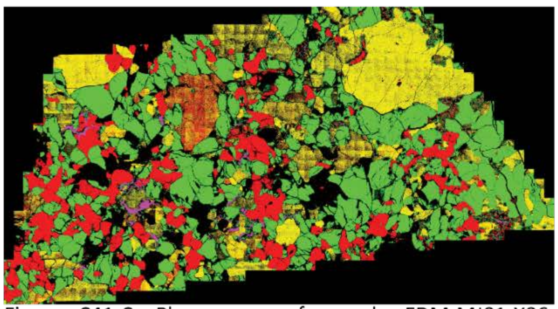

Figure C41-C. Phase map of sample FDM-MJ01-X06, generated by the AZtec software based on the EBSD dataset. Each mineralogical phase is represented by a different color: green is olivine, yellow is enstatite, red is diopside, and magenta is chromite. Black pixels are non-indexed portions of the map.

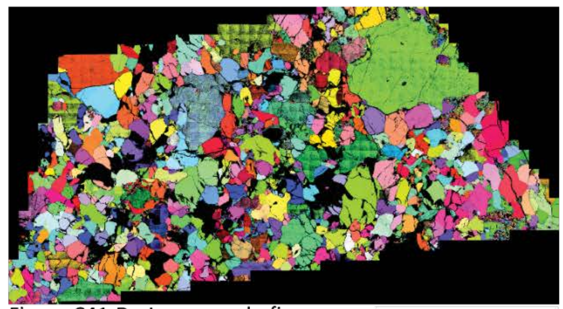

Figure C41-D. Inverse pole figure map of sample FDM-MJ01-X06, generated by the AZtec analysis software (v. 3.0 SP1). Coloring of crystallographic orientations are shown with respect to the x-direction (e.g., inverse pole figure of olivine, right).

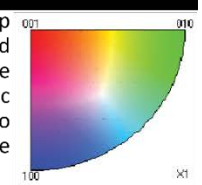

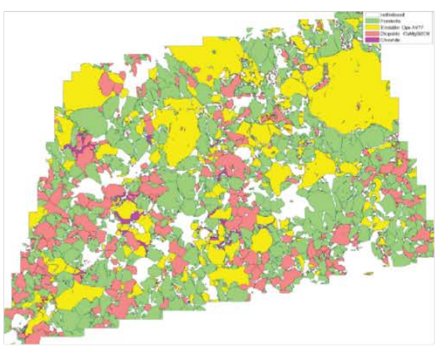

Figure C41-E. Phase map of sample FDM-MJ01-X06, generated using the MTEX toolbox (v. 3.5.0), shows the reconstructed grain set comprising the noise-reduced EBSD dataset. Non-indexed regions are not removed from the dataset during the production of this map.

Figure C41-F. Phase map of sample FDM-MJ01-X06, generated using the MTEX toolbox (v. 3.5.0), shows the reconstructed grain set comprising the one-point-per-grain (1ppg) dataset. Non-indexed regions are removed from the dataset during the production of this map.

VOLCANIC CENTER: MARUJUPU PEAK, FOSDICK MOUNTAINS
XENOLITH ID: FDM-RN01-X01

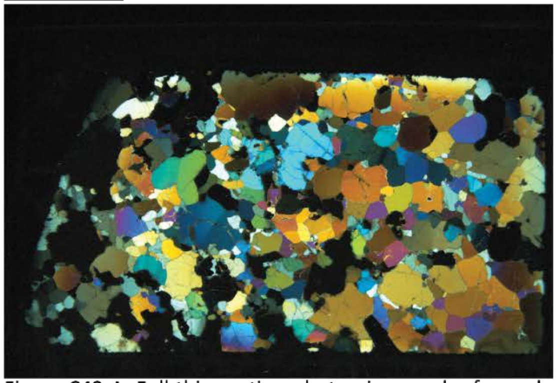

Figure C42-A. Full thin section photomicrograph of sample FDM-RN01-X01 viewed through cross-polarized light (XPL).

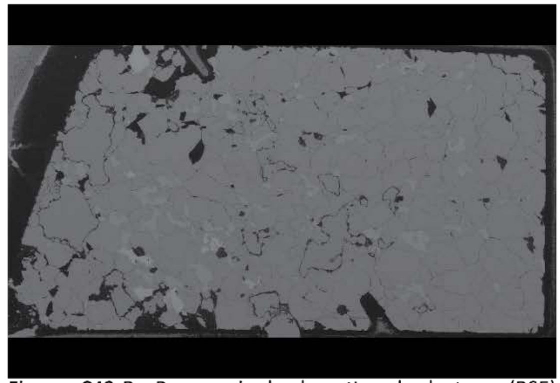

Figure C42-B. Panoramic back-scattered electron (BSE) image of sample FDM-RN01-X01.

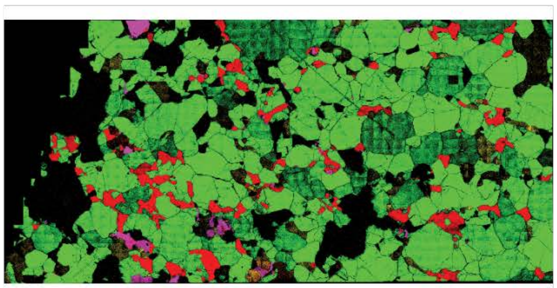

Figure C42-C. Phase map of sample FDM-RN01-X01, generated by the AZtec software based on the EBSD dataset. Each mineralogical phase is represented by a different color: green is olivine, yellow is enstatite, red is diopside, and magenta is chromite. Black pixels are non-indexed portions of the map.

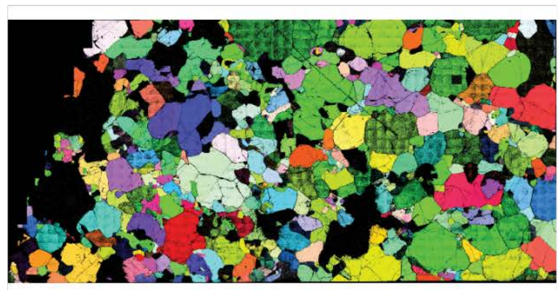

Figure C42-D. Inverse pole figure map of sample FDM-RN01-X01, generated by the AZtec analysis software (v. 3.0 SP1). Coloring of crystallographic orientations are shown with respect to the x-direction (e.g., inverse pole figure of olivine, right).

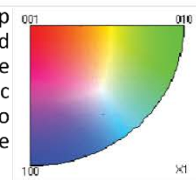

Figure C42-E. Phase map of sample FDM-RN01-X01, generated using the MTEX toolbox (v. 3.5.0), shows the reconstructed grain set comprising the noise-reduced EBSD dataset. Non-indexed regions are not removed from the dataset during the production of this map.

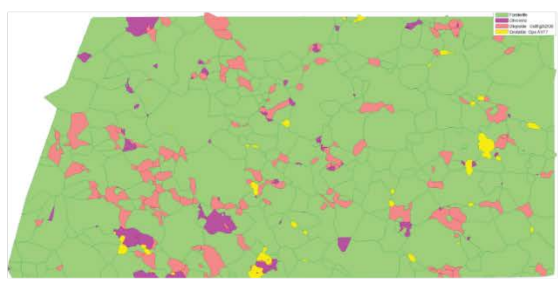

Figure C42-F. Phase map of sample FDM-RN01-X01, generated using the MTEX toolbox (v. 3.5.0), shows the reconstructed grain set comprising the one-point-per-grain (1ppg) dataset. Non-indexed regions are removed from the dataset during the production of this map.

VOLCANIC CENTER: MARUJUPU PEAK, FOSDICK MOUNTAINS
XENOLITH ID: FDM-RN02-X01

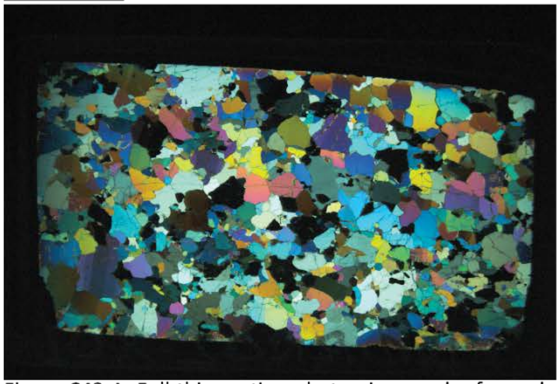

Figure C43-A. Full thin section photomicrograph of sample FDM-RN02-X01 viewed through cross-polarized light (XPL).

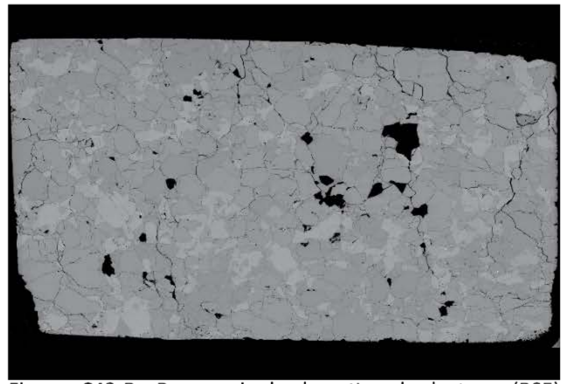

Figure C43-B. Panoramic back-scattered electron (BSE) image of sample FDM-RN02-X01.

Figure C43-C. Phase map of sample FDM-RN02-X01, generated by the AZtec software based on the EBSD dataset. Each mineralogical phase is represented by a different color: green is olivine, yellow is enstatite, red is diopside, and magenta is chromite. Black pixels are non-indexed portions of the map.

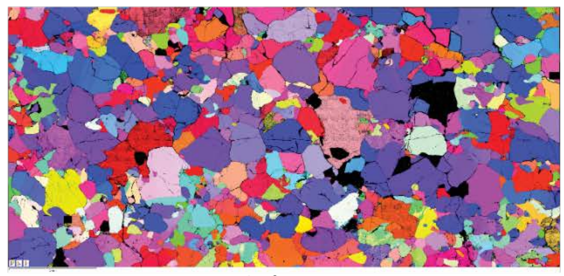

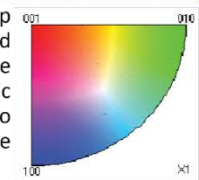

Figure C43-D. Inverse pole figure map of sample FDM-RN02-X01, generated by the AZtec analysis software (v. 3.0 SP1). Coloring of crystallographic orientations are shown with respect to the x-direction (e.g., inverse pole figure of olivine, right).

Figure C43-E. Phase map of sample FDM-RN02-X01, generated using the MTEX toolbox (v. 3.5.0), shows the reconstructed grain set comprising the noise-reduced EBSD dataset. Non-indexed regions are not removed from the dataset during the production of this map.

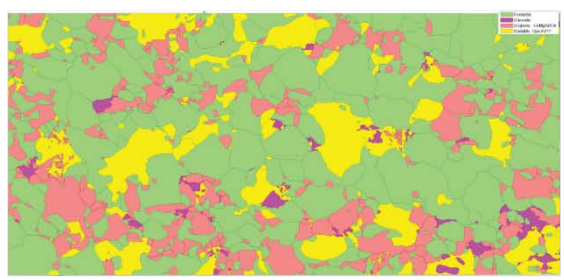

Figure C43-F. Phase map of sample FDM-RN02-X01, generated using the MTEX toolbox (v. 3.5.0), shows the reconstructed grain set comprising the one-point-per-grain (1ppg) dataset. Non-indexed regions are removed from the dataset during the production of this map.

Volcanic Center: Marujupu Peak, Fosdick Mountains
Xenolith ID: FDM-RN03-X01

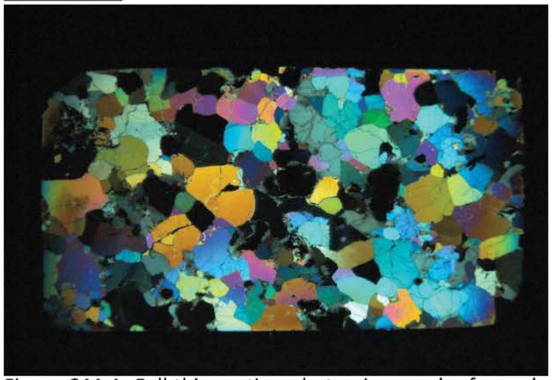

Figure C44-A. Full thin section photomicrograph of sample FDM-RN03-X01 viewed through cross-polarized light (XPL).

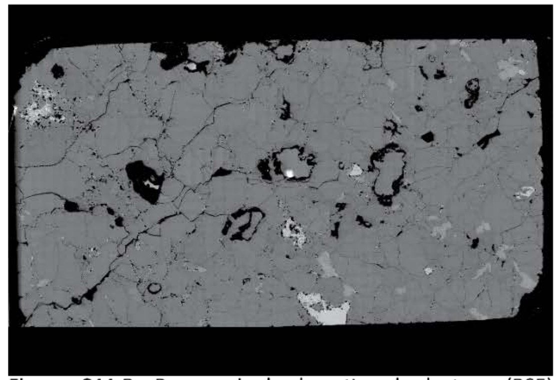

Figure C44-B. Panoramic back-scattered electron (BSE) image of sample FDM-RN03-X01.

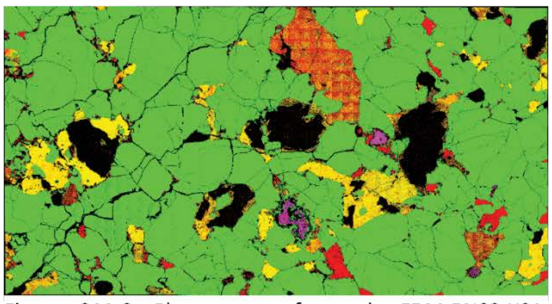

Figure C44-C. Phase map of sample FDM-RN03-X01, generated by the AZtec software based on the EBSD dataset. Each mineralogical phase is represented by a different color: green is olivine, yellow is enstatite, red is diopside, and magenta is chromite. Black pixels are non-indexed portions of the map.

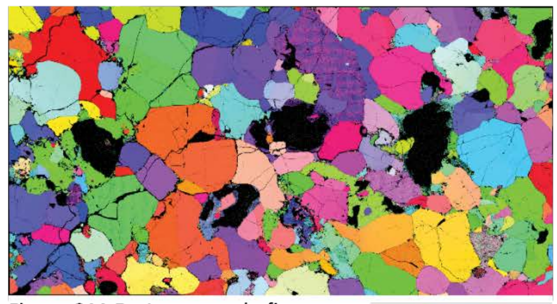

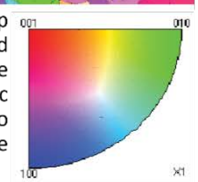

Figure C44-D. Inverse pole figure map of sample FDM-RN03-X01, generated by the AZtec analysis software (v. 3.0 SP1). Coloring of crystallographic orientations are shown with respect to the x-direction (e.g., inverse pole figure of olivine, right).

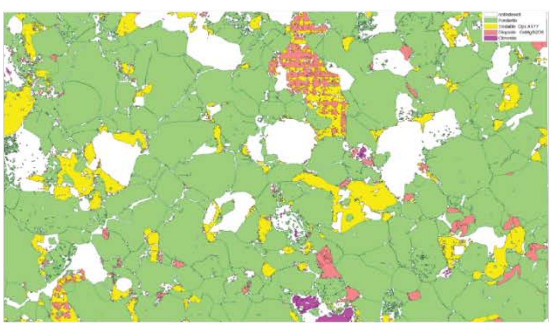

Figure C44-E. Phase map of sample FDM-RN03-X01, generated using the MTEX toolbox (v. 3.5.0), shows the reconstructed grain set comprising the noise-reduced EBSD dataset. Non-indexed regions are not removed from the dataset during the production of this map.

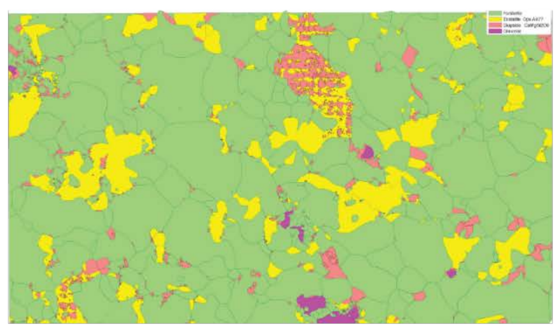

Figure C44-F. Phase map of sample FDM-RN03-X01, generated using the MTEX toolbox (v. 3.5.0), shows the reconstructed grain set comprising the one-point-per-grain (1ppg) dataset. Non-indexed regions are removed from the dataset during the production of this map.

VOLCANIC CENTER: MARUJUPU PEAK, FOSDICK MOUNTAINS
XENOLITH ID: FDM-RN04-X01

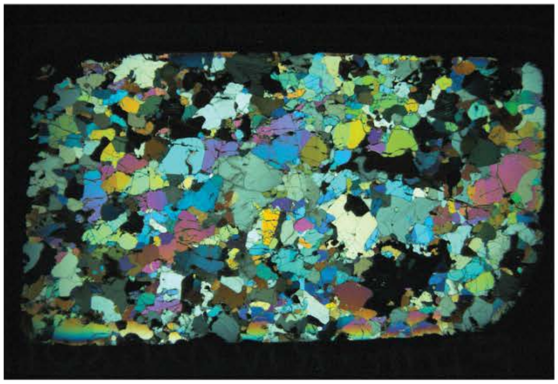

Figure C45-A. Full thin section photomicrograph of sample FDM-RN04-X01 viewed through cross-polarized light (XPL).

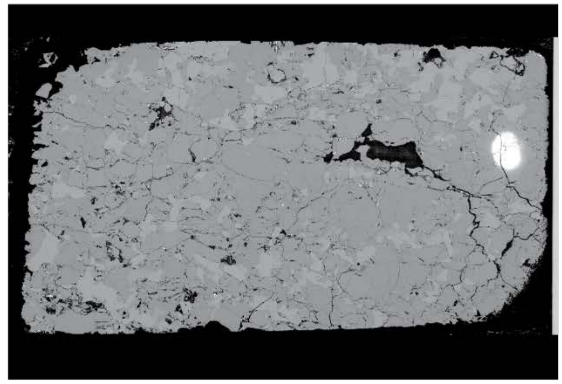

Figure C45-B. Panoramic back-scattered electron (BSE) image of sample FDM-RN04-X01.

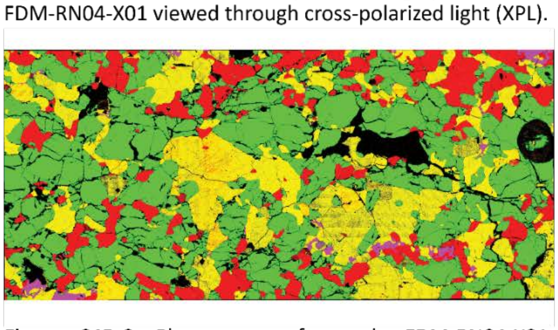

Figure C45-C. Phase map of sample FDM-RN04-X01, generated by the AZtec software based on the EBSD dataset. Each mineralogical phase is represented by a different color: green is olivine, yellow is enstatite, red is diopside, and magenta is chromite. Black pixels are non-indexed portions of the map.

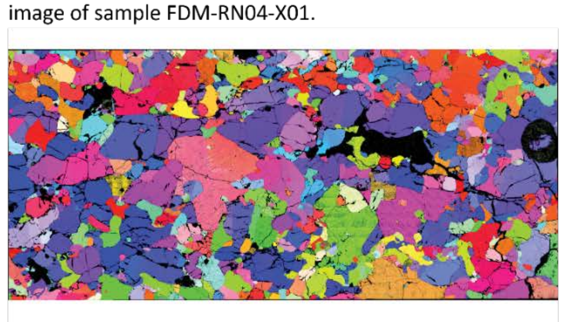

Figure C45-D. Inverse pole figure map of sample FDM-RN04-X01, generated by the AZtec analysis software (v. 3.0 SP1). Coloring of crystallographic orientations are shown with respect to the x-direction (e.g., inverse pole figure of olivine, right).

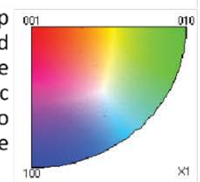

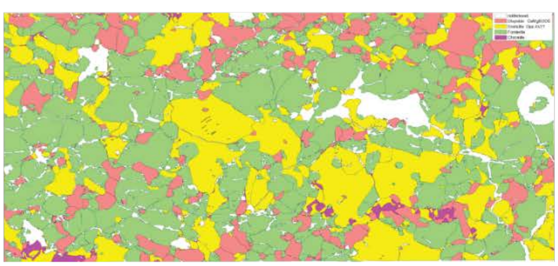

Figure C45-E. Phase map of sample FDM-RN04-X01, generated using the MTEX toolbox (v. 3.5.0), shows the reconstructed grain set comprising the noise-reduced EBSD dataset. Non-indexed regions are not removed from the dataset during the production of this map.

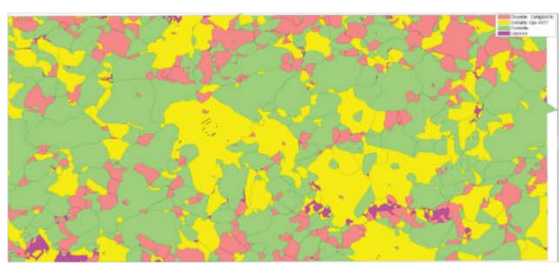

Figure C45-F. Phase map of sample FDM-RN04-X01, generated using the MTEX toolbox (v. 3.5.0), shows the reconstructed grain set comprising the one-point-per-grain (1ppg) dataset. Non-indexed regions are removed from the dataset during the production of this map.

APPENDIX D

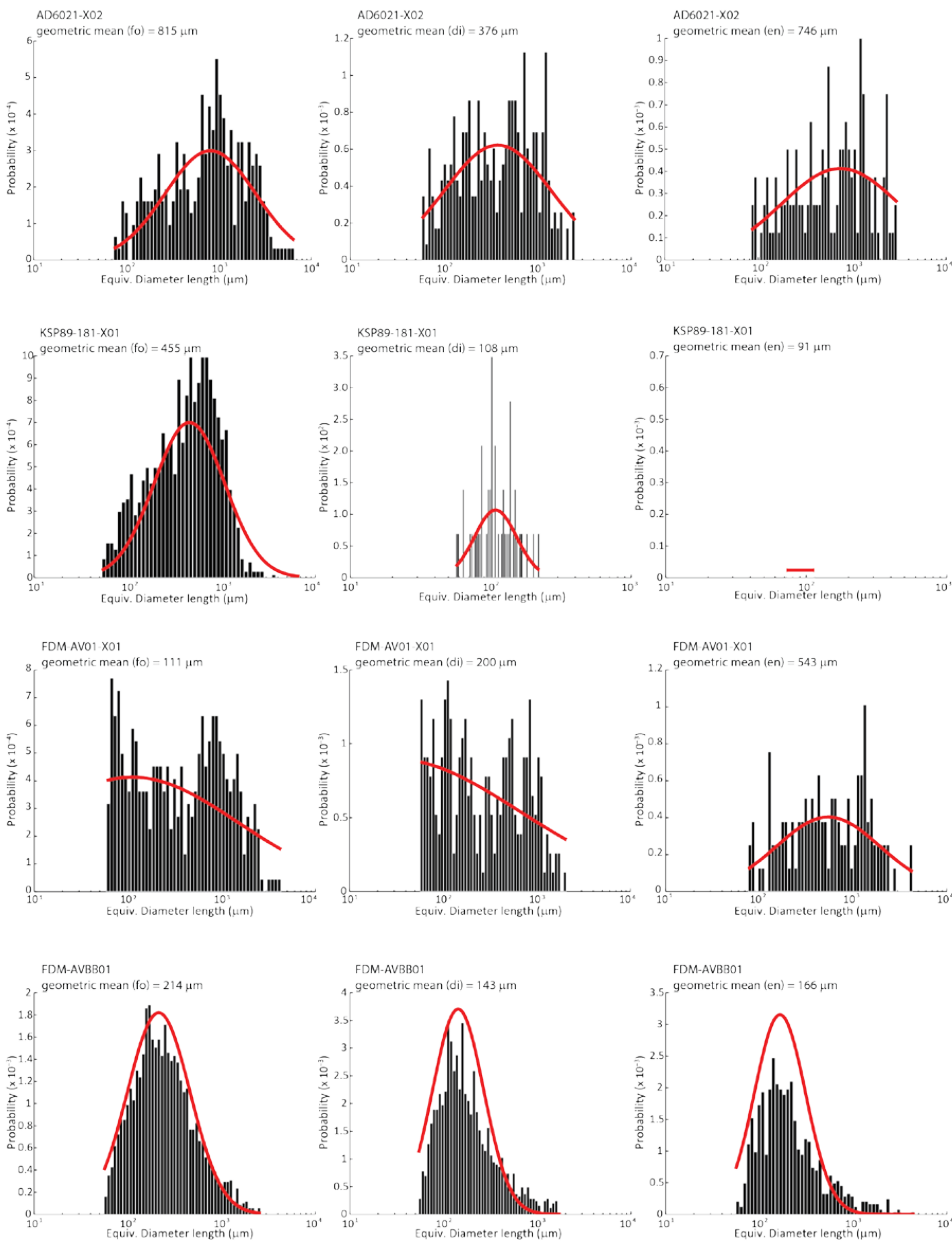
AD6021-X02
geometric mean (fo) = 815 μm
AD6021-X02
geometric mean (di) = 376 μm
AD6021-X02
geometric mean (en) = 746 μm
KSP89-181-X01
geometric mean (fo) = 455 μm
KSP89-181-X01
geometric mean (di) = 108 μm
KSP89-181-X01
geometric mean (en) = 91 μm
FDM-AV01-X01
geometric mean (fo) = 111 μm
FDM-AV01-X01
geometric mean (di) = 200 μm
FDM-AV01-X01
geometric mean (en) = 543 μm
FDM-AVBB01
geometric mean (fo) = 214 μm
FDM-AVBB01
geometric mean (di) = 143 μm
FDM-AVBB01
geometric mean (en) = 166 μm
Probability
Equiv. Diameter length (μm)

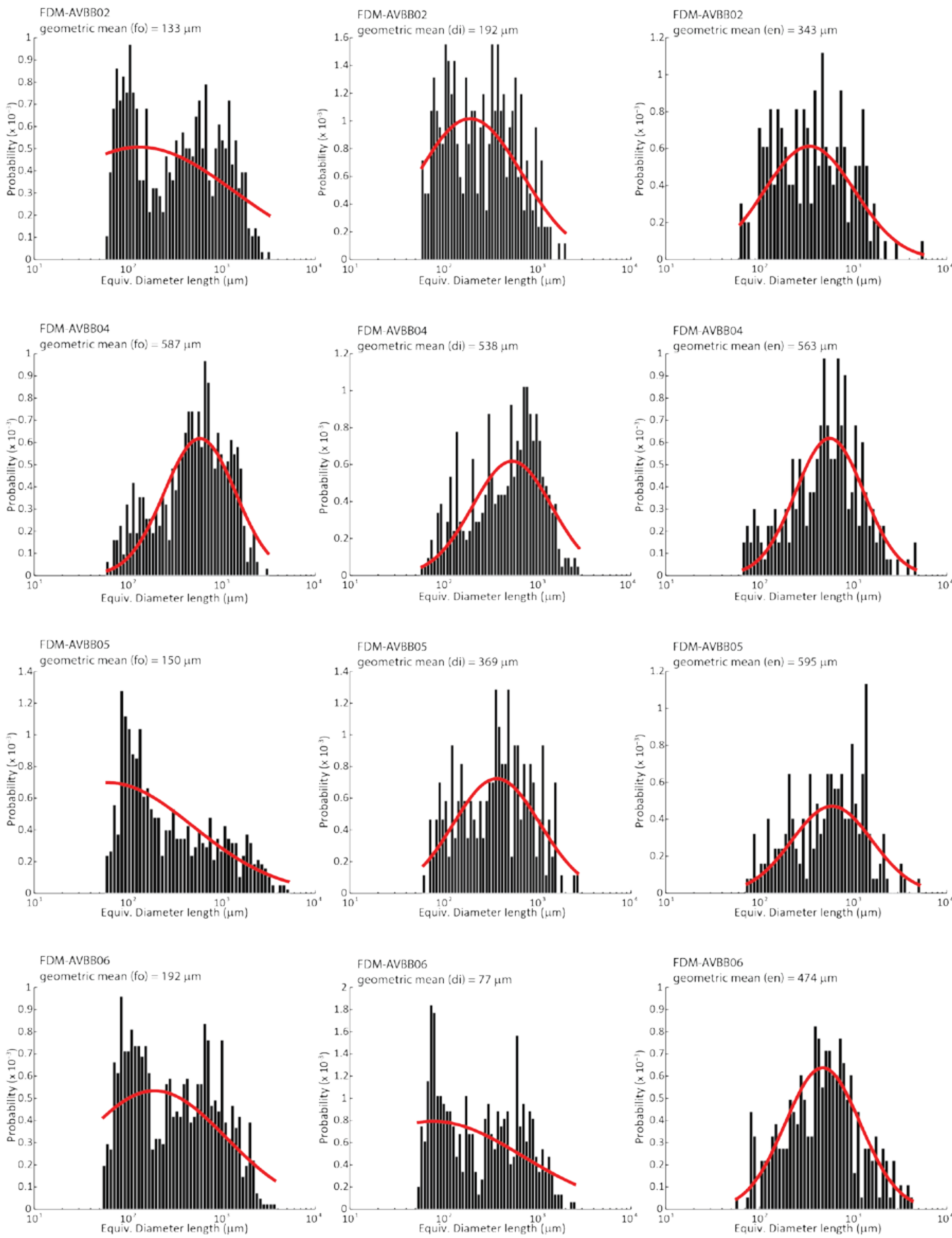
FDM-AVBB02
geometric mean (fo) = 133 μm
FDM-AVBB02
geometric mean (di) = 192 μm
FDM-AVBB02
geometric mean (en) = 343 μm
FDM-AVBB04
geometric mean (fo) = 587 μm
FDM-AVBB04
geometric mean (di) = 538 μm
FDM-AVBB04
geometric mean (en) = 563 μm
FDM-AVBB05
geometric mean (fo) = 150 μm
FDM-AVBB05
geometric mean (di) = 369 μm
FDM-AVBB05
geometric mean (en) = 595 μm
FDM-AVBB06
geometric mean (fo) = 192 μm
FDM-AVBB06
geometric mean (di) = 77 μm
FDM-AVBB06
geometric mean (en) = 474 μm
Probability
Equiv. Diameter length (μm)

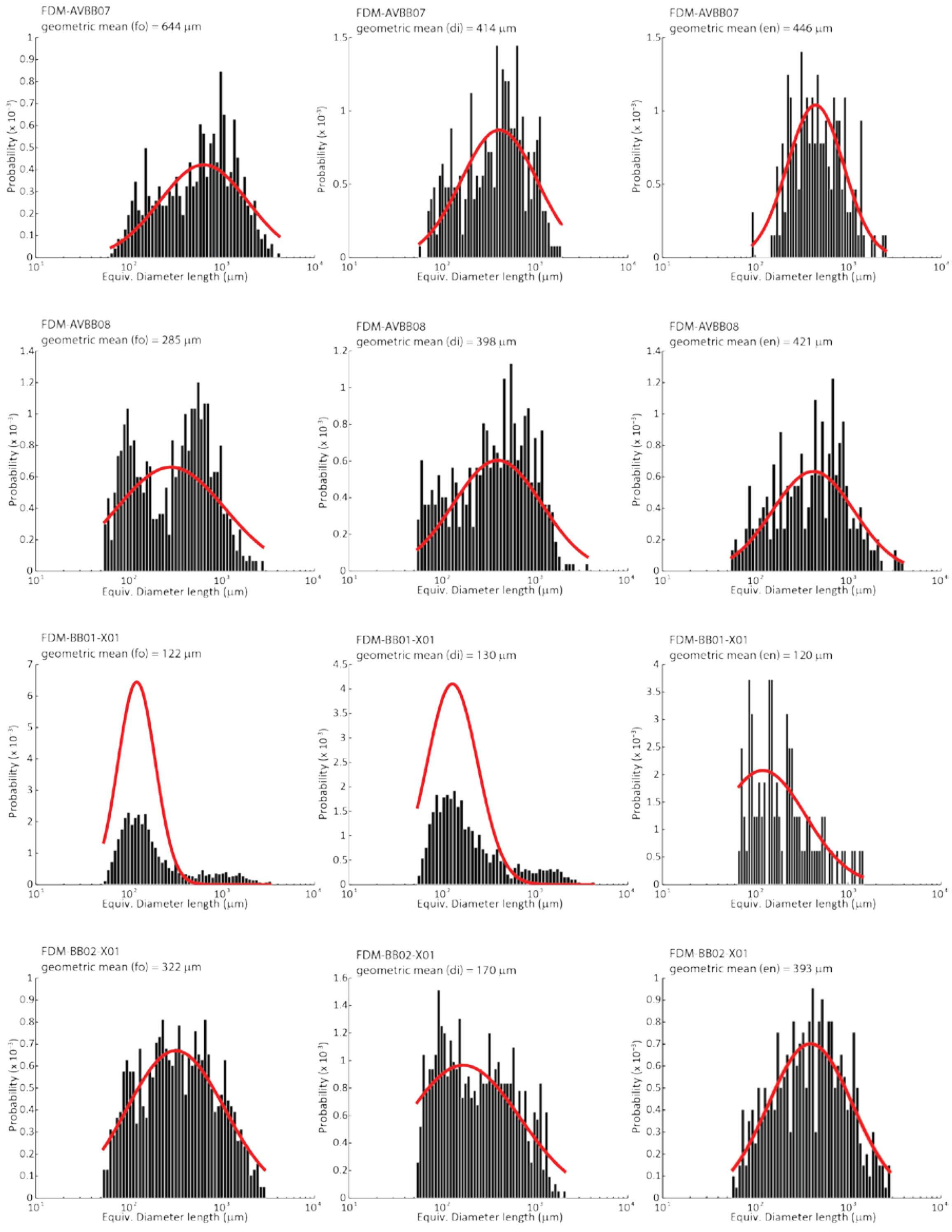
FDM-AVBB07
geometric mean (fo) = 644 μm
FDM-AVBB07
geometric mean (di) = 414 μm
FDM-AVBB07
geometric mean (en) = 446 μm
FDM-AVBB08
geometric mean (fo) = 285 μm
FDM-AVBB08
geometric mean (di) = 398 μm
FDM-AVBB08
geometric mean (en) = 421 μm
FDM-BB01-X01
geometric mean (fo) = 122 μm
FDM-BB01-X01
geometric mean (di) = 130 μm
FDM-BB01-X01
geometric mean (en) = 120 μm
FDM-BB02-X01
geometric mean (fo) = 322 μm
FDM-BB02-X01
geometric mean (di) = 170 μm
FDM-BB02-X01
geometric mean (en) = 393 μm
Probability (x 10⁻³)
Equiv. Diameter length (μm)

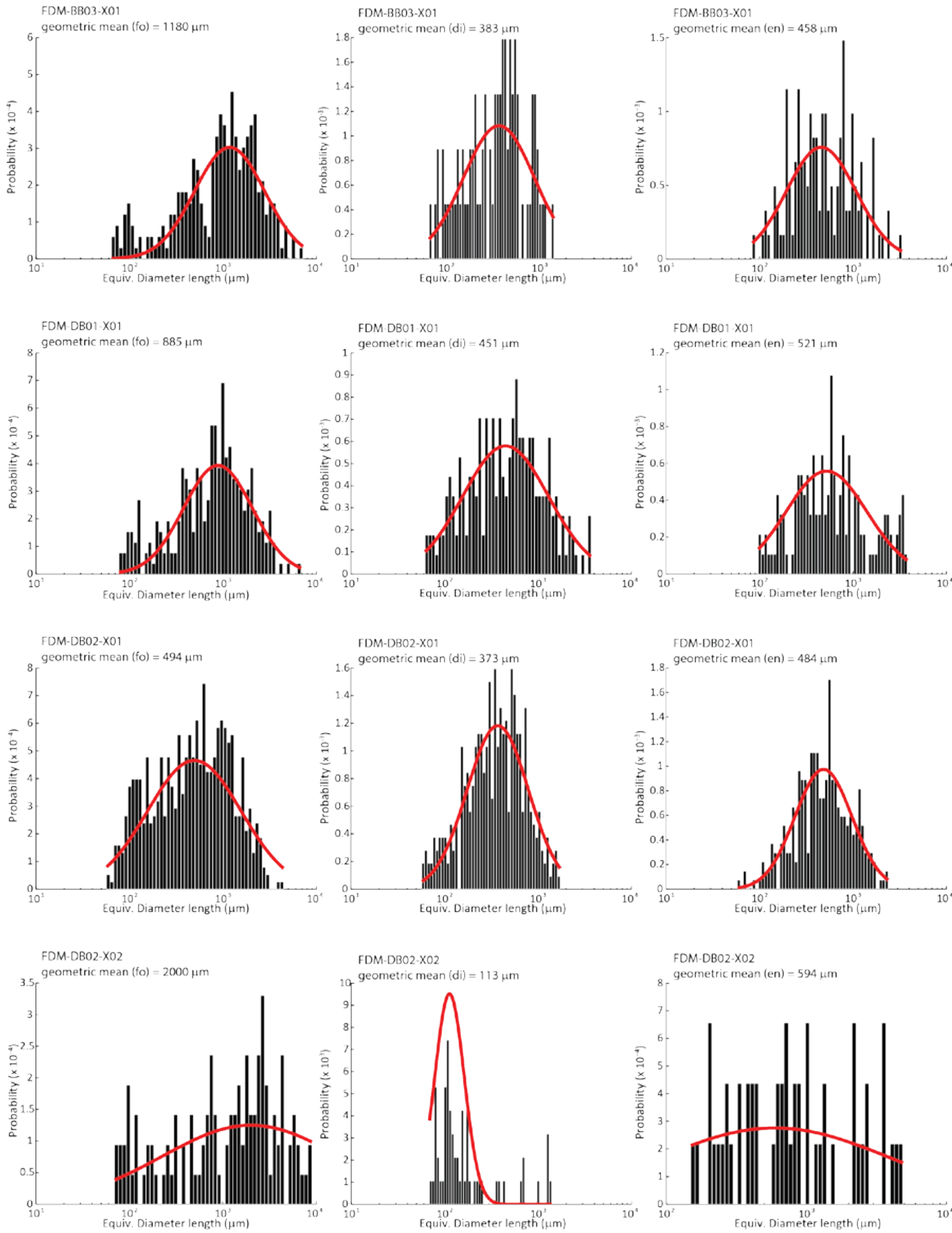
FDM-BB03-X01
geometric mean (fo) = 1180 μm
FDM-BB03-X01
geometric mean (di) = 383 μm
FDM-BB03-X01
geometric mean (en) = 458 μm
FDM-DB01-X01
geometric mean (fo) = 885 μm
FDM-DB01-X01
geometric mean (di) = 451 μm
FDM-DB01-X01
geometric mean (en) = 521 μm
FDM-DB02-X01
geometric mean (fo) = 494 μm
FDM-DB02-X01
geometric mean (di) = 373 μm
FDM-DB02-X01
geometric mean (en) = 484 μm
FDM-DB02-X02
geometric mean (fo) = 2000 μm
FDM-DB02-X02
geometric mean (di) = 113 μm
FDM-DB02-X02
geometric mean (en) = 594 μm
Equiv. Diameter length (μm)
Probability

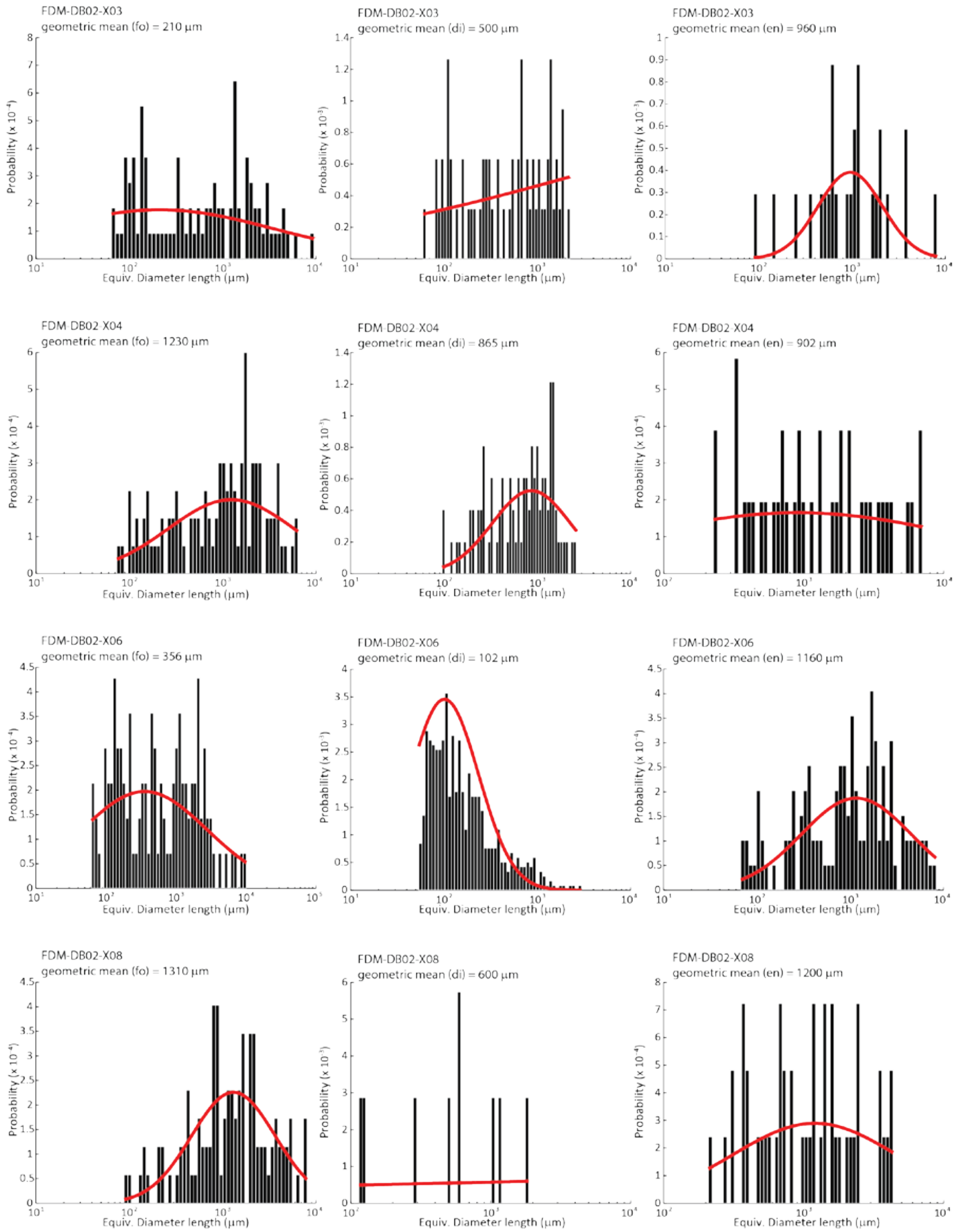
FDM-DB02-X03
geometric mean (fo) = 210 μm
FDM-DB02-X03
geometric mean (di) = 500 μm
FDM-DB02-X03
geometric mean (en) = 960 μm
FDM-DB02-X04
geometric mean (fo) = 1230 μm
FDM-DB02-X04
geometric mean (di) = 865 μm
FDM-DB02-X04
geometric mean (en) = 902 μm
FDM-DB02-X06
geometric mean (fo) = 356 μm
FDM-DB02-X06
geometric mean (di) = 102 μm
FDM-DB02-X06
geometric mean (en) = 1160 μm
FDM-DB02-X08
geometric mean (fo) = 1310 μm
FDM-DB02-X08
geometric mean (di) = 600 μm
FDM-DB02-X08
geometric mean (en) = 1200 μm
Probability (x 10⁻⁴)
Probability (x 10⁻³)
Equiv. Diameter length (μm)

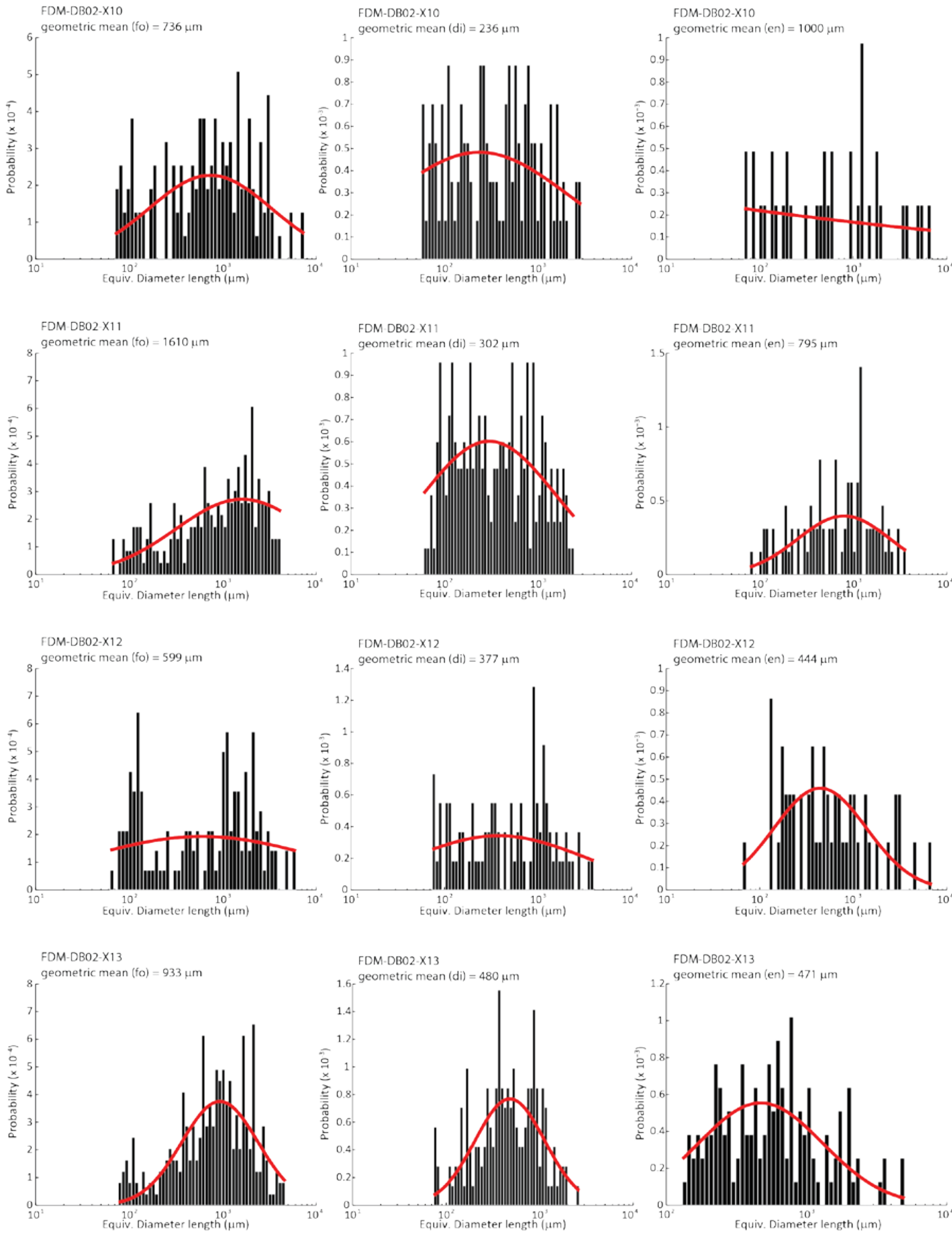
FDM-DB02-X10
geometric mean (fo) = 736 μm
FDM-DB02-X10
geometric mean (di) = 236 μm
FDM-DB02-X10
geometric mean (en) = 1000 μm
FDM-DB02-X11
geometric mean (fo) = 1610 μm
FDM-DB02-X11
geometric mean (di) = 302 μm
FDM-DB02-X11
geometric mean (en) = 795 μm
FDM-DB02-X12
geometric mean (fo) = 599 μm
FDM-DB02-X12
geometric mean (di) = 377 μm
FDM-DB02-X12
geometric mean (en) = 444 μm
FDM-DB02-X13
geometric mean (fo) = 933 μm
FDM-DB02-X13
geometric mean (di) = 480 μm
FDM-DB02-X13
geometric mean (en) = 471 μm
Probability (x 10⁻⁴)
Probability (x 10⁻³)
Equiv. Diameter length (μm)

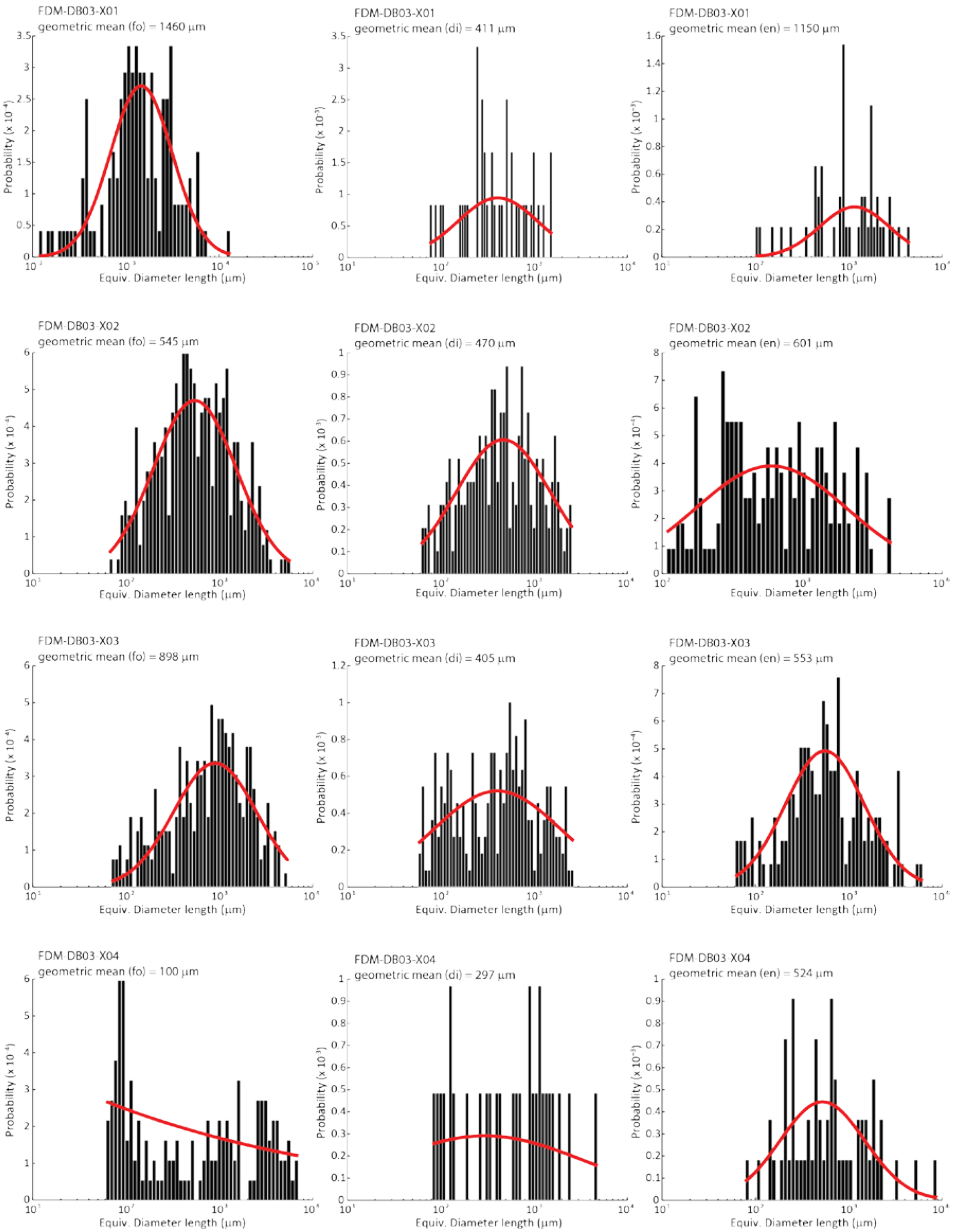
FDM-DB03-X01
geometric mean (fo) = 1460 μm
FDM-DB03-X01
geometric mean (di) = 411 μm
FDM-DB03-X01
geometric mean (en) = 1150 μm
FDM-DB03-X02
geometric mean (fo) = 545 μm
FDM-DB03-X02
geometric mean (di) = 470 μm
FDM-DB03-X02
geometric mean (en) = 601 μm
FDM-DB03-X03
geometric mean (fo) = 898 μm
FDM-DB03-X03
geometric mean (di) = 405 μm
FDM-DB03-X03
geometric mean (en) = 553 μm
FDM-DB03-X04
geometric mean (fo) = 100 μm
FDM-DB03-X04
geometric mean (di) = 297 μm
FDM-DB03-X04
geometric mean (en) = 524 μm
Probability
Equiv. Diameter length (μm)

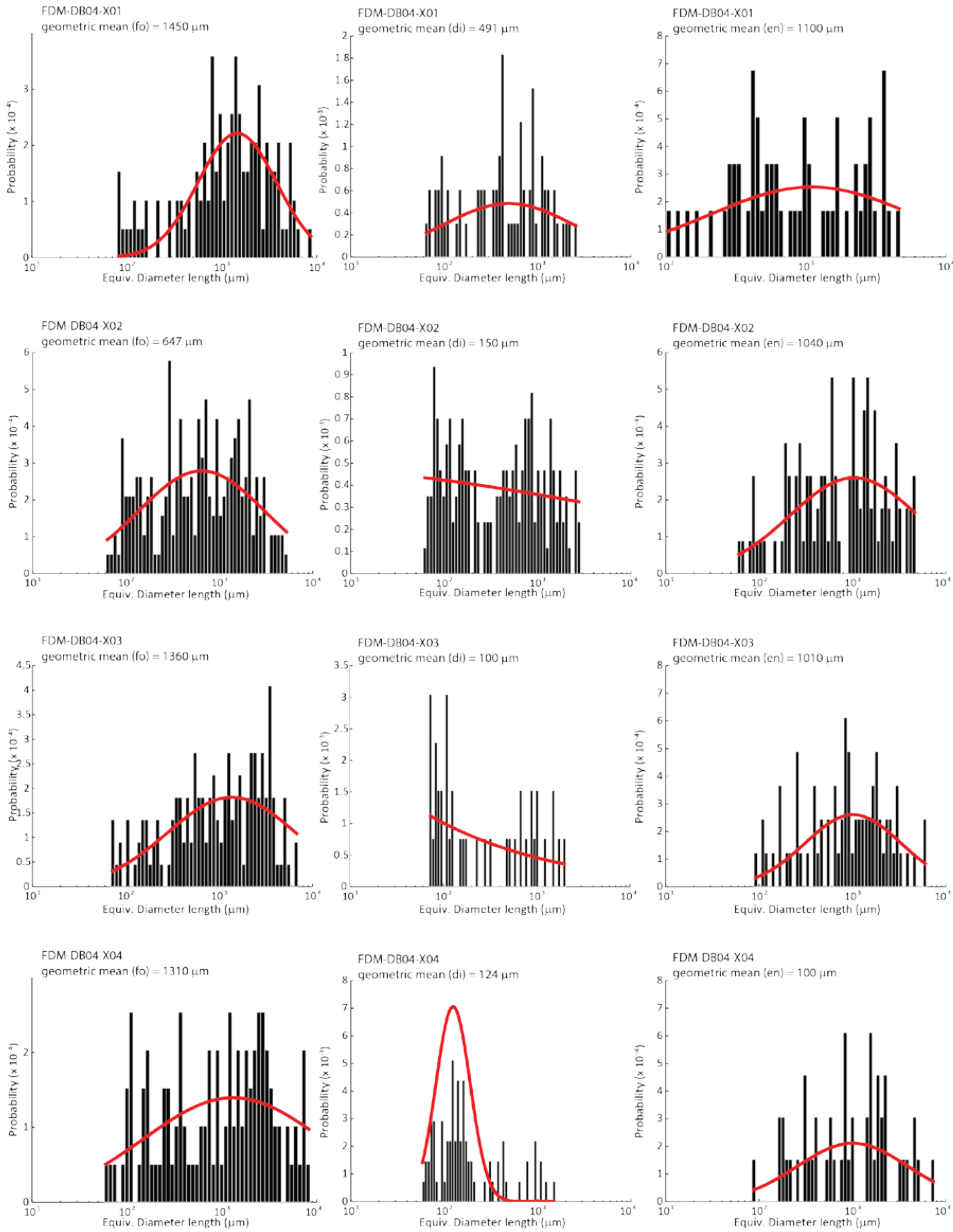
FDM-DB04-X01
geometric mean (fo) = 1450 μm
FDM-DB04-X01
geometric mean (di) = 491 μm
FDM-DB04-X01
geometric mean (en) = 1100 μm
FDM-DB04-X02
geometric mean (fo) = 647 μm
FDM-DB04-X02
geometric mean (di) = 150 μm
FDM-DB04-X02
geometric mean (en) = 1040 μm
FDM-DB04-X03
geometric mean (fo) = 1360 μm
FDM-DB04-X03
geometric mean (di) = 100 μm
FDM-DB04-X03
geometric mean (en) = 1010 μm
FDM-DB04-X04
geometric mean (fo) = 1310 μm
FDM-DB04-X04
geometric mean (di) = 124 μm
FDM-DB04-X04
geometric mean (en) = 100 μm
Probability
Equiv. Diameter length (μm)

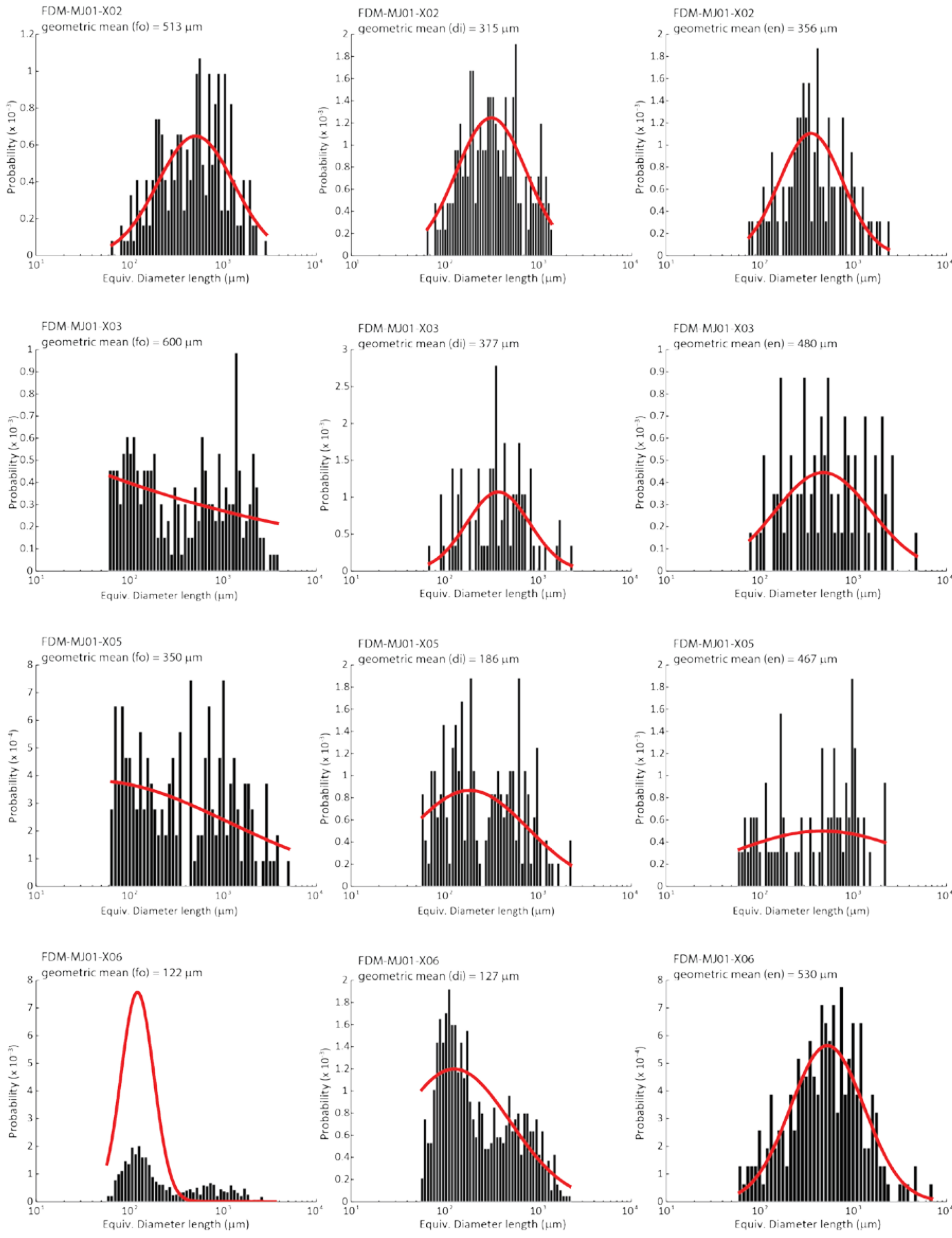
FDM-MJ01-X02
geometric mean (fo) = 513 μm
Probability (x 10⁻³)
Equiv. Diameter length (μm)
FDM-MJ01-X02
geometric mean (di) = 315 μm
Probability (x 10⁻³)
Equiv. Diameter length (μm)
FDM-MJ01-X02
geometric mean (en) = 356 μm
Probability (x 10⁻³)
Equiv. Diameter length (μm)
FDM-MJ01-X03
geometric mean (fo) = 600 μm
Probability (x 10⁻³)
Equiv. Diameter length (μm)
FDM-MJ01-X03
geometric mean (di) = 377 μm
Probability (x 10⁻³)
Equiv. Diameter length (μm)
FDM-MJ01-X03
geometric mean (en) = 480 μm
Probability (x 10⁻³)
Equiv. Diameter length (μm)
FDM-MJ01-X05
geometric mean (fo) = 350 μm
Probability (x 10⁻⁴)
Equiv. Diameter length (μm)
FDM-MJ01-X05
geometric mean (di) = 186 μm
Probability (x 10⁻³)
Equiv. Diameter length (μm)
FDM-MJ01-X05
geometric mean (en) = 467 μm
Probability (x 10⁻³)
Equiv. Diameter length (μm)
FDM-MJ01-X06
geometric mean (fo) = 122 μm
Probability (x 10⁻³)
Equiv. Diameter length (μm)
FDM-MJ01-X06
geometric mean (di) = 127 μm
Probability (x 10⁻³)
Equiv. Diameter length (μm)
FDM-MJ01-X06
geometric mean (en) = 530 μm
Probability (x 10⁻⁴)
Equiv. Diameter length (μm)

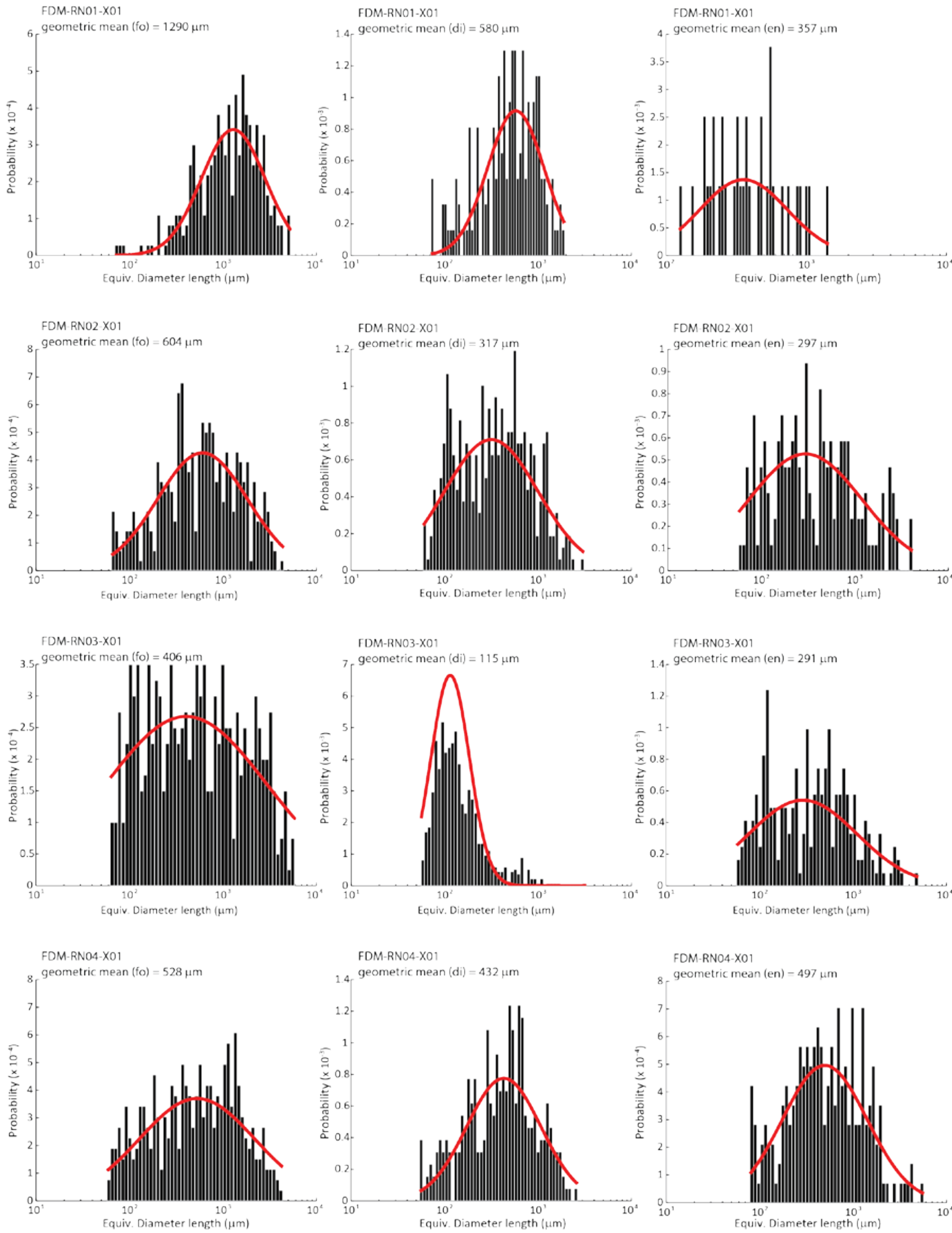
FDM-RN01-X01
geometric mean (fo) = 1290 μm
FDM-RN01-X01
geometric mean (di) = 580 μm
FDM-RN01-X01
geometric mean (en) = 357 μm
FDM-RN02-X01
geometric mean (fo) = 604 μm
FDM-RN02-X01
geometric mean (di) = 317 μm
FDM-RN02-X01
geometric mean (en) = 297 μm
FDM-RN03-X01
geometric mean (fo) = 406 μm
FDM-RN03-X01
geometric mean (di) = 115 μm
FDM-RN03-X01
geometric mean (en) = 291 μm
FDM-RN04-X01
geometric mean (fo) = 528 μm
FDM-RN04-X01
geometric mean (di) = 432 μm
FDM-RN04-X01
geometric mean (en) = 497 μm
Probability (x 10⁻⁴)
Probability (x 10⁻³)
Equiv. Diameter length (μm)

APPENDIX E

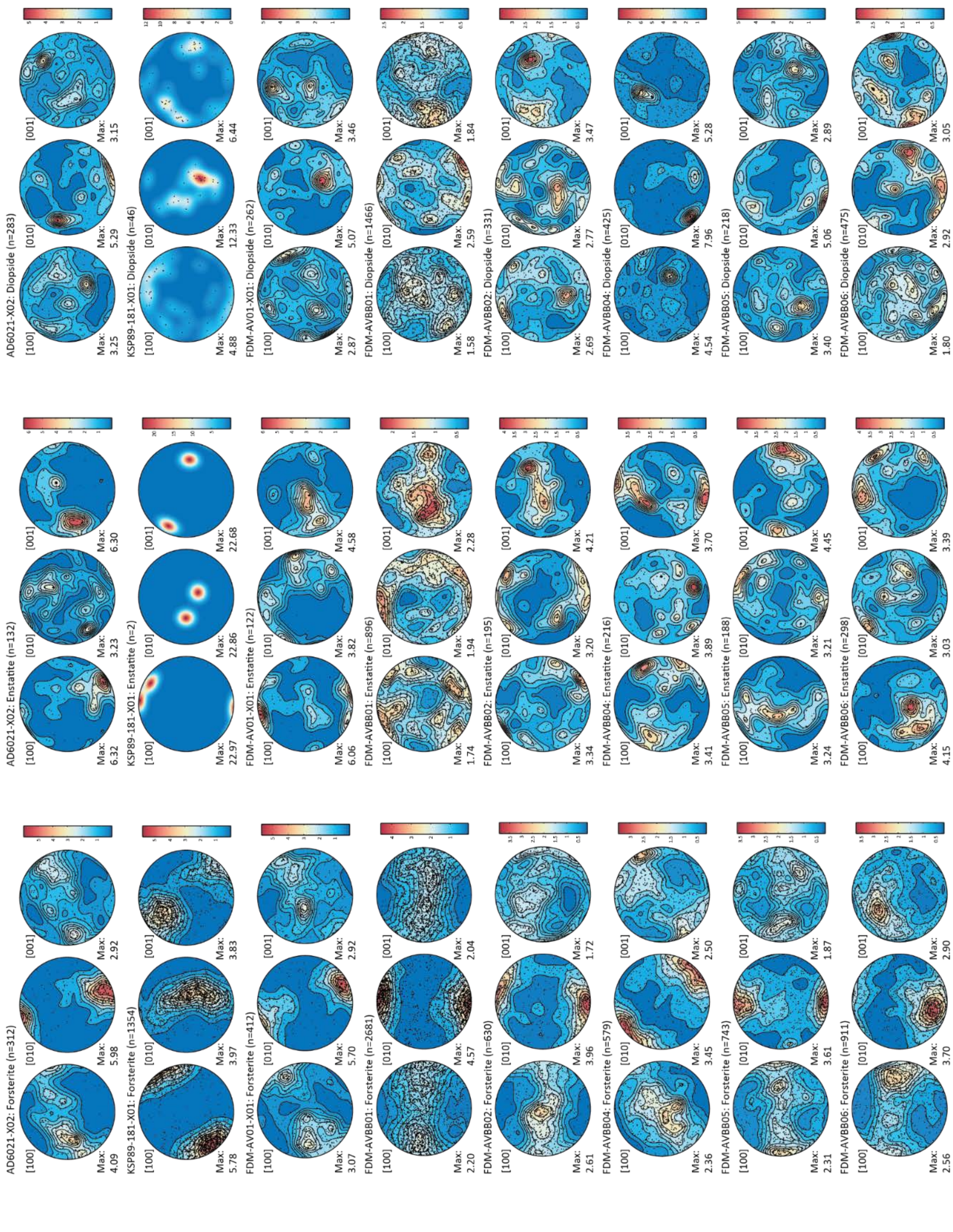
AD6021-X02: Diopside (n=283)
KSP89-181-X01: Diopside (n=46)
FDM-AV01-X01: Diopside (n=262)
FDM-AVBB01: Diopside (n=1466)
FDM-AVBB02: Diopside (n=331)
FDM-AVBB04: Diopside (n=425)
FDM-AVBB05: Diopside (n=218)
FDM-AVBB06: Diopside (n=475)
AD6021-X02: Enstatite (n=132)
KSP89-181-X01: Enstatite (n=2)
FDM-AV01-X01: Enstatite (n=122)
FDM-AVBB01: Enstatite (n=896)
FDM-AVBB02: Enstatite (n=195)
FDM-AVBB04: Enstatite (n=216)
FDM-AVBB05: Enstatite (n=188)
FDM-AVBB06: Enstatite (n=298)
AD6021-X02: Forsterite (n=312)
KSP89-181-X01: Forsterite (n=1354)
FDM-AV01-X01: Forsterite (n=412)
FDM-AVBB01: Forsterite (n=2681)
FDM-AVBB02: Forsterite (n=630)
FDM-AVBB04: Forsterite (n=579)
FDM-AVBB05: Forsterite (n=743)
FDM-AVBB06: Forsterite (n=911)

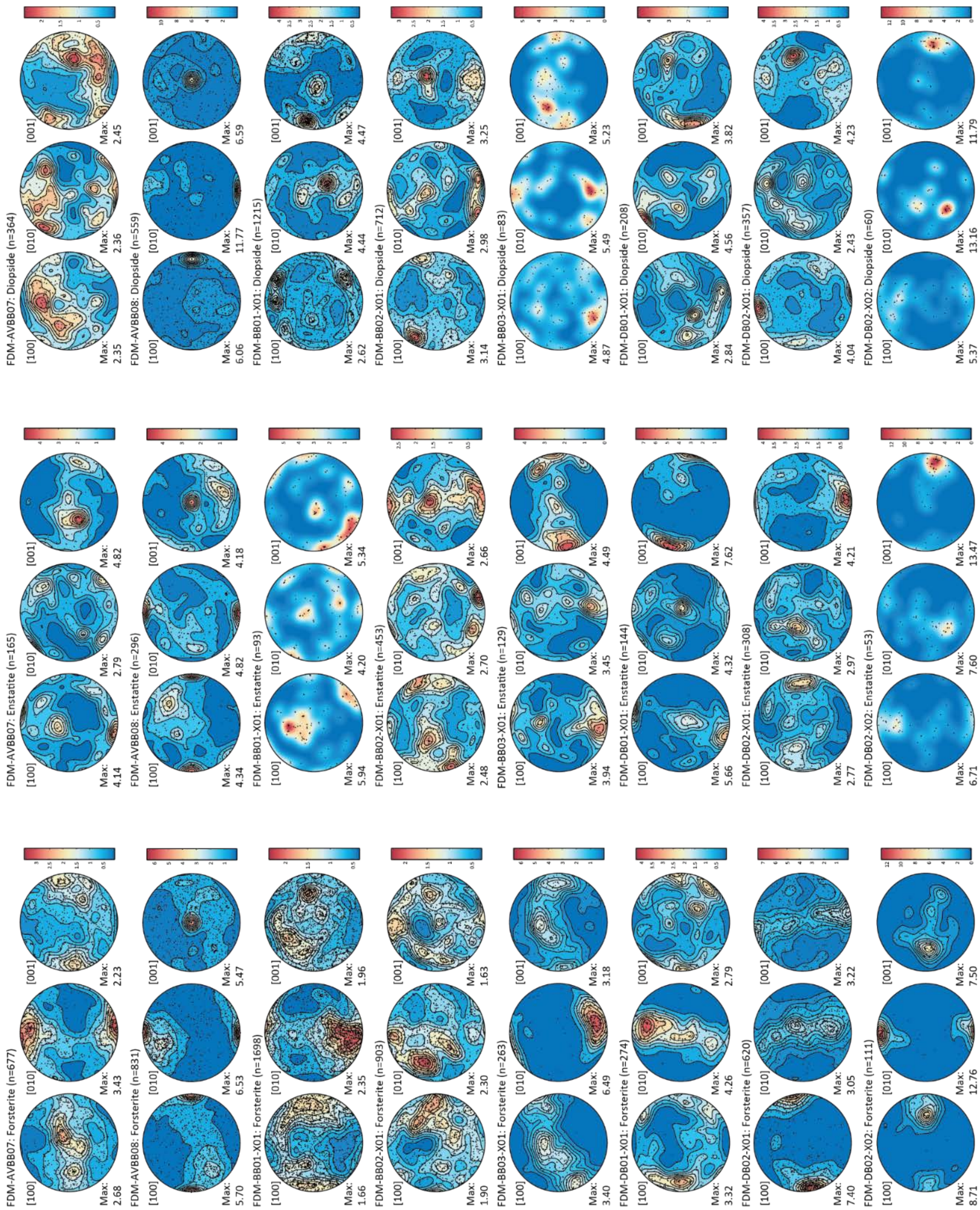
FDM-AVBB07: Diopside (n=364)
[100] Max: 2.35
[010] Max: 2.36
[001] Max: 2.45
FDM-AVBB08: Diopside (n=559)
[100] Max: 6.06
[010] Max: 11.77
[001] Max: 6.59
FDM-BB01-X01: Diopside (n=1215)
[100] Max: 2.62
[010] Max: 4.44
[001] Max: 4.47
FDM-BB02-X01: Diopside (n=712)
[100] Max: 3.14
[010] Max: 2.98
[001] Max: 3.25
FDM-BB03-X01: Diopside (n=83)
[100] Max: 4.87
[010] Max: 5.49
[001] Max: 5.23
FDM-DB01-X01: Diopside (n=208)
[100] Max: 2.84
[010] Max: 4.56
[001] Max: 3.82
FDM-DB02-X01: Diopside (n=357)
[100] Max: 4.04
[010] Max: 2.43
[001] Max: 4.23
FDM-DB02-X02: Diopside (n=60)
[100] Max: 5.37
[010] Max: 13.16
[001] Max: 11.79
FDM-AVBB07: Enstatite (n=165)
[100] Max: 4.14
[010] Max: 2.79
[001] Max: 4.82
FDM-AVBB08: Enstatite (n=296)
[100] Max: 4.34
[010] Max: 4.82
[001] Max: 4.18
FDM-BB01-X01: Enstatite (n=93)
[100] Max: 5.94
[010] Max: 4.20
[001] Max: 5.34
FDM-BB02-X01: Enstatite (n=453)
[100] Max: 2.48
[010] Max: 2.70
[001] Max: 2.66
FDM-BB03-X01: Enstatite (n=129)
[100] Max: 3.94
[010] Max: 3.45
[001] Max: 4.49
FDM-DB01-X01: Enstatite (n=144)
[100] Max: 5.66
[010] Max: 4.32
[001] Max: 7.62
FDM-DB02-X01: Enstatite (n=308)
[100] Max: 2.77
[010] Max: 2.97
[001] Max: 4.21
FDM-DB02-X02: Enstatite (n=53)
[100] Max: 6.71
[010] Max: 7.60
[001] Max: 13.47
FDM-AVBB07: Forsterite (n=677)
[100] Max: 2.68
[010] Max: 3.43
[001] Max: 2.23
FDM-AVBB08: Forsterite (n=831)
[100] Max: 5.70
[010] Max: 6.53
[001] Max: 5.47
FDM-BB01-X01: Forsterite (n=1698)
[100] Max: 1.66
[010] Max: 2.35
[001] Max: 1.96
FDM-BB02-X01: Forsterite (n=903)
[100] Max: 1.90
[010] Max: 2.30
[001] Max: 1.63
FDM-BB03-X01: Forsterite (n=263)
[100] Max: 3.40
[010] Max: 6.49
[001] Max: 3.18
FDM-DB01-X01: Forsterite (n=274)
[100] Max: 3.32
[010] Max: 4.26
[001] Max: 2.79
FDM-DB02-X01: Forsterite (n=620)
[100] Max: 7.40
[010] Max: 3.05
[001] Max: 3.22
FDM-DB02-X02: Forsterite (n=111)
[100] Max: 8.71
[010] Max: 12.76
[001] Max: 7.50

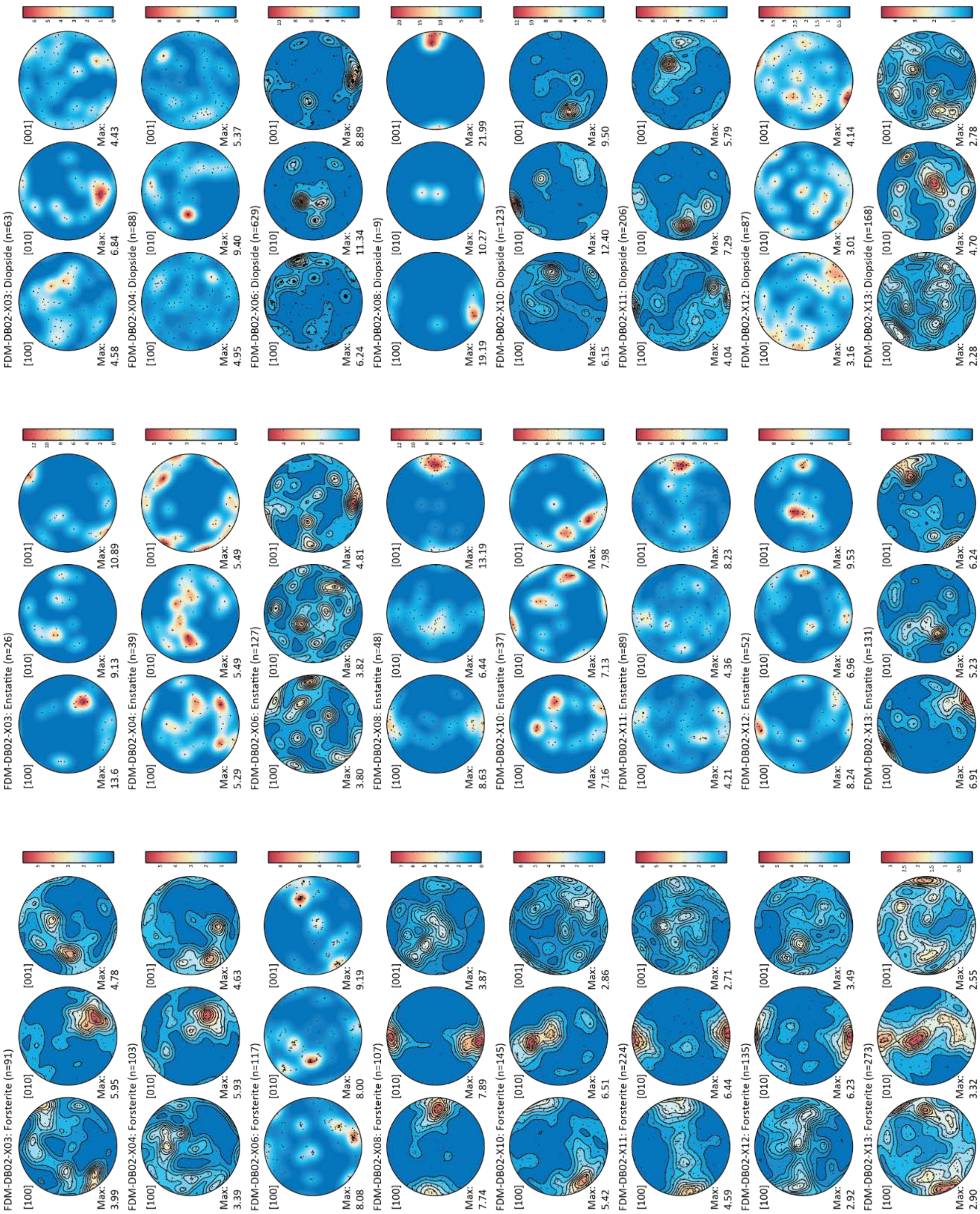
FDM-DB02-X03: Diopside (n=63)
[100] Max: 4.58 [010] Max: 6.84 [001] Max: 4.43
FDM-DB02-X04: Diopside (n=88)
[100] Max: 4.95 [010] Max: 9.40 [001] Max: 5.37
FDM-DB02-X06: Diopside (n=629)
[100] Max: 6.24 [010] Max: 11.34 [001] Max: 8.89
FDM-DB02-X08: Diopside (n=9)
[100] Max: 19.19 [010] Max: 10.27 [001] Max: 21.99
FDM-DB02-X10: Diopside (n=123)
[100] Max: 6.15 [010] Max: 12.40 [001] Max: 9.50
FDM-DB02-X11: Diopside (n=206)
[100] Max: 4.04 [010] Max: 7.29 [001] Max: 5.79
FDM-DB02-X12: Diopside (n=87)
[100] Max: 3.16 [010] Max: 3.01 [001] Max: 4.14
FDM-DB02-X13: Diopside (n=168)
[100] Max: 2.28 [010] Max: 4.70 [001] Max: 2.78
FDM-DB02-X03: Enstatite (n=26)
[100] Max: 13.6 [010] Max: 9.13 [001] Max: 10.89
FDM-DB02-X04: Enstatite (n=39)
[100] Max: 5.29 [010] Max: 5.49 [001] Max: 5.49
FDM-DB02-X06: Enstatite (n=127)
[100] Max: 3.80 [010] Max: 3.82 [001] Max: 4.81
FDM-DB02-X08: Enstatite (n=48)
[100] Max: 8.63 [010] Max: 6.44 [001] Max: 13.19
FDM-DB02-X10: Enstatite (n=37)
[100] Max: 7.16 [010] Max: 7.13 [001] Max: 7.98
FDM-DB02-X11: Enstatite (n=89)
[100] Max: 4.21 [010] Max: 4.36 [001] Max: 8.23
FDM-DB02-X12: Enstatite (n=52)
[100] Max: 8.24 [010] Max: 6.96 [001] Max: 9.53
FDM-DB02-X13: Enstatite (n=131)
[100] Max: 6.91 [010] Max: 5.23 [001] Max: 6.24
FDM-DB02-X03: Forsterite (n=91)
[100] Max: 3.99 [010] Max: 5.95 [001] Max: 4.78
FDM-DB02-X04: Forsterite (n=103)
[100] Max: 3.39 [010] Max: 5.93 [001] Max: 4.63
FDM-DB02-X06: Forsterite (n=117)
[100] Max: 8.08 [010] Max: 8.00 [001] Max: 9.19
FDM-DB02-X08: Forsterite (n=107)
[100] Max: 7.74 [010] Max: 7.89 [001] Max: 3.87
FDM-DB02-X10: Forsterite (n=145)
[100] Max: 5.42 [010] Max: 6.51 [001] Max: 2.86
FDM-DB02-X11: Forsterite (n=224)
[100] Max: 4.59 [010] Max: 6.44 [001] Max: 2.71
FDM-DB02-X12: Forsterite (n=135)
[100] Max: 2.92 [010] Max: 6.23 [001] Max: 3.49
FDM-DB02-X13: Forsterite (n=273)
[100] Max: 2.90 [010] Max: 3.32 [001] Max: 2.55

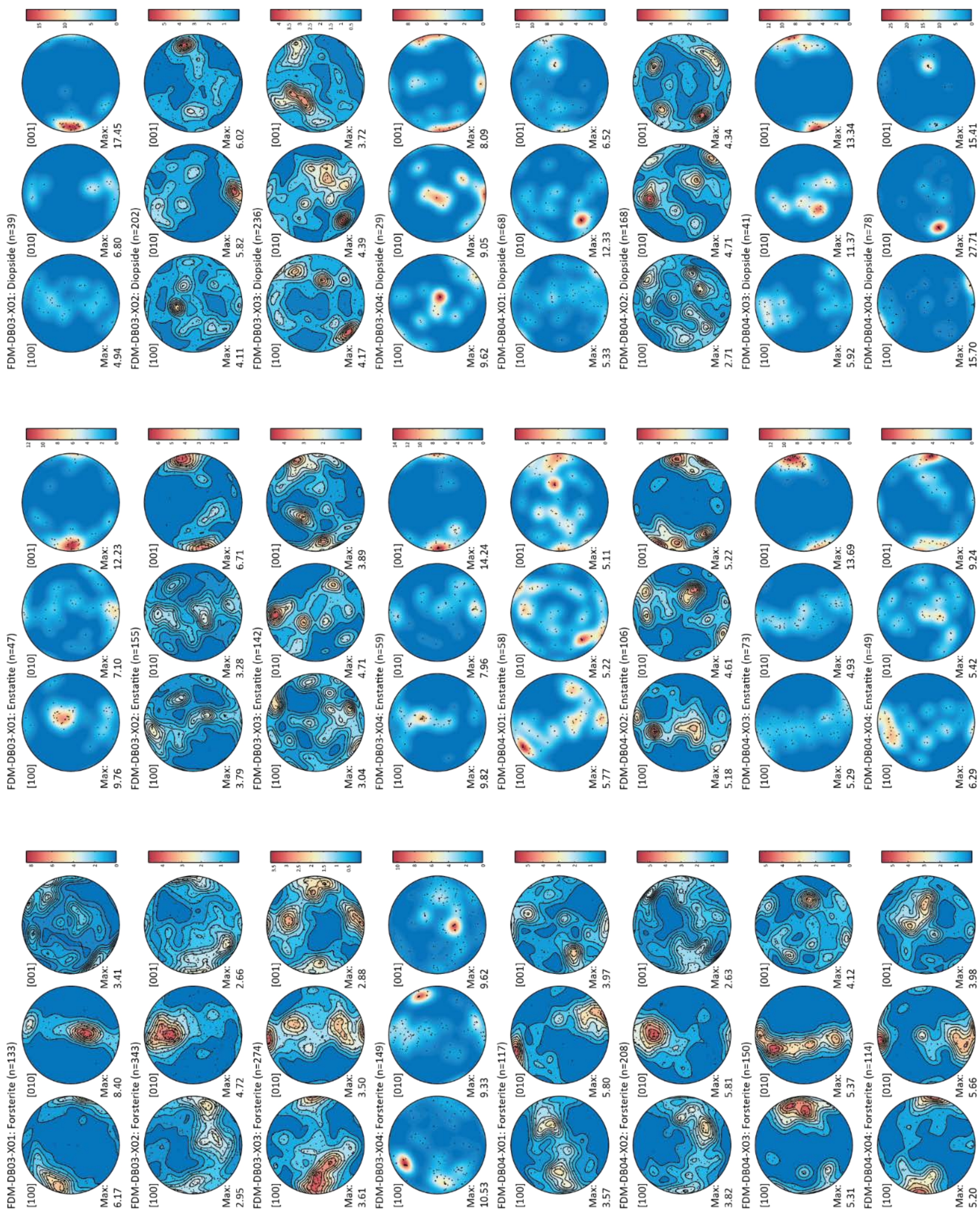

FDM-DB03-X01: Diopside (n=39)
[100] Max: 4.94 [010] Max: 6.80 [001] Max: 17.45
FDM-DB03-X02: Diopside (n=202)
[100] Max: 4.11 [010] Max: 5.82 [001] Max: 6.02
FDM-DB03-X03: Diopside (n=236)
[100] Max: 4.17 [010] Max: 4.39 [001] Max: 3.72
FDM-DB03-X04: Diopside (n=29)
[100] Max: 9.62 [010] Max: 9.05 [001] Max: 8.09
FDM-DB04-X01: Diopside (n=68)
[100] Max: 5.33 [010] Max: 12.33 [001] Max: 6.52
FDM-DB04-X02: Diopside (n=168)
[100] Max: 2.71 [010] Max: 4.71 [001] Max: 4.34
FDM-DB04-X03: Diopside (n=41)
[100] Max: 5.92 [010] Max: 11.37 [001] Max: 13.34
FDM-DB04-X04: Diopside (n=78)
[100] Max: 15.70 [010] Max: 27.71 [001] Max: 15.41
FDM-DB03-X01: Enstatite (n=47)
[100] Max: 9.76 [010] Max: 7.10 [001] Max: 12.23
FDM-DB03-X02: Enstatite (n=155)
[100] Max: 3.79 [010] Max: 3.28 [001] Max: 6.71
FDM-DB03-X03: Enstatite (n=142)
[100] Max: 3.04 [010] Max: 4.71 [001] Max: 3.89
FDM-DB03-X04: Enstatite (n=59)
[100] Max: 9.82 [010] Max: 7.96 [001] Max: 14.24
FDM-DB04-X01: Enstatite (n=58)
[100] Max: 5.77 [010] Max: 5.22 [001] Max: 5.11
FDM-DB04-X02: Enstatite (n=106)
[100] Max: 5.18 [010] Max: 4.61 [001] Max: 5.22
FDM-DB04-X03: Enstatite (n=73)
[100] Max: 5.29 [010] Max: 4.93 [001] Max: 13.69
FDM-DB04-X04: Enstatite (n=49)
[100] Max: 6.29 [010] Max: 5.42 [001] Max: 9.24
FDM-DB03-X01: Forsterite (n=133)
[100] Max: 6.17 [010] Max: 8.40 [001] Max: 3.41
FDM-DB03-X02: Forsterite (n=343)
[100] Max: 2.95 [010] Max: 4.72 [001] Max: 2.66
FDM-DB03-X03: Forsterite (n=274)
[100] Max: 3.61 [010] Max: 3.50 [001] Max: 2.88
FDM-DB03-X04: Forsterite (n=149)
[100] Max: 10.53 [010] Max: 9.33 [001] Max: 9.62
FDM-DB04-X01: Forsterite (n=117)
[100] Max: 3.57 [010] Max: 5.80 [001] Max: 3.97
FDM-DB04-X02: Forsterite (n=208)
[100] Max: 3.82 [010] Max: 5.81 [001] Max: 2.63
FDM-DB04-X03: Forsterite (n=150)
[100] Max: 5.31 [010] Max: 5.37 [001] Max: 4.12
FDM-DB04-X04: Forsterite (n=114)
[100] Max: 5.20 [010] Max: 5.66 [001] Max: 3.98

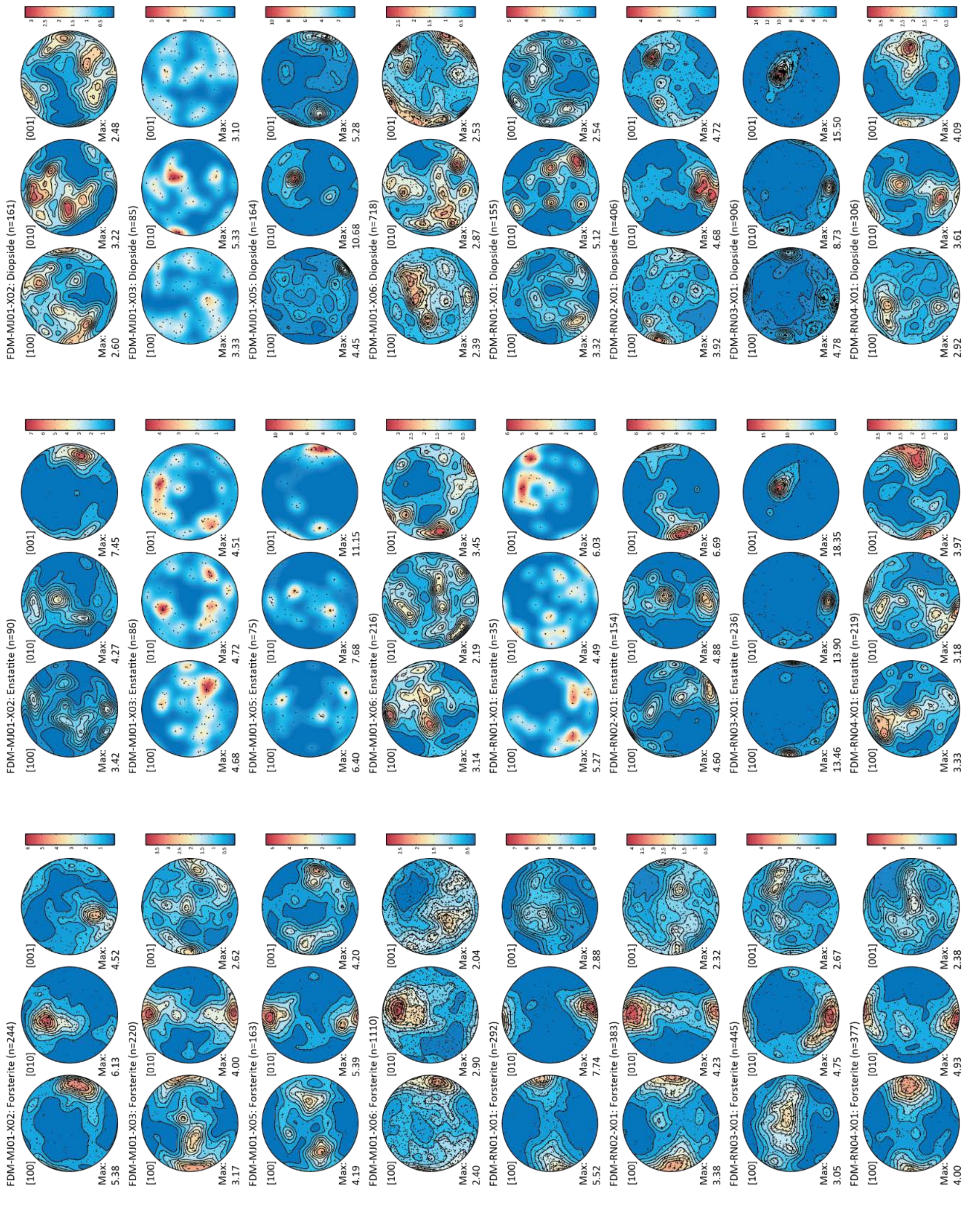
FDM-MJ01-X02: Diopside (n=161)
[100] Max: 2.60 [010] Max: 3.22 [001] Max: 2.48
FDM-MJ01-X03: Diopside (n=85)
[100] Max: 3.33 [010] Max: 5.33 [001] Max: 3.10
FDM-MJ01-X05: Diopside (n=164)
[100] Max: 4.45 [010] Max: 10.68 [001] Max: 5.28
FDM-MJ01-X06: Diopside (n=718)
[100] Max: 2.39 [010] Max: 2.87 [001] Max: 2.53
FDM-RN01-X01: Diopside (n=155)
[100] Max: 3.32 [010] Max: 5.12 [001] Max: 2.54
FDM-RN02-X01: Diopside (n=406)
[100] Max: 3.92 [010] Max: 4.68 [001] Max: 4.72
FDM-RN03-X01: Diopside (n=906)
[100] Max: 4.78 [010] Max: 8.73 [001] Max: 15.50
FDM-RN04-X01: Diopside (n=306)
[100] Max: 2.92 [010] Max: 3.61 [001] Max: 4.09
FDM-MJ01-X02: Enstatite (n=90)
[100] Max: 3.42 [010] Max: 4.27 [001] Max: 7.45
FDM-MJ01-X03: Enstatite (n=86)
[100] Max: 4.68 [010] Max: 4.72 [001] Max: 4.51
FDM-MJ01-X05: Enstatite (n=75)
[100] Max: 6.40 [010] Max: 7.68 [001] Max: 11.15
FDM-MJ01-X06: Enstatite (n=216)
[100] Max: 3.14 [010] Max: 2.19 [001] Max: 3.45
FDM-RN01-X01: Enstatite (n=35)
[100] Max: 5.27 [010] Max: 4.49 [001] Max: 6.03
FDM-RN02-X01: Enstatite (n=154)
[100] Max: 4.60 [010] Max: 4.88 [001] Max: 6.69
FDM-RN03-X01: Enstatite (n=236)
[100] Max: 13.46 [010] Max: 13.90 [001] Max: 18.35
FDM-RN04-X01: Enstatite (n=219)
[100] Max: 3.33 [010] Max: 3.18 [001] Max: 3.97
FDM-MJ01-X02: Forsterite (n=244)
[100] Max: 5.38 [010] Max: 6.13 [001] Max: 4.52
FDM-MJ01-X03: Forsterite (n=220)
[100] Max: 3.17 [010] Max: 4.00 [001] Max: 2.62
FDM-MJ01-X05: Forsterite (n=163)
[100] Max: 4.19 [010] Max: 5.39 [001] Max: 4.20
FDM-MJ01-X06: Forsterite (n=1110)
[100] Max: 2.40 [010] Max: 2.90 [001] Max: 2.04
FDM-RN01-X01: Forsterite (n=292)
[100] Max: 5.52 [010] Max: 7.74 [001] Max: 2.88
FDM-RN02-X01: Forsterite (n=383)
[100] Max: 3.38 [010] Max: 4.23 [001] Max: 2.32
FDM-RN03-X01: Forsterite (n=445)
[100] Max: 3.05 [010] Max: 4.75 [001] Max: 2.67
FDM-RN04-X01: Forsterite (n=377)
[100] Max: 4.00 [010] Max: 4.93 [001] Max: 2.38

APPENDIX F

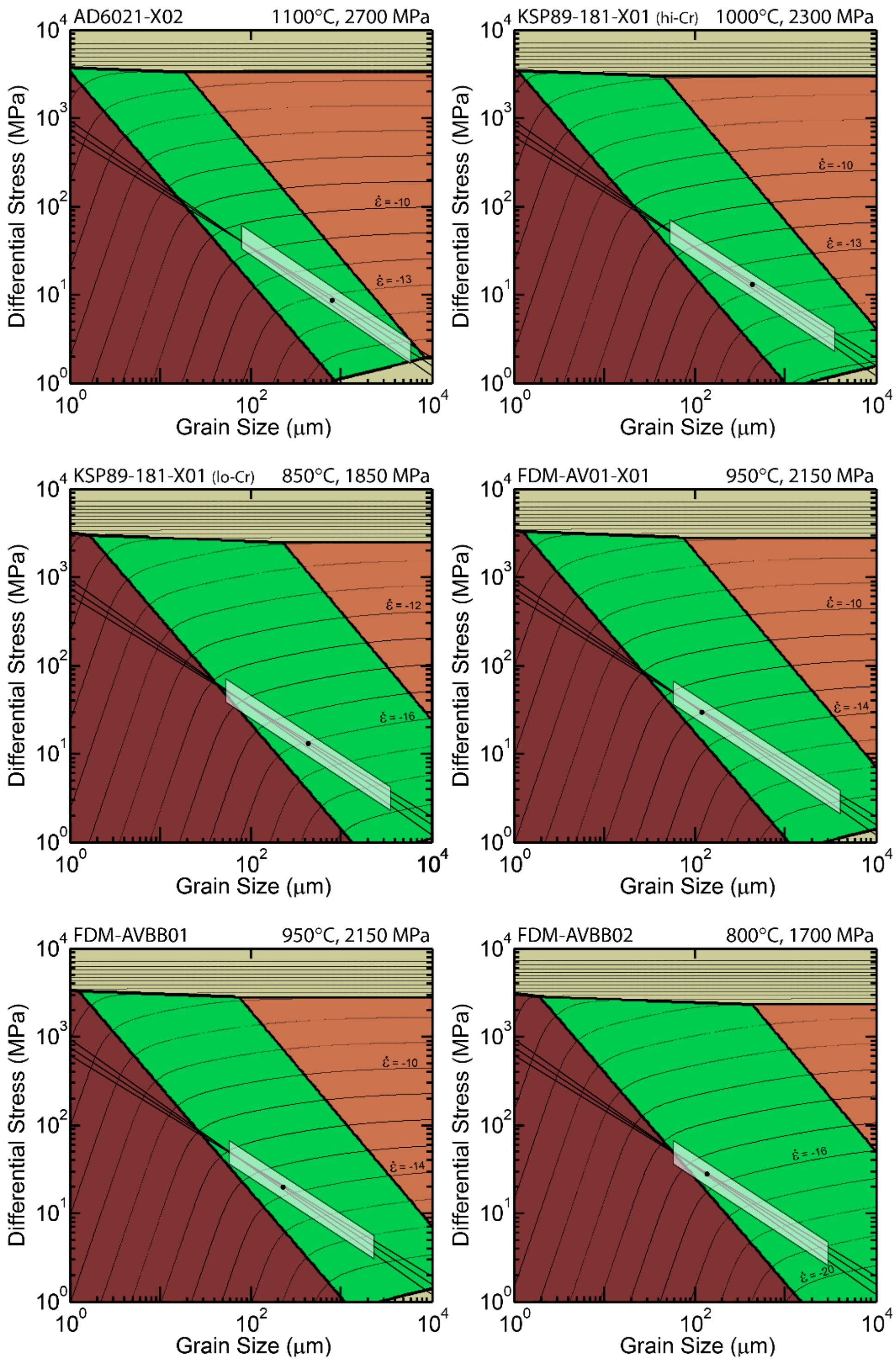

AD6021-X02
1100°C, 2700 MPa
KSP89-181-X01 (hi-Cr)
1000°C, 2300 MPa
KSP89-181-X01 (lo-Cr)
850°C, 1850 MPa
FDM-AV01-X01
950°C, 2150 MPa
FDM-AVBB01
950°C, 2150 MPa
FDM-AVBB02
800°C, 1700 MPa
Differential Stress (MPa)
Grain Size (μm)

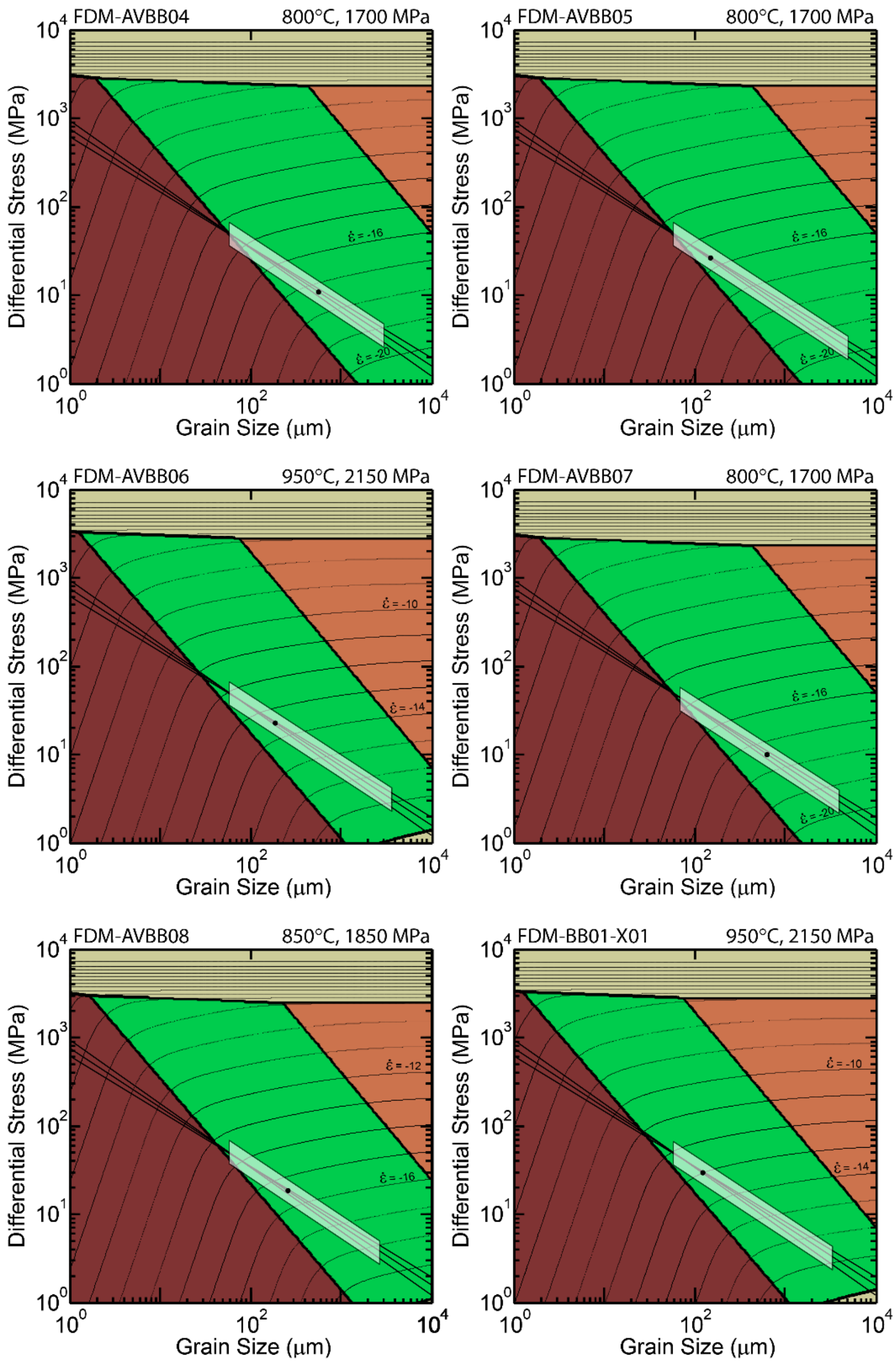

FDM-AVBB04
800°C, 1700 MPa
FDM-AVBB05
800°C, 1700 MPa
FDM-AVBB06
950°C, 2150 MPa
FDM-AVBB07
800°C, 1700 MPa
FDM-AVBB08
850°C, 1850 MPa
FDM-BB01-X01
950°C, 2150 MPa
Differential Stress (MPa)
Grain Size (μm)
$\dot{\varepsilon}$ = -16
$\dot{\varepsilon}$ = -20
$\dot{\varepsilon}$ = -10
$\dot{\varepsilon}$ = -14
$\dot{\varepsilon}$ = -12

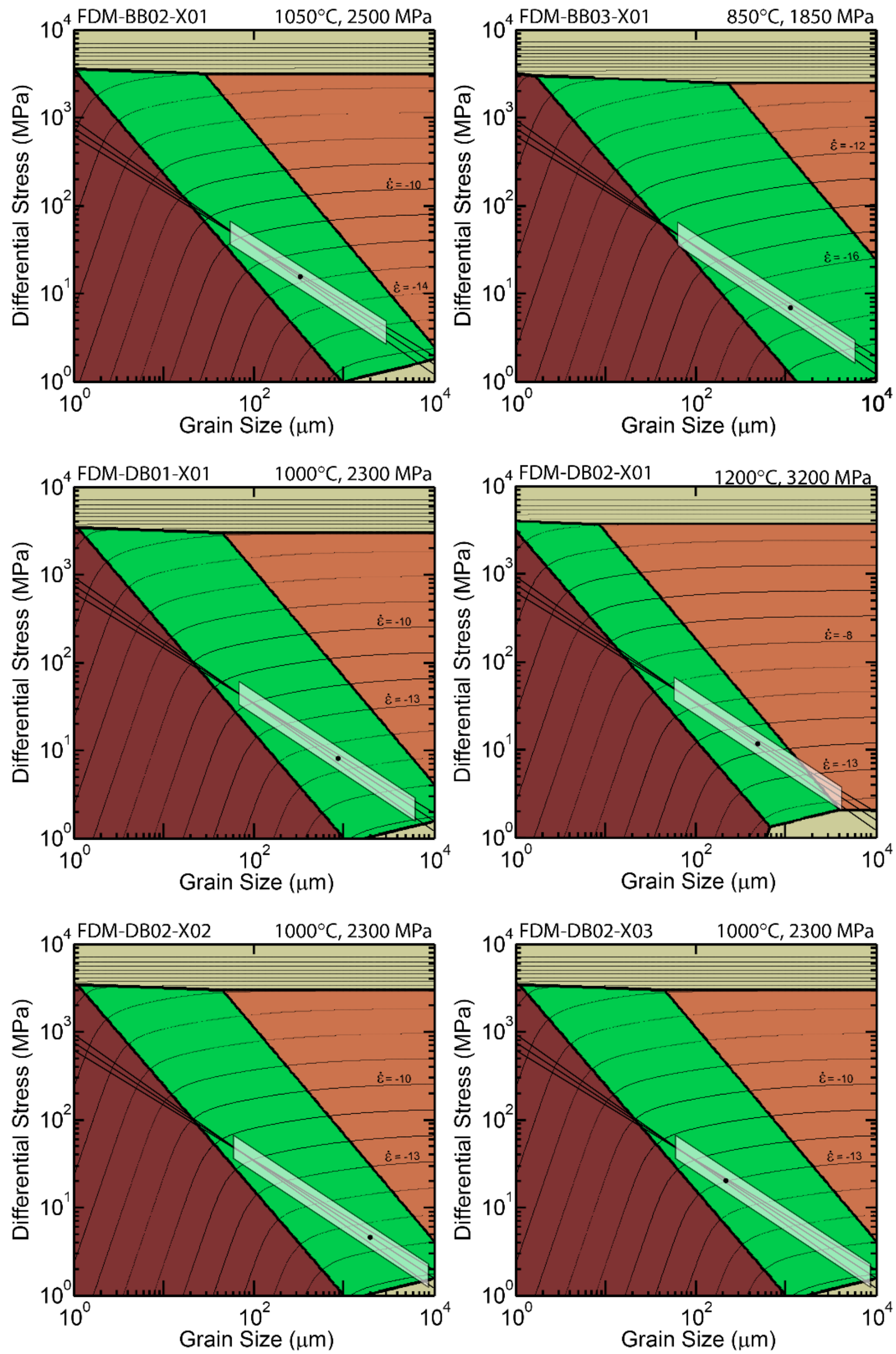
FDM-BB02-X01
1050°C, 2500 MPa
ε̇ = -10
ε̇ = -14
FDM-BB03-X01
850°C, 1850 MPa
ε̇ = -12
ε̇ = -16
FDM-DB01-X01
1000°C, 2300 MPa
ε̇ = -10
ε̇ = -13
FDM-DB02-X01
1200°C, 3200 MPa
ε̇ = -8
ε̇ = -13
FDM-DB02-X02
1000°C, 2300 MPa
ε̇ = -10
ε̇ = -13
FDM-DB02-X03
1000°C, 2300 MPa
ε̇ = -10
ε̇ = -13
Differential Stress (MPa)
Grain Size (μm)

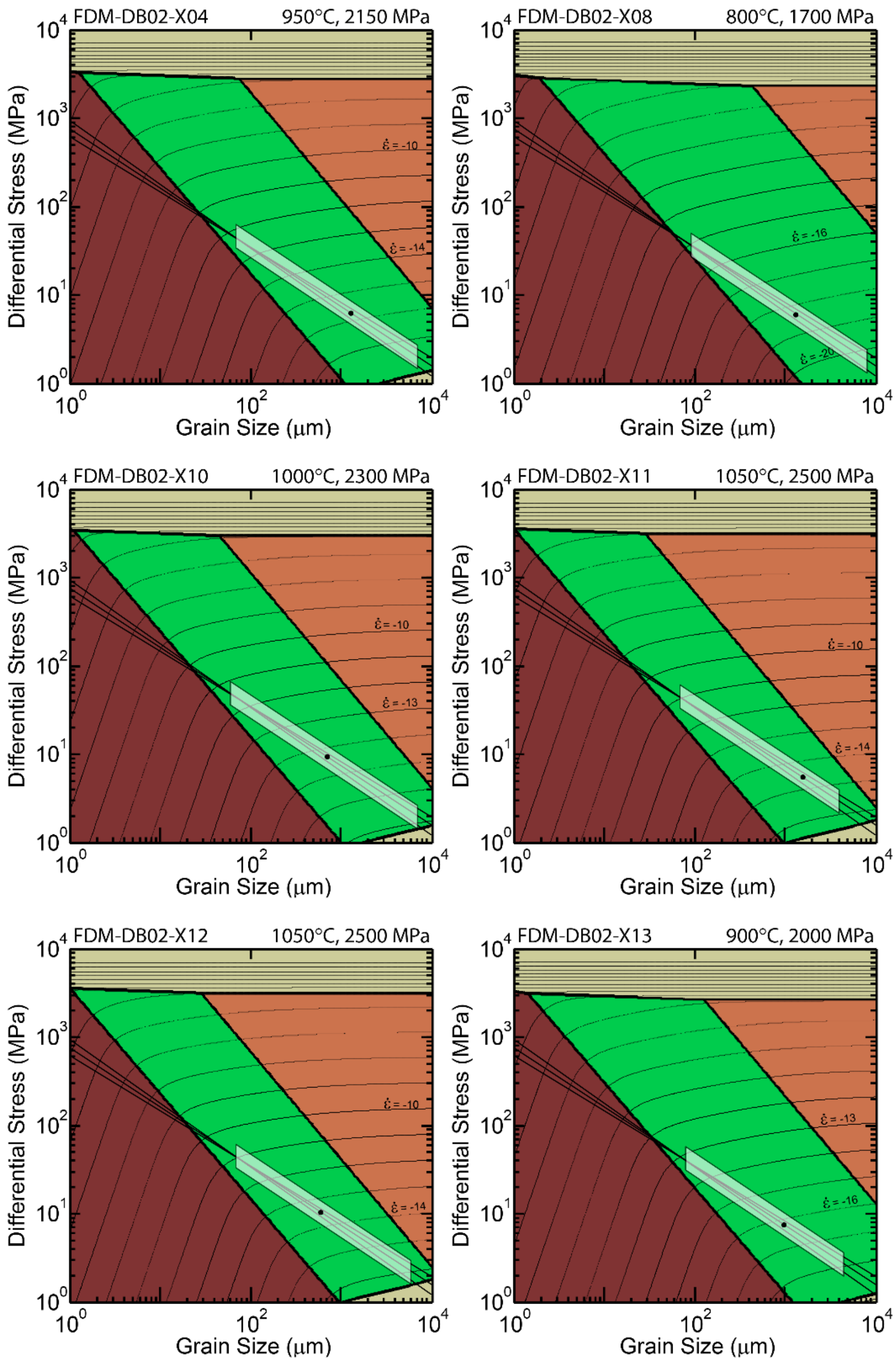

FDM-DB02-X04
950°C, 2150 MPa
FDM-DB02-X08
800°C, 1700 MPa
FDM-DB02-X10
1000°C, 2300 MPa
FDM-DB02-X11
1050°C, 2500 MPa
FDM-DB02-X12
1050°C, 2500 MPa
FDM-DB02-X13
900°C, 2000 MPa
Differential Stress (MPa)
Grain Size (μm)

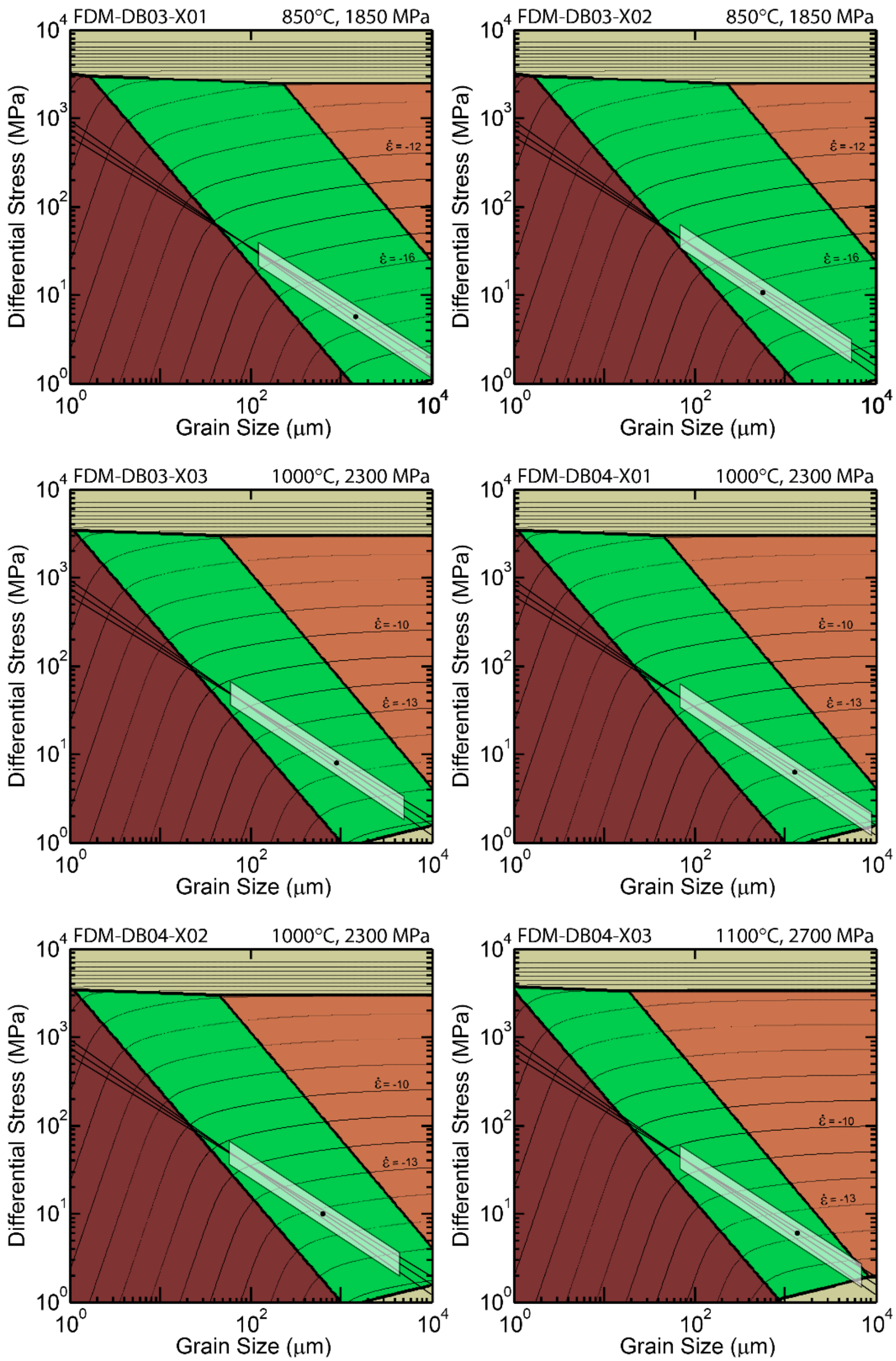
FDM-DB03-X01
850°C, 1850 MPa
FDM-DB03-X02
850°C, 1850 MPa
FDM-DB03-X03
1000°C, 2300 MPa
FDM-DB04-X01
1000°C, 2300 MPa
FDM-DB04-X02
1000°C, 2300 MPa
FDM-DB04-X03
1100°C, 2700 MPa
Differential Stress (MPa)
Grain Size (μm)
ε̇ = -12
ε̇ = -16
ε̇ = -10
ε̇ = -13

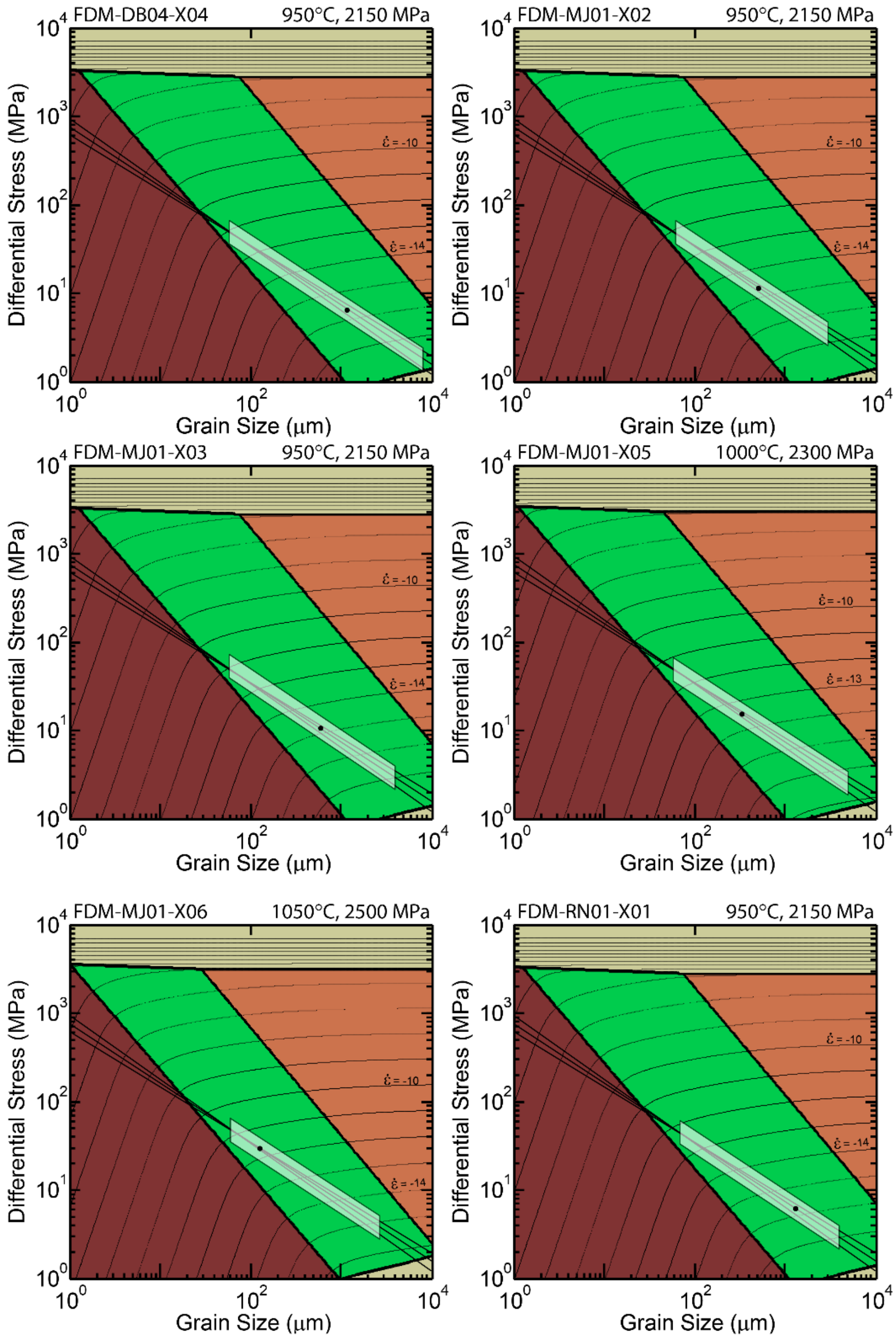
FDM-DB04-X04
950°C, 2150 MPa
FDM-MJ01-X02
950°C, 2150 MPa
FDM-MJ01-X03
950°C, 2150 MPa
FDM-MJ01-X05
1000°C, 2300 MPa
FDM-MJ01-X06
1050°C, 2500 MPa
FDM-RN01-X01
950°C, 2150 MPa
Differential Stress (MPa)
Grain Size (μm)
10^0
10^1
10^2
10^3
10^4
$\dot{\varepsilon}$ = -10
$\dot{\varepsilon}$ = -13
$\dot{\varepsilon}$ = -14

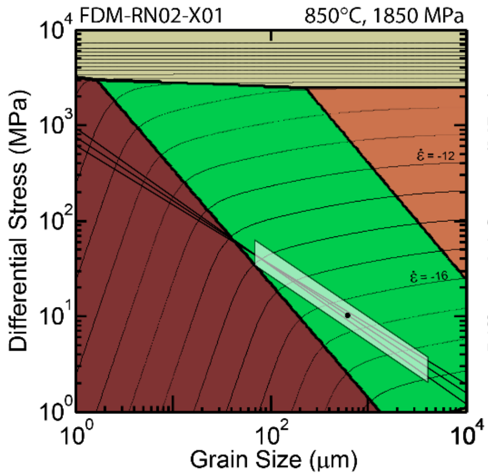
FDM-RN02-X01
850°C, 1850 MPa
Differential Stress (MPa)
Grain Size (μm)
10^0
10^1
10^2
10^3
10^4
$\dot{\varepsilon}$ = -12
$\dot{\varepsilon}$ = -16

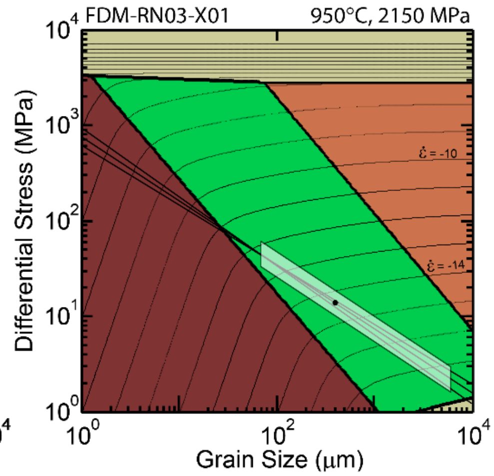
FDM-RN03-X01
950°C, 2150 MPa
Differential Stress (MPa)
Grain Size (μm)
10^0
10^1
10^2
10^3
10^4
$\dot{\varepsilon}$ = -10
$\dot{\varepsilon}$ = -14

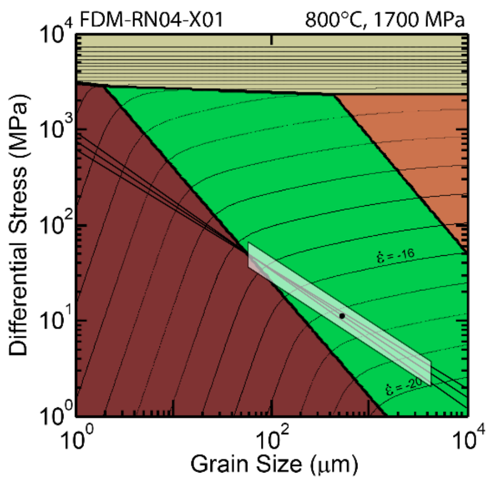
FDM-RN04-X01
800°C, 1700 MPa
Differential Stress (MPa)
Grain Size (μm)
10^0
10^1
10^2
10^3
10^4
$\dot{\varepsilon}$ = -16
$\dot{\varepsilon}$ = -20